STRUCTURE AND FUNCTIONS OF THE ADHESION COMPLEX AND P116 PROTEIN OF Mycoplasma pneumoniae AND Mycoplasma genitalium

Marina Marcos Silva

UAB
Universitat Autònoma de Barcelona

STRUCTURE AND FUNCTIONS OF THE ADHESION COMPLEX AND P116 PROTEIN OF *Mycoplasma pneumoniae AND Mycoplasma genitalium*

Marina Marcos Silva

STRUCTURE AND FUNCTIONS OF THE ADHESION COMPLEX AND P116 PROTEIN OF *Mycoplasma pneumoniae AND Mycoplasma genitalium*

Marina Marcos Silva

2024

Doctoral thesis submitted to obtain the Doctoral of Philosophy Degree in Biochemistry, Molecular Biology and Biomedicine

This work was developed at the Institut de Biotecnologia i Biomedicina (IBB) and at the Biochemistry and Molecular Biology Department of the Universitat Autònoma de Barcelona (UAB), group of Molecular Biology, under the supervision of Dr. Jaume Piñol Ribas and Dr. Òscar Quijada Pich

Dr. Jaume Piñol Ribas Dr. Òscar Quijada Pich

08193-Cerdanyola del Vallès ibb@uab.es http://ibb.uab.es Phone +34 935868952 marina.marcos@uab.cat

“The Only way to learn is to live”

The midnight library

Matt Haig

A mi madre Choni

Al meu pare Mario

A mis yayos

A mi tete Óscar

I a tots els que han fet possible aquesta experiència...

TABLE OF CONTENTS

ACKNOWLEDGEMENTS

(AGRAÏMENTS/AGRADECIMIENTOS)

Parece que, llegado este punto, con este escrito de agradecimiento, toca poner fin a una etapa. Me encuentro sentada, papel y bolígrafo en mano, con la intención de empezar a escribir el borrador de estas palabras y de repente, emocionada, creo que lo acabo de ver claro. Siento que soy muy afortunada. El "Doctorado" no solo ha sido una etapa más de estudios y formación. Durante todo este tiempo he tenido la suerte de vivir una experiencia completa. La sensación más intensa que uno pueda encontrar en un parque de atracciones. Una aventura que no hubiera sido posible sin las personas que han estado a mi lado y me han acompañado.

A lo largo de todo este tiempo, todas y cada una de estas personas, ya sea durante más o menos tiempo, me han aportado algo, permitiéndome avanzar, aprender y crecer. No estoy segura de que solo con estas palabras sea suficiente para llegar a expresar el agradecimiento que siento, pero espero podéroslo transmitir, aunque solo sea a pequeñas dosis, como las que dispensa esta micropipeta.

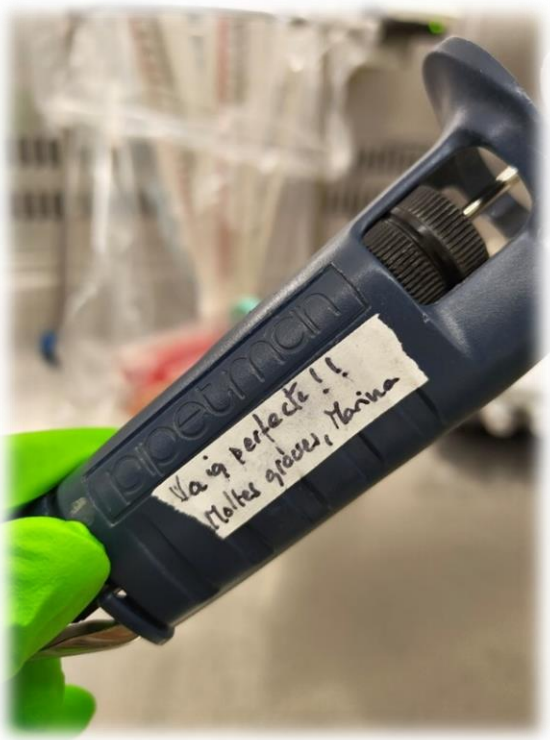

Me gustaría empezar por las personas que de alguna forma me introdujeron en la cola para esta montaña rusa. Sin ellas, literalmente, ni me lo hubiera planteado. Cronológicamente, tal y como más o menos sucedió. Òscar, et vaig conèixer com a professor quan em vas donar una assignatura de pràctiques a segon de grau. GRÀCIES per proposar-me de fer les "practiques externes de laboratori" a Bio Mol. Aquell gest em va donar un vot de confiança en mi mateixa que va despertar el meu esperit científic i em va impulsar/motivar a seguir i acabar el grau. Des de llavors que he seguit els meus estudis sempre vinculats aquí al laboratori. Sergi, vas ser tu qui des del principi em vas ensenyar tot i més. La teva amabilitat no té límits i GRÀCIES a tu i amb tu, no només vaig trobar un referència o un exemple a seguir, sinó també una amistat. Sempre que necessiti qualsevol cosa, relacionada amb la ciència o no, sé que puc comptar amb tu, com sempre m'has demostrat. Lucía, inicialmente compañera de grado. Enseguida empezaste también las prácticas en el lab y entonces empezó nuestra amistad. A veces incluso nos fusionábamos, yo era tú, y tú eras yo, pero eso que quede entre nosotras. Estoy agradecida por haber compartido contigo ese tiempo aprendiendo y trabajando

pipeta con pipeta en la poyata y fuera de ella. GRACIAS por contar conmigo para todo tipo de planes, aprendiendo calle. Tuviste la oportunidad e iniciaste el Doctorado en otro laboratorio, y aunque un pequeño distanciamiento era inevitable, hemos seguido estando muy cerquita. Sigo teniendo la esperanza de que el IBB nos ponga esa "barra" que comunique nuestros laboratorios directamente. Espero que sigamos compartiendo momentos y la multitud de planes que se nos vayan ocurriendo. Carlos, vas ser el darrer a marxar del laboratori, tot just quan jo pràcticament acabava de començar el Doctorat. Et vull donar les GRÀCIES per compartir amb mi tot el teu coneixement i la teva forma de treballar, però sobretot per deixar-me per fi el teu escriptori al despatx, la teva col·lecció d'articles llegits i els teus bolígrafs pilot. També gràcies a tu em vaig iniciar en el món del "SAFing" i "running", que m'ha vingut tan bé en segons quin moment. Jaume, GRÀCIES per recolzar-me i creure en mi des d'un principi. He pogut aprendre moltíssim de tu i treballant amb tu, també a la "poyata". Durant aquest temps has sigut el principal responsable de mantenir les meves ganes de seguir amb la ciència, transmetin-me aquesta sensació de pau i tranquil·litat, com un pare al laboratori.

Seguidamente me gustaría continuar con las personas que después de la larga cola, siguieron a mi lado, subiendo conmigo a esta atracción. Mi familia, sois los primeros a los que me gustaría mencionar. A mis padres, GRACIAS. Me disteis la vida y habéis sido la base para llegar a ser la persona que soy ahora. Papa, enfermaste y me dejaste en la subida justo hacia la caída más espectacular del recorrido. Sabía que no te gustaban las atracciones de emociones fuertes, pero tranquilo, ya he comprendido muchas cosas que finalmente me han hecho sentir con más fuerza para seguir. Te he llegado a sentir conmigo y estoy convencida de que hubieras estado a mi lado, dándome todo tu apoyo. Mama, GRACIAS por ser mi apoyo incondicional y creer en mí incluso cuando yo dudaba. Si tuviera que designar una persona como pilar que sustenta mi vida serías tu sin duda alguna. GRACIAS por la paciencia, constancia, perseverancia y las ganas de constante aprendizaje con las que me has enseñado a vivir. Yaya y Yayo, GRACIAS. Habéis estado conmigo en todo momento, des de que nací. Junto a vosotros di mis primeros pasos, dije mis primeras palabras, rodé mis primeros metros en bicicleta, leí mis primeros libros, y dimos las primeras nociones matemáticas con las sumas y restas. Me habéis hecho apreciar muchos valores de la vida, y aunque ahora ya toca que os cuide yo a vosotros un poco más, sigo aprendiendo día tras día a vuestro lado. Lo único que no he conseguido es que acabéis de entender bien a qué me he dedicado todo este tiempo. Pero lo importante es que habéis estado ahí junto a mí. Tete, biológicamente tan parecidos, pero tan diferentes a la vez. Una de las cosas por las que me siento más afortunada es la relación que tenemos. GRACIAS por poder contar contigo siempre, para lo que sea. No hubiera podido tener mejor hermano mayor que tú. En este apartado también entras tu Xavier, GRACIAS. Quizás eres el que está más acostumbrado a estos escritos de agradecimiento por mi parte. Des de que nos conocimos hemos vivido todo tipo de experiencias que nos han hecho crecer y evolucionar juntos como pareja, como personas, y sobre todo como amigos. Durante todo este tiempo me has dado un apoyo invaluable, has sido mi punto

de anclaje, como los raíles que mantienen el tren en línea. Ahora formamos parte uno del otro y espero poder seguir embarcándome en nuevas aventuras junto a ti. Aprovecho para extender mi agradecimiento también a tu familia. Mari, Javi, Sandra, Fini, Conchi, Juan, Sara, Sebas, Yayo Juan, Trini. El mismo tiempo hace que nos conocemos y me siento agradecida por cómo me acogisteis des del primer día. Nuestra relación también ha evolucionado, como en todos los caminos hay puntos más complicados que te pueden hacer actuar de una forma que realmente no quieres, pero hemos aprendido unos de los otros y eso es de lo que se trata. Sois encantadores y os quiero dar las GRACIAS por vuestro apoyo constante y que en muchas ocasiones me ha servido como fuente de reflexión e inspiración. Y a mis tíos Isa y Susi. Habéis estado ahí, tanto en los momentos buenos y malos, y a veces vuestro apoyo ha sido la chispa que necesitaba, GRACIAS por encenderla. A mis primos, Noelia y Alejandro. GRACIAS por ser como mis hermanos pequeños, aunque ya no tan pequeños. Nos hemos criado prácticamente juntos y no me imagino una vida sin compartir momentos junto a vosotros. Noe, tú sí que eres una buena compi de atracciones, de todo tipo. Alejandro, cree en ti, y persigue lo que te haga más feliz. Yo por mi parte seguiré a vuestro lado, para lo que necesitéis. También a mi tío Juan Carlos, GRACIAS por estar en los momentos críticos. Con tu manera de llevar las situaciones, hace que todo parezca más fácil, siempre con ese particular humor que tanto me recuerda a mi Padre.

Todo este proceso no hubiera sido posible sin la ayuda de otras personas del IBB o que formaron parte en su momento. Jara, GRACIAS por haberme hecho sentir que formaba parte de algo ya des de que nos conocimos. Aunque tú ya estabas embarcada en tu aventura, siempre has tenido tiempo para todo y para todos. Tienes una capacidad increíble para poder llevar muchas cosas y sacarlas adelante. También admiro muchísimo tu forma de ser, siempre tan positiva y preocupándote de todos. De ti también he aprendido a disfrutar de cada momento vivido, porque a veces, un simple café puede ayudarte a reenfocar el camino para mejor. Lo que sin duda sigo dejando solo para ti es tu capacidad para aguantar el picante. Una mención especial también para Arturo, Ana, Miguel, Luis, Helena, Jaime, Eloi, Jossy, Eddi, Pau, Andreas, Alba, David, Marcel, Diego, Sergi, Eric, Marta, Mireya…nombres de personas que me han acompañado a lo largo de este recorrido o una parte y a las que doy gracias de haber conocido. Con vosotros he compartido momentos y experiencias de todo tipo, pero todos inolvidables. No soy mucho de fiestas, pero os tengo que reconocer que habéis sido el alma de las Fondues del IBB. Muchas GRACIAS a Laia, Joana, Anabel, Marta, Andrea, Jesús, Maurici y Wan Lu. Alumnos de prácticas en Bio Mol. Con vosotros, me he visto reflejada en muchas ocasiones y aunque hayan sido períodos cortos de tiempo, espero haberos inculcado nociones que os hayan servido de buena base. Con vuestras dedicación y ganas de trabajar, conseguiréis lo que os propongáis. ¡Mucha suerte en vuestros nuevos caminos! Y quiero acordarme especialmente de mis compañeros de lab. Aunque vuestra afiliación sea diferente, poder compartir el laboratorio con vosotros estos últimos años ha sido un auténtico placer y una enorme suerte. Paula, siguiendo una línea de tren paralela, compartimos la misma experiencia. No han hecho falta muchas palabras para

entendernos. GRACIAS por haberme mostrado tu serenidad en momentos un poco agobiantes. Esos madrugones para las clases de piscina fueron claves, y me gustaría seguir comentando esos hobbies que compartimos. Miquel, nunca me olvidaré de nuestro momento Álex Ubago de una de esas tardes de "karaoke". GRACIAS por esa alegría y "gloria vendita" que siempre consigue sacarme una sonrisa. Siempre nos quedará Sevilla. Inma, eres una gran compañera, pero sobre todo maravillosa persona. Me encanta encontrarme notitas tuyas de vez en cuando por mi mesa o por el lab. GRACIAS, sin ti, no sé cómo hubiéramos conseguido organizarnos en la cabina. Siguiendo con la filosofía de compartir laboratorio, no quería olvidarme de mencionar a Inelvis. Me ha encantado conocerte. Nunca dudé que llegarías a conseguirlo, me alegro mucho por ti. GRACIAS también por descubrirme que el plátano no es solo un postre. Tampoco me gustaría olvidarme de mencionar a personas que, aunque no compartimos despacho, son muy importantes y forman parte del grupo de Bio Mol. GRACIAS a Enrique, Juan, Ángel y especialmente a tu Pepo, per la teva ajuda durant tot aquest temps.

También quiero acordarme de personas de fuera del laboratorio, pero vinculadas al IBB, que también han sido imprescindibles en mi día a día. Miguel, mil gracias por haber sido mi centro de logística de Amazon particular durante todo este tiempo. También por haber hecho de la gestión de los pedidos del laboratorio una de mis actividades favoritos. GRACIAS a toda la gente de Serveis (Toni, Araís, Fran, Holga, Paquis, Roger, Carles, Anna, Martí, Cris) y con especial cariño a Manuela, por tu gran ayuda y paciencia en mis días de citómetro. GRACIAS también a los técnicos (Paqui, Àngels, Almudena, Francesca, Cristina) por hacernos mucho más fácil el trabajo día tras día. Un abrazo enorme.

Y a continuación cómo no, quiero mencionar a las personas de fuera de la autónoma que también me han acompañado durante todo este tiempo. En primer lugar, y todavía dentro del ámbito académico, quiero expresar mi agradecimiento a David Vizárraga, Ignacio, David Aparicio y Jesús. No sólo habéis demostrado ser grandes colaboradores, también sois unas bellísimas personas que me han apoyado y valorado en todo momento. También muchas GRACIAS a Roberta, Alba, Antonio, Ferran, Tania, Marta, Cristina. Grandes personas que hicieron de mi estancia en Nápoles una gran experiencia. Y Annalisa, desde que nos conocimos llevo una parte de ti conmigo para siempre. Sabes que eres capaz de lo que te propongas, así que sigue luchando, porque te mereces lo mejor ¡Ti voglio tanto bene! En el ámbito más personal, me gustaría mencionar a una familia que para mí también ha sido muy importante. María, Quim, Dolors, Xavi, Julio, Silvia. Em sento molt agraïda de que ens haguem trobat en les nostres vides. Cada vegada que ens veiem sento com si el temps no hagués passat. Aquesta sensació, de tant en tant és molt reconfortant, especialment si és en la nostra llar de foc que tants hiverns ens ha escalfat.

En un cierto punto de esta aventura, después de iniciarme en el "SAFing" decidí asistir a alguna clase dirigida. Y allí me encontré con el grupo de personas más dispares que uno pueda pensar, pero que considero para mí como otra gran familia, los "SúperCachas" nos llamamos. GRACIAS a Montse, Eloy, Carlos, Lilia, Eric, Agustí, Eli, David, Naty, por ser esos monitores de 10 que después de un día duro,

sales de vuestras clases casi sin poder pestañear, pero a la vez sintiendo que vuelves a poder con todo. Carles, a tu necessito fer-te una menció a part, perquè per mi has sigut molt especial. També ets monitor però, crec que tots els teus alumnes coincidim en què, estàs a un nivell que pertany a un altre planeta. GRÀCIES per les teves súper classes amb aquesta energia, pels teus consells, les teves cançons i els teus xurros amb xocolata (vertadera raó de que anem a les teves classes). Alberts, Sergi, Juan, Ana Paula, Sara, Ona, Paqui, Verònica, Pedro, Estheres, Olga, Alex, Alícia, Jaume, Isabel, Joan, Eva, Natàlia, Jordi, Núria, Pilar, Aleix, Begoña, Edwin, Cerni, Cistina, todos compis de sufrir esas clases mañaneras y la verdadera razón de haber mantenido mi asistencia. Y no me he olvidado de vosotros, Conrad y Marcela, aquel "Desafío" nos unió mucho más y me siento muy agradecida por ello. Espero llegar a conoceros mucho más y que no nos falten retos para practicar. Os deseo lo mejor. Y por supuesto que no me he olvidado de ti, Seila. Mi italiana friolera, pero de carácter hirviente. GRACIAS por abrazarme de esa manera, por ser la mejor compañera y por no romperme las gafas aquel día. Mi corazoncito ya tiene un reservado para ti, y tu familia. Otro reservado dentro de mi corazón es para mis "Fenómenas". No podría estar más agradecida de haberme iniciado en esta actividad que compartimos con tanta pasión, porque si no, no hubiera conocido a este grupo de mujeres a cuál más increíble. GRACIAS a vosotras he tenido mis momentos de escapatoria y desahogo. En nuestras infinitas salidas nos hemos explicado de todo y nos hemos llegado a conocer hasta el punto de necesitarnos mutuamente. Meli, Raquel, Raquelilla, Silvia, Bego, Fanny, Marta, Mery y especialmente tu Yolanda. GRACIAS por haberme escuchado, comprendido y consolado en tantas ocasiones, por cómo me has cuidado y preocupado por mí. Ya sea a y media o menos cuarto, sé que cuando yo te avise tu seguirás bajando.

Y como sucede en los créditos de las películas, esta aventura no hubiera sido lo mismo sin una buena banda sonora. En este sentido me gustaría mencionar a las personas que la Música me ha atraído y a las cuales estoy muy agradecida. Esther y Ruth, madre e hija, ambas asombrosas músicas que me han formado en este arte. A todas las personas que han pasado por "La coral Oxalá" y "JAMyX". Josselyn, la Música nos unió y detonó la gran amistad que ahora compartimos. Me encanta pasar el tiempo contigo y toda tu familia. Tenéis y transmitís una positividad que te llega de verdad. Para todo lo que necesites "estoy a la orden". Y Anna, no hay nada que no sepas. Te siento cómo una hermana pequeña a la que por vueltas que de la vida no voy a olvidar. Cree en todo lo haces y te haga feliz. Allá dónde la vida te lleve, no habrá distancia física que pueda separarnos. ¡Estamos juntas incluso cuando no lo estamos!

Ya de frenada, volviendo al punto de partida de esta atracción, dispuesta a levantarme del asiento y ponerme de nuevo en pie, solo me queda acabar volviendo a daros las GRACIAS. Solo espero que, durante este tiempo, haya podido devolver a todos y cada uno de vosotros, aunque sea una pequeña porción de todo lo que me habéis aportado. Des de lo más profundo de mi corazón, os estoy y estaré eternamente agradecida. Hasta siempre, Marina.

ABBREVIATIONS

bla	Ampicillin resistance gene
bp	Base pare
CAP	Community-Acquired Pneumonia
cat	Chloramphenicol acetyl transferase
Cm	Chloramphenicol
COSY	Correlation Spectroscopy
Cryo-EM	Cryo-Electron Microscopy
CS	Cleavage Site
C-ter	Carboxy-terminus
DMSO	Dimethyl sulfoxide
DNA	Deoxyribonucleic acid
Dnase	Deoxyrribonucleic acid nuclease
dNTP	Deoxy-nucleotide triphosphate
DR	Downstream region
EDTA	Ethylenediaminetetraacetic acid
eYFP	Enhanced yellow fluorescent protein
FBS	Fetal bovine serum
FC	Flow Citometry
FSC-H	Forward Scatter-Height
gDNA	Genomic DNA
HA	Hemadsorption
HEPES	4-(2-hydroxyethyl)-1-piperazineethsnesulfonic acid
HIV	Human immunodeficiency virus
HMW	High molecular weight
HP	Hypothetical protein
HR	Homologous recombination
HSQC	Heteronuclear Single-Quantum Coherence
IPTG	Isopropyl β-D-1-thiogalactopyranoside
IR	Inverted repeat
kb	Kilobase
kDa	Kilodalton
KO	Knock-Out
LB	Lysogenic broth
LC-MS	Liquid chromatography-mass spectrometry
LVVs	Live vector vaccines
mA	Miliampere
MD	Molecular Dynamics
Mge	*M. genitalium*
MgPar	MgPa repeat
Mpn	*M. pneumoniae*
MiniTnp	Minitransposon
MM	Molecular Mechanics
MPP	Mneumonia caused by *M. pneumoniae*

Mr	Molecular relative mass
mQ	Milli-Q wàter
MS	Mass spectrometry
NAAT	nucleic acid amplification test
NGU	Non-gonococcal urethritis
NMR	Nuclear Magnetic Resonance
NOESY	Nuclear Overhauser Effect
NOESY	Nuclear Overhauser Effect Spectroscopy
nt	Nucleotides
N-ter	Amino terminal
OD	Optical Density
O/N	Overnight
ORF	Open reading frame
pac	Puromycin acetyl transferase
PBS	Phosphate buffer saline
PC	Phosphatidylcholine
PCR	Polymerase chain reaction
pDNA	Plasmidic DNA
PEG	Polyethylene glycol
PID	Pelvic Infiammatory Disease
PIPES	Piperazine-N,N'-bis (2-ethanesulfonic acid)
Pm	Puromycin
PMSF	Phenylmethane sulfonyl fluoride
ppm	Parts per million
PVDF	Polyvinylidene fluoride
RBC	Red Blood Cell
R-M	Restriction-modification
RNA	Ribonucleic acid
Rnase	Ribonucleic acid nuclease
rpm	Revolutions per minute
RT (ºC)	Room temperature
RTIs	Respiratory tract infections
SDS	Sodium dodecyl sulphate
SDS-PAGE	SDS-polyacrilanúde gel electrophoresis
Siglecs	Sialic Acid-Binding Immunoglubuline-Type Lectins
SLBR	Siglec-like Binding Region
SM	Sphingomyelin
SNFG	Symbol Nomenclature For Glycans
SO	Sialylated oligosaccharides
SOE-PCR	Splicing by overlap extension-PCR
SP4	Spiroplasma medium 4
SSC-H	Side Scatter-Height
STD NMR	Saturation Transfer Difference NMR
sTa-Thr	Sialyl-T-antigen
STI	Sexually transmitted infections
Supp.	Supplementary
TEMED	N,N,N,N’-tetramethylethane-1,2-diamine
Tet	Tetracycline

tetM438	Tetracycline resistance gene with MG_438 promoter
TMA	Transcription-mediated amplification
tr-NOESY	transferred-NOESY
TSS	Transcription start site
TO	Terminal organelle
TOCSY	Total Correlation Spectroscopy
UR	Upstream region
UV	Ultraviolet light
V	Volt
WBC	White Blood Cell
WT	Wild-type strain
X-Gal	5-bromo-4-chloro-3-indolyl-β-D-galactopyranoside
3'SLn	3' Sialyl N-acetyl lactosamine
6'SLn	6' Sialyl N-acetyl lactosamine

GENERAL INTRODUCTION

GI. 1. The class Mollicutes. Basic biology of *Mycoplasmas*: a unique bacterial genus

GI. 2. *Mycoplasma pneumoniae* and *Mycoplasma genitalium*: a comparison of two closely related human pathogens

GI. 3. Cytoskeleton: a unique morphology and cell structure

GI. 1. The class Mollicutes. Basic biology of *Mycoplasmas*: a unique bacterial genus

The class Mollicutes constitute a distinct phylogenetic lineage that have arisen from Gram-positive ancestors by reductive or degenerative evolution, which underwent successive and drastic genetic losses[1] [**Woese C. R. *et al.*, 1980**]. All genera within the Mollicutes class are characterized by small genomes ranging from 0.6 to 2.2 Mb[2–4] [**Fraser C. M. *et al.* 1995; Tully J. G. *et al.*, 1995; do Nascimento N. C. *et al.*, 2013**], the complete absence of a cell-wall, limited metabolic capacity and a low G+C content[5,6] [**Razin S., 1985; Barré, A. *et al.*, 2004**] (**Table GI. 1_1**).

Table GI. 1_1. Properties of representative mycoplasma species. Adapted from **Dybvig K. and Voelker L. L., 1996**.

Organism	Genome size (kb)	Mol% G+C	Host	Phylogenetic group
M. arthritidis	840	31	Rodent	Hominis
M. bovis	1100	28-33	Cow	Fermentans
M. capricolum	1100	25	Goat	Mycoides
M. fermentans	1160	27	Human	Fermentans
M. flocculare	1200	ND	Pig	Hyorhinis
M. gallisepticum	1000	31	Bird	Pneumoniae
M. genitalium	580	32	Human	Pneumoniae
M. ominis	700	30	Human	Hominis
M. hyopneumoniae	1100	28	Pig	Hyorhinis
M. hyorhinis	820	27	Pig	Hyorhinis
M. iowae	1300	25	Bird	Pneumoniae
M. mobile	780	24	Fish	Hyorhinis
M. mycoides	1300	25	Cow, Goat	Mycoides
M. pneumoniae	800	40	Human	Pneumoniae
M. pulmonis	950	28	Rodent	Fermentans
M. salivarium	900	29	Human	Hominis
M. amphoriforme (*A39* strain)	1030	32	Human	Pneumoniae

M. penetrans	1360	26	Human	Pneumoniae
M. testudineum (*BH29* strain)	961	28	Tortoises	Pneumoniae (hominis subgroup)

ND, not determined.

Mollicutes are among the smallest cells known and they are pleomorphic, varying from flask-shaped, spherical or branched[7] [**Krieg N.R. *et al.*, 2011**]. Their membranes are rich in cholesterol and lipoproteins, and the lack of peptidoglycan layer confers them intrinsic resistance to penicillins[8] [**Taylor-Robinson D. and Bébéar, C., 1997**]. Mollicutes only have one or two rRNA operons, fewer than other bacteria[7,9] [**Krieg N.R. *et al.*, 2011; Gaurivaud P. *et al.*, 1996**] and, in some genus (*Ureoplasma, Mycoplasma, Spiroplasma and Mesoplasma*) the UGA codon encodes for tryptophan instead of the usual stop codon[10–12] [**Inamine J. M. *et al*., 1990; Citti C. *et al*., 1992; Navas-Castillo J. *et al*., 1992**].

The first species shown to be involved in an outbreak of pleuropneumonia in cattle was isolated in 1898. For this reason, the scientific community began to refer to them as *pleuropneumonia-like-organisms* (*PPLO*). They were considered viruses until 1931, when it was shown that they formed small colonies on agar plates. Under the microscope, it was observed that they had a dense area of central growth surrounded by a lighter peripheral area, in the shape of a "fried egg"[13] [**Harwick H. J. *et al*., 1972**]. Mycoplasmas were also misclassified as eukaryotes or even L-forms[14] [**Klieneberger E., 1935**]. It was not until 1967 that the class Mollicutes was created by the Subcommittee of Taxonomy of the *Mycoplasmatae*[15] [**Edward D. G. and Freundt E. A., 1967**]. Since then, more than 200 different species have been identified.

Mycoplasma is the most well-known genus among the class Mollicutes and they are considered as the smallest free-living microorganisms[16] [**Razin S., 2006**]. They underwent a massive genome reduction and, in consequence, these microorganisms have a severe dependence on the host for nutrients because of its extremely limited metabolic pathways[17] [**Baseman J. B. and Tully J. G., 1997**], which forces them to lead a parasitic lifestyle on a wide range of hosts[18] [**Combaz-Söhnchen N. and Kuhn A., 2017**]. They are parasites of mammals, birds, reptiles, fish, insects and plants and usually present a marked host and tissue specificity[19] [**Razin S. *et al*., 1998**]. These highly demanding microorganisms need very rich and complex media for *in vitro* growth. Most of the species isolated from animals belong to the order of *Mycoplasmatale*s, family of *Mycoplasmataceae*, which includes the genus *Mycoplasma* (**Table GI. 1_2**) and noteworthy many of these species are emerging as important pathogens of animals including humans, insects and plants.

Table GI. 1_2. Taxonomy of genera included in the *Mollicutes* class according to Tully J. G. *et al.*, 1993.

Order	Family	Genus	Number of species (subspecies)	Host
Mycoplasmatales	*Mycoplasmataceae*	*Mycoplasma*	119 (4)	Animal, Human
		"Ca. Mycoplasma"	13 (2)	
		Ureaplasma	7	Animal, Human
		Eperythrozoon	2	Animal
Haloplasmatales	*Haloplasmataceae*	*Haloplasma*	1	Sea
Entomoplasmatales	*Entomoplasmataceae*	*Entomoplasma*	6	Insect, Plants
		Mesoplasma	12	Insect, Plants
	Spiroplasmataceae	*Spiroplasma*	36	Insect, Plants
Acholeplasmatales	*Acholeplasmataceae*	*Acholeplasma*	15	Animal, Plants
		"Ca. Phytoplasma"	38	Insect, Plants
Anaeroplasmatales	*Anaeroplasmataceae*	*Anaeroplasma*	4	Bovine, Ovine
		Asteroleplasma	1	Bovine, Ovine

Mycoplasma cells are small, ranging from 0.2 to 0.8 µm. Their small size and the plasticity of their membranes allow them to pass through 0.22 µm filters[20] [Nikfarjam L. and Farzaneh P., 2012]. This fact, together with their innate resistance to antibiotics targeting the bacterial cell wall, makes them a primary cause of cell culture contamination. In addition, contaminated cultures are not evident, since no turbidity or cell damage is observed after a mycoplasma infection. Thus, the incidence of mycoplasma contamination in cell cultures was astonishingly high some years ago[21] [Rottem S. and Barile M. F., 1993]. . Fortunately, the detection of these

microorganisms has been greatly improved in recent years, and contaminated cell cultures are rarely seen nowadays.

There are more than a hundred *Mycoplasma* species known (**Table GI. 1_2**), sixteen of them have a human origin and most of them are thought to be commensal species[22] [**Taylor-Robinson D. and Jensen J. S., 2011**]. However, at least six exhibit some pathogenic properties (**Table GI. 1_3**). Mycoplasma species from non-human hosts might cause severe pathogenesis as it is the case of *Mycoplasma mycoides*, *Mycoplasma agalactiae* and *Mycoplasma bovis*, which infect ruminants and are related to respiratory diseases, mastitis and arthritis[23–25] [**Kumar A. *et al.*, 2014; Nicholas R. A. J. & Ayling R. D., 2003; Provost A. *et al.*, 1987**]. *Mycoplasma hyorhinis* and *Mycoplasma hyopneumoniae* are swine pathogens that cause arthritis and the enzootic pneumonia, respectively[26,27] [**Barden J. A. and Decker J. L., 1971; Maes D. *et al.*, 2018**]. And there are also avian parasites as *Mycoplasma gallisepticum*, responsible for the chronic respiratory disease in poultry, and *Mycoplasma synoviae*, the causative agent of synovitis and upper respiratory diseases in chickens and turkeys[28] [**Stipkovits L. and Kempf I., 1996**]. These microorganisms have a great impact on animal welfare and represent a massive economic burden[29] [**Minion F. C., 2002**].

Table GI. 1_3. Primary sites of colonization, metabolism and pathogenicity of mycoplasmas isolated from humans. Adapted from **Taylor-Robinson D., 1997**.

Species	Primary site colonized		Metabolism		Considered pathogenic
	Genital tract	Respiratory tract	Glucose	Arginine	
M. hominis	+	±[b]	-	+	Yes
M. fermentans	±	+	+	+	Yes
U. urealyticum[c]	+	+	-	-	Yes
M. salivarum	-	+	-	+	Non-pathogenic[a]
M. primatum	+	-	-	+	Non-pathogenic
M. pneumoniae	±	+	+	-	Yes
M. orale	-	+	-	+	Non-pathogenic

M. buccale	-	+	-	+	Non-pathogenic
M. faucium	-	+	-	+	Non-pathogenic
M. lipophilum	-	+	-	+	Non-pathogenic
M. genitalium	+	±	+	-	Yes
M. pirum	+	-	+	+	Non-pathogenic
M. spermatophilum	+	-	-	+	Non-pathogenic
M. penetrans	+	-	+	+	Yes
M. amphoriforme	-	+	+	-	Non-pathogenic

a "Non-pathogenic" means that no evidence for pathogenicity is available.
b Primary site occasionally.
c Metabolizes urea.

GI. 1.1. Genome reduction and plasticity

Genomes of mycoplasmas are among the smallest ones in all the bacterial world, ranging from 580 kb in *M. genitalium* and 1360 kb in *M. penetrans* (**Table GI. 1_1**). Thus, mycoplasmas have evolved from Gram-positive clostridia through an extensive genome reduction and loss of genes redundancy[30] [**Woese C. R., 1987**]. Mycoplasmas with larger genomes are considered evolutionary older Mollicutes than mycoplasmas with smaller genomes. Moreover, their genomes have a characteristic low G+C content (**Table GI. 1_1**), ranging between 25-35% average; and intergenic regions are particularly rich in A+T content (often about 90%). Besides, mycoplasmas have an AT-biased codon usage and use UGA as tryptophan codon. Consequently, they lack the stop codon-recognizing peptide chain release factor 2 (RF2)[31,32] [**Inagaki Y. *et al.*, 1993 and 1996**].

Despite this extremely genome size reduction, most mycoplasma genomes contain repetitive elements such as insertion-like sequence elements (IS-like) or genomic repeats. In some species, these genomic repeats have been associated with antigenic variation and pathogenicity[33,34] [**Kenri T. *et al*., 1999; Rocha E. P. C. and Blanchard A., 2002**]. On the other hand, IS-like elements in mycoplasmas have shown to be capable of transposition within the chromosome, with the notable exception of IS1138 of *Mycoplasma pulmonis*[35] [**Bhugra B. and Dybvig K., 1993**].

Extrachromosomal DNA is rarely found in mycoplasmas, although several plasmids and replicative phage genomes have been identified[36] [Maniloff J. and Dybvig K., 1983]. The most studied mycoplasma extrachromosomal plasmids are found in *Mycoplasma mycoides* and they code for factors implicated in plasmid maintenance[37] [King K. W. and Dybvig K., 1992]. The most characterized mycoplasma viruses are P1 (infecting *M. pulmonis*)[38] [Tu A. H. *et al*., 2001] and MAV1 (infecting *Mycoplasma arthritidis*). Of note, the latter encodes a viral factor that increases bacterial virulence[39] [Voelker L. L. and Dybvig K., 1999].

GI. 1.2. Phylogeny and Taxonomy

In the 1960s, mycoplasmas were designated members of the class Mollicutes, which derives from Latin words *mollis*: "soft" or "pliable" and *cutis:* "skin". The phylogeny of mycoplasmas was first elucidated via analyses of 16S rRNA, 5S rRNA, and tRNA sequences[1,40,41] [Maniloff J., 1983; Rogers M. J. *et al*., 1985; Woese C. R. *et al*., 1980]. Additional data support the results of these studies. and amino acid sequences encoded by many mycoplasma housekeeping genes are more closely related to homologues from gram-positive bacteria than to those from Gram-negative bacteria.

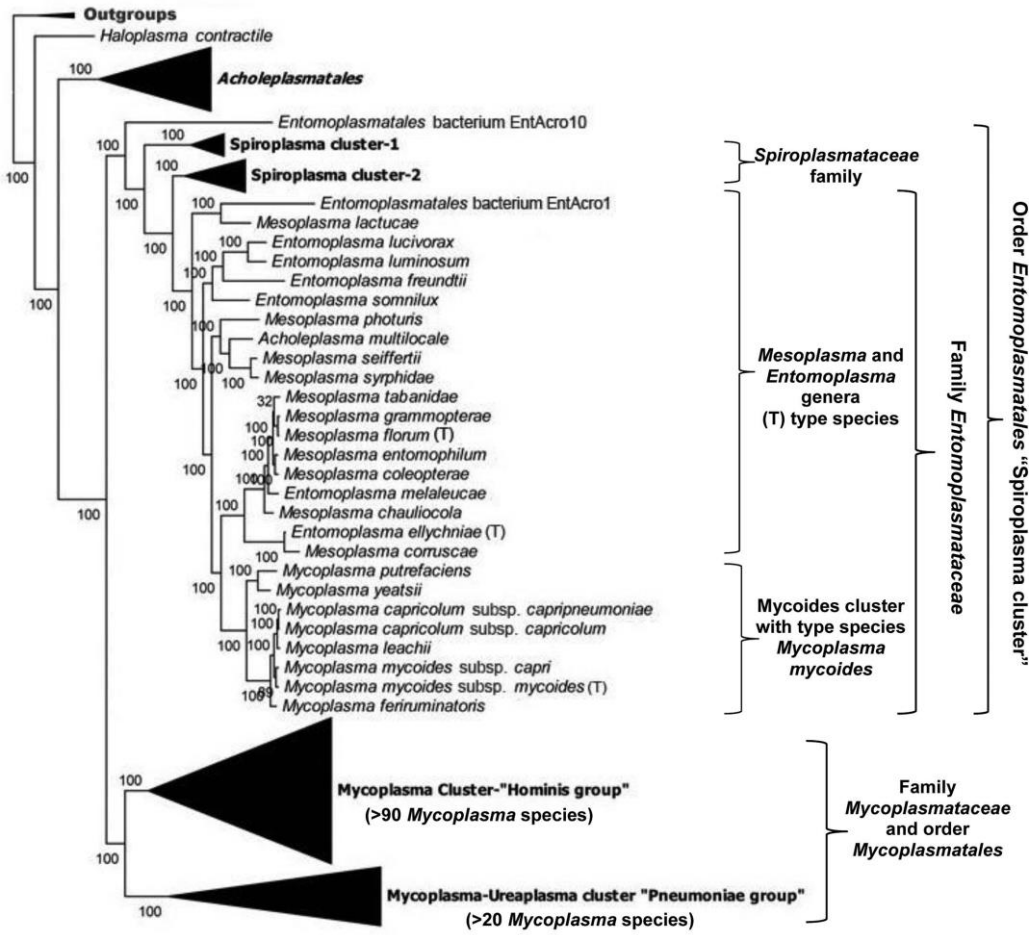

Figure GI. 1.2_1. Classification scheme for the *Mollicutes* species prior to 2018. Image from Gupta R. S. and Oren A., 2020.

Species of *Mycoplasma* have been subdivided into several different phylogenetic groups based on 16S rRNA sequence analysis (**Table GI. 1_2 and Figure GI 1.2_1**). Until 2018, the current taxonomic designations included in class Mollicutes comprise 4 orders, 5 families, 8 genera, and about 200 known species that have been detected in humans, vertebrate animals, arthropods, and plants. However, it was clear from the earliest studies based on 16S rRNA gene sequences that the existing classification for this group of species was highly problematic. As an example, one of these groups, the *pneumoniae* group, also contains the *ureaplasmas*[42] [**Weisburg W. G. *et al.*, 1989**]. The phylogeny and taxonomy of Mollicutes is particularly confusing in the *mycoides* group. *Mycoplasma mycoides* and *Mycoplasma capricolum* are more closely related to the *spiroplasmas* than they are to the other groups of *Mycoplasma*[42] [**Weisburg W. G. *et al.*, 1989**], and certain species within the mycoides group were recently reclassified into two new genera, *Entomoplasma* and *Mesoplasma*[43] [**Tully J. G. *et al.*, 1993**]. Thus, the number of recognized genera of Mollicutes is currently eight, and as a result of this reclassification of species, the mycoides group contains species that are phylogenetically closely related but subdivided into three distinct genera (*Mycoplasma, Entomoplasma,* and *Mesoplasma*).

This and other problems concerning the nomenclature and classification of the Mollicutes species are widely known and have also been discussed by the Subcommittee on the taxonomy of Mollicutes, but no solutions to resolve these problems have emerged. Recently, a new taxonomic proposal has been released[44] [**Gupta R. S. and Oren A., 2020**]. This new approach uses a large amount of evolutionary methodologies to build a new taxonomic proposal (**Figure GI 1.2_2**). This proposal could provide resolve all significant taxonomic anomalies that have afflicted this group of organisms, but it is not yet known if it will be accepted and implemented.

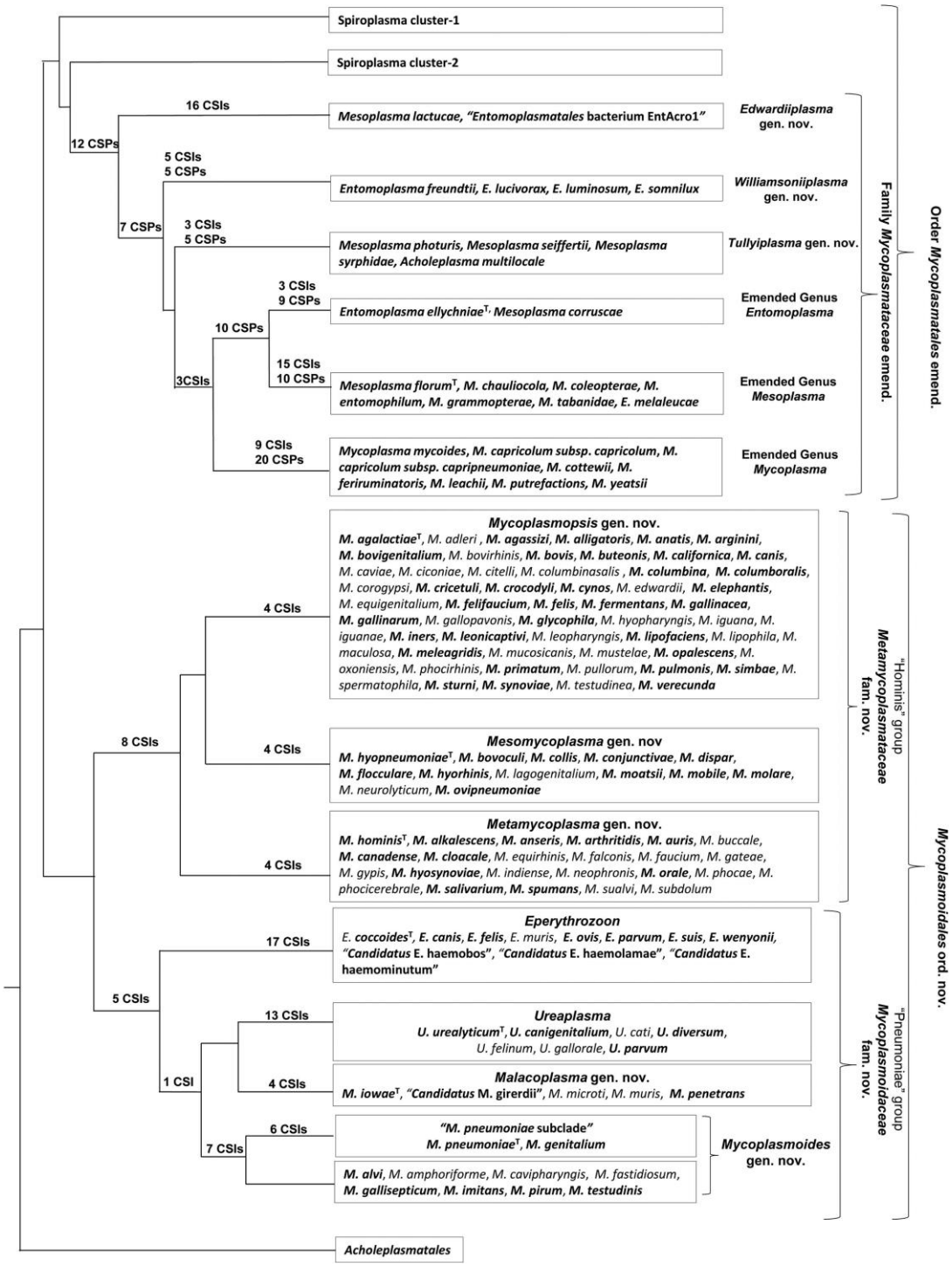

Figure GI. 1.2_2. Revised classification of the *Mollicutes* species based on genomic analyses[45,46] [Gupta R. S. *et al.*, 2018; Gupta R. S. *et al.*, 2019]. The abbreviation CSI refers to conserved signature inserts and deletions, which are uniquely shared by the members of the indicated clades**.** Image from Gupta R. S. and Oren A., 2020.

GI. 1.3. Isolation of mycoplasmas and culture

A major impediment to mycoplasma research and laboratory diagnosis has been the difficulty to cultivate them. *Mycoplasmas* have a wide repertoire of nutritional requirements that challenge the *in vitro* culture of these microorganisms. In fact, most mycoplasmas are isolated

using eukaryotic cell-assisted co-cultivation methods. This is particularly useful for identification and later classification of mycoplasma clinical isolates[47] [Hamasuna R. *et al*., 2007]. In the other hand, cultivable mycoplasmas grow very slowly even on optimized media, possibly due to their lack of most anabolic pathways. For example, both *M. genitalium* and *M. pneumoniae* lack all the genes involved in amino acid synthesis, making them totally dependent on the exogenous supply of the complete spectrum of amino acids[48] [Himmelreich R. *et al*., 1996].

Mycoplasma culture media are usually based on heart infusion, yeast extract, peptone, salts, glucose and serum. In particular, being sterols and fatty acids are critical to support mycoplasma growth[49] [Yus E. *et al.,* 2009]. Thus, most culture media include high amounts of foetal calf serum or horse serum that provide the lipids and cholesterol required for membrane synthesis. Despite these nutritional requirements, it has been proposed that some mycoplasmas may not grow in rich complex mediums because of the presence of toxic components or inhibitors. Therefore, mycoplasma cultivation is an exceptionally fastidious task. A particular feature of mycoplasmas is that they grow in solid surfaces in very small colonies and most of them have a "fried-egg" appearance[50] [Meloni G. A. *et al.*, 1980], due to the embedding of the central zone of the colony into the agar (Figure GI. 1.3_1).

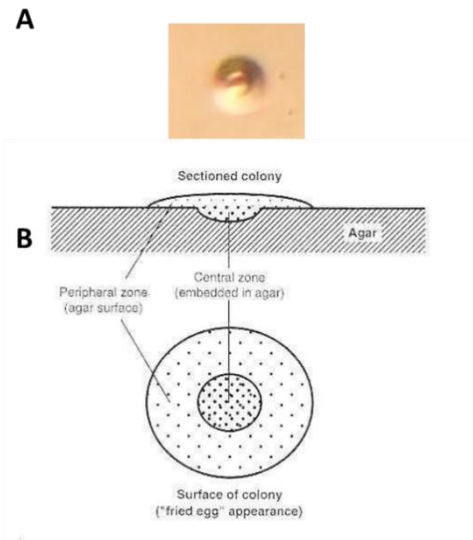

Figure GI. 1.3_1. Mycoplasma growing in a solid surface. A) *Mycoplasma genitalium* colony on mycoplasma agar, magnification 50X. **B)** Morphology of a typical "fried-egg" mycoplasma colony. Extracted image from Razin S., 1996.

GI. 1.4. Metabolism of mycoplasmas

The extreme genome reduction and the parasitic lifestyle of mycoplasmas has led to a dramatic decrease in the number of genes related to cell metabolism and catabolism. All mycoplasmas rely on fermentation of several substrates or arginine hydrolysis for energy production (Table GI. 1_3), which results in poor ATP yields and relatively large quantities of metabolic end products[51] [Miles R. J., 1992]. Some mycoplasmas are capable of oxidation of organic acids using

alternative metabolic pathways[52] [Taylor R. R. *et al.*, 1994], but the contribution of these substrates to the energy provision is unclear. Indeed, there are only three recognized mechanisms of energy generation in these bacteria: the fermentation of sugars to lactate, the oxidation of lactate or pyruvate, and the metabolism of L-arginine[53] [Keçeli S. A. and Miles R. J., 2002]. Therefore, mycoplasmas must rely on the host in order to import several essential nutrients as purines, amino acids and sterols[54] [Pollack J. D., 1997].

Genome streaming has also a big impact on genes from the biosynthetic pathways. Mycoplasmas have lost most genes involved in amino acid and cofactor biosynthesis. Lack of all these genes has resulted in a small genome, but it also has increased their dependence on robust metabolite transport systems[19] [Razin S. *et al.*, 1998]. Moreover, mycoplasmas incorporate host phospholipids and large quantities of exogenous cholesterol into their cell membranes to regulate membrane fluidity despite their lack of endogenous fatty acid biosynthesis networks[55] [Dahl J., 1993].

Large studies on the metabolome of *Mycoplasma pneumoniae* have been conducted[49,56] [Yus E. *et al.*, 2009; Maier T. *et al.*, 2013]. Despite the data integration of multiple metabolic pathways and reaction, several enzymatic activities are still carried out by "orphan enzymes" or by uncharacterized moonlighting proteins (Figure GI. 1.4_1).

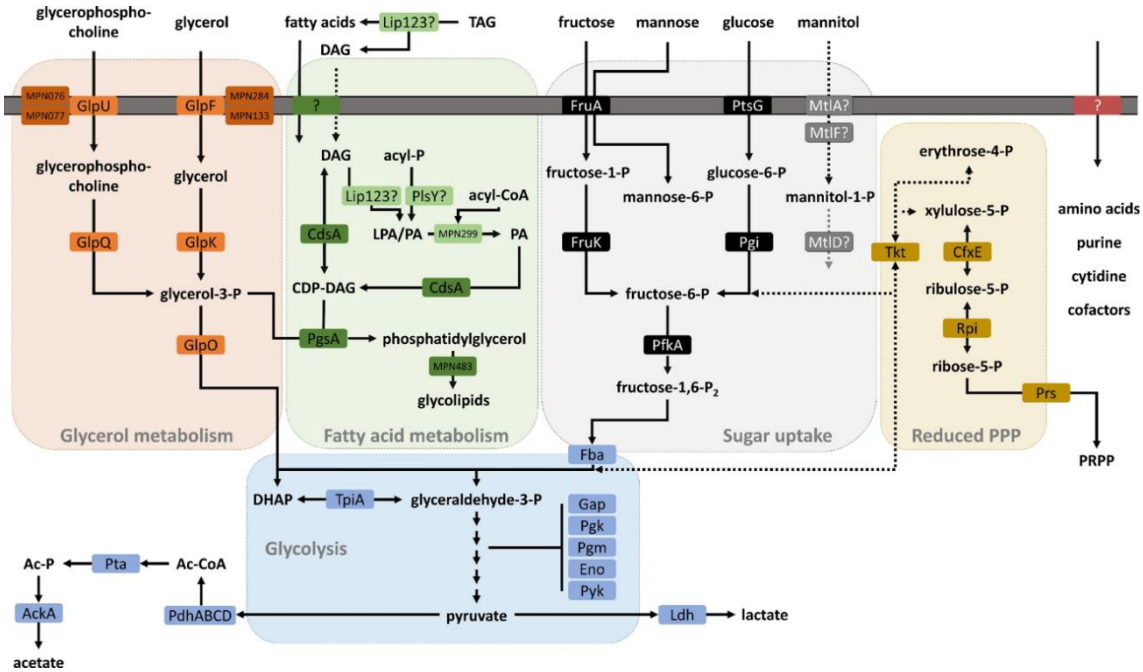

Figure GI. 1.4_1. General overview of the metabolism of *M. pneumoniae* and the relation between glycerol and the metabolism of fatty acids. General overview of the metabolism in *M. pneumoniae* based on experimental and genomic data. *Mycoplasma pneumoniae* is able to metabolize several different sugars. Note that mannitol cannot be utilized, even utilization pathway for this carbohydrate has been predicted. Most mycoplasmas, including *M. pneumoniae*, do not encode enzymes for fatty acid, amino acids, purine, cytidine and cofactor syntheses. These compounds are taken up by unknown import systems and interconverted if necessary. Dashed lines indicate pathways that are not experimentally

proven. Question marks indicate that the enzyme activity is not known or the enzymes themselves could not be identified so far. Ac, acetyl; CDP, cytidine diphosphate; CoA, coenzyme A; DAG, diacylglycerol; DHAP, dihydroxyacetone phosphate; LPA; lysophosphatic acid; P, phosphate; PA, phosphatic acid; PRPP, phosphoribosylpyrophosphate; TAG, triacylglycerol. Image extracted from **Blötz C. and Stülke J., 2017**.

GI. 1.5. Minimal recombination machinery and DNA repair systems of *Mycoplasmas*

The ability to repair DNA that contains mismatched bases or is damaged in some other respect is of central importance for cell survival. *Mycoplasmas* have retained only the enzymes that are strictly necessary for DNA repair[57] [**Carvalho F. M. *et al.*, 2005**]. The number of ORFs related to DNA repair found in *Mycoplasma* varied from 18 to 24 ORFs, whereas in *Escherichia coli* around 73 ORFs have been described. Considering this reduced genome model, the integrity of DNA necessary for life seems to be maintained by nucleotide excision repair (NER), which is the only complete repair pathway[58] [**Dillingham M. S. *et al.*, 2001**], and both base excision repair (BER)[59] [**Estevao S. *et al.*, 2014**] and recombination[60] [**Witte G. *et al.*, 2008**]. Excision repair in *E. coli* is catalysed by the enzymes UvrA, UvrB, and UvrC, and sequences homologous to the *uvrA* and *uvrB* genes have been found in *M. capricolum, M. genitalium* and *M. pneumoniae*[2,61] [**Bork P. *et al.*, 1995; Fraser C. F. *et al.*, 1995**]. Thus, excision repair is probably more common in mycoplasmas than previously thought.

Final steps in both NER and BER repair pathways involve the activity of translesion DNA polymerases and ligases to finally generate a corrected DNA strand. DNA polymerase IV and a similar DNA polymerase I (Pol-I-like) found in some mycoplasma species such as *M. genitalium*[57] [**Carvalho F. M. *et al.*, 2005**] could be involved in correction of chromosomal errors. However, its role in DNA repair has not been addressed yet.

Mycoplasmas also have an efficient rudimental machinery to perform homologous combination (HR) between homologous strands, although it has not been studied in depth. Furthermore, homologous recombination repair system has been questioned as a Δ*recA* mutant of *M. genitalium* had similar DNA repair capabilities than the WT strain upon exposure to DNA-damaging agents[62] [**Burgos R. *et al.*, 2012**].

As in many other prokaryotes, mycoplasmas encode restriction and modification (R-M) systems in their genomes[63] [**Brocchi M. *et al.*, 2007**]. Type I R-M systems are largely widespread, but some species like *M. genitalium* only have the gene coding for the S subunit of a vestigial R-M system (HsdS, MG438), perhaps suggesting a moonlight function for this subunit[64] [**Calisto B. M. *et al.*, 2005**]. Type II and III R-M systems are less common but have also been found in some mycoplasmas[65] [**Dybvig K. *et al.*, 2007**]. It is thought that DNA methylation in mycoplasmas protects the chromosome against possible DNA intrusions, but unique Gm^{6}ATC methylase

activity not related to DNA protection has been observed in several species as well[66] [**Bergemann A. D. *et al.*, 1990**], with no defined role so far. As with other enzymes purified from many bacterial species, *Mycoplasma fermentans Mfe*I endonuclease (which recognizes CAATTG as the target sequence) has been included in the common restriction enzymes available on the market[67] [**Halden N. F. *et al.*, 1989**].

GI. 1.6. Infection and disease: clinical implications of species of the genus *Mycoplasma*

Mycoplasma infections are typically very fastidious and persistent in time. The initial steps of mycoplasma infection involve the attachment and possible internalization into the host cells. Adhesion to host tissue is an essential step for colonization and infection and it relies on cytadhesins or mycoplasma specialized lipoproteins as well as other accessory membrane proteins[68–72] [**Krause D. C. and Baseman J. B., 1982; Fisseha M. *et al.*, 1999; Burgos R. *et al.*, 2006; Pich O. Q. *et al.*, 2008; Indiková I. *et al.*, 2013**] (further explained below). It has been shown that mycoplasmas need sialydated lipids or sialydated glycoproteins present in host cell membranes for attachment[73–75] [**Razin S. *et al.*, 1981; Baseman J. B. *et al.*, 1982; Aparicio D. *et al.*, 2018**]. Although it has been clearly established in some cases, whether most animal mycoplasmas can invade epithelial cells during infection is still a matter of debate[76–80] [**Taylor-Robinson D. *et al.*, 1991; Lo S. C. *et al.*, 1993; Jensen J. S. *et al.*, 1994; Winner F. *et al.*, 2000; Blaylock M. W. *et al.*, 2004**]. The exact mechanism used to enter the host cells is not well understood, though some mycoplasmas such us *M. genitalium*, *M. pneumoniae* or *M. penetrans* use a specialized tip structure (known as terminal organelle) to facilitate this process[81] [**Ueno P. M. *et al.*, 2008**]. In some species, internalization in target cells can be halted using actin polymerization inhibitors such as cytochalasin D[82] [**Andreev J. *et al.*, 1995**]. This internalized reservoir could have major implication in infection persistence and immune evasion[17,83] [**Baseman J. B. and Tully J. G., 1997; McGowin C. L. *et al.*, 2009a**].

While most mycoplasmas are commensals living innocuously within their host, some species have been associated to several diseases. Pathogenic mycoplasmas infect and colonize the respiratory membranes, the genitourinary tract, the conjunctiva, the mammary glands or joints, causing both acute and chronic diseases.

In the *Mycoplasmataceae* family there are mycoplasmas with clinical implications in humans belonging to the genus *Mycoplasma* and *Ureaplasma*[84] [**Shepard M. C. *et al.*, 1974**]. In 1937 Dienes L. and Edsall G. described the first isolation in humans, *Mycoplasma hominis*[85] [**Dienes L. and Edsall G., 1937**]. In successive years, more and more cases of mycoplasmas that were isolated in humans began to be known, almost always from samples of the respiratory and

genital tract. The pathogenic role of some is quickly reflected in species such as *Ureaplasma urealyticum, Mycoplasma pneumoniae* or *Mycoplasma genitalium*[86] [**Taylor-Robinson D. and Furr P. M., 1998**]; while in others, such as *Mycoplasma fermentans* or *M. hominis*, their pathogenicity was not evident until several years later[84] [**Shepard M. C. *et al.*, 1974**].

In humans, the most common mycoplasma infections are caused by *M. penumoniae*, *M. genitalium*, *Mycoplasma hominis, M. penetrans, Ureaplasma urealyticum* and *Ureaplasma parvum*. *M. pneumoniae* is the main agent causing primary atypical pneumonia or "walking pneumonia" as well as chronic lung conditions due to vigorous immune responses[87] [**Waites K. B. and Talkington D. F., 2004**]. *M. genitalium* infections are sometimes asymptomatic[88–90] [**Clarivet B. *et al.*, 2014; Henning D. *et al.*, 2014; Philibert P. *et al.*, 2014**], but can cause non-gonococcal urethritis (NGU), cervicitis, vaginal discharge and pelvic inflammatory diseases[91] [**Manhart L. E., 2013**]. *M. hominis* can cause bacterial vaginosis, pelvic inflammatory disease, post-partum fevers and male infertility[92] [**Mardh P. A., 1983**]. *U. urealyticum* and *U. parvum* infections have been linked as causants of NGU as well as abortions or preterm birth, although their exact role in developing these illnesses is not yet clear[93–95] [**Ireland D. J. and Keelan J. A., 2014; Zhang N. *et al.*, 2014; Sweeney E. L. *et al.*, 2017**]. *M. penetrans* pathogenesis is still a matter for debate, although some studies have established a link between *M. penetrans* infection and HIV progression[96,97] [**Blanchard A. and Montagnier L., 1994; Grau O. *et al.*, 1995**] or nephropathies[98] [**Jiang X. *et al.*, 2013**]. Some mycoplasmas infecting humans have also oncogenic potential and can induce chromosome aberrations in prolonged infections[99] [**Tsai S. *et al.*, 1995**] (**Table GI. 1_3 and Table GI. 1.6**).

Table GI. 1.6. Relevant aspects of the species of the genus *Mycoplasma* that may have clinical implications in humans. Adapted from **Gómez Rufo D. *et al*., 2021**.

Specie	Isolation in man	Clinical significance	Antimicrobials recommended
M.amphoriforme	Yes	Sí	Macrolides, tetracyclines and fluoroquinolones
M. arginini	Yes	Sí	Macrolides, tetracyclines and quinolones
M. arthritidis	Yes	ND	ND
M. bovis	Yes	ND	Tetracyclines
M. buccale	Yes	ND	ND
M. canis	Yes	ND	ND
M. edwardii	Yes	ND	ND
M. faucium	Yes	Yes	Macrolides, tetracyclines and fluoroquinolones
M. felis	Yes	Yes	Intravenous ampicillin/sulbactam and doxycycline
M. fermentans	Yes	Yes	Doxycycline and ciprofloxacin
M. genitalium	Yes	Yes	Azithromycin, moxifloxacin and doxycycline. Pristinamycin and minocycline alternatives
M. haemofelis	Yes	ND	Doxycycline
M. hominis	Yes	Yes	Doxycycline, moxifloxacin and macrolides
M. hyorhinis	Yes	It has been associated with several types of cancer and their malignancy	ND
M. lipofaciens	Yes	Yes	ND
M. lipophilum	Yes	ND	ND
M. maculosum	Yes	Yes	Sensitivity testing is necessary
M. orale	Yes	Yes	It is necessary to take into account the patient's immunological situation to avoid relapses
M. ovis	Yes	Yes	Doxycycline or levofloxacin. Combine rifampicin if there is suspicion of coinfection with Bartonella henselae
M. penetrans	Yes	Yes	Azithromycin, clarithromycin, erythromycin and tetracyclines
M. phocicerebrale	Yes	Yes	Tetracycline. Aureomycin as an alternative
M. pirum	Yes	Yes	It is sensitive to macrolides except erythromycin
M. pneumoniae	Yes	Yes	Macrolides, preferably azithromycin over erythromycin. Resistance has been documented. Alternatively use tetracyclines and fluoroquinolones
M. primatum	Yes	ND	ND
M. pulmonis	Yes	ND	ND
M. salivarium	Yes	Yes	Doxycycline and clindamycin
M. spermatophilum	Yes	ND	ND
M. suis	Yes	ND	ND
U.parvum	Yes	Yes	Doxycycline and erythromycin
U. urealyticum	Yes	Yes	Doxycycline and moxifloxacin; in pregnant women use erythromycin

GI. 2. *M. pneumoniae* and *M. genitalium*: a comparison of two closely related human pathogens

GI. 2.1 *Mycoplasma genitalium*

M. genitalium was initially identified in patients with non-gonococcal urethritis (NGU) in 1981, and it was later isolated from respiratory and synovial tissues as well[3,100,101] [**Tully J. G. *et al.*, 1981; Tully J. G. *et al.*, 1995; Taylor-Robinson D. *et al.*, 1994**]. Recently, with the new taxonomically classification that has been proposed for Mollicutes, *M. genitalium* can also be called Mycoplasmoides genitalium[45,102] [Tully J. G. et al. 1983; Gupta R. S. et al. 2018].

M. genitalium is a human pathogen that is parasitic in the genitourinary tract and causes acute and chronic NGU in men. In women, *M. genitalium* has been implicated in a range of reproductive tract diseases in women, including cervicitis, endometritis, pelvic inflammatory disease (PID), tubal factor infertility and pre-term birth[103] [**McGowin C. L. and Anderson-Smits C., 2011**]. *M. genitalium* has been reported to be the cause of 15%–20% of non-gonococcal urethritis (NGU), 20%–25% of non-chlamydial NGU, and 30% of recurrent or persistent urethritis[104] [**Harish S., 2021**]. According to the 2017–2018 National Health and Nutrition Examination Survey, the overall prevalence of urogenital *M. genitalium* among adults aged 14–59 years in the United States is 1.7%. According to the survey, males had a 1.8% frequency, while females had a 1.7% prevalence[105] [**Torrone E. A. *et al.*, 2021**].

M. genitalium is also reported to for its capacity to bind to red blood cells[75] [**Aparicio D. *et al.*, 2018**] and co-infect with other pathogens, such as human immunodeficiency virus (HIV), *Chlamydia trachomatis*, *Neisseria gonorrhoeae*, and *Trichomonas vaginalis*[106] [**Gnanadurai R. and Fifer H., 2020**]. Clinical data indicate that sexually transmitted infections by *M. genitalium* have become more serious worldwide, especially given their marked and rapid propensity for developing antimicrobial resistance[107] [**Fernández-Huerta M. *et al.*, 2020**]. Unfortunately, few antibiotics are available to treat *M. genitalium* infections, and there has been a marked rise in resistance to the antibiotics azithromycin and moxifloxacin, two antibiotics often used to treat *M. genitalium* infections[108–111] [**Jensen J. S. *et al.*, 2016; van der Schalk T.E. *et al.*, 2020; Machalek D.A. *et al.*, 2020; Manhart L.E. *et al.*, 2011**] (**Table GI. 1.6**). Therefore, uncovering the pathogenic mechanism and virulence factors of *M. genitalium* will be greatly beneficial for therapeutics and vaccine development.

GI. 2.2. *Mycoplasma pneumoniae*

M. pneumoniae belongs to class Mollicutes and with a 816-kb genome, is also a model organism for a minimal cell[112] [**Lluch-Senar, M. *et al.* 2015**]. Among pathogenic *Mycoplasma*, *M.*

pneumoniae is the most predominant and intensely studied species. It was isolated for the first time in 1944 in tissue culture from the sputum of a patient with primary atypical pneumonia[113] [**Eaton M. D. *et al*., 1944**]. Recently, with the new taxonomically classification that has been proposed for Mollicutes, *M. pneumoniae* can also be called Mycoplasmoides pneumoniae[45,114] [Somerson N. L. et al. 1963; Gupta et al. R. S. 2018].

M. pneumoniae causes both upper and lower respiratory tract infections (RTIs), and in most cases the clinical symptoms are non-specific[87,115] [**Waites K. B. and Talkington D., 2004; Waites K.B. *et al*., 2017**]. Tracheobronchitis is the most common type of lower respiratory infection, the incidence of which is about 20 times that of pneumonia, and 10–40% of respiratory tract infections caused by *M. pneumoniae* will eventually develop into pneumonia[116] [**Søndergaard M.J. et al., 2018**]. While most pneumonia caused by *M. pneumoniae* (MPP) cases are benign, some cases may develop into severe pneumonia and refractory pneumonia with pleural effusion, multi-organ dysfunction, and serious long-term sequelae, including bronchiolitis obliterans and bronchiectasis[117] [**Gao L.W. *et al*., 2019**].

Community-acquired pneumonia (CAP) is associated with high morbidity and mortality, and the disease is also a major threat to public health worldwide[118] [**Zhu Y.G. *et al*., 2018**]. Based on the reported cases in China, *M. pneumoniae* infections accounted for 19.2% of all CAP cases in adults, and the prevalence of CAP in children and teenagers, ranged from 10% to 30%[118,119] [**Zhu Y.G. *et al*., 2018; Xu W. *et al*., 2018**]. In the USA, a recent study of hospitalized children with CAP showed that 8% children with median age of 7 years were positive for *M. pneumoniae* by polymerase chain reaction (PCR)[120] [**Kutty P.K. *et al.*, 2019**]. Airborne droplets containing *M. pneumoniae* can be transmitted and spread among people through coughing and sneezing.

Although CAP is the most significant disease caused by *M. pneumoniae*, the pathogen is known to cause upper respiratory tract infections. Pharyngitis is commonly reported while rhinosinusitis and otitis media are less frequently encountered in upper respiratory tract infections caused by *M. pneumoniae*[115] [**Waites K.B. *et al.*, 2017**].

M. pneumoniae respiratory infections are associated with asthma exacerbation during which patients will suffer from a combination of symptoms including sudden or progressive coughing, respiratory distress, wheezing or chest pain[121,122] [**Kumar S. *et al*., 2019; Kassisse E. *et al*., 2018**]. The onset of asthma is due to the release of *Mycoplasma*-mediated cytokine in infected patients[123] [**Esposito S. *et al*., 2002**]. Respiratory infections caused by *M. pneumoniae* are also associated with a wide array of extrapulmonary manifestations such as meningoencephalitis, myocarditis, nephritis, atherosclerosis and mucocutaneous eruptions, etc.[124–128] [**Narita M., 2010; Narita M., 2016; Giavina-Bianchi P. and Kalil J., 2016; Wang K. *et al*., 2011; Takahashi N. *et al*., 2016**]. More importantly, *M. pneumoniae* also induces mucositis and mucocutaneous

diseases including the Stevens-Johnson syndrome. These mucocutaneous diseases are frequently associated with systemic inflammation and higher risk of the occurrence of long-term sequelae[129–132] [**Meyer Sauteur P.M. *et al*., 2020; Meyer Sauteur P.M. *et al*., 2012; Harr T. and French L.E., 2010; Prindaville B. *et al*., 2014**].

Although *M. pneumoniae* infection is generally self-limiting and does not require antibiotic treatment, patients of all age groups can develop severe, life-threatening or extrapulmonary diseases[133] [**Meyer Sauteur P.M. *et al*., 2016**]. Antibiotics such as tetracycline and fluoroquinolone have been reported to be effective in eliminating *M. pneumoniae* infections[134] [**de Groot R.C.A. *et al*., 2017**] but tetracyclines cause discoloration of bones and teeth in young children. Fluoroquinolones can also affect the muscle, joint and tendon. Instead, macrolides, which have fewer side effects, have been the drug of choice for treating *M. pneumoniae* infection in past years[135] [**Spuesens E.B.M. *et al*., 2014**] (**Table GI. 1.6**). More worrisome is that the extensive use of macrolides in China has led to a particularly high rate of macrolide resistance in this organism (69%~95%)[136] [**Cao B. *et al*., 2017**]. The emergence of antibiotic resistance represents another challenge regarding the treatment of *M. pneumoniae* infections. Failure in antibiotic treatment has caused an increase in mortality rate during recent years[137] [**Khoury T. *et al*., 2016**]. Although the clinical outcomes of infections caused by macrolide-susceptible and -resistant *M. pneumoniae* isolates are not significantly different, patients infected with macrolide-resistant isolates had a longer febrile period, length of hospital stay, antibiotic drug courses, and defervescence time after macrolide treatment compared to patients infected with macrolide-sensitive isolates[138] [**Chen Y. C. *et al*., 2020**]. Furthermore, macrolide-resistant strains may be associated with more extrapulmonary complications, and severe clinical and radiological features[133,139] [**Meyer Sauteur P.M. *et al*., 2016; Zhou Y. *et al*., 2014**]. Hence, determination the pathogenic mechanism and virulence factors of *M. pneumoniae* will be greatly beneficial for therapeutics and the development of vaccines against *M. pneumoniae* infections is a potential solution for the prevention of infections caused by this pathogen.

GI. 2.3. *M. genitalium* and *M. pneumoniae* as a systems biology and minimal genome model

M. genitalium was the second bacteria with its genome completely sequenced[2] [**Fraser C. M. *et al*., 1995**], only behind *Haemophilus influenzae*. At the time, with 580 kb and only 470 predicted coding regions, the unraveling of its sequence marked the start of the minimal genome race. A few years after, it was speculated that the essential genes of *M. genitalium* would range between 265 and 350[140] [**Hutchison C. A. *et al*., 1999**].

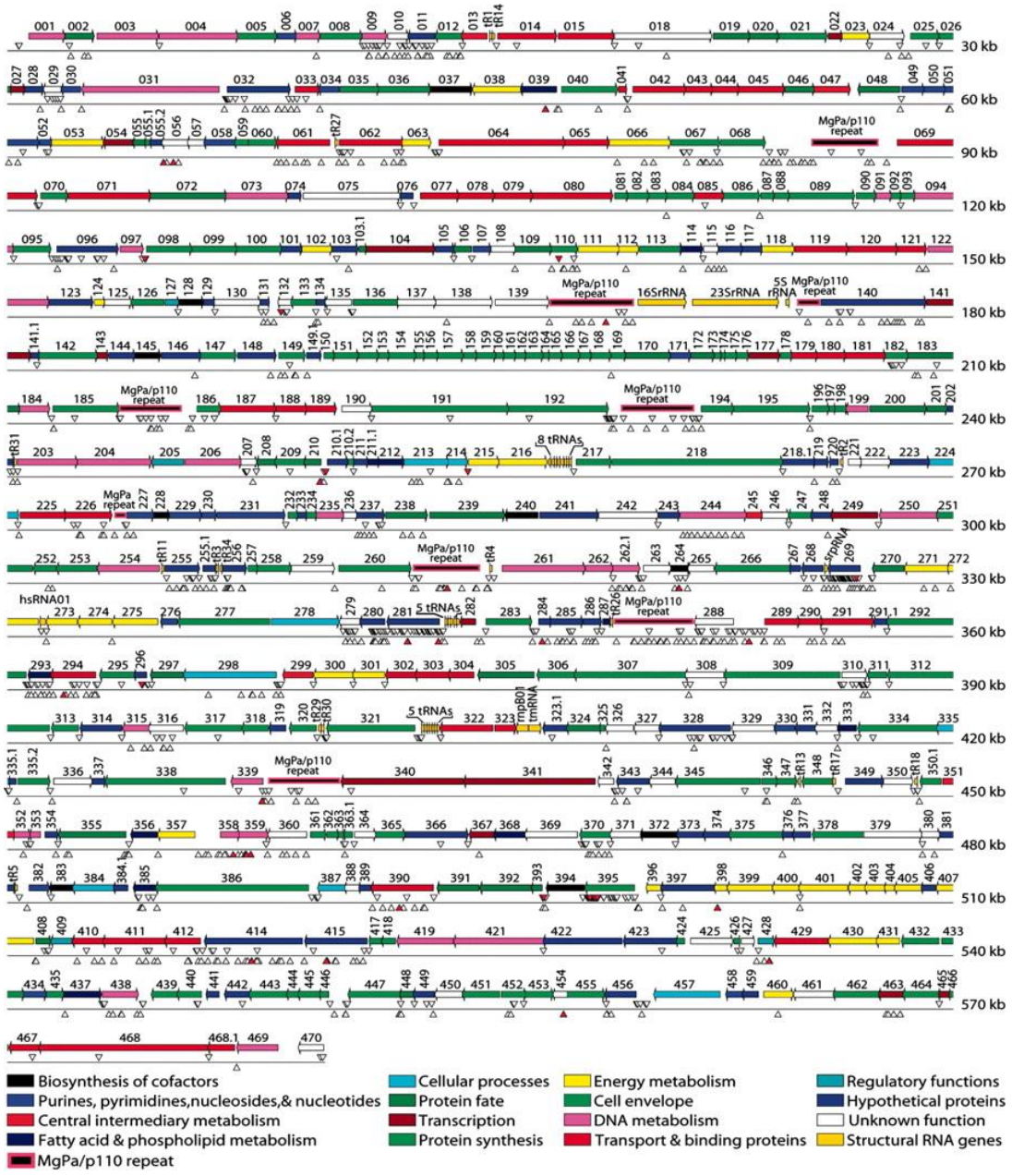

Figure GI. 2.3_1. Gene essentiality of *M. genitalium* determined by global transposition mutagenesis. Glass and his coworkers sequenced the transposon insertion site of hundreds of colonies to find out which genes were dispensable. A red triangle represents 10+ insertions. Large genomes zones without insertions can be observed, while it is also evident the existence of hot spots: genome localizations with an elevated number of transposon insertions. Image extracted from **Glass J. I. *et al.*, 2006**.

Since then, essentiality studies have been performed on its chromosome[141] [**Glass J. I. *et al.*, 2006**] and in the closely related species *M. pneumoniae*[112] [**Lluch-Senar M. *et al.*, 2015**] to determine the smallest set of genes that can sustain autonomous life. Regarding the former, they found through global transposon mutagenesis that 382 genes of *M. genitalium* were essential (**Figure GI. 2.3_1**), 28% of them coding for proteins of unknown function. As for the latter, the study in *M. pneumoniae* revealed the importance of non-coding regions, as they

unveiled that non-coding RNAs (ncRNAs) were involved in the regulation of the expression of essential ORFs, thus adding another layer of complexity to the minimal genome studies. The relevance of non-coding elements, including intergenic segments of unknown function, in essentiality was also addressed by a report on *Caulobacter crescentus* several years before[142] [**Christen B. *et al*., 2011**].

The *M. genitalium* genome was also the first one to be produced synthetically[143] [**Gibson D. G. *et al.*, 2008**]. It was followed by the genome synthesis of the ruminant pathogen *M. mycoides*, a genome comprising 1.19 Mb and 867 predicted protein-coding genes[144] [**Gibson D. G. *et al*., 2010**]. The latter was transplanted into a *M. capricolum* recipient cell and was capable of self-replication. An attempt to unravel the minimal number of genes necessary for autonomous life was performed with *M. mycoides*, and its genome was thoroughly reduced to 531 kb and 438 protein-coding genes (with a striking 31.5% of genes coding for proteins of unknown function)[145] [**Hutchison C. A. *et al*., 2016**]. Although the expected minimal genome proposed in his 1999 paper was expected to be roughly half of the experimentally determined final size, Hutchinson and his colleagues described in the 2016 report the existence of *quasi-essential* genes, not strictly needed for cell viability but required for robust growth.

In the present days, the race towards the discovery of the minimal set of genes necessary for self-replicating life has apparently come to a halt, as the interest for a minimal genome has shifted to more industry-suitable microorganisms than the slow-growing and highly demanding mycoplasmas[146] [**Vickers C. E., 2016**].

Despite these changes in the model microorganisms chosen for synthetic biology, *M. genitalium* and *M. pneumoniae* remain two of the most characterized mycoplasmas and they have become model organisms for systems biology[147] [**Balish M. F., 2014**]. Several large studies have been conducted to better understand these minimal cells in the fields of transcriptomics[148–151] [**Weiner J. *et al*., 2000; Güell M. *et al*., 2009; Maier T. *et al*., 2011; Yus E. *et al*., 2012**], proteomics[152–155] [**Kühner S. *et al*., 2009; Schmidl S. R. *et al*., 2010; Párraga-Niño N. *et al*., 2012; van Noort V. *et al*., 2012**], metabolomics[49,56,156] [**Yus E. *et al*., 2009; Maier T. *et al*., 2013; Wodke J. A. H. *et al*., 2013**] and genetic methylome[157] [**Lluch-Senar M. *et al*., 2013**]. Integration of all these data permitted the generation of a whole-cell computational model that aimed at providing accurate predictions on *M. genitalium* cell behaviour and biological functions[158] [**Karr J. R. *et al*., 2012**]. However, the fact that there are still more than 100 genes of *M. genitalium* with unknown function enhances the importance of single-gene characterization studies in these microorganisms.

GI. 2.4. Virulence and pathogenicity

To date, there are no known toxins secreted by *M. genitalium*. Thus, virulence of this small pathogen is mainly associated with its capacity to stimulate the host immune response[159] [McGowin C. L. and Totten P. A., 2017]. In fact, it has been proposed that the actual primary source of damage upon mycoplasma infections is self-inflicted by an inefficient immune response[19] [Razin S. *et al.*, 1998]. This topic has been thoroughly assessed in *M. pneumoniae*[87] [Waites K. B. and Talkington D. F., 2004], as it has been observed that potent immune system reactions are strongly associated with more severe pulmonary injuries[160,161] [Ito S. *et al.*, 1995; Radisic M. *et al.*, 2000].

The immunomodulation caused by mycoplasmas has been linked to its ability to persist inside the host and establish chronic infections[19] [Razin S. *et al.*, 1998]. Their exposed lipoproteins play a critical role in modulating the host immune response to a mycoplasma infection. It was evidenced in the mid-nineties that lipoproteins present on mycoplasma membranes could induce the production of proinflammatory cytokines, although by a different mechanism than lipopolysaccharides[162] [Rawadi G. and Roman-Roman S., 1996]. A few years later, it was demonstrated that the uncharacterized lipoprotein MG309 of *M. genitalium* elicited a potent proinflammatory response via toll-like receptors (TLR)[163] [McGowin C. L. *et al.*, 2009b]. Similarly, other researchers linked the inflammatory response induced by the lipoproteins of this pathogen to the activation of NF-κB[164] [Wu Y. *et al.*, 2008]. Notably, it was reported that contact with lung epithelial cells triggered a differential expression of genes coding for lipoproteins in *M. pneumoniae*[165] [Hallamaa K. M. *et al.*, 2008], and a similar phenomenon was observed in the human-pathogen *M. hominis*, as it changed expression of lipoprotein-encoding genes upon contact with human dendritic cells[166] [Goret J. *et al.*, 2016]. There has also been proposed that autophagy might also play a role in the inflammatory response induced by mycoplasma cytadherence[167] [Shimizu T., 2016].

Production of hydrogen peroxide (H_2O_2) and mycoplasma pathogenicity are intimately entwined. This reactive oxygen species (ROS) is generated as a by-product of glycerol metabolism[168] [Halbedel S. *et al.*, 2007b], an essential carbon source for mycoplasma growth that is part of one of the few catabolic pathways conserved in Mollicutes[49] [Yus E. *et al.*, 2009]. Glycerol also constitutes a bridge between glycolysis and fatty acid metabolism (**Figure GI. 1.4_1**), as glycerol-3-phosphate can be removed from the former and used for lipid synthesis[169] [Blötz C. and Stülke J., 2017]. Although glycerol can pass the membrane by passive diffusion, mycoplasmas encode a glycerol facilitator, a membrane transporter similar to aquaporins that,

in addition to glycerol uptake, also allows the facilitate diffusion of urea[170] [Stroud R. M. *et al.*, 2003].

As it was demonstrated in a highly virulent strain of the ruminant pathogen *M. mycoides*, the uptake of glycerol is directly related to production of H_2O_2 and virulence, as this particular strain contained an operon coding for an additional glycerol transporter[171] [Vilei E. M. and Frey J., 2001]. The correlation between glycerol metabolism and virulence was also proved in *M. pneumoniae*, as a mutant strain with an impaired glycerol metabolism was unable to produce H_2O_2 and did not cause any detectable damage to host cells in vitro[172] [Schmidl S. R. *et al.*, 2011]. However, production of H_2O_2 is not the only toxic factor secreted by mycoplasmas, as non-ROS producing mutants are still virulent[173,174] [Hames C. *et al.*, 2009; Szczepanek S. M. *et al.*, 2014]. The virulence of H_2O_2 is connected to its vast reactivity and the oxidative damage that it causes. ROS can harm DNA, proteins and lipids[175] [Cross C. E. *et al.*, 1987]. Of note, human phagocytes (as neutrophils or macrophages) also use H_2O_2 as a microbiocidal, a mechanism that is called respiratory burst[176] [Thomas D. C., 2017]. Thus, the production of ROS is a double-edged sword, as it can damage both the pathogen and the host. This is especially true for most mycoplasmas, as they do not have a gene coding for a catalase to remove H_2O_2.

Lipoproteins and peroxide production are, thus, widespread virulence factors for all mycoplasmas. Remarkably, *M. pneumoniae* also produces a toxin termed as Community Acquired Respiratory Distress Syndrome (CARDS) toxin. This protein has ADP-ribosyltransferase activity and elicits vacuolization and cell death of the host cells[177] [Kannan T. R. and Baseman J. B., 2006]. The toxin holds some similarity to the pertussis toxin and its immunodominance has been evidenced. In an animal model, it was observed that the CARDS toxin alone could replicate the inflammation associated with an *M. pneumoniae* infection[178] [Hardy R. D. *et al.*, 2009]. In addition, a high expression of the toxin along with an also elevated expression of the pro-inflammatory cytokine TNF-α has been associated with more severe prognosis[179] [Li G. *et al.*, 2019]. **Figure GI. 2.4_1 and Table GI. 2.4_1** show the main pathogenic mechanism and the virulence factors associated with *M. pneumoniae* infection, respectively.

Recent advances in the pathogenicity of *M. genitalium* have evidenced that biofilm formation can contribute to the survival and perseverance of this bacterium[180] [Daubenspeck J. M. *et al.*, 2020]. *M. genitalium* biofilms also decreases antibiotic access, leading to a lower-level exposure and increased survival, thus increasing the risk for the development of resistance. The main pathogenic components and the key virulence factors associated with *M. genitalium* infection are shown in **Figure GI. 2.4_1 and Table GI. 2.4_2**, respectively.

Table GI. 2.4_1. Key virulence factors of *M. pneumoniae*. Adapted from Jiang Z. *et al*., 2021.

Pathogenic Mechanism	Virulence Factor	Gene Annotation
Adherence	P1	MPN141
	P30	MPN453
	P40 (Protein C)	MPN142
	P90 (Protein B)	MPN142
	P200	MPN567
	Hypothetical protein HMW1-3 (high molecular weight)	MPN447/310/452
	P116	MPN213
	P65	MPN309
	Elongation factor thermo unstable (EF-Tu)	MPN665
	Pyruvate dehydrogenase subunit B	MPN392
	Glycolytic enzymes enolase	MPN606
	TopJ	MPN119
Immune evasion	Nuclease	MPN491
	Immunoglobin binding protein (IbpM)	MPN400
Inflammation injury	H_2O_2	/
	Reactive oxygen species (ROS)	/
	H_2S	/
	HapE enzyme	MPN487
	Oxidase GlpO	MPN051
	Membrane lipids	/
	Membrane lipoproteins	/
	Capsular materials	/
Cytotoxicity	Community-Acquired Respiratory Distress Syndrome (CARDS) toxin	MPN372
	Cytotoxic nuclease	MPN133
Gliding motility	P65	MPN309
	P30	MPN453
	Hypothetical protein MPN387	MPN387
	P24	MPN312
	P41	MPN311

Table GI. 2.4_2. Putative factors for immune evasion and sustained survival of *M. genitalium*. Adapted from **Yueyue W. *et al*., 2022**.

Virulence factors	Subcellular location	Function
P140	Transmembrane	Adhesion; Motility; Antigenic variation; Internalization
P110	Transmembrane	Adhesion; Motility; Antigenic variation; Internalization
MG428	Unclear	Recombination regulator
RecA (mg339)	Cytoplasm	Recombination regulator
RuvA (mg358)	Unclear	Recombination regulator
RuvB (mg359)	Unclear	Recombination regulator
RecU (mg352)	Cytoplasm	Recombination regulator
RrlA (mg220)	Transmembrane	σ accessory protein
RrlB	Unclear	σ accessory protein
MG281	Transmembrane	Protein M, Antibody-binding
Duf31 domain protein	Unclear	Cleavage of Igs (Predicted)
MG186	Cell membrane; Lipid-anchor	Nuclease, Degradation of NETs (Predicted)
MG408	Cytoplasm	MsrA; Defenses against oxidative stress
MG448	Cytoplasm	MsrB
MG454	Unclear	Ohr; Detoxification of oxidants
MG149	Cell membrane; Lipid-anchor	OsmC, Maintaining cellular integrity; Degrading ROS
MG427	Cytoplasm	OsmC, Detoxification

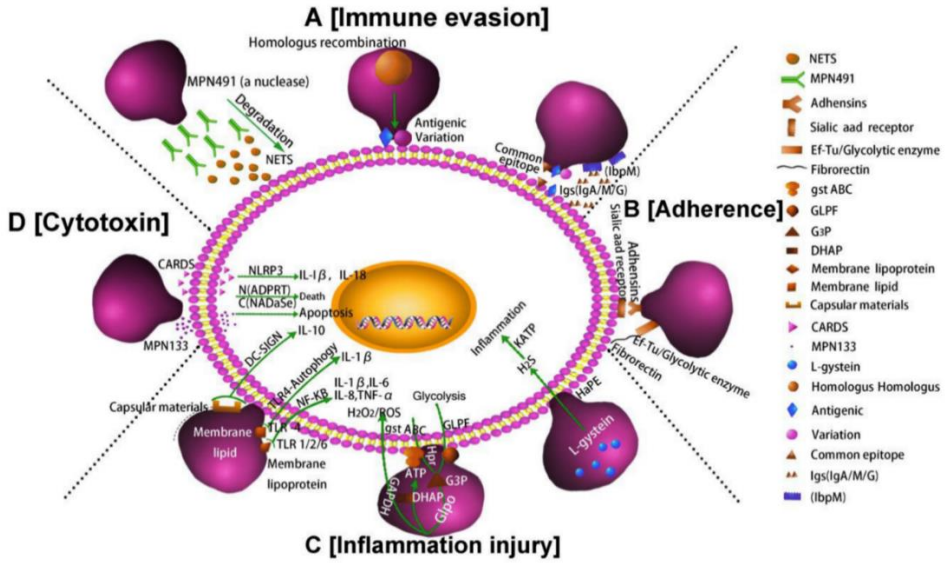

Figure GI. 2.4_1. Pathogenic mechanisms of *M. pneumoniae*. A) Nuclease and IbpM in *M. pneumoniae* enable immune evasion, and homologous DNA recombination leads to antigen variation. **B)** *M. pneumoniae* adhesion causes cell damage. Additionally, the P1 adhesin protein binds to the sialic acid receptor on the host cell surface contributing to *M. pneumoniae* adherence and gliding. Furthermore, elongation factor Tu (EF-Tu) can bind strongly to a diverse range of host molecules (such as fibronectin), contributing to adhesion. **C)** Inflammation-inducing factors (HapE enzyme, oxidase GlpO, membrane lipids, lipoproteins, and capsular materials) activate host cell inflammatory pathways. **D)** *M. pneumoniae* secretes cytotoxic nuclease (catalytic protein encoded by MPN133) and CARDS toxin. Image from **Jiang Z. *et al*., 2021**.

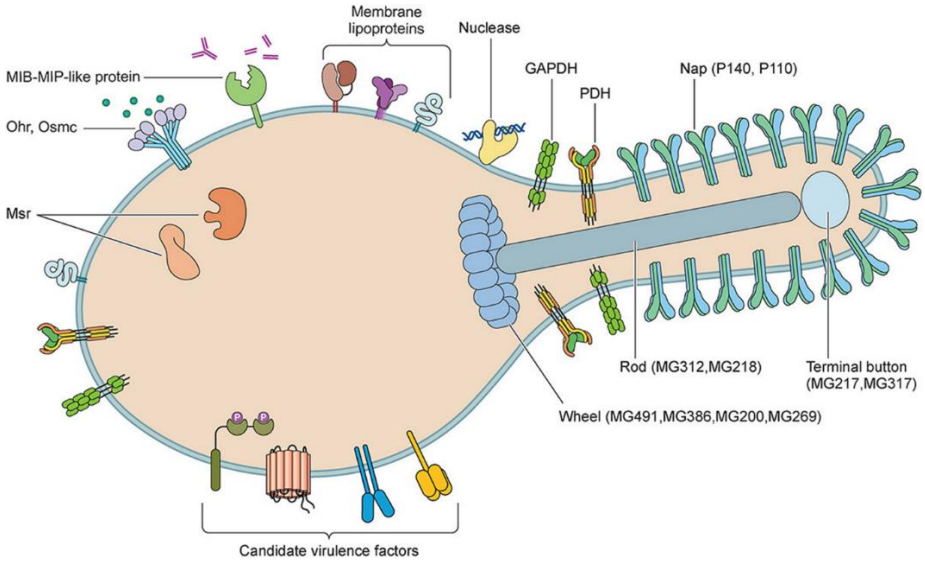

Figure GI. 2.4_2. Diagrammatic representation of the pathogenic components of *Mycoplasma genitalium*. The pathogenesis and virulence of *M. genitalium* include invasiveness, toxic nuclease, and membrane lipoproteins. Numerous factors contribute to invasiveness, including proteins involved in adhesion, gliding motility, and antigenic variation, detoxifying enzymes involved in immune evasion (methionine sulphoxide reductase (Msr), organic hydroperoxide reductase (Ohr), osmotically inducible protein C (OsmC), and immunoglobulin proteases), and biofilms involved in antibiotic resistance and persistent infection. Additionally, glycosyltransferase, serine/threonine kinase, and serine/threonine phosphatase are considered candidate virulence factors of *M. genitalium.* Image from **Yueyue W. *et al*., 2022**.

GI. 2.5. Treatment and vaccine development

At present, no vaccine is available for protection against *M. pneumoniae* or *M. genitalium* infections. The lack of cell wall in *M. pneumoniae* and *M. genitalium* greatly reduces the choice of current antibiotics. Treatment strategies for M. genitalium are based on the knowledge that it is susceptible to antibiotics belonging to the drug classes of macrolides, tetracyclines and quinolones[181] [**Renaudin H. *et al*., 1992**]. More recent studies have shown that a single dose of azithromycin is more effective than an extended dose of doxycycline. It has replaced the use of tetracyclines which were the first agents used to treat NGU before the recognition of *M. genitalium*[182,183] [**Haggerty C. *et al*., 2008; Björnelius E. *et al*., 2008**]. Failure of tetracyclines or older quinolones to treat *M. genitalium*-associated male urethritis has been recognised and persistent infection from poor efficacy has resulted in chronic NGU[184–187] [**Falk L. *et al*., 2003; Falk L. *et al*., 2004; Wikstrom A. and Jensen J. S., 2006; Jensen J.S., 2006**].

Treatment of *M. pneumoniae* infections on a case-by-case basis has been guided primarily by its well-known and consistent susceptibilities to drugs in the macrolide, tetracycline, and fluoroquinolone classes that are available for oral administration. Appreciation of *M. pneumoniae* as a significant respiratory tract pathogen and the numerous new drugs in the macrolide and fluoroquinolone classes that have become available since the early 1990s have led to the performance of several trials involving adults and children with community-acquired pneumonia in which the clinical efficacies of various antimicrobials were evaluated. Newer fluoroquinolones are being used extensively for treatment of respiratory tract infections in adults. However, fluoroquinolones are not recommended for use in children due to possible toxicity to developing cartilage[188] [**Ferwerda A. *et al*., 2001**].

Furthermore, the increased number of refractory infections caused by macrolide-resistant *M. pneumoniae* makes clinical treatment extremely difficult, especially for children. Although the mortality and disability rates caused by *M. pneumoniae* infection are low, complications, and even fatal pneumonia, can occur in susceptible individuals (children between 5–15 years, adolescents, and the elderly of more than > 60 years) in an epidemic area.

Multidrug resistance (MDR) strains are becoming frequent in Europe and are a real threat in regions as Australia (9.8% of the identified *M. genitalium* strains were MDR), Japan (30.8%) and China[189,190] [**Guo D. X. *et al*., 2019; Wang Y. *et al*., 2021**] mainly due to an inappropriate use of the current antibiotics[191] [**Braam J. F. *et al*., 2017**]. In consequence, treatment failures are becoming more common[91] [**Manhart L. E. *et al*., 2013**]. Despite that alternative antibiotics as pristinamycin and solithromycin are being employed to treat MDR infections, further studies are needed to determine optimal dosages for those antibiotics in order to achieve clinical cure and

prevent the appearance of new resistances[192] [**Couldwell D. L. and Lewis D. A., 2015**]. This emphasizes the urgent need of effective vaccines for preventing *M. genitalium* and *M. pneumoniae* infections.

There are various types of *M. pneumoniae* vaccines including inactivated, live-attenuated, and subunit vaccines. These vaccines are mainly administered via the nasal route or hypodermic needle. Whole-cell vaccines can be either inactivated or live-attenuated vaccines. Inactivated vaccines were found to elicit weak immune responses, and some individuals who did not produce antibodies after vaccination experienced severe immune responses on reinfection with *M. pneumoniae*. Vaccines based on M*. pneumoniae* adhesion proteins (P1, P30 and P116) have been considered as promising options. Hypodermic inoculation with a protein subunit vaccine results in effective immune protection[193] [**Zhang Q. *et al*., 2011**]. However, the generation of a protein subunit vaccine can be challenging because they are accompanied by several inevitable shortcomings and technical difficulties. (1) The protein expression level in vitro is usually very low. Besides, purification of recombinant proteins is a complicated process[194,195] [**Lahiry A. *et al*., 2018; Yu H. *et al*., 2016**]. (2) Protein subunit vaccines do not have a self-replicating ability compared with live attenuated vaccines or DNA vaccines, so multiple immunization is usually required[196] [**Fitch W. M. *et al*., 1993**]; (3) The protein subunit may lose its natural conformation when being expressed in heterologous systems[197] [**Pal S. *et al*., 2001**]. DNA vaccines trigger both cell-mediated and humoral immunity, but the injected DNA cannot be consistently replicated in mammalian cells. These challenges need to be overcome in the future to develop effective vaccines.

M. pneumoniae infections in immunocompetent patients induce antibody responses that mainly direct against the terminal organelle-associated proteins in *M. pneumoniae*[198] [**Dumke R. and Jacobs E., 2016**]. Thus, vaccine based on this adhesin can induce specific immunoglobulins that inhibit the adherence of *M. pneumoniae* to the respiratory epithelium of the host[198] [**Dumke R. and Jacobs E., 2016**]. However, due to their weak humoral immunogenicity when used alone without aluminium adjuvant, a fusion protein with an adjuvant, such as hepatitis B virus capsid HN-144 fragment, is a preferred immunization strategy. Although live vector vaccines (LVVs) using probiotics as expression vectors are still in its exploratory stage, it is believed that LVV could be a promising vaccine strategy against *M. pneumoniae* infections in the near future. Regardless of the vaccine type, the immunogenicity, safety, effectiveness, and functional mechanisms of vaccines used in humans need to be thoroughly researched before further clinical trials can be commenced.

Furthermore, prioritizing the characterization of surface-exposed antigenic epitopes, which are crucial for antibody-mediated elimination, is essential for the potential development of successful drugs and vaccines targeting bacterial pathogens[199] [**Nogueira W. G., *et al*., 2021**]. Reverse vaccinology, a powerful strategy that has transformed the landscape of vaccine development, offers a promising approach to address this urgency[200] [**Moxon R. *et al*., 2019**]. This innovative approach enables the systemic prediction and selection of antigens, primarily focusing on both T-cell and B-cell epitopes, which have the potential to trigger a robust immune response against the pathogen[201] [**Khan S. *et al*., 2022**]. A very recent study also proposes a new computational pipeline, , to identify immunogenic epitopes and design peptide vaccines with optimized T-cell and B-cell epitopes that target specific antigens of *M. genitalium*[202] [**Akter A. *et al.,* 2024**].

GI. 2.6. Immune evasion strategies and antigenic variation of minimal cells

Pathogenic mycoplasmas continuously evolve due to the pressure of host immune system as well as the use of antibiotic drugs. Antigenic variation is one of the most common strategies employed by pathogenic microorganisms to evade immune surveillance is. and is successfully employed by various bacterial pathogens, including *Neisseria* spp.*, Mycoplasma* spp.*,* and *Treponema pallidum*[203] [**Vink C. *et al*. 2012**]. It is also effectively used by viral pathogens, such as influenza virus[204] [**Shao W. *et al*. 2017**]. Antigenic variation leads to continuous alterations or modifications of the surface molecules that are mainly targeted by the host immune systems. Consequently, the humoral (antibody) response generated against the previous ("old") surface molecules cannot effectively recognize and neutralize the modified ("new") molecules, allowing the pathogen to persist in the infected host for a prolonged period of time[205,206] [**Dehon P. M. and McGowin C. L. 2017; Qin L. *et al*. 2019**].

Despite their reduced genomes and limited set of genes, mycoplasmas have developed a wide range of strategies to generate variants of their surface exposed proteins. Generally, all strategies are based on rapid and reversible genetic changes that can produce variants in a combinatorial manner. These strategies include DNA slippage, site-specific recombination, gene rearrangement, gene conversion and reciprocal recombination[207] [**Citti C. *et al*., 2010**].

Antigenic variation is also hypothesized to be involved in the repeated epidemics caused by *M. pneumoniae*[208] [**Dumke R. *et al*. 2008**]. In this species, as well as in *M. genitalium,* this antigenic variation is predicted to be generated through homologous recombination between specific, repetitive DNA elements that are dispersed throughout their genomes[34] [**Rocha E. P. and Blanchard A. 2002**]. These repetitive elements encode the antigenic surface molecules P1 and MgPa of *M. pneumoniae* and *M. genitalium*, respectively (**Figure GI. 2.6_1**).

While antigenic variation through homologous recombination may be crucial for the propagation of *Mycoplasma* species in human populations, a major issue for these organisms is the maintenance of the integrity of their genomes, in particular because these genomes are much more compact than the genomes of most other bacterial taxa. Interestingly, the DNA repair systems that are involved in maintaining genome integrity may also be involved in the recombination between repetitive DNA elements. Consequently, the DNA repair machinery of these organisms may be directly involved in antigenic variation. Remarkably, the recombination of MgPa repeats that generates phase and antigenic variation in *M. genitalium* is promoted by an alternative sigma factor encoded in the *mg428* gene[209,210] [**Torres-Puig S. *et al.*, 2015; Torres-Puig S., 2017**]. Notably, mutants lacking MG428 were defective in generating *mg191mg192* (P140 and P110 gene) variants[211] [**Burgos R. and Totten P. A. 2014**]. Interestingly, overexpression of MG428 increased expression of *ruvA, ruvB, recA,* as well as other genes, and was associated with increased P140 and P110 gene variation[209,211] [**Burgos R. and Totten P. A. 2014; Torres-Puig S. *et al.* 2015**]. These findings highlight the complexity of the regulation of recombination events in *M. genitalium,* and possibly in *M. pneumoniae.*

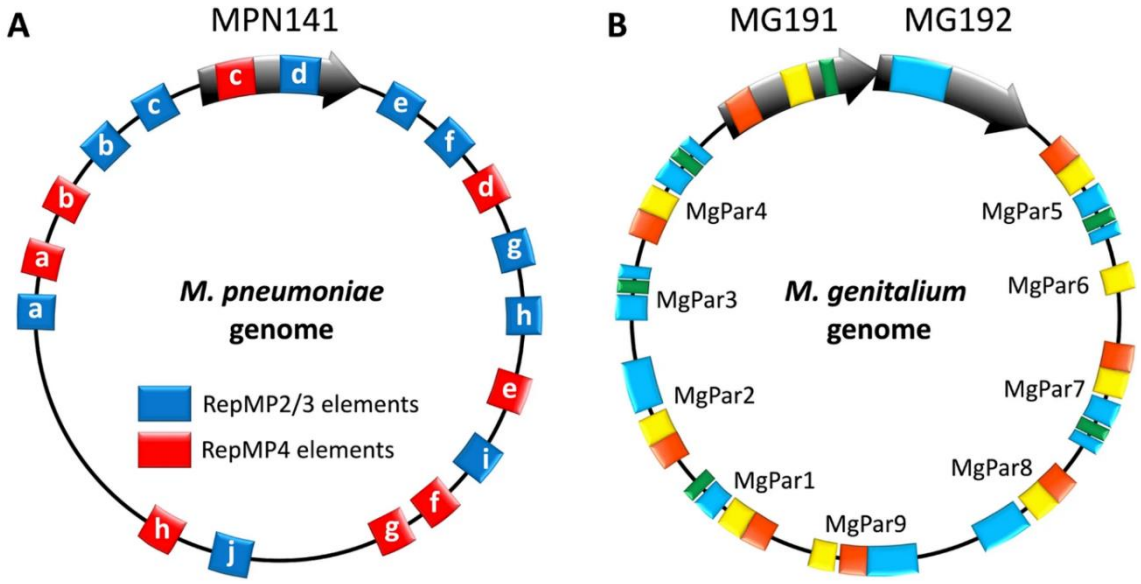

Figure GI. 2.6_1. Repetitive elements in the genome of *Mycoplasma pneumoniae* and *Mycoplasma genitalium*. A) The P1 gene (ORF MPN141) of *M. pneumoniae* contains two variable DNA elements, RepMP2/3 and RepMP4. Multiple variants of RepMP2/3 and RepMP4 elements are dispersed within the genome of *M. pneumoniae*. There are ten variants of RepMP2/3 and each variant is labeled 'a' to 'j' in blue. For RepMP4, there are eight variants and each variant is labeled 'a' to 'h' in red. **B)** The MgPa operon of *M. genitalium* contains two variable genes, *mgpB* (ORF MG191) and *mgpC* (ORF MG192). There are three MgPar homologous regions within the MG191 gene, indicated as repeat regions B (orange), EF (yellow), and G (green), while there is only one, large MgPar homologous region within the MG192 gene, indicated as repeat region JKLM (light blue). Invariable, conserved regions within each gene are indicated in black. Nine homologous MgPar sequences, containing diverse copies of *mgpB*- and *mgpC*-associated homologous regions, are present in the genome of *M. genitalium*. Homologous sequences are indicated in the same colour. Image from **Hakim M. S. *et al.*, 2021**.

The genomes of *M. pneumoniae* and *M. genitalium* contain a significant amount of repeated DNA regions, approximately a fraction of 8% and 4% of the genome, respectively[48,212] [**Himmelreich R. *et al*. 1996; Peterson S. N. *et al*. 1993**]. These repeated elements, which are dispersed throughout the genome, display a high level of sequence similarity, but are not identical. In *M. pneumoniae,* these regions are referred to as Rep MP (RepMP2/3 and RepMP4) elements; while in *M. genitalium* they are named MgPa repeats (MgPars)[2,213–215] [**Fraser C. M. *et al*. 1995; Peterson S. N. *et al*. 1995; Ruland K. *et al*. 1990; Su C. J. *et al*. 1988**]. Interestingly, some of the copies of the repeated DNA elements were found to form part of genes encoding antigenic surface proteins. Among these proteins are the cytadhesins P1 and P40/90 of *M. pneumoniae*[48] [**Himmelreich R. *et al.* 1996**] and P140 and P110 of *M. genitalium*[2,75] [**Aparicio D. *et al*. 2018; Fraser C. M. *et al.* 1995**]. It has been demonstrated that the repeated DNA elements can undergo homologous DNA recombination, which may result in sequence variation, such as the antigenic variation of the cytadhesins proteins[213,214,216,217] [**Ma L. *et al*. 2007; Peterson S. N. *et al*. 1995; Ruland K. *et al*. 1990; Spuesens E. B. *et al*. 2009**], allows the generation of a virtually unlimited set of antigenic variants of these adhesins.

For *M. pneumoniae*, it has been hypothesized that homologous recombination between RepMP elements may occur through gene conversion-like processes. This hypothesis was supported by analysis of the RepMP elements from a collection of 23 *M. pneumoniae* isolates. Sequence analysis of all 10 variants of RepMP2/3 and all 8 variants of RepMP4 from these isolates indicated that one or more 'donor' RepMP variants appeared to have been copied to other ('recipient') RepMP variants, including those located within the P1 operon[217] [**Spuesens E. B. *et al*. 2009**]. The same phenomenon was also observed among RepMP5 variants, resulting in amino acid changes in another surface-exposed cytadhesin protein, named P40[218] [**Spuesens E. B. *et al*. 2011**]. In addition, analysis of an additional set of 23 *M. pneumoniae* clinical isolates also showed a significant rate of reorganization through recombination events between these repetitive elements[112] [**Lluch-Senar M. *et al*. 2015**].

Sequence analysis of the *M. genitalium mgpB* (*MG_191*) and *mgpC* (MG_192) genes coding for adhesins P140 and P110 strongly supports the hypothesis that recombination with MgPar sequences results in antigenically diverse adhesin variants both in vitro and in clinical isolates[216,219–222] [**Fookes M. C. *et al.* 2017; Iverson-Cabral S. L. *et al*. 2006, 2007; Ma L. *et al*. 2007, 2014**]. In an experimental chimpanzee model of *M. genitalium* infection, sequence variation within the *mgpC* gene initially occurred within five weeks post infection and accumulated progressively[223] [**Ma L. *et al.* 2015**]. Interestingly, in the majority of the cases, MgPa recombination events in *M. genitalium* were found to be caused by reciprocal DNA

recombination events, in contrast to the homologous recombination events found in *M. pneumoniae*, which all appeared to have resulted from gene conversion events. Another difference between the recombination processes in these mycoplasmas is that recombination events occur at a significantly higher frequency in *M. genitalium* than in *M. pneumoniae*[203] [**Vink C. *et al*. 2012**].

Because both the *M. pneumoniae* P1 protein and the *M. genitalium* P140 protein are highly immunogenic[224] [**Razin S. and Jacobs E. 1992**], the recombination-induced antigenic variation of these proteins may play a crucial role in the pathogenicity. Consequently, antigenic variation may be a critical factor in allowing *M. pneumoniae* and *M. genitalium* to persist in infected humans for prolonged periods of time[203,220,225,226] [**Atkinson T. P. *et al*. 2008; Hardy R. D. *et al*. 2002; Iverson-Cabral S. L. *et al*. 2006; Vink C. *et al*. 2012**]. In support of this notion, persistent infections with these bacteria were observed in animal models of infection[226–228] [**Hardy R. D. *et al*. 2002; McGowin C. L. *et al*. 2010; Wood G. E. *et al*. 2017**]. In addition, the antigenic variation of P1 and MgPa proteins are surface-exposed proteins that function in the attachment of the bacteria to host cells[222] [**Ma L. *et al*. 2014**].

GI. 2.7. Transformation of mycoplasmas and available genetic tools for the study of minimal cells.

Despite their lack of cell wall, transformation of mycoplasmas with exogenous DNA has proven to be problematic, probably due to the high activity of mycoplasma membrane nucleases[229] [**Minion F. C. *et al.*, 1993**] and the presence of R-M systems[230] [**Dybvig K. *et al.*, 1998**]. First reported transformation of mycoplasmas was achieved via PEG in *M. pulmonis* using the Tn*916* transposon derived from *Enterococcus faecalis* encoding the tetracycline resistance marker *tetM*[231] [**Dybvig K. and Cassell G. C., 1987**]. Since then, several gene delivery systems have been developed, for instance calcium chloride treatment followed by PEG[232] [**King K. W. and Dybving K., 1991**], liposome-mediated delivery[233] [**Minion F. C. and Kapke P. A., 1998**] or electroporation[234] [**Hedreyda C. T. *et al.*, 1993**]. Transformation protocols vary depending on the mycoplasma species and usually requires relatively hight amounts of DNA.

Mycoplasmas have evolved from Gram-positive ancestors by a process of massive genome reduction until being self-replicating organisms with the smallest genomes known[42] [**Weisburg W. G. *et al.*, 1989**]. Due to this evolutionary reduction process, they are the most suitable cells for the study of minimal genes essential for the life and determine the unsolved question of which is the minimal set of genes required for life[141,235] [**Glass J. I. *et al.*, 2006; Xavier J. C. *et al.*, 2014**].

However, despite their suitability for these studies, available genetic tools for engineering these microorganisms are limited. Replicative plasmids are only functional in some mycoplasmas species such as *Mycoplasma hyopneumoniae*[236] [Maglennon G. A. *et al.*, 2013], *Mycoplasma capricolum* subs. *Capricolum, M. pulmonis*[237] [Cordova C. M. *et al.*, 2002], *Mycoplasma gallisepticum*[238] [Lee S. W. *et al.*, 2008], *Mycoplasma imitans*[239] [Lee S. *et al.*, 2008], *Mycoplasma agalactiae* and *Mycoplasma bovis*[240] [Sharma S. *et al.*, 2015] while site directed mutagenesis by homologous recombination is also limited to *M. genitalium*[241] [Dhandayuthapani S. *et al.*, 1999], *M. pulmonis*[242] [Mahairas G. G. and Minion F. C., 1989a] and some strains of *M. pneumoniae*[243] [Krishnakumer R. *et al.*, 2010]. Therefore, the most extended technique is the use of transposons and minitransposons to deliver the desired sequences and to isolate randomly truncated mutants[244–246] [Pich O. Q. *et al.*, 2006a; Hasselbring B. M. *et al.*, 2006a; Pich O. Q. *et al.*, 2006b]. Moreover, all of these techniques rely on the introduction of an antibiotic resistance gene and genetic modifications in the same strain will be limited to the number or selective markers available and phenotypic analyses can be biased by the presence of selectable markers. For mycoplasmas four antibiotic resistance genes have been reported conferring resistance to gentamycin, tetracycline, chloramphenicol and puromycin[231,247–249] [Mahairas G. G. and Minion F. C., 1989b; Dybvig K. and Cassell G. C., 1987; Hahn T. W., *et al.*, 1999; Algire M. A. *et al.*, 2009].

The basic tools for functional genomic analyses in M. *genitalium* are mostly limited to random mutagenesis with transposons and targeted mutagenesis by allele exchange. Targeted gene disruption through homologous recombination with a suicide plasmid was first described in *M. genitalium* twenty years ago[241] [Dhandayuthapani S. *et al.*, 1999]. This is not a common feature among mycoplasmas, as the generation of mutants in this species was strictly associated with the laborious process of random mutagenesis and screening. Notably, in the closely related species *M. pneumoniae*, double crossover events are rare and strain-specific[243] [Krishnakumar R. *et al.*, 2010]. To cope with these problems, a phage recombinase from *Bacillus subtilis* has been engineered for oligo recombineering in *M. pneumoniae* (Piñero-Lambea et al 2020 ACS Synth. Biol. 2020, 9, 1693−1704). This system allows to obtaining targeted genome modifications very efficiently when used in combination with the Cas9 enzyme and a guide RNA directed to sequence to be deleted or modified. While this system provides a generic method for targeted mutagenesis in mycoplasmas, the Cas9 enzyme is not selective enough to effciently counterselect small modifications like single point mutations.

Random mutagenesis by transposon delivery has been the main genetic tool available for mycoplasmas. The most widely used transposon in mycoplasma has been the Tn4001 isolated from *Staphylococcus aureus*[250] [Lyon B. R. *et al.*, 1984], which was later successfully proved in

M. pneumoniae[234] [Hedreyda C. T. *et al.*, 1993] and also in *M. genitalium*[251] [Reddy S. P. *et al.*, 1996]. This transposon was used for the first global transposon mutagenesis in *M. genitalium*[140] [Hutchison C. A. *et al.*, 1999]. Its instability once transposed (probably due to an inadequate expression of the transposase) was later improved with the creation of the MiniTn4001, in which the transposase was placed outside the inverted repeats to diminish unwanted transposition events[252] [Pour-El I. *et al.*, 2002]. The MiniTn4001 transposon was then further optimized for *M. genitalium*[244] [Pich O. Q. *et al.*, 2006b]. A new transposon which transformation efficiency is reportedly higher than the MiniTn4001 was recently engineered[253] [Montero-Blay A. *et al.*, 2019]. In this transposon, the regulatory region of the transposase and the selectable marker are changed to improve their transcription in a broad range of *Mycoplasma* species.

Due to the lack of cell wall, there are few selectable markers available in mycoplasmas. In *M. genitalium*, the three most widely-used antibiotic resistance markers have been the *tetM* gene providing tetracycline resistance, the aac(6')-aph(2'') gene providing aminoglycoside resistanceand the *cat* gene for chloramphenicol resistance. Few years ago, a new functional marker in *M. genitalium* was described: the pac gene from *Streptomyces alboniger*[249] [Algire M. A. *et al.*, 2009] which codes for puromycin *N*-acetyltransferase .

In the last ten years, there has been an increasing development and adaptation of genetic tools for use in mycoplasmas. The discovery of functional extrachromosomal DNA elements could represent a breakthrough in mycoplasma studies. Although replicative plasmids were observed in *M. mycoides*[254] [Bergemann A. D. *et al.*, 1989], the evidence of these elements in mycoplasmas was scarce. However, studies with constructed oriC plasmids in different mycoplasma species[255] [Lartigue C. *et al.*, 2003] laid the groundwork for more recent publications reporting the creation of several oriC plasmids for many mycoplasma species: there are now functional replicative plasmids for *M. gallisepticum*[238] [Lee S. W. *et al.*, 2008], *M. synoviae*[256] [Shahid M. A. *et al.*, 2014], *M. bovis*[257] [Li J. *et al.*, 2015], *M. hyopneumoniae*[258] [Ishag H. Z. A. *et al.*, 2016] and *M. hyorhinis*[259] [Ishag H. Z. A. *et al.*, 2017]. Until recently, though, there were no stable extrachromosomal DNA elements described in *M. genitalium*. Two years ago, it was reported that a replicative plasmid containing the oriC of *M. pneumoniae* could be used in *M. genitalium*[260] [Blötz C. *et al.*, 2018]. Unfortunately, previous experiments in this laboratory with oriCplasmid revealed high rates of chromosome integration[210] [Torres-Puig S. *et al.*, 2017]. Moreover, the Cre-lox technology was adapted to *M. genitalium* in our laboratory[261] [Mariscal M. *et al.*, 2016]. This could be of great relevance for future studies in *M. genitalium*, as it provides the possibility of unmarked genetic modifications in a bacterium with a limited pool of functional selectable markers, thus allowing consecutive rounds of genome edition. To ensure a tight control of the Cre recombinase, its transcription was under the control of a modified

version of the inducible promoter P*xyl*/*tet*O2, previously described as functional in *M. agalactiae*[262] [**Breton M. *et al*., 2010**].

Finally, the promising CRISPRi (CRISPR interference) technology has also been studied in our laboratory. This is a modification of the CRISPR system that uses a Cas9 without endonuclease activity. Therefore, when this modified Cas9 is co-expressed with a guide RNA, it is able to effectively repress the expression of several target genes[263] [**Qi L. S. *et al*., 2013**]. This method was proved in *M. pneumoniae* and targeted gene regulation was achieved[264] [**Mariscal M. *et al*., 2018**]. The generation of knockdowns could be of major interest when studying essential genes encoded in the *M. genitalium* genome.

GI. 3. Cytoskeleton: a unique morphology and cell structure

GI. 3.1. A complex ultrastructure: the terminal organelle (TO)

Some *mycoplasma* species present a characteristic tip structure or a protrusion at one of the poles of the cell. It is called terminal organelle (TO) or attachment organelle in the members of *pneumoniae* cluster[265] [Hatchel J. M. and Balish M. F., 2008]. The TO has been traditionally studied in *M. pneumoniae* and *M. genitalium* cells (Figure GI. 3.1_1). This organelle hides a unusually complex cytoskeletal structure and is involved in pivotal functions like adhesion, gliding motility, cell division and virulence.

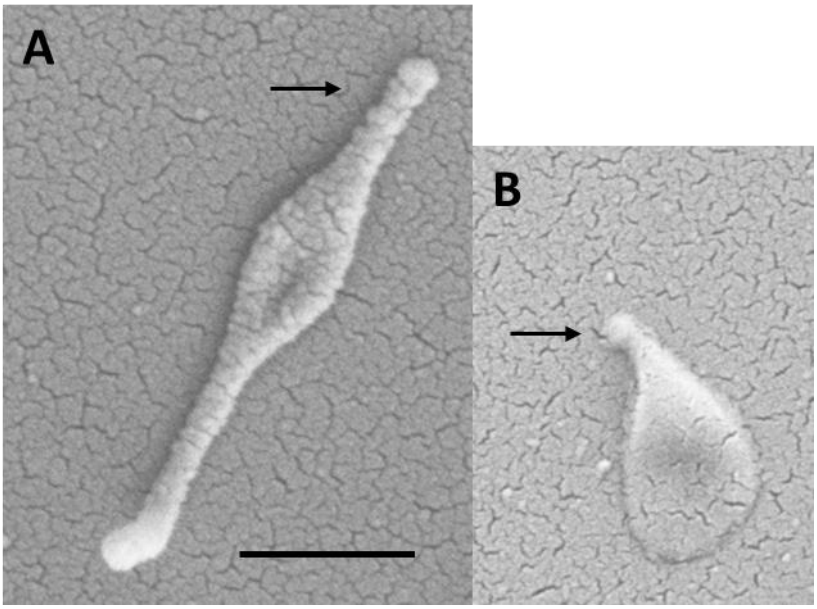

Figure GI. 3.1_1. Scanning electron (SEM) micrographs of *M. pneumoniae* (A) and *M. genitalium* (B) cells. Terminal organelle is pointed with a black arrow. Images are shown at the same magnification. Scale bar 500 nm.

M. pneumoniae cytoskeleton was first observed in 1980 using different chemicals to remove the cell membrane, allowing the observation of the internal structure[266] [Meng K. E. and Pfister R. M., 1980]. Further studies by Cryo electron tomography (Cryo-ET) improved the resolution of the different substructures forming the attachment organelle and generated 3D reconstructions of the electron-dense core[267–269] [Seybert A. *et al.*, 2006; Henderson G. P. and Jensen G. J., 2006; Kawamoto A. *et al.*, 2016]. Based on these studies, four substructures conforming the cytoskeleton can be identified: the adhesion complexes in the surface, the terminal button in the most apical region, the segmented paired plates (also called rod) in the central region and the wheel or bowl complex in the most proximal part. It must be stated that this electron-dense core is surrounded by an electron-lucent area, suggesting the absence of proteins in this area (Figure GI. 3.1_2).

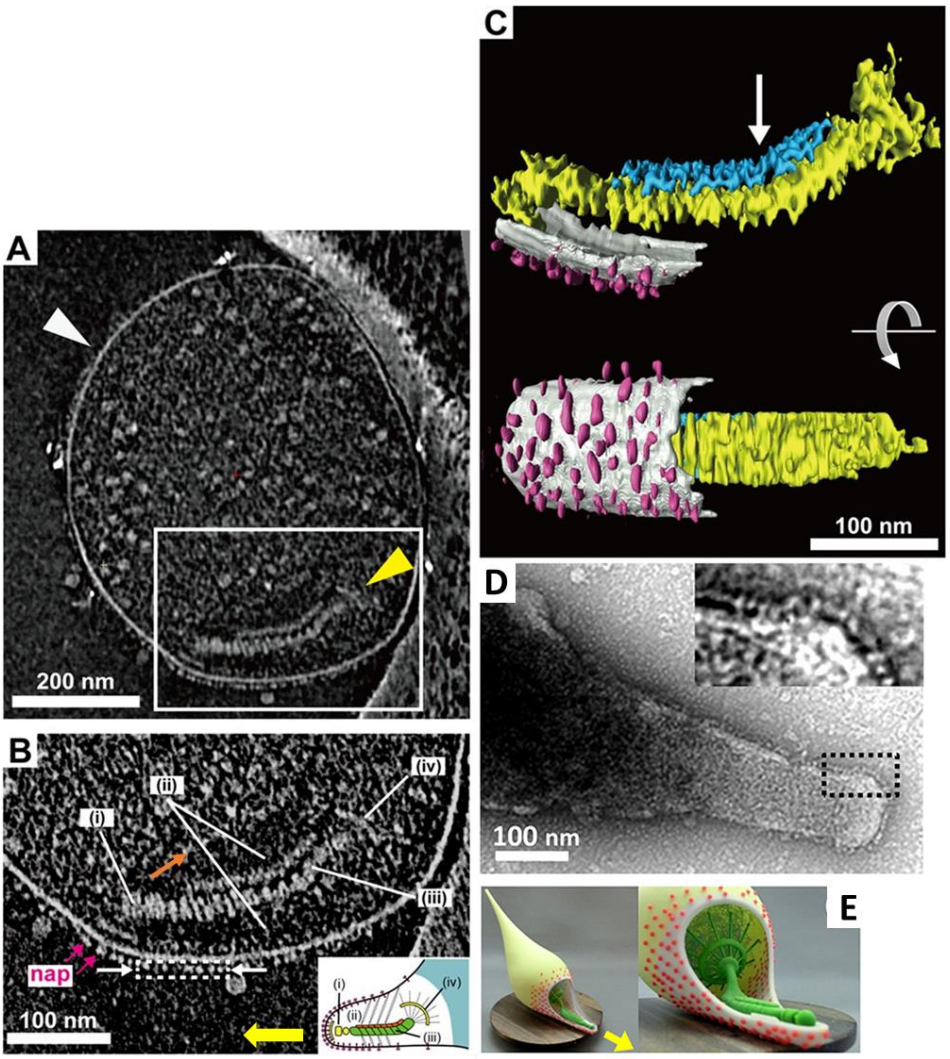

Figure GI 3.1_2. *M. pneumoniae* terminal organelle (TO) image reconstituted ultrastructure visualized by electron microscopy (EM). A) Images of 15-nm-thick slices through the tomograms of wild-type cells. The TO can be observed in the white box. **B**) Image of a 16-nm-thick slice through the tomogram of a TO. Top: the image shows a dense array of the knoblike particles on the membrane surface (Nap) and the terminal button (i), translucent area (ii), paired plates (iii), and bowl (wheel) complex (iv). The outline of the translucent area is marked with an orange arrow. Inset: schematic diagram of the TO. **C**) Rendered three-dimensional image of the tomogram shown in **B** depicting the knoblike particles (pink), membranes (light gray), and thin (blue) and thick (yellow) plates of the internal core. The bend is marked with an arrow. **D**) Nap structure. The area outlined by the dashed box is magnified in the inset. **E**) Schematic three dimensionally model of cell structure. The surface and internal structures of the TO are coloured red and green, respectively. The upper side of the cell membrane on the TO is omitted to show the internal structures. The gliding direction is shown by a yellow arrow. Images adapted from **Kawamoto A. *et al*., 2016 and Nakane D. *et al*., 2011**.

High-resolution studies of the *M. genitalium* terminal organelle have been also performed. The treatment of *M. genitalium* cells with Triton X-100 to isolate the cytoskeleton structure shows a terminal organelle morphology very similar to its close relative *M. pneumoniae* with the difference of a less defined electron lucent area surrounding the terminal organelle[270] [**Gonzalez-Gonzalez L., 2015**] (**Figure GI. 3.1_3**).

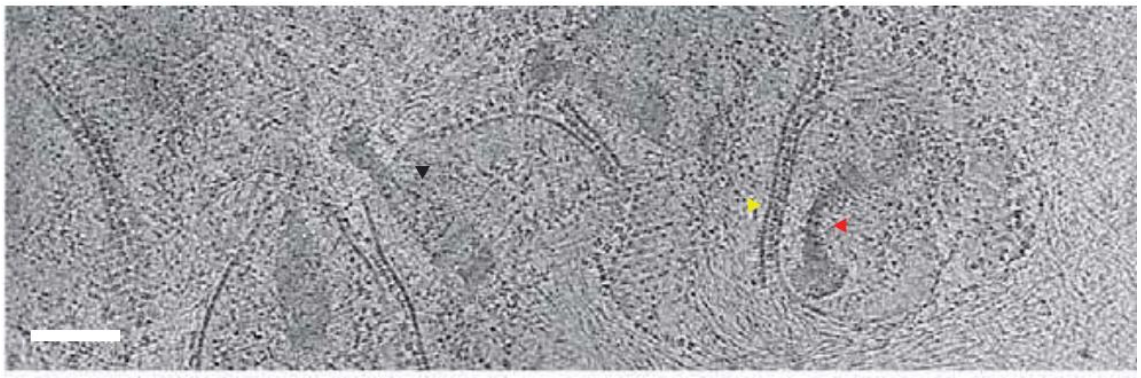

Figure GI. 3.1_3. General view of ghost cells from *M. genitalium* by Cryo-electron microscopy. The image shows the average projection of fifteen 0.85 nm thick slices through the reconstructed volume of G37 ghost cells treated with Triton-X-100. Black arrowhead indicates top view of the cytoskeleton. Red arrowhead points a side view of the terminal organelle. Yellow arrowhead indicates a junction of a Nap with the adjacent mycoplasma membrane. Scale bar 100 nm. Image from **Gonzalez-Gonzalez L., 2015**.

Table GI. 3.1_1 Orthologue terminal organelle proteins of *M. genitalium* and *M. pneumoniae*.

M. genitalium		*M. pneumoniae*			
Locus	Protein	Locus	Protein	Identity (%)	Function
MG_053	ManB	MPN_066	CpsG	62	Gliding
MG_191	P140	MPN_141	P1	45	Adhesion
MG_192	P110	MPN_142	P40/P90	50	Adhesion
MG_200	MG200	MPN_119	TopJ	35	Gliding
MG_217	MG217	MPN_309	P65	42	Gliding
MG_218	HMW2	MPN_310	HMW2	57	Adhesion
MG_219	MG219	MPN_312	P24	16	Gliding
MG_239	Lon	MPN_332	Lon	78	Gliding
MG_269	MG269	MPN_387	MPN387	49	Gliding
MG_312	HMW1	MPN_447	HMW1	33	Adhesion
MG_317	HMW3	MPN_452	HMW3	33	Adhesion
MG_318	P32	MPN_453	P30	43	Adhesion
MG_386	MG386	MPN_567	P200	30	Gliding
MG_491	P41	MPN_311	P41	53	Gliding

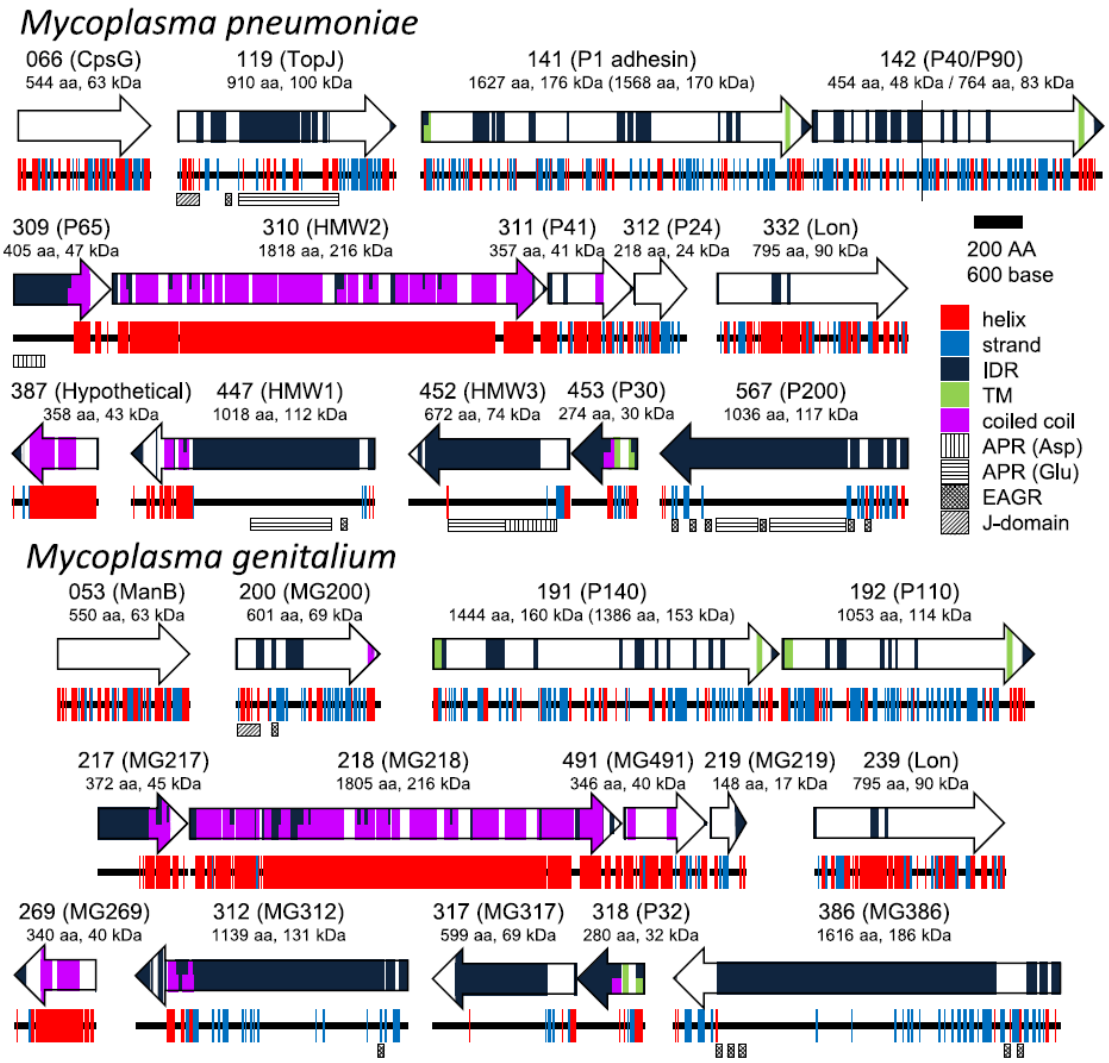

Figure GI. 3.1_4. Protein components of the terminal organelle (TO). Fifteen and fourteen proteins coded in nine loci on the genome are presented with their MPN (*M. pneumoniae*) and MG (*M. genitalium*) codes, respectively and the protein name. α-helix (helix), β-strand (strand), intrinsically disordered region (IDR), transmembrane segment (TM), coiled coil, Aspartic acid, and Proline rich region (APR Asp), Glutamic acid and Proline rich region (APR Glu), Enriched in Aromatic and Glycine Residues (EAGR), and the J-domain are predicted and marked. The amino acid number and predicted mass are shown beneath the protein name. The size after processing is shown in parentheses for MPN141 (P1 adhesin) and MG191 (P140). The cleavage site between P40 and P90 is shown by a broken line. *M. pneumoniae* and *M. genitalium* are presented as upper and lower panels, respectively. Image from **Miyata M. and Hamaguchi T., 2016**.

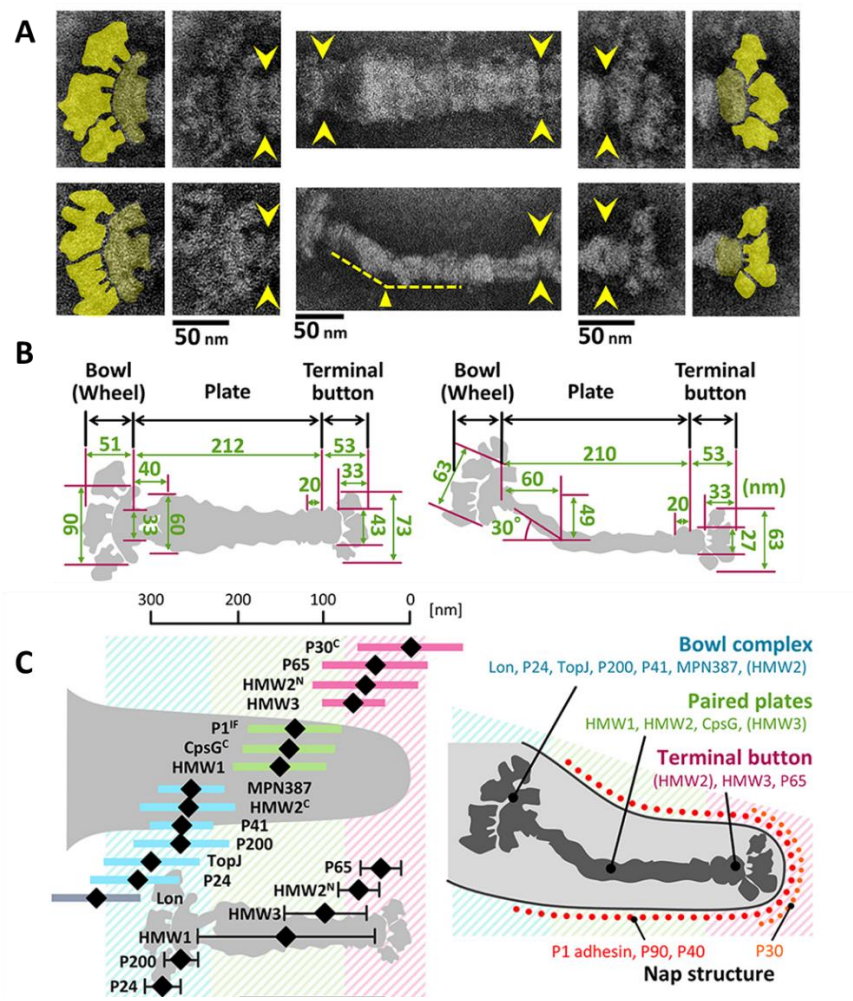

Figure GI. 3.1_5. Structure and scheme of component proteins localized in the terminal organelle (TO). **A)** Negative staining EM images of the isolated internal core of the TO. Structural features of the internal core. Top and side views of the structures are shown in the upper and the lower panels, respectively. Yellow arrowheads indicate the boundaries between the core components. The original and coloured images are shown in the adjacent panels for the bowl complex and terminal buttons in the left and the right, respectively. The thin plate is not visible in this preparation. A bend is observed in the side view around 60 nm from the back end, as marked by the yellow triangle. **B)** Schematics and dimensions of bold (left) and slim (right) types of internal core averaged for 40 structures extracted from A images. **C)** Mapping and assignment of component proteins on the TO. *M. pneumoniae* protein positions based on EYFP fluorescence microscopy. The average position in individual cells and standard deviation relative to the cell edge are plotted with a black diamond and a coloured bar, respectively. The mapping data based on immuno EM are plotted as a black diamond with a black bar in the lower. The proteins are mapped onto three localization groups, the terminal button (pink), the paired plates (green), and the bowl complex (blue). Images from **Miyata M. and Hamaguchi T., 2016** modified from **Nakane D. *et al*., 2015**.

GI. 3.2. Proteins involved in the terminal organelle structure

As schematized in **Figure GI. 3.1_4**, , 15 proteins have been identified to date as components of the terminal organelle[147,271–273] [**Krause D. C. and Balish M. F., 2004; Miyata M. and Nakane D., 2013; Balish M. F., 2014; Nakane D. *et al*., 2015**]. Each protein has been mapped on the organelle image systematically in nanometer order by fluorescence microscopy and immuno

EM[271], as shown in **Figure GI. 3.1_5C** [**Nakane D. *et al*., 2015**]. The features of this organization are grouped and summarized in **Figure GI. 1.3_4**, including a new concept, intrinsically disordered region (IDR), which cannot form a stable three dimensional structure but can achieve it when it binds to other structures[274] [**Dyson J. H. and Wright P. E., 2005**]. Interestingly, the sequences of P65 (MPN309), HMW1 (MPN447), HMW3 (MPN452), P30 (MPN453), and P200 (MPN567) are mostly predicted as IDR. In **Figure GI. 3.2_1** all of 15 proteins are assigned onto the schematic structure of the attachment organelle, based on the information that is currently available in *M. pneumoniae* and *M. genitalium*.

The protein composition of the cytoskeleton has been studied also by obtaining mutant strains that present deficiencies in the terminal organelle structure or function and by proteomic approaches after detergent treatment to isolate the cytoskeleton[70,71,154,245,246,275–287] [**Burgos R. *et al*., 2006; Pich O. Q. *et al*., 2006a; Burgos R. *et al*., 2007; Pich O. Q. *et al*., 2008; Burgos R. *et al*., 2008; Pich O. Q. *et al*., 2009; García-Morales L. *et al*., 2016; Párraga-Niño N. *et al*., 2012; Stevens M. K. and Krause D. C., 1992; Hahn T. W. *et al*., 1998; Balish M. F. *et al*., 2001; Krause D. C. and Balish M. F., 2001; Willby M. J. and Krause D. C., 2002; Willby M. J. *et al*., 2004; Hasselbring B. M. *et al*., 2006a; Chaudhry R. *et al*., 2007, Relich R. F. and Balish M. F., 2011; Cloward J. M. and Krause D. C., 2011**].

In *M. pneumoniae* these studies have been complemented with protein localization by immunofluorescence, immune electron microscopy and using autofluorescent protein fusion proteins tagging TO proteins[288–294] [**Seto S. and Miyata M., 2003; Balish M. F. *et al*., 2003; Seto S. *et al*., 2001; Hasselbring B. M. *et al*., 2006b; Kenri T. *et al*., 2004; Hasselbring B. M. and Krause D. C., 2007b; Cloward J. M. and Krause D. C., 2009**].

In *M. genitalium* the exact localization of terminal organelle proteins has been only determined for MG217 and P32[276,278] [**Burgos R. *et al*., 2008; García-Morales L. *et al*., 2016**]. The assignment of the other TO proteins to the different substructures is based in their homology to *M. pneumoniae* proteins (**Table GI. 3.1_1, Figure GI. 3.1_4 and GI. 3.1_5**) and in the phenotypic analyses of the mutant strains[295] [**Miyata M. and Hamaguchi T., 2016**].

Below are presented the proteins assigned to each substructure of the terminal organelles in basis of the previous studies cited. A drawing with the location of each protein is shown in **Figure GI. 3.1_5C**.

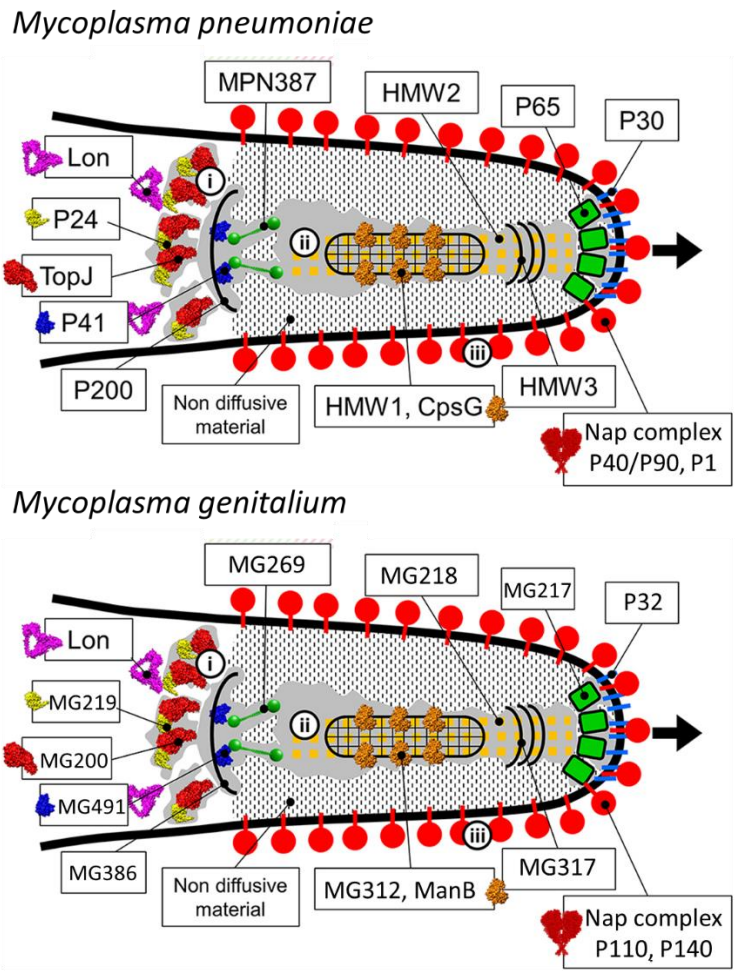

Figure GI. 3.2_1. Mapping and assignment of component proteins on the terminal organelle (TO). Assignment of the component proteins onto the schematic of the attachment organelle based on EM. *M. pneumoniae* and *M. genitalium* are presented as upper and lower panels, respectively. The gliding direction is shown by a black arrow. In the gliding mechanism, the force may be generated at the bowl complex (i), transmitted through the paired plates (ii), and modulated by the Nap adhesion complex (iii). Nap structure extracted from Aparicio D. *et al*., 2020 and Vizarraga D. *et al*., 2020 studies. The protein structures were predicted by Phyre2[296] [Kelley L. A. and Sternberg M. J. E., 2009] whenever possible. Images modified from Miyata M. and Hamaguchi T., 2016.

GI. 3.2.1. Nap

The Nap complex contains the adhesins and is located on the membrane surrounding the terminal organelle. It is formed by the P110 and P140 proteins in *M. genitalium*[270] [Gonzalez-Gonzalez L., 2015] and P1 and P40/P90 in *M. pneumoniae*[271] [Nakane D. *et al*., 2015]. In *M. pneumoniae* it has been determined that the Nap complex contains two molecules of P1 adhesin and two molecules of P40/P90[297,298] [Layh-Schmitt G. *et al*., 2000; Nakane D. *et al*., 2011] as well as for the P110 and P140 complex from *M. genitalium*[299] [Scheffer M. P. *et al*., 2017] (Figure GI. 3.2_2). These proteins are essential for cell adhesion (Burgos et at 2006) and real-time microscopy studies have shown that after the addition of anti-P1 antibody to *M. pneumoniae*

cells, gliding cells stopped just before to unbound from the glass surface[300] [Seto S. *et al.*, 2005]. Moreover, P110 and P140 proteins are required for terminal organelle development in *M. genitalium*[70,277] [Pich O. Q. *et al.*, 2009; Burgos R. *et al.*, 2006] and play a major role in gliding motility[278] [García-Morales L. *et al.*, 2016].

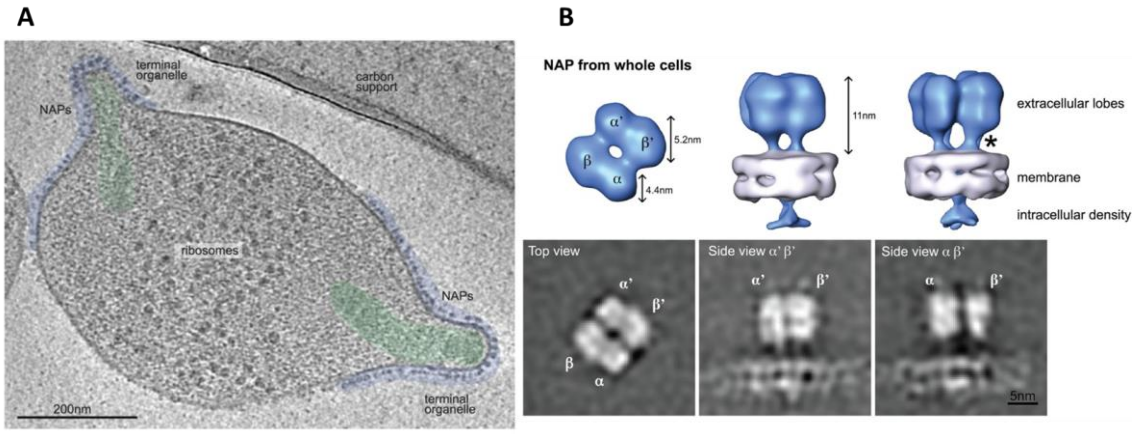

Figure GI. 3.2_2. Tomogram of an intact mycoplasma cell. A) Terminal organelle cores are highlighted in green and Nap complexes are highlighted in blue. The two terminal organelles observed in this cell are typical of mycoplasmas in division process. **B)** Sub-tomogram averages of the Nap complex by Cryo-ET revealing the tetrameric complex with C2 symmetry. An asterisk marks the stalk domain. The stalk corresponds to the small C-domain that is followed in sequence by a predicted transmembrane helix, which imposes the proximity of this C-domain to the cell membrane. Images from Scheffer M. P. *et al.*, 2017.

Sub-tomogram averaging of the Nap obtained from intact mycoplasma cells shows that this complex consists of an extracellular domain, a transmembrane segment with a stalk domain and a short intracellular domain (Figure GI. 3.2_2). The stalk domain corresponds to a small domain that reaches the cell membrane and crosses it with the single transmembrane helix predicted from the sequence of both proteins[301] [Iverson-Cabral S. L. *et al.*, 2015]. So that, it is reasonable to think that some factors would modulate the complex conformation and therefore the function of the Nap. Possibly, catalytic residues located in the stalk domain and residues implicated in the interplay between P110 and P140 may contribute to this event. Our laboratory, in collaboration with the group of Ignacio Fita at the "Parc Científic de Barcelona" have determined the crystal structure of the extracellular region of the P110 adhesin (erP110), identified its sialic acid binding domain and confirmed its lectin activity[75] [Aparicio D. *et al.*, 2018]. The information in the crystal structure guided the design of several point mutations in residues likely implicated in receptor binding. The resulting *M. genitalium* mutants exhibited important cythadherence defects *in vivo*. In addition, pre-treatment of human red blood cells (hRBCs) with neuraminidase prompted a dramatic decrease of the cytadherence capacity of *M.*

genitalium, in agreement with the idea that hemadsorption is mediated through the interaction with sialylated receptors[75] [**Aparicio D. *et al*., 2018**].

GI. 3.2.2. Terminal button

The terminal button is the most apical substructure of the cytoskeleton. Proteins P30, P65 and HMW3 have been localized in the terminal button in *M. pneumoniae*[271,279,288,290,302] [**Nakane D. *et al*., 2015; Stevens M. K. and Krause D. C., 1992; Jordan J. L. *et al*., 2001; Seto S. and Miyata M., 2003; Seto S. *et al*., 2001**]. P30 (MPN453) is a transmembrane protein located at the most apical region of the cell membrane, with its C-terminal oriented towards the outside of the cell[303] (**Figure GI. 3.1_4**) [**Chang H. Y. *et al*., 2011**] and plays an important role in adhesion and gliding motility[286,304,305] [**Relich R. F. and Balish M. F., 2011; Hasselbring B. M. *et al*., 2005; Romero-Arroyo C. E. *et al*., 1999**]. The subcellular localization of this protein is at the end of the attachment organelle[271,288,290] (**Figure GI. 3.1_5 and GI. 3.2_1**) [Seto S. et al., 2001; Seto S. and Miyata M., 2003; Nakane D. et al., 2015]. Moreover, chemical cross-linking studies suggest close proximity between P30 and P1 adhesin[297] [Layh-Schmitt G. et al., 2000]. The overexpression of the ortholog in *M. genitalium*, P32 (MG318), rescues the instability of the Nap complex in MG491 mutant strains[278] [García-Morales L. et al., 2016]. P32 and P30 probably share similar roles because both P30 and P32 can rescue the adhesion and gliding defects of cells from *M. pneumoniae* strains lacking P32[286] [**Relich R. F. and Balish M. F., 2011**].

P65 needs the P30 for proper localization[302] [**Jordan J. L. *et al*., 2001**]. A mutant with a disruption in P65 coding gene has been isolated and shows a reduced gliding speed. However, it is not clear if this phenotype is directly due to P65 absence or to polar effects from transposon insertion affecting the stability of other terminal organelle proteins[306] [**Hasselbring B. M. *et al*., 2012**]. This last hypothesis is supported by the fact that MG217, the P65 homologous protein from *M. genitalium*, has been localized in the *M. genitalium* terminal button by TEM immunogold, determines the gliding direction by modifying the curvature of the terminal organelle and mutants lacking this protein have a normal gliding speed[276] [**Burgos R. *et al*., 2008**]. HMW3 protein is believed to anchor the terminal button to the electron-dense core[71,271] [**Nakane D. *et al*., 2015; Pich O. Q. *et al*., 2008**].

GI. 3.2.3. Segmented paired plates or rod

The segmented paired plates are the central part of the terminal organelle and are surrounded by an electron-lucent area. The paired plates are composed by two straited plates separated by a gap of around 7 nm[267–269] [**Henderson G. P. and Jensen G. J., 2006; Seybert A. *et al*., 2006; Kawamoto A. *et al*., 2016**] and a flexible bend of approximately 30 degrees in the middle. Thin

and thick plate have been clearly defined in *M. pneumoniae* (**Figure GI. 3.1_5**) but have not been observed in the rod structure of *M. genitalium*.

HMW1 and HMW2 are the proteins localized in this substructure[271,289] [**Nakane D. *et al.*, 2015; Balish M. F. *et al.*, 2003**]. Both proteins are involved in cell morphology and adhesion, and are critical for terminal organelle formation in both microorganisms[71,275,280,307,308] [**Pich O. Q. *et al.*, 2008; Burgos R. *et al.*, 2007; Krause D. C. *et al.*, 1997; Popham P. L. *et al.*, 1997; Hahn T. W. *et al.*, 1998**]. HMW1 protein from *M. genitalium* and *M. pneumoniae* are slightly different: while in *M. pneumoniae* it is a membrane-associated protein[282] [**Balish M. F. *et al.*, 2001**] it has not been found in cell membrane extracts from *M. genitalium*[154] [**Párraga-Niño *et al.*, 2012**]. Moreover, *M. genitalium* HMW1 has a modular double function: C-terminal domain is involved in cytadherence and terminal organelle assembly (as its *M. pneumoniae* homologue protein) while the N-terminal domain is involved in gliding motility[275] [**Burgos R. *et al.*, 2007**]. The N-terminal domain contains a EAGR box (enriched in aromatic and glycine residues), supporting the implication of this EAGR motif in gliding motility[246,282,294,309] [**Calisto B. M. *et al.*, 2012; Pich O. Q. *et al.*, 2006a; Balish M. F. *et al.*, 2001; Cloward J. M. and Krause D. C., 2009**]. The finding that *M. genitalium* mutant lacking HMW2 and overexpressing of P32 are motile suggests that segmented paired plates are not directly involved in the movement generation[278] [**García-Morales L. *et al.*, 2016**]. CpsG phosphomannomutase of *M. pneumoniae* has also been localized in this structure[271] [**Nakane D. *et al.*, 2015**] but the role of this enzyme in the TO is still unclear.

GI. 3.2.4. Wheel or bowl complex

The wheel or bowl complex is the structure located at the most proximal part of the terminal organelle. MPN387, P41, P200, TopJ, P24 and Lon proteins have been localized in the wheel complex[271,292,294] [**Kenri T. *et al.*, 2004; Cloward J. M. and Krause D. C., 2009; Nakane D. *et al.*, 2015**]. The proteins P200 and MG386, both containing EAGR domains, are involved in gliding motility but not in cell adhesion[246,310] [**Jordan J. L. *et al.*, 2007; Pich O. Q. *et al.*, 2006a**] as well as the proteins MPN387 and MG269[293,311] [**Hasselbring B. M. and Krause D. C., 2007a; Kawakita A. *et al.*, 2016**]. TopJ and MG200 proteins are involved in cell motility and also contain one EAGR box[246,294,309] [**Cloward J. M. and Krause D. C., 2009; Pich O. Q. *et al.*, 2006a; Calisto B. M. *et al.*, 2012**]. Moreover, their N-terminal contain a DnaJ domain which has been shown to be involved in stabilizing the main adhesins in both strains[287,312,313] [**Cloward J. M. and Krause D. C., 2011; Cloward J. M. and Krause D. C., 2010; Broto A., 2015**], explaining the implication of these proteins in cell adhesion.

Protein P41 from *M. pneumoniae* and MG491 from *M. genitalium* plays a key role in gliding motility[293,314,315] [**Hasselbring B. M. and Krause D. C., 2007b; Hasselbring B. M. and Krause D.**

C., 2007a; Martinelli L. *et al*., 2016]. Moreover, it also has a role in connecting the TO to the main cell body since mutant strains lacking this protein are prone to show TOs escaping from the cell body[293,314,315] [Hasselbring B. M. and Krause D. C., 2007b; Hasselbring B. M. and Krause D. C., 2007a; Martinelli L. *et al*., 2016]. Fluorescence studies of P41 in *M. pneumoniae* cells have shown that P41 is one of the earliest proteins incorporated to the nascent TOs just before cell division. P24 and MG219 proteins are are also involved in gliding motility[270,293] [Hasselbring B. M. and Krause D. C., 2007b; Gonzalez-Gonzalez L., 2015]. Interestingly, all the proteins localized in the wheel complex (except the Lon protease which has not been deeply studied) are involved in gliding motility and have a minor impact in cell adhesion, supporting the idea that the wheel complex is the structure responsible for the movement generation[295] [Miyata M. and Hamaguchi T., 2016].

GI. 3.2.5. Translucent Area

As stated before, the core is surrounded by an electron lucent area from which the dense complexes are excluded[288,316,317] [Wilson M. H. and Collier A. M., 1976; Shimizu T. and Miyata M., 2002; Seto S. and Miyata M., 2003]. The structure of this area has been examined by treating fixed cells with Triton X-100, showing the presence of thin filamentous structures connecting the electron-dense core and the periphery of the cell[318] [Hegermann J. *et al*., 2002]. It has been also proposed that the translucent area was created by the exclusion of macromolecules via the repeated movement of the electron-dense core[268] [Henderson G. P. and Jensen G. J., 2006]. However, this hypothesis is unlikely because the translucent area can be observed in all cells even if they are not in conditions optimized for gliding[288,317] [Shimizu T. and Miyata M., 2002; Seto S. and Miyata M., 2003]. This area may be occupied by stiff, less diffusive materials invisible in EM, which may play a role in transmitting the movements of the paired plates originated in the bowl complex[267–269] (Figure GI. 3.1_5C and GI. 3.2_1) [Henderson G. P. and Jensen G. J., 2006; Seybert A. *et al*., 2006; Kawamoto A. *et al*., 2016].

GI. 3.3. Motility of mycoplasmas

Motility is an important strategy for searching resources, allowing the colonization of a variety of habitats. Hence, it is a valuable virulence factor in the infection process and also allowing evasion of cellular immune systems. Mollicutes share many features related to motility. For instance, they form a protrusion at one of the cell poles, bind to sialylated oligosaccharides (SOs) fixed on solid surfaces through this protrusion, and glide in the direction of protrusion, at a speed ranging 0.1–4.5 µm/s.

All of them present a cytoskeleton structure, supporting the direct relationship between the cytoskeleton and the ability to glide[265] [Hatchel J. M. and Balish M. F., 2008]. Interestingly,

Mycoplasma gliding does not involve flagella or pili and is entirely unrelated to other bacterial motility systems and the conventional motor proteins that are common in eukaryotic motility systems[319–321] (**Figure GI. 3.3_1**) [**McBride M. J., 2001; Jarrell K. F. and McBride M. J., 2008; Miyata M. *et al*., 2020**].

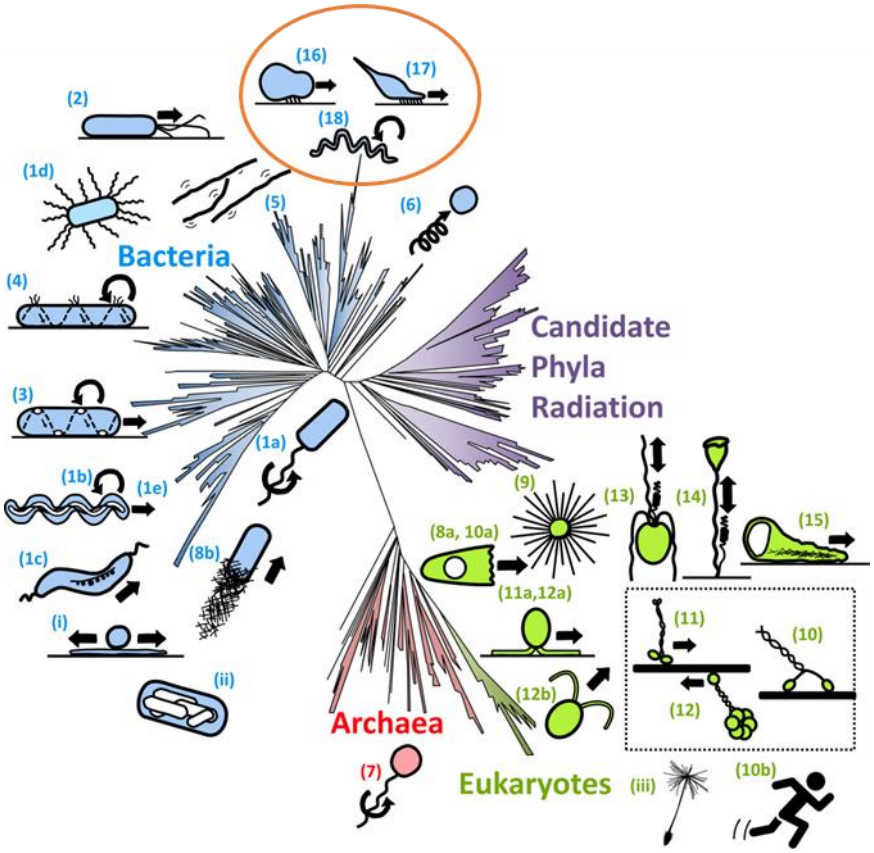

Figure GI. 3.3_1. Tree of motility: various types of motility systems. Cartoons of those systems are assigned to the relative positions in Tree of Life[322,323] [**Hug L. A. *et al*. 2016; Castelle C. J. and Banfield J. F., 2018**]. (1a) bacterial flagellar swimming, (1b) spirochetes flagellar swimming, (1c) magnetotactic bacterial flagellar swimming, (1d) bacterial flagellar swarming, (1e) Leptospira crawling motility, (2) bacterial pili motility, (3) Myxococcus xanthus adventurous (A) motility, (4) Bacteroidetes gliding, (5) Chloroflexus aggregans surface motility, (6) Synechococcus nonflagellar swimming, (7) archaella swimming, (8a) amoeba motility based on actin polymerization, (9) heliozoa motility based on microtubule depolymerization, (10) myosin sliding, (11) kinesin sliding, (12) dynein sliding, (10a) amoeba motility driven by contraction of cortical actin–myosin. (10b) animal muscle contraction, (11a, 12a) flagellar surface motility (FSM), (12b) flagellar swimming, (13) haptonemal contraction, (14) spasmoneme contraction, (15) amoeboid motility of nematode sperm, (8b) actin-based comet tail bacterial motility, (16) Mycoplasma mobile gliding, (17) Mycoplasma pneumoniae gliding, (18) Spiroplasma swimming, (i) bacterial sliding, (ii) gas vesicle, (iii) dandelion seed. The three eukaryotic conventional motor proteins are shown in the dotted box. The orange circle highlights the position of mycoplasmas motility in this motility tree. Image adapted from **Miyata M. *et al*., 2020**.

More than twenty species of *Mycoplasma* have been reported to be motile. *Mycoplasma mobile* and *M. pulmonis* in the *Hominis* subgroup and most species in the *Pneumoniae* subgroup have gliding capability (**Figure GI. 3.3_2**). Motile mycoplasmas glide over solid surfaces without

using flagella, pili or other known machineries used by other bacteria[319,320] [**McBride M. J., 2001; Jarrell K. F. and McBride M. J., 2008**]. The mechanism behind this gliding motility of mycoplasmas is not completely understood but two different models have been proposed: the inchworm and centipede models[324] [**Miyata M., 2008**]. The proteins involved in the actual mechanisms of both models do not show any similarities in amino acid sequence or gene arrangement. These observations suggest that these two systems developed independently, achieving similar results through convergent evolution.

The centipede model for motility in *M. mobile* cells is the best characterized mechanism (**Figure GI. 3.3_3**). This model is based in a motile machinery involving four main proteins (Gli349, Gli123, Gli521 and P42) that form a flexible leg complex. Multiple flexible legs are distributed in the cell membrane of the tip structure and a coordinated cycle of attach-stroke-movement-release generates the cell movement[325–327] (**Figure GI. 3.3_3**) [**Mizutani M. *et al.*, 2018; Nishikawa M. S. *et al.*, 2019; Matsuike D. *et al.*, 2023**]. Energy from ATP hydrolysis inside the cells is transmitted to these legs, which are connected to the internal cytoskeleton. This model has also been proposed to explain the motility of *M. pneumoniae* cells, and the Nap complex would function as the flexible leg[295,327,328] [**Miyata M., 2010; Miyata M. and Hamaguchi T., 2016; Matsuike D. *et al.*, 2023**].

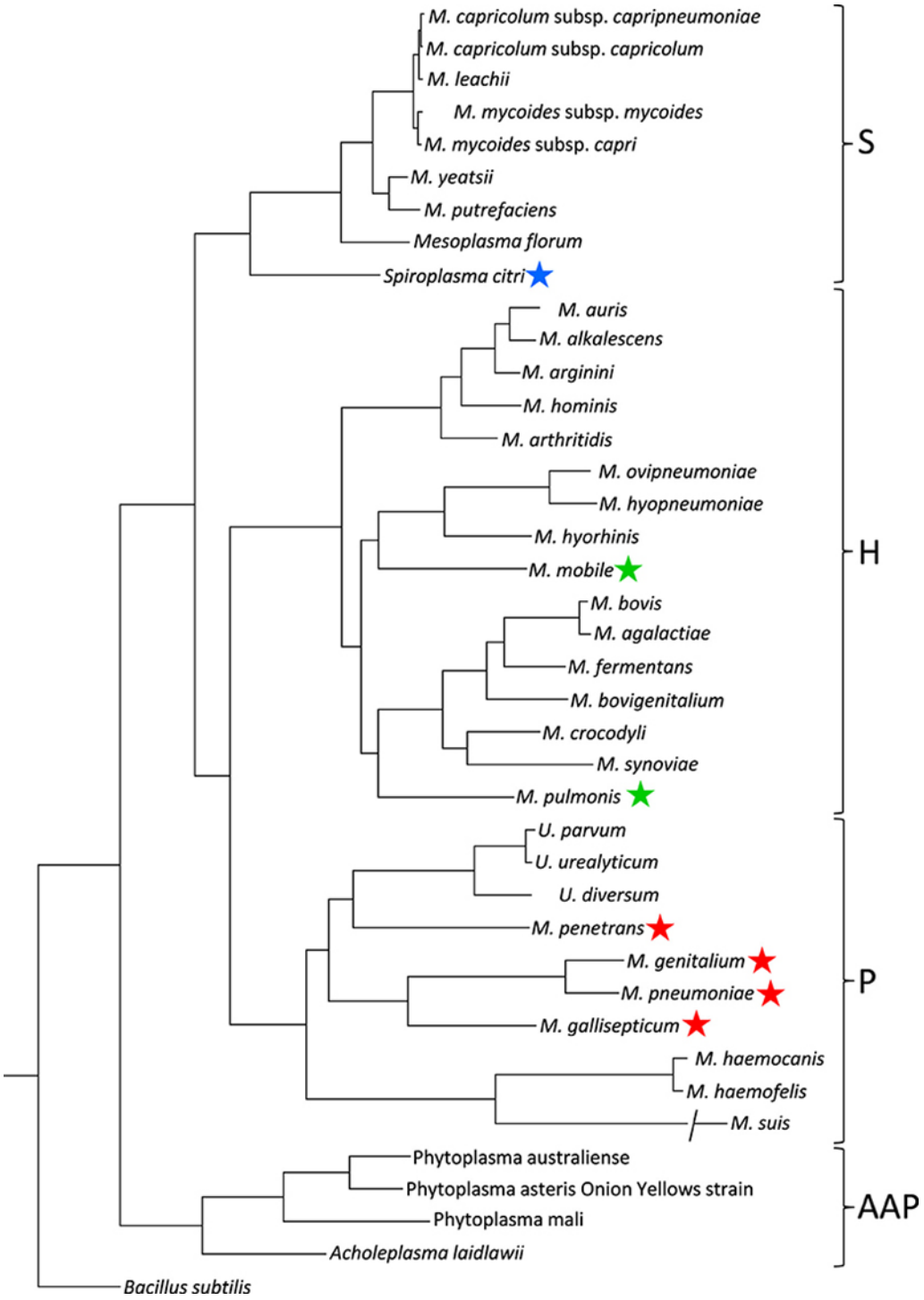

Figure GI. 3.3_2. Phylogenetic tree inferred using multiple alignments depicting mycoplasma motile species. Main phylogenetic subgroups are indicated: S, *Spiroplasma*; H, *Hominis*; P, *Pneumoniae*; AAP, *Acholeplasma/Anaeroplasma/Phytoplasma*. Motile species are marked by blue, green, and red stars for the motility types represented by *S. citri, M. mobile*, and *M. pneumoniae*, respectively. Image from **Miyata M. *et al.*, 2016**.

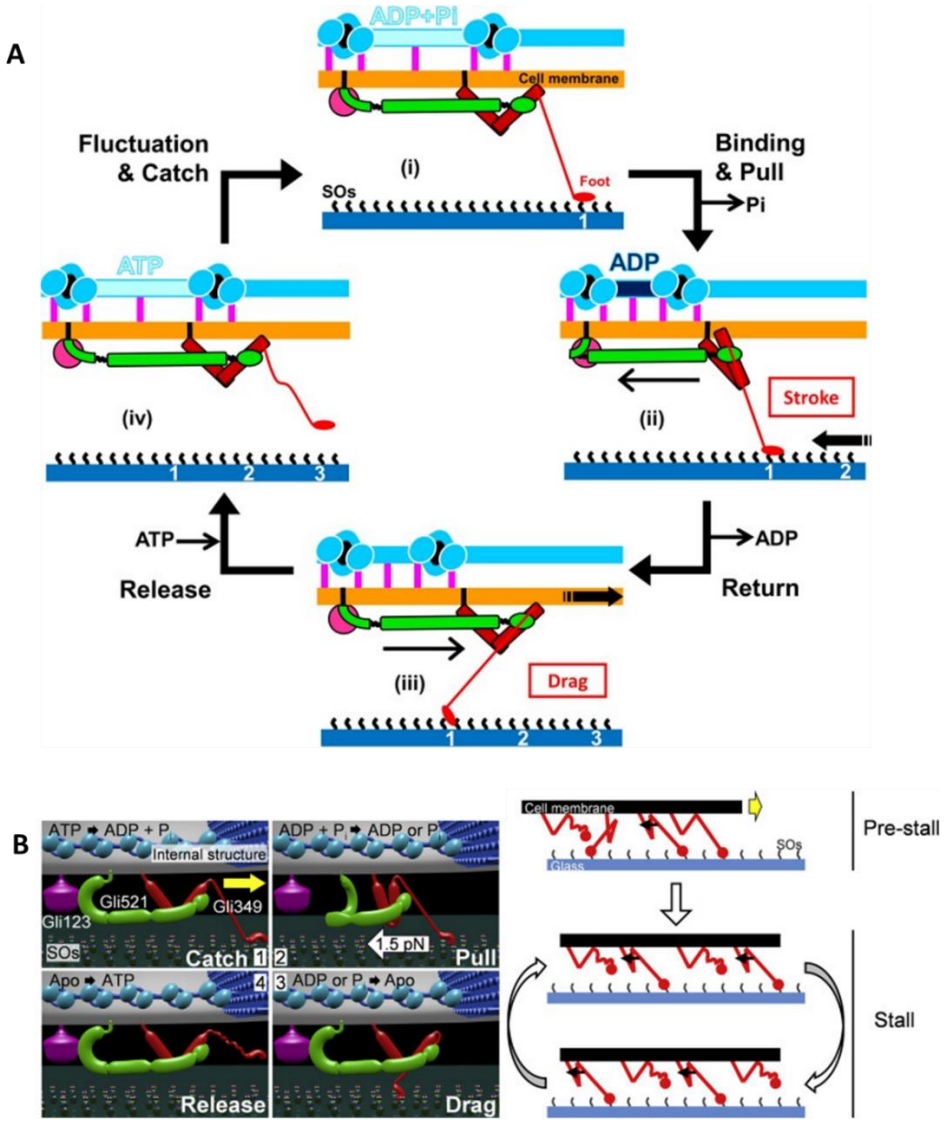

Figure GI. 3.3_3. The centipede model. A) Schematic illustrations of the updated working model for the gliding mechanism. Gli123, Gli521, and Gli349, essential for gliding, are presented in magenta, green, and red, respectively. The bridges between jellyfish-like structure and cell membrane are shown by pink vertical bars. The gliding occurs through stages i to iv. Image from **Nishikawa M. S. *et al.*, 2019**. **B)** Lineal schematic illustration of the gliding mechanism focusing on the single unit of machinery. The unit consists of an internal structure (upper blue) and three huge proteins: Gli123 (purple), Gli349 (red), and Gli521 (green) on the cell surface. The mechanism is divided into stages (1) through (4). The gliding direction is shown by a yellow arrow. Image from **Mizutani M. *et al.*, 2018**.

The inchworm model (**Figure GI. 3.3_4**), proposed for *M. pneumoniae* and *M.genitalium* cells. is based in the theory that longitudinal changes of the segmented paired plates drives the motion of cells by repetitive cycles of attach-contract-step-detach-extend[329] [**Wolgemuth C. W. *et al.*, 2003**] (**Figure GI. 3.3_4**). F studies suggested that motion might be a consequence of changes in the bending of the segmented paired plates[267,268] [**Seybert A. *et al.*, 2006; Henderson G. P. and Jensen G. J., 2006**]. It has been proposed that the wheel complex is the structure where the movement is generated and then is transmitted to the cell through the segmented paired plates

while the terminal button will be in charge of the gliding direction determination. However, the mechanistic model for gliding motility is still controversial and it has been shown that the rod component is not essential for the gliding motility[278] [García-Morales L. *et al.*, 2016]. The direct energy source for *M. pneumoniae*-type gliding motility has been elusive for many years[330] [Jurkovic D. A. *et al.*, 2013]. However, a recent work provides some evidence that ATP might by the energy source[331] [Mizutani M. and Miyata M., 2019]. Other recent studies, including the work described in this thesis, will help to understand this gliding motility mechanism, based on *M. pneumoniae* and *M. genitalium* Nap 3D structure determination (Figure GI. 3.3_4B).

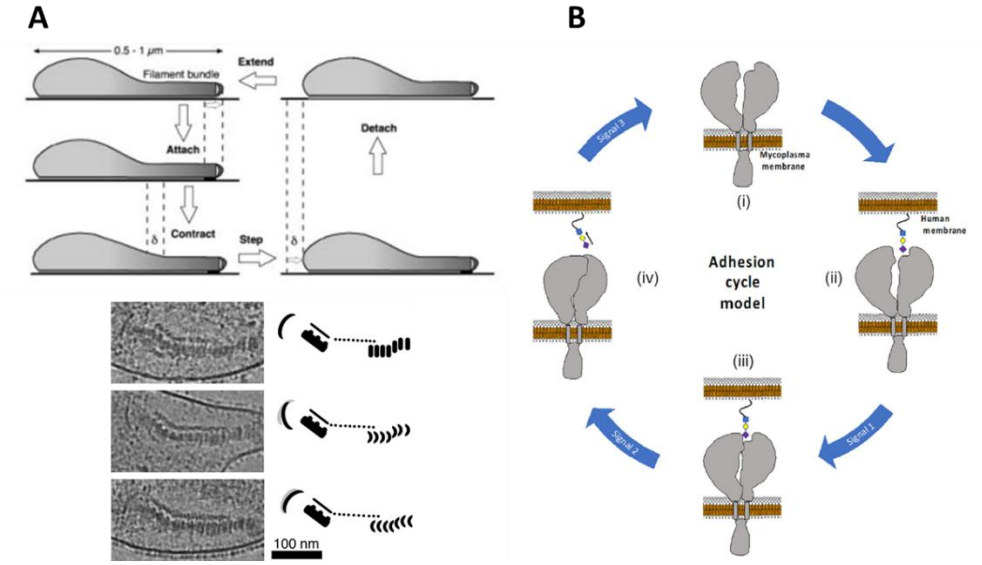

Figure GI. 3.3_4. The inchworm model. A) Schematic of the proposed mechanochemical cycle for the cell. The filament bundle attaches at the front and contracts, stretching the cell body. The elastically coupled cell body slides forward, consolidating the forward step. Finally, the nose detaches and extends, completing the cycle. Images from Wolgemuth C. W. *et al.*, 2003; Henderson G. P. and Jensen G. J., 2006. **B)** *M. pneumoniae* and *M. genitalium* model depicting the Nap adhesion cycle to the receptor based on protein structures. It begins with the Nap in an open state (i) followed by the binding of sialylated sugars to P40/P90 or to P110 (ii). Receptor binding likely induces conformational changes (signal 1) (iii) that subsequently trigger posttranslational modification (signal 2), which drives the Nap to its closed state, where the sugar is released (iv). Finally, an additional signal (either a post-translational modification or a conformational change) allows the Nap to revert to the open state (i) completing the cycle. Image from Vizarraga D. *et al.*, 2021.

GI. 3.4. Implication of the terminal organelle in cell division

Cell division is an essential process that is subjected to a tight and extremely complex regulation to ensure the cell viability[332] [Vicente M. *et al.*, 1998]. In the model organism *Escherichia coli*, the **d**ivision and **c**ell **w**all (*dcw*) cluster contain up to sixteen genes that encapsulate the whole division process: from the biosynthesis of the peptidoglycan wall to the cytokinesis[333] [Ayala J. A. *et al.*, 1994], in which the tubulin-like FtsZ protein plays a major role. In contrast, Mollicutes also encode a shortened version of the *dcw* operon[334] (Figure GI. 3.4_1) [Zhao Y. *et al.*, 2004].

In mycoplasmas cell division is done by binary fission of the cell. Besides the role of their cytoskeleton in adhesion and gliding motility, this structure has been thought to participate also in cell division in the earliest works when it was demonstrated that the duplication of the (TO) and its migration to the opposite pole precede cytokinesis in *Mycoplasma pneumoniae*[281] [Krause D. C. and Balish M. F., 2001].

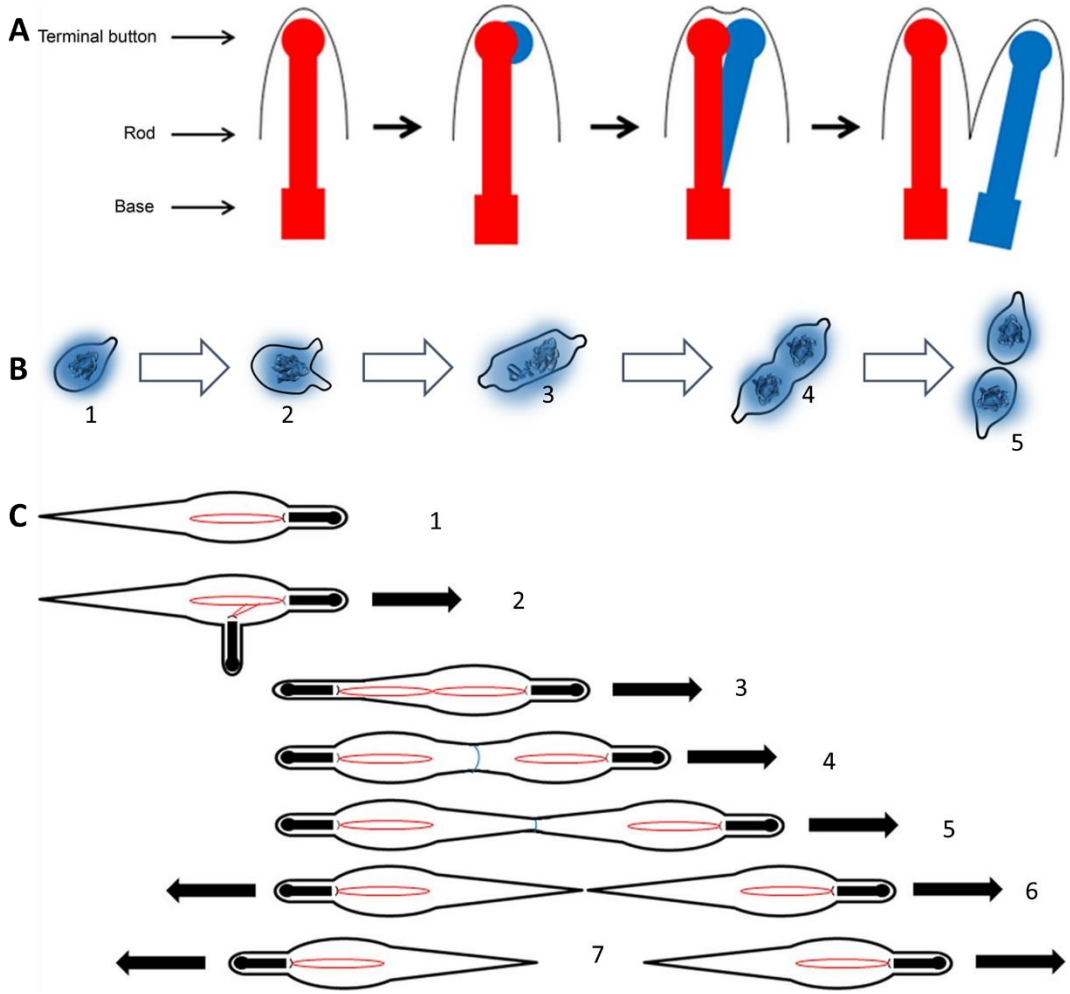

Figure GI. 3.4_1. Cell division and cytokinesis models in Mycoplasma. A) Model of template-driven duplication of the TO core in *M. pneumoniae* and its relatives. Several lines of data suggest that duplication of the core begins at the distal terminal button and proceeds toward the cell interior in a TopJ- and P24-dependent manner. Red, original, motility-competent core; blue, new, motility-incompetent core. Image from Balish M. F., 2014. **B)** Terminal Organelle (TO) duplication and cell division in *M. genitalium* applicable to other mycoplasmas. From left to right: a single cell (1) with a chromosome (highlighted in blue) duplicates its TO before DNA replication (2). The chromosome replication begins once the TO has ended its migration to the opposite pole (3) and then gliding motility is partially resumed to carry out cytokinesis (4) and eventually produce two daughter cells (5). Image from Martínez-Torrò C. 2020. **C)** Model of *M. pneumoniae* cell division also applicable to other mycoplasmas. (1) In a pre-divisional cell, the TO contains an electron-dense core (solid black), to the base of which (black arc) the nucleoid (red) is attached. (2) Using the TopJ/P24-dependent mechanism, the core duplicates, resulting in a second TO with newly replicated DNA attached. (3) Movement of the cell body, driven by motility of only the old TO, pulls the new TO to the rear of the cell. At this point, the new TO is not motility active. (4) As the dividing cell grows, two nascent daughter cells become apparent as the old TO continues to stretch and pull the

cell body. Constriction of FtsZ (blue) at midcell contributes to the separation of the daughter cells. (5) The continued combination of pulling and constriction leads to the formation of a filament that connects the nascent daughter cells. (6) When the connecting filament ruptures, cytokinesis has occurred. The cell with the old TO continues its forward motion, and the other daughter cell remains inactive for some amount of time. (7) The new TO becomes activated for motility, and both daughter cells are now motile. Image from **Balish M. F., 2014**.

M. pneumoniae and *M. genitalium* have one TO per cell[271,290,291,335] (**Figure GI. 3.1_1**) [**Bredt W., 1968; Seto S. *et al*., 2001; Hasselbring B. M. *et al*., 2006b; Nakane D. *et al*., 2015**], suggesting that the formation of the nascent organelle occurs precisely coupled with cell growth and division. This connection has been traced by fluorescence microscopy in both fixed and live cells[290,291,336] [**Seto S. *et al*., 2001; Hasselbring B. M. *et al*., 2006b; Martínez-Torrò C. 2021**]. These studies have shown that the nascent organelle is formed adjacent to the preexisting one (**Figure GI. 3.4_1a**) and yhen, the new TO moves laterally to the other pole (**Figure GI. 3.4_1b,c**). However, the cell images highlighting organelle formation vary in terms of the number of attachment organelles, with the next nascent organelle sometimes emerging before the end of cytokinesis (**Figure GI. 3.4_2**). It was also evidenced that there was no variation in DNA content between cells with one TO and cells with a nascent TO near the original, suggesting that the duplication of the TO is the first step of cell division[290] [**Seto S. *et al*., 2001**]. Another study suggested that gliding motility ceased upon the creation of a new organelle and it was only resumed once the new TO moves to the opposite pole[291] [**Hasselbring B. M. *et al*., 2006b**], thus implying a remarkable coordination between motility and division.

From the previous studies emerges a picture of the whole process. Cell division starts with the terminal organelle duplication. Once the new terminal organelle is completely formed and functional, it migrates to the opposite pole and the gliding motility of both TOs help to the cytokinesis to separate the daughter cells[147,291,337] [**Lluch-Senar M. *et al*., 2010; Hasselbring B. M. *et al*., 2006b; Balish M. F., 2014**]. It has been reported that multiple TO duplication can occur before the cytokinesis in *M. pneumoniae* cells (**Figure GI. 3.4_3 and Figure GI. 3.4_2A**), suggesting a simultaneous initiation of cell division. However, in *M. genitalium* cells, the frequency of cells with multiple organelles is much lower than in *M. pneumoniae* (**Figure GI. 3.4_1B**). This difference can be controlled by the proteins P110 and P140 since mutants with lower amounts of these proteins present a high increase in cells with multiple TOs[277] [**Pich O. Q. *et al*., 2009**].

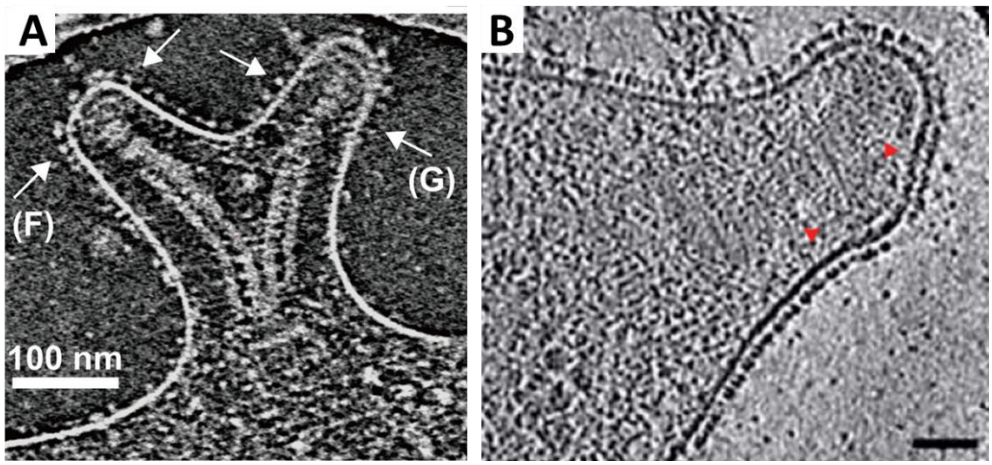

Figure GI. 3.4_2. Analysis of the terminal organelle (TO) surface by Cryo-ET. A) Early stages of TO duplication in *M. pneumoniae*. Bifurcated TO of *M. pneumoniae* cell. White arrows point the two terminal organelles. Image from. **B)** *M. genitalium* G37-WT cell in an early stage of TO division. Red arrows delimitate a nascent terminal button almost 90º of the rod. Scale bar of 50 nm. Image from González-González L., 2015.

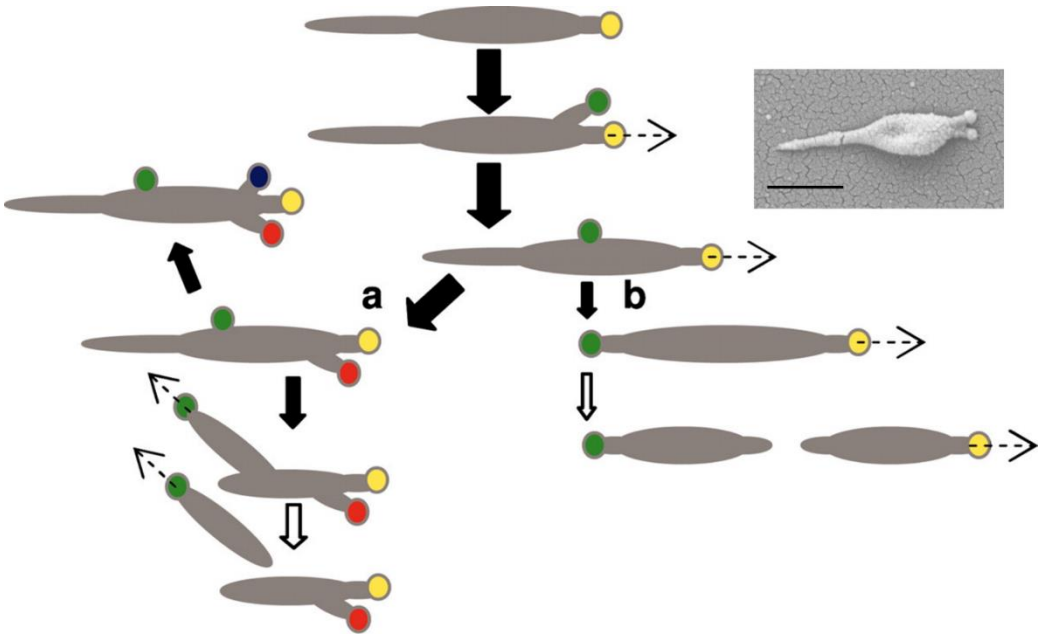

Figure GI. 3.4_3. Model for *M. pneumoniae* terminal organelle (TO) duplication and growth cycle. The yellow circle represents the initial TO, and green, red, and blue circles represent subsequent organelles, appearing in that order. The dashed arrows reflect movement of the indicated TO, and open arrows indicate cytokinesis. Solid arrows indicate steps in the cell cycle, with arrow size reflecting relative frequency. In most cases, multiple duplications of the terminal organelle occur before daughter cells emerge (a), although rarely some cells undergo a single duplication of the terminal organelle followed by cytokinesis (b). Scale bar of 0.5 µm. Schematic image from Hasselbring B. M. *et al.*, 2006b.

Studies with fluorescent proteins tagging some proteins conforming the attachment organelle of *M. pneumoniae* has enlighten the process of the terminal organelle formation during its replication[291] [Hasselbring B. M. *et al.*, 2006b]. It seems that proteins are sequentially added when new terminal organelles are assembled. In this way, P41 protein is among the first proteins identified in nascent terminal organelles, before that P30 and P65 could be detected. Since P41

is located in the wheel complex and P30 and P65 are located in the terminal button, the wheel complex could be the first structure that is assembled in nascent terminal organelles[291] [Hasselbring B. M. *et al.*, 2006b]. This hypothesis is in disagreement with electron microscopy images of *M. pneumoniae* cells where cells showing bipartite attachment organelles can be observed[269,318] (Figure GI. 3.4_2A) [Hegermann J. *et al.*, 2002; Kawamoto A. *et al.*, 2016]. Cryo-electron microscopy images of *M. genitalium* cells also show cells with two terminal buttons, suggesting that the terminal organelle duplication may start from its most apical extreme[270] (Figure GI. 3.4_2B) [Gonzalez-Gonzalez L., 2015]. Therefore, more studies are required to fully understand the mechanism of terminal organelle duplication and division process.

The strict relationships between gliding motility and cytokinesis are probably conserved in the closely related species *M. genitalium* and *M. pneumoniae*. However, phase variants and mutant cels with no adhesins are non-motile but these cells are viable and they grow quite normally[246] [Pich O. Q. *et al.*, 2006a]. Despite the TO has specific mechanisms to segregate the cytoskeletons in the daughter cells just before cytokinesis, the previous data and suggest that the TO might collaborate in cytokinesis but is not essential for cell division.

GI. 3.5. Cell Division

The dcw cluster of most mycoplasma only contains four genes: *mraZ*, *mraW*, a gene that codes for a hypothetical protein and *ftsZ* (Figure GI. 3.5_1). Little was known about the exact function of MraZ and MraW in cell division, in spite of the vast conservation of the two genes in which they are encoded, even in their position inside the operon, as the two genes are always placed at the beginning of the cluster[332] [Vicente M. *et al.*, 1998]. However, their presence even in the cell-wall-less Mollicutes implies a global role beyond cell wall synthesis.

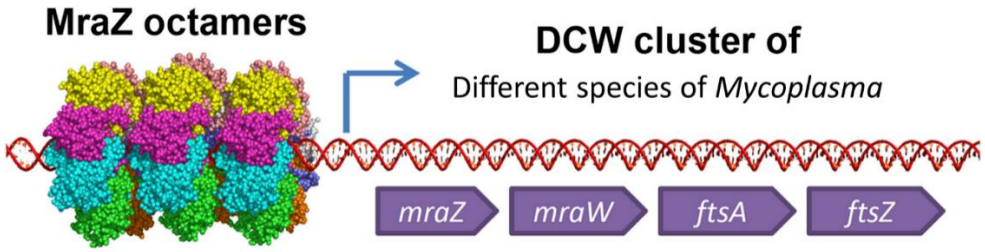

Figure GI. 3.5_1. Recognition site of the MraZ-family regulator of *Mycoplasma gallisepticum*, which is conserved in many species of different clades within class *Mollicutes*. MraZ binds to a single repeat as an octamer complex. MraZ can also bind a single binding site or a series of repeats with different spacer lengths (2–4 nt); thus, it may play a role in the regulation of multiple operons in *Mollicutes*. Image from Fisunov G. Y. *et al.*, 2016.

The first gene of the operon is *mraZ*, which codes for a transcriptional regulator (**Figure GI. 1.5_1**). A few years ago, it was unveiled that MraZ acts as a transcriptional repressor of the *dcw* operon in *E. coli*[338] [**Eraso J. M. *et al.*, 2014**]. Eraso and his collaborators evidenced that MraZ could negatively regulate its own expression as well as the transcription of the first eleven genes of the cluster. In addition, they determined through Electronic Mobility Shift Assays (EMSA) that MraZ binds to direct repeats contained in its immediate upstream region (**Figure GI. 3.5_2**). The conserved motif consists of three GTG(G/T) boxes separated by six nucleotides. There is an additional fourth box in *M. genitalium*[336] [**Martínez-Torró C. *et al.*, 2021**]. Interestingly, the deletion of this highly conserved gene is not correlated with a discernible phenotype in *E. coli* cells (Eraso et al 2014), although its overexpression was proven to be detrimental for cell growth.

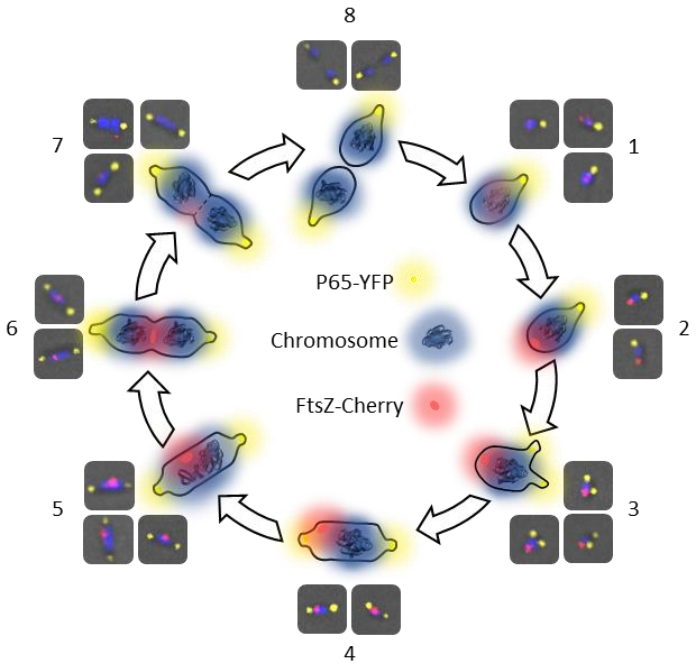

Figure GI. 3.5_2. Fluorescent tracking of the cell cycle of *M. genitalium* from a single cell until complete cytokinesis. Each stage is illustrated by a fluorescence microscopy micrographs of the *mraZ ftsZ*Ch 217YFP strain. Image from **Martínez-Torrò C. *et al.*, 2021**.

Increased levels of MraZ lead to cell filamentation in *Corynebacterium glutamicum*[339] [**Maeda T. *et al.*, 2016**] and *Mycoplasma gallisepticum*[340] [**Fisunov G. Y. *et al.*, 2016**]. In this latter work, it was also confirmed that MraZ negatively regulates the transcription of the *dcw* operon. In *M. genitalium*, the depletion of MraZ activates transcription of the division and cell wall operon, which is associated with a severe growth delay and an impaired cytokinesis. However, overexpression of *mraZ* causes a transcriptional activation of the operon, although it is milder than the associated with the loss of the regulator[336] [**Martínez-Torró C. *et al.*, 2021**]. However, this data might be controversial since it has been also described the transcriptional activation of

the dcw cluster upon *mraZ* overexpression [**Fisunov G. Y. *et al.*, 2016**]. Thus, MraZ culd function both as a transcriptional repressor and activator of the dcw cluster.

Regarding the gene product of *mraW*, the second gene of the *dcw* operon in *M. genitalium*, it has been published that MraW is an RNA methyltransferase that targets the 16S rRNA[341] [**Kimura S. and Suzuki T., 2010**]. Although its function has not been determined yet, there are several studies that address the effects of its deletion. **Kimura S. and Suzuki T.** reported that the *mraW* mutant had an altered non-AUG initiation and translation fidelity, thus suggesting that MraW could be potentially playing a role in start codon selection. The defective mutant of *mraW* in *S. aureus* also exhibited an anomalous translation fidelity, a slight increase in doubling time and a higher sensitivity to oxidative stress[342] [**Kyuma T. *et al.*, 2015**]. It was found that the tolerance to aminoglycosides in *E. coli* decreased in the *mraW* mutant[343] [**Zou J. *et al.*, 2018**]. And a more recent study in enterohaemorrhagic *E. coli* linked the deletion of *mraW* to a reduced motility and a decreased DNA methylation in a wide range of promoters and genes[344] [**Xu X. *et al.*, 2019**]. In *M. genitalium*, loss of MraW does not change the gene expression patterns, although it slightly increases the duplication time and it is associated with a higher expression of FtsZ[336] [**Martínez-Torró C. *et al.*, 2021**].

MraZ and MraW are strictly related. It is described that the toxic effects caused by the overexpression of *mraZ* could be blocked by co-overexpressing *mraW*[338] [**Eraso J. M. *et al.*, 2014**]. In addition, the *mraZ* gene is always accompanied by *mraW* at the beginning of the *dcw* operon. Remarkably, no chromosomes with orphan *mraZ* genes have been documented. However, a small number of bacteria has a copy of *mraW* despite they lack *mraZ*, suggesting the existence of an MraZ-independent activity for MraW.

In *M. genitalium*, the third gene of the operon (MG223) codes for a hypothetical protein of unknown function. However, in the mollicute *Spiroplasma kunkelii*, the third gene was characterized as ftsA[334] [**Zhao Y. *et al.*, 2004**]. However, but the sequence gene is poorly conserved among species and no solid conclusions about the role of third locus of the dcw operon can be drawn.

The *ftsZ* gene is almost universally conserved in bacteria[345] [**Margolin W., 2000**]. It is essential in *E. coli*[346] [**Dai K. and Lutkenhaus J., 1991**] and *B. subtilis*[347] [**Beall B. and Lutkenhaus J., 1991**]. It codes for FtsZ, a GTPase that is the ancestral homologue of tubulin[348] [**Margolin W. *et al.*, 1996**]. This protein is able to assemble in a polymer-dynamic ring-like structure named the Z ring[349] [**Sun Q. and Margolin W., 1998**]. The assembly serves as a scaffold for other division-related proteins that are recruited into the structure to effect cell division[350] [**Errington J. *et al.*, 2003**]. Notably, in spite of its high conservation among bacteria and its critical function in cell division, it was evidenced in our laboratory that *ftsZ* is not essential in *M. genitalium* for *in vitro* growth,

suggesting that cells are able to perform binary fission without the FtsZ protein[337] [**Lluch-Senar M. *et al.*, 2010**]. However, spontaneous adherence mutants, which appeared quite frequently among wild-type cells, cannot be recovered from the mutant strain lacking FtsZ, reinforcing the importance of TO in the division process and suggesting that the gliding motility can undertake feasible cytokinesis in the absence of FtsZ[337] [**Lluch-Senar M. *et al.*, 2010**]. Then, FtsZ and gliding motility could be considered as redundant mechanisms for cytokinesis and cell division in *M. genitalium* and probably all motile mycoplasma species.

GI. 3.6. Infection process mediated through adhesion

The adhesion of Mollicutes to host cells is a prerequisite infection. The loss of adhesion capacity is linked to the loss of infectivity as well as reversion to the cytadherence phenotype also reverts their virulence and infectivity[16] [**Razin S., 2006**]. The adhesion of some mycoplasmas, as *M. pneumoniae*, *M. genitalium* and *M. mobile*, to the host cells has been demonstrated to be mediated by specific sialylated oligosaccharides that can be found in the membrane cell and would be recognized by adhesin proteins of the mycoplasma surface[75,351–354] [**Kasai T. *et al.*, 2013; Nagai and Miyata M., 2006, Loomes L. M. *et al.*, 1984; Aparicio D. *et al.*, 2018; Vizarraga D. *et al.*, 2020**].

The first step for bacterial infection and colonization is the adhesion to host urogenital epithelial cells[83,355] [**Rottem S., 2003; McGowin C. L. *et al.*, 2009a**]. *In vitro* studies with vaginal epithelial cells have demonstrated that *M. genitalium* attaches to host cells by the TO (**Figure GI. 3.6_1**) just before to be internalized by these cells[83] [**McGowin C. L. *et al.*, 2009a**]. After adhesion, a subset of *M. genitalium* cells can invade cytoplasm of the host epithelial cell by an unknown mechanism, but it is characterized by the presence of clathrin-coated pits[356] [**Mernaugh G. R. *et al.*, 1993**]. Once internalized, this microorganism has been located within perinuclear vesicles, and possibly the nucleus[81,163] [**Ueno P. M. *et al.*, 2008; McGowin, C. L. *et al.*, 2009**], of different cell lines[83,356–358] [**McGowin C. L. *et al.*, 2009a; Mernaugh G. R. *et al.*, 1993; Baseman J. B. *et al.*, 1995; Dallo S. F. and Baseman J. B. 2000**]. Hence, mycoplasma cells invade its target cells and survive within the intracellular environment, which provides a safe harbor from host immunological responses[83,358] [**McGowin C. L. *et al.*, 2009a; Dallo S. F. and Baseman J. B. 2000**] and antibiotic treatments[186] [**Wikström A. and Jensen J. S., 2006**]. This feature also explains the persistence and chronic nature of *M. genitalium* infections[359,360] [**Cohen C. R. *et al.*, 2007; Citti C. and Blanchard A., 2013**], the recurrence of the NGU symptoms even after antibiotic treatments and their latent asymptomatic subsistence[358] [**Dallo S. F. and Baseman J. B. 2000**]. Regarding *in vivo* studies, *M. genitalium* cells have been found inside human vaginal cells of clinical samples using confocal immunoanalysis[80] [**Blaylock M. W. *et al.*, 2004**]. However, *M.*

genitalium is also capable of binding to human spermatozoa and can thus be transported by motile spermatozoa. Male infertility may be caused by injuries from *M. genitalium*-bound sperm, such as those resulting from agglutination and immobility. In addition, the motile sperm may deliver *M. genitalium* to the ciliated epithelia in the uterus and fallopian tubes, leading to genital diseases and infertility in females[361,362] [**Svenstrup H. F. *et al.*, 2003; Collier A. M., 1990**].

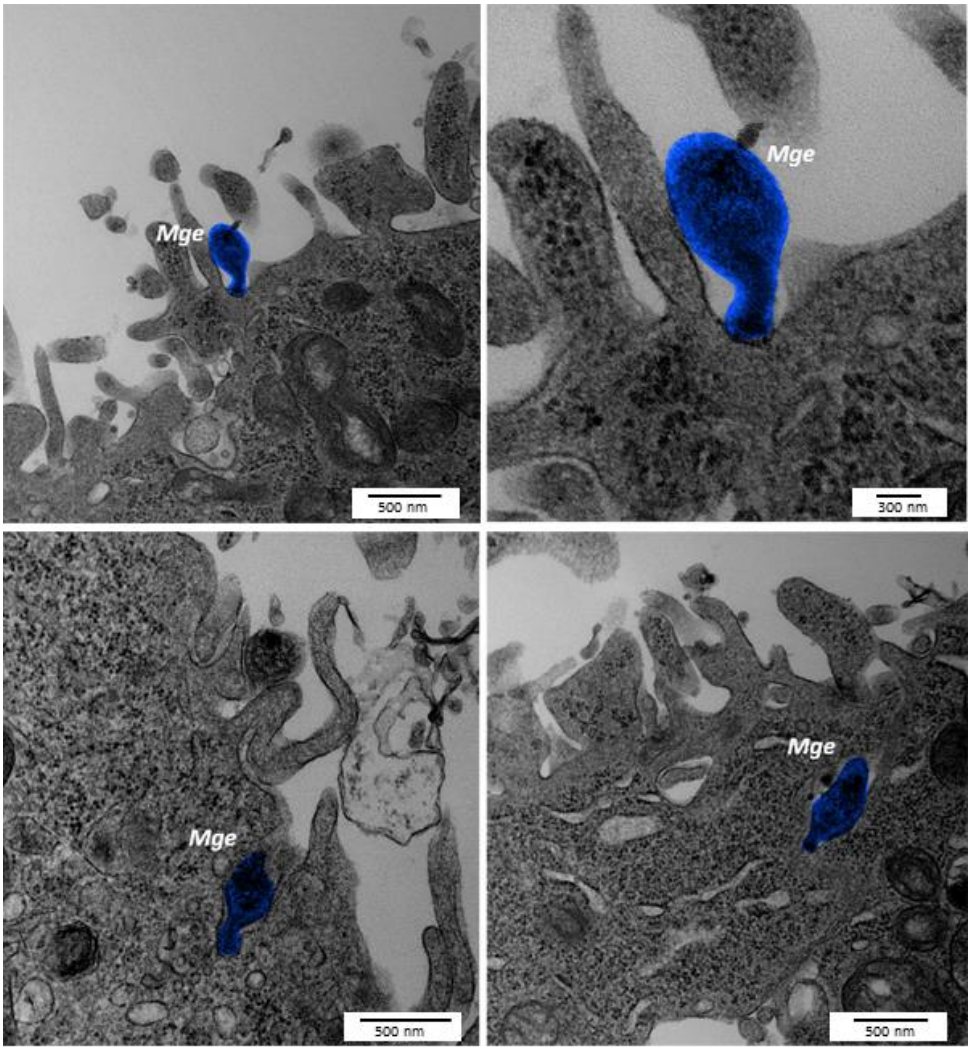

Figure GI. 3.6_1. Transmission electron micrograph of *Mycoplasma genitalium* cells. *M. genitalium* adhered to human cell surface (upper images) and entering to the cytoplasm of the cell (images below). Images have been modified for clarity purposes and mycoplasma cells are false coloured in blue and named *Mge*.

Adhesion to host cells is critical for its virulence and adhesins plays a key role in this process[87] [**Waites K. B. and Talkington D. F., 2004**]. P140 and P110, the two major *M. genitalium* adhesins, are also the most important virulence factors of thisd microorganism[75,363] [**Burgos R. *et al.*, 2007; Aparicio D. *et al.*, 2018**]. P140 exhibits high sequence homology and a wide range of immunological cross-reactivities with the P1 cytadhesin of *M. pneumoniae*. P140 and/or P110 mutants exhibit distorted morphologies, hypoplasia of terminal organelles, and loss of

adhesion[75,221,241] [Aparicio D. *et al.*, 2018; Dhandayuthapani S. *et al.*, 1999; Iverson-Cabral S. L. *et al.*, 2007]. As stated before, these important virulence proteins interact to form a transmembrane complex called Nap[299] [Scheffer M. P. *et al.*, 2017], which is expected to be instrumental for adherence and gliding motility in mycoplasmas belonging to the *pneumoniae* cluster such as *M. genitalium*[298,315] [García-Morales L., 2016; Nakane D. *et al.*, 2011]. Although not as critical as P140 and P110, other adhesins like P32, are also of significant importance in the adherence and motility of *M. genitalium*[364] [Reddy S. P. *et al.*, 1995].

Apart from adhesins located in the terminal organelle that binds to sialylated compounds[351] [Kasai T. *et al.*, 2013], it has been reported that proteins ef-Tu and E1 beta subunit of pyruvate dehydrogenase complex binds to fibronectin[365,366] [Dallo S. F. *et al.*, 2002; Balasubramanian S. *et al.*, 2008]. A number of pyruvate dehydrogenase subunits and some glycolic enzymes also bind to plasminogen[367–370] [Thomas C. *et al.*, 2013; Gründel A. *et al.*, 2015a; Gründel A. *et al.*, 2015b; Yueyue W. *et al.*, 2022]. In addition, some reports indicate that glyceraldehyde-3-phosphate dehydrogenase (GAPDH) acts also as an adhesin for *M. genitalium* binding to fibrinogen and mucin [371] [Dumke R. *et al.*, 2011]. As a key enzyme of the glycolytic pathway, the primary functional domain of GAPDH is localized in the cytosol. However, further analysis revealed that 10% of the total GAPDH was localized to the membrane, although the concentration of surface-exposed GAPDH varied among *M. genitalium* subpopulations[372] [Alvarez R. A. *et al.*, 2003]. The differences in GAPDH profile relocation between individual mycoplasmas may govern the ability of *M. genitalium* subpopulations to adhere to or invade target cells. Piruvate dehidrogease (PDH) subunits A and B have been identified also as mucin-binding proteins, explaining why GAPDH epitope blocking by antibodies only reduces the binding of *M. genitalium* to mucin by 70%[372] [Alvarez R. A. *et al.*, 2003]. These findings established the fact that the relocation of glycolytic enzymes to the *M. genitalium* membrane surface imparts completely independent and unforeseeable properties, such as mucin-binding activity. Given the reduced genome of *M. genitalium*, this microorganism makes use of moonlighting proteins with a distinctive compartmentalization and localization to facilitate the colonization and invasion of host tissues.

All these proteins may play a secondary role in adhesion to host cells once the TO has initiated the binding[115] [Waites K. B. *et al.*, 2017]. Interestingly, a nearly nonmotile M. *pneumoniae* mutant, retaining the 60% of its cythaderence ability compared to wild-type cells, is avirulent[373] [Szczepanek S. M. *et al.*, 2012], suggesting that in gliding motility is also a key virulence factor. Therefore, TO proteins (**Table GI. 3.1_1**) and the more recently discovered CARDS toxin[177,374] [Kannan T. R. and Baseman J. B., 2006; Techasaensiri C. *et al.*, 2010] are the main virulence

factors of *mycoplasmas*, which are able to proliferate and persist for a long time period after infecting a suitable host, even faced with a sophisticated immune system.

There is a need to explore novel therapeutic strategies to control *M. genitalium* and *M. pneumoniae* infections. Anti-adherence molecules, aimed to prevent the first stages of infection, arise as attractive non-antibiotic drugs[375,376] [**Ofek I. *et al*., 2003; Sharon N., 2006**]. Since anti-adherence agents do not act by killing or arresting the growth of pathogens, resistance to these agents is expected to emerge at very low rates. However, design of efficient anti-adherence therapies, based on receptor analogs or neutralizing antibodies, requires a deep understanding of the cytadherence structure, the gliding mechanisms and the immune properties of the adhesion complexes.

OBJECTIVES

CHAPTER I: STRUCTURE AND MECHANISM OF THE NAP ADHESION COMPLEX FROM THE HUMAN PATHOGEN *Mycoplasma genitalium*

The broad objective is to get mechanistic insights into the function of the Nap adhesion complex of *M. genitalium* to gain a better understanding of the mechanisms of adhesion and gliding motility by combining molecular biology tools and *in vivo* analyses.

As particular objectives:

- To determine the structure of the Nap adhesion complex.
- To investigate the biological role of the potassium binding pocket by characterizing *M. genitalium* strains carrying mutations in residues with special relevance based on the P110 3D structure (Y830A, R834G, D836L, W838F and G839).
- To investigate the interaction between P110 and P140 adhesins by characterizing *M. genitalium* strains carrying mutations in residues R600A, Q460A and D461A from P110.
- To examine the possible catalytic role of P140 residues H381 and H382 by characterizing *M. genitalium* strains carrying mutations in these residues.
- To compare the epitope maps between P140 from *M. genitalium* and the homologous P1 adhesin from *M. pneumoniae*.
- To investigate the presence of phosphorylated residues in P140 and P110 adhesins
- To determine the role of phosphorilations by characterizing *M. genitalium* strains bearing mutations in selected phosphorylated residues.
- To investigate the role of protein phosphatase PrpC (MG_108) and protein kinase PrkC (MG_109) in in gliding motility and cell growth.

CHAPTER II: MOLECULAR BASIS OF BACTERIAL LECTINS RECOGNITION OF EUKARYOTIC GLYCANS: THE CASE OF *Mycoplasma pneumoniae* AND *Mycoplasma genitalium*

The broad objective is to better understand the structural features governing the recognition of sialoglycan ligands by the main adhesins from *M. pneumoniae* and *M. genitalium* by combining spectroscopic, computational and biophysical approaches.

As particular objectives:

- To understand the physical binding of sialylated *N*- and *O*-glycans to the adhesins of *M. pneumoniae* and *M. genitalium*.
- To identify the structural determinants required for sialoglycans recognition.
- To identify the ligand epitopes accommodated in the protein binding sites to explore the conformational behavior of *N*- and *O*-glycans interacting with the adhesins.
- To depict 3D models of protein-ligand complexes.
- To compare the mode of action of mycoplasma adhesins with that of other bacterial adhesins.
- To understand the role of the potassium binding pocket in the stabilization and functioning of the Nap adhesion complex.

CHAPTER III: DYNAMICS OF THE NAP COMPLEX AND ADHESION MECHANISMS OF THE HUMAN PATHOGENS *Mycoplasma pneumoniae* AND *Mycoplasma genitalium*

The broad objective is to obtain a complete view of the Nap dynamics in adhesion and gliding motility by combining molecular biology tools and *in vivo* analysis.

As particular objectives:

- To obtain the structure of the complex formed by P1 and the antigen binding fragment (Fab) from a neutralizing monoclonal antibody that halts motility of *M. pneumoniae* cells.
- To get a better knowledge of the attachment/detachment of Naps to sialic acids from host human cells.
- To study the movement transmission from the mycoplasma inner cell to the Nap complex.
- To understand the antibody neutralization of P110 adhesin and elucidate the Nap areas most effective for antibody neutralization.

CHAPTER IV: ESSENTIAL PROTEIN P116 EXTRACTS CHOLESTEROL AND OTHER INDISPENSABLE LIPIDS FOR *Mycoplasmas*

The broad objective is to get mechanistic insights of the function of the P116 protein of *Mycoplasma pneumoniae* by combining molecular biology tools and *in vivo* analysis.

As particular objectives:

- To determine the structure of the P116 protein.
- To investigate the contribution of the P116 to the host-cell adhesion.
- To elucidate the function and biological role of P116 protein.
- To compare the P116 protein from *M. pneumoniae* with orthologous proteins from other mycoplasma species.

CHAPTER V: HETEROLOGOUS EXPRESSION OF *Mycoplasma pneumoniae* MAJOR ADHESINS IN THE CLOSE RELATED SPECIES *Mycoplasma genitalium*

The broad objective is to get mechanistic insights into the function of the Nap adhesion complex of *M. pneumoniae* by introducing an ectopic copy of the genes coding for the Nap proteins in *M. genitalium* cells.

As particular objectives:

- To assess if *M. genitalium* can be used as a surrogate host to express and characterize *M. pneumoniae* adhesins.
- Characterize the morphology, cytadherence and motility properties of *M. genitalium* strains expressing *M. pneumoniae* adhesins.
- To validate the catalytic cleavage of *M. pneumoniae* P40/P90 adhesin by introducing mutations in residues carrying the predicted target for proteolytic cleavage.

CHAPTER I

STRUCTURE AND MECHANISM OF THE NAP ADHESION COMPLEX FROM THE HUMAN PATHOGEN *Mycoplasma genitalium*

CI. 1. Introduction

CI. 2. Results

CI. 3. Discussion

Results presented in this chapter have been partially published in:

Aparicio, D.*, Scheffer, M.P.*, **Marcos-Silva, M.***, Vizarraga, D., Sprankel, L., Ratera, M., Weber, M.S., Seybert, A., Torres-Puig, S., Gonzalez-Gonzalez, L., Reitz, J., Querol, E., Piñol, J., Pich, O.Q., Fita, I., Frangakis, A.S. **Structure and mechanism of the Nap adhesion complex from the human pathogen *Mycoplasma genitalium*.** Nature communications. **2020**. DOI: 10.1038/s41467-020-16511-2. https://doi.org/10.1038/S41467-020-16511-2 *These authors contributed equally.

STRUCTURE AND MECHANISM OF THE NAP ADHESION COMPLEX FROM THE HUMAN PATHOGEN *Mycoplasma genitalium*

Mycoplasma genitalium is a human pathogen responsible for urethritis in men and cervicitis and pelvic inflammatory disease in women. Adherence of *M. genitalium* to host target epithelial cells is mediated through an adhesion complex called Nap, which is essential for infectivity. The Nap is a trans-membrane dimer of heterodimers comprising the adhesin proteins P110 and P140. The crystal structure of P110 revealed the binding site for the sialylated host cell receptor moiety. However, the structure and mechanism of the Nap, which is a prime target for antimicrobial development, had yet to be determined. Here we report the crystal structures of P140 both alone and in complex with the N-terminal domain of P110. The P140-P110 structure was also confirmed in solution by single-particle Cryo-electron microscopy (Cryo-EM) at 4.1 Å. These structures show that the sialic acid binding site is not accessible when the P140-P110 complex is formed. In addition, the structure of the whole Nap was determined in two different conformations by Cryo-EM and Cryo-electron tomography (Cryo-ET) at 9.8 Å and 15 Å respectively. The Cryo-EM structure shows a "closed" Nap conformation, where the interaction between the P140 and P110 subunits of a heterodimer are the same as in the P140-P110 crystal structure. In turn, the Cryo-ET structure shows an "open" conformation, where interfaces between the four subunits of a Nap are loose, with P110 ready-to-bind to sialic acid receptor moieties. Conformational changes comprise the rearrangement of the four subunits around the central Nap two-fold axis. Structural information, in combination with functional studies, suggests a mechanism for attachment and release of *M. genitalium* to the host cell receptor, in which the Nap complex alternates between “open” and “closed” conformations to sustain motility and guarantee infectivity.

My specific contribution to this chapter:

I have conducted all the experiments involving the construction and analysis of *M. genitalium* mutants by microcinematography and flow cytometry. These experiments are described in sections: CI. 2.4, CI. 2.5, CI. 2.7, CI. 2.8, CI. 2.9, CI. 2.10 and CI. 2.11. I have also contributed to the manuscript writing.

CI. 1. Introduction

Adherence of bacteria and viruses to their intended host cells is usually mediated by lectins[377] [**Moonens K. and Remaut H., 2017**]. Lectins are carbohydrate-binding proteins that exhibit an exquisite specificity for their cognate cellular receptors. These proteins, ubiquitous in nature, recognize the sugar moieties present in glycoproteins and lipids. The sexually transmitted bacterium *Mycoplasma genitalium* binds to eukaryotic cells by means of its main adhesins, P110 and P140[378,379] [**Mernaugh G. R. *et al*., 1993; Burgos R. *et al*. 2006**]. These important virulence proteins interact to form a transmembrane complex called Nap[380] [**Scheffer M. P. *et al*. 2017**], which is expected to be instrumental for adherence and gliding motility in mycoplasmas belonging to the *pneumoniae* cluster such as *M. genitalium*[381,382] [**García-Morales L. *et al*., 2016; Nakane D *et al*., 2011**]. In addition to their role in adherence and locomotion, P110 and P140 are immunodominant proteins and constitute the main target of host antibodies during infection[5–7] [**Wood G. E. *et al*., 2013; Ma L. *et al*, 2015; Wood *et al*., 2017**]. In a previous study, we determined the crystal structure of the P110 adhesin, identified its sialic acid binding domain and confirmed its lectin activity[383] [**Aparicio D. *et al*., 2018**]. However, the P110 structure also raised important questions regarding the possible function of a potassium binding pocket identified in the C-terminal domain, or the interplay with the other adhesin, P140.

Performance of bacterial lectins is often controlled by other proteins in response to specific signals. During colonization of host tissues, bacteria must withstand the mechanical stress of being removed by fluid flow or epithelial turnover. Therefore, many adhesion proteins display increased binding capacity under physical stress[384] [**Otto M., 2014**]. This is the case of the clumping factor A of *Staphylococcus aureus*[385] [**Herman-Bausier P. *et al*., 2018**], a bacterium frequently associated with bloodstream infections, or the fimbriae protein FimH of *Escherichia coli*[386] [**Connell *et al*., 1996**]. Indeed, FimH contributes decidedly to the pathogenesis of *E coli* in the urinary tract and exhibits increased binding capacity in response to high flow[387] [**Sauer M. M. *et al*., 2016**]. At the molecular level, conformational changes between the lectin binding (N-terminal) and the pilin binding (C-terminal) domains, modulate the affinity of FimH for glycan receptors. Two different FimH conformations have been described: an extended state showing high affinity and a compressed one with low affinity. Remarkably, transition between the two conformations requires the participation of the pilus assembly chaperone FimC, which prevents the interaction between the lectin and pilin binding domains and promotes a tight binding to oligosaccharides[388] [**Choudhury D. *et al*., 1999**]. As *M. genitalium* is a urogenital pathogen, it is reasonable to think that some factors would also modulate the affinity of P110 for oligosaccharides. Moreover, control of the binding capacity is particularly important in adhesion

proteins involved in motilitys as it is the case in mycoplasmas[328] [Miyata M., 2010]. As with eukaryotic cells[389] [Greenwood J. A. and Murphy-Ullrich J. E. *et al*., 1998], we anticipate that *M. genitalium* motility relies on a tight coordination of receptor catch and release.

Structural data often provides pivotal information to understand protein function. In recent years, Cryo-electron microscopy (Cryo-EM) has emerged as the most versatile method unrivalled, to study large and flexible macromolecular assemblies. Remarkably, recent advances in Cryo-EM methodology have decreased the size for which Cryo-EM is applicable and it is becoming a powerful and widespread approach to resolve the structure of large proteins and small oligomers[390,391] [Laverty D. *et al*., 2019; Sartori-Rupp A. *et al*., 2019]. Cryo-EM can be used to determine the three-dimensional structure of biomacromolecules in near native condition at close to atomic resolution[392] [Hospenthal M. K. *et al*., 2017] and has the potential to reveal conformations of dynamic molecular complexes. In addition, combination of Cryo-EM and X-ray crystallography may be instrumental to understand the function of multifaceted molecular machines[393] [Li H. and Thanassi D. G. *et al*., 2009]. For instance, the crystal structure of the coronavirus spike protein lectin domain, implicated in the recognition of different cellular receptors and undergoing conformational transitions, was determined in 2012[394] [Peng G. *et al*., 2012]. More recently, Cryo-EM has provided data on the structural and functional evolutions of spike proteins[395] [Shang J. *et al*., 2018] and revealed important information regarding antibody recognition[396] [Walls A. C. *et al*., 2016]. On the other hand, Cryo-electron tomography (Cryo-ET) is another method that allows the visualization of whole cells and their dynamics such as super-resolution light microscopy. It provides a crucial link between whole-cell imaging and high-resolution structure determination and molecular resolution 3D images of cellular landscapes. Technological advances in Cryo-ET now enable *in situ* structural studies at 3-4 nm resolution. While in favorable cases Cryo-EM can provide near-atomic resolution, even at nanometer resolution, the cellular environment offers a tremendous potential to discover unexpected scenarios[397,398] [Turk M. and Baumeister W., 2020 and Lučič V. *et al*., 2013]. Recently, using Cryo-ET, the structure of the complete native Nap complex has been determined *in-situ*, elucidating some new insights of the dynamics that these complexes could experience[399] [Sprankel L. *et al*., 2023].

Several studies demonstrate that *M. genitalium* is rapidly developing resistance to all current antibiotics[192,400–402] [Cao B. *et al*., 2010; Parrott G. L. *et al*., 2016; Bradshaw C. S. *et al*., 2006; Couldwell D. L. *et al*., 2015]. Therefore, it is necessary to explore novel therapeutic strategies to control *M. genitalium* infections. Anti-adherence molecules, aimed at preventing the establishment of infection, arise as attractive non-antibiotic drugs[375,403] [Ofek I. *et al*., 2003; Sharon N. 2006]. Since anti-adhesive agents do not act by killing or arresting the growth of the

pathogens, resistance to these agents should emerge at a markedly low rate. However, design of efficient anti-adherence therapies, based on receptor analogs or neutralizing antibodies, requires a profound understanding of the cytadherence mechanism and the immunogenic properties. A deep understanding of the Nap structure and adhesion mechanism will facilitate the development of anti-adherence therapies. In a previous work, we had determined the crystal structure of the extracellular region of P110 and demonstrated its binding to sialic acid receptors[383] [Aparicio D. *et al.*, 2018] (Figure CI. 1_1). In this chapter, we combined X-ray crystallography, Cryo-EM, Cryo-ET and *in vivo* experiments to get important mechanistic insights of the function of the main adhesion complex of *M. genitalium* and reveal an intricate interplay between P110 and P140.

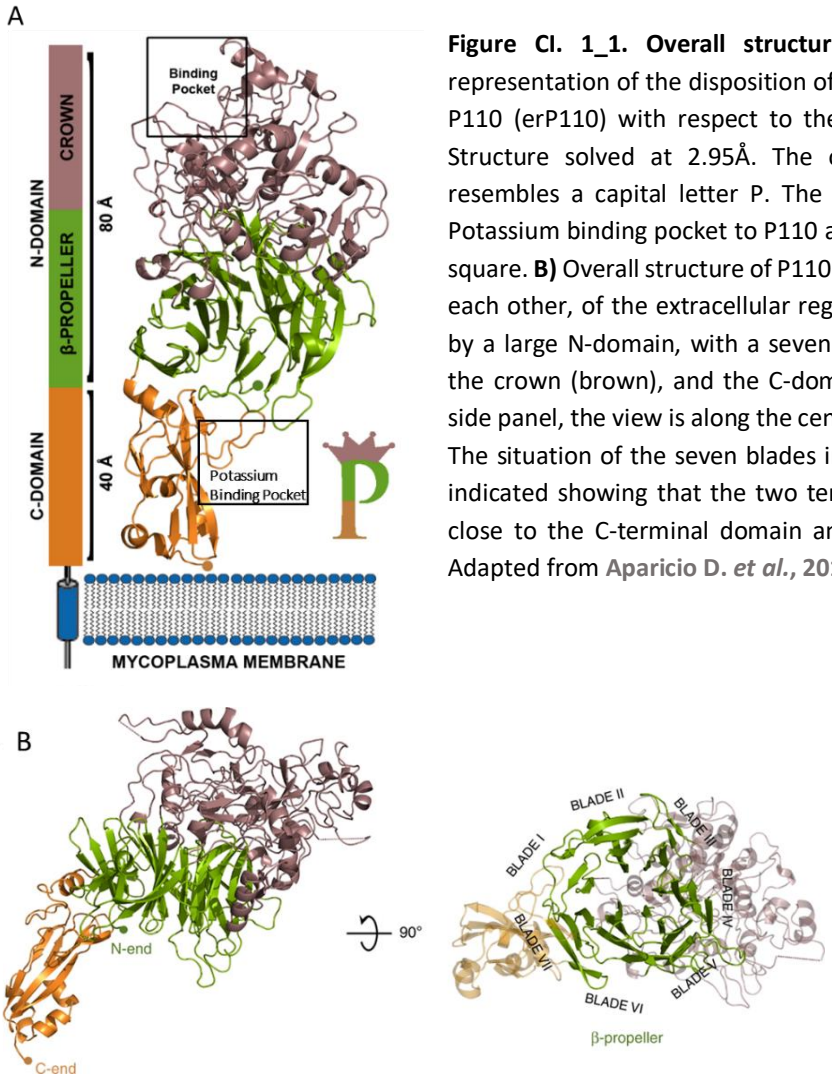

Figure CI. 1_1. Overall structure of P110. A) Schematic representation of the disposition of the extracellular region of P110 (erP110) with respect to the mycoplasma membrane. Structure solved at 2.95Å. The overall structure of P110 resembles a capital letter P. The Receptor binding and the Potassium binding pocket to P110 are highlighted with a black square. **B)** Overall structure of P110. Two views, 90° apart from each other, of the extracellular region of P110 that is formed by a large N-domain, with a seven blade β-propeller (green), the crown (brown), and the C-domain (orange). In the right-side panel, the view is along the central axis of the β-propeller. The situation of the seven blades in the propeller is explicitly indicated showing that the two terminal blades I and VII are close to the C-terminal domain and opposite to the crown. Adapted from Aparicio D. *et al.*, 2018.

CI. 2. Results

CI. 2.1. Crystal structure of P140 and in complex with P110N

Crystals were obtained from the extracellular region of P140 (erP140) (residues 23–1351) (**Figure CI. 2.1_1**), which excludes the signal secretion peptide at the N-end (residues 1-23) and the transmembrane and intracellular regions at the C-end (1352-1445). Crystals were obtained both alone and in complex with the N-terminal domain of P110 (P110N: residues 23–827) (**Figure CI. 2.1_1**). The structure of P140, for which there were no molecular models or experimental phases available, was determined by density modification techniques, starting with a mask derived from the sub-tomogram-averaged map of the whole Nap obtained by Cryo-ET. With four heterodimers in the asymmetric unit, the P140–P110N crystals were refined at 2.65 Å resolution to a final model with agreement R and R_{free} factors of 18.7 and 22.4, respectively. (**Appendices Table A. CI. 1.7**).

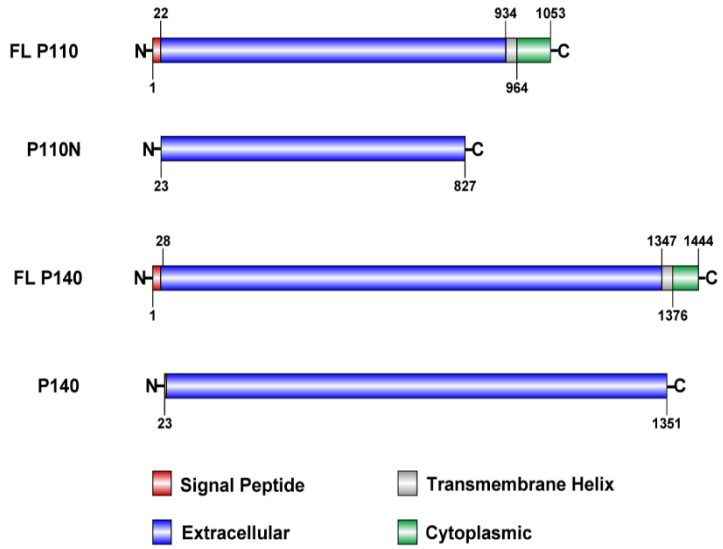

Figure CI. 2.1_1. **Proteins and constructs used in this study**. The Psi-Pred server[404] [Jones D. T., 1999] was used to predict the location of signal peptides (red), extracellular regions (lilac), transmembrane helices (grey) and cytoplasmic regions (green) in the full length (FL) P140 and P110 proteins. Constructs of the extracellular regions of P140 and P110 are also shown. In P110N the C-domain was excluded. Numbers indicate the residues at the boundaries. Adapted from Aparicio D. *et al.*, 2020.

The four erP140-P110N heterodimers found in the crystal asymmetric unit of the erP140-P110N crystals are organized as two dimers, each having two erP140-P110N heterodimers (**Figure CI. 2.1_2**). Dimers are not identical, as orientation of the erP140-P110N heterodimers with respect to the local two-fold axis of each dimer differs by ~3°. This variability and the presence in solution, as observed by MALS (**Appendices Figure A. CI. 1.7_1**), only of heterodimers erP140-

erP110, but not tetrameric complexes, indicates that interactions between the two heterodimers P140-P110 forming a Nap are weak in the extracellular regions.

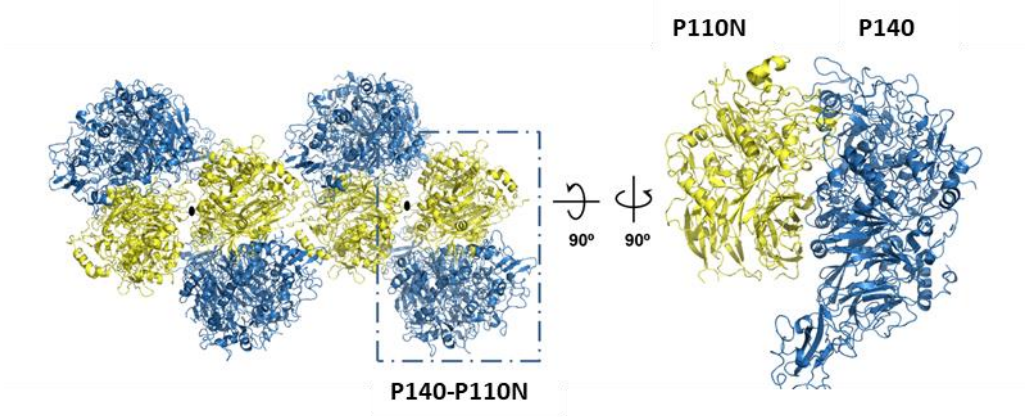

Figure CI. 2.1_2. **Asymmetric units content of P140-P110N crystals.** The P140-P110N crystals contain four P140-P110N heterodimers in the asymmetric unit that are arranged as two dimers with a local, non-crystallographic, two-fold axis (black oblong dots). The P140 construct (blue) includes the N- and C-domains, while the P110N construct (yellow) corresponds only to the N-domain of P110. Adapted from **Aparicio D. *et al.*, 2020**.

Sialylated oligosaccharides were recently shown to be the main cell host receptors of *M. genitalium*[383] [**Aparicio D. *et al.*, 2018**]. Structures of erP110 in complex with either 3´-sialyllactose (3SL: where the neuraminic acid moiety forms a α2-3 linkage to a lactose monosaccharide) or 6´-sialyllactose (6SL: with a α2-6 linkage) proved that both oligosaccharides bind into the same binding site, which is located in a protruding β-hairpin in the upper part of the P110 crown. Binding was reported to involve just a few P110 residues, in particular the sialic-acid-binding motif[405,406] [**Loukachevitch L.V. *et al.*, 2016; Pyburn T.M. *et al.*, 2011**] X-Phe/Tyr-Ser/Thr (Ser456-Phe457-Ser458) at the β-hairpin. In the structure of the erP140-P110N heterodimer, the sialic binding site is at the interface of P140 and P110, with the P110 β-hairpin that contains the sialic-binding motif making several hydrogen bonds and Van der Waals interactions with P140 (**Figure CI. 2.1_2A-D**).

Comparing the reported structures of erP110-alone (**Figure CI. 1_1**) with the structure of P110N determined now, the main structural changes correspond to the sialic binding β-hairpin itself and to two protein loops (residues 468-480 and 524-533) in the close vicinity of the sialic binding site (**Figure CI. 2.1_4C**). Another significant difference between the reported structures of P110 and the structure of P110N is found in the lower part of the β-propeller at the interface with the C-domain. Here changes appear to be triggered by the steric clashes that would occur in the heterodimer if P110 retains in the complex the conformation reported for the structure of P110 alone: i) P140 residues 704-707 clashing with the P110 loop residues 805-808; ii) P140 loops

(residues 157-160 and 492-495) clashing with the C-terminal P110 strand (873-883) (see below). Therefore, interactions between P140 and P110 in the heterodimer introduce some strain affecting to the linkage with the C-domain in P110. Steric strain might also provide an explanation to the difficulties obtaining crystals of erP140-erP110 complexes when erP110 includes the C-domain.

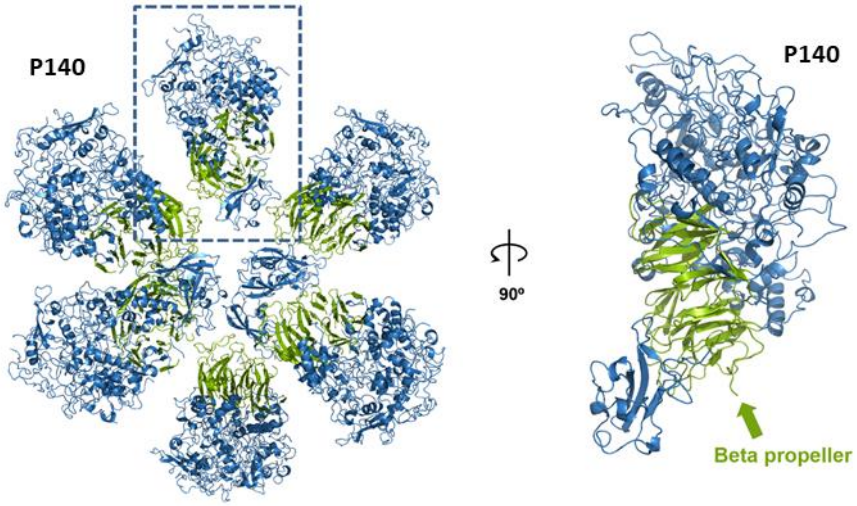

Figure CI. 2.1_3. **Asymmetric units content of P140-alone crystals.** The P140-alone crystals contain six P140 subunits in the asymmetric unit. β-propellers are explicitly indicated (green).

Main changes between the P140 structures from the erP140-P110N and erP140-alone crystals (**Figure CI. 2.1_3**), such as the rearrangement of the 807-827 residues, occur also in the vicinity of the sialic binding site (**Figure CI. 2.1_4C,D**). Interestingly, the structural changes observed in the erP140-P110N heterodimer will sterically interfere with the binding of oligosaccharides to the sialic binding site. In agreement with the structural information, binding of 3SL or 6SL was clear (by Surface Plasmon Resonance) for erP110-alone[383] [**Aparicio D. *et al.*, 2018**] but was not detected either for erP140-alone or for erP140-erP110 heterodimers. The sialic binding site is directly and importantly involved in the formation of the P140-P110 heterodimer interface. Mutants at the sialic binding site can affect to sialic binding as already reported[407] [**Krissinel E. and Henrick K., 2007**] but mutants at this site can also affect the stability of the P140-P110 heterodimer. Close to the sialic binding site, there is a cavity in P140, lined by two contiguous and highly conserved histidine residues (381-382) pointing towards some un-interpreted electron density (present in both the erP140-alone and the erP140-erP110 crystals), that might correspond to a possible active site with an unknown catalytic activity (**Figure CI. 2.1_4E**).

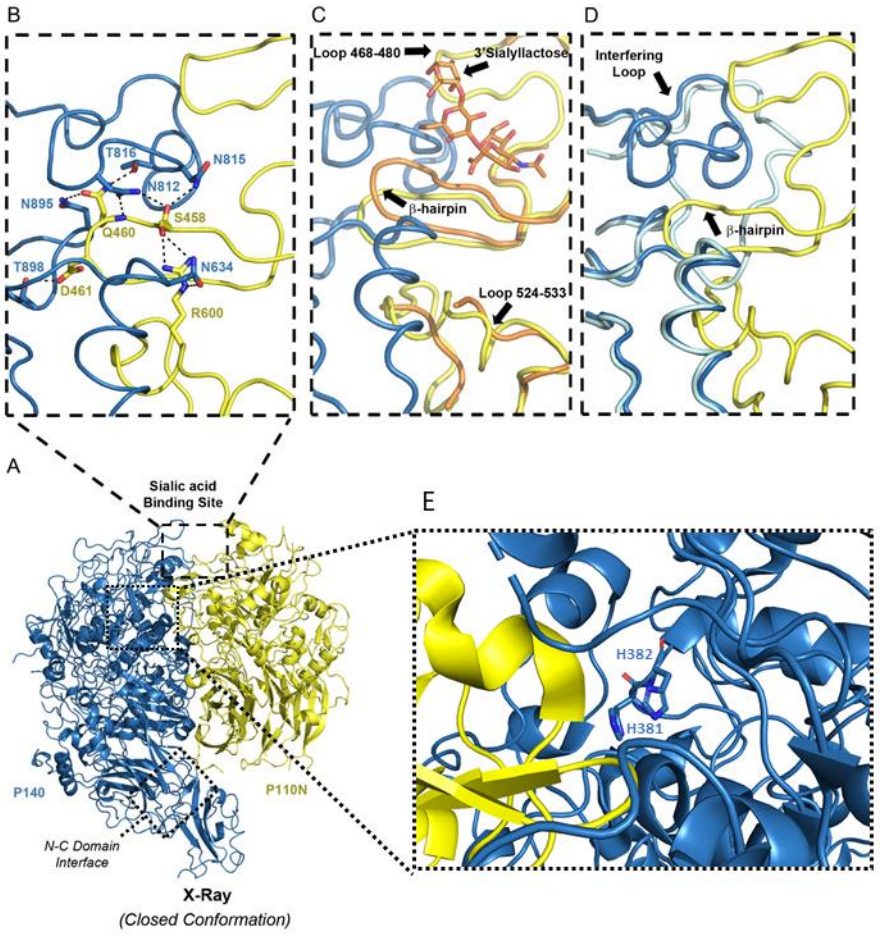

Figure CI. 2.1_4. **Close conformation of the P140-P110 heterodimers by X-rays. A)** X-ray crystal structure of the P140–P110N heterodimer. **B)** Network of hydrogen bonds in the vicinity of the oligosaccharide-binding site between P140 (blue) and P110N (yellow). Rearrangements experienced by P110N (**C**) and P140 (**D**) with respect to the structures of P110 alone (orange) and P140 alone (light blue), respectively. Rearrangements of the ß-hairpin and the interfering loop are indicated with red arrows. Oligosaccharide 3SL (**C**) is depicted as it was found in the structure of P110 alone[383] [**Aparicio D. *et al.*, 2018**], showing that it would have steric clashes in the closed conformation of the P140–P110N complex. **E)** P140 cavity containing the highly conserved histidine residues H381 and H382. Adapted from **Aparicio D. *et al.*, 2020**.

Electron density is well defined for all the residues from the P140 C-domain in both the erP140-P110N complex and the erP140-alone crystals. In turn, crystals of the erP140-P110N complex show poor density in several regions from the P140 N-domain: before residue 59 (the first residue modeled) and in five solvent exposed loops (residues 106-109, 228-231, 783-788, 1090-1096, 1160-1163), none at the upper part of the crown. Crystals of erP140-alone show poor density also for the P140 loop of residues 261-266. This loop is stabilized by interactions with P110N in the erP140-P110N complex. Moreover, there is a stretch of twenty residues long from P140 (807-827) that in the erP140-P110N complex is well defined and interacts with the receptor binding site of P110 (see below), while in the erP140-alone crystals presents some disorder with possible alternative conformations in some subunits.

CI. 2.2. Overall structure of P140 and structural similarities with P110

The overall structure of the extracellular region of P140 (erP140), consists of a large N-domain (residues 23-1243) and a smaller C-domain (residues 1244-1351) (**Figure CI. 2.2_1**). Both domains, containing mainly β-strands secondary structures, present clear similarities to the overall organization found for P110 (**Figure CI. 2.2_2A**).

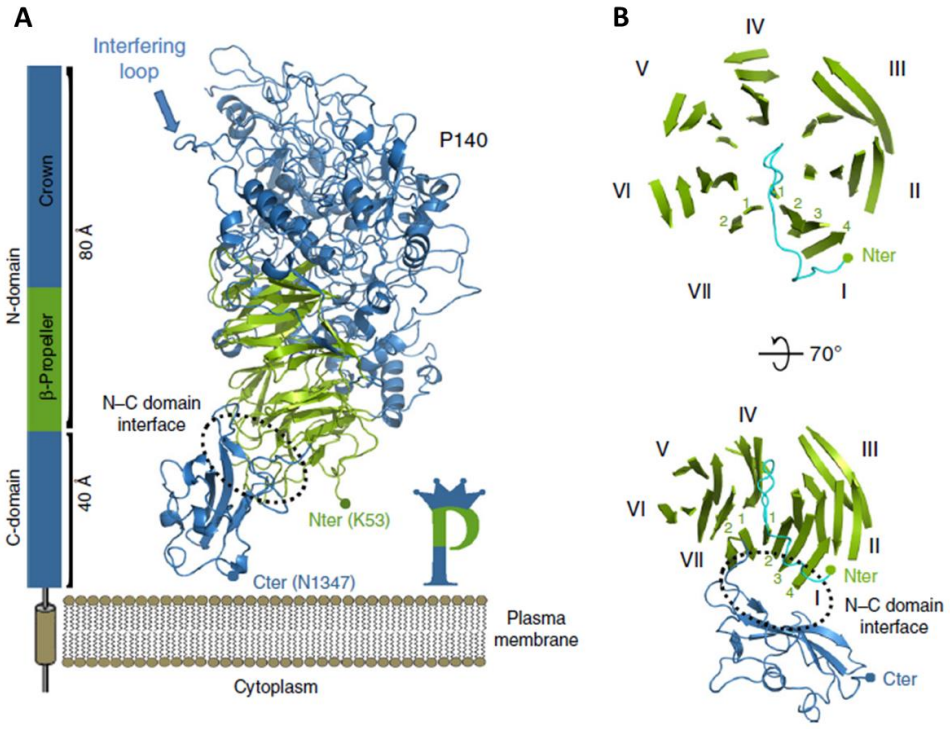

Figure CI. 2.2_1. Structure of P140. A) P140 contains a large N-terminal domain and a smaller C-terminal domain, which is followed in sequence by a predicted transmembrane helix. The N-terminal domain has two distinct regions: the β-propeller (green) and the crown (blue). **B)** Two views of the β-propeller, 70° apart. The first and last β-sheets of the propeller (I and VII, respectively) interact with the C-terminal domain and are structurally contiguous in the propeller ring. A large β-bulge (residues 69–77, in cyan) occludes the center of the propeller ring. The presence of only two strands in the last β-sheet (VII) constrains the interface between the N-terminal and C-terminal domains. Adapted from **Aparicio D. *et al.*, 2020**.

As in P110, the N-domain of P140 has a β-sheet propeller topology of seven consecutive blades or β-sheets and a "crown" formed by the clustering of the long polypeptide segments that emerge from the propeller (**Appendices Figure A. CI. 1.7_2**). Each β-sheet have four antiparallel strands with the only exception of β-sheet VII (the last β-sheet in the propeller that connects directly with the C-terminal domain) that contains only two strands. The absence of the last two strands in β-sheet VII, the last β-sheet of the propeller, affects importantly to the linkage with the following C-domain (**Figure CI. 2.2_2B**). On the contrary, β-sheet I, which in P110 had only three strands, has four in P140 (**Figure CI. 2.2_2B**). This "extra" first strand in the first β-sheet of P140 situates the N-end of the domain in the propeller face opposite to the one in P110 (**Figure**

CI. 2.2_2B). This "extra" first strand in β-sheet I starts with a large β-bulge (residues 69-77) that occludes the centre of the propeller, contrary to what happens in P110, where the centre is empty (**Figure CI. 2.2_2B**). Therefore, the first and last blades, structurally contiguous in the propeller, present the largest differences between P140 and P110. Connections between β-strands vary widely in length and accordingly the number of residues that each β-sheet spans is very diverse, ranging from 44 to 197 for β-sheets V and IV, respectively. The length of links between β-sheets is also very diverse, going from just two residues, between sheets VI and VII, to 253 residues between sheets IV and V. Residues from the long connections, both between β-strands and β-sheets, cluster together creating a crown-like structure, above β-sheets III-IV and V, that is related with the crown observed in P110, although both crowns present many differences. According to these observations, superimposition of N-domains from P110 and P140 gives a RMSD of 3.5 Å between the Cα atoms of 359 structurally equivalent residues for 359 equivalent residues (~28%), which include most of the residues from the β-strands in the propeller β-sheets. The small C-terminal domain of erP140 presents a three stranded antiparallel β-sheet that interacts extensively with β-sheets I, II and VII from the N-domain. Superimposition of C-domains from P110 and P140, gives a RSMD of 2.2 Å for 74 equivalent residues (~71%). Therefore, C-domains from P110 and P140 are clearly structurally related, in spite topology appears somehow different as two of the five strands forming a β-barrel that is central to the P110 structure, are missing in P140.

Localization of C-domains with respect to the propeller ring is different in both adhesins. The C-domains protrudes radially from the ring in P110 while in P140 the C-domain is tangential and with a large interdomain interface. These differences, together with the analysis of the relative orientations of domains in all the structures of P110 and P140 subunits available and the compactness of the β-propeller rings, suggest that hinge movements between the N- and C-domains are likely rather limited in P140, but might be larger in P110.

The overall shape of erP140 can be described, similarly to what was proposed for P110, as a capital letter **P** (of ~130 Å in length), with the round and leg parts of the **P** corresponding to the N- and C-domains, respectively (**Figure CI. 2.2_1 and 2.2_2A**). In this representation, the C-end of the C-domain is located at the very bottom of the **P**, while the crown is at the top of the **P** above the β-sheets of the propeller that are located opposite to the C-domain. As for P110 the C-end of erP140, predicted to be followed by the trans-membrane helix (**Figure CI. 2.1_1**), was expected to be close to the mycoplasma outer membrane surface and this is now fully confirmed for both adhesins by the fitting of P110 and P140 into the map obtained from Cryo-ET images of *M. genitalium* "ghost" cells at ~10 Å resolution (see below). In summary, both the topology and

the overall organization of domains from the extracellular regions of P140 and P110 present clear structural relationships, even despite the significant differences in size, of more than 400 residues (with P140 being ~400 residues larger than P110). Structural similarities strongly suggest that P110 and P140 are evolutionarily related, likely having a common ancestor not too distant in the past, although the degree of conservation differs for the N-terminal and C-terminal domains (**Figure CI. 2.2_1**).

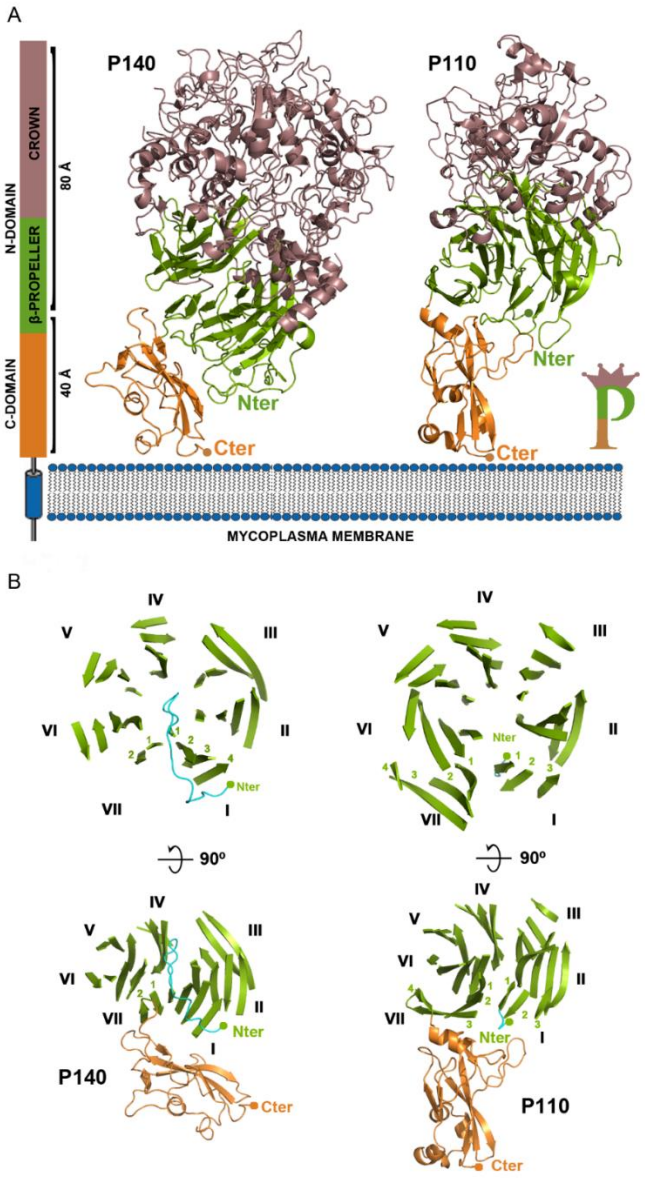

Figure CI. 2.2_2. Structural comparison of P140 and P110. A) P140 and P110 present a similar domain organization with small C-domains (orange) and large N-domains in the extracellular regions of the proteins. The N-terminal domains contain two distinct regions, a seven blade β-propeller (green) and a crown (brown), with the β-propellers situated between the C-terminal domains and the crowns. Also, in both proteins, the C-terminal domains are followed in sequence by a (predicted) transmembrane helix and a cytosolic region with about a hundred residues. **B)** Two views of the β-propellers of P140 and P110, 90° apart. The N-domain of both P140 and P110 has a β-sheet propeller topology of seven consecutive blades or β-sheets. Adapted from **Aparicio D. *et al.*, 2020**.

CI. 2.3. Single-particle Cryo-EM of the P140-P110 extracellular region

Using a sample of P140–P110 complexes, with the complete extracellular region included for both subunits (P140 residues 23–1351 and P110 residues 23–938), we performed single-particle Cryo-EM. We obtained a map with an overall resolution of 4.1 Å, although non-isotropic (**Figure CI. 2.3_1 and 2.3_2, Appendices Table A. CI. 1.6_1 and Appendices Figure A. CI. 1.6_1**). The P140–P110N X-ray structure could be fitted as a rigid-body without modifications into the P140–P110 Cryo-EM map, indicating no conformational changes, with UCSF Chimera[408] [**Pettersen E. F. *et al.*, 2004**] (**Figure CI. 2.3_2 and Appendices Table A. CI. 1.6_2**).

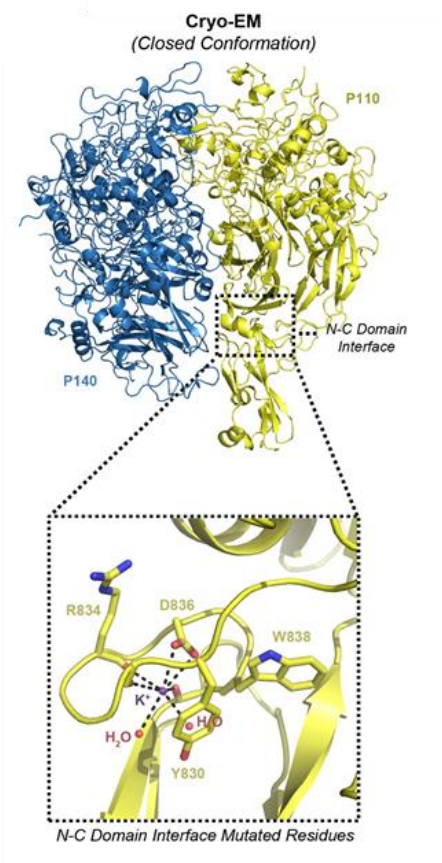

Figure CI. 2.3_1. Cryo-EM structure of the P140–P110 heterodimer. The C-terminal domain of P140 is missing in the structure because it was not defined in the Cryo-EM map (**Figure 2.4_2**). The C-terminal domain of P110 was visible in the Cryo-EM map, although with a local resolution lower than that for the N-terminal domains. Spotted square shows the details of the interface between the N-terminal and C-terminal domains, close to where a potassium ion was found in the structures of P110 alone[383] [**Aparicio D. *et al.*, 2018**]. R^2 for each fitting curve: WT (0.8576), dP110 (0.9054), P110-WT (0.9921), P110-Y830A (0.9663), P110-W838F (0.8339), P110-R834G (0.8757), P110-D836L (0.9993), P110-R600A (0.8663), and P110-RQD (0.9999). Adapted from **Aparicio D. *et al.*, 2020**.

Therefore, the structure of the P140–P110 complex found by Cryo-EM corresponds to the conformation of the X-ray P140–P110N structure, where access to the sialylated oligosaccharides binding site is occluded (closed conformation). In the P140–P110 Cryo-EM map, there is no density for the C-terminal domain of P140, whereas the C-terminal domain of P110, which is absent in the P140–P110N complex, is visible in the P140-P110 Cryo-EM, albeit with a weak density (**Figure CI. 2.3_1 and 2.3_2**). This indicates a significant flexibility of the C-terminal domains with respect to the bulkier N-terminal domains. In the P140–P110 complex found by Cryo-EM, the interface between subunits spans 2758 Å2 with 30 hydrogen bonds and an

estimated Gibbs free energy of –20 kcal/mol, resulting in a 100% probability of the formation of the complex (PISA server[407] [Krissinel E. and Henrick K., 2007]).

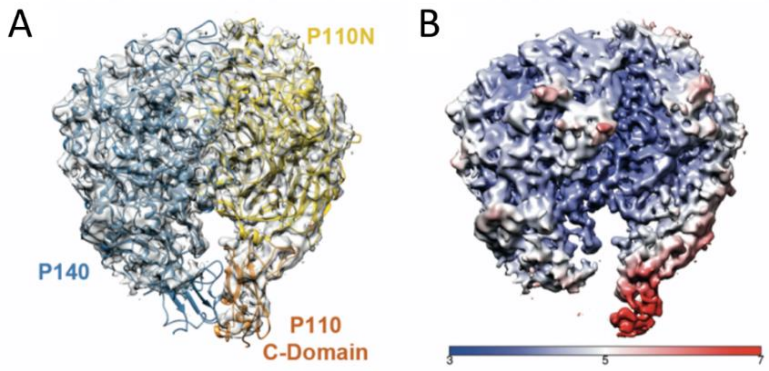

Figure CI. 2.3_2. Cryo-EM of the P140-P110 extracellular region. **A)** Cryo-EM map of the extracellular region of the P140-P110 heterodimer. The structure of P140-P110N, fitted into the map density, is also shown with P140 in blue and P110 in yellow. There is no density for the C-domain of P140, while density is visible, although weak, for the C-domain of P110 that was fitted independently into the Cryo-EM map (orange). **B)** Local resolution of the Cryo-EM map. The lowest resolution corresponds to the C-terminal domains, which indicates a significant flexibility of these domains, in particular of the C-terminal domain from P140, with respect to the bulkier N-domains. Adapted from Aparicio D. *et al.*, 2020.

CI. 2.4. Assessment of the cytadherence capacity of *M. genitalium* strains carrying target mutations in P140 or P110

In previous works in our laboratory, we demonstrated the suitability of a FACS-based hemadsorption (HA) assay to quantify and compare the cytadherence capacity of *M. genitalium* mutants[383,409] [García-Morales L. *et al*. 2014, Aparicio D. *et al*. 2018] (see methods for further procedure explanation). The resulting Flow Citometry (FC) data can be later modelled using a kinetic approach, allowing the quantification of the HA activity of a particular mycoplasma strain by standard K_d and B_{max} parameters[409]. Similar to other kinetic analyses performed on binding reactions involving a ligand and a receptor, the lower K_d and the higher B_{max} are indicative of the stronger HA activity of the tested mycoplasma cells.

Moreover, we showed that pre-treatment of the human red blood cells (hRBCs) with neuraminidase has a dramatic impact on the cytadherence capacity of *M. genitalium*, confirming that hemadsoption of this human pathogen is mediated through the interaction with sialylated receptors[383] [Aparicio D. *et al*. 2018]. Herein, we used FACS to assess HA of thecytadhesin mutant strains created in this study.

Both, the conformation and proximity of P140 histidines 381 and 382 strongly advocate for the presence of acatalytic function in this adhesin. To examine the role of these residues in the function of the adhesion complex, we obtained a mutant strain (P140-HH) carrying a double H381A-H382A substitution (**Table CI. 2.4 and Table MM. CI. 1.1.1**). The mutated P140 allele was

introduced by transposon delivery into a *M. genitalium* strain lacking the gene coding for P140[379] [Burgos R. *et al*., 2006]. For control purposes, the P140 wild type allele was also introduced by transposon delivery to the same strain background to create the P140-WT mutant (see methods for further explanation). For each strain, several clones were isolated and analyzed. Polyacrylamide gels demonstrated that both P140 and P110 proteins were expressed in the P140-WT and P140-HH mutants (**Figure CI. 2.4_1A**). In all the P140-HH clones isolated, P140 expression was slightly reduced as compared to the WT or the P140-WT strains. Cytadherence capacity of the P140-WT mutant was undistinguishable from that of the WT strain. However, expression of the P140 variant with mutated histidines prompted important cytadherence defects. In particular, the binding analysis featured a high K_d, indicating a lower affinity of this mutant for hRBCs compared to the WT or the P140-WT strains. Nonetheless, mycoplasmas were still able to adhere, especially at the highest hRBCs concentrations (**Figure CI. 2.4_1B**).

Table CI. 2.4. Strains used in this chapter.

Strain Name	Genotype	Reference
G37	Wild-type	ATCC 33530
ΔMG_192	Deletion of the MG_192 gene by allelic exchange (G37 ΔMG_192::tetM438)	Burgos *et al.,* 2006
P110-WT	Re-introduction of a MG_192 wild-type allele in a ΔMG_192 mutant	Aparicio, D. *et al.,* 2018
P110-R600A	Introduction of a MG_192 allele bearing a R600A substitution in a ΔMG_192 mutant	This work
P110-RQD	Introduction of a MG_192 allele bearing a R600A, Q460A and D461A substitutions in a ΔMG_192 mutant	This work
P110-Y830A	Introduction of a MG_192 allele bearing a Y830A substitution in a ΔMG_192 mutant	This work
P110-R834G	Introduction of a MG_192 allele bearing a R834G substitution in a ΔMG_192 mutant	This work
P110-D836L	Introduction of a MG_192 allele bearing a D836L substitution in a ΔMG_192 mutant	This work
P110-W838F	Introduction of a MG_192 allele bearing a W838F substitution in a ΔMG_192 mutant	This work
P110-G389F	Introduction of a MG_192 allele bearing a G839F substitution in a ΔMG_192 mutant	This work
ΔMG_191	Deletion of the MG_191 gene by allelic exchange (G37 ΔMG_191::tetM438)	Burgos *et al.,* 2006
P140-WT	Re-introduction of a MG_191 wild-type allele in a ΔMG_191 mutant	This work

P140-HH	Introduction of a MG_191 allele bearing a H831A and H832A substitutions in a ΔMG_191 mutant	This work

The binding site for the sialylated oligosaccharides, identified in the structure of P110[383] [Aparicio D. *et al.*, 2018], is located at the interface between P140 and P110 in the crystal structure of the P140–P110N complex (**Figure CI. 2.1_4**). Interaction of the two subunits changes the position of the sialic binding β-hairpin while the interfering loop (P140 residues 807–827) inserts into the binding pocket of P110N, thereby sterically interfering with the binding of oligosaccharides to the P140-P110 complex (**Figure CI. 2.1_4C,D**). In agreement with this picture, surface plasmon resonance analysis shows that, in solution, sialylated compounds 3SL and 6SL (neuraminic acid forming an α2–3 or an α2–6 linkage to a lactose monosaccharide, respectively), which bind to P110 alone[383] [Aparicio D. *et al.*, 2018], do not bind either to P140 alone or to P140–P110 complexes (**Appendices Figure A. CI. 1.7_3**). The structure of the P140–P110N complex suggests that P110 residues Q460–D461, from the binding β-hairpin, and R600, which is close to the receptor-binding site, play an important role in the interaction with P140 (**Figure CI. 2.1_4A**).

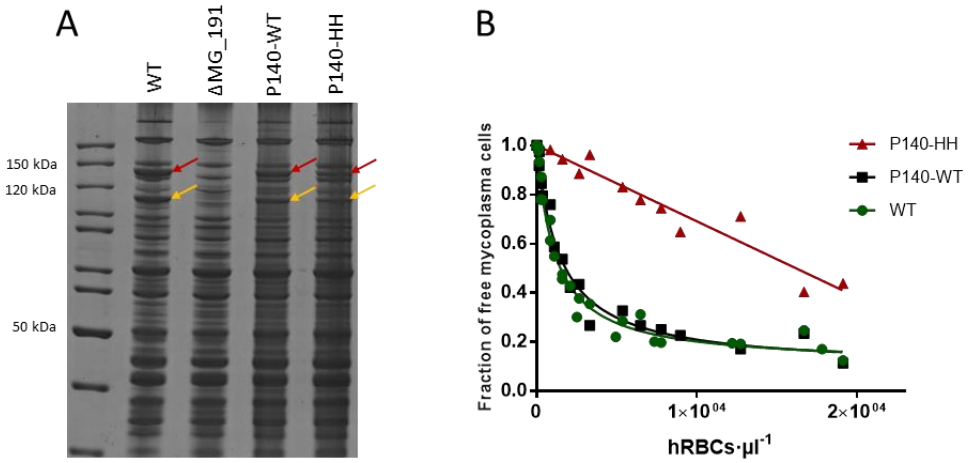

Figure CI. 2.4_1. Characterization of the mutant strains carrying P140 adhesin variants. A) SDS-PAGE of whole cell lysates from the WT, ΔMG_191 strain and the different P140 adhesin mutants. Red and orange arrows indicate the presence of P140 and P110 adhesins, respectively. **B)** HA assays determined by FACS analysis. Graphic represents inverse Langmuir plots containing a fixed amount of mycoplasma cells and increasing amounts of hRBCs. Plots were generated using data from, at least two biological repeats for each strain.

Structural analysis indicates that P110 residues R600, Q460 and D461 may play an important role in the interaction with P140 and therefore, mutations in these amino acids could prevent the formation of the erP140-P110g heterodimer. To test this hypothesis, we obtained mutants carrying a R600A substitution (P110-R600A) or a triple substitution R600A, Q460A and D461A (P110-RQD) (**Table CI. 2.4 and Table MM. CI. 1.1.1**). Similarly, the mutated P110 alleles were

introduced by transposon delivery into a *M. genitalium* lacking the gene coding for P110[379] [Burgos R. *et al.*, 2006]. Again, several transformants were isolated and analyzed for each mutant. In this case, the control strain bearing a transposon-encoded copy of the P110 allele was already obtained and characterized in a previous study[383] [Aparicio D. *et al.* 2018]. Whole-cell lysates of these mutants were analyzed in polyacrylamide gels, but the P110-R600A and P110-RQD variants were not detected. This result suggests that P110-R600A and P110-RQD are unstable and degraded, which precludes the *in vivo* characterization of the resulting strains.

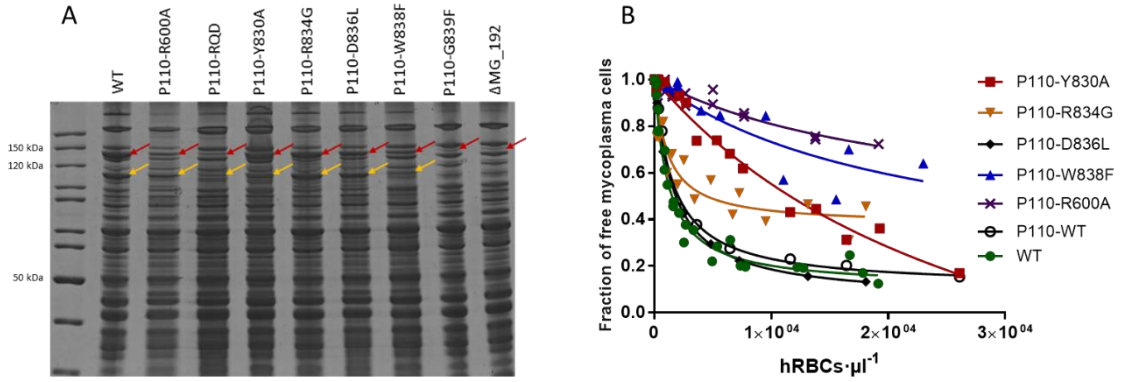

Figure CI. 2.4_2. Characterization of the mutant strains carrying P110 adhesin variants. A) SDS-PAGE of whole cell lysates from the WT, ΔMG_192 strain and the different P110 adhesin mutants. Red and orange arrows indicate the presence of P140 and P110 adhesins, respectively. **B)** HA assays determined by FACS analysis. Graphic represents inverse Langmuir plots containing a fixed amount of mycoplasma cells and increasing amounts of hRBCs. Plots were generated using data from, at least two biological repeats for each strain. Adapted from Aparicio D. *et al.*, 2020.

Despite the earlier identification of a potassium binding pocket within the C-terminal region of the P110 adhesin, the role of this pocket in P110 function has not been addressed. Remarkably, this pocket is located at the leg of the P110 adhesin, that is, near the transmembrane domain and away from the receptor binding pocket. To gain insight into the function of this pocket we constructed a series of mutants involving several residues of the potassium binding pocket of P110: Y830A, R834G, D836L, W838F and G389A (**Table CI. 2.4 and Table MM. CI. 1.1.1**). SDS-PAGEs demonstrates the expression of the all the P110 variants except P110-G389A (**Figure CI. 2.4_2A**) and thislatter mutant strain was not characterized further. All mutant strains analyzed exhibited cytadherence defects, with the only exception of the P110-D836L strain (**Figure CI. 2.4_2B**). The P110-Y830A and P110-R834G variants showed intermediate hemadsorption phenotypes, characterized by unusually high B_{max} values. Binding of the P110-W838F mutant was similar to that of the P140-HH strain, characterized by a high K_d. In contrast, the cytadherence profile of the P110-R838F mutant featured anomalous B_{max} values, suggesting that the cell population tested was heterogeneous and a significant number of cells was non-

adherent, even at the highest hRBC concentration. Therefore, our results suggest a possible role for potassium in the regulation of *M. genitalium* cyatdherence.

CI. 2.5. Assessment of the motility of *M. genitalium* strains carrying target mutations in P140 or P110

We examined the gliding activity of cells from the different mutants described above by time-lapse microcinematography to monitor the movements of individual cells for 120 s (**Figure CI. 2.5_1 and Table CI. 2.5**). In the P110-W838F mutant, cells were completely non-motile and, in agreement with this extreme phenotype, phase contrast images revealed the presence of large aggregates (**Figure CI. 2.5_1**). The presence of large cell aggregates has been correlated in previous works with the existence of severe gliding deficiencies[379] [**Burgos R. *et al*., 2006**]. The Y830A, R834G, and D836L variants also exhibited altered gliding velocities, indicating that structural integrity at the interface between the N-terminal and C-terminal domains, away from the cell receptor-binding site, is critical for motility in *M. genitalium,* but these differences were not found to be statistically significant.

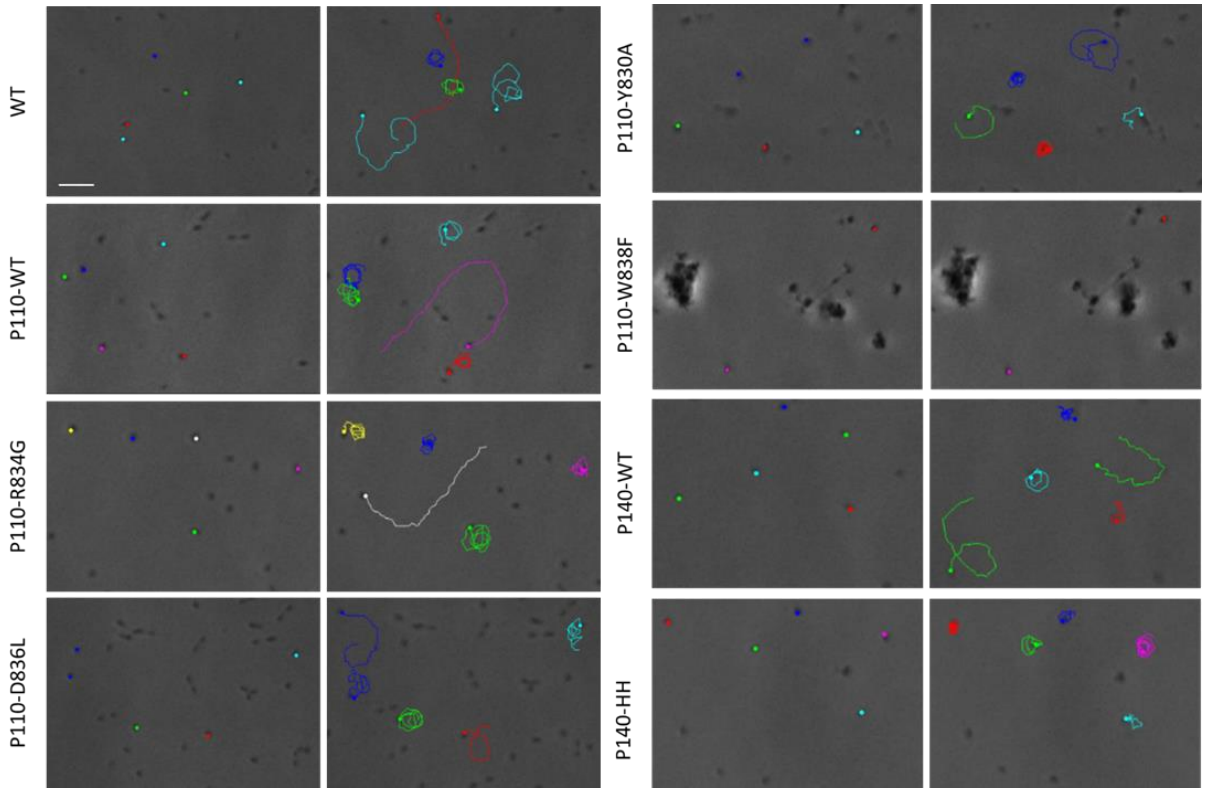

Figure CI. 2.5_1. **Time-lapse microcinematography and expression analysis for WT and selected strain variants**. Representative tracks of *M. genitalium* G37 Wild Type (WT), P110-WT and P140-WT cells, and P110-R834G, P110-D836L, P110-Y830A, P110-W838F and P140-HH mutant cells. Although cells from P110-W838F were found to have severe hemadsorption deficiencies by flow cytometry, these cells attached properly to the plastic surface of Ibidi slides. This behavior is somewhat common and has been

previously described[410] [Burgos R. et al., 2006]. Bar is 5 µm. All pictures are shown at the same magnification. Adapted from Aparicio D. *et al.*, 2020.

Motility of the P140-WT and P110-WT strains was comparable to that of the WT strain (**Table CI. 2.5**). However, we found that gliding velocity of cells from the P140-HH mutant was significantly reduced (**Table CI. 2.5**). Moreover, when examining this mutant, we observed a reduced frequency of cells drawing non-circular tracks (**Figure CI. 2.5_2**) and a significantly reduced diameter of the circular tracks (**Table CI. 2.5 and Figure CI. 2.5_3**)**.** All these results reinforce the role of H381 and H382 in the function of the Nap complex.

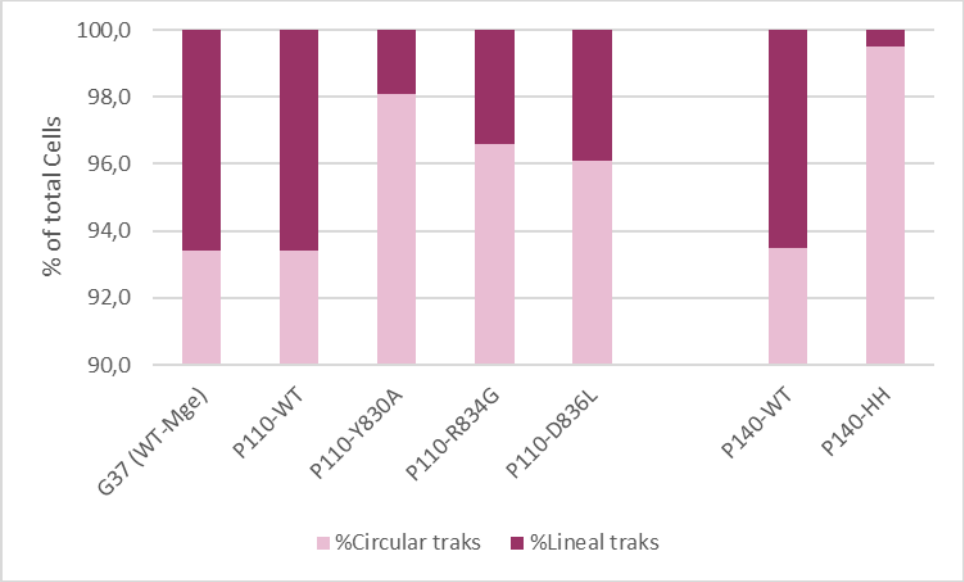

Figure CI. 2.5_2. Characterization of the motile properties in the reference and all mutant strains. Percentage of cells describing circular and non-circular tracks.

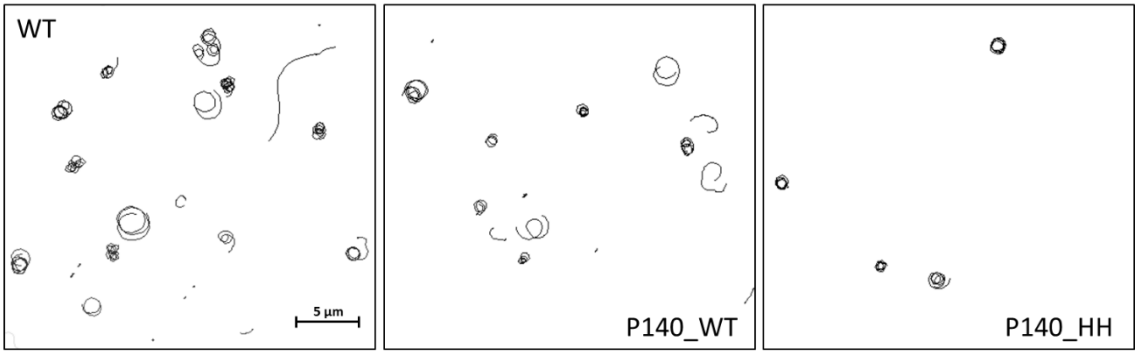

Figure CI. 2.5_3. Representative tracks described by mycoplasma cells. P140-HH mutant strain present a reduced frequency of cells drawing non-circular tracks and a significantly reduced diameter of the circular tracks.

Table CI. 2.5. Gliding motility parameters of *M. genitalium* G37 wild-type cells and all different mutant strains obtained.

Strain	n (Motility)	Individual Motile cells (%)	n (Velocity)	Velocity (µm/s)[a]	Motility loss (%)	Circular Tracks (%)	Non-circular Tracks (%)	Diameter of circular tracks (µm)[a]
G37 (WT)	~250	88.5	25	0.126±0.002	-	93.4	6.6	1.076±0.041
P110-WT	~250	77.4	25	0.119±0.014	5.6	93.4	6.6	1.077±0.033
P110-Y830A	~250	78.8	25	0.100±0.011*	20.6	98.1	1.9	1.075±0.039
P110-R834G	~250	86.8	25	0.114±0.007	9.5	96.6	3.4	1.070±0.024
P110-D836L	~250	86.5	25	0.102±0.009*	19.0	96.1	3.9	1.075±0.035
P110-W838F	~64	0	25	0	100	-	-	-
P140-WT	~250	83.7	25	0.124±0.005	1.6	93.5	6.5	1.084±0.036
P140-HH	~250	85.8	25	0.080±0.010*	36.5	99.5	0.5	0.810±0.028*

[a]Velocities are shown as mean values +/- standard error. n=25 biologically independent cells, from different fields, different preparations and different microcinematographies.

*Statistically significant values (T (25) = 2.06; p<0.05). Statistical significance was assessed with the Paired Student's two-sided T-test. Velocity p-values: 0.02, 0.01, $3.96 \cdot 10^{-12}$; Diameter P140-HH p-value=: $3.04 \cdot 10^{-3}$ (Table order).

CI. 2.6. Single-particle analysis of the Nap

Next, we performed single particle Cryo-EM using a purified sample of Nap complexes, obtained as previously described[380] [**Scheffer M. P. *et al.*, 2017**]. The purified Nap complexes contain full-length P140 and P110 proteins, including the transmembrane helices and cytoplasmic regions, which are required for formation of tetramers. Classification indicated that only ~15–20% of the images corresponded to complete Nap particles where the extracellular region was well defined. The best map, with an overall resolution of 9.8 Å, allowed accurate rigid-body fitting with Chimera[408] [**Pettersen E. F. *et al.*, 2004**] of the P140 structure alone and the P110 structure alone, confirming the presence of a dimer of P140–P110 heterodimers in each Nap (**Figure CI. 2.6_1A–C, Appendices Figure A. CI. 1.6_2 and Appendices Table A. CI. 1.6_1**). The arrangement of P140–P110 heterodimers is essentially identical to the X-ray and Cryo-EM P140–P110 structures, with the interactions between both subunits preventing access to the sialylated oligosaccharide binding site. This is the "closed" conformation of the Nap. C-terminal domains act like stalks connecting the large N-terminal domain of each subunit with the outer surface of the cell membrane. The two P110 subunits are almost parallel to the dimer axis and face away from each other, while the two P140 subunits of the Nap adopt a "V-shaped" arrangement with the C-terminal domains very close to each other (**Figure CI. 2.6_1C**).

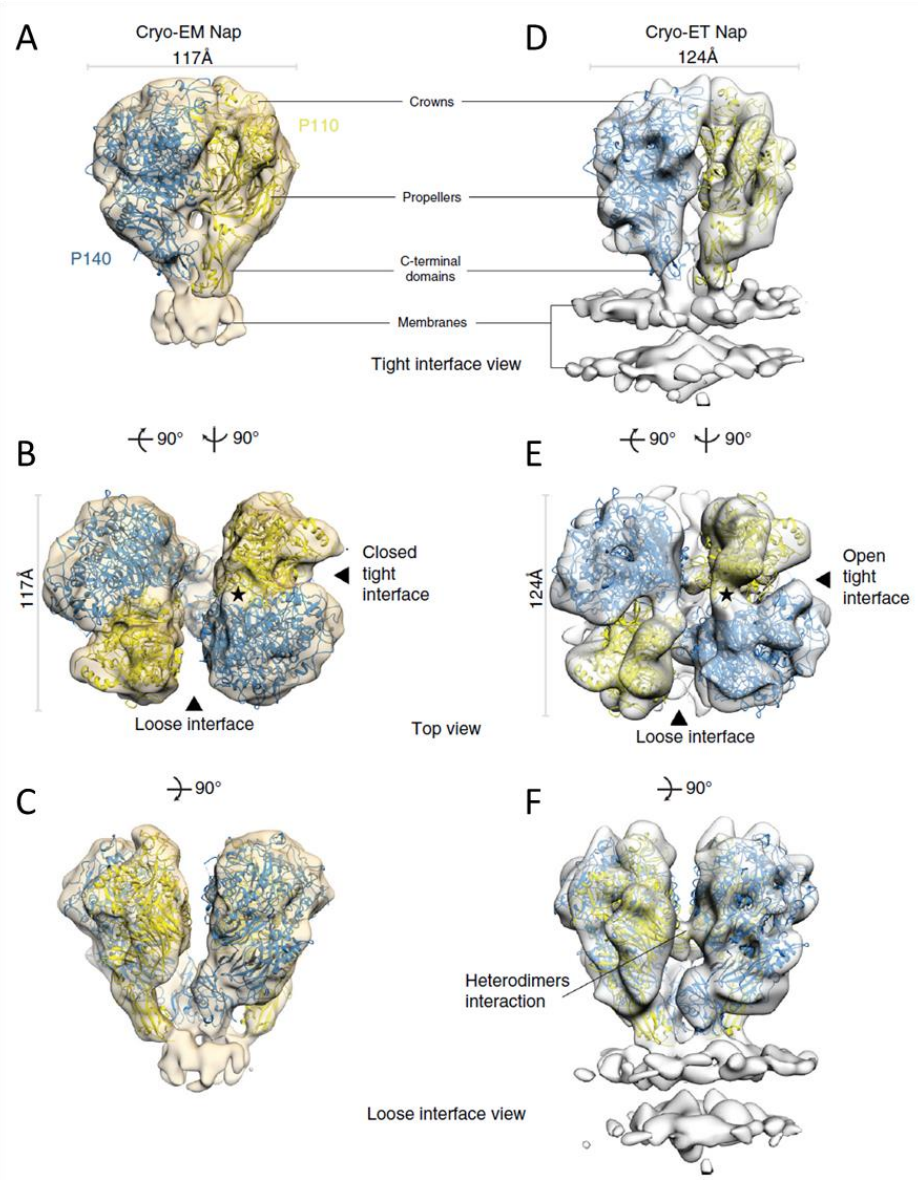

Figure CI. 2.6_1. The structure of Nap by single-particle Cryo-EM and in situ Cryo-ET. A–C) Three different views of the single-particle Cryo-EM from the Nap (beige surface) with the structures of P140 (blue) and P110 (yellow) fitted into the density. In **A** the crown, propeller, and C-terminal domain are indicated. **B)** Top view of the Nap, depicting the loose and tight interfaces. An approximate twofold axis perpendicular to the cell membrane relates the pair of P110–P140 heterodimers of a Nap. Fitting of the P140 and P110 subunits is unambiguous. The interface between the P110 and P140 subunits, defined as tight in the Cryo-EM structure of the Nap, is the same found in the Cryo-EM structure of the P140–P110 heterodimer. The interfering loop and the binding site are indicated with a black star. **C)** The lateral view along the loose interface shows the V-like shape adopted by the two P140 subunits. **D–F)** Three views of the Cryo-ET map of the Nap, with the structures of P140 and P110 accurately fitted. The membrane bilayer of the mycoplasma cell is clearly defined in the lower part of the lateral views (**D, F**). **E)** The top view shows that the tight interface is wider in the Cryo-ET "open" conformation than in the Cryo-EM "closed" conformation of the Nap. **F)** The lateral view along the loose interface shows an interaction between heterodimers. Adapted from **Aparicio D. *et al.*, 2020**.

The distance between heterodimers is large (**Figure CI. 2.6_1B,C**), suggesting that their interaction is weak. This is in agreement with MALS measurements where only heterodimers

are detected when mixing equimolecular amounts of constructs from the extracellular regions of P110 and P140 (**Appendices Figure A. CI. 1.7_1**). Therefore, there are two interfaces in the Nap between the extracellular regions of P140 and P110, which we name the "tight" and "loose" interfaces (**Figure CI. 2.6_1B,E**). The Cryo-EM map of the Nap shows density corresponding to the Nap transmembrane region and the positions of the transmembrane helices (their N-terminal ends) can be seen (**Figure CI. 2.6_1A,C**). The close proximity of the P140 C-terminal domains also brings the N-terminal ends of the corresponding transmembrane helices closer together. For P140 and P110, sequence analysis indicates the presence of one transmembrane helix containing one and two Engelman motifs (GXXXG, with X any residue, in general hydrophobic), respectively, which are characteristic of high-affinity interactions in membrane helices[411,412] [**Russ W. P. and Engelman D. M., 2000; Seto S. *et al.*, 2005**].

CI. 2.7. Cryo-electron tomography of the "in-situ" Nap

The structure of the native Nap complex was also investigated *in situ* by Cryo-ET from mildly lysed *M. genitalium* cells[380] [**Scheffer M. P. *et al.*, 2017**]. Classification of Nap volumes and subsequent sub-tomogram averaging provided an improved map for the most abundant class (~85%) at 15 Å resolution, in which the four subunits, two from P110 and two from P140, are clearly distinguished and present a nearly perfect twofold symmetry (**Figure CI. 2.6_1D-F and 2.7_1**).

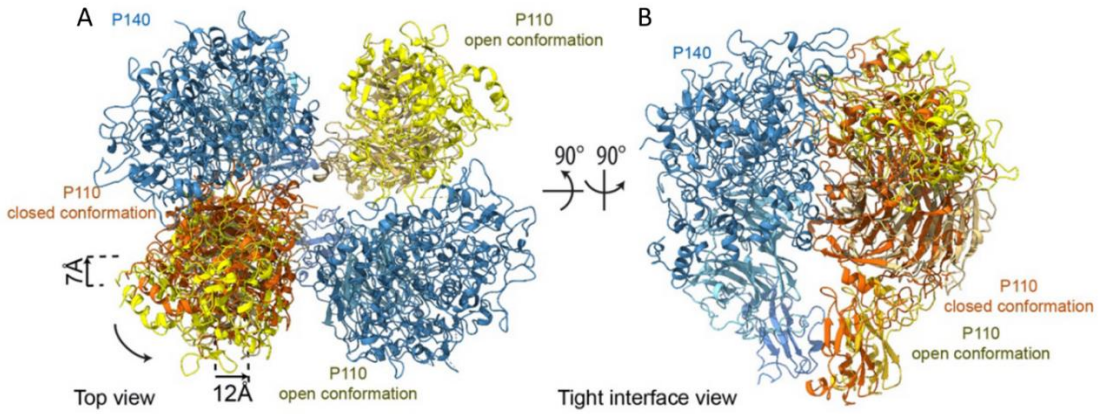

Figure CI. 2.7_1. Transition between the open and closed conformations through the movement of P110. A) Top view and (**B**) a tight interface view of a dimer of P140-P110 heterodimers showing the relative movement of P110 from the closed conformation (orange) as it retracts 7Å from its position at the tight interface and moves 12 Å closer to P140 across the loose interface to form the open conformation (yellow). P140 (blue) is kept unchanged as a reference. Adapted from **Aparicio D. *et al.*, 2020**.

The rigid-body fitting of the structures of P110 alone and P140 alone into the Cryo-ET density with Chimera[408] [**Pettersen E. F. *et al.*, 2004**] reveals major differences from the Cryo-EM structure of the Nap (**Figure CI. 2.6_1, 2.7_2A and Appendices Table A. CI. 1.6_2**). In the Cryo-ET structure, the longest axis of the four subunits runs parallel to the axis of twofold symmetry of the Nap. This implies that between the Cryo-ET and Cryo-EM structures there is a rotation of P110 relative to P140 in the heterodimer and an increase of 10 Å in the closest distance between the C-terminal domains of P140 subunits (**Figure CI. 2.7_2B,C and Appendices Figure A. CI. 1.4_2**). The loose interface between P140 and P110 subunits, which is very wide in the Cryo-EM structure of the Nap, is narrower in the Cryo-ET structure, with a few interactions between P140 and P110 (in particular, P140 residues 1175–1179 interacting with the P110 loop 750–755) that are absent in the Cryo-EM Nap (**Figure CI. 2.6_1C,F**). The tight interface between P140 and P110, which is in the "closed" conformation in the Cryo-EM structure of the Nap, undergoes major rearrangements in the Cryo-ET structure, becoming on average ~7 Å wider (**Figure CI. 2.6_1A-E**). This widening "opens" the sialylated oligosaccharide-binding site, making it accessible for binding in the Cryo-ET structure of the Nap. Therefore, the Cryo-ET and Cryo-EM structures of the Nap correspond to conformations that, with respect to the sialylated host cell receptors, are respectively "open", with the binding site accessible and ready for binding, and "closed", with the binding site occluded and not accessible for binding. In the Cryo-ET map, the cell membrane surrounding the Nap is visible as a double layer that is perpendicular to the Nap twofold axis. The positions of the C-terminal domains are largely different between the Cryo-ET and Cryo-EM Nap structures, changing from a squared to rhomboid shape, respectively (**Figure CI. 2.7_2B**). These differences also affect the positions of the transmembrane helices that follow in sequence immediately after the C-terminal domains, which provide a mechanism for communication between the Nap extracellular and intracellular regions. On the intracellular side, the Cryo-ET map shows a compact density, similar to the one reported previously[380] [**Scheffer M. P. *et al.*, 2017**], with a volume suited to about 400 residues and an approximate twofold symmetry, where the four subunits appear to interact closely as they cannot be individualized at the resolution available.

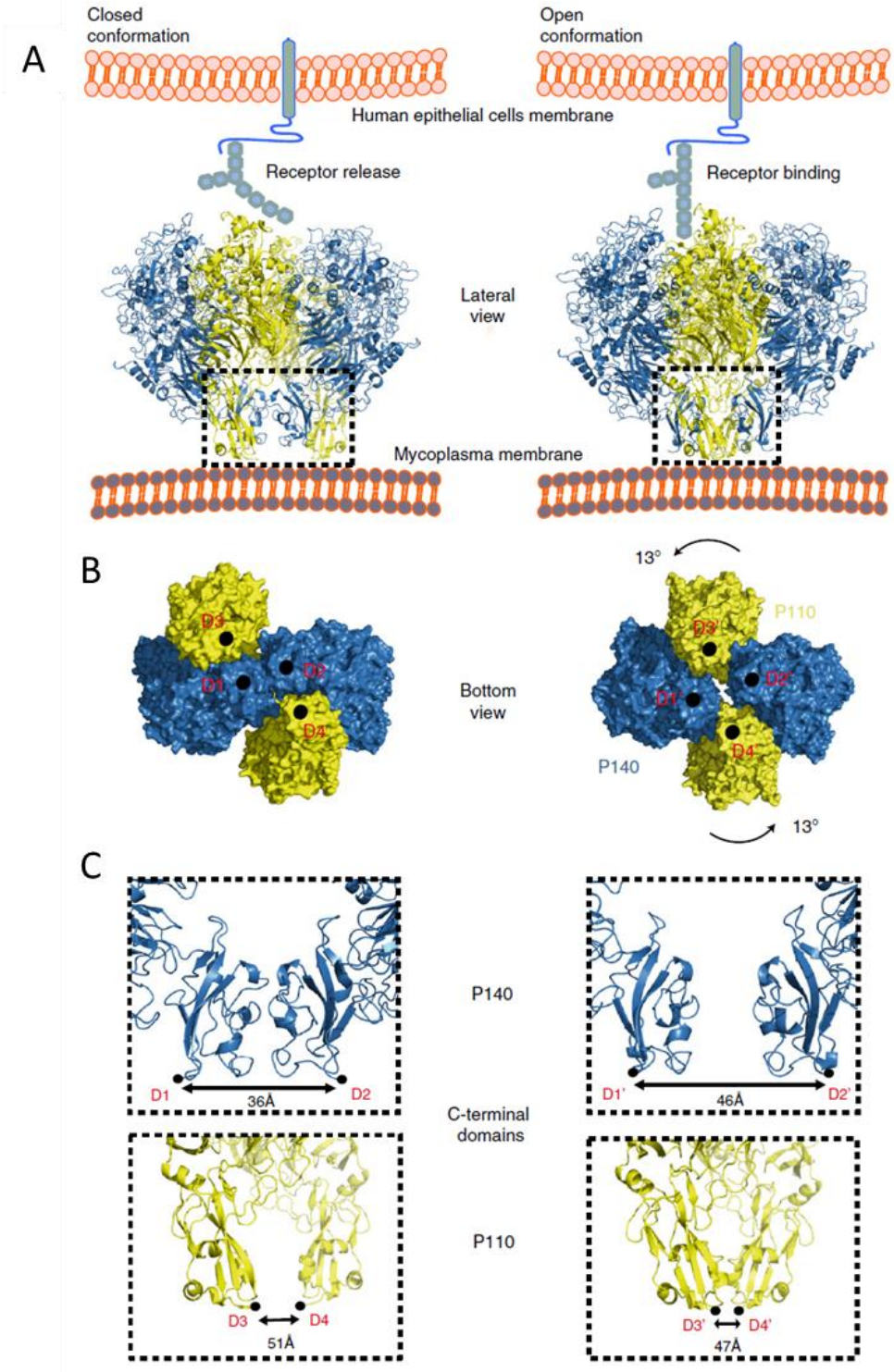

Figure CI. 2.7_2. Structural rearrangements between "open" and "closed" conformations. A) "Closed" (left panel) and "open" (right panel) conformations of the Nap complex. The "closed" conformation associated with the release state of the sialylated oligosaccharides cell receptors. The "open" conformation associates with the bound and ready-to-bind state. **B)** Bottom view along the Nap twofold axis, depicting points of contact (black circles) between subunits and the mycoplasma cell outer membrane. These points also mark the start (the N-terminal ends) of the transmembrane helices. The N-terminal end positions are changing from a squared to rhomboid shape, when transitioning from the closed to the open conformation. **C)** Changes to the relative positions of the C-terminal domains from P140 (upper panels) and P110 (lower panels). Adapted from **Aparicio D. *et al.*, 2020**.

CI. 2.8. Epitope maps comparison between P1 from *M. pneumoniae* and P140 from *M. genitalium*

Untreated infections by *M. pneumoniae* and *M. genitalium* can be persistent, highlighting a remarkable ability to evade the host immune response. The main adhesins of *M. genitalium* (P140 and P110) and *M. pneumoniae* (P1 and P90/P40) are among the most immunogenic proteins of these pathogens. These adhesins feature variable regions located predominantly at the solvent-exposed surface that could function as a decoy to prevent antibody recognition of key cytoadherence domains. Epitopes for monoclonal antibodies (mAbs) and sera from *M. pneumoniae* infected patients, are mainly exposed on the surface of P1[413] [**Vizarraga D. *et al.*, 2020**]. However, the immunogenicity of *M. genitalium* P140 has not been examined in the context of the 3D structure of this adhesin. We investigated the presence in the P140 adhesin of known P1 (PDB:6RC9) epitopes from mAbs and sera using Clustal-O alignments. Accessibility of residues in the identified P140 epitopes was examined by PyMOL in the 3D structure of this adhesin (PDB:6S3U).

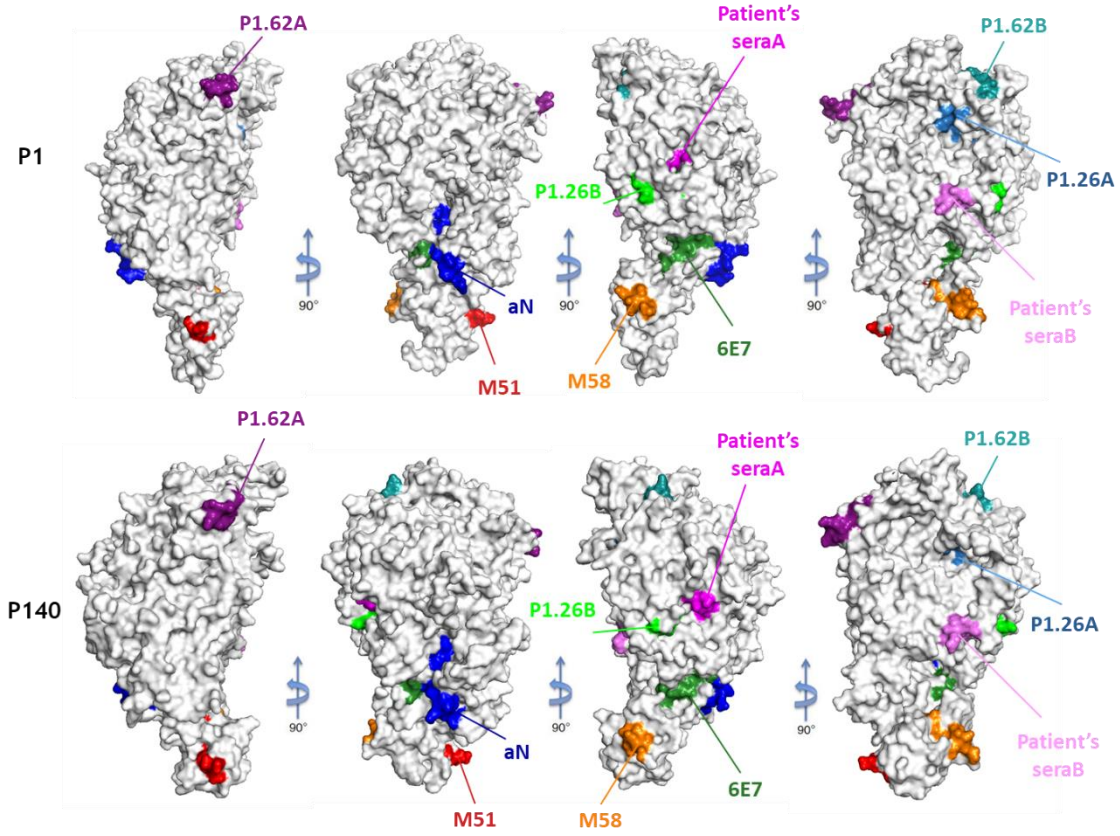

Figure CI. 2.8_1. 3D structure of the *M. penumoniae* P1 (PDB:6RC9) and *M. genitalium* P140 (PDB:6S3U) adhesins. Different views, 90° apart from each other, of the P1 and P140 surfaces. Location of known epitopes in the P1 adhesin and predicted P1-like epitopes in the P140 adhesin. Their location was comparable to that in P1. Predicted P140 epitopes were examined by PyMOL. Adapted from **David V. *et al.*, 2020**.

Comparative structural analyses indicate that P1 and P140 adhesins show similar immunogenicity properties. We determined the location of the epitopes for six known adhesion-inhibiting mAbs and patient's sera in the structure of P1 (**Figure CI. 2.8_1**). Epitopes were located manly exposed in the surface of this adhesin (**Table CI. 2.8**), suggesting that they are accessible to the antibodies. P1-like epitopes are located mainly exposed on the surface of P140, suggesting that they are also accessible to the antibodies. P1.26 mAb binds to dual epitopes and one of them might become hidden in the resulting Nap adhesin complex. A similar scenario is predicted for the A epitope from patients' sera. The location of P1-like epitopes was pinpointed in the structure of the P140 adhesin and location was comparable to that in P1, with the sole exception of epitope A from mAb P1.26, which is exposed in the surface of P1 but it is predicted to be buried in the P140 structure.

Table CI. 2.8. Location of epitopes in P1 (*M. pneumoniae*) and P140 (*M. genitalium*). Presence in the P140 adhesin of known P1 epitopes from mAbs and sera. Predictions were made by examining Clustal-O alignments of both adhesins.

	M. penumoniae				*M. genitalium*		
mAbs epitopes	**Sequence**	**Residues**	**Extracellular Domain**	**Location**	**Sequence**	**Residues**	**Exposure**
aN	NAINPRLTPWTYRN	Asn60-Asn74	N-terminal	Surface	QAVDETLTPWTWNN	Gln59-Asn72	Surface
P1.26-A	NALSFTNK	Asn980-Lys987	N-terminal	Hidden	NALTFTNK	Asn895-Lys902	Hidden
P1.26-B	DVVGVGRL	Asp1362-Leu1369	N-terminal	Surface	SEIGI	Ser1209-Ile1213	Surface
P1.62-A	EVKKKSDS	Glu290-Ser297	N-terminal	Surface	EVERGSQS	Glu282-Ser287	Surface
P1.62-B	ENHTKFTS	Glu910-Ser917	N-terminal	Surface	IPFEQ	Ile845-Gln849	Surface
M58	SVNPKMVR	Ser1450-Arg1457	C-terminal	Surface	GFDQASIR	Gly1294-Arg1301	Surface
M51	NEQSLGLR	Asn1466-Arg1473	C-terminal	Surface	ENQTLGVR	Glu1310-Arg1317	Surface
6E7	GIVRTPLAELLDG	Gly1383-1395	N-terminal	Surface	GVVSTPLVNLING	Gly1227-Gly1239	Surface

	M. pneumoniae				*M. genitalium*		
Patient sera epitopes	**Sequence**	**Residues**	**Extracellular Domain**	**Location**	**Sequence**	**Residues**	**Exposure**
A	WIGNGYRY	Trp810–Tyr817	N-terminal	Hidden	WIGNGKPF	Trp770-Phe777	Hidden
B	FTDFVKPR	Phe1124–Arg1131	N-terminal	Surface	FTDFIRPR	Phe1031-Arg1038	Surface

CI. 2.9. Determination of post-translational modifications (phosphorylation by TiO2)

To investigate the presence of phosphorylated residues in P140 and P110 adhesins, we analysed them in-liquid digested samples by LC-MS/MS. First, a non-enriched sample was directly analysed by LC-MS/MS. After database search, 170 protein groups were identified in this sample and the two most abundant proteins according to the PSMs were P140 (P20796) and P110 (P22747). The sequences of these two proteins are 100% homologous with the sequences that were submitted to the proteomics facility (P110 6His with P22747 and P140 with P20796). The coverage obtained for both proteins was around 60% but no phosphorylated peptide was detected. Next, an enriched sample analysis was performed. After database search, 162 protein groups were identified and the two proteins of interest had around a 70% of coverage. In this case, five and seven phosphorylated peptides were detected for protein P110 and P140, respectively (**Appendices Figure A. CI. 1.8_1 and A. CI. 1.8_2**). To confirm these phosphopeptides, a LC-MS/ MS analysis in target mode was performed, acquiring only the spectra corresponding to the phosphopeptides of interest m/z. **Appendices Table A. CI. 1.8_1** show the sequences identified in the enriched sample analysis by data dependent mode (without list of peptides) and in target mode (specifying which m/z was fragmented). As can be seen, ten out of twelve phosphopeptides were confirmed by the target analysis. In this way, five phosphosites were confirmed in P140 protein, and four phosphosites in P110 protein, all with a ptmRS confidence higher than 90% (**Table CI. 2.9**).

Table CI. 2.9. List of phosphosites confirmed for P140 and P110 adhesins by target mode.

P140	P110
T237	S178
S265	S368
S1418	S1035
T1430	S1048
T1118	

CI. 2.10. Characterization of *M. genitalium* strains carrying mutations in the possible phosphosites in P140

Proteomics analyses confirmed five phosphosites in P140 adhesin and four in P110 adhesin. In order to investigate/elucidate the importance of these post translational modifications, we generated a series of mutant strains carrying substitutions in residues in the vicinity or that directly belong to the phosposites of P140, trying to understand the effect that one C-terminal modification could have. We obtained, by transposon delivery into a *M. genitalium* strain lacking the gene coding for P140, mutants carrying single substitutions: P140-S1406A, P140-T1401A, P140-T1415A, P140-S1418A, P140-S1418E and P140-T1428A; and double substitutions: P140-S1406A+T1401A, P140-S1406E+T1401E, P140-S1418A+T1428A and P140-S1418E+T1428E (**Table CI. 2.10_1 and Table MM. CI. 1.1.1**).

Table CI. 2.10_1. Strains used in this study.

Strain Name	Genotype	Reference
G37	Wild-type	ATCC 33530
ΔMG_191	Deletion of the MG_191 gene by allelic exchange (G37 ΔMG_191::*tet*M438)	Burgos *et al.*, 2006
P140-WT	Re-introduction of a MG_191 wild-type allele in a ΔMG_191 mutant	This work
a: P140-S1406A	Introduction of a MG_191 allele bearing a S1406A substitution in a ΔMG_191 mutant	This work
b: P140-T1401A	Introduction of a MG_191 allele bearing a T1401A substitution in a ΔMG_191 mutant	This work
c: P140-T1415A	Introduction of a MG_191 allele bearing a T1415A substitution in a ΔMG_191 mutant	This work
dA: P140-S1418A	Introduction of a MG_191 allele bearing a S1418A substitution in a ΔMG_191 mutant	This work
dE: P140-S1418E	Introduction of a MG_191 allele bearing a S1418E substitution in a ΔMG_191 mutant	This work
e: P140-T1428A	Introduction of a MG_191 allele bearing a T1428A substitution in a ΔMG_191 mutant	This work
dAeA: P140-S1418A + T1428A	Introduction of a MG_191 allele bearing a S1418A and T1428A substitutions in a ΔMG_191 mutant	This work
dEeE: P140-S1418E + T1428E	Introduction of a MG_191 allele bearing a S1418E and T1428E substitutions in a ΔMG_191 mutant	This work
abA: P140-S1406A + T1401A	Introduction of a MG_191 allele bearing a S1406A and T1401A substitutions in a ΔMG_191 mutant	This work
abE: P140-S1406E + T1401E	Introduction of a MG_191 allele bearing a S1406E and T1401E substitutions in a ΔMG_191 mutant	This work

The mutated P140 allele was introduced by transposon delivery into a *M. genitalium* strain lacking the gene coding for P140[379] [Burgos R. *et al.*, 2006], as previously described. For each strain, several clones were isolated and analyzed. For control purposes, the previously described P140-WT strain was used. Polyacrylamide gels demonstrated that both P140 and P110 proteins were expressed in all mutants generated at the same level compared to the WT strain (**Figure CI. 2.10_1A and 2.10_2A**).

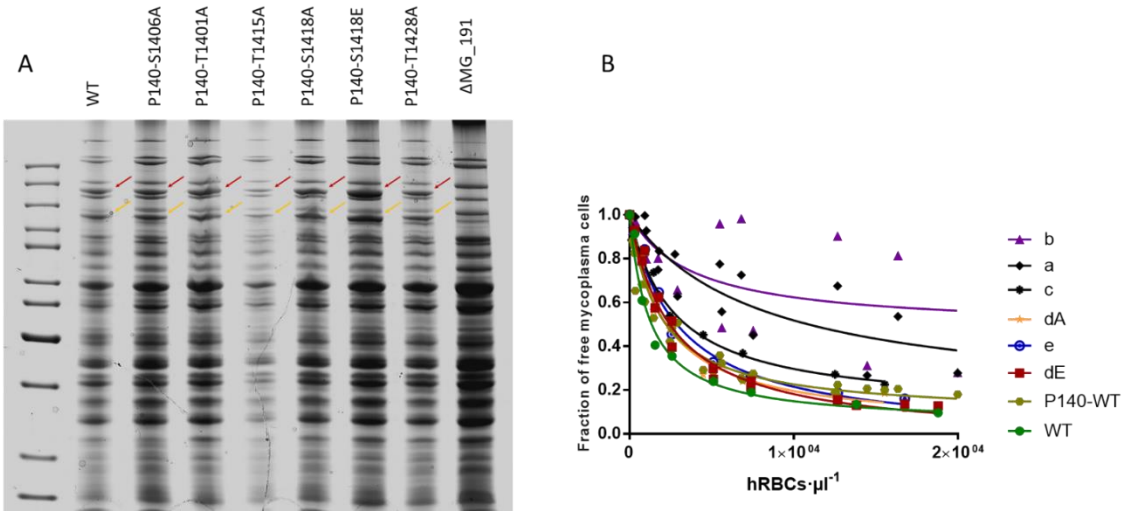

Figure CI. 2.10_1. Characterization of the single mutant strains carrying P140 adhesin variants. A) SDS-PAGE of whole cell lysates from the WT, ΔMG_191 strain and the different P140 adhesin mutants. Red and orange arrows indicate the presence of P140 and P110 adhesins, respectively. **B)** HA assays determined by FACS analysis. Graphic represents inverse Langmuir plots containing a fixed amount of mycoplasma cells and increasing amounts of hRBCs. Plots were generated using data from, at least two biological repeats for each strain.

All mutants analyzed exhibited some cytadherence defects. Nonetheless, mycoplasmas were still able to adhere, especially at the highest hRBCs concentrations (**Figure CI. 2.10_1B and 2.10_2B**). P140- S1418E+T1428E presented the most striking cytadherence phenotype. In particular, the binding analysis featured a high K_d, indicating a lower affinity of this mutant for hRBCs when compared to the WT or the P140-WT strains (**Appendices Table A. CI. 1.3**) suggesting that phosphosites S1418 and T1428 are the most important for P140 function.

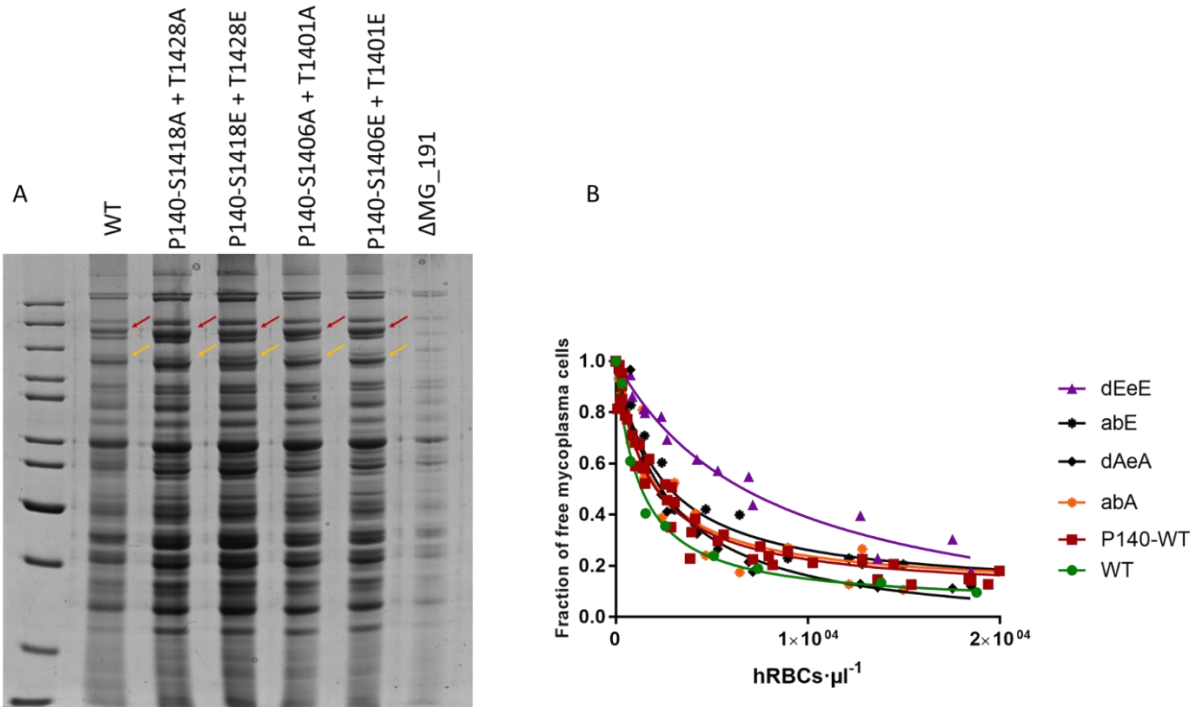

Figure CI. 2.10_2. Characterization of the double mutant strains carrying P140 adhesin variants. A) SDS-PAGE of whole cell lysates from the WT, ΔMG_191 strain and the different P140 adhesin mutants. Red and orange arrows indicate the presence of P140 and P110 adhesins, respectively. **B)** HA assays determined by FACS analysis. Graphic represents inverse Langmuir plots containing a fixed amount of mycoplasma cells and increasing amounts of hRBCs. Plots were generated using data from, at least two biological repeats for each strain.

We also examined the gliding activity of cells from the different mutants described above by time-lapse microcinematography to monitor the movements of individual cells for 120 s (**Figure CI. 2.10_3, 2.10_4 and Table CI. 2.10_2**). We found that gliding velocity of cells from all mutant was significantly reduced (**Table CI. 2.10_2**), especially in the case of the mutants that present double substitutions/point mutations. Moreover, when examining this mutant, we observed a reduced frequency of cells drawing non-circular tracks and a significantly reduced diameter of the circular tracks (**Table CI. 2.10_2, Figure CI. 2.10_3A,B and 2.10_4**)**.** All these results reinforce the role of the phosphorylation modifications that P140 present in the function of the Nap complex. Interestingly, some mutants presented high frequency of paired cells, suggesting that these cells are stalled in the cytokinesis process[337] [**Lluch-Senar M. *et al.*, 2010**] (**Table CI. 2.10_2 and Figure CI. 2.10_5**). These data are in agreement with the fact that cells from the strain bearing P140-S1418E+T1428E substitution have severe impairments both in adhesion and motility.

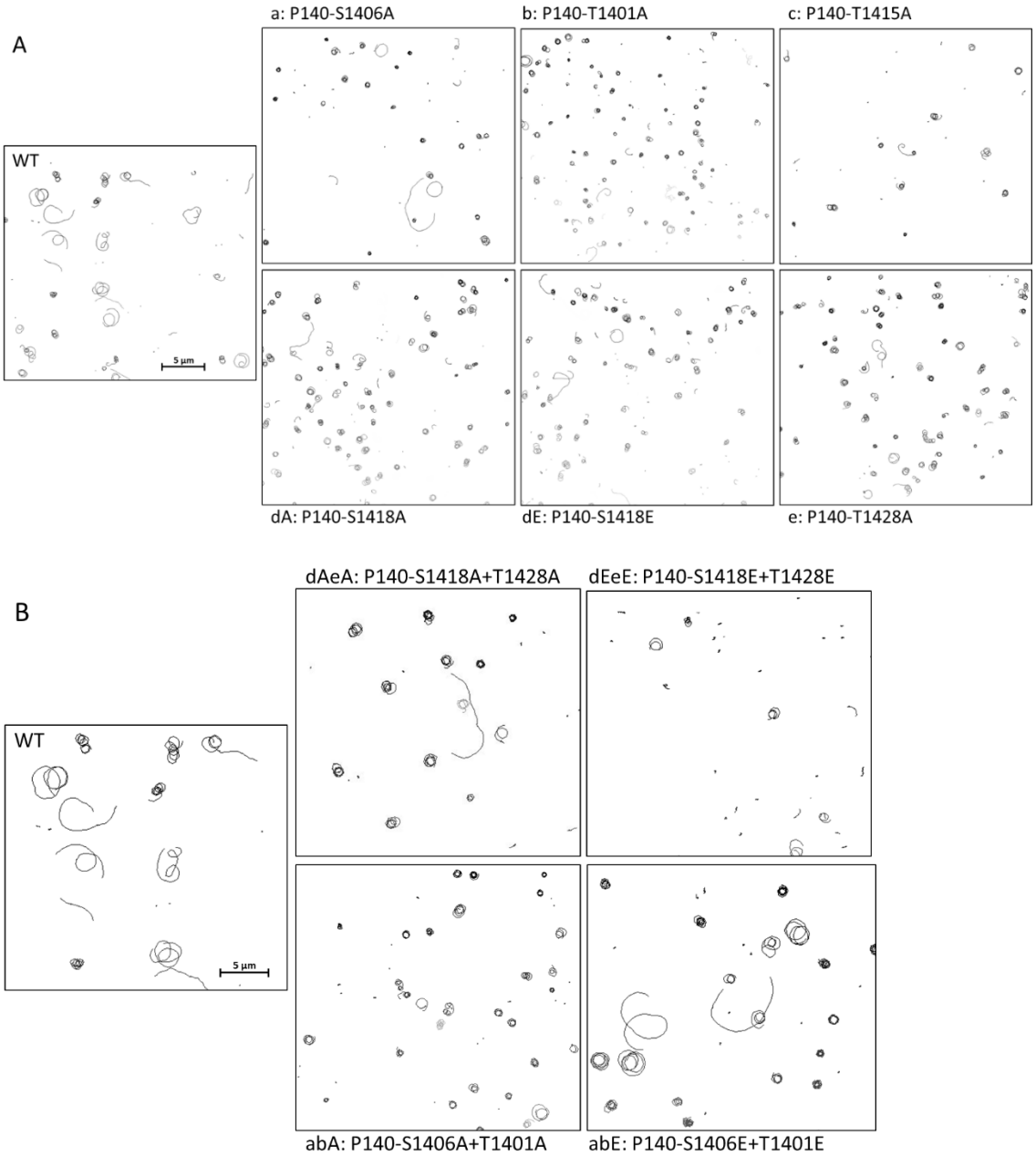

Figure CI. 2.10_3. Representative tracks described by mycoplasma cells. Compared with the WT strain, single P140 mutant strains (**A**) and double P140 mutant strains (**B**) present a reduced frequency of cells drawing non-circular tracks and a significantly reduced diameter of the circular tracks.

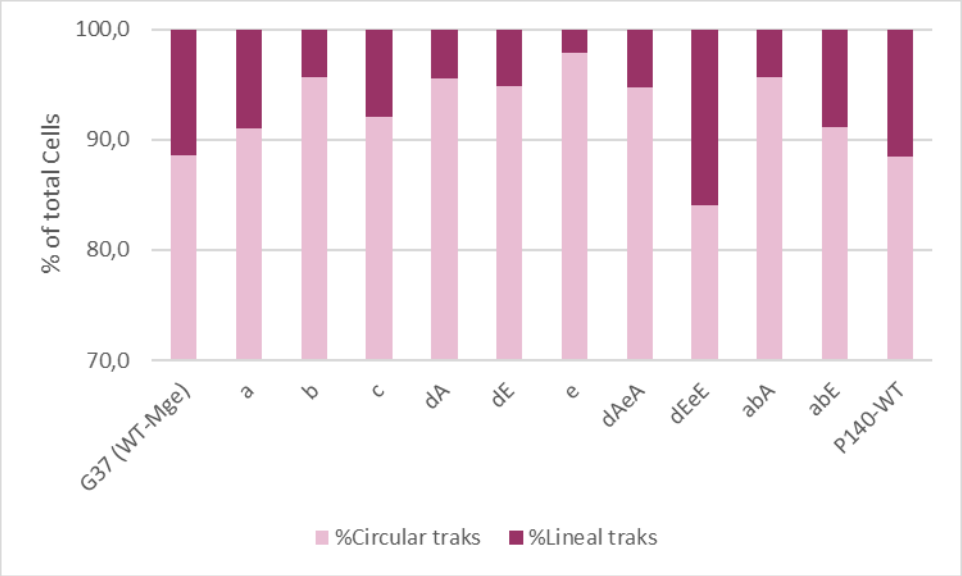

Figure CI. 2.10_4. Characterization of the motile properties in the reference and all mutant strains. Percentage of cells describing circular and non-circular tracks.

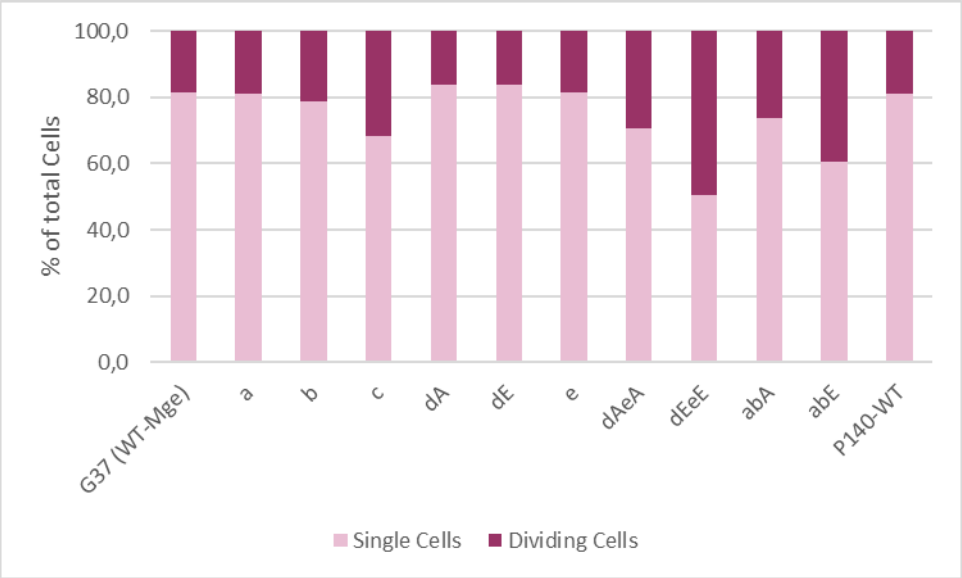

Figure CI. 2.10_5. Characterization of the motile properties in the reference and all mutant strains. Percentage of cells stocked in the division process (in pairs) and individual cells.

Table CI. 2.10_2. Gliding motility parameters of *M. genitalium* G37 wild-type cells and all different mutant strains obtained.

Name	Strain	n	Paired Cells (%)	Motile cells (%)	Individual Motile Cells (%)	Velocity (µm/s)[a]	Velocity preserved (%)	Motility loss (%)	Circular Tracks (%)	Diameter of Circular Tracks (µm)[a]
WT	G37	~700	18.7	76.7	87.6	0.125±0.002	100(ref.)	-	88.6	1.057±0.034
P140-WT	ΔMG_191::MTn*Pac*MG_191	~700	18.9	75.0	88.1	0.120±0.004	94.5	5.5	88.5	1.001±0.025
a	P140-S1406A	~700	19.0	74.7	75.1	0.083±0.002*	65.4	34.6	91.0	0.698±0.024*
b	P140-T1401A	~700	21.2	76.6	82.1	0.069±0.001*	54.3	45.7	95.6	0.721±0.027*
c	P140-T1415A	~700	31.8	63.0	85.7	0.087±0.003*	68.5	31.5	92.0	0.749±0.039*
dA	P140-S1418A	~700	16.4	80.7	94.9	0.072±0.001*	56.7	43.3	95.5	0.815±0.029*
dE	P140-S1418E	~700	16.2	79.0	94.6	0.068±0.001*	53.5	46.5	94.8	0.798±0.032*
e	P140-T1428A	~700	18.4	80.0	94.7	0.071±0.001*	55.9	44.1	97.9	0.687±0.024*
dAeA	P140-S1418A + T1428A	~700	29.4	69.0	91.0	0.058±0.001*	46.4	53.6	94.7	0.736±0.029*
dEeE	P140-S1418E + T1428E	~700	49.7	42.1	83.8	0.045±0.002*	36.1	36.9	84.0	0.857±0.028*
abA	P140-S1406A + T1401A	~700	26.4	76.3	92.7	0.059±0.002*	46.9	53.1	95.6	0.670±0.024*
abE	P140-S1406E + T1401E	~700	39.5	53.2	88.0	0.062±0.002*	49.3	50.7	91.1	0.760±0.025*

[a]Velocities are shown as mean values +/- standard error. n=25 biologically independent cells, from different fields, different preparations and different microcinematographies.

*Statistically significant values (T (25) = 2.06; $p<0.05$). Statistical significance was assessed with the Paired Student's two-sided T-test. Velocity p-values: $2.23\cdot10^{-48}$, $2.40\cdot10^{-85}$, $2.52\cdot10^{-21}$, $8.14\cdot10^{-82}$, $1.27\cdot10^{-67}$, $2.45\cdot10^{-55}$, $9.06\cdot10^{-56}$, $1.11\cdot10^{-90}$, $1.85\cdot10^{-50}$, $3.74\cdot10^{-72}$; Diameter p-values: $1.97\cdot10^{-11}$, $4.66\cdot10^{-10}$, $5.03\cdot10^{-7}$, $6.12\cdot10^{-6}$, $3.49\cdot10^{-6}$, $2.54\cdot10^{-11}$, $4.14\cdot10^{-10}$, $2.02\cdot10^{-4}$, $1.93\cdot10^{-12}$, $2.21\cdot10^{-8}$.

CI. 2.11. Characterization of *M. genitalium* MG_108 and MG_109 (Ser/Thr kinase/phosphatase couple, PrkC/PrpC) null mutant strains

Transcriptional control in mycoplasmas appears unique, as these prokaryotes possess relatively few regulatory factors compared with other bacteria, possibly due to reduced genome size[414] [**Himmelreich R. *et al.*, 1997**] and their successful adaptation to host environments[148] [**Weiner J. *et al.*, 2000**]. Compared with more complex bacteria, *M. genitalium* lacks the majority of known transcription factors and regulatory pathways. However, despite the apparently reduced gene regulatory toolbox, both environmental stresses and metabolic insults induce complex, specific transcriptional responses in this bacterium[39,40] [**Zhang W. and Baseman J.B., 2010; Zhang W. and Baseman J.B., 2011**]. Thus, posttranslational regulation might be important for these bacteria.

PrpC is a member of a family termed "eukaryotic-like" Ser/Thr phosphatases (eSTPs) despite a growing recognition of their ubiquity in eubacteria. PrpC and its homologs are often partnered with the cognate kinase PrkC, a highly conserved eukaryotic-like Ser/Thr kinase (eSTK). Mutant analysis in *Bacillus subtilis* has shown that homologs to these enzymes regulate sporulation and cell wall development by reversible phosphorylation[415–417] [**Absalon C. *et al.*, 2009; Pereira F. F. *et al.*, 2011; Shah I. M. *et. al.*, 2008**]. It has been shown that posttranslational modification of cytadherence proteins by PrkC is essential for the development and function of the *M. pneumoniae* terminal organelle[153]. [**Schmidl S. R. *et al.*, 2010**]. Transposon insertions in the only annotated Ser/Thr protein kinase gene (*prkC*; MPN248) and its cognate phosphatase gene (*prpC*; MPN247) in *M. pneumoniae* resulted in significant and contrasting effects on gliding frequencies. *prkC* mutant cells glided at approximately half the frequency of wild-type cells, while *prpC* mutant cells glided more than twice as frequently as wild-type cells. Collectively, these data suggest that PrkC and PrpC work in opposition in *M. pneumoniae* to influence gliding frequency[418] [**Page C. A. *et al.*, 2013**].

To get more insights into the importance of the reversible phosphorylation events in *M. genitalium*, we decided to analyze the effect of the complete loss of the PrpC (MG_108 protein in *M. genitalium)* by deleting the *mg108* coding region completely by homologous recombination. For this purpose, the suicide plasmid pBEΔMG_108 was engineered to contain the *Cm*M438 selectable marker flanked by *lox* sequences and the flanking regions of *mg108* (see methods). A double recombination event between plasmid pBEΔMG_108 and the mycoplasma genome promotes the substitution of bases 22 to 517 of *mg*108 (63.4 % of the *mg*108 coding region) by the *Cm*M438 marker. Several chloramphenicol-resistant clones were isolated after electroporation of G37 (WT) *M. genitalitum* in the presence of pBEΔMG_108. Electroporation

of this mutant with the pCre plasmid[261] [Mariscal A. M. *et. al.*, 2016] that contains the Cre recombinase allows us to obtain the G37ΔMG_108 without any antibiotic selectable marker. The deletion was confirmed by PCR and sequencing reactions (see methods).

At the same time, we also analized/characterize a *M. genitalium* strain knock out (KO) for the MG_109 protein, the supposed PrkC in this bacterium. This strain was obtained previously in the laboratory by Carlos Martinez Torrò (unpublished).

In order to determine if any of the mutants present growth difficulties, we analyzed the duplication times that G37ΔMG_108 and G37ΔMG_109 present. For this purpose, we adapted a colorimetric assay previously reported by Karr and colleagues[419] [Karr J. R. *et al.*, 2012]. This method was adapted in our laboratory (by Carlos Martinez Torrò[420] [Martínez-Torrò C., 2020] and is exhaustively described in Materials and Methods section. The calculated duplication time for the G37ΔMG_109 strain was 10.66 ± 0.97 h, while the wild-type and the G37ΔMG_108 strains were clocked at 8.94 ± 0.58 h and 8.92 ± 0.37 h, respectively (**Figure CI. 2.11_1**). This significative increase of the duplication time for the G37ΔMG_109 strain is consistent with the time of culture that were necessary for G37ΔMG_109 mutant cells to grow compared with the WT strain.

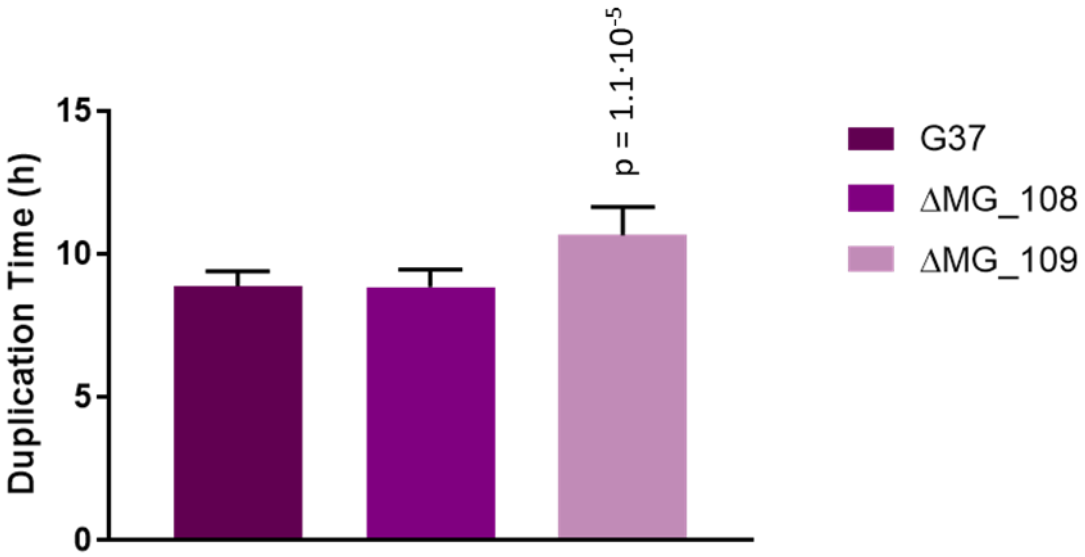

Figure CI. 2.11_1. Growth rate of *M. genitalium* reference, G37ΔMG_108 and G37ΔMG_109 strains. The duplication time data was collected after several independent biological repeats. Statistical significance was assessed using a paired T-test and statistically significant values (p-value< 0.05) are stated above the upper standard error bar of each strain.

As previously described, we also examined the gliding activity of cells from G37ΔMG_108 and G37ΔMG_109 mutants by time-lapse microcinematography. We found that gliding velocity of cells from the two mutants was significantly reduced, but especially in the case of G37ΔMG_109

mutant, cells glided at approximately half the frequency of wild-type cells (**Table CI. 2.11**). Moreover, when examining these mutants, no significant differences were observed neither in the frequency of cells drawing non-circular tracks nor in the diameter of the circular tracks drown (**Table CI. 2.11 and Figure CI. 2.11_2**). Another important observation is that, contrary to what happened with other mutants described previously described, G37ΔMG_108 strain not seem to present a high percentage of cells in couples (**Figure CI. 2.11_3**). All these results reinforce the importance of the phosphorylation modifications in the gliding motility in *M. genitalium*.

Table CI. 2.11. Gliding motility parameters of *M. genitalium* G37 wild-type cells and G37ΔMG_108 and G37ΔMG_109 mutant strains.

Name	Strain	n	Paired Cells (%)	Motile cells (%)	Individual Motile Cells (%)	Velocity (µm/s)[a]	Velocity preserved (%)	Motilitty loss (%)	Circular Tracks (%)	Diameter of Circular Tracks (µm)
WT	G37	~700	18.9	76.7	87.6	0.125±0.002	100(ref.)	-	98.6	1.06±0.03
ΔMG_108	G37 ΔMG_108	~700	10.4	86.2	96.2	0.103±0.003*	84.4	15.6	97.7	1.00±0.03
ΔMG_109	G37 ΔMG_109	~700	20.9	74.5	94.4	0.064±0.002*	52.5	47.5	98.3	1.07±0.05

[a]Velocities are shown as mean values +/- standard error. n=25 biologically independent cells, from different fields, different prparations and different microcinematographies.

*Statistically significant values (T (25) = 2.06; p<0.05). Statistical significance was assessed with the Paired Student's two-sided T-test. G37ΔMG_108 $p= 2.78 \cdot 10^{-5}$; G37ΔMG_109 $p= 7.33 \cdot 10^{-15}$.

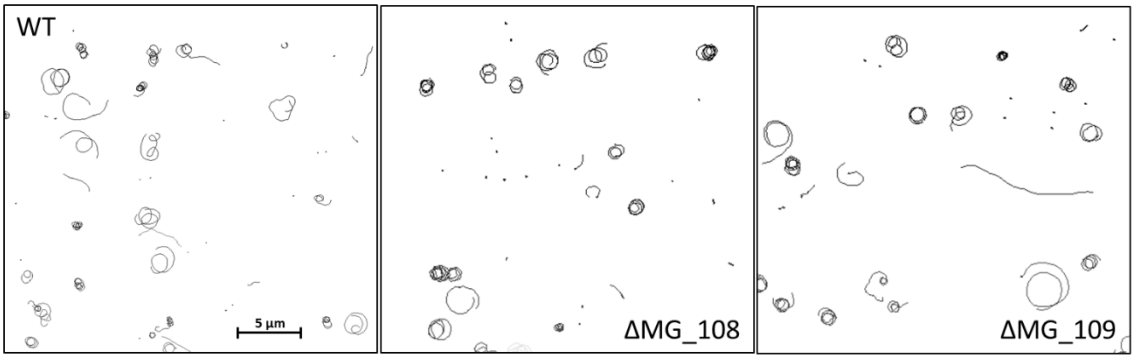

Figure CI. 2.11_2. Representative tracks described by mycoplasma cells. Compared with the WT strain, G37ΔMG_108 and G37ΔMG_109 KO strains, did not present significant differences in the frequency of cells drawing non-circular tracks or in the diameter of the circular track drown.

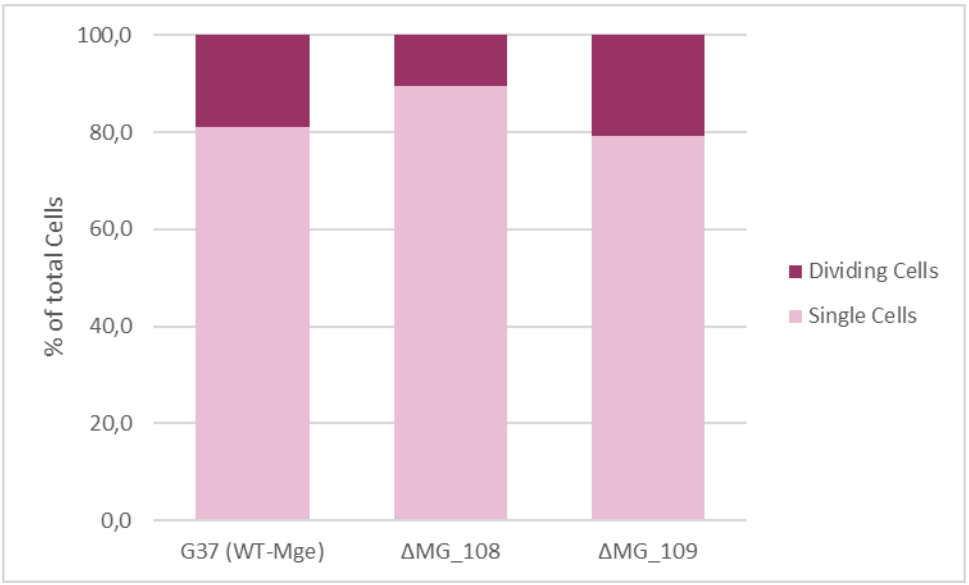

Figure CI. 2.11_3. Characterization of the motile properties in the reference G37ΔMG_108 and G37ΔMG_109 strains. Percentage of cells stocked in the division process (in pairs) and individual cells.

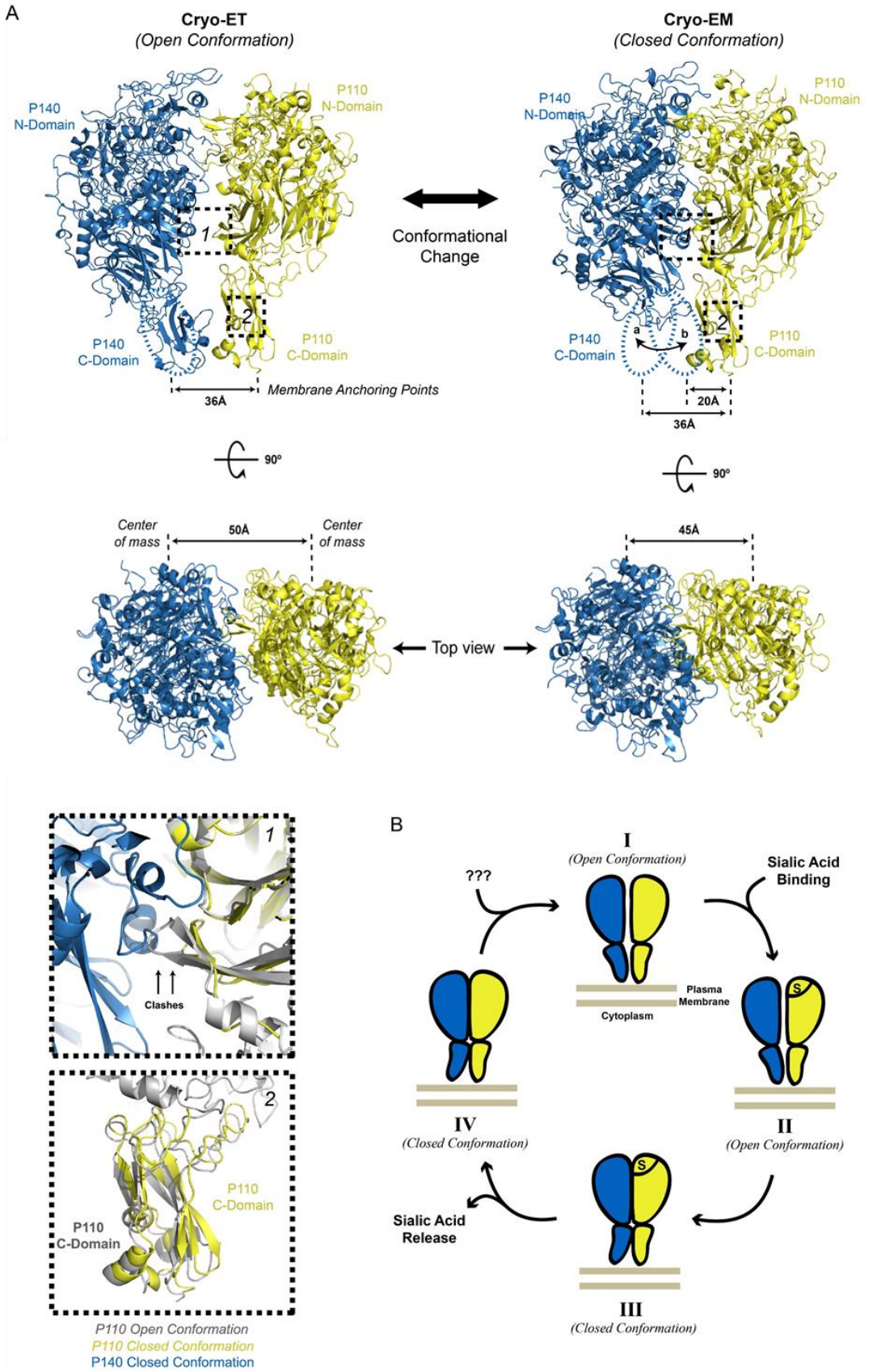

Figure CI. 3_1. Conformational transition between the open and close states of the P140-P110 heterodimers. Adapted from **Aparicio D. *et al.*, 2020**.

CI. 3. Discussion

Integration of the information obtained from the different structural approaches used in this work indicates that P140-P110 heterodimers comprising the Nap, have a loose interface between them in the extracellular region. This suggest that subunits in the Nap are held together mainly by interactions in the intracellular and trans-membrane regions. Naps undergo large structural rearrangements, thereby alternating between "open" and "closed" conformations, which are associated with attachment and release to the cell receptor, respectively (**Figure CI. 2.7_1 and 2.7_2**). The "open" conformation is very common in the Nap complexes examined *in situ*, where the P140 and P110 extracellular regions from the four subunits of a Nap interact only weakly with each other, allowing P110 to remain in a conformation ready-to-bind to sialylated cell receptors. The "closed" conformation corresponds to an *in situ* less abundant state, where the tight interaction of the extracellular regions of P140 and P110 occlude the cell receptor binding site. To avoid been trapped in the overall most stable state, the cycling between "open" and "closed" conformations would require an i energy nput of at the level of every Nap.

Transitions between the open and closed conformations of the P140-P110 heterodimers imply concerted structural changes mainly in three locations from both P110 and P140: i) at the crowns, in the adhesins regions surrounding the cell receptor binding site (**Figure CI. 2.1_4A-D**); ii) at the interfaces between N- and C-domains (**Figures CI. 2.1_4A and 2.3_1**) and iii) at the connections between the C-domains and the transmembrane helices. The structural rearrangements in the Nap extracellular region might be transmitted to the inner cell by the repositioning of the trans-membrane helices (**Figure CI. 3_1**). Thus, we hypothesize (**Figure CI. 3_1B**) that the Cryo-ET open conformation captures an "in vivo" long-lived ready-to-be-bound (empty) receptor state (I in **Figure CI. 3_1B**) that, by binding to sialylated cell receptors, initiates conformational changes (II-III in **Figure CI. 3_1B**) ending in the "in vivo" short-lived release receptor state captured in the closed Cryo-EM conformation (IV in **Figure CI. 3_1B**).

We have taken advantage of the structural data obtained for the Nap and biological *in vivo* data from the P110 and P140 proteins to design and generate several *M. genitalium* strains with mutations in key residues of these proteins. Our results reveal that cythadherence capacity and gliding motility of this bacterium can be modulated by introducing single amino acid substitutions in P110 and P140. Of note, residues located outside of the sialic acid receptor binding site are also important to sustain adherence and motility.

Many mycoplasmas, including *M. genitalium*, have curved terminal organelles and draw circular paths when they glide over solid surfaces[246,421] [**Pich O. Q. *et al.*, 2006a; Jennifer M. H. *et al.*, 2008**]. Since gliding is essential for infection on mucosal surfaces[422] [**Jarrat L. J. *et al.*, 2007**] and

the curvature of *M. genitalium* terminal organelle correlates well with the diameter of the circular tracks[276] [**Burgos R. *et al.*, 2008**], this type of movement could be important for mycoplasma pathogenicity. Interestingly, P140-HH mutant strain shows an increased frequency of cells describing circular paths, also with a reduced diameter when compared to that exhibited by WT cells. The same is observed in all the *M. genitalium* strains with mutations in the P140 phosphosites. Similarly, P110-Y830A strain also exhibited an increased frequency of cells describing circular tracks, but in this case the diameter of circular paths was very similar to that exhibited by WT cells.

The presence of several residues with a potential regulatory role makes the Nap complex an excellent candidate to integrate the signals from different external and internal stimulus and to provide a response by modulating the gliding motility and cytadherence capacity of mycoplasma cells. Unfortunately, how the Nap could internalize and transmit the signals to intracellular effectors is still unknown. However, the phosphosites found in P110 and P140, and the phenotype characterization of these phosphorylated residues mutant strains, could help to understand the cross-talk communication between extra- and intracellular regions. All these results together reinforce the view that the Nap complex is not a passive element to attach mycoplasmas to solid surfaces and reveal that adhesins are able to modulate the mycoplasma movements.

The comparative study of P1 and P140 reveals that both adhesins share similar immunogenic properties and provides several polypeptide candidates to be used for *M. genitalium* serological diagnostic. This information combined with structural and biochemical studies enhance our understanding of *M. genitalium* immune evasion strategies and may facilitate the rational design of candidate vaccines against this human pathogen. Identification of P1-like epitopes in the P140 protein could facilitate the development of serological tests for diagnosis of *M. genitalium* infections.

In summary, our results about the role of mycoplasma adhesins, indicate critical residues for the Nap functioning. These results, together with previous studies showing the potential of pneumococcal adhesin based vaccines[423] [**Seo J-Y. *et al.*, 2002**], pave the way to the development of alternative strategies of anti-adhesion therapies based on blocking the first stages of the infection by mycoplasmas from the *pneumoniae* cluster. Development of non-antibiotic therapies is essential when antibiotic-based therapies are increasingly failing in the treatment of infections with these microorganisms, which depicts a severe thread for public health in the next years.

CHAPTER II

MOLECULAR BASIS OF BACTERIAL LECTINS RECOGNITION OF EUKARYOTIC GLYCANS: THE CASE OF *Mycoplasma pneumoniae* AND *Mycoplasma genitalium* CYTOADHESINS

Results presented in this chapter have been partially published in:

Angela Marseglia, Maria Concetta Forgione, **Marina Marcos-Silva**, Cristina Di Carluccio, Yoshiyuki Manabe, David Vizarraga, Ferran Nieto-Fabregat, Maria Pia Lenza, Koichi, Fukase, Antonio Molinaro, Oscar Q. Pich, David Aparicio, Alba Silipo, Roberta Marchetti. **Molecular basis of bacterial lectins recognition of eukaryotic glycans: the case of *Mycoplasma pneumoniae* and *Mycoplasma genitalium* cytoadhesins.** *International Journal of Biological Macromolecules*. **2024**. DOI: 10.1016/j.ijbiomac.2024.135277. https://doi.org/10.1016/j.ijbiomac.2024.135277

MOLECULAR BASIS OF BACTERIAL LECTINS RECOGNITION OF EUKARYOTIC GLYCANS: THE CASE OF *Mycoplasma pneumoniae* AND *Mycoplasma genitalium* CYTOADHESINS

Mycoplasma pneumoniae and *Mycoplasma genitalium* are two emerging bacterial pathogens that colonize the human respiratory and urogenital epithelia, respectively. Both pathogens express cell surface cytoadhesins that play a crucial role in the interaction with the host, mediating the attachment to sialylated glycan receptors and triggering infection. The design of competitive binding inhibitors of *Mycoplasma* cytoadhesins has potential to disrupt these interactions and lessen bacterial pathogenesis. To this end, we report here molecular insights into the adhesion mechanisms of *M. pneumoniae* and *M. genitalium*, which are largely mediated by sialylated glycans on the host cell surface. In detail, a combination of NMR spectroscopy, fluorescence analysis and computational studies allowed us to explore the recognition by the cytoadhesins P40/P90 in *M. pneumoniae* and P110 in *M. genitalium* of sialylated N- and O-glycans. We reveal that, unlike other bacterial adhesins, which are characterized by a wide binding pocket, *Mycoplasma* cytoadhesins principally accommodate the sialic acid residue, in a similar manner to mammalian Siglecs. These findings represent crucial insight into the future development of novel compounds to counteract *Mycoplasma* infections by inhibiting bacterial adherence to host tissues.

My specific contribution to this chapter:

I have conducted the experiments involving the construction and analysis of the *M. genitalium* mutant and the molecular dynamics simulations described in sections CII. 2.3 and CII. 2.6, respectively. Of note, these experiments involve the use of techniques that I learned during my 3-month stay in Naples. I have also contributed to the manuscript writing.

CII. 1. Introduction

Bacterial adhesion to host cells is one of the initial stages of infection and is a key step in pathogenesis. This process is mediated by dedicated bacterial surface structures that enable microorganisms to specifically target host molecular signatures such as carbohydrate signalling molecules[424] [Pizarro-Cerdá J. and Cossart P., 2006]. Several *Mycoplasma* species, including *Mycoplasma pneumoniae* and *Mycoplasma genitalium*, have been shown to infect host cells via this adhesion pathway[425,426] [Loveless W. and Feizi T., 1989; Williams C.R. *et al.*, 2020]. Mycoplasmas are cell wall-less microorganisms, phylogenetically related to Gram-positive bacteria, and are capable of invading and replicating within eukaryotic cells[206] [Qin L. *et al.*, 2019]. Among these species, *M. pneumoniae* is an exclusively human parasite[87] [Waites K. B. and Talkington D. F., 2004] that primarily affects the conducting airways, and is the leading cause of upper and lower respiratory tract infections[225,427] [Atkinson T. P. *et al.*, 2008; Talkington D. F. *et al.*, 2001]. It is estimated that *M. pneumoniae* is responsible for up to 40% of community-acquired pneumonias (CAPs) in children and adults worldwide. Atypical CAPs, also caused by *M. pneumoniae*, may also involve extrapulmonary organs, including, for example, head, eyes, ears, skin, or gastrointestinal tract[428] [Kashyap S. and Sarkar, M., 2010]. On the other hand, *M. genitalium* is a sexually transmitted bacterium that frequently co-infects the urogenital tract with other pathogens, such as HIV, *C. trachomatis*, and *N. gonorrhoeae*[367] [Yueyue W. *et al.*, 2022]. In women, it is responsible for several inflammatory reproductive tract syndromes, including cervicitis, pelvic inflammatory disease (PID), and infertility[103] [McGowin C. L. and Anderson-Smits C., 2011]; in men, it is the leading cause of 30-40% cases of urethritis[429] [Ona S. *et al.*, 2016]. Additionally, *M. genitalium* has been associated with preterm birth, spontaneous abortion, and HIV acquisition[430] [Smullin C. P. *et al.*, 2020].

Cytoadherence and gliding motility of these two pathogens are essential for colonization of the human tissues and are mediated primarily by a complex attachment organelle that consists of an intracellular region and a specialized surface-exposed structure. This surface structure comprises accessory proteins[271] [Nakane D. *et al.*, 2015] that form the adhesion complex, a peplomer-like structure termed Nap[431] [Hu P. C. *et al.*, 1982]. The Nap is essential for infectivity and displays a tetrameric organization composed of heterodimers of the cytadhesin proteins P140 and P110 in *M. genitalium*, and their homologs P1 and P40/P90 in *M. pneumoniae*[75,353] [Aparicio D. *et al.*, 2018; Vizarraga D. *et al.*, 2020]. These cytadhesins possess a similar domain organization, consisting of a large extracellular domain (the crown), a transmembrane helix, and a short cytoplasmic tail (C-domain). The extracellular portion is further divided into two subdomains: a small *C*-terminal domain and an *N*-terminal region containing a seven bladed β-

propeller in the shape of a crown, where the sialic acid binding site is located[432] [**Aparicio D. *et al.*, 2020**]. Given the similar topology of the cytadhesin structures of *M. genitalium* and *M. pneumoniae* and neuraminidase proteins from influenza A viruses, it has been suggested that P110 and P40/P90 proteins contain a putative catalytic site, located close to the sialic acid binding site[433] [**Vizarraga D. *et al.*, 2021**] and characterized by the presence of an RLP (Arg-Leu-Pro) motif (**Figure CII. 1_1**) usually found in non-viral sialidases[434,435] [**Taylor G., 1996; Gaskell A. *et al.*, 1995**].

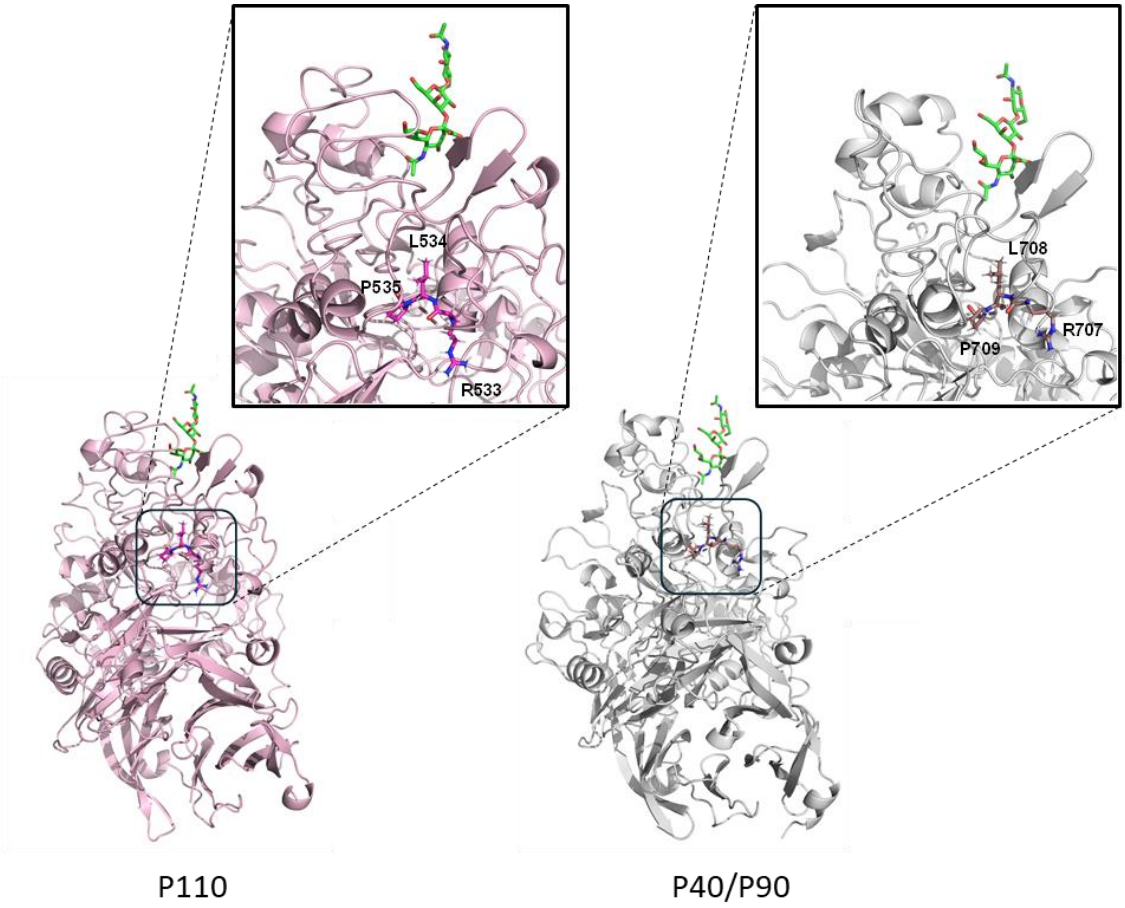

Figure CII. 1_1. 3D view of the putative catalytic site of P110 and P40/P90. The aa of the RLP (Arg-Leu-Pro) motif of the putative catalytic site of P110 (in pink) and P40/P90 (in grey), are represented as sticks. Adapted from **Marseglia A. *et al.*, 2024**.

Sialic acids are negatively charged nine-carbon monosaccharides, found in abundance on cell surface structures of humans and other mammals and involved in various biological functions, including cell adhesion and immune responses. This class of monosaccharides, often the terminal residue of both *N*- and *O*-glycans on cell surfaces, can act as receptor ligands for certain pathogens, allowing them to attach and infect host cells[436] [**Varki N. M. and Varki A., 2007**]. The interaction of *Mycoplasma* adhesins with specific sialylated glycans on target host cells has been

shown to be a prerequisite for the development of Mycoplasmas-associated infectious diseases[427,437] [**Roberts D. D. *et al*., 1989; Talkington D. F. *et al*., 2001**].

Given the critical roles that *Mycoplasma* cytadhesins play in bacterial adhesion to host cells, they are attracting increasing attention as promising targets for anti-adhesive therapy of *Mycoplasma* infections. Notably, anti-adhesive agents are not bactericidal and therefore much less likely than antibiotics to induce the evolution and spread of resistant strains.

We previously elucidated the structural features of the main cytadhesins from *M. genitalium* and *M. pneumoniae*[433] [**Vizarraga D. *et al*., 2021**], and Cryo-ET studies have been recently published describing the structure of the major adhesion complex from *Mycoplasma genitalium*[399] [**Sprankel L. *et al*., 2023**]; however, the resolution of the Cryo-ET data was not sufficient to visualize the sialylated oligosaccharides and the adhesion mechanism of *Mycoplasma* cells remains not fully understood. Thus, further molecular insights on sialoglycan recognition and binding by *Mycoplasma* cytadhesins are needed to design effective anti-adhesion strategies, either by reducing the contact between host tissues and pathogens, and/or by prevention of adhesion of the infectious agent. To further this aim, we dissect herein the recognition profiles and binding modes of different sialoglycans with P110 from *M. genitalium* and P40/P90 from *M. pneumoniae*. We employ an integrated approach that combines NMR spectroscopy, fluorescence analysis, and computational studies, rendering in three-dimensional, atomic-level detail the adhesin-sialoglycan complexes. These findings accurately defined the ligand-epitope maps and their bioactive conformations, together with the protein structural features involved in sialoglycan recognition and their respective binding affinities (**Figure CII. 1_2**). In addition, our outcomes allow us to pinpoint molecular differences in the sugar-binding mode of *Mycoplasma* cytoadhesins with respect to other bacterial Siglec-like adhesins, such as those expressed by streptococcal species[438] [**Di Carluccio C. *et al*., 2021**].

Given the high incidence of pathologies related to *M. pneumoniae* and *M. genitalium*, the absence of a vaccine for *M. pneumoniae* in contrast to other respiratory pathogens, and the rapid increase of antibiotic resistance of *Mycoplasma* pathogens[439] [**Chernova O. A. *et al*., 2016**], our results are of critical importance and lay the foundation for the future development of therapeutic strategies based on the inhibition of *Mycoplasma*-host cell adhesion and infection.

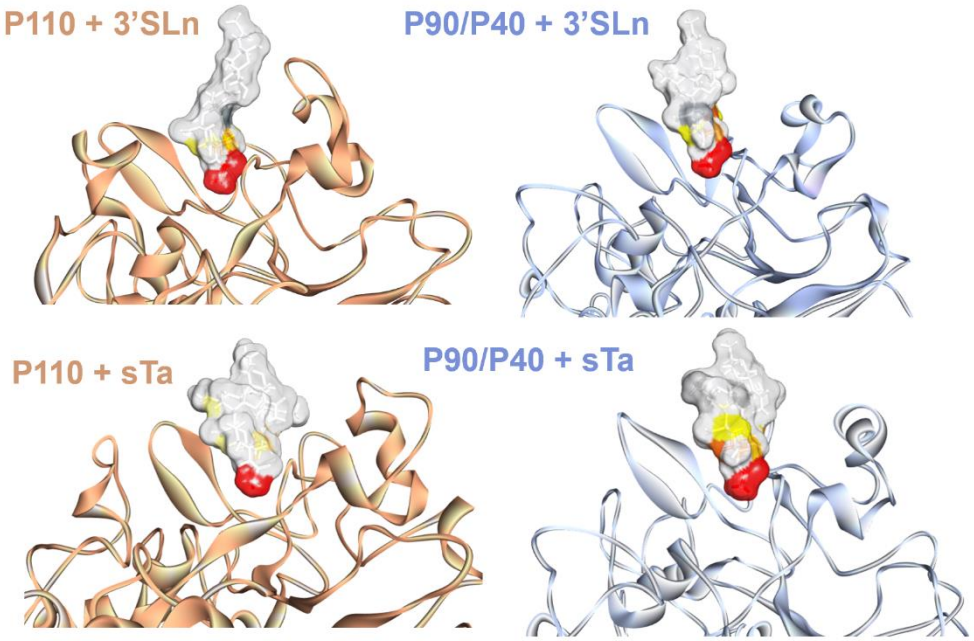

Figure CII. 1_2. Comparison of sialoglycans recognition by *M. genitalium* P110 and *M. penumoniae* P40/P90 adhesins. Predicted models of 3'SLn and/or sTa-Thr bound to *Mycoplasma* cytoadhesins, P110 and P40/P90. In all the predicted complexes the ligand surface is colored according to the STD-derived epitope mapping. A combination of NMR spectroscopy, fluorescence analysis and computational studies allowed us to explore the recognition by the cytoadhesins P40/P90 in *M. pneumoniae* and P110 in *M. genitalium* of sialylated *N*- and *O*-glycans. Adapted from **Marseglia A. *et al*., 2024**.

CII. 2. Results

The association between *Mycoplasma* cytadhesins, P110 (from *M. genitalium*) and P40/P90 (from *M. pneumoniae*), and both *N*- and *O*-glycans typically decorating the host cell surface (**Figure CII. 2_1**) was initially assessed by fluorescence spectroscopy (**Figure CII. 2_2**).

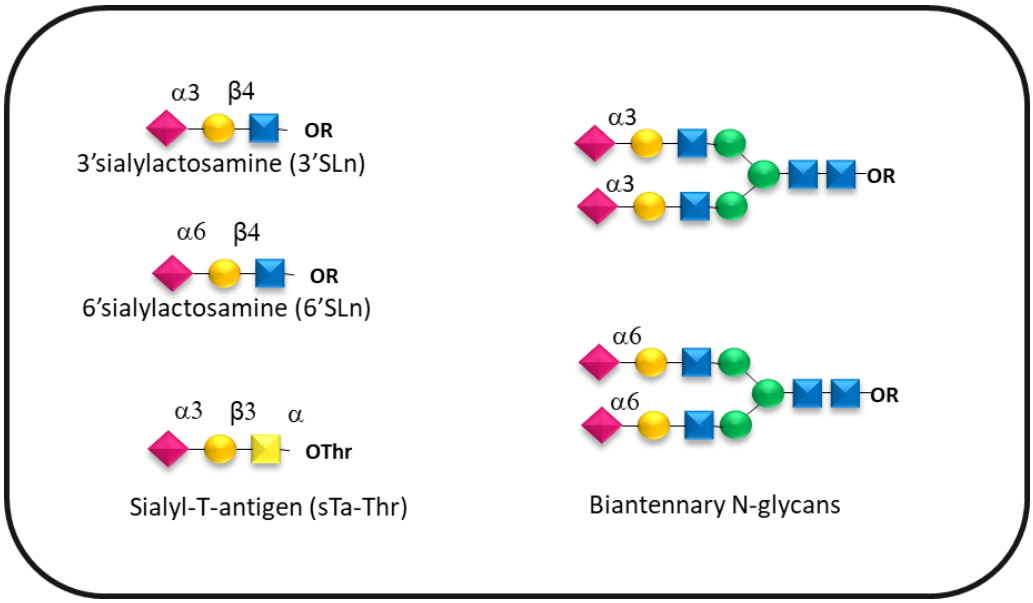

Figure CII. 2_1. Depiction of investigated sialoglycans. List of sialoglycans studied in interaction with P110 and P40/P90 depicted by using the SNFG representation. Adapted from **Marseglia A. *et al.*, 2024**.

Briefly, a fixed concentration of both proteins was titrated with increasing amounts of each sialoglycan (3'SLn, 6'SLn, biantennary *N*-glycans and sTa-Thr) to derive the binding isothermal curves for all protein-ligand mixtures and, consequently, obtain information regarding the binding affinities. The results demonstrated the ability of both cytadhesins (P110 and P40/P90) to similarly recognize different Neu5Ac-containing ligands, as the estimated binding constants (Kb) were all in the micromolar range (**Figure CII. 2_2**). Notably, these findings align with equilibrium dissociation constants previously established through SPR measurements[75,353] [**Aparicio D. *et al.*, 2018; Vizarraga D. *et al.*, 2020**]. To elucidate the mechanism of cell adhesion and gliding of *M. genitalium* and *M. pneumoniae*, the molecular recognition of the different sialylated ligands by cytadhesins was further investigated by using complementary techniques. As described in the following sections, Saturation Transfer Difference NMR (STD NMR) was applied to reveal the ligand binding epitopes, and transferred-NOESY (tr-NOESY) experiments were employed to investigate their conformational behaviour[440] [**Di Carluccio C. *et al.*, 2021**]. In combination with NMR results, Molecular Dynamic (MD) simulations were also carried out to provide 3D models of the complexes.

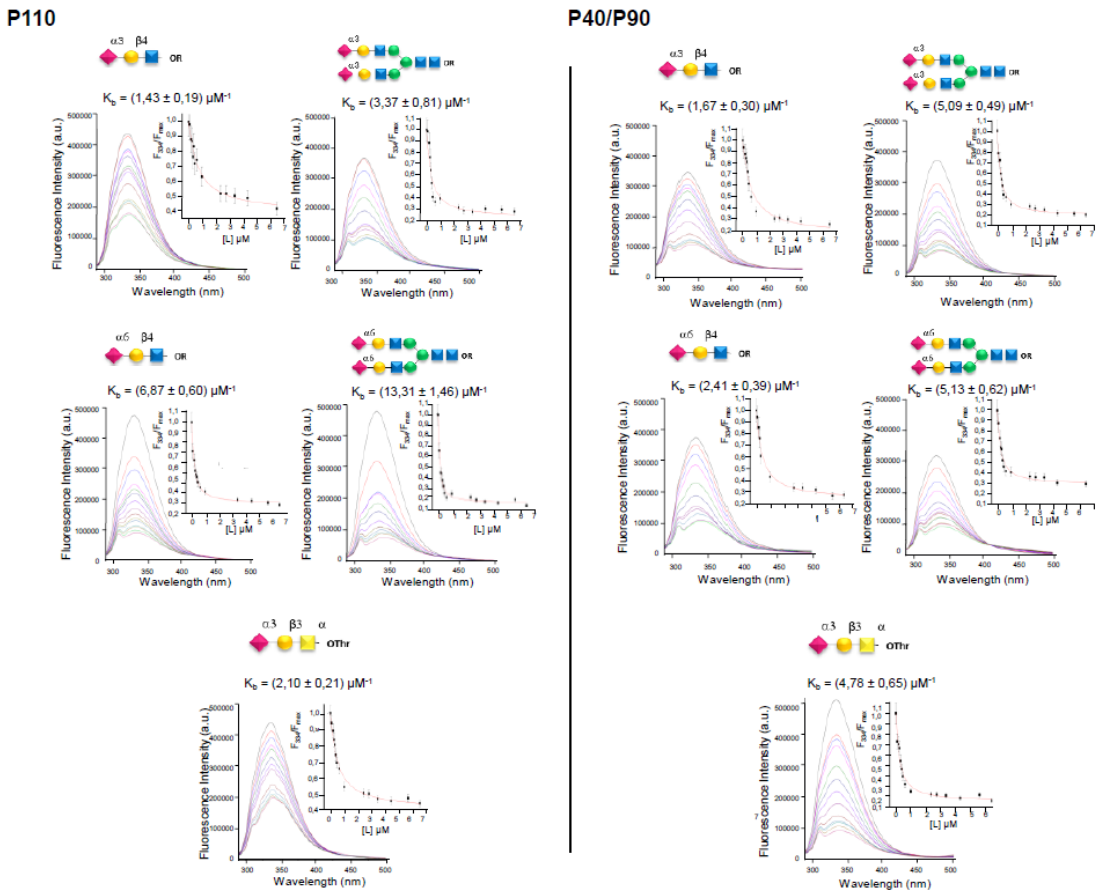

Figure CII. 2_2. Measurement of sialoglycans affinity for P110 and p40/P90 by fluorescence spectroscopy. Quenching of intrinsic fluorescence of *M. genitalium* P110 (left panel) and *M. pneumoniae* P40/P90 (right panel) in the presence of increasing amounts of 3'SLn, 6'SLn, sTa-Thr and biantennary sialoglycans, respectively. The binding isotherms were obtained by plotting the values of F/F_{max} versus the total ligand concentration, where F is the fluorescence intensity observed at each addition of ligand, and F_{max} is the maximum fluorescence intensity observed. The resulting binding constants (K_b) were reported in the insets. Error bars indicate standard deviations of representative experiments performed in triplicate. Adapted from **Marseglia A. *et al.*, 2024**.

CII. 2.1. 3'SLn recognition by P110 and P40/P90

The analysis of the STD NMR spectra of the mixture P110/3'SLn clearly showed that the protein binding pocket was selective towards the Neu5Ac moiety (**Figure CII. 2.1_1A, left panel**). As suggested by the STD NMR enhancements, the entire Neu5Ac was recognized by the receptor and received a good magnetization transfer from P110. The strongest relative STD NMR effect belonged to the acetyl group of Neu5Ac unit, followed by the protons H6 and H7, which had an STD NMR percentage above 40%. Other protons of Neu5Ac (H4, H5, H8 and H9) showed STD signals but to a lesser extent. The other sugar residues did not participate in the recognition process, in agreement with the crystal structure of P110 in complex with 3'SLn[75] [**Aparicio D. *et al.*, 2018**].

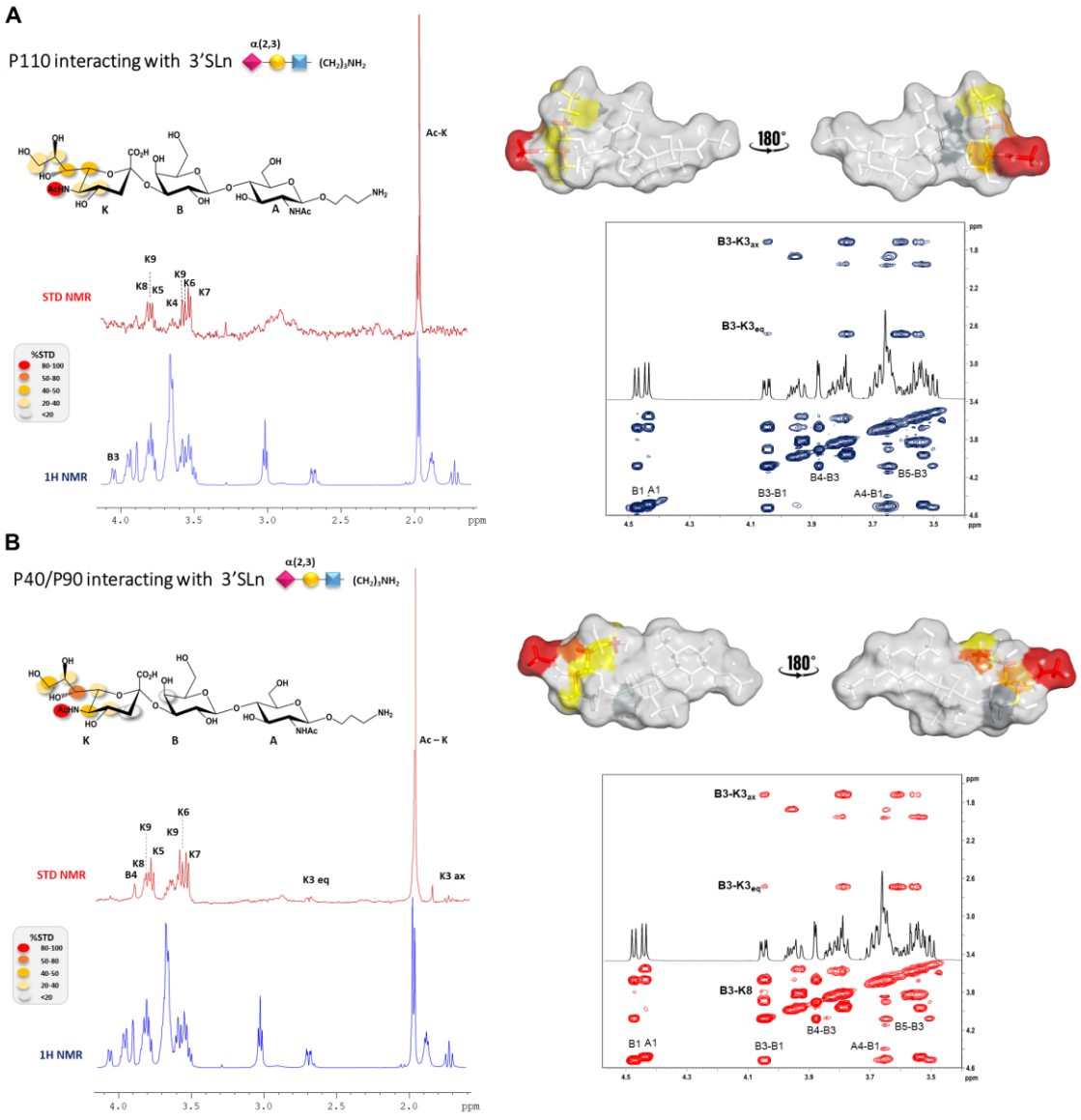

Figure CII. 2.1_1. NMR analysis of 3'SLn bound to P110 and P40/P90. **A)** Superimposition of the STD NMR spectrum (red) and the unsaturated reference spectrum (blue) of 3'SLn interacting with P110.The ligand epitope map has been calculated by $(I_0 - I_{sat})/I0$, where $(I_0 - I_{sat})$ was the signal intensity in the STD-NMR spectrum and I0 was the peak intensity of the off-resonance spectrum Tr-NOESY spectrum on the 1:50 P110-3'SLn mixture and the ligand bioactive conformation are showed on the right. The ligand surface was colored according to the STD derived epitope mapping. **B)** The superimposition of STD NMR spectrum (black) and the unsaturated reference spectrum (blue) together with the epitope map of the 3'SLn interacting with P40/P90 are reported on the left. Tr-NOESY spectrum 1 of 1:50 P40/P90–3'SLn mixture and STD-derived epitope mapping of 3'SLn in its bioactive conformation are showed on the right. Adapted from **Marseglia A. *et al.*, 2024**.

Tr-NOESY experiments and MD simulations then allowed us to describe the ligand's bioactive conformation. The conformational behaviour of 3'SLn has been extensively analyzed in free solution and displays an equilibrium between different conformations, namely *t*, *g* and *-g,* according to the different values of the Φ(C1-C2-O-C3') dihedral angle around the Neu5Ac-α-(2,3)-Gal glycosidic linkage[441] [**Forgione R. E. *et al*., 2020**]. Here, the conformation of the ligand in the presence of P110 was analyzed; the glycosidic torsion trajectories of 3'SLn were monitored during a simulation of the bound state within the P110 binding pocket and indicated a preference of the ligand for the *t* conformer (**Figure CII. 2.1_2**). This agreed with the tr-NOESY derived calculated distances for 3'SLn in the presence of P110 (**Figure CII. 2.1_1A, right panel**). In particular, the presence of the key NOEs between the diastereotopic protons at position 3 of the Neu5Ac and the proton H3 of the Gal residue, as well as the absence of the H3 Gal – H8 Neu5Ac NOE contact, suggested that the 3'SLn mainly adopted a *t* conformation in solution when accommodated in the protein binding pocket.

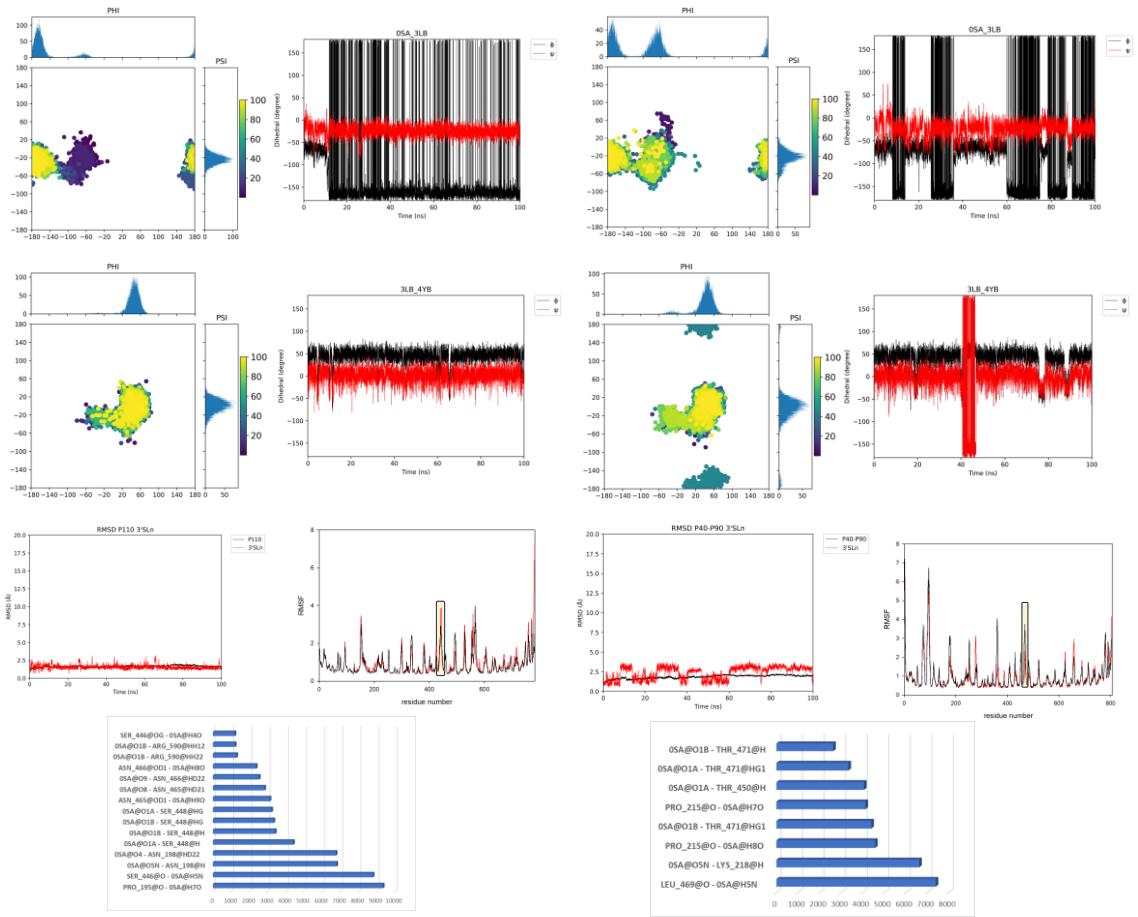

Figure CII. 2.1_2. MD analysis of P110 (left panel) and P40/P90 (right panel) in the interaction with 3'SLn. 3'SLn dihedral angles analysis in the bound state with P110 (left panel) and P40/P90 (right panel) represented as scatter plots of the φ torsion against ψ, during the MD simulation with the relative histograms to represent the most populated energies. RMSD of the protein (black) and the ligand (red) are reported. The ligand RMSD was calculated in reference to the protein. The overall flexibility of the proteins in the free (red line) and bound (black line) state was measured via the average root mean square

fluctuation (RMSF) values during the MD trajectory of P110 (left) and P40/P90 (right) bound to 3'SLn. RMSF measures the average amplitude of each atom's motions relative to a mean reference position. The higher value of RMSF represents higher flexibility. The protein-ligand H-bonds (acceptor – donor H) established during the 100 ns MD are also shown. Adapted from **Marseglia A. *et al.*, 2024**.

A cluster analysis of the MD (**Figure CII. 2.1_3**) indicated that the sialic acid was the main residue involved in the binding interaction between P110 and 3'SLn, in agreement with the STD NMR results. In addition, numerous hydrogen bonds were observed at the protein-ligand interface; for example, H-bonds were established between Neu5Ac carboxyl group and Arg600 and Ser458. Asn200 exhibited two interactions with Neu5Ac: one with the OH at position 4 and the other with its acetamide moiety; while Pro197 formed a H-bond with the hydroxyl proton 7 of Neu5Ac. In addition, Asn475 established crucial H-bonds with hydroxyl protons 8 and 9 of the glycerol chain of Neu5Ac, which strongly contributed to the stabilization of the complex and resulted in the flexible loop region (471-482 aa) moving closer to the Neu5Ac binding site (**Figure CII. 2.1_3A and 2.1_2 left panel**). As shown in **Figure CII. 2.1_3A**, the ligand was positioned with the acetamide group of the Neu5Ac in a hydrophobic pocket close to Phe457, which also helped to stabilize the binding. Another significant contact was observed between the amide nitrogen of Neu5Ac and Ser456, forming a hydrogen bond that was stable during the MD simulation, in accordance with the high STD contribution.

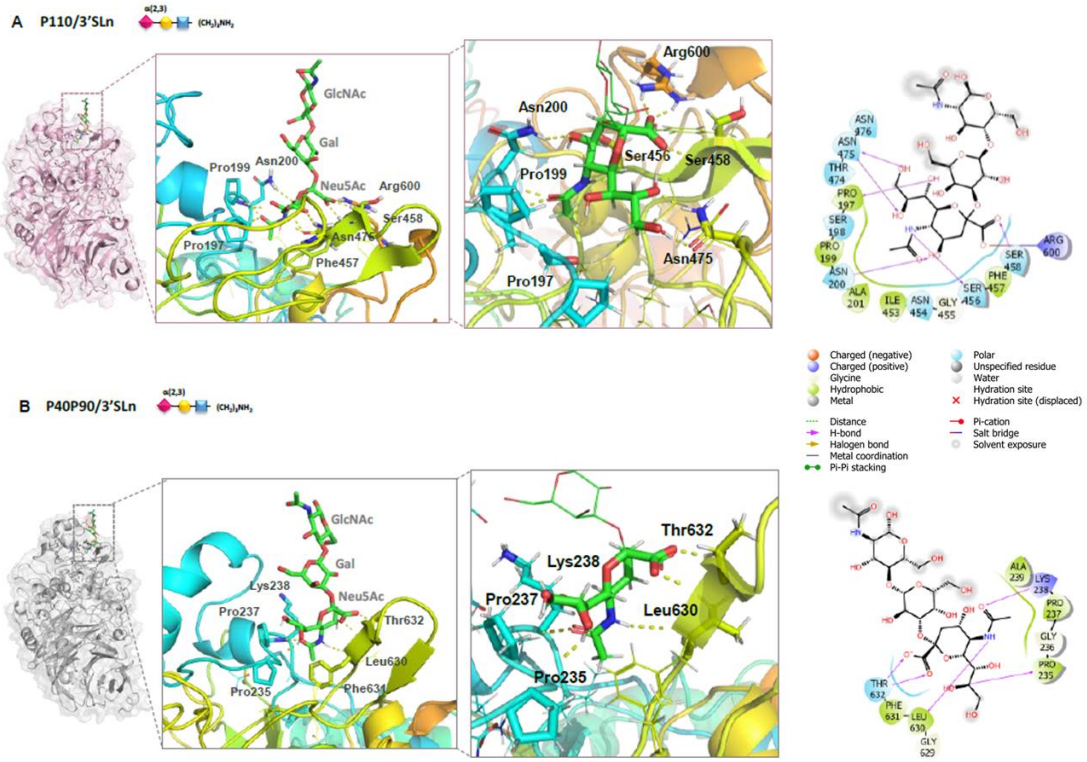

Figure CII. 2.1_3. P110–3'SLn and P40/P90–3'SLn predicted complexes. A) 3D view of P110-3'SLn predicted complex. **B)** 3D view of P40/P90-3'SLn complex. The aa of the binding pocket involved in the

binding with Neu5Ac are represented as sticks. The flexible loop moving closer to the binding site upon binding is represented in yellow. For clarity, zoom on the Neu5Ac is also reported. On the right, two-dimensional plots highlighting the main protein-ligand interactions are shown. Solid arrows represent hydrogen bonds with the functional groups of the backbone; the other residues in the binding pocket participate in polar and hydrophobic interactions. Adapted from **Marseglia A. *et al.*, 2024**.

Upon comparison of these results to the interactions observed in the crystal structure of P110 in complex with 3'SLn, it was evident that the majority of contacts align with previous findings, mainly involving the residues Ser 458, Ser 456, Asn200 and Pro197, although in the crystal the ligand is accommodated in the protein binding site with a different conformation relative to that derived from the NMR data (**Figure CII. 2.1_4A**).

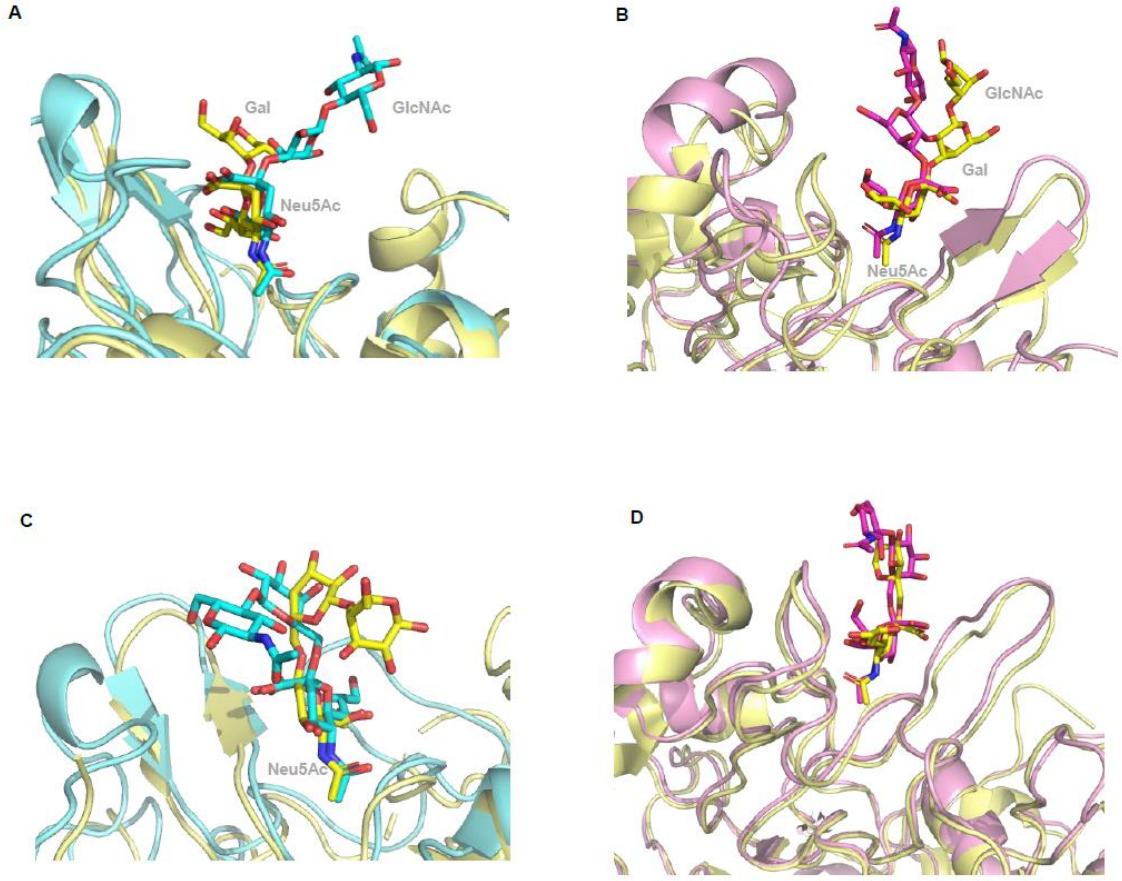

Figure CII. 2.1_4. Superimposition of P110 and P40/P90 - sialoglycans complexes derived from MD simulations and X-Ray. Upper panel: Superimposition of P110–3'SLn and P40/P90–3'SLn complexes. **A)** 3D view of the P110-3'SLn complexes as derived by MD simulation (in cyan) and from crystallographic analysis (PDB: 6r41 in yellow). **B)** 3D view of the P40/P90-3'SLn complexes as derived by MD simulation (in pink) and from crystallographic analysis (PDB: 6tlz in yellow). Lower panel: Superimposition of P110–6'SLn and P40/P90–6'SLn complexes. **C)** 3D view of the P110-6'sLn complexes as derived by MD simulation (in cyan) and from crystallographic analysis (PDB: 6r43 in yellow). **D)** 3D view of the P40/P90-6'SLn complexes as derived by MD simulation (in pink) and from crystallographic analysis (PDB: 6tl0 in yellow). Adapted from **Marseglia A. *et al.*, 2024**.

Analogously, the recognition of 3'SLn by the *M. pneumoniae* cytadhesin P40/P90 was studied. Similarly, to P110, the STD NMR analysis revealed a selective binding mode mainly involving the Neu5Ac moiety (**Figure CII. 2.1_1B, left panel**). The highest magnetization transfer was again observed for the acetyl group of Neu5Ac. The proton at position 7 of the Neu5Ac also exhibited a significant STD effect above 50%, while the protons H5, H6, and H9 contributed to the binding but with lower STD percentages between 50% and 20%. Very slight STD enhancements were also observed for the diastereotopic protons of the Neu5Ac and the proton at position 4 of the Gal unit.

Computational studies were also performed to further describe the conformational behaviour of 3'SLn upon binding to P40/P90. In accordance with tr-NOESY data (**Figure CII. 2.1_1B, right panel**), MD results revealed that 3'SLn could be accommodated in the binding pocket upon adopting two different conformations, namely *t* and *-g*, with the Φ dihedral angle around the glycosidic linkage between Neu5Ac-Gal at 180° and -60°, respectively. This is likely due to the higher flexibility (**Figure CII. 2.1_2, right panel**) and the different orientation of a loop region (642-653 aa) of P40/90 relative to P110, resulting in a wider binding pocket.

Regardless of the conformation adopted by the ligand, the main interactions with the protein were established only with the Neu5Ac moiety, as already revealed by the NMR analysis and in agreement with the previously published X-ray data (**Figure CII. 2.1_4B**). Indeed, in the main representative conformation of the complex (**Figure CII. 2.1_3B**), the Neu5Ac was the only sugar residue entirely accommodated in the protein binding pocket, while Gal and GlcNAc residues were more distant from the protein surface. Specifically, a stable contact occurred between the amide group at position 5 of Neu5Ac and the Leu630 that was present for about 70% of MD simulation time.

The Neu5Ac carboxyl group also established H-bonds with the side chain of Thr632. Consistent with STD NMR results, the OH at position 7 interacted with Pro235 and the oxygen of the acetyl moiety established a contact with Lys238. The presence of hydrophobic residues near the binding site, in particular Phe631, contributed to stabilize the complex and anchor the Neu5Ac unit to the protein via hydrophobic contacts.

CII. 2.2. 6'SLn recognition by P110 and P40/P90

The binding mode and the conformational behaviour of 6'SLn when interacting with P110 and P40/P90 were also investigated by combining NMR experiments and computational approaches. Also, in this case, in accordance with the previous crystallographic data (**Figure CII. 2.1_4 lower panel**), Neu5Ac was the ligand motif most involved in cytadhesin binding. The STD NMR analysis and the resulting epitope map of 6'SLn bound to P110 showed that the highest STD NMR effect

was given by the acetyl group of Neu5Ac (**Figure CII. 2.2_1**). Also, the proton H7 contributed significantly to the interaction, with a STD NMR relative percentage close to 50%. A minor contribution was given by H6, H8 and H9 protons of the Neu5Ac.

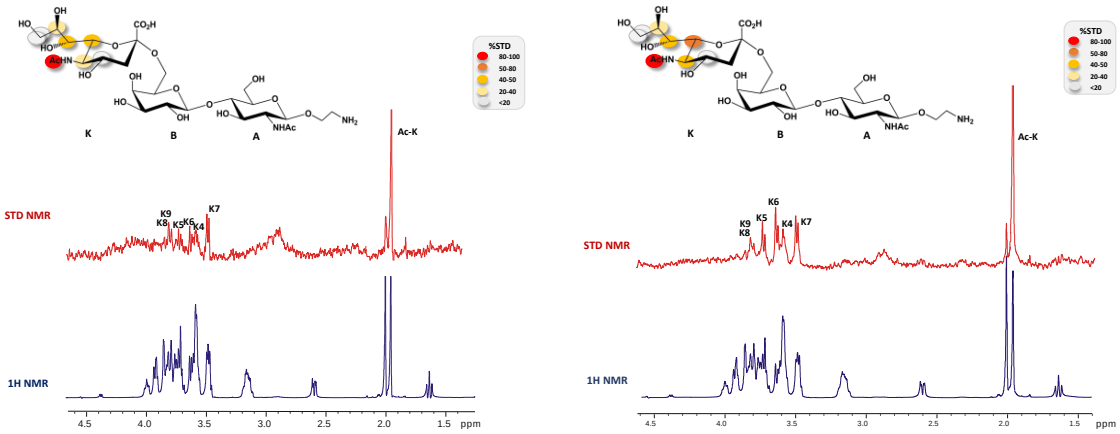

Figure CII. 2.2_1: NMR analysis of 6'SLn bound to P110 (left panel) and P40/P90 (right panel). STD NMR spectra (red) and the unsaturated reference spectrum (blue) together with the epitope map of the ligand interacting with P110 (left panel) and P40/P90 (right panel) are reported. Adapted from **Marseglia A. *et al.*, 2024**.

MD data corroborated the experimental results, clearly indicating the key role of the sialic acid in the binding interaction and showed numerous H-bonds established between the protein amino acids and the terminal Neu5Ac residue, also stabilized by hydrophobic contacts with Phe457 (**Figure CII. 2.2_2 and CII. 2.2_3**). Recurring interactions above 90% of the simulation time were formed between Pro197 and the Neu5Ac hydroxyl group at position 7, while the amide group established an interaction with the carbonyl oxygen of Ser456. Other H-bonds occurred between Asn200 and both the carbonyl oxygen of the acetyl moiety and the OH at position 4. The hydroxyl protons at positions 8 and 9 of the glycerol chain of Neu5Ac interacted with Asn475. In addition, the hydroxyl group of Ser458 also mediated a crucial interaction with the carboxyl group of Neu5Ac. While the Neu5Ac was the residue most involved in the interaction, in all the complexes derived from the MD cluster analysis, transient interactions between the protein and some protons of the GlcNAc unit were also observed.

Consistent with the results observed for the cytoadhesin P110, the STD-NMR experiments acquired on the mixture P40/P90-6'SLn suggested that the protein selectively recognized the Neu5Ac residue (**Figure CII. 2.2_2**). As shown by the epitope map (**Figure CII. 2.2_1**), the most involved group was the acetyl moiety of the Neu5Ac; protons H6 and H7 also exhibited high STD enhancements upon 50%, while the glycerol chain and the other protons of Neu5Ac contributed less to the interaction. These data agreed with MD results and the previously published crystallographic complex showing that 6'SLn established a crucial interaction with amino acids of the binding pocket mainly via the Neu5Ac residue. In detail, its carboxyl group formed a H18

bond with Thr632[432] [Aparicio D. *et al.*, 2020]; the acetamide group of Neu5Ac interacted with the Leu630 and Lys238; and the Pro235 displayed an interaction with the hydroxyl group at position 8 of the glycerol side chain.

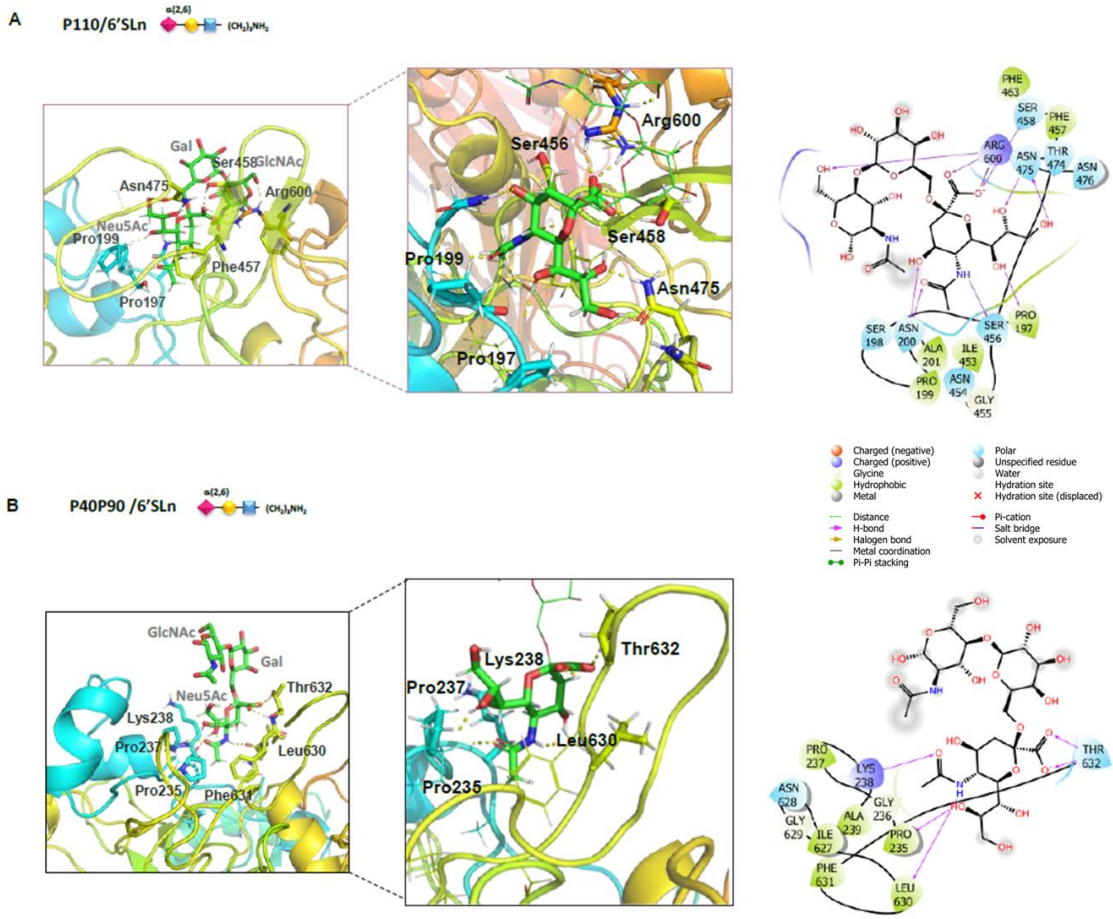

Figure CII. 2.2_2. P110–6'SLn and P40/P90–6'SLn predicted complexes. A) 3D view of the P110-6'sLn complex. **B)** 3D view of the P40/P90-6'sLn complex. The aa of the binding pocket involved in the binding with Neu5Ac are represented as sticks. Two-dimensional plots highlighting the main protein-ligand interactions are also reported. Solid arrows represent hydrogen bonds with the functional groups of the backbone; the other residues in the binding pocket participate in polar and hydrophobic interactions. Adapted from Marseglia A. *et al.*, 2024.

As already observed for the complexes with 3'SLn, MD simulation analysis also revealed higher flexibility of the ligand when bound to P40/P90 than with P110. Given the presence of the additional ω torsion angle in the 6'SLn with respect to 3'SLn, the ligand could sample a population distribution in equilibrium between different rotamers, namely *gt*, *tg* and *gg*, according to the different values of ω angle (60°, 180° and -60° respectively)[442] [Poppe L. *et al.*, 1992]. Specifically, in the free state, the *gt* and *tg* rotamers were the most populated, while the *gg* rotamer population was minor. Interestingly, MD results revealed that, upon binding to P110, the ligand was mainly accommodated in the *gt* conformation (Figure CII. 2.2_3). On the other

hand, when 6'SLn bound to P40/P90, an equilibrium was observed between two different rotamers (*gt* and *tg*) that were similarly accommodated in the protein binding pocket, with the *tg* conformation as the more populated one.

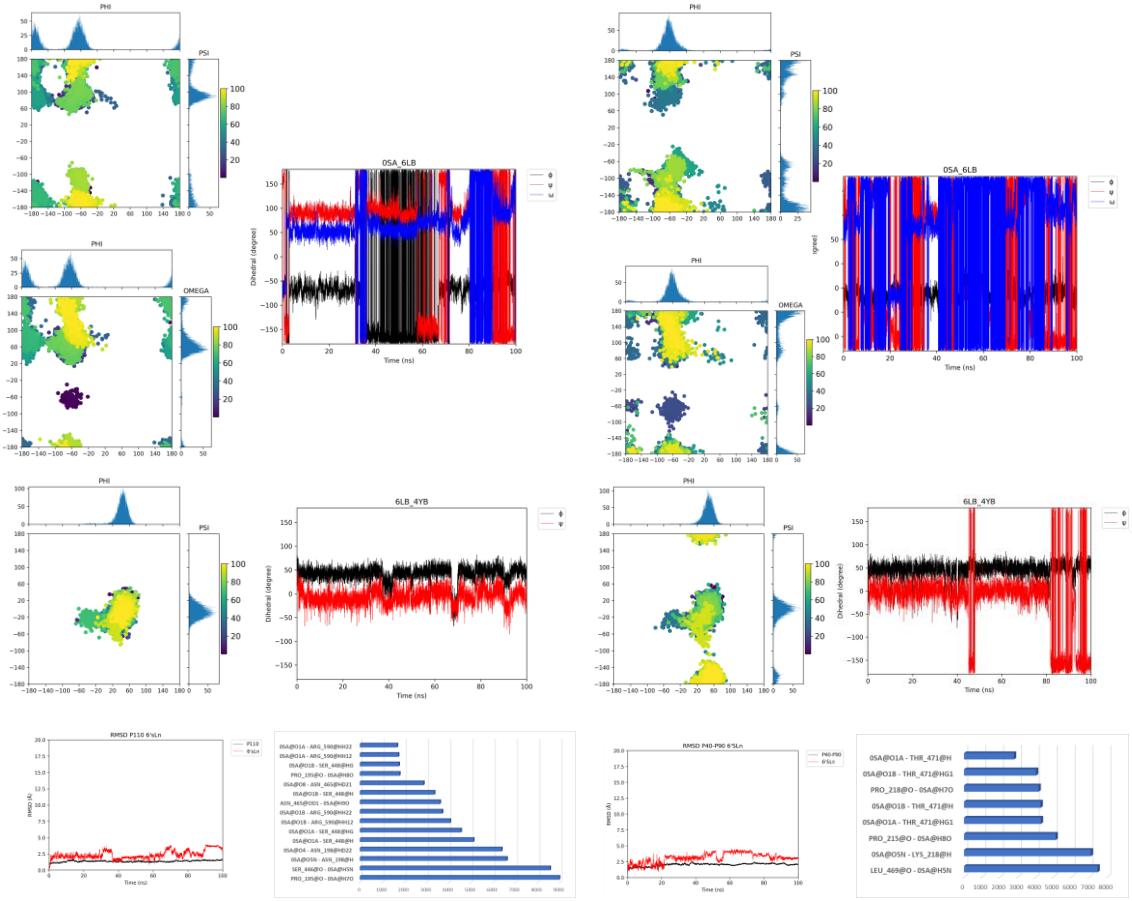

Figure CII. 2.2_3. MD analysis of P110 (left panel) and P40/P90 (right panel) in the interaction with 6'SLn. 6'SLn dihedral angles analysis in the bound state with P110 (left panel) and P40/P90 (right panel) represented as scatter plots of the Φ torsion against ψ or w, during the MD simulation with the relative histograms to represent the most populated energies. RMSD of the protein (black) and the ligand (red) are reported. The ligand RMSD was calculated in reference to the protein. The protein-ligand H-bonds (acceptor – donor H) established during the 100 ns MD are also shown. Adapted from **Marseglia A. *et al.*, 2024**.

CII. 2.3. Transient interactions with the Neu5Ac moiety observed in *M. genitalium* P110

The cluster analysis of the Molecular Dynamics previously explained (**Figure CII. 2.1_3 and 2.2_2**) indicated that the sialic acid was the main residue involved in the binding interaction between P110 and the ligands 3'SLn and 6'SLn, in agreement with the STD NMR results. In the Molecular Dynamics also appears "new" interactions, with moieties different to the sialic acid, that could be more transient but they exist. With these results we determined that the binding site of P110 were composed by the following residues which are involved in hydrogen bonds with the sialic acid moiety: Asn 182, Asn 476, Asn 475, Asn 200, Ser 458, Ser 456 and Pro 197, located in two

different regions of the protein (**Figure CII. 2.3_1A,B**). In the Apo form, *Mge* N182 is away from the binding pocket. However, in the MD simulations Asn 182 seems to be closer to the binding site, especially with the 3'SLn ligand (**Figure CII. 2.3_1A**). The transient or more flexible interaction with this residue could be important for the conformational change of the loop involved in the P140 interaction and therefore the functioning of the Nap complex.

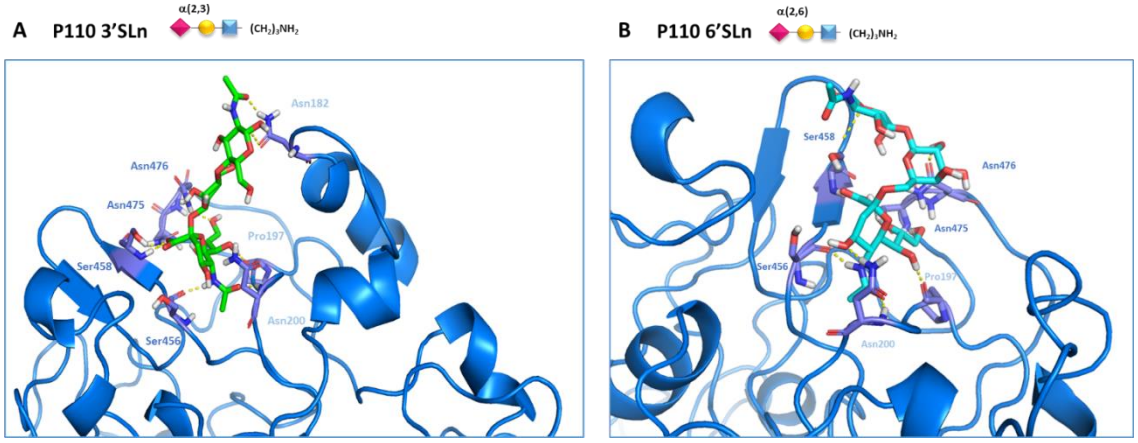

Figure CII. 2.3_1. MD simulation, illustrating the interactions between the sialylated trisaccharide 3'SLn (A), 6'SLn (B) and the residues in the binding site of the protein. The binding site of P110 is composed by the residues highlighted which are involved in hydrogen bonds with the sialic acid. These residues are located in two different regions of the P110 differentiated by the dark or light blue colour. **A)** P110 interacting with 3'SLn in one of the main representative conformation (*t* conformation). **B)** P110 interacting with 6'SLn in one of the main representative conformation (g*t* conformation/rotamer).

With this observation, we decoded to introduce by transposon delivery, a P110 variant carrying an Asn182Ala substitution, into *M. genitalium* null mutant (ΔMG_192) (**Table CII. 2.3**). The strain expressing the P110-N182A variant show a non-adherent phenotype consistent with the barely detectable level of expression of the adhesin (**Figure CII. 2.3_2**). This fact, indicates that this residue seems to be important for the folding and in this strain adhesins are unstable and degrade, preventing further characterization and from taking conclusions regarding the protein-ligand interaction behaviour.

Table CII. 2.3. *M. genitalium* strains used in this chapter.

Strain Name	Genotype	Reference
G37	Wild-type	ATCC 33530
ΔMG_192	Deletion of the MG_192 gene by allelic exchange (G37 ΔMG_192::tetM438)	Burgos *et al.*, 2006

P110-WT	Re-introduction of a MG_192 wild-type allele in a ΔMG_192 mutant	Aparicio, D. *et al.*, 2018
P110-N182A	Introduction of a MG_192 allele bearing a N182A substitution in a ΔMG_192 mutant	This work

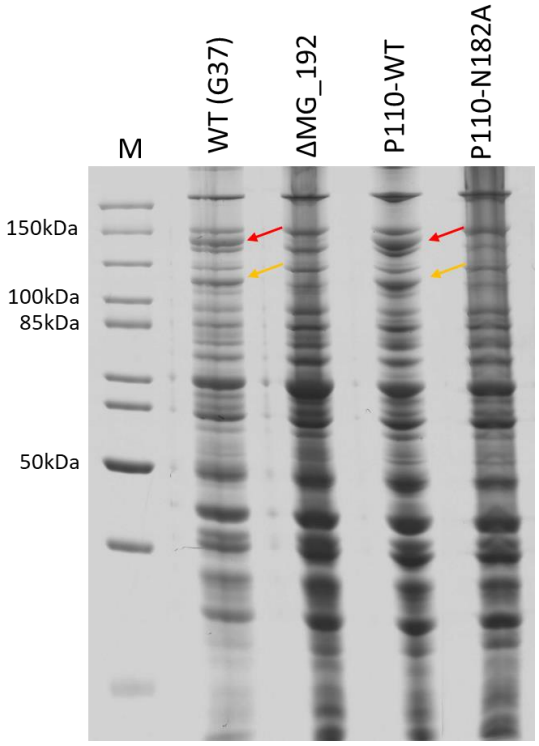

Figure CII. 2.3_2. SDS-PAGE of whole cell lysates from the G37 (WT-*Mge*), ΔMG_192 strain, P110-WT complemented strain and the P110-N182A mutant strain generated. Red and orange arrows indicate the presence of P140 and P110 adhesins, respectively.

CII. 2.4. Recognition of complex type *N*-glycans by P110 and P40/P90

To acquire additional insights into *N*-glycans recognition by P110 and P40/P90, longer ligands, which mimic natural complex type biantennary *N*-glycans containing the Neu5Ac-α-(2,3)-Gal or Neu5Ac-α-(2,6)–Gal epitopes at their terminal end, were also investigated (see supporting information). STD-NMR analyses carried out on branched undecasaccharides (**Figure CII. 2.4_1 and 2.4_2**) reinforced selective protein recognition for the Neu5Ac residues, whereas the other sugar units did not contribute to the binding process. These results were comparable with those obtained on smaller trisaccharides. Again, the acetyl group of the Neu5Ac displayed the highest STD enhancement, while some other STD signals of strong intensity belonging to the protons of the sialic acid sugar backbone, in particular H7 and H6, were also observed.

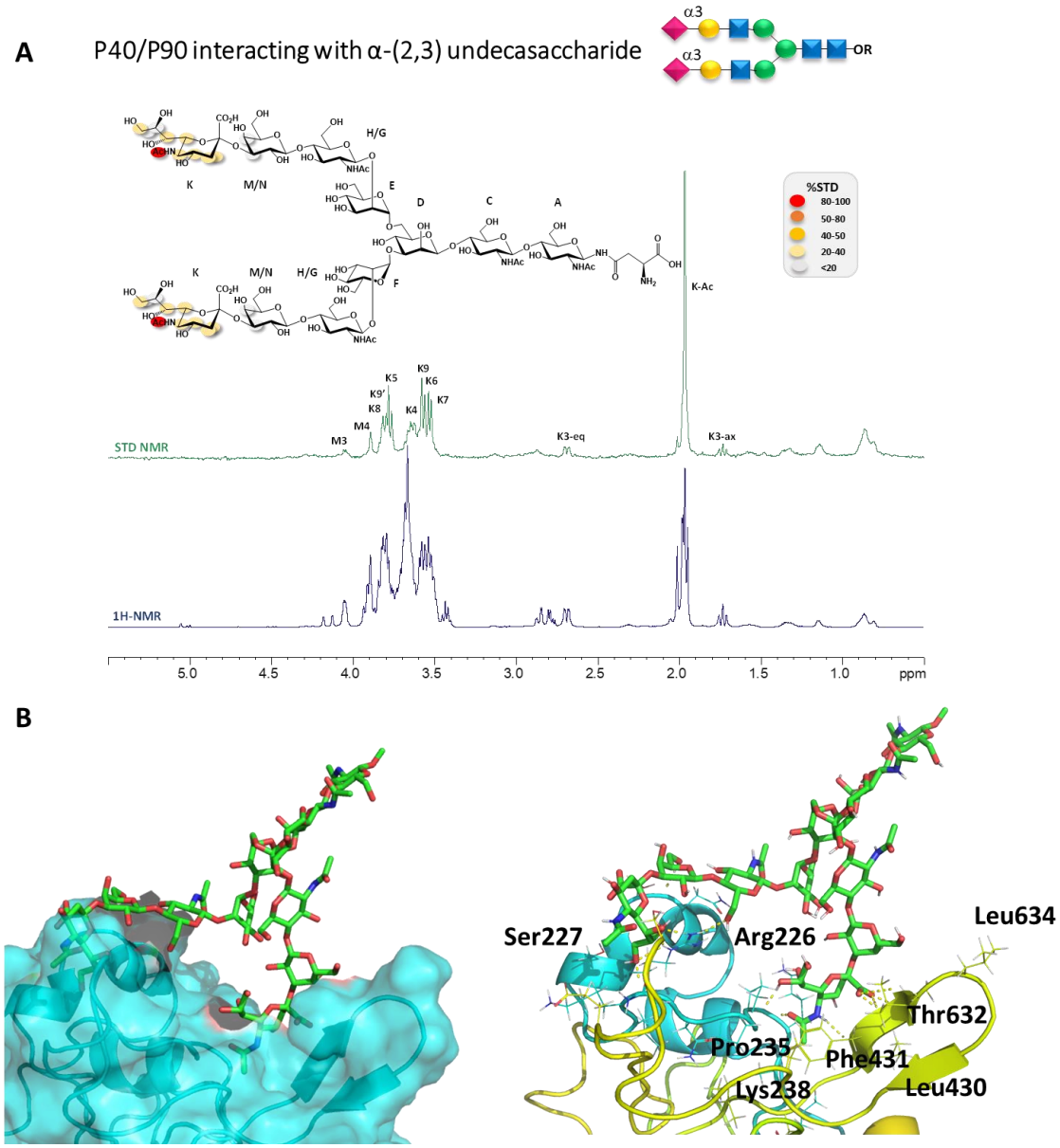

Figure CII. 2.4_1. NMR and MD analysis of complex glycan bound to P40/P90. **A)** STD-NMR spectrum (green) and the unsaturated reference spectrum (blue) of the undecasaccharide containing the Neu5Ac-α-(2,3)-Gal epitope at its terminal end interacting with P40/P90. The ligand epitope map is also showed. **B)** 3D view of the P40/P90-undecasaccharide predicted complex. Adapted from Marseglia A. *et al.*, 2024.

On the contrary, the resonances of the protons belonging to the other sugar units were not visible in the spectra, indicating that they were solvent exposed. These data were in full agreement with the results of MD simulations. Indeed, as showed in the predicted model depicted in **Figure CII. 2.4_1**, the longer, complex N-glycan was anchored to the protein surface with the sialic acid on one antenna mainly establishing polar contacts with Leu634 and Thr632 and hydrophobic interactions involving Phe631, as previously reported for the trisaccharide ligand. Moreover, additional interactions were observed in the predicted model between the Neu5Ac unit positioned at the terminal end of the other glycan branch and Arg226 and Ser227

residues. This result agreed with the values of the binding constants measured by fluorescence analysis, which revealed a protein affinity for each undecasaccharide that was approximately two-fold higher than the one measured for the corresponding trisaccharide, further supporting the possibility of a branched binding mode involving both sialic acid residues on the longer sialoglycans.

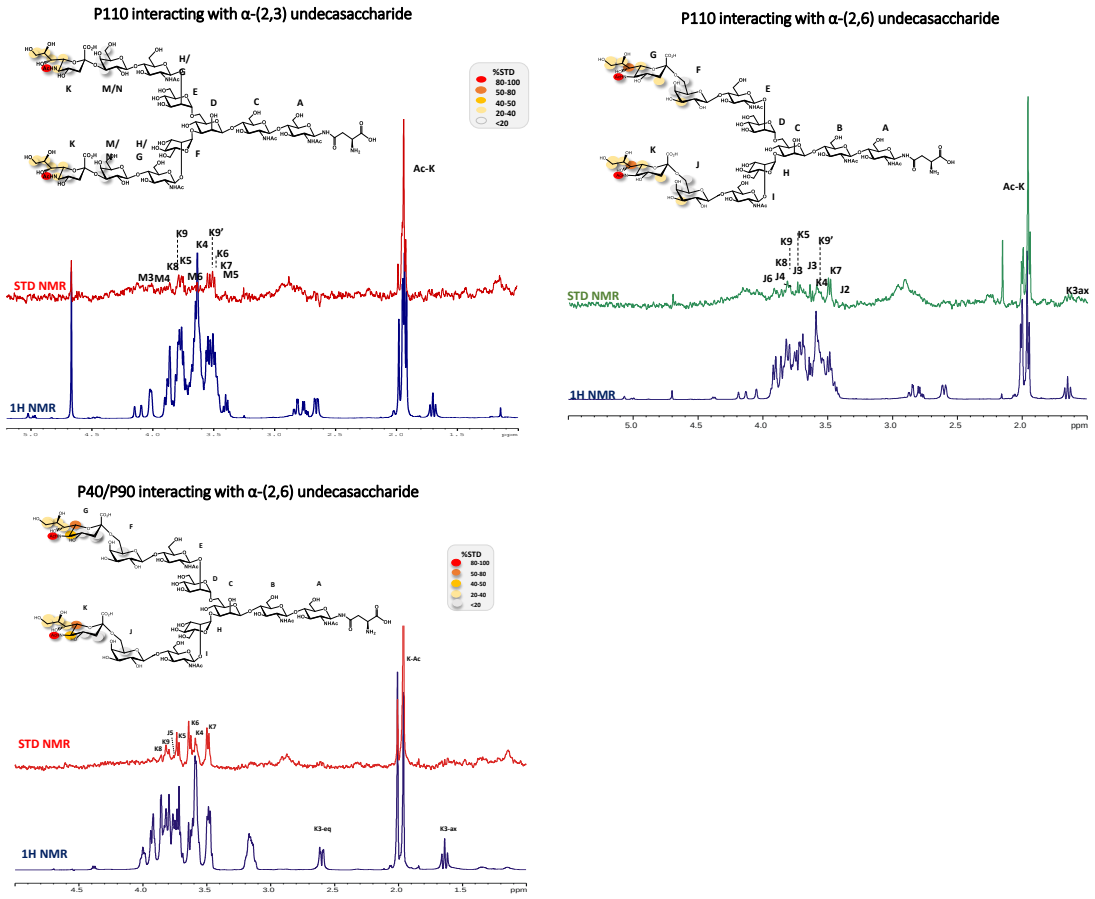

Figure CII. 2.4_2. NMR analysis of complex-type biantennary N-glycans bound to P110 and P40/P90. The STD NMR spectra (red) and the unsaturated reference spectrum (blue) together with the epitope map of α-2,3 and α2,6 undecasaccharides interacting with P110 and P40/P90 are reported. Adapted from **Marseglia A. *et al.*, 2024**.

CII. 2.5. sTa-Thr recognition by P110 and P40/P90

The molecular basis of the interactions between *Mycoplasma* cytadhesins and the *ad hoc* synthesized, threonine-linked sialyl-T-antigen, sTa-Thr, was also assessed. As revealed by the STD NMR analysis, both proteins were able to recognize the *O*-glycan in a similar manner (**Figure CII. 2.5_1**). The STD NMR spectra showed that the Neu5Ac displayed the highest STD contribution, the galactose unit slightly contributed to the interaction, and the reducing GalNAc, as well as the Thr residue, did not receive any magnetization transfer from the protein.

Regarding P110, the acetyl group of Neu5Ac showed a strong contribution to the binding, followed by H7, H5, H6, H8 and H9 protons, which displayed STD NMR relative percentages upon

50%. On the other hand, H4 of Neu5Ac and H4 and H6 of the Gal were less involved in the binding event, showing %STD values below 40%.

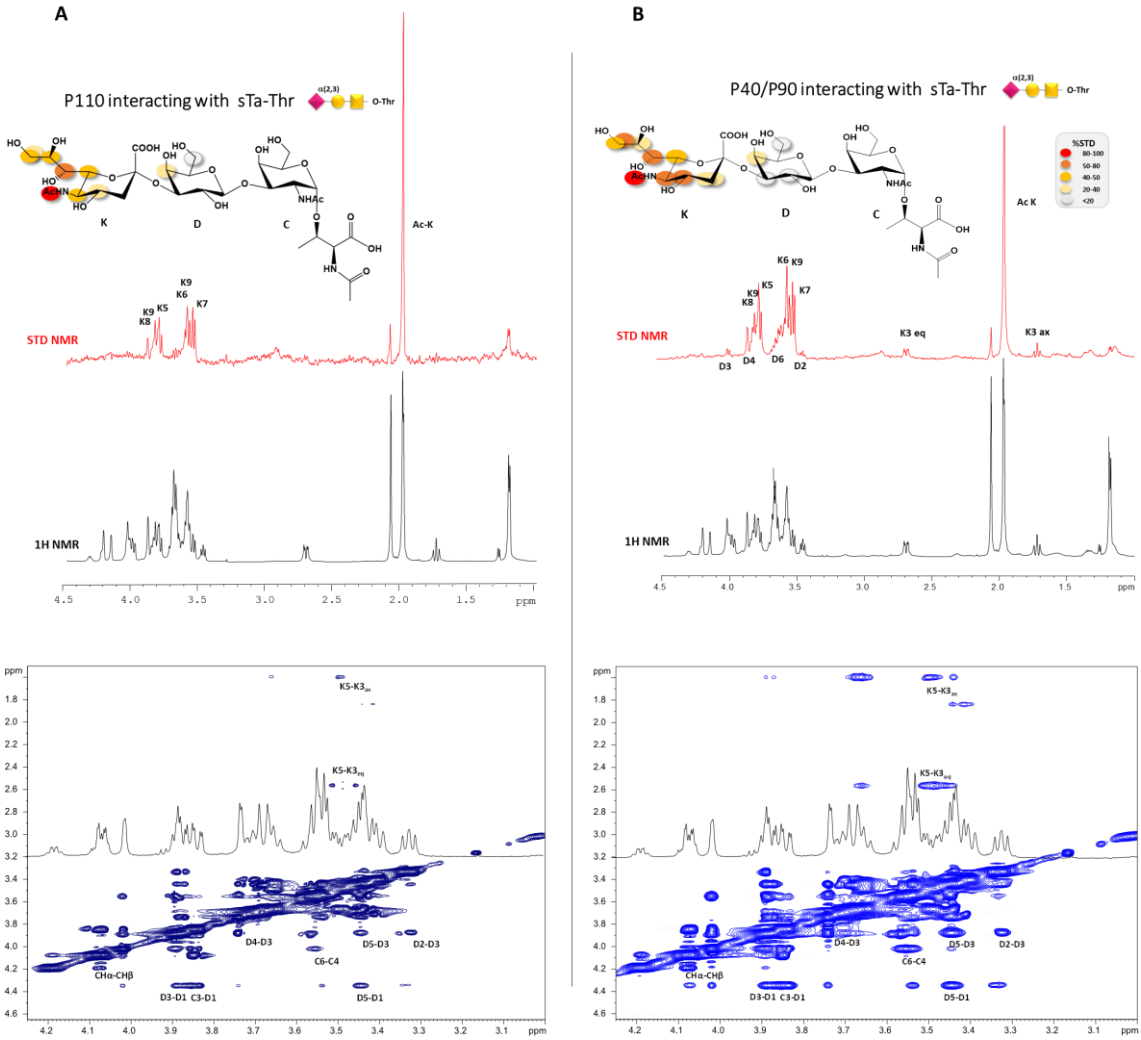

Figure CII. 2.5_1. NMR analysis of sTa-Thr bound to P110 and P40/P90. **A)** Superimposition of STD-NMR spectrum (red) and the unsaturated reference spectrum (black) of sTa-Thr interacting with P110 and the corresponding ligand epitope map. are reported. On the bottom, Tr-NOESY spectrum of 1:50 P110-sTa-Thr mixture is reported. **B)** Superimposition of STD NMR spectrum (red) and the unsaturated reference spectrum (black) of sTa-Thr interacting with P40/P90 and the corresponding ligand epitope map. On the bottom, Tr-NOESY spectrum of 1:50 P40/P90 -sTa-Thr mixture is reported. Adapted from **Marseglia A. *et al.*, 2024**.

In the case of P40/P90, a strong saturation transfer was also detected for the acetyl group and H7 of the Neu5Ac, showing the highest STD NMR effects (**Figure CII. 2.5_1**). H4, H5 and H9 further contributed to the binding with STD NMR enhancements greater than 50%. Protons at positions 8, 6 and 3 of the Neu5Ac chain underwent less magnetization transfer exhibiting a %STD NMR lower than 50%. Moreover, slight STD effects were observed also for the galactose moiety that exhibited a weaker contribution to the binding; galactose protons H4, H3, H6 and H2 displayed STD NMR percentages lower than 20%.

Once the ligands interacting epitopes were established, the binding profile of the complexes of P110 and P40/P90 with sTa-Thr were further investigated via computational approaches and tr-NOESY analysis. As shown in **Figure CII. 2.5_2**, the sTa-Thr was accommodated in the same protein binding pocket as the previously analyzed ligands. Regarding 1 the P110/sTa-Thr predicted complex, interactions occurred between Pro197 and the hydroxyl group at position 7 of Neu5Ac and between Ser456 and the amide nitrogen of the sialic acid. The Asn200 residue also interacted with the OH group at position 4 of Neu5Ac and Ser458 established two H-bonds with the carboxyl group of this residue, as seen in the crystal structures[75,432] [**Aparicio D. *et al.*, 2018; Aparicio D. *et al.*, 2020**]. Also, the MD simulation of P40/P90 in complex with sTa-Thr revealed a selective recognition toward Neu5Ac. The most stable contact occurred between Leu630 and the amide group of Neu5Ac, according to the observed high STD NMR value. The Neu5Ac carboxyl moiety also established stable H-bonds with Thr632. Other significant contacts were observed for OH at C7 of Neu5Ac, forming a hydrogen bond with Pro235, which was stable during the MD simulation in accordance with the high STD contribution of H7 (around 80%). In addition, Lys218 formed a hydrogen bond with the Neu5Ac acetyl group.

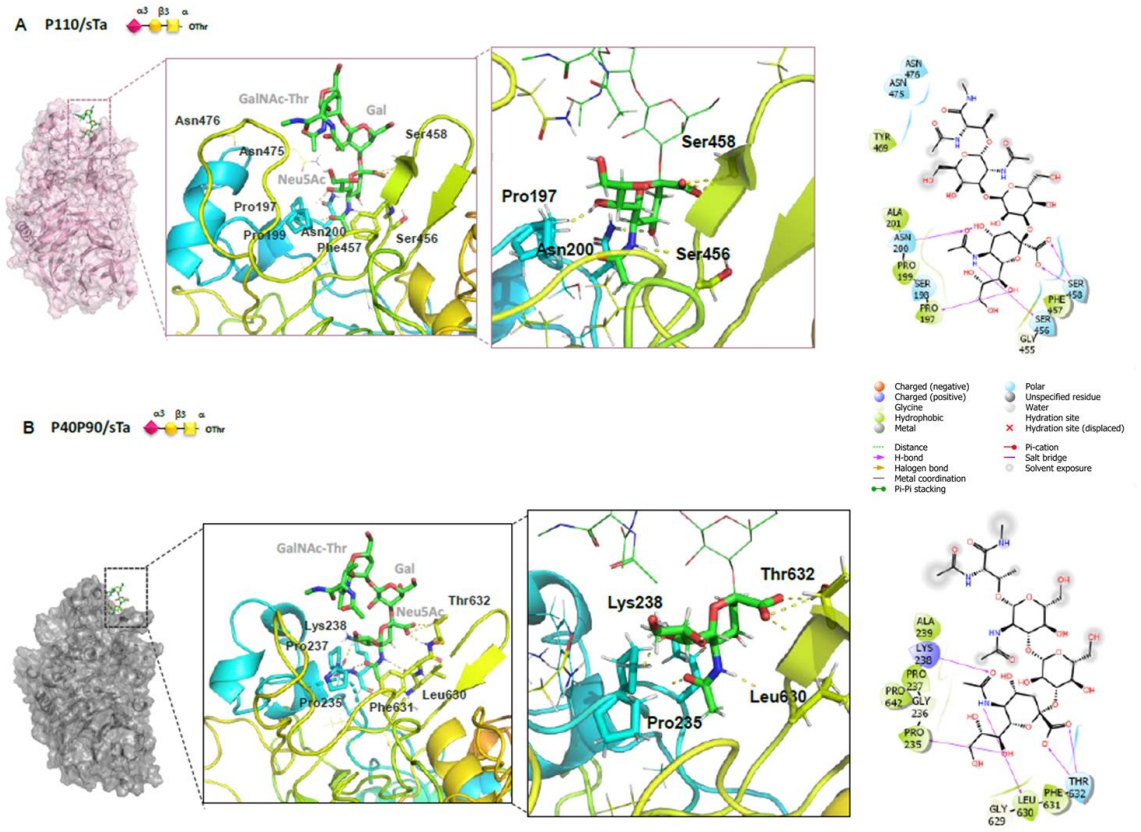

Figure CII. 2.5_2. P110 and P40/P90–sTa-Thr predicted complexes. **A)** 3D view of the P110-sTa-Thr complex. **B)** 3D view of the P40/P90-sTa complex. For clarity, zoom on the Neu5Ac is also reported. The aa of the binding pocket involved in the binding with Neu5Ac are represented as sticks. Two-dimensional plots highlighting the main protein-ligand interactions are also shown. Solid arrows represent hydrogen

bonds with the functional groups of the backbone; the other residues in the binding pocket participate in polar and hydrophobic interactions. Adapted from **Marseglia A. *et al.*, 2024**.

The trajectories of ligand glycosidic torsions were sampled during the MD simulations in the free and bound states for both systems to evaluate the sTa-Thr conformational behaviour (**Figure CII. 2.5_3**). The sTa-Thr shape and conformation were mainly influenced by the glycosidic torsion angles, namely Φ (C1-C2-O-C3')/ψ (C2-O-C3'-H3') around Neu5Ac-α-(2,3)-Gal and Φ (H1– C1–O–C3')/ ψ (C1–O–C3'–H3') around the Gal-β-(1,3)–GalNAc bonds. Interestingly, a conformer selection was observed upon binding with P110. Indeed, in the bound state only the minimum characterized by the value of Φ torsional angle at -60° was populated. On the other hand, no significant conformational differences between the free and bound state were observed for the sTa-Thr interacting with P40/P90, which mainly adopted two conformations with the Φ torsion angle along the Neu5Ac -α-(2,3)-Gal unit at 180° and -60°.

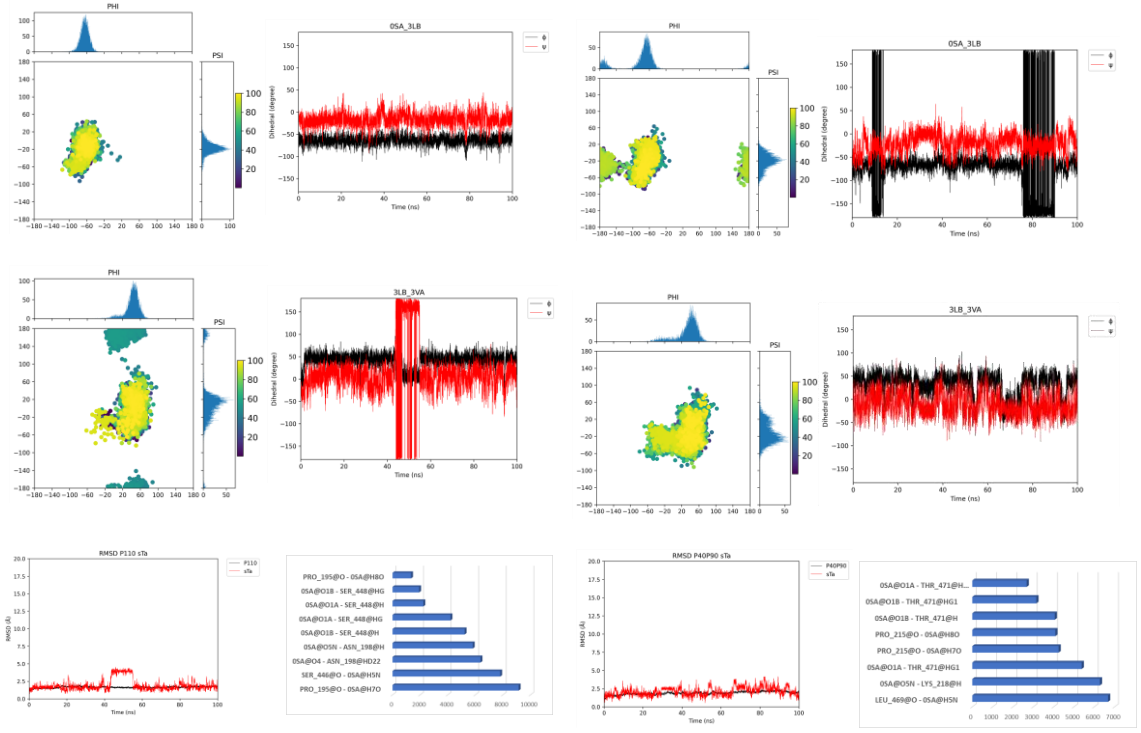

Figure CII. 2.5_3. MD analysis of P110 (left panel) and P40/P90 (right panel) in the interaction with sTa-Thr. sTa-Thr dihedral angles analysis in the bound state with P110 (left panel) and P40/P90 (right panel) represented as scatter plots of the Φ torsion against ψ or w, during the MD simulation with the relative histograms to represent the most populated energies. RMSD of the protein (black) and the ligand (red) are reported. The ligand RMSD was calculated in reference to the protein. The protein-ligand H-bonds (acceptor – donor H) established during the 100 ns MD are also shown. Adapted from **Marseglia A. *et al.*, 2024**.

CII. 2.6. Role of the potassium ion binding site in the stabilization of the Nap complex (or the P110 adhesin) and the ligand interaction

As has been described1 in a previous chapter, we determined the crystal structure of the P110 adhesin, and the structure showed a potassium ion bound to the C-domain[383]. [**Aparicio D. *et al.*, 2018**] (**Figure CII. 2.6_1 and 2.6_4**). The potassium ion binding site is located in a hydrophilic cage of the C-domain close to the interface with the N-domain (**Figure CII. 2.6_1A**). Potassium ion is coordinated with three oxygens of the main chain (from residues Thr831, Arg834, and Gly839), with two water molecules and with one of the carboxylate oxygens from Asp836[75] (**Figure CII. 2.6_1B**) [**Aparicio D. *et al.*, 2018**]. The cage is covered by the Tyr830 side chain, which maintains all the carbon atoms of the phenolic ring at ~4 Å from the potassium. In the absence of potassium, the binding cage opens by reorienting the Tyr830 side chain, and the Asp836 side chain rotates outside the cage pointing its carboxylic group toward the displaced side chain of Arg834 (**Figure CII. 2.6_1C**). These changes also result in some rearrangements of neighbour residues, in particular Pro877 and Pro926. Though many roles have been described for potassium ions, its function in P110 activity is unclear[443,444] [**Page M. J. and Di Cera E., 2006; Black, C. B. *et al.*, 1994**].

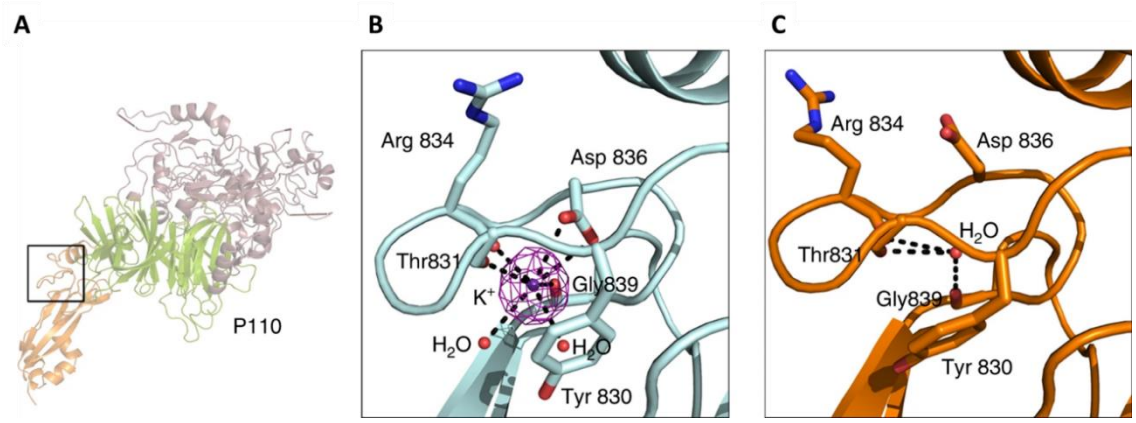

Figure CII. 2.6_1. Binding of Potassium to P110. A) Overall views of the potassium binding site (indicated by a rectangle) in the C-terminal domain of P110. Detail of the potassium binding site in the presence **(B)** and in the absence **(C)** of potassium.. Adapted from **Aparicio D. *et al.*, 2020**.

We decided next to study in more detail the implications that the potassium ion biding site could represent for the hole complex and we subjected the P110 (PDB: 5OX7) to MD simulations in AMBER. Comparing the MD simulations of the P110 with and without the K^+ ion, we observed that, from the RMSF graphs (**Figure CII. 2.6_2**), there exist conformational changes in some parts of the protein (**Figure CII. 2.6_3A,B**). It seems that in general, the protein is stabilized in the presence of the K^+ ion, from the lower values of the RMSF in the presence of the ion (**Figure CII. 2.6_2**).

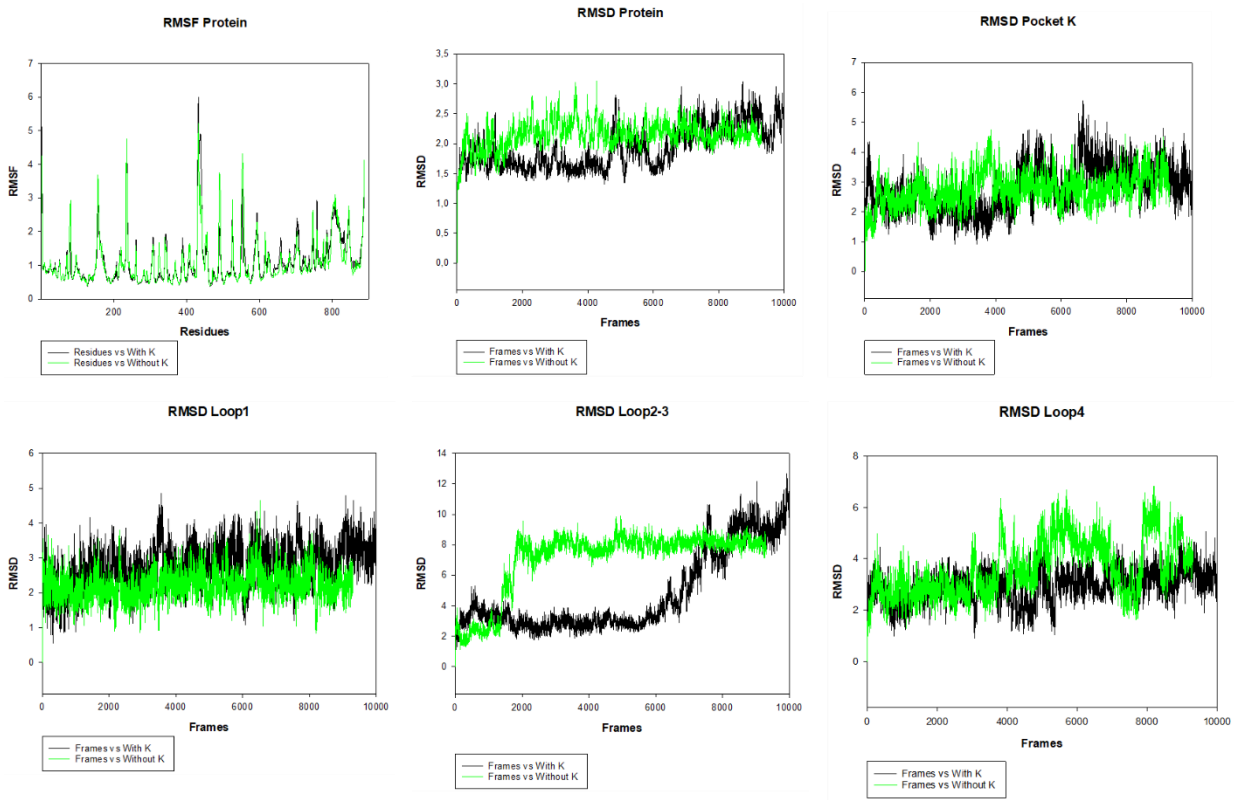

Figure CII. 2.6_2. MD simulation of P110 (PDB: 5OX7) with and without the presence of a potassium (K^+) ion in the potassium binding site. Conformational analysis of the protein and the "Loops" designated in the P110 structure. The ligand RMSD was calculated in reference to the protein. The overall flexibility of the protein with (black line) and without (green line) potassium ion was measured via the average root mean square fluctuation (RMSF) values during the MD trajectory of P110. RMSF measures the average amplitude of each atom's motions relative to a mean reference position. The higher value of RMSF represents higher flexibility. The MD simulation was performed during 100 ns.

Comparing the PDB structures of the main representative conformation of the protein, with the information of the RMSF values, we determined the parts of the protein "affected" conformationally by the ion presence and designated as different loops (**Figure CII. 2.6_4A**). These loops are located in the globular part of the protein. Specifically, in parts that are surface exposed and/or surface exposed but located in the interface with the P140 in the Nap complex. We also subjected the complex P110-3'SLn to MD simulations and the differences observed in the ligand configuration between the complex with and without the presence of the ion could be explained by the conformational changes observed in the protein (**Figure CII. 2.6_4B**). In both simulations, the ligand (3'SLn) is able to interact and it seems to be stable, however more in the presence of the K^+ ion (**Figure CII. 2.6_5**).

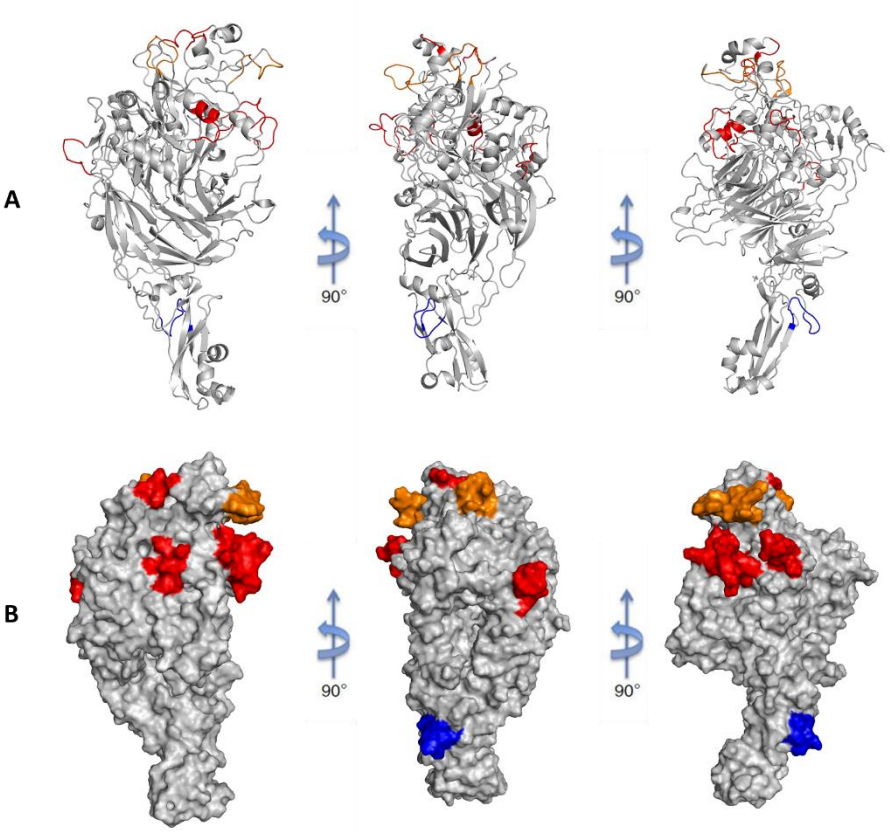

Figure CII. 2.6_3. Cartoon (A) or surface (B) representation of P110 (PDB: 5OX7) depicting parts of the protein altered in the MD simulation with and without the potassium (K^+) ion. The coloured zones, represents parts or fragments of the protein differently stabilized from the RSMF spectra comparation: the potassium binding pocket (in blue), part stabilized from the low RMSF values with the ion (in red) and parts no stabilized from the high RMSF values with the ion (in orange).

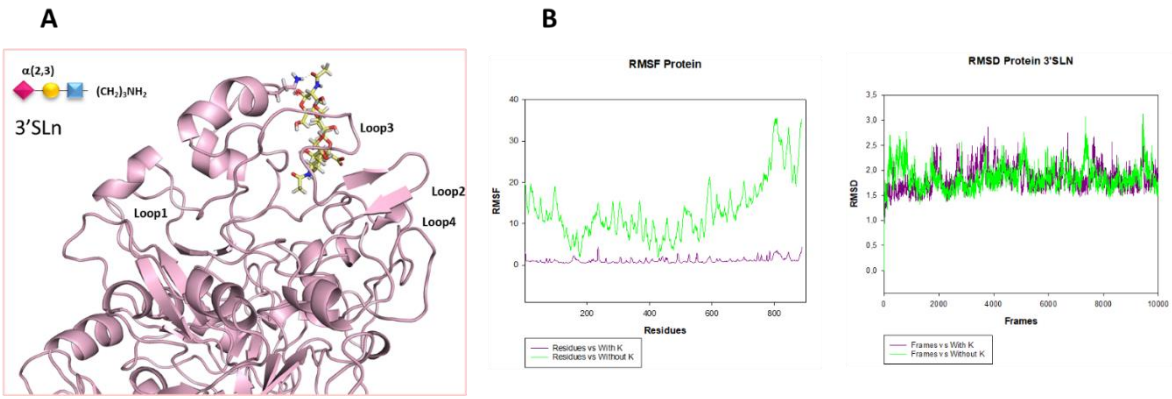

Figure CII. 2.6_4. MD simulation of P110 (PDB: 5OX7) with and without the potassium (K^+) ion, in the interaction with the ligand 3'SLn. A) Loops 1 to 4, designated in the structure of the P110, that are altered during the MD simulation. **B)** Conformational analysis of the protein. The overall flexibility of the protein with (purple line) and without (green line) potassium ion was measured via the average root mean square fluctuation (RMSF) values during the MD trajectory of P110 bound to 3'SLn. RMSF measures the average amplitude of each atom's motions relative to a mean reference position. The higher value of RMSF represents higher flexibility. The MD simulation was performed during 100 ns.

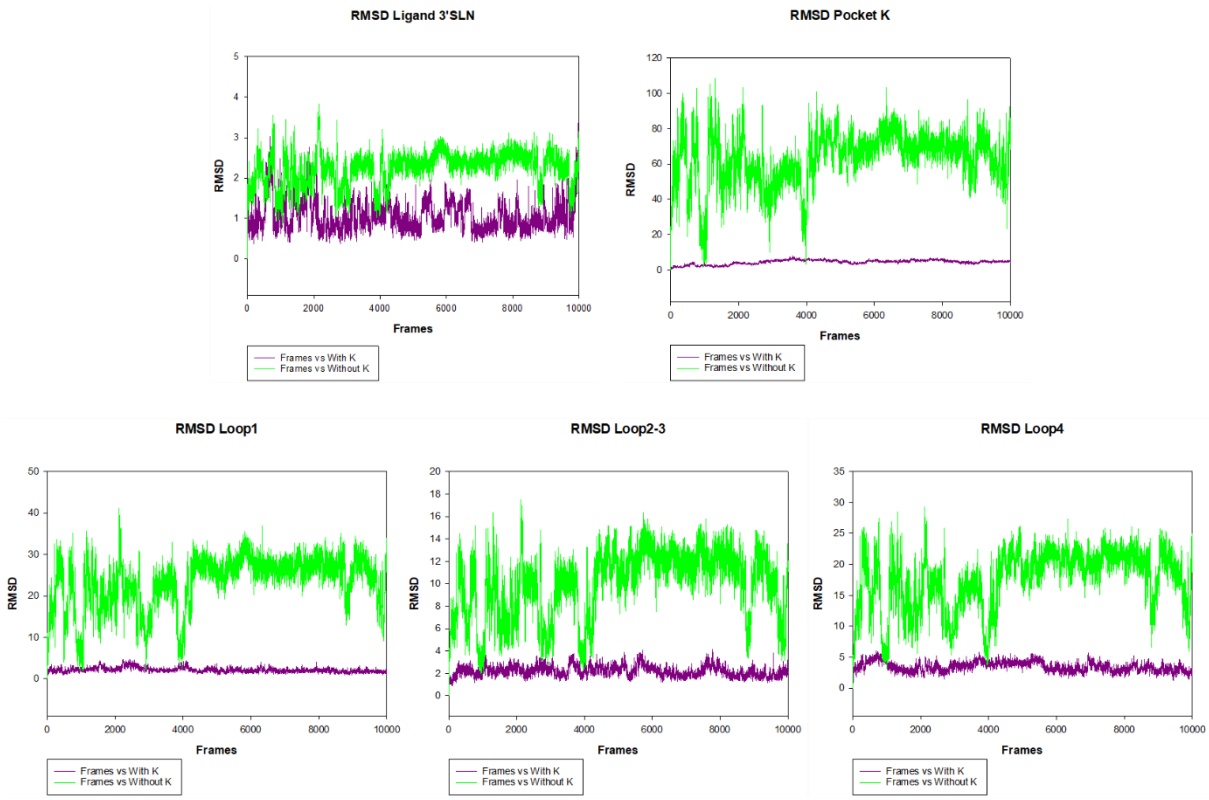

Figure CII. 2.6_5. MD simulation of the P110 (PDB: 5OX7) with and without the potassium (K^+) ion, in the interaction with the ligand 3'SLn. Conformational analysis of the protein and "Loops" designated in the P110 structure. The ligand RMSD was calculated in reference to the protein. The overall flexibility of the protein with (purple line) and without (green line) potassium ion was measured via the average root mean square fluctuation (RMSF) values during the MD trajectory of P110 bound to 3'SLn. RMSF measures the average amplitude of each atom's motions relative to a mean reference position. The higher value of RMSF represents higher flexibility. The MD simulation was performed during 100 ns.

CII. 3. Discussion

Sialic acid-containing glycans are highly abundant on vertebrate cell surfaces and play essential roles in a plethora of biological functions of relevance both in healthy and diseased states. They serve as critical modulators of cell division, cell signalling, and cell-cell recognition, regulating a wide range of immune responses. Thus, it is not surprising that many pathogenic organisms have evolved to exploit host sialoglycans to facilitate association with and entry into target cells. Among them, several species from the bacterial genus *Mycoplasma* have been shown to interact with sialylated glycoproteins on the exterior of eukaryotic cells to mediate adhesion and subsequent infection[351,445,446] [**Kasai T. *et al*., 2013; Manchee R. J. and Taylor-Robinson D. 1962; Sobeslavsky O. *et al*., 1968**]. Given the increasing emergence of antibiotic resistance documented in Mycoplasmas, such as the respiratory pathogen *M. pneumoniae* and the urogenital pathogen *M. genitalium*, the development of alternative therapeutic strategies to prevent and combat Mycoplasmas-associated infections is urgently needed. Specifically, interference with this sialylated glycoprotein-mediated adhesion pathway represents a promising therapeutic route to treat *Mycoplasma* infection. Despite recent efforts to understand the mechanism of this bacterial adhesion pathway, the molecular basis of the interaction remained obscure. We report here the atomic-level characterization of the recognition modes of the *Mycoplasma* cytadhesins, P40/P90 and P110, interacting with host sialylated *N*- and *O*-glycans.

To elucidate in-depth the structural details of sialoglycans recognition by bacterial cytadhesins, a combination of biophysical techniques and computational methods were employed. This integrated approach allowed us to identify the ligand epitopes accommodated in the protein binding site, to explore the conformational behaviour of *N*- and *O*-glycans interacting with the bacterial cytadhesins, and to predict 3D models of protein-ligand complexes. The analysis and comparison of P110 and P40/P90 binding showed the ability of both proteins to recognize different sialoglycans. We here provide the first experimental evidence of *Mycoplasma* cytadhesins binding to *O*-glycans. The study of the interaction between P110 and P90/40 with *ad hoc* synthesized sTa covalently linked to a threonine (sTa- Thr), representing a natural *O*-glycan exposed on membrane cells, was performed. This further revealed the ability of these *Mycoplasma* cytadhesins to recognize *O*-glycans with a similar epitope of *N*-glycans.

In all predicted complexes, the sialic acid is the residue that principally contributes to the binding, although the two cytadhesins show different binding sites and shapes. Sialoglycans interacting with P110 always show the recurrent H-bonds between the carboxylate group of Neu5Ac and Ser458, NHAc at position 5 with Ser456 and the proton at position 7 with Pro197,

all residues exhibiting high STD responses. In P40/P90, Thr632 is involved in the H-bond with carboxyl group of Neu5Ac, the proton at position 7 always interacts with Pro235, but the NHAc at position 5 makes a H-bond with Leu630. Although amino acids of hydrophobic nature in proximity to the protein binding pocket contributed to stabilize the complexes, the network of hydrogen bonds between the terminal sialic acid residue and the protein binding site was by far the most relevant mediator of the protein-ligand interaction. Indeed, a preliminary 3D model of binding between *Mycoplasma* cytadhesins and longer, complex *N*-glycans, such as those occurring on the host cell surface, suggest that the interaction was governed only by the terminal Neu5Ac residues without the involvement of the other, solvent-exposed, sugar residues. Thus, we here demonstrate that P110 and P90/P40 similarly recognize *N*- and *O*-glycans that show similar epitopes; however, the more open binding site and the higher flexibility of some loops close to the binding site of P40/P90 allows the accommodation of sialoglycans that maintain their conformational freedom as in the free state, as opposed to in the binding site of P110, where conformer selections are observed.

The information obtained guided the design of a P110 variant not possible characterized as the protein is unstable and degrade. These observations suggest is structurally critical, with Asn182 being important for the proper processing and stability of P110 *in vivo*. Therefore, as indicated by the structural data, our *in vivo* analysis corroborates that this residue plays a key role in the interaction of *M. genitalium* with host cell receptors. In addition, MD simulations has revealed that the potassium ion binding site located in the P110[383] [**Aparicio D. *et al*., 2018**] may play an important role in the stabilization of the protein and the interaction with the ligand. Notably, these data demonstrate that the mode of action of *Mycoplasma* cytadhesins is very different from that of bacterial adhesins, such as Siglec-like streptococcal adhesins, despite a remarkable topological similarity with their sugar binding site (**Figure CII. 3_1**). We previously indicated that the Siglec-like binding region of adhesins exposed on the surface of *Streptococcus gordonii*, SLBRHsa and SLBRGspB and SLBRUB10712,have a wide binding pocket, allowing the accommodation of sialoglycans via interactions with sugar residues in addition to the terminal Neu5Ac[438,447] [**Di Carluccio C. *et al*., 2021; Di Carluccio C. *et al*., 2024**]. There are some similarities between streptococcal Siglec-like adhesins and *Mycoplasma* cytadhesins, such as a similar recognition of *N*- and *O*-glycans, with the carboxylate group of Neu5Ac establishing the key H-bond with a threonine amino acid residue (Ser458 for P110 and Thr632 for P90/P40). However, the flexible loops in the Siglec like adhesins influence their selectivity for sialoglycans containing only Neu5Ac-α-(2-3)-Gal glycosidic linkages and also influence the conformation of those sialoglycans in the binding site, while also allowing the recognition of extended ligand epitopes. On the contrary, our data clearly showed a binding mode for Mycoplasma cytadhesins that is

very similar to that of several mammalian Siglecs, that preferentially accommodated into their binding site the terminal Neu5Ac, and rarely establish additional interactions with the adjacent galactose residue.

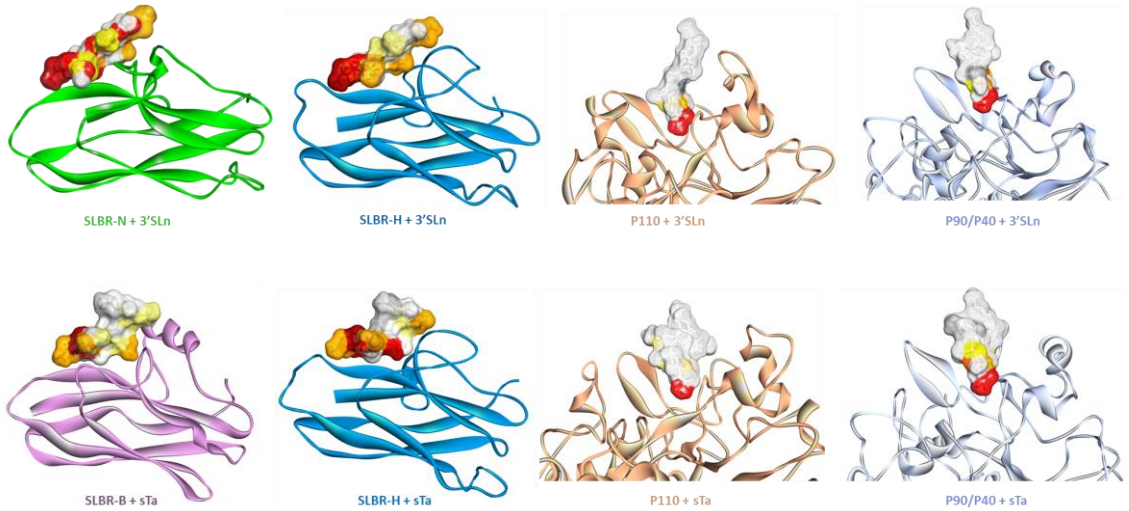

Figure CII. 3_1. Comparison of sialoglycans recognition among bacterial Siglec-like adhesins. Predicted models of 3'SLn and/or sTa-Thr bound to i) streptococcal adhesins, $SLBR_{UB10712}$, $SLBR_{Hsa}$ and $SLBR_{GspB}$, (previously published in[438,447] [Di Carluccio, C. *et al.*, 2021; Di Carluccio, C. *et al.*, 2024]) and *Mycoplasma* cytoadhesins, P110 and P40/P90. In all the predicted complexes the ligand surface is colored according to the STD-derived epitope mapping, highlighting the different binding mode of streptococcal Siglec-like adhesins compared to that of *Mycoplasma* cytoadhesins. The PDB codes of the proteins used for computational analyses of the bound states in the previously[438,447] [Di Carluccio, C. *et al.*, 2021; Di Carluccio, C. *et al.*, 2024] published papers are 6EFF[448] [Bensing, B.A. *et al.*, 2022],45 6EFD[448] [Bensing, B.A. *et al.*, 2022], 45 and 5IUC[406] [Pyburn, T.M. *et al.*, 2011] 46 for $SLBR_{UB10712}$, $SLBR_{Hsa}$ and $SLBR_{GspB}$, respectively. Adapted from Marseglia A. *et al.*, 2024.

Moreover, we here hypothesize that *Mycoplasma* adhesins could recognized longer complex *N*-glycans by using a branched binding mode involving both sialic acid residues, located at the termini of the two antennae, in the interaction. NMR experiments on isotopically labelled glycans, together with mutagenesis experiments followed by binding measurements need to be performed to further validate the proposed model of the interaction. Notably, the ability of the serine-rich repeat adhesin $SLBR_{SrpA}$ to bind complex sialoglycans containing two sialic acid residues had previously been hypothesized, thanks to the presence of arginine residues corresponding to both a bacterial and mammalian sialoglycan binding pocket[405] [Loukachevitch L. V. *et al.*, 2016]. However, the lack of a crystal structure as well as a model of branched glycans bound to $SLBR_{SrpA}$ hampers the comparison of this binding mode with that of *Mycoplasma* adhesins.

To conclude, our results provide a more comprehensive knowledge of the structural features governing the recognition of sialoglycan ligands by the main cytadhesins from *M. pneumoniae*

and *M. genitalium*, defining the molecular basis of ligand specificity of these bacterial virulence factors. Our analysis provides a critical, atomic-level picture of these interactions, which can be used to identify competitive binding compounds able to selectively inhibit bacterial adherence to host target cells. This, in turn, paves the way to the development of novel strategies to treat bacterial infections based on cytoadherence inhibition.

CHAPTER III

DYNAMICS OF THE NAP COMPLEX AND ADHESION MECHANISMS OF THE HUMAN PATHOGENS *Mycoplasma pneumoniae* AND *Mycoplasma genitalium*

Results presented in this chapter has been published in the BioRxiv preprint server:

David Vizarraga*, Akihiro Kawamoto*, Marina Marcos-Silva*, Jesús Martín, Fumiaki Makino, Tomoko Miyata, Jorge Roel-Touris, Enrique Marcos, Òscar Q. Pich, David Aparicio, Ignacio Fita, Makoto Miyata, Jaume Piñol, Keiichi Namba, Tsuyoshi Kenri. **Dynamics of the Nap complex and adhesion mechanisms of the human pathogens *Mycoplasma pneumoniae* and *Mycoplasma genitalium*. 2024**. DOI: 10.1101/2023.07.31.551205. https://doi.org/10.1101/2023.07.31.551205. *These authors contributed equally.

DYNAMICS OF THE NAP COMPLEX AND ADHESION MECHANISMS OF THE HUMAN PATHOGENS *Mycoplasma pneumoniae* AND *Mycoplasma genitalium*

Mycoplasma pneumoniae is a bacterial wall-less human pathogen and the etiological agent of atypical pneumonia and tracheobronchitis in both adults and children. *M. pneumoniae* infectivity, gliding motility and adherence to host target respiratory epithelial cells are mediated by adhesin proteins P1 and P40/P90 forming a transmembrane complex (Nap) that binds to sialylated oligosaccharides human cell ligands. Here we report the Cryo-EM structure of P1 bound to the Fab fragment of monoclonal antibody P1/MCA4, which stops gliding and induces detachment of motile *M. pneumoniae* cells. On the contrary, polyclonal antibodies generated against the N-domain of P1 or against the whole ectodomain of P40/P90 have little or no effects on adhesion or motility. The epitope of P1/MCA4, centred on loop Thr1426-Asp1438 in the small C-terminal domain of P1, is inaccessible to antibodies in the "open" conformation of the adhesion complex, when ready for attachment to sialylated oligosaccharides. Mutations in the highly conserved Engelman motifs found in the transmembrane helix of P40/P90 also alter adhesion and motility. During the attachment/detachment cycle of the adhesion complex, the C-terminal domain of P1 experiences large conformational rearrangements that are hindered by the antibodies against the domain. Interfering with the gliding of mycoplasma cells suggests new ways to confront *M. pneumoniae* infections.

My specific contribution to this chapter:

I have conducted the *in vivo* experiments, including the generation and complete characterization of the mutants. These experiments are described in sections: CIII. 2.1, CIII. 2.4, CIII. 2.5, CIII. 2.6, CIII. 2.7 and CIII. 2.8. I have also contributed to the manuscript writing.

CIII. 1. Introduction

Mycoplasma pneumoniae is a human pathogen inducing respiratory diseases and one of the leading microorganisms causing community acquired bacterial pneumonias[449] [**Waites K. B. *et al.*, 2017**]. Coinfections of *M. pneumoniae* with other respiratory pathogens, such as SARS-CoV-2, Adenovirus or *Chlamydia pneumoniae*, have been associated with importantly increased morbidities[449–451] [**Parrott G. L. *et al.*, 2016; Rangroo R. *et al.*, 2022; Waites K. B. *et al.*, 2017**]. Recent pneumonia outbreaks in Europe and Asia due to the re-emergence of *M. pneumoniae* also underlines the clinical relevance of this human pathogen[452] [**Sauteur P. M. *et al.*, 2024**]. However, the tropism for respiratory tissues of *M. pneumoniae* might be exploited for biomedical applications, and attenuated strains of this mycoplasma have been recently engineered to be used as living pills to treat pulmonary diseases[453] [**Mazzolini R. *et al.*, 2023**].

M. pneumoniae exhibits a membrane protrusion at a cell pole, referred as the "attachment" or "terminal" organelle (TO), that is instrumental for infection and gliding motility. *M. pneumoniae* cells bind to glass surfaces coated with sialylated oligosaccharides (SOs), which are abundant on the human epithelial surfaces, and glide in the direction of the TO[454–456] [**Henderson G. P. and Jensen G. J, 2006; Miyata M. and Hamaguchi T., 2016; Seybert A. *et al.*, 2006**]. The type of motility presented by *M. pneumoniae* is shared only by mycoplasma species belonging to the pneumoniae cluster[455,457] [**Miyata M. and Hamaguchi T., 2016; Nakane D. *et al.*, 2015**]. The molecular machinery for motility is located in the TO and involves about fifteen different proteins organized as surface structures and internal parts[457–459] [**Kawamoto A. *et al.*, 2016; Mizutani M. *et al.*, 2021; Nakane D. *et al.*, 2015**]. The main and most abundant surface structure is the adhesion complex, also known as the Nap complex, which comprises the transmembrane adhesin proteins P40/P90 and P1[460–462] [**Krause D. C. *et al.*, 1982; Scheffer M. P. *et al.*, 2017; Vizarraga D. *et al.*, 2020**]. A similar organization of the adhesins P110 and P140 forming a 540 kDa membrane complex is found in the closely related human pathogen *Mycoplasma genitalium*[459,463] [**Mizutani M. *et al.*, 2021; Vizarraga D. *et al.*, 2021**]. Adhesins play an essential role in attachment to surfaces by binding to the SOs ligands[463,464] [**Vizarraga D. *et al.*, 2021; Williams C. R. *et al.*, 2020**].

During the last few years, several high-resolution structures have been determined for adhesins P1 and P40/P90[462] [**Vizarraga D. *et al.*, 2020**] and also for the closely related orthologous proteins from *M. genitalium* P140 and P110[465–467] [**Aparicio D. *et al.*, 2020, 2018; Sprankel L. *et al.*, 2023a**]. The Nap complexes were proposed to cycle between "open" and "closed" conformations where the SOs binding pockets become accessible or inaccessible, respectively. The SO binding pocket is located in the P40/P90 N-terminal domain, although accessibility to the

pocket is determined by the interaction with the N-terminal domain of P1 that is tighter in the "closed" conformation. Adhesins P1 and P40/P90, together with protein P116, are the most immunogenic proteins of *M. pneumoniae*[462,468] [Sprankel L. *et al.*, 2023b; Vizarraga D. *et al.*, 2020]. To study the immunogenic and functional properties of P1, monoclonal antibodies were generated against a fragment of this adhesin spanning from residue Ala1160 to Gln1518, (P1:1160-1518 peptide) (Table CIII. 1). One of the monoclonal antibodies obtained (henceforth referred as P1/MCA3) was reported some years ago to progressively reduce gliding speed, removing mycoplasma cells from surfaces in a concentration-dependent way, while having little effect on non-moving cells[469] [Seto S. *et al.*, 2005]. These observations led to the conclusion that during gliding, P1 has to experience important conformational changes participating like a leg in a "power stroke" that propels the cell, with epitope exposure to antibody P1/MCA3 significantly reduced in non-moving cells.

Table CIII. 1. MCA Monoclonal antibodies generated against the rP1 antigen (A1160-Q1518).

Clone No.	ELISA screening against rP1	Western blot against M129 lysate	Binding to live M129 cells	Inhibition of hemadsorption (HA)	Inhibition of gliding
3	+	+	+	+	+
4	+	+	+	+	+
5	+	+	+	+	+
8	+	+	+	+	+
18	+	+	+	+	+
102	+	-	-	-	-
104	+	+	-	-	-
115	+	+	-	-	-
127	+	+	-	-	-
128	+	+	-	-	-

How the functioning of the Nap complex is related to the motility of mycoplasma cells remains elusive. Monoclonal antibody P1/MCA3 is no longer available, but we have now solved by Cryo-EM the structure of P1 in complex with the Fab fragment of P1/MCA4, which was obtained at the same time as P1/MCA3 against the same P1:1160-1518 peptide (Table CIII. 1). P1/MCA4 also affects motility and enhances detachment of moving mycoplasma cells similarly to P1/MCA3. The determined structure provides a snapshot of the "closed" conformation of P1 that prevents the Nap complex from attachment to SOs. We also investigated how motility is affected by polyclonal antibodies against the whole ectodomains of adhesins P1 and P40/P90 and those against constructs of the N-terminal domain of P1. Mutations in the highly conserved Engelman

motifs, found in the transmembrane helices of adhesins, can also alter adhesion and motility, providing information about how extra- and intra-cellular regions communicate with each other. Altogether, these results provide a deep insight into the Nap complex function and explain the specific neutralization mechanism deployed by antibodies against the C-terminal domain of P1.

CIII. 2. Results

CIII. 2.1. Monoclonal antibody P1/MCA4 and its binding to P1

Monoclonal antibody P1/MCA4, raised against the P1:1160-1518 peptide, exhibited strong hemadsorption inhibitory activity (in a 10 µg/ml concentration) for *M. pneumoniae.* In the presence of P1/MCA4, gliding mycoplasma cells reduce rapidly their speed and eventually halt and detach from (sialylated) glass surfaces, while non-moving cells are not affected by the presence of P1/MCA4 and remain attached to surfaces. As mentioned in the introduction, a similar behaviour had been reported for antibody P1/MCA3 [469] [**Seto S. *et al.*, 2005**]. It is worth mentioning that this behaviour is also observed in three additional monoclonal antibodies raised in the same batch as P1/MCA3 and P1/MCA4 (**Table CIII. 1**). The P1:1160-1518 peptide corresponds to a fragment of the N-terminal domain (residues Ala1160-Thr1399) and to (almost) the whole C-terminal domain (Ala1400-Gln1518) according to the structural information now available[462] [**Vizarraga D. *et al.*, 2020**].

cDNA sequencing of P1/MCA4 mRNAs in hybridoma cells showed the presence of a single IgG heavy chain mRNA but two different light chain mRNAs (**Appendices Figure A. CIII. 3.5**). N-terminus analysis of samples from antibody P1/MCA4 (obtained as indicated in the Material and Methods) confirmed the presence of one heavy chain but two different light chains (roughly 70% for the most abundant). The heterogeneity of light chains might explain in particular the failure of numerous crystallization attempts involving P1/MCA4. Analysis by multi-angle light scattering (MALS) showed the formation of a stable and homogeneous P1-Fab(P1/MCA4) complex, in a solution with equimolecular amounts of P1/MCA4 Fabs and the whole P1 ectodomain (residues Thr29-Asp1521), indicating that the two kinds of Fab found in P1/MCA4 bind efficiently to P1 (**Appendices Figure A. CIII. 3.7_1**).

Antibody P1/MCA4 presents high affinity for a construct corresponding to the C-terminal domain of P1, proving that this small domain contains the epitope. Moreover, western blotting analysis performed using different segments of P1 showed that residues Thr1426-Asp1438 are a key part of the epitope (**Figure CIII. 2.1_1**). An additional observation that could have clinical implications is that P1/MCA4 presents affinity also for the C-terminal domain of P140 (residues Lys1220-Asp1351) from *M. genitalium,* even stopping the movement of cells, although after treatments of more than one hour (longer than with *M. pneumoniae*), in agreement with the high sequence and structural similarities between the C-terminal domains of the two human pathogens *M. pneumoniae* and *M. genitalium* (**Figure CIII. 2.1_2**).

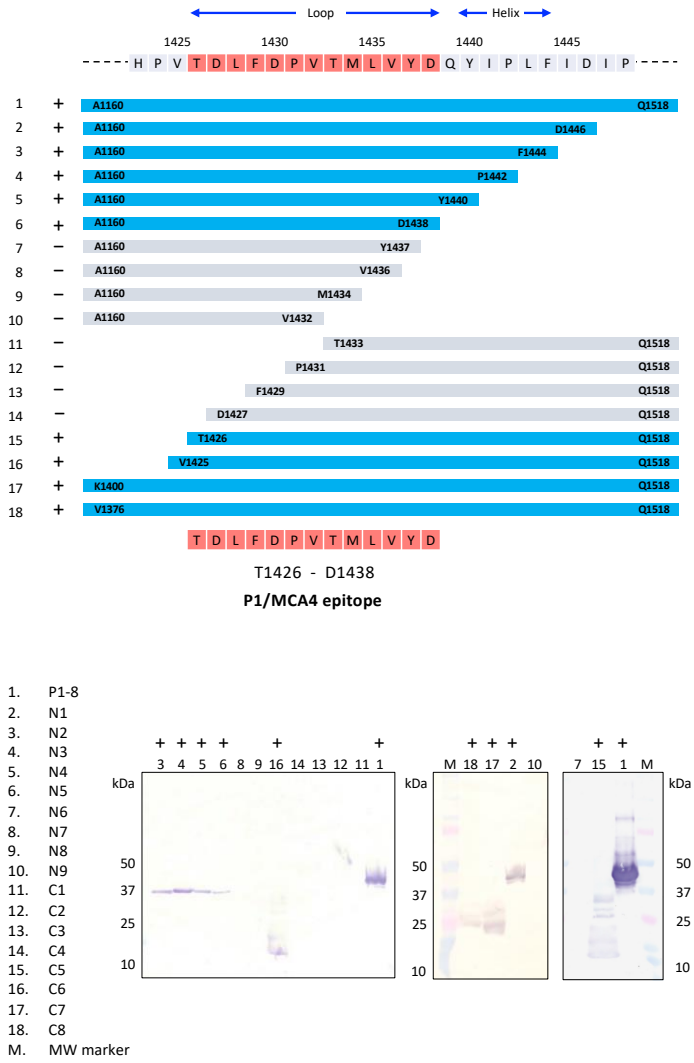

Figure CIII. 2.1_1. P1 epitope mapping of Mab P1/MCA4.

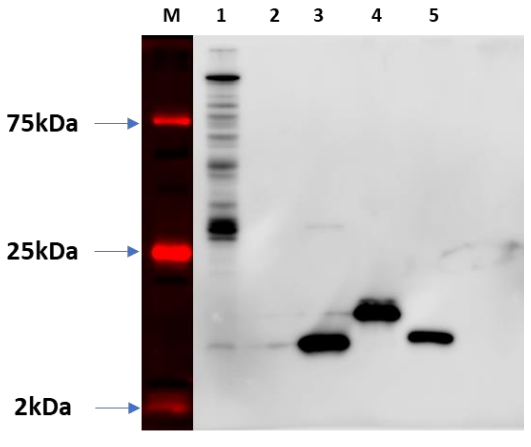

Figure CIII. 2.1_2. Western blotting analysis performed using Mab P1/MCA4 and different constructs from P1 (*M. pneumoniae*) and from P140 (*M. genitalium*). 1) *Mpn*-WT (MPN129); 2) P1Glob. Thr29-Ala1375; 3) P1 C-terminal A1400-D1521; 4) P1 C-terminal K1376-D1521; 5) C-terminal P140 S1244-D1351. The key peptide in the epitope of P1 (1426 TDLFDPVTMLVYD 1438) presents a high sequence identity with the corresponding peptide in P140 (1270 TELFDPNTMFVYD 1282).

CIII. 2.2. Cryo-EM structure of the P1-Fab(P1/MCA4) complex

The structure of the ectodomain of P1 bound to the Fab fragment of P1/MCA4 was determined by Cryo-EM single particle analysis with an overall resolution in the final map of 2.4 Å (**Figure CIII. 2.2_1A, Appendices Figures A. CIII. 3.8_1, 3.8_2 and Appendices Table A. CIII. 3.8**).

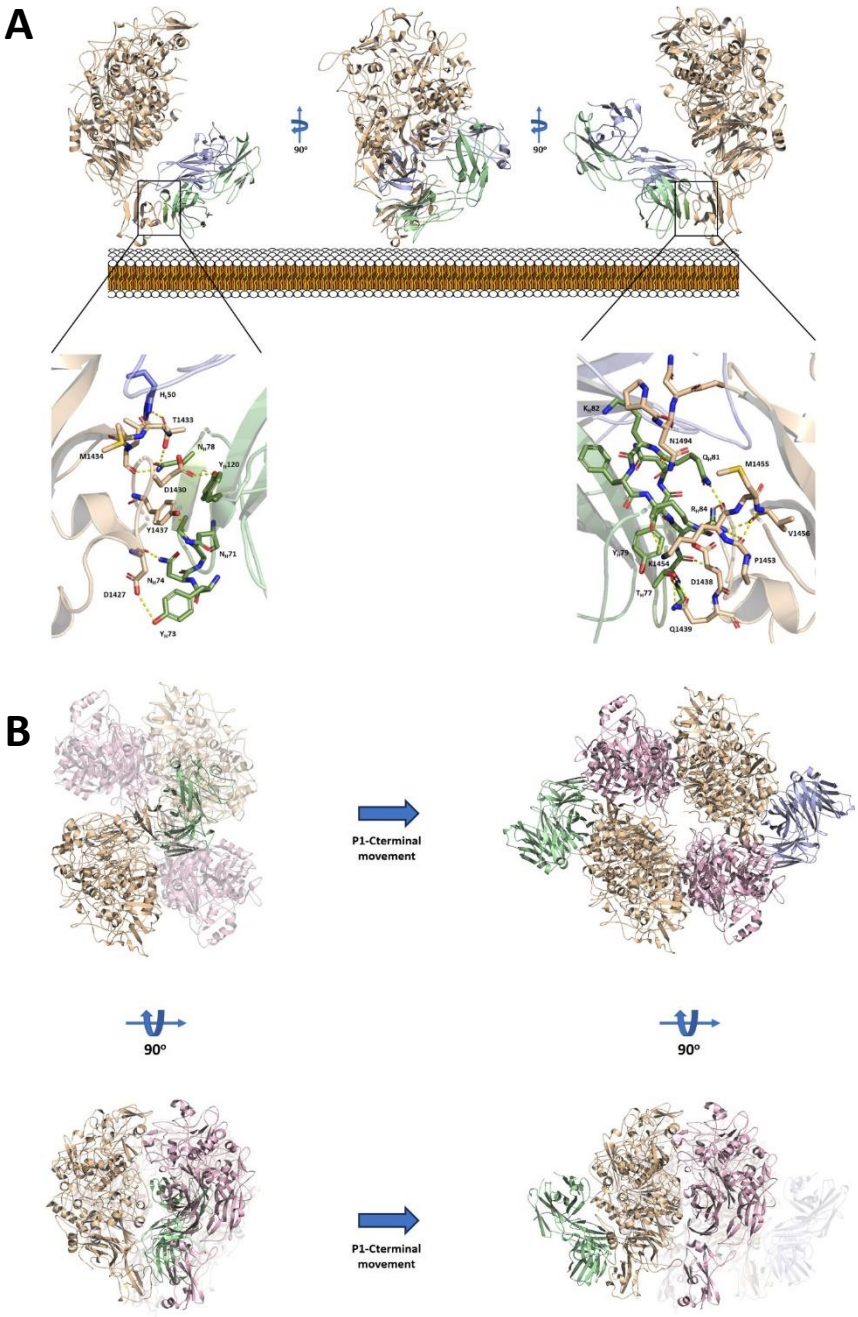

Figure CIII. 2.2_1. **Cryo-EM structure of the P1-Fab(P1/MCA4) complex. A)** Ribbon representations, with three 90° apart views, of the complex between P1 (brown) and the Fab fragment of monoclonal antibody P1/MCA4 (light and heavy chains in blue and green, respectively). Insets showing the recognition interactions between P1 and P1/MCA4. The epitope is located in the C-terminal domain of P1, close to

the mycoplasma membrane displayed as a reference. **B)** Two 90° apart views of the Nap in the "open" conformation with one of the P1 subunits replaced by the P1-Fab(P1/MCA4) complex (left panels). The P1/MCA4 epitope, buried at the Nap center, is totally inaccessible to antibodies in the "open" conformation and the Fab would catastrophically clash with GPC subunits. The C-terminal domain has to experience an important hinge rearrangement to expose the epitope avoiding steric clashes (right panels).

The high quality of the map allowed accurate modelling of the structure from P1 and the Fab variable domains, defining clearly the paratope-epitope interface. The Fab constant domains were less well defined, indicating some flexibility in the Fab elbow. The sequence observed for the Fab corresponded to the one with light chain L1. The structure of P1 consists of a large N-terminal domain (residues 60-1399) and a smaller C-terminal domain (1400-1521), in full agreement with the structures of P1 reported previously[462] [**Vizarraga D. *et al.*, 2020**]. Superposing the P1 structure determined here with the P1 crystal structure (PDB code 6rc9), gives a root mean square deviation (rmsd) of 1.80 Å for 1236 aligned residues (from a total of 1339 in the model) (**Figure CIII. 2.2_2**).

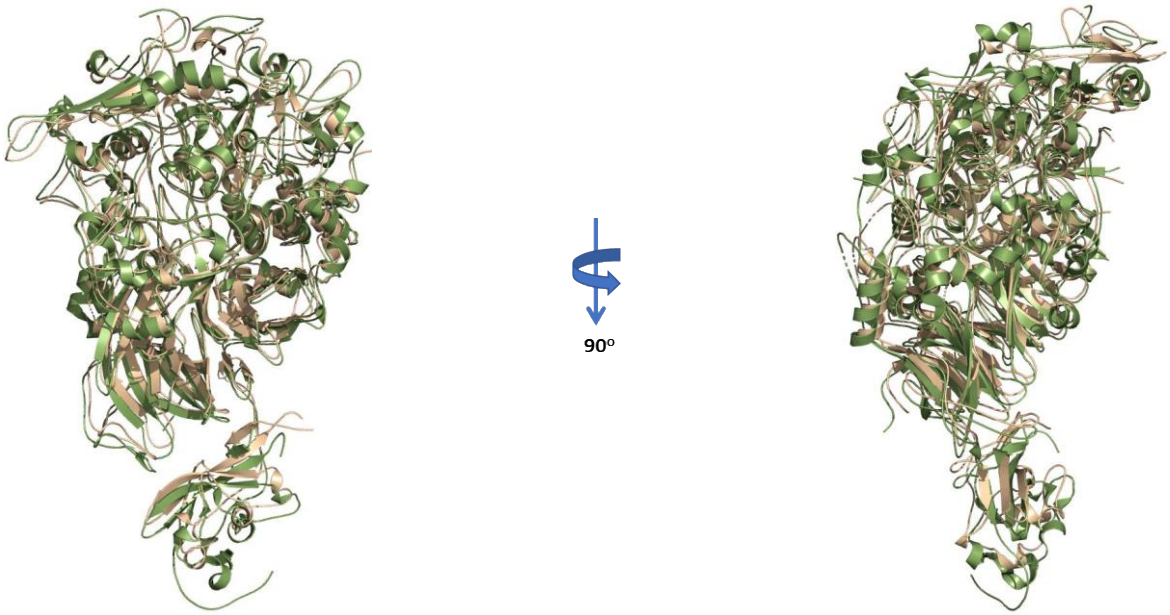

Figure CIII. 2.2_2. Superposition of P1 structures. Two 90° apart views of the superposition of the P1 structures determined by X-ray crystallography (PDB code 6RC9) and in this work in the complex P1-Fab(P1/MCA4) (in brown and green, respectively).

When the superposition is done separately for the N-terminal and C-terminal domains, rmsds are 1.65Å (1151 aligned residues out of 1226) and 1.20Å (97 aligned out of 104), respectively. These results show the high plasticity of P1, in particular for the N-terminal domain, which experiences significant changes although it participates only indirectly in the interaction with the P1/MCA4 Fab. Comparison of the crystal (6rc9) and the new (in the complex of P1-Fab) structures of P1, indicates a 7.7° rotation of the C-terminal domain relative to the N-terminal

domain, confirming hinge movements between the two domains as had suggested the Cryo-EM structure of P1 where the C-terminal domain was disordered[462] [Vizarraga D. *et al.*, 2020]. The structure of the P1-Fab complex shows that the epitope of P1/MCA4 is conformational, although involving residues from the C-terminal domain only, in particular from loop Val1425-Asp1438 in agreement with the epitope mapping analysis (**Figure CIII. 2.2_1A and Appendices Figure A. CIII. 3.8_1**). The quality of the Cryo-EM map was high enough to even allow the localization in the N-terminal domain of a significant number of solvent molecules, most of them also present in the crystal structure of P1 (**Appendices Figure A. CIII. 3.8_2**). It is worth mentioning that docking using a previous Cryo-EM map determined at lower resolution, correctly predicted the overall binding interface between P1 and the Fab(P1/MCA4), with the largest deviations arising from the inaccuracy on the fitting of the P1 C-terminal domain (**Figure CIII. 2.2_3**).

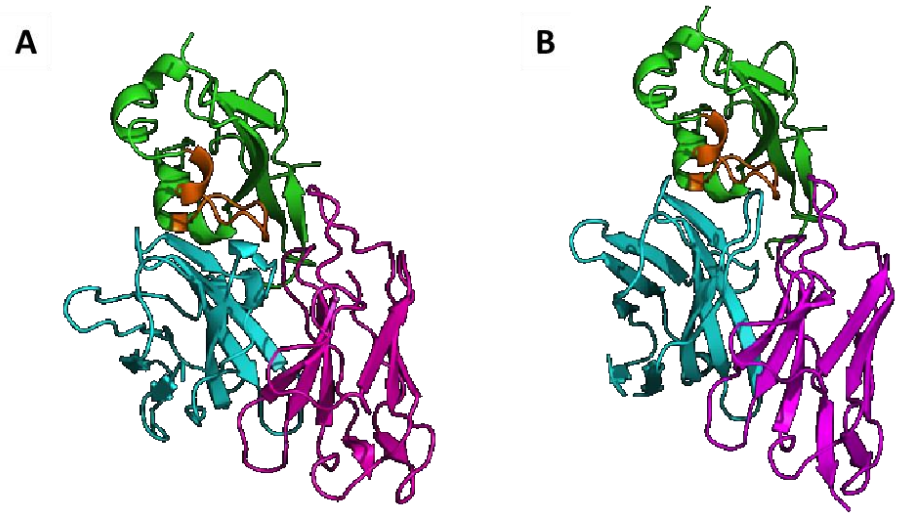

Figure CIII. 2.2_3. Docking calculations on the binding interface between the Fab and the C-terminal domain of P1. a) Interface observed in the 2.3 Å resolution map. (b) Top-ranked model obtained from HADDOCK[470] [van Zundert G. C. P. *et al.*, 2016] docking simulations performed with a lower resolution map, the P1 crystal structure and the AlphaFold2[471,472] [Jumper J. *et al.*, 2021; Evans R. *et al.*, 2022] prediction of the Fab. Docking models were ranked based on Haddock docking score (-66.44 arbitrary units), buried surface area (1457 Å^2), and correlation with the Cryo-EM map (0.85, as calculated with Chimera[408] [Pettersen E. F. *et al.*, 2004]). The C-terminal domain of P1 is colored in green, the loop Val1425-Asp1438 in orange, and the heavy and light chains of the Fab in cyan and magenta, respectively. For clarity, only the variable fragment of the Fab is shown.

Importantly, superposing the structure of P1-Fab(P1/MCA4) onto the Nap complex in a "open" conformation available for *M. genitalium*[465] [Aparicio D. *et al.*, 2020] by superposing the P1 and P140 structures, results in a catastrophic steric clash of the Fab against the adhesins, indicating that the epitope of P1/MCA4 is totally inaccessible to antibodies in the "open" conformation of the Nap complex (**Figure CIII. 2.2_1B**). Therefore, this complex must experience important structural rearrangements between the "open" conformation and when the epitope of P1/MCA4 is fully exposed.

CIII. 2.3. Attempts to obtain the ternary complex P40/P90-P1 Fab(P1/MCA4)

A solution with equimolecular amounts of Fab(P1/MCA4) and of ectodomains from P1 (residues 29-1521) and from P40/P90 (residues 23-1114) produced a mixture of several complexes where the ternary complex P40/P90-P1-Fab(P1/MCA4) was not clearly identified, while heterodimers P40/P90-P1 and P1-Fab(P1/MCA4) were abundant (**Appendices Figure A. CIII. 3.7_2**). Cryo-EM confirmed the mixture of different complexes in the classifications (**Figure CIII. 2.3_1**). Attempts to determine the structure of a ternary complex gave a map with an overall resolution lower than 10Å (**Appendices Table A. CIII. 3.8**).

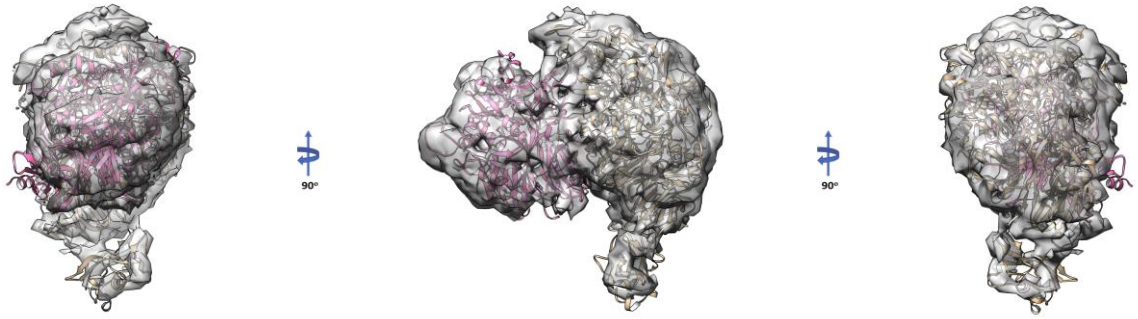

Figure CIII. 2.3_1. Cryo-EM structure determination of the ternary P40/P90-P1-Fab(P1/MCA4) complex.

The best-defined part of this map corresponds to the N-terminal domains of P40/P90 and P1 that interact tightly with each other similarly to what had been determined for the "closed" structures of orthologue adhesins P110 and P140 from *M. genitalium*[465] [Aparicio D. *et al.*, 2020]. Density corresponding to the C-terminal domain of P1 was quite strong, although fitting of the domain presented some ambiguities due to the limited resolution and small size of the domain. Density was missing for the C-terminal domain of P40/P90 and uninterpretable for the Fab. Docking the structure of the P1-Fab binary complex by superimposing the N-terminal domains of P1, resulted in steric clashes between the Fab and P40/P90 although their footprints on P1 do not overlap, suggesting that P40/P90 might compete with the Fab for the formation of the ternary complex (**Figure CIII. 2.3_2**). However, steric problems could be relieved by a hinge rotation of the P1 C-terminal domain and the scarcity of the ternary complex shows that the energy required by the hinge rotation is larger than the energy provided by the binding to P1 of either P40/P90 or the Fab.

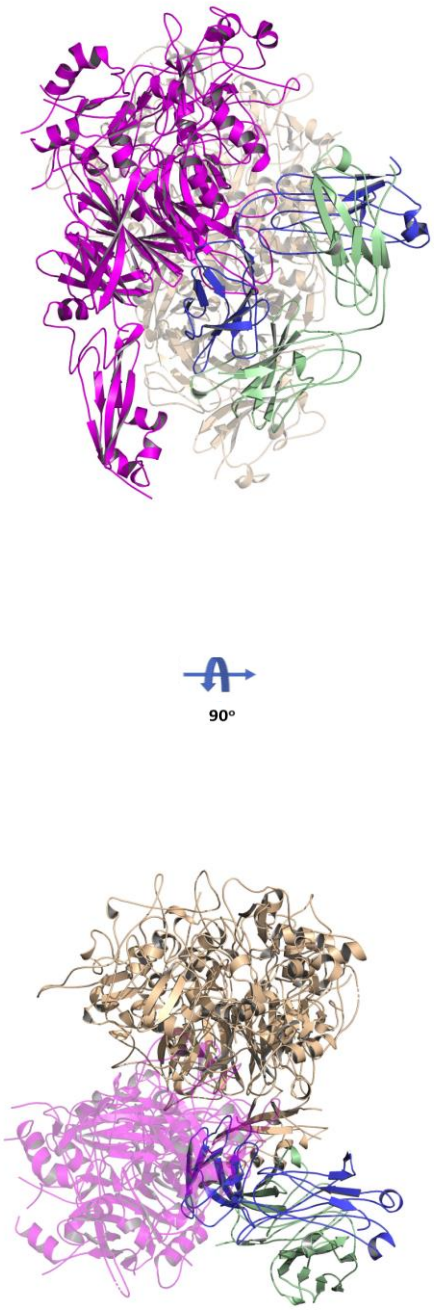

Figure CIII. 2.3_2. Modelling the ternary complex P40/P90-P1-Fab(P1/MCA4). Ribbon representation of the ternary complex modelled using the information obtained in the Cryo-EM attempts. Steric clashes between P40/P90 (cyan) and the Fab light chain (blue) (heavy chain in green) when they are bound to P1 (brown) can explain the difficulties to obtain the ternary complex.

CIII. 2.4. Polyclonal antibodies against the P40/P90 and P1 ectodomains and against the N-terminal domain of P1

Polyclonal antisera against the ectodomains of P40/P90 (residues Ala25-Pro1113) and of P1(residues Thr29-Asp1521) were obtained by immunizing mice with recombinant versions of these polypeptides (**Table CIII. 2.4 and Appendices Table A. CIII. 3.9**). Polyclonal antisera against

the N-terminal domain of P1 were obtained by immunizing mice with the P1 N-terminal domain (residues Thr29-Ala1375). These antisera were tested by ELISA, Western Blotting and immunofluorescence assays on whole *M. pneumoniae* cells, and titers higher than 1/2000 were obtained for all the antisera. Effects of these antisera on *M. pneumoniae* motility and attachment were investigated by incubating *M. pneumoniae* cells and antisera in the presence[464] [**Williams C. R. *et al.*, 2020**] or absence[469] [**Seto S. *et al.*, 2005**] of 3% gelatin in the SP4 medium.

Table CIII. 2.4. Motile and adhesion effect of the different polyclonal antibodies against *M. pneumoniae* Naps and P1/MCA4 monoclonal antibody.

SP4	Before[#]	After[#]		
PCA	**%Motility ± SE**	**%Motility ± SE**	**RT_{50} (min ± SE)[&]**	**% Detached cells ± SE**
P1	89,4±0,6	1,8±1,8	4,65±1,19	72,3±2,4
P40/P90	87,5±3,9	74,3±4,4	NA	45,2±26,1
P1N-ter	95,6+0,1	85,4±1,6	NA	59,8±0,1
Negative Control[$]	89,9±1,2	76,1±4,8	NA	51,5±4,3
SP4+3%Gelatin	**Before[#]**	**After[#]**		
PCA	**%Motility ± SD**	**%Motility ± SE**	**RT50 (min ± SE)[&]**	
P1	96,5±0,5	3,4±2,8	4,05±0,35	
P40/P90	96,4±0,4	95,7±0,3	NA	
P1N-ter	88,9±3,2	88,2±2,7	NA	
Negative Control[$]	96,3±0,3	96,5±0,1	NA	
MCA				
P1/MCA4	97,3±0,7	0±0	2,6±0,26	

All values are shown as mean values +/- standard error from three different and independent microcinematographies.

[$] Negative control. PBS with no antibody was added.

[#] Measurements made "before" or "after" adding antibodies or a control PBS solution.

(NA): Not applicable. (–): Not performed. SE: standard error.

[&] RT_{50} is the antibody incubation time required to stop the movement of 50% of motile cells.

Because *M. pneumoniae* cells spontaneously detach at high frequencies from the observation surface [468] [**Sprankel L. *et al.*, 2023b**] more reproducible and consistent results were obtained

when gliding motility was analyzed with SP4 medium supplemented with gelatin. In the absence of antibodies most of the cells remained motile during the observation time. In contrast, P1 ectodomain antisera stopped the movement of mycoplasma cells (after five minutes of incubation in the absence of gelatin), which then detach in a way similar to the one described for the P1/MCA4 monoclonal antibody[469] [Seto S. *et al*., 2005]. When gelatin was present the P1 ectodomain antisera stopped the movement of mycoplasma cells in a very reproducible way after four minutes of incubation, but stopped cells did not detach from the surface. No significant effects on mycoplasma gliding were detected neither for the antisera against the P1 N-terminal domain nor for the P40/P90 ectodomain, even at the lowest dilution tested. It is also worth mentioning that cell adhesion was inhibited when cells were added to media that already contained antisera against the ectodomains of either P1 or P40/P90, suggesting that these antibodies can interfere with their binding to SOs via steric hindrance, but their epitopes are not accessible when the cells are attached to surfaces.

Binding of antibodies to epitopes whose accessibility varies during a conformational transformation interferes with the dynamics of the adhesion complex. According to this idea, the attachment/detachment cycle is halted by antibody P1/MCA4 against the C-terminal domain of P1 that experiences important rearrangements during the cycle. Instead, the attachment/detachment cycle is not altered, or very little, by antibodies against P40/P90 or against the N-terminal domain of P1, indicating that accessibility of their epitopes must remain essentially unchanged during the Nap cycle.

CIII. 2.5. Mutations in the Engelman motifs

The transmembrane domains of P1 and P40/P90, predicted to be single helices, appear right after the C-terminal domains of the globular part of these proteins. Remarkably, these helices contain one Engelman motif in P1 and two Engelman motifs in P40/P90 (**Figure CIII. 2.5_1**). These three Engelman motifs are highly conserved in the pneumonia cluster of mycoplasmas. Engelman motifs, which are frequently involved in high-affinity interactions between membrane helices, have the sequence GXXXG, with X being any residue but often hydrophobic[411] [Russ W. P. and Engelman D. M., 2000]. We have investigated by mutational analysis, possible contributions of the Engelman motifs from adhesins to the organization and functioning of the Nap complex. The study was performed with *M. genitalium* because simple genetic methods to introduce point mutations are available in this microorganism and transmembrane helices from orthologue adhesins of *M. pneumoniae* and *M. genitalium* present high sequence identities (**Figure CIII. 2.5_1**).

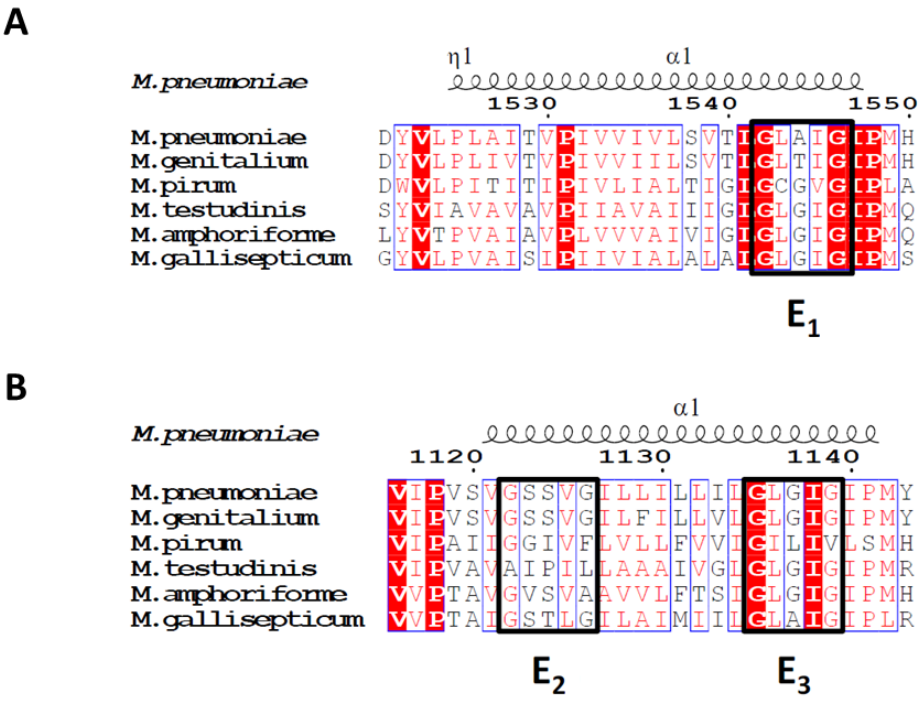

Figure CIII. 2.5_1. Sequence alignments of transmembrane helices from the adhesins of species belonging to the pneumonia cluster of mycoplasmas. Orthologues from P1 **(A)** and from P40/P90 **(B).**

The Engelman motif at the C-end of the P140 transmembrane helix, close to the internal side of the cell membrane, will be referred as E1 and the two Engelman motifs in P110 as E2 and E3, close to the external and to the internal sides of the cell membrane, respectively (**Figure CIII. 2.5_2A**). Mutations were introduced by transposon delivery in a *M. genitalium* null mutant G37ΔAdh (G37ΔMG_191-ΔMG_192), to obtain isogenic strains bearing Gly to Phe double point mutations of the glycine residues of P140 and/or P110 Engelman motifs (**Table CIII. 2.5 and Table MM. CIII. 1.1.3**). The protein profile analysis of these mutant strains showed that adhesins bearing the different mutations (**Figure CIII. 2.5_3B**) were expressed at similar levels to P140 and P110 in wild type (WT) cells (**Figure CIII. 2.5_3A**).

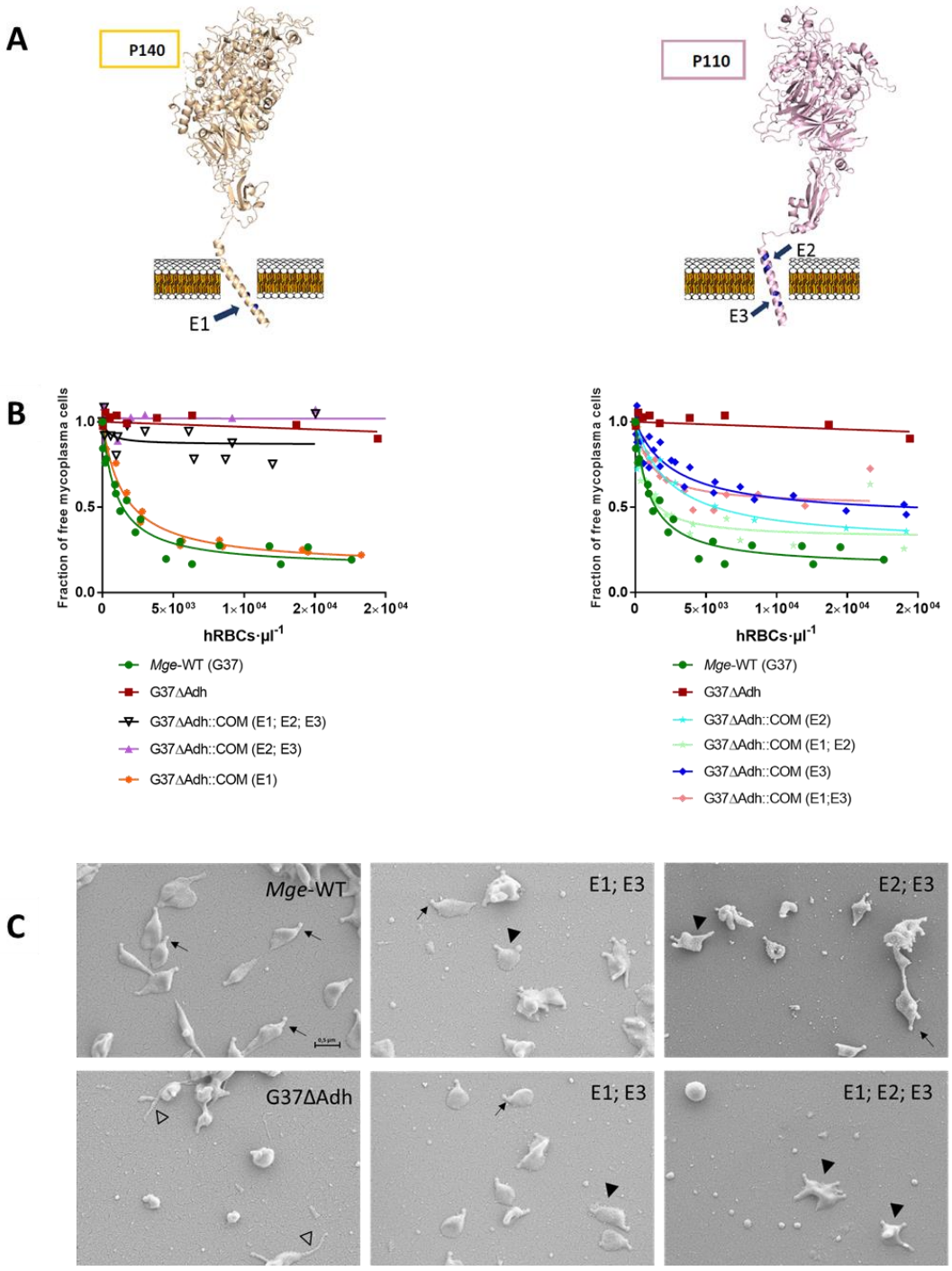

Figure CIII. 2.5_2. Engelman motifs in adhesins. A) Transmembrane helices of adhesins from the pneumonia cluster of mycoplasmas contain three highly conserved Engelman motifs (GxxxG sequences), referred as E1 (P140) and E2, E3 (P110) in *M. genitalium*. **B)** Mutational analysis, performed in the Engelman motifs of P140 and P110, indicate that motifs E2 and E3 from P110 have important and synergic contributions to adhesion. On the contrary, no effects were observed when E1 from P140 was mutated. **C)** Changes in adhesion correlate with increasing rates of cells presenting multiple TOs phenotypes. The empty triangles point to the filaments observed. Arrows point to the TO of the cells. The filled triangle point to a cell with multiple TOs.

Table CIII. 2.5. Strains used in this chapter.

Strain Name	Synonyms	Genotype	Reference
G37	WT-*Mge*	*Mycoplasma genitalium* Wild-type	NCTC:10195 (ATCC 33530)
MPN129	WT-*Mpn*	*Mycoplasma pneumoniae* Wild-type	ATCC 29342
G37ΔAdh	G37ΔMG_191-ΔMG_192	Deletion of the MG_191 and MG_192 genes by allelic exchange.	This work
G37ΔAdh::COM	G37ΔMG_191-ΔMG_192::MG_191-MG_192	Re-introduction, by transposon insertion, of a MG_191 and MG_192 wild-type alleles in a G37ΔAdh mutant. It is resistant to puromycin.	This work
G37ΔAdh::COM (MutE1)	G37ΔAdh::COM (E1)	Re-introduction of a MG_191 and MG_192 alleles bearing P140E1: G1372F-G1376F substitutions, in a G37ΔAdh mutant. It is resistant to puromycin.	This work
G37ΔAdh::COM (MutE2; MutE3)	G37ΔAdh::COM (E2; E3)	Re-introduction of a MG_191 and MG_192 alleles bearing P110E2: G947F-G951F and P110E3: G960F-G964F substitutions, in a G37ΔAdh mutant. It is resistant to puromycin.	This work
G37ΔAdh::COM (MutE1; MutE2; MutE3)	G37ΔAdh::COM (E1; E2; E3)	Re-introduction of a MG_191 and MG_192 alleles bearing P140E1: G1372F-G1376F, P110E2: G947F-G951F and P110E3: G960F-G964F substitutions, in a G37ΔAdh mutant. It is resistant to puromycin.	This work
G37ΔAdh::COM (MutE2)	G37ΔAdh::COM (E2)	Re-introduction of a MG_191 and MG_192 alleles bearing P110E2: G947F-G951F substitutions, in a G37ΔAdh mutant. It is resistant to puromycin.	This work
G37ΔAdh::COM (MutE3)	G37ΔAdh::COM (E3)	Re-introduction of a MG_191 and MG_192 alleles bearing P110E3: G960F-G964F substitutions, in a G37ΔAdh mutant. It is resistant to puromycin.	This work
G37ΔAdh::COM (MutE1; MutE2)	G37ΔAdh::COM (E1; E2)	Re-introduction of a MG_191 and MG_192 alleles bearing P140E1: G1372F-G1376F and P110E2: G947F-	This work

		G951F substitutions, in a G37ΔAdh mutant. It is resistant to puromycin.	
G37ΔAdh-COM (MutE1; MutE3)	G37ΔAdh-COM (E1; E3)	Re-introduction of a MG_191 and MG_192 alleles bearing P140E1: G1372F-G1376F and P110E3: G960F-G964F substitutions, in a G37ΔAdh mutant. It is resistant to puromycin.	This work

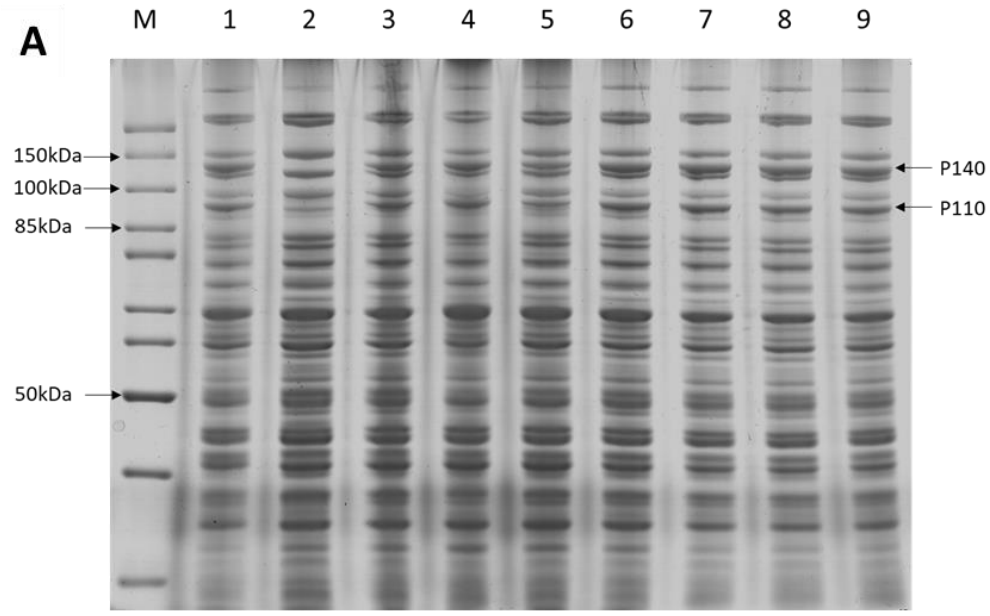

B

E1: G1372F-G1376F (P140)

1371Leu-**Gly**-Leu-Thr-Ile-**Gly**-Ile ⟶ 1371Leu-**Phe**-Leu-Thr-Ile-**Phe**-Ile

225680-TTG**GGA**TTAACGATT**GGA**ATT ⟶ 225680-TTG**TTT**TTAACGATT**TTT**ATT

E2: G947F-G951F (P110)

946Val-**Gly**-Ser-Ser-Val-**Gly**-Ile ⟶ 946Val-**Phe**-Ser-Ser-Val-**Phe**-Ile

228741-GTA**GGT**TCTTCAGTT**GGG**ATC ⟶ 228741-GTA**TTT**TCTTCAGTT**TTT**ATC

E3: G960F-G964F (P110)

959-Leu-**Gly**-Leu-Gly-Ile-**Gly**-Ile ⟶ 959-Leu-**Phe**-Leu-Gly-Ile-**Phe**-Ile

228780-TTA**GGA**CTTGGGATT**GGG**ATC ⟶ 228780-TTA**TTT**CTTGGGATT**TTT**ATC

Figure CIII. 2.5_3. SDS-PAGE with protein extracts from *M. genitalium* mutant strains. A) 1) *Mge*-WT (G37); 2) G37 ΔAdh; 3) G37 ΔAdh::COM (E1;E2;E3); 4) G37 ΔAdh::COM (E1); 5) G37 ΔAdh::COM (E2;E3); 6) G37 ΔAdh::COM (E2); 7) G37 ΔAdh::COM (E3); 8) G37 ΔAdh::COM (E1;E2); 9) G37 ΔAdh::COM (E1;E3). **B)** Schematization of the different mutations introduced in P140 and P110 adhesins.

CIII. 2.6. Assessment of the cytadherence capacity of *M. genitalium* strains carrying target mutations in the Engelman motifs

The properties of the adhesins variants were tested by quantitative hemadsorption assay (**Figure CIII. 2.5_2B**). The E1 mutant strain cells showed hemadsorption values very similar to those of WT cells and also similar to what is obtained when a WT copy of both adhesin coding genes were delivered by transposition to the null mutant G37ΔAdh (ΔAdh::COM (WT)). In contrast, E2 mutants showed an intermediate adherence phenotype and E3 mutants had a more severely impaired hemadsorption phenotypes, characterized by low B_{max} values (see in Material and Methods). As expected, E1-E2 and E1-E3 mutant strains exhibited phenotypes similar to E2 and E3, respectively. In addition, E2-E3 and E1-E2-E3 mutant strains showed a non-adherent phenotype characterized by very low B_{max} and very high K_d values, similar to the ones of the G37ΔAdh null mutant strain. Immunolabeling with a polyclonal antiserum against the Nap complex from *M. genitalium*, seemed to indicate that labelling concentrates at the tip of the triple mutated (E1-E2-E3) cells, as found for the P110 and P140 WT adhesins (**Figure CIII. 2.6_1**).

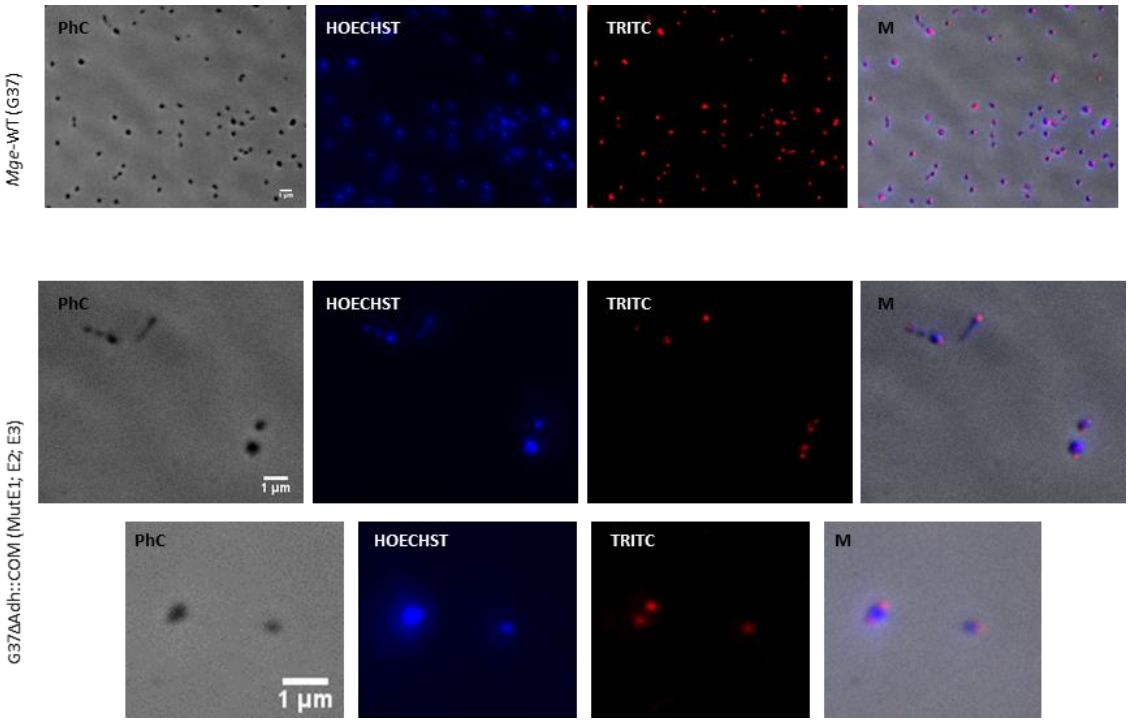

Figure CIII. 2.6_1. Immunolabeling for the localization of the Nap complexes in *M. genitalium* WT and MutE1; E2; E3 cells. Phase contrast (PhC) immunofluorescence microscopy images of cells using labeling with polyclonal antibodies against Naps. Labelling for the Nap seems to concentrates at the tips of the cells. PhC: phase contrast; TRITC: P1 mouse *Mge* Nap polyclonal antibody; Hoechst: Hoechst 33342 nucleic acid staining; M: merge.

CIII. 2.7. Morphological characterization of *M. genitalium* strains carrying target mutations in the Engelman motifs

Cells from E1 mutants exhibited normal morphologies when analyzed by Scanning Electron Microscopy. Remarkably, all cell variants where E2 or E3 was mutated showed a multiple TO phenotype. The fraction of cells presenting multiple TOs (MOTs) increased from a small percentage in E2 variants to most cells in E2-E3 and E1-E2-E3 variants (**Figure CIII. 2.5_2C**). Nascent TOs develop adjacent to a preexistent TO with gliding providing the strength to deliver the new TOs to the opposite cell pole, a process that is hindered in cells having adhesion and motility deficiencies[473] [**Pich O. Q. *et al.*, 2009**], which can explain the correlation found in the Engelman mutated variants between reduced adhesion and increasing rates of MOT cells. Moreover, it had been shown that the P110 and P140 adhesins are essential for TO development[474] [**Burgos R. *et al.*, 2006**], which indicates that these adhesins are properly formed and positioned in the TOs of the Engelman variant mutant cells. Therefore, mutational analysis allows to conclude that Engelman motifs from P110, but unexpectedly not from P140, have a critical and synergic contribution to adhesion, strongly suggesting that interactions between the transmembrane helices of the two P110 subunits are required to achieve a functional "open", ready for binding, conformation of the Nap complex.

CIII. 2.8. Motility analysis of the mutants. Time-lapse cinematographic studies of *M. genitalium* strains carrying target mutations in the Engelman motifs

We examined the gliding activity of cells from the different mutants described above by time-lapse microcinematography to monitor the movements of individual cells for 120 s (**Table CIII. 2.8**). When examining the mutants still able to adhere to the flask-culture, no differences in the frequency of cells drawing circular tracks were found when comparing with the WT or G37ΔAdh::COM strains (**Table CIII. 2.8 and Figure CIII. 2.8_1**). We also observed that the motility of the G37ΔAdh::COM (WT), G37ΔAdh::COM (E1) and G37ΔAdh::COM (E2) strains was comparable to that of the G37 WT strain (**Table CIII. 2.8**). The percentage of the individual motile cells and the velocity were very similar. However, we found that gliding velocity of cells from the G37ΔAdh::COM (E3), G37ΔAdh::COM (E1; E2) and G37ΔAdh::COM (E1; E3) mutants was significantly reduced (**Table CIII. 2.8**).

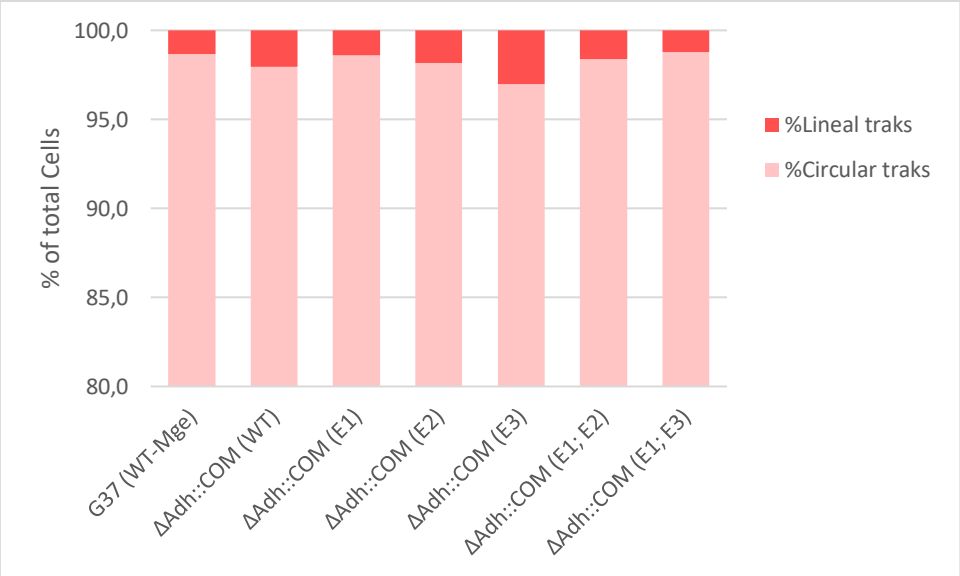

Figure CIII. 2.8_1. Characterization of the motile properties of the G37 (WT), ΔAdh::COM (WT) and all mutant strains. Percentage of cells describing circular and non-circular tracks.

Table CIII. 2.8. Gliding motility parameters of *M. genitalium* G37 wild-type cells and all different mutant strains obtained.

Strain	n (Motility)	Individual Motile cells (%)	n (Velocity)	Velocity (µm/s)[a]	Velocity preserved (%)	Motility loss (%)	Circular Tracks (%)	Non-circular Tracks (%)
G37 (WT)	~500	94.7	25	0.112±0.003	100 (ref.)	-	98.7	1.3
G37ΔAdh::COM	~500	94.0	25	0.115±0.004	100	-	97.9	2.1
G37ΔAdh::COM (E1)	~500	95.5	25	0.105±0.004	93.5	6.5	98.6	1.4
G37ΔAdh::COM (E2)	~500	86.6	25	0.110±0.004	98.1	1.9	98.2	1.8
G37ΔAdh::COM (E3)	~500	85.1	25	0.093±0.002*	82.5	17.5	97.0	3.0
G37ΔAdh::COM (E1; E2)	~500	87.8	25	0.098±0.002*	87.1	12.9	98.4	1.6
G37ΔAdh-COM (E1; E3)	~500	83.8	25	0.098±0.003*	87.5	12.5	98.8	1.2

[a]Velocities are shown as mean values +/- standard error. n=25 biologically independent cells, from different fields, different preparations and different microcinematographies.

*Statistically significant values (T (25) = 2.06; $p<0.05$). Statistical significance was assessed with the Paired Student's two-sided T-test. Velocity p-values: $3.86 \cdot 10^{-5}$, $6.82 \cdot 10^{-4}$, $9.61 \cdot 10^{-4}$.

CIII. 3. Discussion

The pneumonia cluster of mycoplasmas has developed a unique, strikingly complex, molecular machinery for gliding motility that consists of internal and surface structures located in the TO, a morphologically conspicuous cell protrusion. A gliding model has been proposed based mainly on biophysical and structural data of the internal structures[455,457,458] [**Kawamoto A. *et al.*, 2016; Miyata M. and Hamaguchi T., 2016; Nakane D. *et al.*, 2015**]. The model is a variant of the "inchworm" model, in which repeated contractions and extensions, synchronized with alternative attachment and detachment of the TO front and rear sides, enable the smooth gliding of cells[454,475,476] [**Henderson G. P. and Jensen G. J., 2006; Miyata M., 2008; Seybert A. *et al.*, 2018**]. According to this model, adhesins P1 and P40/P90 forming the Nap complex, which is the main surface structure of the TO, have a key contribution to both attachment and movement, by going throughout an iterative four stages cycle during gliding[459] [**Mizutani M. *et al.*, 2021**]. In the last few years a wealth of high resolution structural data has been obtained for the Nap complex[459,463] [**Mizutani M. *et al.*, 2021; Vizarraga D. *et al.*, 2021**].

The structure of the complex of *M. pneumoniae* adhesin P1 and the Fab fragment from the monoclonal antibody P1/MCA4, determined in this work, shows that the P1/MCA4 epitope involves residues of the C-terminal domain of P1 only (**Figure CIII. 2.2_1A**). This epitope is totally inaccessible to antibodies in the "open" (ready for binding to SOs) conformation of the Nap complex (**Figure CIII. 2.2_1B**). Therefore, for the P1/MCA4 epitope to be exposed, the adhesion complex has to experience a major rearrangement with respect to the "open" conformation. The conformation where P1/MCA4 binds must be unsuitable for attachment to SOs, as binding of antibody P1/MCA4 slows and induces detachment of moving *M. pneumoniae* cells only. Together with the available information, our results allow now to model accurately the four stages of the Nap complex cycle (**Figure CIII. 3_1**) explaining how internal and surface structures interact with each other.

Stage I: The cycle starts with the "open" conformation that is ready for binding to the SOs. The extracellular region from the "open" conformation of the Nap was built according to the structure determined *in situ* by Cryo-ET for *M. genitalium*[465] [**Aparicio D. *et al.*, 2020**]. The Engelman motifs found in the transmembrane helix of P40/P90 have a critical role to stabilize the "open" conformation, suggesting that the helices from the two P40/P90 subunits interact with each other.

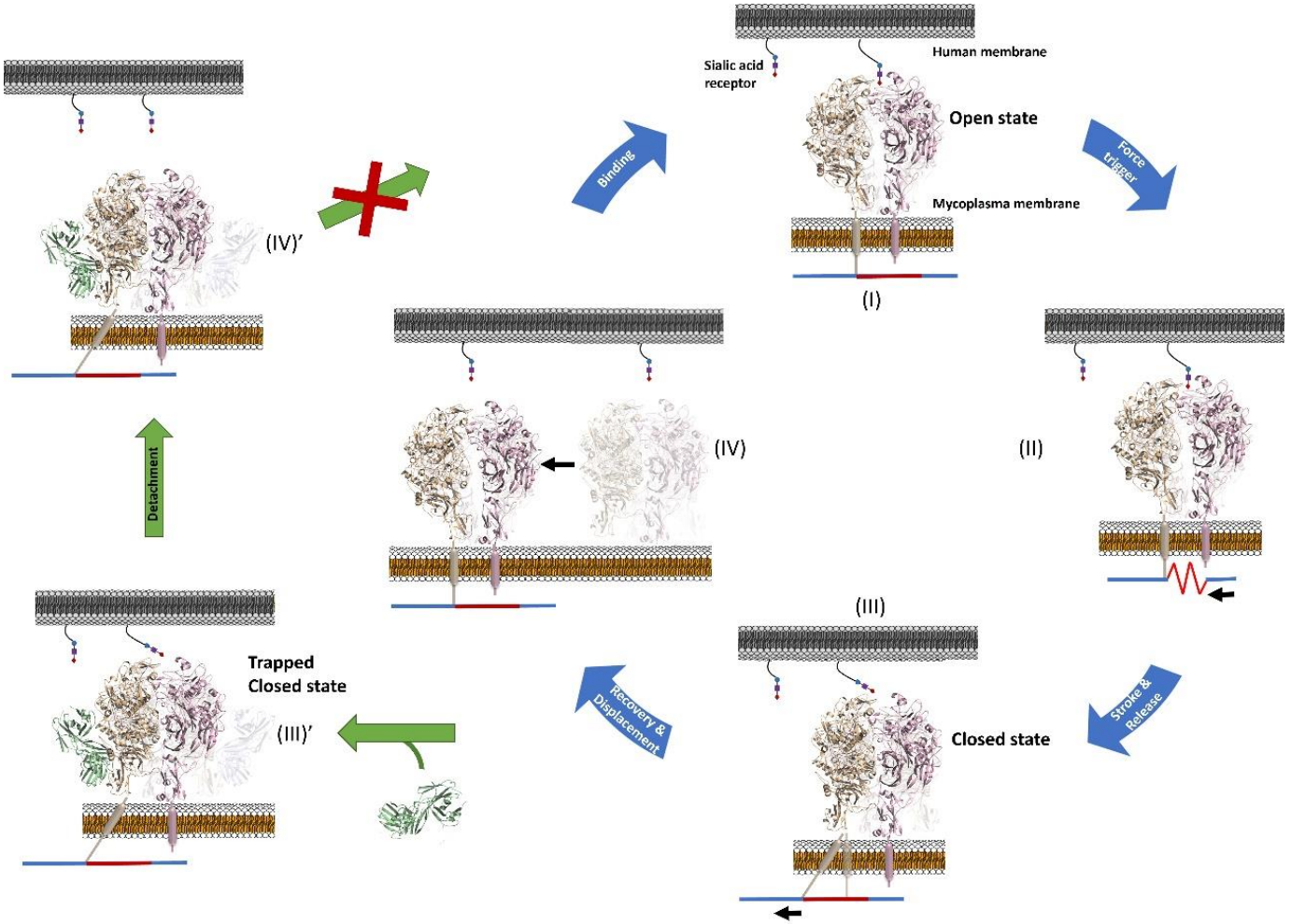

Figure CIII. 3_1. The attachment and detachment cycle of the Nap complex. The Nap complexes participating in adhesion and motility cycle between "open" and "closed" states, with the binding site to sialic oligosaccharides becoming alternatively accessible and inaccessible for binding. During the cycle, structural rearrangements are experienced mainly by the C-terminal domain of P1, with hinge rotations of about 175°. Movements of the C-terminal domain of P1 may be driven by the force, generated by ATP hydrolysis, transmitted from the back end of the TO (at the right of images) through the rod, which is represented as a line composed of elastic (red) and rigid (blue) parts. Displacements are shown by black arrows. Binding of the monoclonal antibody P1/MCA to the C-terminal domain of P1 halts the cycle, trapping the "closed" conformation and inducing detachment in motile cells only.

Stage II: Binding to SOs triggers the transition of the Nap complex towards the "closed" conformation. During the transition the exposed surfaces of the P40/P90 subunits remain unchanged, in agreement with the restraints imposed by the interactions between the transmembrane helices of the two P40/P90 subunits and previous studies showing that the two SOs binding sites of the Nap complexes are probably involved[477,478] [Kasai T. *et al.*, 2013; Mizutani M. and Miyata M., 2019]. In turn, the C-terminal domain of P1 has to experience an important rearrangement to allow the exposure of the P1/MCA4 epitope (Figure CIII. 3_2).

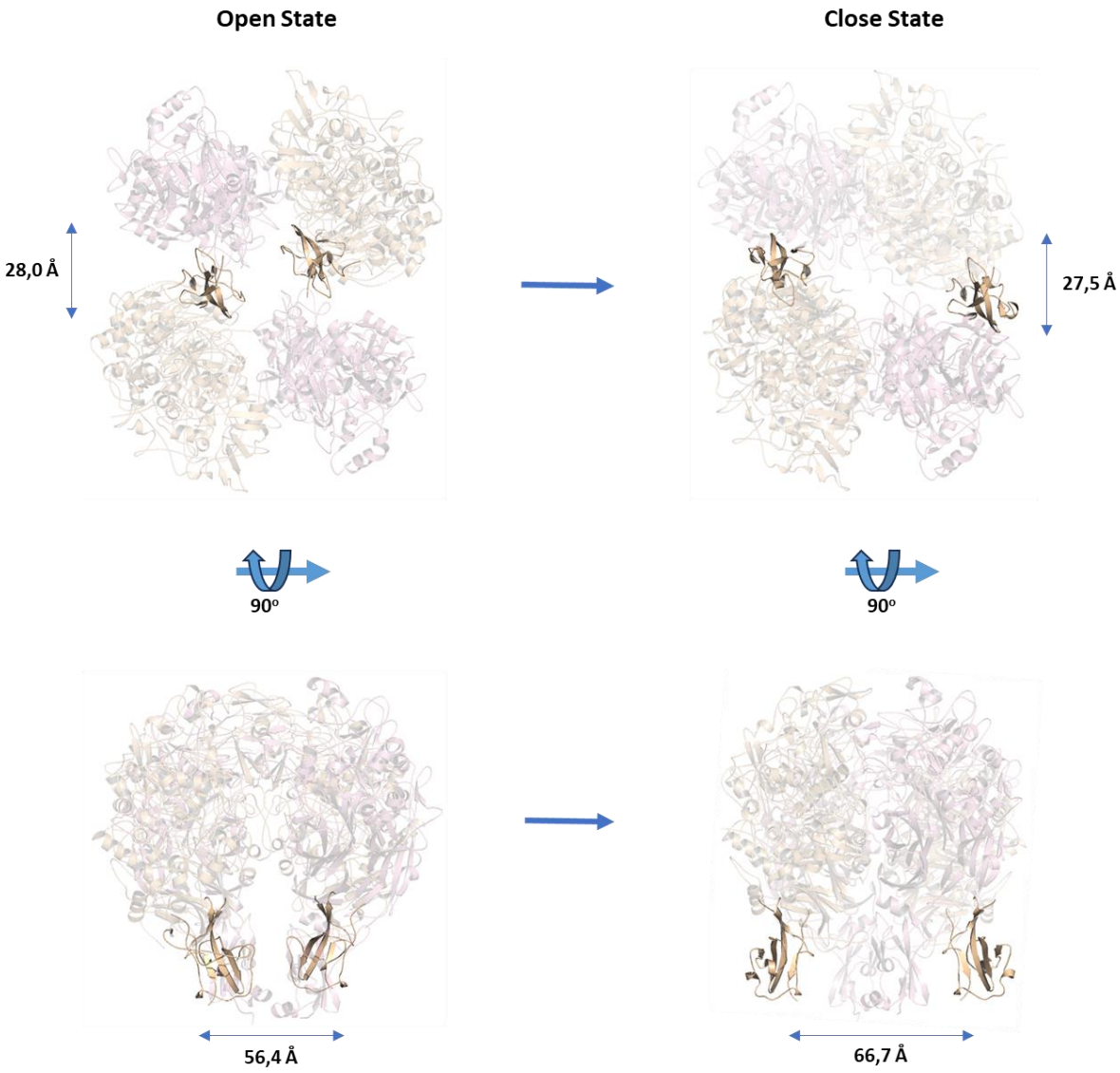

Figure CIII. 3_2. C-terminal domain of P1 movements during the "open" to "closed" transition. Top and side views (upper and lower panels, respectively) of the Napss (adhesins) ectodomains in the "open" and "closed" conformations (left and right panels, respectively). Values correspond to the distances (in that perspective) between the C-ends of the C-terminal domains of the two P1 subunits in the Nap. Besides the linear displacements the C-terminal domain experiences a hinge rotation of about 175º.

Stage III: Reaching the "closed" conformation of the Nap complex, where the N-terminal domains of P1 and P40/P90 interact tightly with each other, forcing the release of SOs and

occluding the binding site. At this stage the C-terminal domain of P1 has completed a hinge rotation of about 175º with respect to the "open" conformation, allowing the epitope of antibody P1/MCA4 to be fully exposed. Hinge movements of the C-terminal domain must be associated with displacements or distortions of the transmembrane helix, contiguous along the P1 sequence, which provides a way to communicate back and forth structural information between extra- and intra-cellular regions.

Binding of antibody P1/MCA4 to the C-terminal domain of P1 traps the Nap complex in the "closed" conformation, which explains why only moving cells are affected by the antibody (left images in **Figure CIII. 3_1**). The increasing number of complexes in the closed, non-adherent conformation slows down the speed of gliding and weakens cell attachment.

Stage IV: Recovering the "open" conformation of the Nap complex. The "open" and "closed" conformations of the unbound adhesion complexes as described here so far, have the same molecular components. Assuming no other elements are at play, the least stable conformation must revert spontaneously towards the most stable, while the transition from the most towards the least stable will require energy. The "open" conformation, the most abundant in an *in situ* Cryo-ET analysis[465] [**Aparicio D. *et al*., 2020**], is likely the most stable, suggesting that the energy input is required for the "open" to "closed" transition associated with the power stroke and the straining of the internal structures (from Stage I to Stage III in **Figure CIII. 3_1**)[459] [**Mizutani M. *et al*., 2021**]. The force is likely generated by ATP hydrolysis at the back end of the TO[478] [**Mizutani M. and Miyata M., 2019**] and transmitted to the adhesins through the contraction and extension of the TO internal rod structure that, by pulling the C-terminal domain of the P1 subunits, causes the transition between the conformations of the Nap complex.

Results provide now a consistent structural framework for the functioning of the Nap complex during the attachment/detachment cycle in which subunit P1, mainly its C-terminal domain, experiences extensive rearrangements pivoting around static P40/P90 subunits anchored by interactions of their Engelman motifs. Results also lay out a clear structural explanation for the efficient neutralization mechanism of antibodies such as P1/MCA4, binding to the dynamic and highly conserved C-terminal domain of P1, suggesting new approaches to confront human pathogens like *M. pneumoniae* and *M. genitalium*.

CHAPTER IV

ESSENTIAL PROTEIN P116 EXTRACTS CHOLESTEROL AND OTHER INDISPENSABLE LIPIDS FOR *Mycoplasmas*

Results presented in this chapter have been partially published in:

Lasse Sprankel, David Vizarraga, Jesús Martín, Sina Manger, Jakob Meier-Credo, **Marina Marcos-Silva**, Josep Julve, Noemi Rotllan, Margot P. Scheffer, Joan Carles Escolà-Gil, Julian D. Langer, Jaume Piñol, Ignacio Fita and Achilleas S. Frangakis. **Essential protein P116 extracts colesterol and other indispensable lipids for *Mycoplasmas***. *Nature Structural & Molecular Biology*. **2023**. DOI: 10.1038/s41594-023-00922-y. https://www.nature.com/articles/s41594-023-00922-y

ESSENTIAL PROTEIN P116 EXTRACTS CHOLESTEROL AND OTHER INDISPENSABLE LIPIDS FOR *Mycoplasmas*

Mycoplasma pneumoniae, responsible for approximately 30% of community-acquired human pneumonia, needs to extract lipids from the host environment for survival and proliferation. Here, we report a comprehensive structural and functional analysis of the previously uncharacterized protein P116 (MPN_213). Single-particle Cryo-EM of P116 reveals a homodimer presenting a previously unseen fold, forming a huge hydrophobic cavity, which is fully accessible to solvent. Lipidomic analysis shows that P116 specifically extracts lipids such as phosphatidylcholine, sphingomyelin and cholesterol. Structures of different conformational states reveal the mechanism by which lipids are extracted. This finding immediately suggests a way to control *Mycoplasma* infection by interfering with lipid uptake.

My specific contribution to this chapter:

I have been involved in the generation of the different polyclonal and monoclonal antibodies to demonstrate that P116 protein is not an adhesin and paved the way to determine the protein function. These antibodies also allowed to perform the protein immunolocalization experiments. These experiments are described in CIV. 2.1 section. I have also contributed to the manuscript writing.

CIV. 1. Introduction

Mycoplasma pneumoniae is a facultative intracellular human pathogen that causes community-acquired pneumonia that can result in severe systemic effects[479] [Tsiodras S. *et al.*, 2005]. Unlike other respiratory pathogens, there is no approved vaccine against *M. pneumoniae*[480] [Jiang Z. *et al.*, 2021]. *Mycoplasma* species lack a cell wall and have the smallest known genomes[481] [Razin S. et al., 1998]. *M. pneumoniae*, with a 816-kb genome, is a model organism for a minimal cell[112] [Lluch-Senar M. *et al*. 2015]. Many of the metabolic pathways that are required to synthesize essential products are absent, which makes uptake by specialized mechanisms necessary. In fact, *M. pneumoniae* cannot synthesize several of the lipids that are important components of the cell membrane, such as sphingomyelin, phosphatidylcholine and cholesterol[482] [Gaspari E. *et al.*, 2020]. Instead, it must take up lipids from the host environment, and it adapts its membrane composition depending on the medium in vitro[483–485] [Razin S. *et al.*, 1963; Leon O. and Panos, C., 1981; Bittman R., 1993]. Cholesterol in particular, which is present in only a few prokaryotes, is essential for *M. pneumoniae* cells and several other *Mycoplasma* species[483] [Razin S. *et al.*, 1963]. It is the most abundant lipid in the membranes, accounting for 35–50% of the total lipid fraction[483] [Razin S. *et al.*, 1963]. Comprehensive studies on other cholesterol-utilizing bacteria are largely lacking; the best characterized organism in this group is *Mycobacterium tuberculosis*, for which it has been proposed that an ABC transporter homolog and other genes from the *mce*4 operon are involved in cholesterol uptake[486] [Mohn W. W. *et al.*, 2008]. *M. tuberculosis* uses cholesterol as a carbon source, enabling long-term infections with the bacteria[487] [Pandey A. K. and Sassetti, C. M., 2008]. It has been shown that *M. pneumoniae* survive long-term in cholesterol-rich atherosclerotic plaques[488] [Damy S. B. *et al.*, 2009]. For other clinically relevant bacteria that use cholesterol, like *Borrelia burgdorferi* or *Helicobacter pylori*, the uptake mechanism remains elusive[489] [Huang, Z. and London E., 2016]. To date, it is unclear how *Mycoplasma* spp. uptake lipids from the environment.

In this work, we report the structural and functional characterization of P116. This protein was originally reported to contribute to host-cell adhesion[490] [Svenstrup H. F. et al., 2002]. Furthermore, P116 is an essential protein for the viability of *M. pneumoniae* cells and is strongly immunogenic, thus making it a promising target for therapeutics[490] [Svenstrup H. F. *et al.*, 2002]. Despite the essential role of P116, the *M. pneumoniae* genome contains only a single copy of *mpn*_213 (gene encoding P116), and, on average, only 34 copies of the protein are present in *M. pneumoniae*[49] [Yus E. *et al.*, 2009]. By contrast, the most immunogenic protein, P1, is not essential, has multiple gene copies present in the genome[159] [McGowin C. L. and Totten, P. A., 2017], and has a 20-fold-higher copy number[49] [Yus E. *et al.*, 2009]. To elucidate the role of P116,

we first determined the structure of the ectodomain by single-particle Cryo-EM. To the best of our knowledge, this structure represents a previously uncharacterized fold (with no matches in the Protein Data Bank) featuring a uniquely large hydrophobic cavity that is fully accessible to solvent. Using mass spectrometry, we identified several different lipids (including cholesterol) bound to P116, some of which are essential, matching observed densities in the hydrophobic cavity. On the basis of these findings, we describe the mechanism by which *Mycoplasma* spp. extract lipids from the environment and possibly also deposit them in their own membrane, thus explaining the essential role of P116 in the survival of *M. pneumoniae* cells.

CIV. 2. Results

CIV. 2.1 P116 is evenly distributed on the cell surface

A construct predicted to span the whole ectodomain of P116 from *M. pneumoniae* (residues 30–957) was overexpressed in *Escherichia coli* and purified by His-tag affinity and gel filtration chromatography (see methods for further explanation; **Figure CIV. 2.1_1**). Immunolabeling with both polyclonal antibodies against this construct showed an intense and uniform distribution of labelling across the whole surface of the *M. pneumoniae* cells (**Figure CIV. 2.1_2**), and adhesion and motility were unaffected by the antibodies (**Table CIV. 2.1 and Appendices Table A. CIV. 4.5**). This distribution contrasts with that of P1, an adhesion protein that concentrates at the tip of the cell and whose inhibition has strong effects on adhesion and motility[491,492] [**Krause D. C. *et al.*, 1982; Baseman J. B. *et al.*, 1982**].

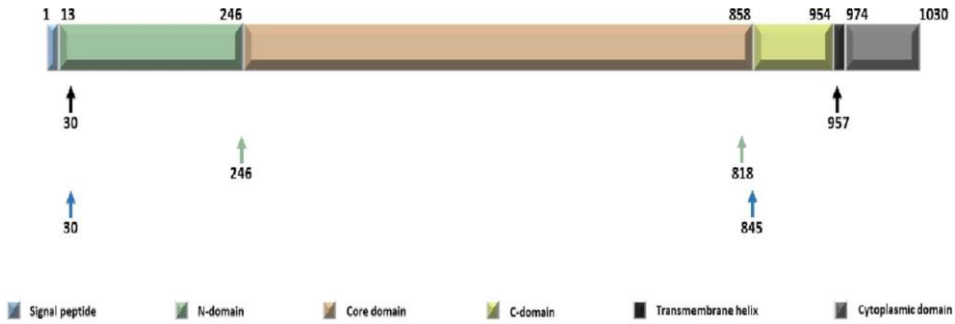

Figure CIV. 2.1_1. P116 constructs. Overview of the different constructs (30–957, 30–818, 246–845) used for expression. For expression purposes a His-tag (KHHHHH) was added at the C-terminus. For the structural analysis by Cryo-EM the construct from 30-957 was used. Adapted from **Sprankel L. *et al.*, 2023**.

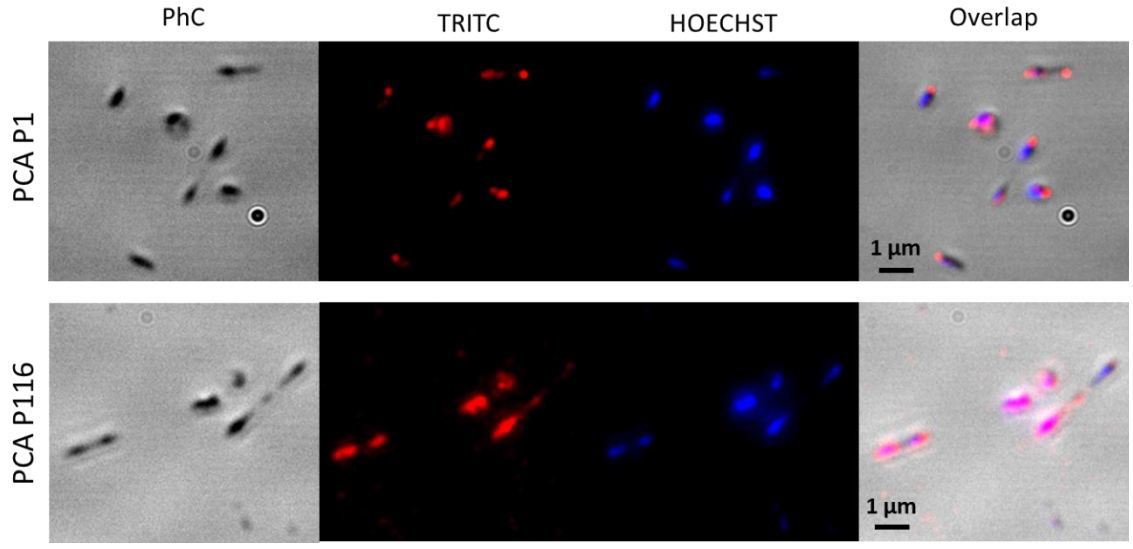

Figure CIV. 2.1_2. Localization of P116 in *Mycoplasma pneumoniae* cells and structure of P116. Phase contrast (PhC) immunofluorescence microscopy images *of M. pneumoniae* cells using labeling with polyclonal antibodies (PCA) against the ectodomains of adhesin P1 (top row; used as a reference) and P116 (bottom row) (two separate experiments with independent samples were performed). Labeling for P1 concentrates at the tip of the cell; for P116, it covers the whole surface homogenously. Adapted from **Sprankel L. *et al.*, 2023**.

Table CIV. 2.1. Adhesion and motility inhibition assay. Number of cell detachments and motility status of *M. pneumoniae* cells before and after adding polyclonal antibodies (PCA) vs P1 and P116.

	Before[#]	After[#]	
PCA	**% Motility ± SE**	**% Motility ± SE**	**% Detached cells ± SE**
P1	95,9 ± 1,9	15,3 ± 6,3	95,1 ± 2,1
P116	91,9 ± 1,5	85,8 ± 2,4	40,2 ± 3,8
Negative Control[$]	89,9 ± 3,0	75,7 ± 5,0	53,8 ± 6,8

All values are shown as mean values +/- standard error from three different and independent microcinematographies.
[$] Negative control. PBS with no antibody was added.
[#] Measurements made "before" or "after" adding antibodies or a control PBS solution.
SE: standard error.

CIV. 2.2 P116 has a previously uncharacterized fold with a lipid-accessible cavity

The structure of P116 (30–957) was determined by single-particle Cryo-EM at 3.3-Å resolution (according to the gold-standard criterion of Fourier shell correlation (FSC) = 0.143; **Appendices Table A. CIV. 4.3 and Appendices Figure A. CIV. 4.3_1**). It is an elongated homodimer of ~240 Å along its longest axis, which adopts an arched shape with an arc diameter of ~20 nm (**Figure CIV. 2.2_1**). Each monomer consists of two distinct domains: the core domain (residues 246–867) and the amino-terminal domain (residues 60–245), situated distal to the dimer axis. The dimerization interface, part of the core domain and proximal to the dimer axis (**Figure CIV. 2.2_1 and Figure CIV. 2.2_2A,B**), is very well resolved. By contrast, the N-terminal domain has substantial hinge mobility with respect to the core domain, evident by the poorer local resolution of the Cryo-EM map (**Appendices Figure A. CIV. 4.3_1**), making model building difficult for the most distal parts of the construct (**Figure CIV. 2.2_2C**). The homodimer displays substantial flexibility with many vibrational modes, as illustrated by a complete vibrational analysis, showing a fluent transition between states (**Figure CIV. 2.2_3**).

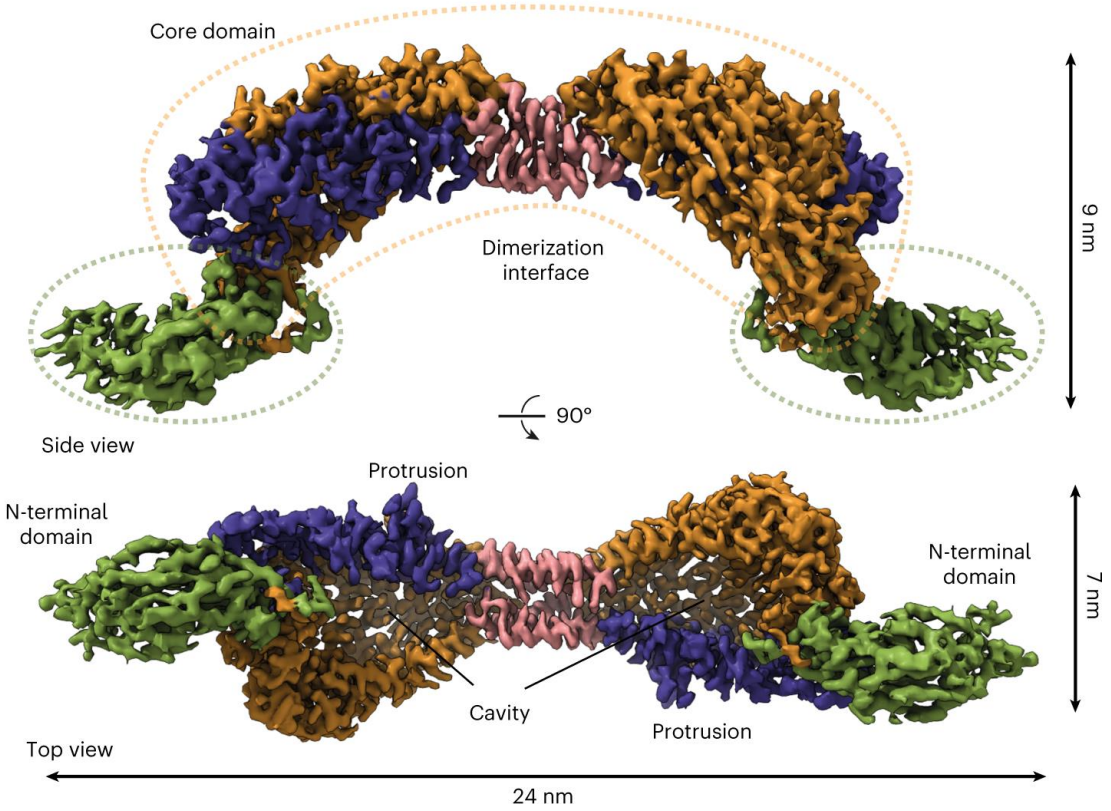

Figure CIV. 2.2_1. Structure of P116. Two views of the Cryo-EM density map of the complete extracellular region of the P116 dimer at 3.3-Å resolution (from 1.3 million particles), 90° apart. The homodimer is held together by the dimerization interface (shown in pink). The core domains have four contiguous antiparallel helices (shown in blue) and a β-sheet with five antiparallel strands (shown in orange). The N-terminal domain is shown in green. The top view displays a huge cavity that is fully accessible to solvent. The cleft providing access to the cavity spans the whole core domain. Each monomer also has a distinct protrusion (shown in blue as part of the antiparallel α-helices). Adapted from **Sprankel L. *et al.*, 2023**.

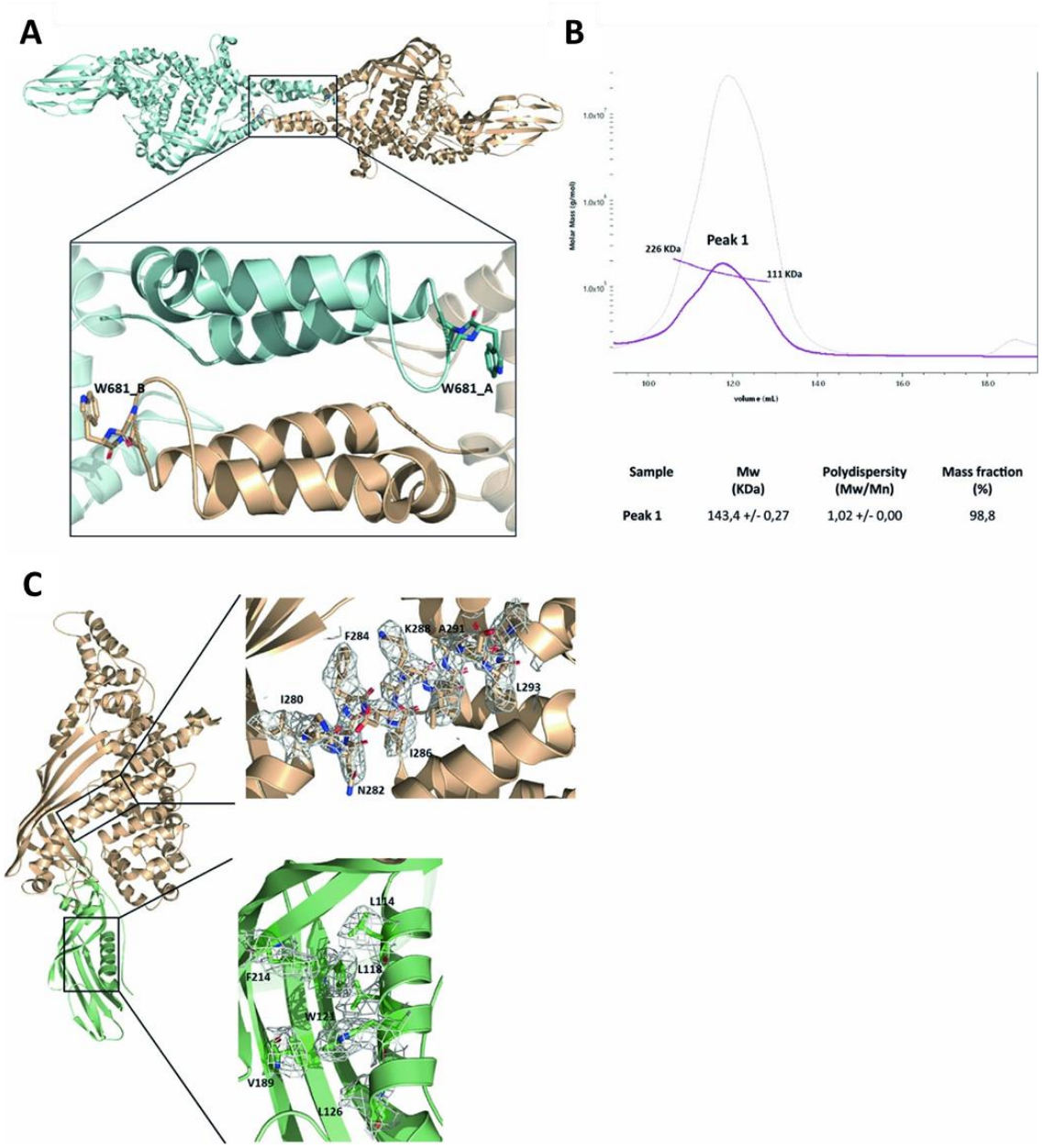

Sample	Mw (KDa)	Polydispersity (Mw/Mn)	Mass fraction (%)
Peak 1	143,4 +/- 0,27	1,02 +/- 0,00	98,8

Figure CIV. 2.2_2. Dimerization interface and model building of P116. A) Detail of the dimerization zone with the two monomers and the TRP-681 residue of both chains contacting the opposite one. **B)** SEC-MALS of P116 W681A. The greatest polydispersity of this sample is observed, which oscillates between a very large MW (molecular weight) range, and the clear decrease in size with respect to the WT due to the now predominance of the monomeric state. **C)** Exemplary superimpositions of the Cryo-EM density and the PDB model for the core and N-terminal domain. Adapted from **Sprankel L. *et al*., 2023**.

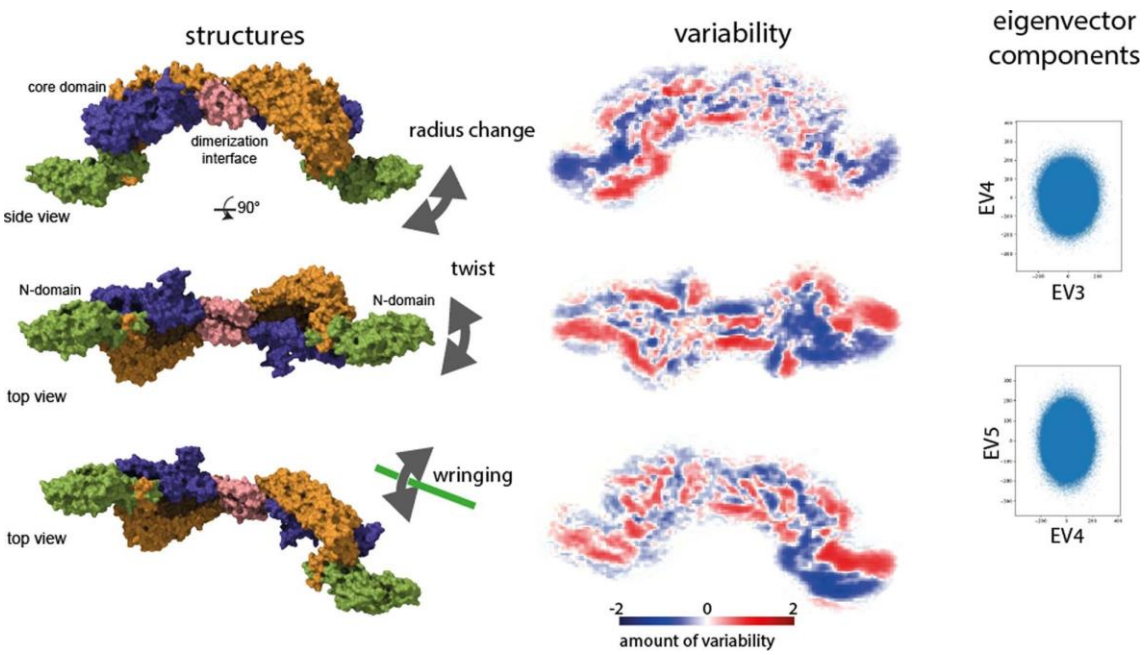

Figure CIV. 2.2_3. Flexibility of P116. Cryo-EM classes display different flexibility modes. Individual reconstructions are shown on the left column. Their variability is shown in the middle column. Plotting of the individual eigenvector weights shows, that no clear distribution is visible and a smooth transition between the individual vibrational modes. Here 'eigenvector 3' (EV3) is plotted against 'eigenvector 4' (EV4) that display the largest resemblance to the radius change and 'eigenvector 4' (EV4) is plotted against 'eigenvector 5' (EV5) that display the largest resemblance to the twist. Adapted from **Sprankel L. *et al.*, 2023**.

The core domain resembles a half-opened left hand, with four contiguous antiparallel pairs of amphipathic α-helices corresponding to the four fingers and the N-terminal domain corresponding to the thumb (**Figure CIV. 2.2_4A**). The dimer interface, which corresponds to the wrist, is composed of helices with a conserved tryptophan residue (Trp681) that interacts tightly with the neighbouring monomer. In the variant with the W681A mutation, the rate of dimers to monomers is 1:4, compared with only dimers in the wild type (**Figure CIV. 2.2_2B**). The palm of the hand includes a long and well-defined central α-helix, namely the bridge helix (residues 268–304), and a rigid β-sheet of five antiparallel strands that extends to the N-terminal domain (**Figure CIV. 2.2_4B**). The hand appears in a half-opened state with a large, elongated cleft across the whole core domain (**Figure CIV. 2.2_4C**). The core domain forms a large cavity that measures 62 Å from the proximal to the distal end and 38 Å from the anterior to the posterior side. The cavity has a volume of ~18,000 $Å^3$. The cavity is completely hydrophobic but is fully accessible to the solvent (**Figure CIV. 2.2_4C**). In addition, the core has two access points, one at the dorsal side and another at the distal side (**Figure CIV. 2.2_5A**). Using the DALI server, we found only very weak structural relationships between P116 and all other experimentally determined protein structures in the Protein Data Bank, which shows that P116 has a unique fold.

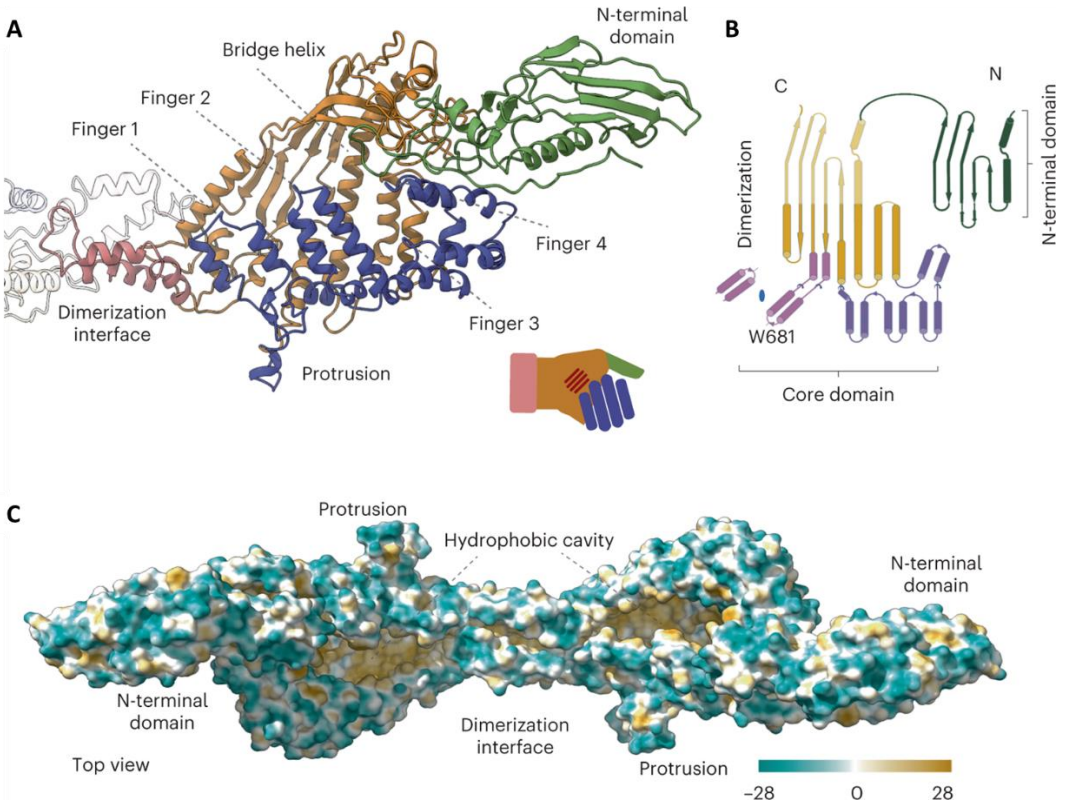

Figure CIV. 2.2_4. P116 structure and hydrophobic areas. A) Ribbon model of the P116 monomer, built from the density shown in **Figure CIV. 2.2_1** and colored also as in **Figure CIV. 2.2_1**. The overall shape of the structure corresponds to a left hand, with the four antiparallel amphipathic α-helices representing fingers (shown in blue), and the bridge helix and β-sheet of five antiparallel strands representing the palm (shown in orange). The N-terminal domain, which is very flexible, corresponds to the thumb. The dimerization helices (shown in pink) correspond to the wrist. **B)** The overall topology of P116. The N-terminal and core domains of P116 share a similar topology, which suggests that P116 might have been generated by duplication of an ancestor domain. Colors correspond to A. **C)** The hydrophobic map of the P116 homodimer shows that the cavity in the core domain is hydrophobic (amino acid hydrophobicity is colored according to the Kyte–Doolittle scale). Adapted from **Sprankel L. *et al.*, 2023**.

The N-terminal domain is compact and organized around a cluster of aromatic residues, at the centre of which is the only tryptophan residue of the domain (W121). The N-terminal and core domains of P116 superimpose for 126 equivalent residues (68% of the N-terminal domain), suggesting that P116 might have been generated by duplication of an ancestor domain. The common secondary structural elements in the N-terminal and core domains consist of a β-sheet and the two helices preceding the β-sheet (**Figure CIV. 2.2._4B**). The core domain is much larger than the N-terminal domain, mainly owing to two insertions containing 12 and 4 helices.

For the inner part of the P116 core domain, the Cryo-EM maps show prominent elongated densities (with a length of 10–19 Å and a width of 4 Å) that fill most of the hydrophobic areas (**Figure CIV. 2.2_5A**). These elongated densities, which are unaccounted for by the structure, cannot be explained by the protein residues missing in the model. Instead, the mass excess of

~13 kDa, consistently measured by multiple angle light scattering (MALS) and mass spectrometry for P116 in different preparations, could be explained by the presence of ligand molecules bound to P116 (**Figure CIV. 2.2_6A**). Mass spectrometry analysis of the same samples from which the structure of P116 was determined showed the presence of several lipid species, predominantly phosphatidylethanolamine (PE) and phosphatidylglycerol (PG) lipids, as well as wax esters (**Figure CIV. 2.2_6B-D and 2.2_7**).

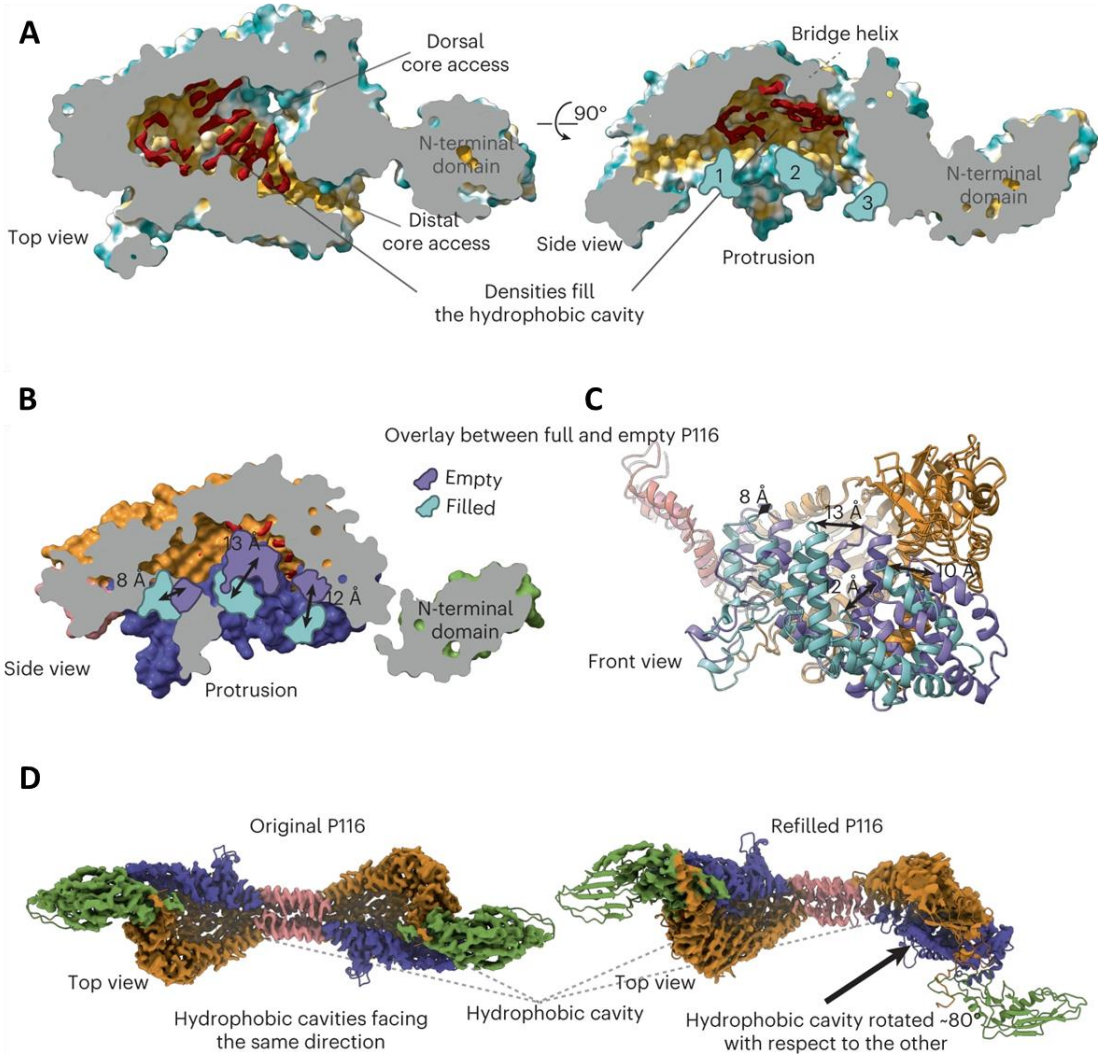

Figure CIV. 2.2_5. Purified P116 is filled with ligands and displays a large conformational variation compared to empty P116. A) A cross-section through the core domain of original P116 exposes a series of elongated densities (shown in red), which cannot be accounted for by the structure. These densities are ~4-Å wide and 10- to 19-Å long and are surrounded by highly conserved hydrophobic residues. The cross-section also reveals that the core domain can be accessed dorsally and distally. The side view of the core domain shows that the densities are aligned to the bridge helix and away from the fingers (shown in red). Numbers indicate individual fingers (finger 4 is not visible in this illustration). **B)** Overlay between empty and full P116. The side view of the cross-section surface view of the empty, and full P116 (palm areas aligned) shows that the fingers of the empty P116 (in purple) have come closer to the palm, massively reducing the cavity. The position of the fingers in the empty P116 (in purple) is markedly different compared with the full P116 (shown in cyan). Finger 1 has moved 8 Å sideways and towards the palm, finger 2 has moved 13 Å towards the palm and finger 3 has moved 12 Å towards the palm. The cavity

in the empty P116 is no longer sufficient to accommodate ligands. **C)** In the ribbon presentation, the conformation differences between the empty and full P116 structures can be seen in the front view. All four fingers have moved towards the palm (shown in orange) of the hand (individual distances are indicated filled conformation in cyan, empty conformation in purple). **D)** Two Cryo-EM classes reveal a wringing movement of P116. Comparison of the two density maps (superimposed with the ribbon diagram of the structure) shows that the wringing movement of P116 allows for the two hydrophobic cavities in the dimer to face almost opposite directions. The top view on the left shows both cavities facing in one direction, and the top view on the right shows the cavities rotated ~80° to each other. Adapted from **Sprankel L. *et al.*, 2023**.

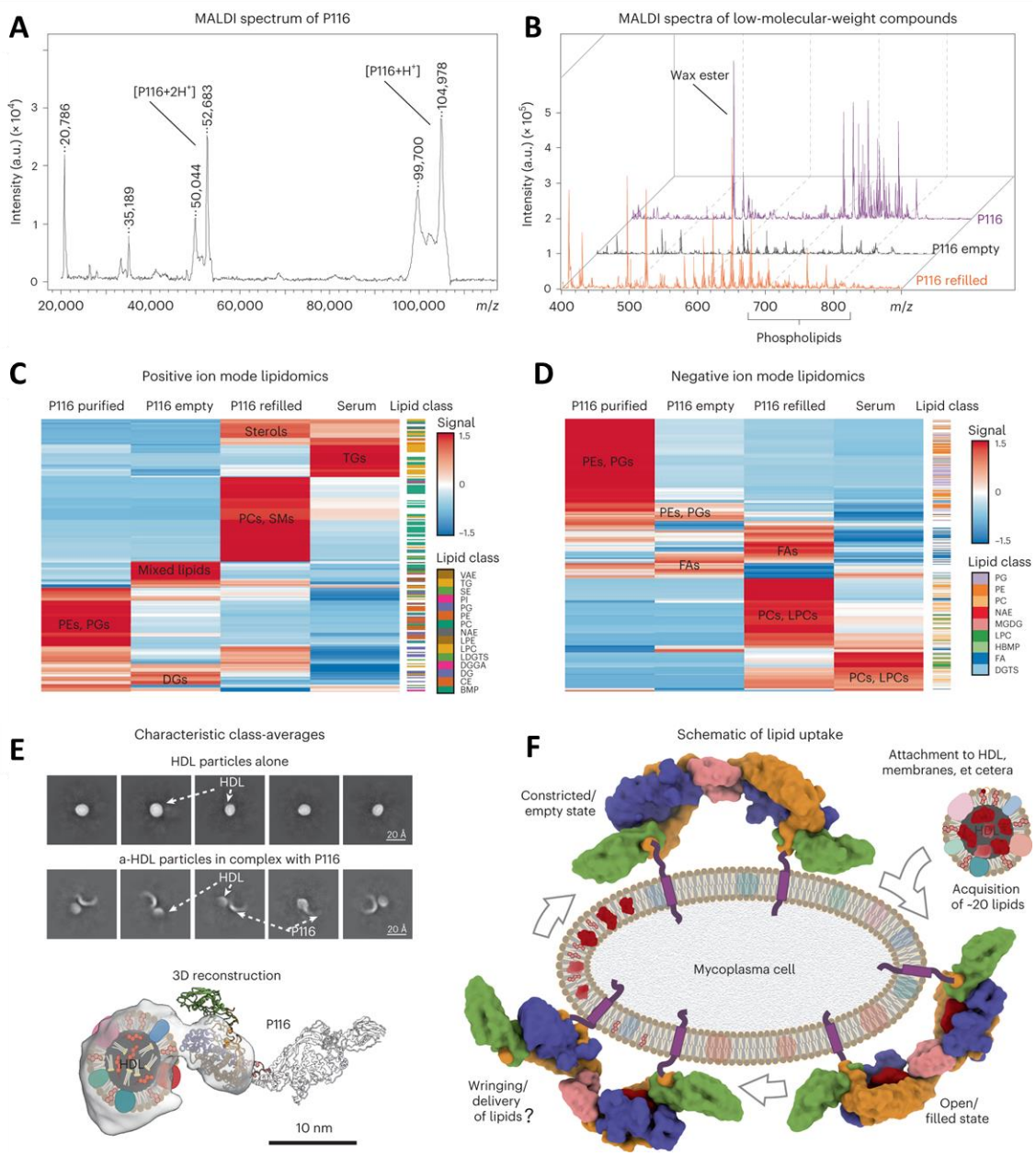

Figure CIV. 2.2_6. Analysis of the lipid spectrum and uptake of P116. A) MALDI-TOF mass spectrum of original P116 sample (linear mode, high mass range), showing a dominant peak at 105 kDa, corresponding to the singly charged full protein, as well as the charged states two, three and four. a.u., arbitrary units. **B)** Stacked MALDI-TOF mass spectra (reflector mode, low mass range) of the original purified P116 (purple, rear), empty P116 (black, middle) and refilled P116 sample (orange, front) showing a change in the lipid distribution among the samples. **C, D)** Hierarchical clustering of lipid compounds identified in positive (**C**)

and negative (**D**) ion mode lipidomics (LC–MS/MS) analyses (reproduced in three independent experiments), showing differential distributions of lipid compositions in original P116 (first column), empty P116 (second column), refilled P116 (third column) and serum (fourth column). The refilled P116 shows a particular affinity to sterols and cholesterol specifically. All data were normalized to the mTIC of all identified compounds in each sample, and row-wise scaling was applied. PE, phosphatidylethanolamine; PG, phosphatidylglycerol; DG, diacylglycerol; PC, phosphatidylcholine; SM, sphingomyelin; TG, triacylglycerol; FA, fatty acid; LPC, lysophosphatidylcholine; VAE, vitamin A fatty acid ester; SE, sterol esters; PI, phosphatidylinositol; NAE, N-acyl ethanolamines; LPE, lysophosphatidylethanolamine; LDGTS, lysodiacylglyceryl trimethylhomoserine; DGGA, diacylglyceryl glucuronide; CE, cholesteryl ester; BMP, bismonoacylglycerophosphate; NAE, N-acyl ethanolamines; MGDG, monogalactosyldiacylglycerol; HBMP, hemibismonoacylglycerophosphate; DGTS, diacylglyceryl trimethylhomoserine. **E)** Cryo-EM analysis of empty P116 incubated with HDL shows that P116 binds HDLs between its N-terminal and core domains. P116 is attached to HDL through its distal core. Owing to the flexibility of P116 and the variability of HDL, only one subunit of P116 can be seen at this threshold. The whole P116 can be seen in the individual class averages. **F)** Schematic of the lipid uptake and conformational variations of P116 (here indicated by its structure anchored in the mycoplasma membrane. Linkers and transmembrane domains not seen in the Cryo-EM structure are shown in purple). P116 starts in an empty, constricted state; incubation with HDL leads to each individual monomer filling up with approximately 20 lipids; and P116 changes to the open/filled state. We hypothesize that, through a wringing motion, lipids are delivered into the mycoplasma membrane. Adapted from **Sprankel L. *et al.*, 2023**.

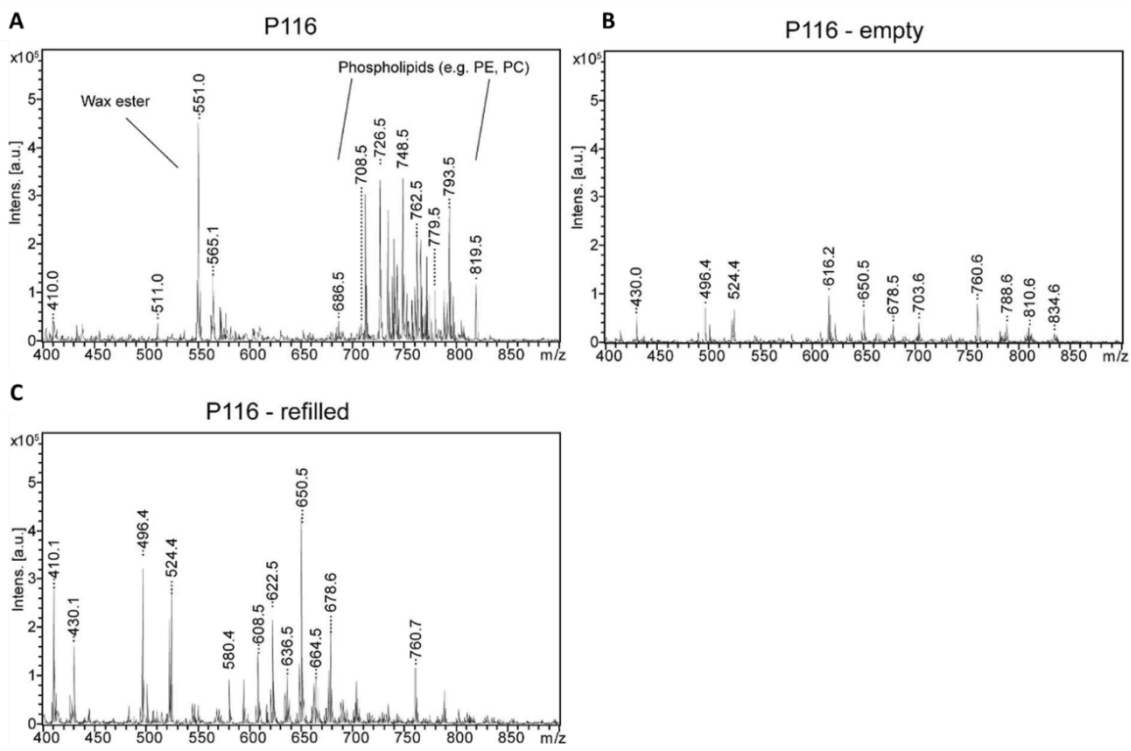

Figure CIV. 2.2_7. MALDI-TOF of P116, P116 empty and P116 refilled. Individual low molecular weight MALDI-MS spectra of P116, P116-empty and P116-refilled as displayed in in **Figure CIV. 2.2_6**. Adapted from **Sprankel L. *et al.*, 2023**.

CIV. 2.3 P116 orthologs in other *Mycoplasma* spp

P116 orthologs were found in at least eight other *Mycoplasma* species, including *M. genitalium* and *M. gallisepticum*. The amino acids lining the hydrophobic cavity are largely conserved (they are either identical or have similar characteristics) (**Figure CIV. 2.3_1A**). Modelling the orthologs of P116 with AlphaFold[471] [**Jumper J. *et al.*, 2021**] resulted in all the models having a similar tertiary structure, in which a large core domain is flanked by a smaller N-terminal domain, but the relative position of the domains does not closely match the experimental structure (**Figure CIV. 2.3_1B**).

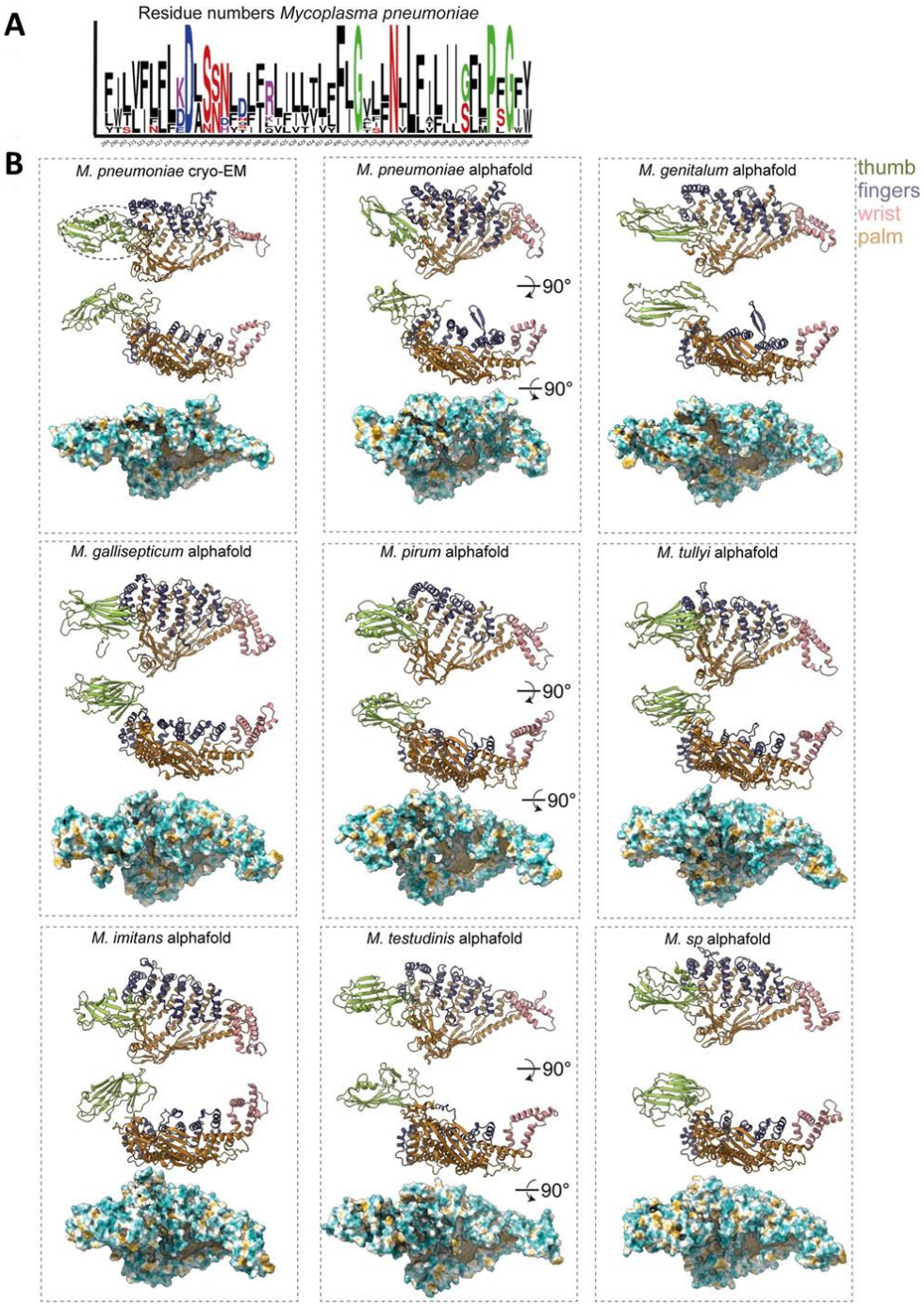

Figure CIV. 2.3_1. P116 in other *Mycoplasma* species. A) Conserved (minimum 55 %) amino acids pointing inwards the hydrophobic cavity. Black indicates amino acids with a hydrophobic character. Red indicates amino acids with a hydrophilic character. Blue indicates amino acids with a negative side chain. Purple indicates amino acids with a positive side chain. Green indicates other amino acids. **B)** Predictions of P116 from different *Mycoplasma spp*. in comparison with the structure resolved with Cryo-EM. The N-terminal and the core domain have been predicted independently and subsequently fitted in the Cryo-EM density map of P116. The coloring of the models is identical to the **Figures CIV. 2.2_1, 2.2_4, 2.2_5 and 2.2_6**. Adapted from **Sprankel L. *et al*., 2023**.

CIV. 2.4 Empty P116 cannot accommodate lipids

To obtain empty P116 that is free of any bound ligands, we treated the P116 samples with the detergent Triton X-100 (see below). Mass spectrometry confirmed a massive reduction of lipids in the sample (**Figure CIV. 2.2_6B**). The structure of the empty P116 sample was solved by Cryo-EM at 4-Å resolution (**Figure CIV. 2.4_1**). Its overall topology is almost identical to that of the original P116 sample; however, the core domain is constricted as a result of fingers 1, 2 and 3 being closer to the palm by 8, 13 and 12 Å, respectively, and finger 4 moving 11 Å sideways to retain the distal core access to the cavity (**Figure CIV. 2.2_5B and 2.4_2**). These changes reduce the volume of the cavity from ~18,000 $Å^3$ to ~6,300 $Å^3$. Consequently, the huge hydrophobic cavity reduces to two pockets that are large enough for lipids to pass through but that appear unoccupied in the Cryo-EM density. A comparison of the filled and empty P116 structures shows that the original densities that were unaccounted for create massive steric clashes in the constricted configuration, demonstrating that the cavity can no longer accommodate lipids. In the empty P116, the dimerization interface is shifted towards the dorsal side of the molecule by 10 Å, resulting in a contraction that changes the arc diameter of the dimer to ~10 nm and shifts the N-terminal domain towards the dimerization interface.

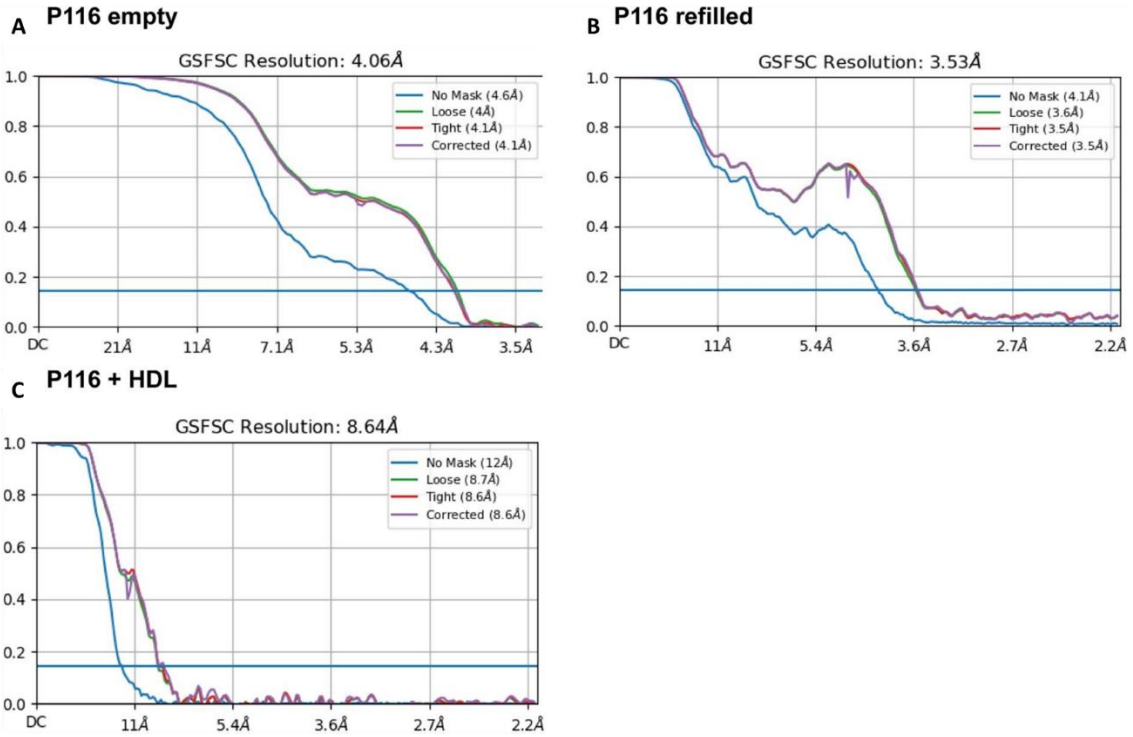

Figure CIV. 2.4_1. Fourier shell correlations of P116 empty, P116 refilled and P116 + HDL. (**a**) Final reported resolution of P116 empty at 4 Å according to the 0.143 cut-off criteria. (**b**) Final reported resolution of P116 refilled at 3.5 Å according to the 0.143 cut-off criteria. (**c**) Final reported resolution of P116 + HDL at 9 Å according to the 0.143 cut-off criteria. Adapted from **Sprankel L. *et al.*, 2023**.

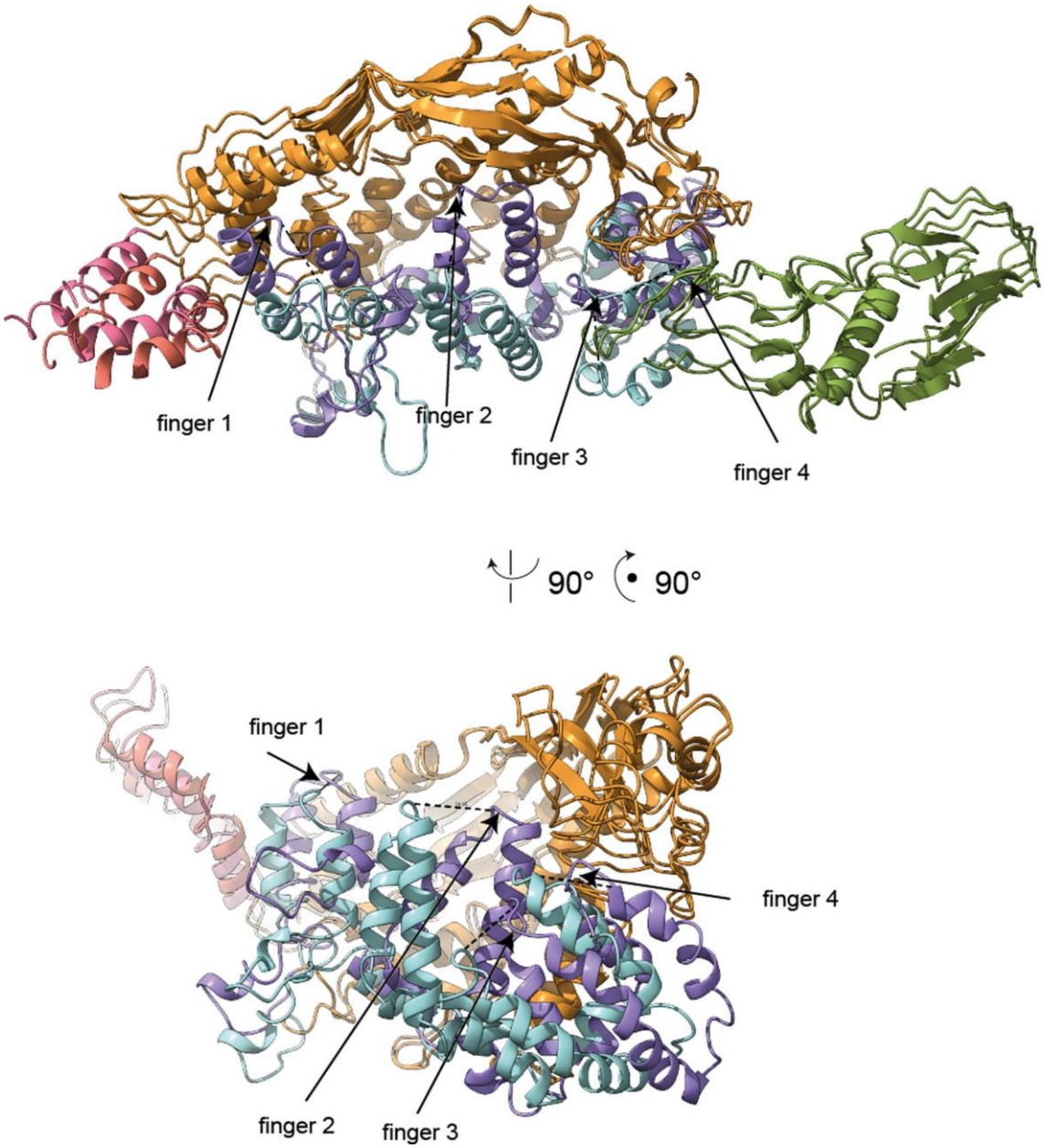

Figure CIV. 2.4_2. Conformational change between P116 and P116 empty. Superimposition of one subunit of P116 with one subunit of P116 empty. The movement of the fingers 1-4 is indicated by dashed lines. Side view of the ribbon representation of the empty and full P116 shows that the fingers (in purple) have come closer to the core domain, massively reducing the available volume. Their new position is markedly different compared to the full P116 (shown in light blue). Finger 1 moved 8 Å sideways and towards the core, finger 2 has moved 13 Å towards the core and Finger 3 has moved 12 Å towards the core. Adapted from **Sprankel L. *et al*., 2023**.

CIV. 2.5 Refilled P116 is identical to the purified P116

We next refilled the empty P116 samples by incubating them either with foetal bovine serum (FBS) or with high-density lipoprotein (HDL) and then re-purified them by affinity chromatography. Medium containing FBS is a common growing broth for *M. pneumoniae* cultures, although lipoproteins, in particular HDL, are efficient substitutes for serum in mycoplasma culture medium, likely because lipoproteins can provide the key lipids, in particular

cholesterol, which are essential for mycoplasma cells[493] [Washburn L. R. and Somerson N. L., 1979]. We solved the structure of the refilled P116 samples at 3.5-Å resolution using Cryo-EM. The structure of the refilled monomer P116 is practically identical to the structure of the original monomer P116 sample, including densities at the palm of the hand that can be assigned to ligands. Mass spectrometry of the refilled samples shows the clear presence of lipids (**Figure CIV. 2.2_6B**).

CIV. 2.6 Conformational flexibility of P116

The structures of the original P116, empty P116 and refilled P116 samples appear predominantly as homodimers. In all cases, the homodimer exhibits substantial flexibility. Most prominently, the arc diameter of the empty structure is approximately 10 nm smaller than that of the original and refilled structures. In addition, a wringing motion is visible in the refilled structure: each monomer is twisted in the opposite direction along the axis perpendicular to the dimer axis by ~80°, and bends up to 20°, depending on its cargo (**Figure CIV. 2.2_5D and 2.2_3**). In all P116 structures, the N-terminal domain is the most flexible. Within the core domain, temperature factors are higher at the fingertips, indicating movement of the antiparallel α-helices. When the fingers approach the palm, this results in the core domain constricting and a clash with the densities therein.

CIV. 2.7 P116 ligands include essential lipids

We next set out to characterize the possible ligands within P116. We first measured the rate of radioactivity transfer to P116 after incubation with HDL particles containing either tritium-labelled cholesterol ([^{3}H]cholesterol) or tritium-labelled cholesteryl oleate as a representative of cholesterol esters (**Table CIV. 2.7**). A substantial fraction of the [^{3}H]cholesterol-containing HDL radiotracer was detected in the P116 samples that had been incubated with HDL and then separated from it by purification (**Figure CIV. 2.7_1**), indicating a net transfer of both cholesterol and cholesterol ester between HDL and P116. The total absence of the most abundant HDL protein (APOA1), cross-checked by immune detection (**Appendices Table A. CIV. 4.4**), verified that no HDL remnants had contaminated the purified P116 samples.

The highest rate of radiotracer transfer was achieved when [^{3}H]cholesterol-containing HDLs were mixed with empty P116. [^{3}H]cholesterol was also transferred. Transfer of [^{3}H]cholesterol esters to P116 would require a direct interaction between HDL and P116, as these esters are buried in the core of the HDL particles (**Table CIV. 2.7**). Passive cholesterol transport from cellular membranes to HDL or from low-density lipoprotein to HDL has been reported[494] [Phillips

M. C., 2014], but the concept that bacteria can actively extract cholesterol from HDL has not been previously characterized.

Table CIV. 2.7. Relative transfer of cholesterol from HDL to P116. Adapted from Sprankel L. *et al*., 2023.

	% of [^{3}H]cholesterol transferred/mL	Nmol cholesterol transferred/mL/h	nmol cholesterol transferred/mg P116[a]
HDL to empty P116			
Free cholesterol	13.12	13.52	59.49 (6.3)
Esterified cholesterol	6.98	7.22	31.75 (3.3)
HDL to original P116			
Free cholesterol	7.89	7.42	32.63 (3.4)
Esterified cholesterol	6.32	6.01	26.44 (2.8)

[a]Numbers in parentheses are the estimated number of cholesterol molecules transferred per P116 subunit (assuming a molecular weight of ~105 kDa for the construct).

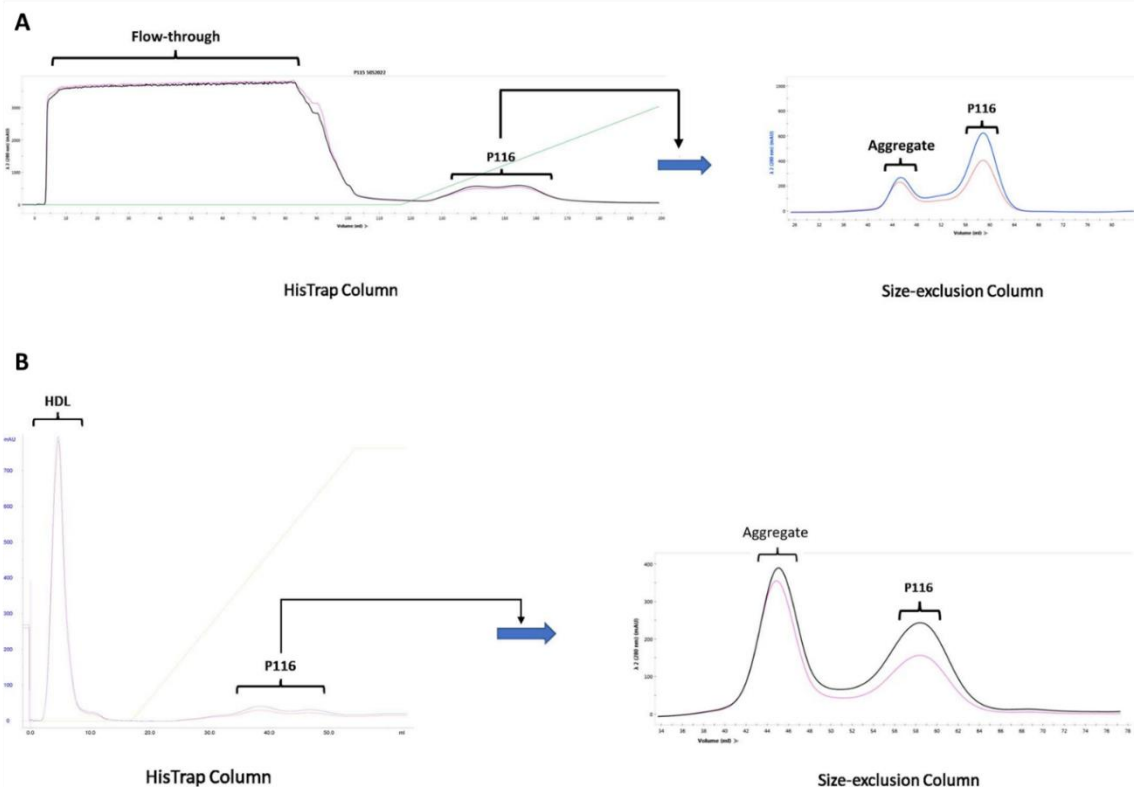

Figure CIV. 2.7_1. His-Traps and Size-exclusion running profiles of the purification. A) Running profile of the purification of the original P116 construct. **B)** Running profile of the separation between P116 and HDL. The green slope indicates the increase of the imidazole concentration during the purification. Adapted from Sprankel L. *et al*., 2023.

We then conducted a detailed matrix-assisted laser desorption/ionization-time of flight (MALDI-TOF) and liquid chromatography electrospray ionization coupled with tandem mass spectrometry (LC-ESI–MS/MS) analysis. We identified more than 500 lipid species in the samples and found striking differences between the original, empty and refilled P116 samples (**Figure CIV. 2.2_6B-D**). In the original P116 sample, the predominant lipid species were PE, PG and wax esters. Wax esters are not known to be required by *M. pneumoniae*, but they were part of the cultivation medium of the *E. coli* strain in which P116 was produced. Incorporation of many lipid species is in agreement with the fact that *M. pneumoniae* adapts its membrane composition to the available lipid spectrum[483–485] [**Razin S. *et al*., 1963; Leon O. and Panos C., 1981; Bittman R., 1993**]. In the empty P116, we observed a substantial reduction of lipids, with no specific lipid class enriched. In the P116 samples refilled from FBS, we observed a clear accumulation of the essential lipid classes phosphatidylcholine (PC) and sphingomyelin (SM), as well as sterols and cholesterol (**Figure CIV. 2.2_6 C, D and Appendices Table A. CIV. 4.4**).

CIV. 2.8 P116 extracts specific lipid classes

To analyse lipoprotein carryover in the FBS-refilled P116, we conducted an additional proteomics LC–MS/MS experiment (data not shown) using ultrasensitive, ion-mobility-assisted LC–MS/MS. In this experiment, we observed limited lipoprotein carryover into the refilled sample. However, on the basis of peptide spectrum match (PSM) numbers and intensity values, we found P116 to be over 30-fold more abundant than the lipoproteins in the refilled sample. If the lipid spectrum in the FBS-refilled P116 sample originated from lipoprotein carryover, we would expect a similar distribution of the lipid classes in both samples. In fact, we observed a specific enrichment of PC and SM in the FBS-refilled sample, whereas TG, the most abundant lipid class in the serum, was decreased and was barely detectable. Thus, although P116 can extract a large range of lipids, it shows a preference for selected lipid species (**Figure CIV. 2.2_6 C,D and Appendices Table A. CIV. 4.4**). We conclude that the lipid composition in the FBS-refilled P116 sample can be attributed predominantly to P116 itself and not to lipoprotein carryover.

CIV. 2.9 P116 binds at defined regions to HDL

Next, we performed Cryo-EM on a sample containing empty P116 and HDL. Of ~58,000 particles that were identified as HDL, ~25,000 were attached to P116. The resulting density at a resolution of 9 Å shows P116 interacting directly with HDL. The structure can be well fitted to the density map. Interestingly, the P116 region between the N-terminal domain and the core interacts with HDL (**Figure CIV. 2.2_6F**). Cryo-electron tomograms of whole *M. pneumoniae* cells indicate that this region faces away from the *M. pneumoniae* membrane and is thus accessible to vesicles and lipids. This presents a possible explanation as to how P116 avoids extracting lipids from the *M.*

pneumoniae membrane itself. However, the unambiguous identification of P116 on the *M. pneumoniae* membrane is challenging owing to the low copy number of P116[49] [Yus, E. *et al.*, 2009], and further experiments are required to better characterize the attachment of P116 with the *M. pneumoniae* membrane (**Figure CIV. 2.9_1**).

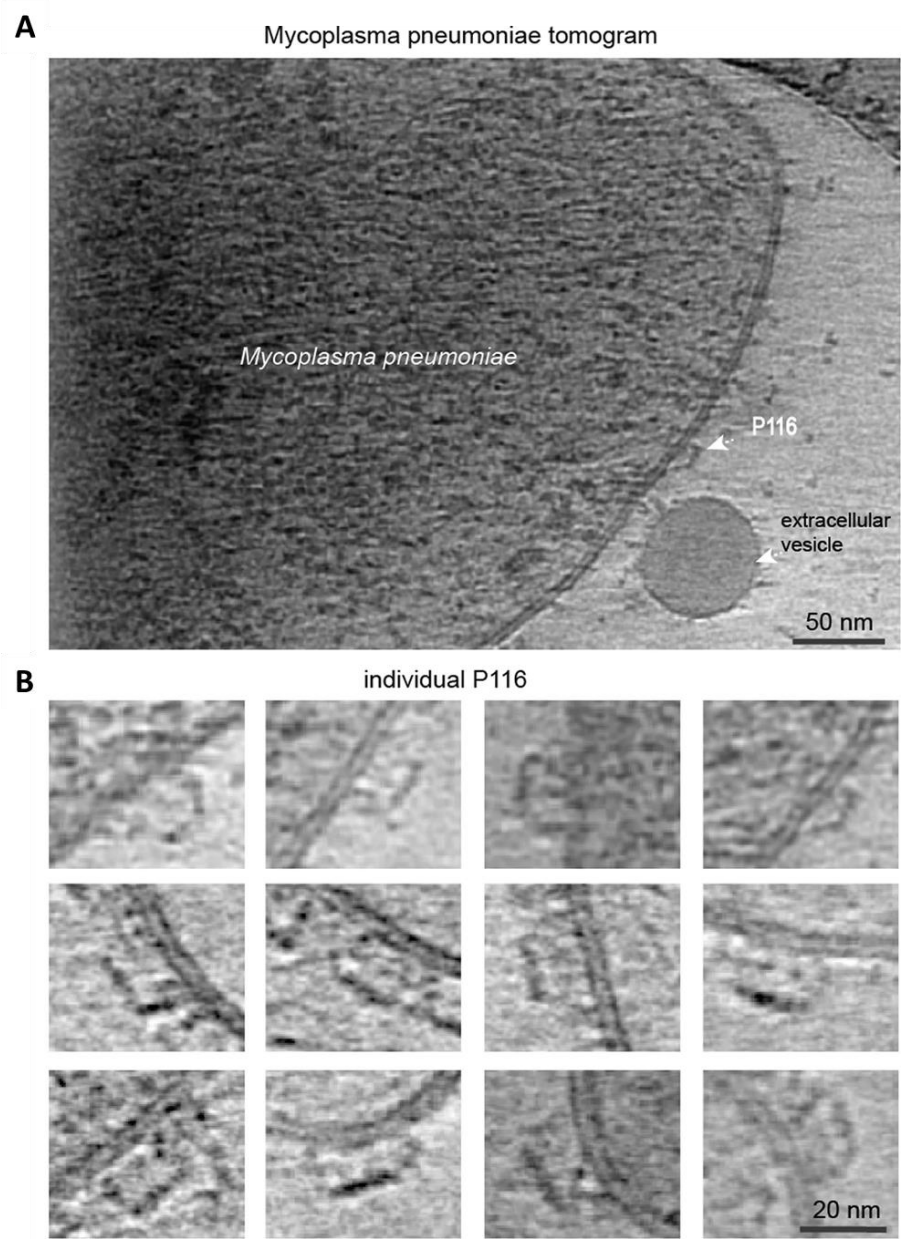

Figure CIV. 2.9_1. Cryo-electron tomogram of a M. pneumoniae cell. A) Representative 10 nm thick slice of a tomographic reconstruction of an individual *M. pneumoniae* cell depicting a possible P116 protein on the surface of the *M. pneumoniae* membrane (One slice from a tomogram is shown – 10 tomograms were recorded). **B)** Gallery of different possible P116 proteins from several tomographic reconstructions depicting P116 attached to the membrane (P116 molecules could be observed from three independent preparations). Tomograms were acquired with a defocus of −3 µm. Adapted from Sprankel L. *et al.*, 2023.

CIV. 3. Discussion

P116 is essential for the viability of the human pathogen *M. pneumoniae*[112] [**Lluch-Senar M. *et al*. 2015**] and is the target of a strong antigenic response in infected people[495] [**Drasbek M. *et al*., 2004**]. The P116 structure has a previously unseen fold with a uniquely large hydrophobic cavity filled with ligands. Mass spectrometry and radioactivity transfer experiments confirm a lipid extraction from serum (FBS) and HDL. Further, the ligands have been identified as essential lipids for the survival of the cells. In fact, we found a high specificity towards cholesterol, PC and SM, which are the most abundant membrane lipids in *M. pneumoniae*[485] [**Bittman R., 1993**]. Crosslinking mass spectrometry studies indicate one weak amino acid-pair interaction between P116 and MPN161 (a protein of unknown function)[496] [**O'Reilly F. J. *et al*., 2020**]. Thus, although the involvement of other proteins in incorporating the extracted lipids into the *Mycoplasma* membrane cannot be excluded, it appears likely, given the observed conformational states upon lipid extraction, that P116 is also responsible for incorporation, thus P116 is responsible for the complete uptake (**Figure CIV. 2.2_6F**). Taken together, the P116 structure and our insights into different P116 conformations and the P116 complex formation with HDL reveal a mechanism by which *Mycoplasma species* extract lipids from the environment and most likely incorporate them into their own membrane.

The transition from a full to an empty P116 molecule involves a ~70% volume reduction of the hydrophobic cavity in concert with a wringing motion of the core domains. During this wringing motion, in which the monomers are each twisted in the opposite direction around their long axis, the hydrophobic cavities face almost opposite directions. Because the N-terminal domain is near the C-terminus, which anchors the protein in the *Mycoplasma* membrane *in vivo*, the core is the domain that experiences the high flexibility seen in our data sets. This flexibility enables an alternating wringing motion whereby one monomer of the core domain faces the *Mycoplasma* membrane (that is, the monomer transferring lipids to the membrane) and the other monomer faces the environment (that is, the monomer extracting lipids from the environment). This wringing motion can be repeated in a continuous manner. In this way, P116 could undergo a rolling movement on the *Mycoplasma* membrane, thus facilitating the transport of cholesterol and other essential lipids in an apparently simple way for lipid transporters (**Figure CIV. 2.2_6F**).

Mycoplasma species have a minimal genome and can incorporate many different lipids into their membranes[483,484] [**Razin S. *et al*., 1963; Leon O. and Panos C., 1981**]. The lipid-binding versatility shown by P116 enables a single molecular system to cope with the transport of diverse lipids required by *Mycoplasma*. Although only *Mycoplasma* shares genes with sequences similar to

that of *p116*, other microorganisms that require uptake of lipids from the environment, including clinically relevant bacterial species such as *B. burgdorferi*, may have similar, as yet undiscovered systems to regulate their cholesterol homeostasis. Whether P116 shares functional similarities with other transfer proteins such as human cholesteryl ester transfer and phospholipid transfer proteins[497,498] [**Zhang L. *et al*., 2012; Zhang M. *et al*., 2018**] requires further investigation. However, the diversity and amount of lipids that P116 can bind appear to be unmatched by any other known prokaryotic or eukaryotic lipid carrier. Interestingly, despite its broad lipid range, P116 still shows a high specificity, largely enriching certain lipids (SM, PC and cholesterol) while excluding others (TGs). This understanding of bacterial lipid uptake presents potential opportunities for treatment of mycoplasma infections and may for the first time[480] [**Jiang Z. *et al*., 2021**] enable the development of a vaccine against *M. pneumoniae*.

CHAPTER V

HETEROLOGOUS EXPRESSION OF *Mycoplasma pneumoniae* MAJOR ADHESINS IN THE CLOSE RELATED SPECIES *Mycoplasma genitalium*

Results described in this chapter have been partially presented in the 25th International Organization for Mycoplasmology Congress (IOM):

Marcos-Silva, M., Vizárraga, D., Fita, I., Pich, O.Q. and Piñol, J. **Heterologous expression of *Mycoplasma pneumoniae* major adhesins in the close related species *Mycoplasma genitalium*.**

HETEROLOGOUS EXPRESSION OF *Mycoplasma pneumoniae* MAJOR ADHESINS IN THE CLOSE RELATED SPECIES *Mycoplasma genitalium*

Mycoplasma pneumoniae (*Mpn*) is a human pathogen that causes primary atypical pneumonia. Elucidation of the tridimensional structure of P1 and P40/P90, the major adhesins of this bacterium, revealed important clues about the function of these proteins essential for infection. The lack of routine tools to introduce targeted mutations in *M. pneumoniae* hinders the construction and evaluation of strains carrying selected cytadhesin variants. To circumvent these problems, we used *Mycoplasma genitalium* (*Mge*) as a surrogate host to express and characterize *M. pneumoniae* adhesins. To this end, target mutations were introduced in P1 and P40/P90 adhesin coding genes which were then used to construct *M. genitalium* strains carrying *M. pneumoniae* adhesin variants for structure-function studies. Several *M. genitalium* mutant strains were obtained by gene replacement methods and transposition: i) a non-adherent Mge^{ad-} strain bearing a deletion of the P140 and P110 coding genes; ii) the Mge^{Mpn} strain is a Mge^{ad-} derivative complemented with the genes coding for WT-P1 and WT-P40/P90; iii) the $Mge^{Mpn\text{-}CS}$ and $Mge^{Mpn\Delta SII}$ strains are Mge^{ad-} derivatives complemented with the alleles coding for WT-P1 and P40/P90 bearing mutations in the cleavage site or a deletion of the insertion loop II (SII), respectively. Adhesin expression was assessed by SDS-PAGE and immunoblotting. Cell morphology was examined by SEM and motility by microcinematography. Cytadherence properties were assessed by flow cytometry and epifluorescence using human red blood cells (hRBCs). Expression of P1 and P40/P90 adhesins in Mge^{Mpn} was confirmed by SDS-PAGE and Western-blotting. These analyses showed that the proteolytic cleavage of P40/P90 was preserved in all mutant strains, suggesting that this adhesin has an auto-processing capacity. Mge^{Mpn} cells were elongated and prone to form small clusters. Introduction of P1 and P40/P90 coding genes restored adhesion properties for hRBCs and motility of Mge^{ad-} cells, suggesting that P1 and P40/P90 are properly folded and functional. However, Mge^{Mpn} cells showed hybrid motile properties, with a gliding velocity comparable to that of *Mge* cells. Adhesion and motile properties of *Mge* cells expressing *Mpn* adhesins indicate that *Mge* is a suitable model to perform structure-function relationship studies. This model could be also helpful to identify mycoplasma factors involved in tissue tropism.

My specific contribution to this chapter:

I have conducted all the experiments described in this chapter. These findings will also be submitted for publication in a peer-reviewed journal.

CV. 1. Introduction

M. genitalium (*Mge*) and *M. pneumoniae* (*Mpn*) have parallel mechanisms for adhesion and gliding, where the Nap emerges as a refined anchoring system to the host target cells[413,432,499] [**Aparicio D. *et al.*, 2018; Aparicio D. *et al.*, 2020; Vizarraga D. *et al.*, 2020**].[102,500] As it has been described in a previous chapter, the Nap is an ensemble of a dimer of heterodimers formed by the cytadhesins P140 and P110 in *M. genitalium*[432,499] [**Aparicio D. *et al.*, 2018; Aparicio D. *et al.*, 2020**]. In *M. pneumoniae* the Nap is formed by theadhesins P1 (homolog to P140 from *Mge*) and P40/P90 (homolog to P110 from *Mge*)[413] [**Vizarraga D. *et al.*, 2020**]. The genes coding for these adhesins, MPN140-MPN141-MPN142, comprise a polycistronic transcriptional unit, which likely facilitates the production of equimolar amounts of the proteins[501,502] [**Inanime J. M. *et al.*, 1988; Waldo R.H. *et al.*, 2006**]. MPN141 encodes the P1 adhesin, a 170 kDa protein comprised of 1627 amino acids[503] [**Inamine J. M. *et al.*, 1988**] while MPN142 encodes a 130 kDa adherence accessory protein comprising 1218 amino acids[504] [**Sperker B. *et al.*, 1991**]. P40/P90 consists of two polypeptides from the proteolytic cleavage of a 130 kDa precursor[504–506] [**Sperker B. *et al.*, 1991; Layh-Schmitt G. and Herrmann R., 1992; Widjaja M. *et al.*, 2015**]. Notably, the predicted 130 kDa precursor is not detectable as it undergoes processing shortly after translation, indicating that the cleavage events are efficient[504,505] [**Layh-Schmitt G. and Herrmann R., 1992; Sperker B. *et al.*, 1991**].

Historically, little attention has been dedicated to P40/P90 and the mechanism of the MPN142 protein cleavage remains unknown[505] [**Layh-Schmitt G. and Herrmann R., 1992**]. Smaller fragments resulting from additional cleavage of the MPN142 polypeptide and with affinity for different host proteins of the extracellular matrix, have also been described[506] [**Widjaja M. *et al.*, 2015**].

It has been previously reported that orthologous gene replacement between different mycoplasma species is possible, but the cytoskeletal protein replaced in this study turned out to not contribute to the different attachment organelle phenotypes that *M. pneumoniae* and *M. genitalium* present[286] [**Relich R. F. and Balish M. F., 2011**]. In this chapter, we are aimed to investigate the possible self-processing of *M. pneumoniae* P40/P90, the importance of this processing for *M. pneumoniae* pathogenesis and if the adhesins are involved in different tissue tropism of *M. genitalium* and *M. pneumoniae*.

CV. 2. Results

CV. 2.1. Construction of a *M. genitalium* strain with a deletion in P140 and P110 coding genes and introduction of genes and gene variants coding for *M. pneumoniae* adhesins

A double mutant strain bearing a deletion of both MG_191 and MG_192 genes was obtained by gene replacement with a selectable marker. This deletion was accomplished by transforming *M. genitalium* cells in the presence of the suicide plasmid pBEΔMG_191/MG_192, which carries a cassette with the chloramphenicol resistance marker and two genomic DNA regions flanking MG_191 and MG_192 genes. The selectable marker in the suicide plasmid was also flanked with *lox* sequences allowing to remove the marker gene by a Cre recombinase approach previously described in chapter I (**Figure CV. 2.1_1**; see Appendices for extended explanation). The obtained strain, designated as *Mge*$^{ad-}$ (**Table CV. 2.1 and Table MM. CV. 1.1.5**), was used as the recipient strain to transform all the pMTnPac plasmids bearing the genes and gene variants coding for *M. pneumoniae* adhesins (**Appendices Table A. CV. 5.2_1**). The presence of the unmarked deletion in *Mge*$^{ad-}$ strain was confirmed by PCR and direct genome sequencing (data not shown).

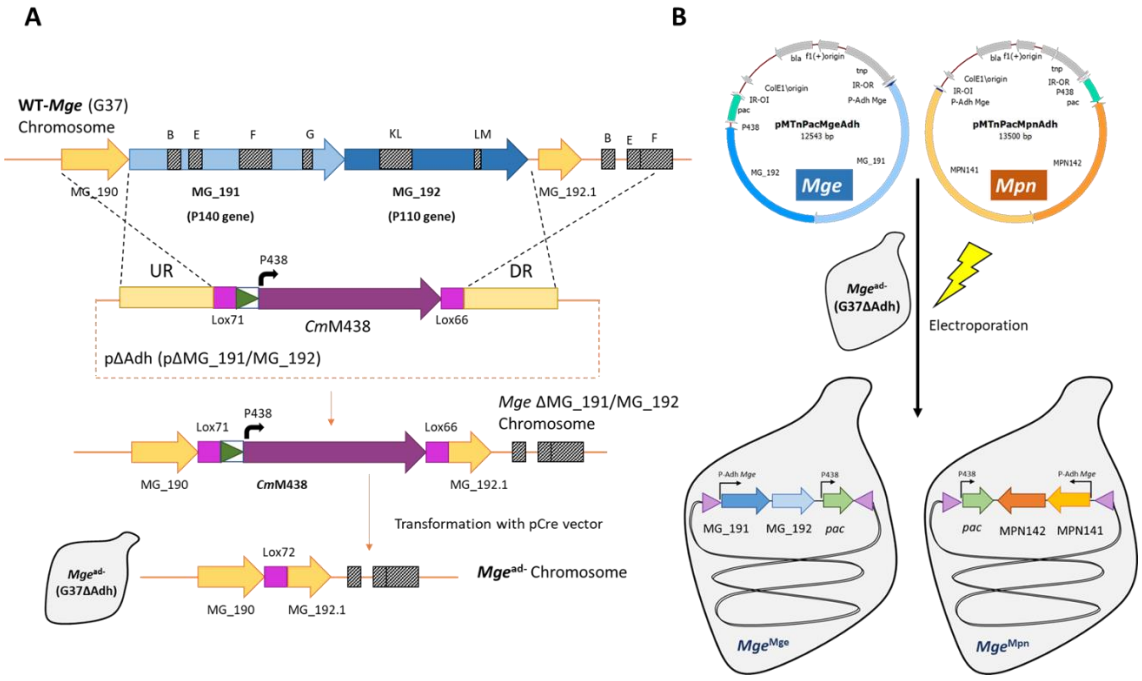

Figure CV. 2.1_1. Schematic representation of the process followed to generate the G37ΔAdh surrogate host (*Mge*$^{ad-}$) and the complemented mutant strains (*Mge*^{Mge} and *Mge*^{Mpn}). A) The upstream and downstream regions (UR and DR) of the adhesin genes, as well as the *Cm*M438 selectable marker, were PCR-amplified. Then, the three amplicons were joined by Splicing by Overlap Extension (SOE) PCR and cloned into an *Eco*RV-digested pBE plasmid. The resulting suicide plasmid (pΔAdh) was transformed into G37 (WT) *Mge* cells to generate a *Mge* null mutant by allelic exchange (*Mge*$^{ad-}$). **B)** The adhesins genes

from *Mge* (pMTnPacMgeAdh) or *Mpn* (pMTnPacMpnAdh) were re-introduced into the *Mge*$^{ad-}$ strain using the pMTnPac minitransposon[507] [Torres-Puig S. *et al.*, 2015].

For control purposes, the MG_191 and MG_192 wild-type (WT) alleles from the chromosome of *M. genitalium* G37 strain were subsequently reintroduced into the G37ΔAdh null mutant strain by transposon delivery to create the complemented strain (*Mge*^{Mge}). To this end we used the pMTn*Pac*[507] [Torres-Puig S. *et al.*, 2015] minitransposon (MiniTnp), which carries both genes (pMTn*Pac*MgeAdh) under the control of its own promoter (see methods for further details) and the puromycin resistance selection marker gen. At the same time and by the same methodology, the MPN141 and MPN142 wild-type (WT) alleles from the chromosome of *M. pneumoniae* MPN129 strain were also reintroduced into the G37ΔAdh null mutant strain to create the strain (*Mge*^{Mpn}). To this end, we also used the pMTn*Pac*MpnAdh minitransposon (MiniTnp), which carries the two *M. pneumoniae* adhesin genes under the control of the *M. genitalium* MG_191 native promoter (see methods for further details). The presence of the different transposon insertions was confirmed by PCR and direct genome sequencing (see below).

Table CV. 2.1. Strains used in this chapter.

Strain Name	Genotype	Reference
G37	*Mycoplasma genitalium* Wild-type	NCTC:10195 (ATCC 33530)
MPN129 (WT-*Mpn*)	*Mycoplasma pneumoniae* Wild-type	ATCC 29342
ΔMG_191	Deletion of the MG_191 gene by allelic exchange (G37 ΔMG_191::*tet*M438)	Burgos R. *et al.*, 2006
ΔMG_192	Deletion of the MG_192 gene by allelic exchange (G37 ΔMG_192::tetM438)	Burgos R. *et al.*, 2006
G37ΔAdh (*Mge*$^{ad-}$)	Deletion of the MG_191 and MG_192 genes by allelic exchange (G37ΔMG_191-ΔMG_192::Lox72)	This work
G37ΔAdh::COM (*Mge*^{Mge})	Re-introduction, by transposon insertion, of a MG_191 and MG_192 wild-type alleles in a G37ΔAdh mutant (G37ΔAdh MG_RS01600 (327226)::MTnPacMG_191/MG_192)	This work
G37ΔAdh::MPN (*Mge*^{Mpn})	Re-introduction, by transposon insertion, of a MPN_141 and MG_142 wild-type alleles in a G37ΔAdh mutant (G37ΔAdh MG_281 (343662)::MTnPacMPN_141/MPN_142)	This work
G37ΔAdh::MPN-CS (*Mge*$^{Mpn-CS}$)	Re-introduction, by transposon insertion, of a MPN_141 and MG_142 alleles bearing P40/P90: R445S-A446S-R455S-A456S substitutions in a G37ΔAdh mutant (G37ΔAdh MgPar7 (313199)::MTnPacMPN_141/MPN_142-R445S-A446S-R455S-A456S)	This work

G37ΔAdh::MPN ΔSII (*Mge*^{MpnΔSII})	Re-introduction, by transposon insertion, of a MPN_141 and MG_142 alleles bearing P40/P90: L395-T414 deletion in a G37ΔAdh mutant (G37ΔAdh MG_067 (82408)::MTnPacMPN_141/MPN_142-ΔL395-T414)	This work
G37ΔMG_317 (ΔHMW3)	MG_317 truncated gene by pMTntetM438 transposon insertion	Pich O. Q. *et al.*, 2009

CV. 2.2. Characterization of the complemented strains obtained: Protein expression and cell growth rate of *M. genitalium* complemented strains

For each transformation with the pMTn*Pac*Adh minitransposons, several colonies were picked, propagated and analyzed. We found that *Mge*^{Mge} (carrying *Mge* adhesins) and *Mge*^{Mpn} (carrying *Mpn* adhesins) strains showed protein profiles comparable to their respective WT-*Mge* and WT-*Mpn* counterpats (**Figure CV. 2.2_1A**). In both cases, adhesin expression was apparent.

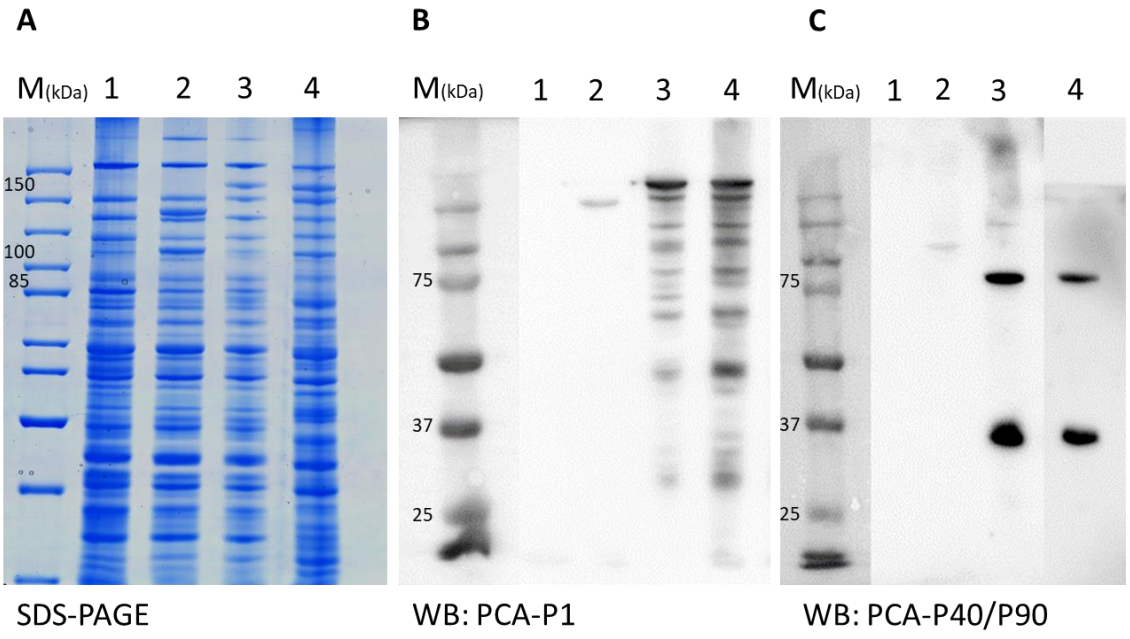

Figure CV. 2.2_1. Characterization/Protein profiles and adhesin expression of the WT and complemented strains. A) SDS-PAGE of whole cell lysates from 1. *Mge*$^{ad-}$ (G37ΔAdh); 2. WT-*Mge* (G37); 3. *Mge*^{Mpn} (G37ΔAdh::MPN); 4. WT-*Mpn* (MPN129)**. B)** Western Blot (WB) analysis using whole-cell lysates and the polyclonal antibodies (PCA) obtained against the *M. pneumoniae* P1. **C)** Western Blot (WB) analysis using whole-cell lysates and the polyclonal antibodies (PCA) obtained against the *M. pneumoniae* P40/P90.

We observed that *Mge*^{Mpn} cultures grew slower than those of the WT-*Mge* or WT-*Mpn* reference strains. Therefore, to evaluate the presence of possible growth defects in the *Mge*^{Mpn} cells, we

calculated the duplication times of all the strains under study (**Figure CV. 2.2_2**). For this purpose, we used the colorimetric assay previously reported by Karr J. R. *et al.* and colleagues[419] [**Karr J. R. *et al.*, 2012**] with some modifications [420] [**Martínez-Torrò C., 2020**]. The duplication times for WT-*Mge* *Mge*^{Mge} and WT-*Mpn* strains were between 8.2 and 8.8 hours. However, as we anticipated, the duplication time for *Mge*^{Mpn} was significantly higher (10.02 ± 0.64 h) than for the other strains tested (**Figure CV. 2.2_2**). Of note, several *Mge*^{Mpn} clones were analyzed and exhibited the growth delay, regardless of the transposon insertion site (**Appendices Table A. CV. 5.2_2**).

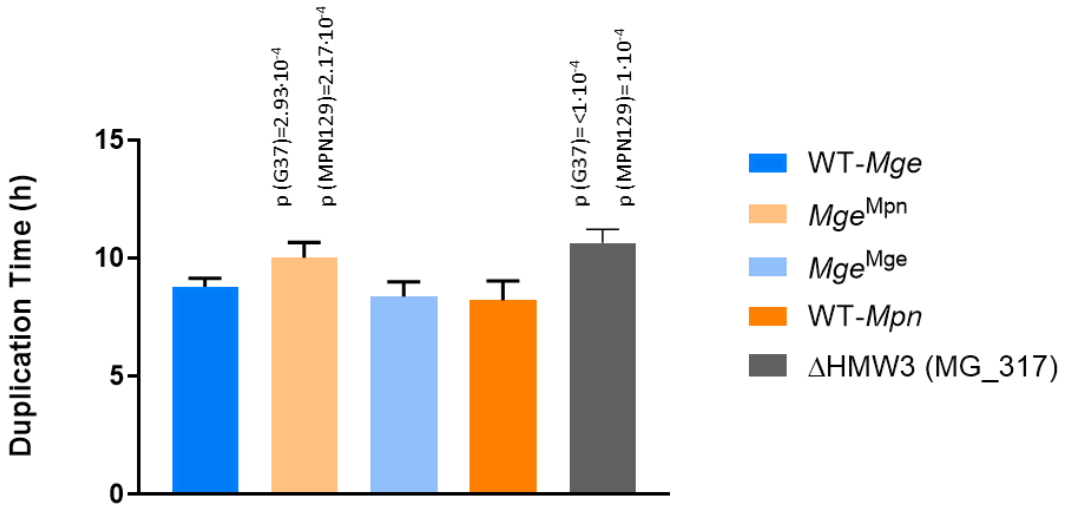

Figure CV. 2.2_2. Growth rate of *M. genitalium* (WT-*Mge*), *M. pneumoniae* (WT-*Mpn*) reference, and complemented strains. The duplication time data was collected after several independent biological repeats. Statistical significance was assessed using a paired T-test and statistically significant values (p-value< 0.05) are stated above the upper standard error bar of each strain.

CV. 2.3. Assessment of the cytadherence capacity of *M. genitalium* strains expressing P1 and P90/P40.

Then, we wondered whether the slow growth exhibited by the *Mge*^{Mpn} strain could be due to defects in cell adhesion, because of cell adhesion and gliding motility play a significant role in cell division, as it has been previously described [336,337] [**Lluch-Senar M. *et al.*, 2010; Martínez-Torrò C. *et al.*, 2021**]. In addition, longer duplication times are observed in many strains with adhesion defects previously isolated in our lab. For instance, the strain ΔMG_317 with a deletion of HMW3 cytadherence related protein[508] [**Pich O.Q. *et al.*, 2008**] has a duplication time of 10.64 ± 0.20 h.

In previous works in our laboratory and as it was described in a previous chapter, we demonstrated the suitability of a FACS-based hemadsorption (HA) assay to quantify and compare the cytadherence capacity of *M. genitalium* mutants[383,409] [**García-Morales L. *et al.***

2014; Aparicio D. *et al*. 2018] (see methods for further procedure explanation). The resulting Flow Citometry (FC) data can be later modelled using a kinetic approach, allowing the quantification of the HA activity of a particular mycoplasma strain by standard K_d and B_{max} parameters[409] [Aparicio D. *et al*. 2018]. Like other kinetic analyses performed on binding reactions involving a ligand and a receptor, the lower K_d and the higher B_{max} are indicative of the stronger HA activity of the tested mycoplasma cells. Herein, we used FACS to assess binding of the *Mge*^{Mge} and *Mge*^{Mpn} strains.

Cells from the *Mge*^{Mge} strain showed a HA parameters very similar to those exhibited by WT-*Mge* cells (**Figure CV. 2.3_1**). This result indicates that the ectopic copies of MG_191 and MG_192 reintroduced in this mutant complementthe non-adherent phenotype. On the other hand, while WT-*Mpn* cells show similar K_d values than WT-*Mge* cells, they present lower B_{max} values. This result suggests that *M. pneumoniae* adhesins bind red blood cells as strongly as *M. genitalium* adhesins, but *M. pneumoniae* cells might be somewhat heterogeneous in their adhesin content when compared to *M. genitalium* cells[509] [García-Morales L. *et al*. 2014]. In contrast, *Mge*^{Mpn} cells exhibit (**Figure CV. 2.3_1 and Table CV. 2.3 and Appendices Table A. CV. 5.3**) higher K_d values than WT-*Mge* and WT-*Mpn* cells, indicating that the heterologous copies of P1 and P90/P40 expressed in the surrogate host do not bing to the erythrocytes as strongly as their counterparts in *M. pneumoniae*. This result might be indicative of the presence of folding defects in the heterologous copies of P1 and P90/P40 adhesins or that these adhesins are not completely functional in *M. genitalium*. However, these defects are not critical for protein function since the heterologous copies of P1 and P90/P40 are still able to attach to erythrocytes.

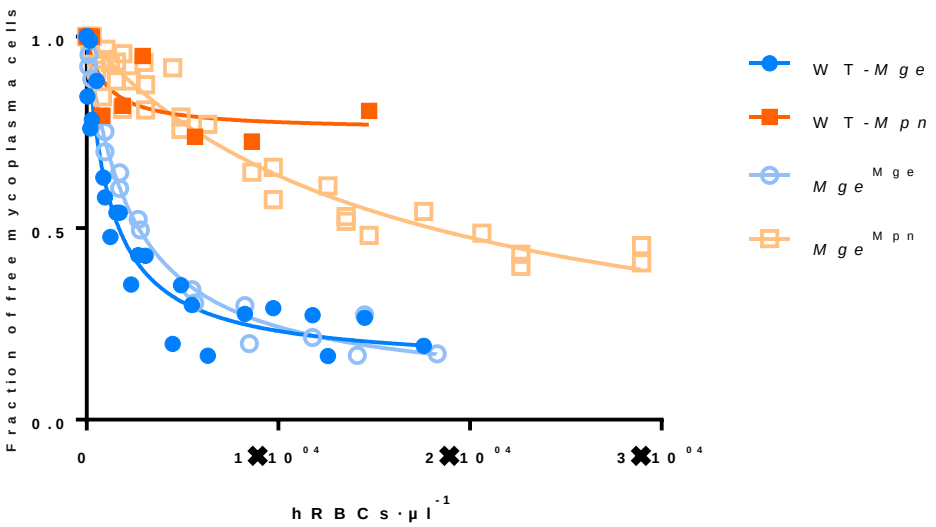

Figure CV. 2.3_1. Quantitative analysis of the cytadherence capacity of G37 (WT-*Mge*), MPN129 (WT-*Mpn*), *Mge*^{Mge} and Mge^{Mpn} complemented mutant strains. The graphic shows the inverse Langmuir plots from hemadsorption (HA) assays[409] [García-Morales L. *et al.*, 2014] by FACS analysis, using a fixed amount of mycoplasma cells and increasing amounts of human red blood cells (hRBCs).

Table CV. 2.3 and Appendices Table A. CV. 5.3. Summary table with the K_d, B_{max} values and other characteristics of all mutant strains analysed in Chapter V.

Strain	K_d values ± SE	B_{max} values ± SE	Affected HA parameter (vs WT-*Mge*)	Affected HA parameter (vs WT-*Mpn*)	Flask-Adherent	Adhesins expression levels[a]
G37 (WT-*Mge*)	$1.2x10^3$±$2.6\ x10^2$	0.86±0.05	-	↑ B_{max}	Yes	4
MPN129 (WT-*Mpn*)	$1.0x10^3$±$1\ x10^3$	0.24±0.06	↓ B_{max}	-	Yes	4
G37ΔAdh::COM	$1.5x10^3$±$2.8\ x10^2$	0.90±0.04	-	↑ B_{max}	Yes	4
G37ΔAdh::MPN	1.6x104±$3.2\ x10^3$	0.95±0.10	↑ K_d, ↑ B_{max}	↑ K_d, ↑ B_{max}	Yes	4

[a] Illustrative value scale from 0 (without adhesins) to 4 (WT).

CV. 2.4. Time-lapse cinematographic studies of the of *M. genitalium* strains expressing P1 and P90/P40

To further test the function of the heterologous copies of P1 and P90/P40 we examined the gliding activity of cells from the different mutants described above by time-lapse microcinematography (**Table CV. 2.4**). Compared to WT-*Mge*, WT-*Mpn* reference strain glide at higher speed, but the percentage of motile individual cells is lower (**Table CV. 2.4**). Cells from the complemented *Mge*^{Mge} mutant strain are completely motile and comparable with the WT-*Mge* reference strain. On the other hand, *Mge*^{Mpn} motile cells glide at a speed similar to that shown by cells of the WT-*Mge* strain. However, *Mge*^{Mpn} cells show a frequency of non-motile cells comparable with the WT-*Mpn* reference strain (**Figure CV. 2.4_1**). Interestingly, *Mge*^{Mpn} cells glide describing circular paths with a frequency very similar to that exhibited by cells from WT-*Mge* reference strain and higher than cells from WT-*Mpn* reference strain. All these observations led us to conclude that *Mge*^{Mpn} presents a hybrid behavior in terms of motility. We should keep in mind that cell aggregates are not motile. In addition, it was also noticeable in microcinematographies *Mge*^{Mpn} and WT-*Mpn* cells an increased frequency of non-motile paired cells that might be reminiscent of cells in cytokinesis previously found in *M. genitalium* mutants of the cell division operon[336,337] [Lluch-Senar M. *et al.*, 2010; Martínez-Torrò C. *et al.*, 2021]. All

these data taken together suggest that the presence of adhesion defects in *Mge*^{Mpn} cells are not critical for cell motility and heterologous copies of P1 and P90/P40 can support the gliding motility in *M. genitalium* cells.

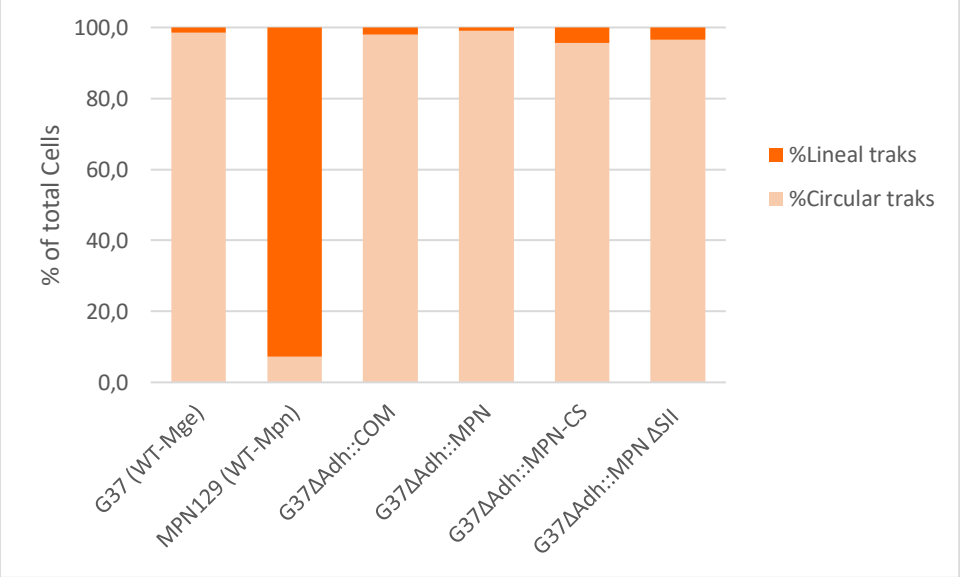

Figure CV. 2.4_1. Characterization of the motile properties in the WT reference and all complemented and mutant strains. Percentage of cells describing circular and non-circular tracks.

Table CV. 2.4. Gliding motility parameters of *M. genitalium* G37 and *M. pneumoniae* wild-type cells and all different complemented and mutant strains obtained.

Strain	n (Motility)	Individual Motile cells (%)	n (Velocity)	Velocity (µm/s)[a]	Circular Tracks (%)	Non-circular Tracks (%)
G37 (WT-*Mge*)	~500	95.9	25	0.122±0.002	98.6	1.4
MPN129 (WT-*Mpn*)	~500	75.8	25	0.290±0.011	7.3	92.7
G37ΔAdh::COM (*Mge*^{Mge})	~500	94.0	25	0.124±0.003	97.9	2.1
G37ΔAdh::MPN (*Mge*^{Mpn})	~500	72.4	25	0.101±0.005*	99.1	0.9
G37ΔAdh::MPN-CS (*Mge*$^{Mpn-CS}$)	~250	54.4	25	0.105±0.006*	95.7	4.3
G37ΔAdh::MPN ΔSII (*Mge*^{MpnΔSII})	~250	81.7	25	0.108±0.005*	96.6	3.4

[a]Velocities are shown as mean values +/- standard error. n=25 biologically independent cells, from different fields, different preparations and different microcinematographies.

*Statistically significant values ($T(25) = 2.06$; $p<0.05$). Statistical significance was assessed with the Paired Student's two-sided T-test. WT-*Mpn* p-values: $4.29 \cdot 10^{-13}$, $6.34 \cdot 10^{-14}$ and $1.17 \cdot 10^{-13}$; WT-*Mge* p-values: $1.35 \cdot 10^{-3}$, 0.01 and 0.03 (Table order).

CV. 2.5. Characterization of the complemented strains obtained: Adhesion inhibition assay with polyclonal antibody against *M. pneumoniae* P1 (PCA P1)

To further test the function of the heterologous copies of P1 and P90/40 we have examined if antibodies against these adhesins can block the gliding motility of *Mge*^{Mpn} cells in the same way that block the movement of WT-*Mpn* cells. In the absence of P1 polyclonal antibodies, *Mge*^{Mpn} and *Mge*^{Mge} motile cells glide during all the observation time. In the absence of antibodies, a small frequency of *Mge*^{Mpn} motile cells detached spontaneously, similar to what happens to WT-*Mpn* reference strain cells^{510} [**Sprankel L. *et al.*, 2023**]. PCA P1 polyclonal antibodies have no impact on WT-*Mge* and *Mge*^{Mge} motile cells. As expected, these antibodies stopped the movement of WT-*Mpn* and *Mge*^{Mpn} (**Table CV. 2.5**). Most of the non-motile cells remained attached to the surface during the observation period. However, some cells from from WT-Mpn and *Mge*^{Mpn} strains detached after movement was prevented by PCA P1 antibodies.

Table CV. 2.5. Motile and adhesion effect after adding polyclonal antibodies (PCA) against *M. pneumoniae* P1 adhesin.

	Before[#]	After[#]		
PCA P1	**%Motility ± SE**	**%Motility ± SE**	**RT_{50} (min) ± SE[&]**	**% Detached cells ± SE**
WT-Mge	93.23±0,26	81.93±0.29	NA	NA
WT-*Mpn*	89.43±0.65	1.80±1.80	4.65±1,19	72.30±2.38
WT-*Mpn* Negative Control[$]	87.42±1.24	66.94±4.75	NA	59.93±4.34
***Mge*^{Mge}**	94.68±0.26	88.51±0.17	NA	NA
***Mge*^{Mpn}**	45.78±4.24	0.00±0.00	2.67±0.00	5.69±0.32

All values are shown as mean values +/- standard error from three different and independent microcinematographies.

[$] Negative control. PBS with no antibody was added.

[#] Measurements made "before" or "after" adding antibodies or a control PBS solution.

(NA): Not applicable. (–): Not performed. SE: standard error.

[&] RT_{50} is the antibody incubation time required to stop the movement of 50% of motile cells.

CV. 2.6. Morphological characterization of the strains expressing heterologous *M. pneumoniae* adhesins

Cells from all the strains were analyzed by Scanning Electron Microscopy (SEM). *Mge*^{Mge} cells have a morphology very similar to WT-*Mge* cells, showing the characteristic flask-shape morphology and a unique TO (**Figure CV. 2.6_1**). Interestingly, *Mge*^{Mpn} cells show an elongated shape and a high % of the cells presenting multiple TOs, a similar morphology that exhibit the cells. Interestingly, most of the paired cells that were detected above by microcinematography also exhibit multiple TOs. It has been previously described that the presence of multiple terminal TOs is the consequence of the early duplication of the TO before the cell can complete the cytokinesis process and might be indicating the presence of adhesion defects in this cell[246] [**Pich O.Q. *et al.*, 2006a**] (**Figure CV. 2.6_1**). In addition, *Mge*^{Mpn} cells shows, the presence of large cell aggregates typically found in *M. genitalium* cells with motile defects[410] [**Burgos R. *et al.*, 2006**], and similar to that is found when examining cells from WT-*Mpn* strain (**Figure CV. 2.6_2**).

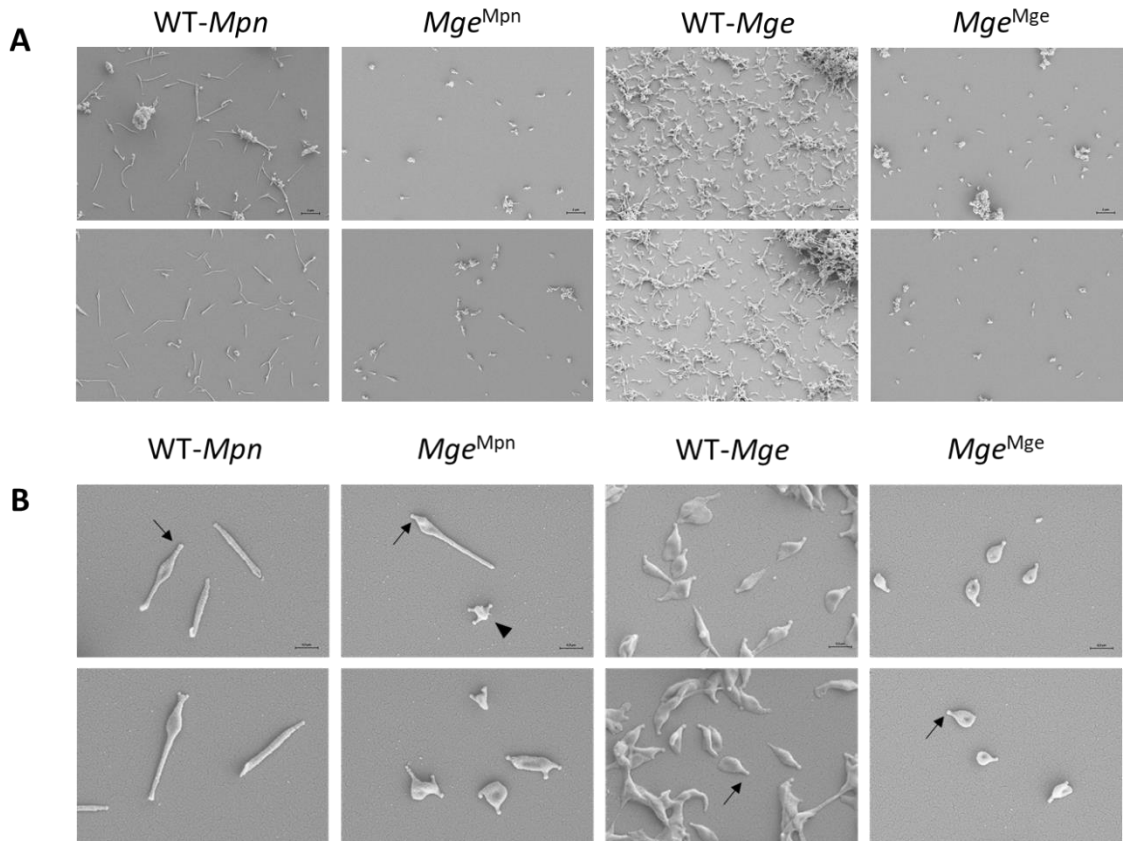

Figure CV. 2.6_1. Scanning Electron Microscopy (SEM) micrograph of the wild-type and the complemented strains. A) SEM micrographs as a general view, taken from afar. **B)** More in detail SEM micrographs, taken closer. Arrows point to the Terminal Organelle (TO) of the cells. Arrowheads point to a cell with multiple TOs.

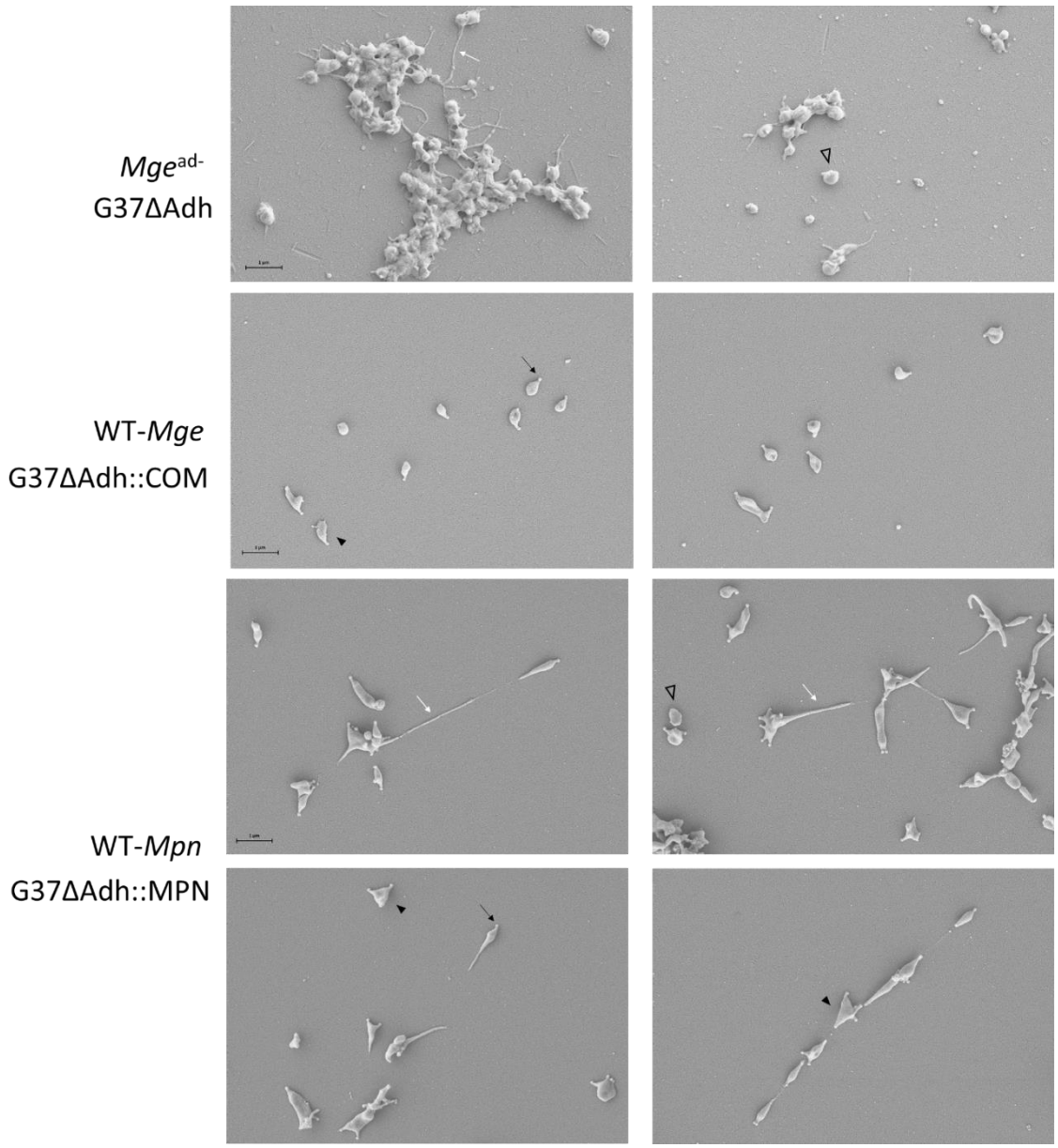

Figure CV. 2.6_2. Scanning Electron Microscopy (SEM) micrograph of the wild-type and the complemented strains. Black arrows point to the Terminal Organelle (TO) of the cells. Arrowheads point to a cell with multiple TOs. The empty arrow heads point to cells with spherical shape, characteristic of the non-adherent strains as the *Mge*$^{ad-}$ (G37ΔAdh) strain generated. White arrows point to the filaments observed.

CV. 2.7. Proteolytic processing P40/P90 adhesin in *M. genitalium*

Expression of P1 and P40/P90 in the strains under study was assessed by Western Blotting using polyclonal antisera to P1 and P40/P90 (**Figure CV. 2.2_1B,C**). We found that the proteolytic cleavage of P90/P40 adhesin was preserved in t*Mge*^{Mpn} strain (**Figure CV. 2.2_1C**). This result raised important questions regarding the molecular mechanisms by with the *M. pneumoniae* P40/P90 is cleaved proteolytically, as it is a process still uncharacterized. It is important to mention that the orthologous protein P110 from *M. genitalium* does not suffer any processing after its expression[383] [**Aparicio D. *et al.*, 2018**].

When examining the sequences and the 3D structure of P110, P40/P90 adhesins, we found two extra insertions that correspond to disordered regions of P40/P90[413] [**Vizarraga D. *et al.*, 2020**] (**Figure CV. 2.7_1**). Furthermore, it is in the second insertion (designated as SII region) where the two proteolytic cleavage sites might be located (**Figure CV. 2.7_1**). Therefore, we decided to generate and characterize an additional *Mge*$^{ad-}$ complemented strain bearing a double point mutation of the residues of the cleavage site (R445-A446 and R455-A456) and another *Mge*$^{ad-}$ complemented strain bearing a complete deletion of the insertion II (SII) (**Table CV. 2.1**).

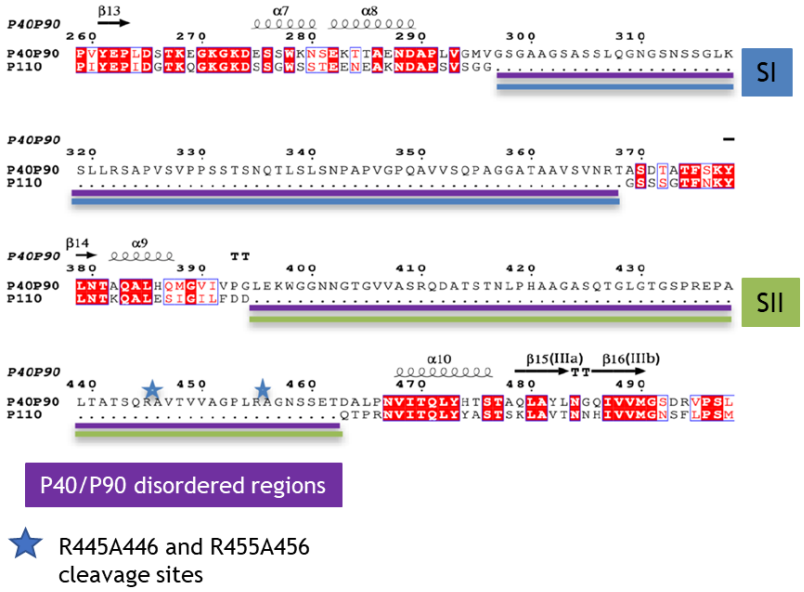

Figure CV. 2.7_1. Structural sequence alignment of P40/P90. Specific part of the structural sequence alignment obtained by the superposition between P40/P90 and the orthologous protein P110 from *M. genitalium* and represented with program Espript[511] [**Robert X. and Gouet P., 2014**]. The DSSP assignment of secondary structure elements for P40/P90 are represented above the sequence, as squiggles (α-helices), arrows (β-strands) and TT (turns). Missing residues, corresponding to disordered regions of P40/P90 in the X-ray structure[413] [**Vizarraga D. *et al.*, 2020**], are indicated with a purple line. The long insertions 1 and 2 (named as SI and SII) are underlined in blue and green, respectively. The two blue stars correspond to the R445-A446 and R455-A456 cleavage sites. Adapted from **Vizarraga D. *et al.*, 2020**.

Following the same approach used to obtain the *Mge*^{Mpn} strain, P90/P40 gene variants with the target mutations were introduced by transposon delivery in a *M. genitalium* null mutant *Mge*$^{ad-}$ to obtain isogenic strains bearing Arg and Ala to Ser double point mutations of the cleavage site residues and the P40/P90 SII deletion (**Appendices Table A. CV. 5.2_1 and Table MM. CV. 1.1.5**). The new mutant strains, designated *Mge*$^{Mpn-CS}$ and *Mge*$^{Mpn-\Delta SII}$, also present a similar protein profile as the WT-*Mpn* reference strain (**Figure CV. 2.7_2A and 2.7_3A**). Unexpectedly, proteolytic cleavage of P40/P90 is also preserved in *Mge*$^{Mpn-CS}$ and *Mge*$^{Mpn-\Delta SII}$ (**Figure CV. 2.7_2B and 2.7_3B**). These results reinforce the auto-processing capacity of *M. pneumoniae* P40/P90.

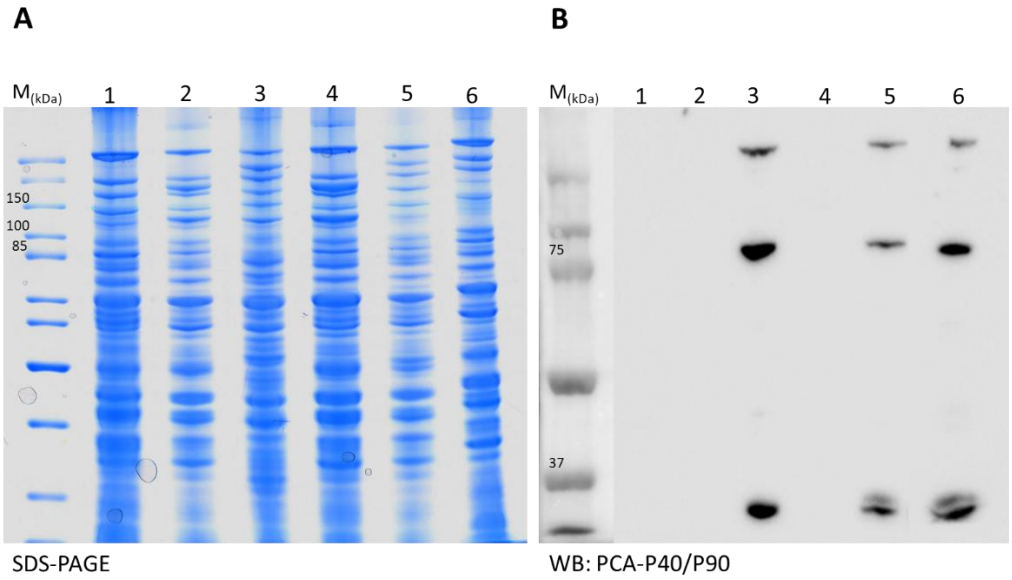

Figure CV. 2.7_2. Characterization/Protein profiles and adhesin expression of the WT and complemented mutant strains. A) SDS-PAGE of whole cell lysates from 1. *Mge*$^{ad-}$ (G37ΔAdh); 2. WT-*Mge* (G37); 3. WT-*Mpn* (MPN129); 4. *Mge*^{Mge} (G37ΔAdh::COM); 5. *Mge*^{Mpn} (G37ΔAdh::MPN); 6. *Mge*$^{Mpn-CS}$ (G37ΔAdh::MPN-CS)**. B)** Western Blot (WB) analysis using whole-cell lysates and the polyclonal antibodies (PCA) obtained against the *M. pneumoniae* P40/P90.

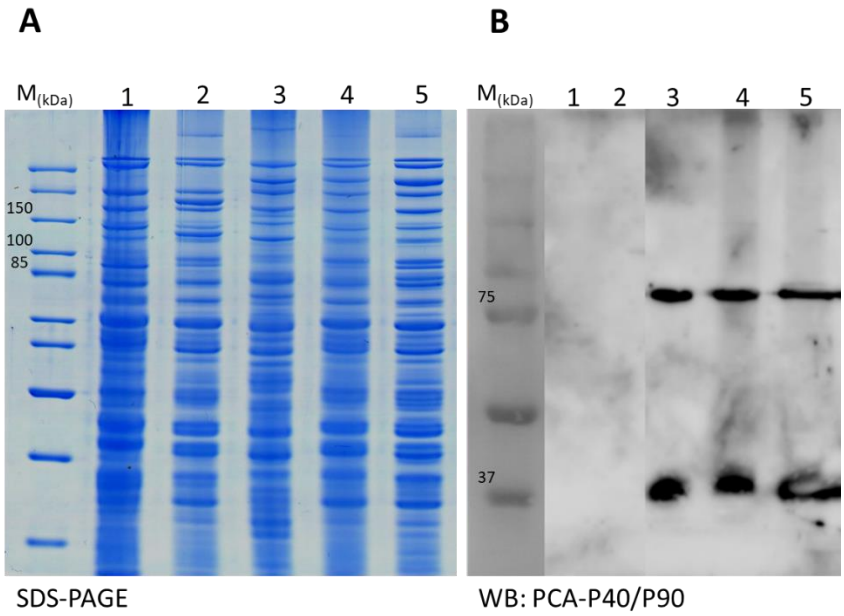

Figure CV. 2.7_3. Characterization/Protein profiles and adhesin expression of the WT and complemented mutant strains. A) SDS-PAGE of whole cell lysates from 1. *Mge*$^{ad-}$ (G37ΔAdh); 2. WT-*Mge* (G37); 3. WT-*Mpn* (MPN129); 4. *Mge*^{Mpn} (G37ΔAdh::MPN); 5. *Mge*^{MpnΔSII} (G37ΔAdh::MPN ΔSII)**. B)** Western Blot (WB) analysis using whole-cell lysates and the polyclonal antibodies (PCA) obtained against the *M. pneumoniae* P40/P90.

We also examined the gliding activity of cells from the two complemented mutant strains by time-lapse microcinematography (**Table CV. 2.4**). As what was observed for the *Mge*^{Mpn} complemented strain, *Mge*$^{Mpn-CS}$ and *Mge*$^{Mpn-ΔSII}$ motile cells glide at a speed more similar to the WT-*Mge* strain. As expected, *Mge*$^{Mpn-ΔSII}$ cells show a frquency of non-motile cells between the values of the two reference strains. However, *Mge*$^{Mpn-CS}$ cells show a significantly low number of motile cells. In addition, *Mge*$^{Mpn-CS}$ and *Mge*$^{Mpn-ΔSII}$ cells glide describing high frequency of circular tracks compared with WT-*Mpn* cells and similar to the one described by cells from WT-*Mge* strain (**Figure CV. 2.4_1**). These results suggest that mutations introduced do not impact the function P40/P90 adhesins.

CV. 3. Discussion

Here we show that the major adhesins from *M. penumoniae*, P1 and P40/P90, are functional when expressed in *M. genitalium*. This result demonstrates the potential use of *Mge* as a surrogate host to study the function of the adhesin proteins from other pathogenic mycoplasmas from the pneumoniae cluster. This strategy might facilitate the analysis of adhesin function (wild type and mutant variants) in a convenient bacterial context, with the advantage that transformation of *Mge* is much easier than in other mycoplasma species and that the tools for genetic engineering of this bacterium are consistent and reliable.

It has been described that cleavage of the P40/P90 polypeptide chain occurs *in vitro* at two exposed Arg–Ala motives (Arg445–Ala446 and Arg455–Ala456) located in the central part of the N-terminal domain, producing two polypeptide chains that can correspond to the P40 and P90 subunits found *in vivo*[504,505] [**Layh-Schmitt G. and Herrmann R., 1992; Sperker B. *et al.*, 1991**] (**Figure CV. 2.7_1**). Recently, it has been suggested that cleavage of P40/P90 is a self-proteolytic process [462] [**Vizarraga D. *et al.*, 2020**]. However, the residues responsible for this enzymatic activity have not been found yet. After the autoproteolytic processing, P40/P90 continues to behave as a single globular protein structurally similar to P110, in agreement with the extensive interface between the P40 and P90 polypeptides and the very stable ensemble they form[413] [**Vizarraga D. *et al.*, 2020**]. However, P40 is located at the outer surface part of the Nap and due to the absence of covalent bonds might become separated from P90 and from the Nap complex under stringent or denaturing conditions. The loss of P40 only in certain conditions could explain the discrepancies in the past about whether P40 was part of the adhesion complex.

Clevage of the MPN142 preprotein (130kDa) into the P40/P90 polypeptides typical of *Mpn* is still observed upon expression in *Mge*. This is important because P110 from Mge is not processed, which might be due to the lack of the corresponding proteolytic enzyme. Moreover, MPN142 cleavage was still observed in mutants *Mge*$^{\text{Mpn-CS}}$ and *Mge*$^{\text{Mpn-ΔSII}}$ strains (**Table CV. 2.1**), mutants in witch the proteolytic cleavage site has been removed, reinforcing the auto-processing capacity P40/P90 adhesin. In other words, the proteolytic processing of P40/P90 in *Mge*$^{\text{Mpn-ΔSII}}$ strain suggests the absence of a specific cleavage site in this adhesin, contrary to that is currently though. This result is in accordance with the importance of the proteolytic processing because it is also critical for function in many virulence factors like viral hemagglutinins[512] [**Russell, C.J. *et al.*, 2018**], for $N_{\omega}V$ eukaryotic viral capsid maturation[513,514] [**Jinghua Tang *et al.*, 2014; John E. Johnson *et al.*, 2021**] and FrpC and FlhB bacterial proteins[515–517] [**Minamino T. and Macnab R.M., 2000; Sadilkova L. *et al.*, 2008; Ann-Catrin B. *et al.*, 2009**]. In addition, it has been found that the residues implicated in this enzymatic activity are normally glutamic acid and aspartic

acid residues located very close to the cleavage site [Matsui T. *et al.*, 2009]. Interestingly, the cleavage site found in the *M. pneumoniae* P40/P90 is surrounded by these residues (**Figure CV. 3.1_1**), specially Glu110 and Asp463.

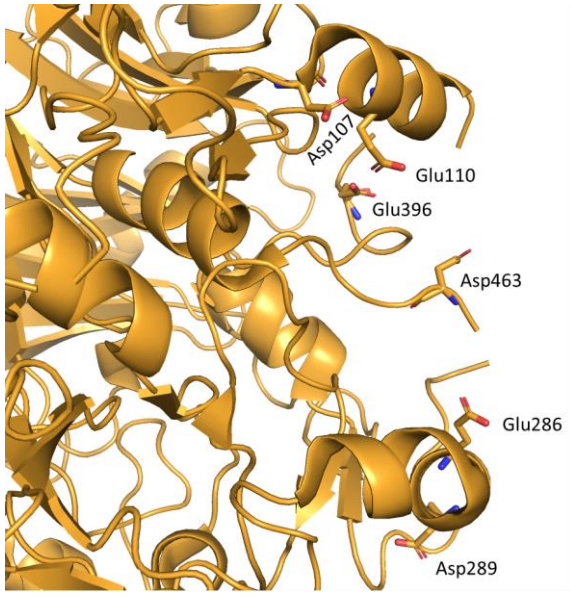

Figure CV. 3.1_1. *M. penumoniae* P40/P90 N-terminal 3D structure. Glutamic acid (Glu) and Aspartic acid (Asp) residues closed to the cleavage site present in P40/P90 are highlighted. PDB: 6RJ1[413] [Vizarraga D. *et al.*, 2020].

Gliding of mycoplasmas from the pneumoniae cluster, including *Mge* and *Mpn*, is thought to be caused by a mechanism where the force, generated by ATP energy[331] [Mizutani M. and Miyata M., 2019], is transmitted to the Nap that appears to work as a leg/ foot on the surface of the mycoplasma cell[269,271,324,326,412,518–520] [Miyata M. and Hamaguchi T., 2016; Nishikawa M. S. *et al.*, 2019; Seto S. *et al.*, 2005; García-Morales L. *et al.*, 2016; Miyata M., 2008; Seybert A. *et al.*, 2018; Nakane D. *et al.*, 2015; Kawamoto A. *et al.*, 2016]. Gliding of *M. pneumoniae* cells is always in the direction of the attachment organelle, which indicates that the gliding machinery, including the Naps at the cell surface, should provide a well-defined directionality. Scanning electron microscopy images from *Mge*^{Mpn} mutants also revealed that cells coupled by the filaments mentioned before, are always oriented in opposite directions, a configuration characteristic of dividing mycoplasma cells. Altogether, these observations suggest that cytokinesis is impaired in *M. genitalium* complemented strain with gliding motility defects that could also explain the growth delay that this strain present (**Figure CV. 2.2_1**). In addition, locomotion clearly contributes to cell dispersion in adherent mycoplasmas, a fact that is supported by the formation of large cell aggregates in liquid flask-cultures of mutants with

gliding deficiencies[432,521] [Pich O.Q. *et al.*, 2006a; Aparicio D., *et al.*, 2020], also observed in the *Mge*$^{Mpn-CS}$ and *Mge*$^{Mpn-\Delta SII}$ complemented mutant strains.

Heterologous expression of P1 and P40/P90 coding genes restored adhesion to hRBCs and motility of *Mge*$^{ad-}$ cells, suggesting that P1 and P40/P90 are functional. However, analysis of the hRBCs binding kinetics reveals higher K_d values in *Mge*^{Mpn} than in the WT-Mge and WT-*Mpn* strains. In addition, *Mge*^{Mpn} cells, and *Mge*$^{Mpn-CS}$ and *Mge*$^{Mpn-\Delta SII}$ mutant cells showed some motile defects when compared to the WT-*Mpn* or WT-*Mge* reference strains (**Table CV. 2.4**). These observations have several possible explanations. The most obvious one is the presence of some folding defect/s in P1 and P40/P90 adhesins when expressed in *Mge*. In fact, *Mge and Mpn* possess a unique TopJ chaperone specific for adhesin trafficking and recycling[287] [Cloward J. M. and Krause D. C., 2011]. In this scenario, TopJ chaperone from *Mge* might not be as efficient when dealing with P1 and P40/P90 as the native TopJ from Mpn. Alternatively, the particular adhesion properties of *Mge*^{Mpn} might also be due to non-proper interactions with the accessory cytadhesion proteins from *Mge*. These interactions are likely mediated by the intracellular C-terminal domain of the adhesins and are critical for protein function[277] [Pich O. Q. *et al.*, 2009]. When examining the sequences of P110 and P40/P90, conspicuous divergences are found in the C-terminal ends of these adhesins (**Figure CV. 3.1_2**). Considering also the striking similarities in adhesion, cell morphology and motility between the *Mge*^{Mpn} strain and strains with short versions of the C-terminal end of P110[277] [Pich O. Q. *et al.*, 2009], it is plausible that interactions C-terminal end of P40/P90 with the cytoskeletal proteins of *Mge* might not suffice for a normal function when this adhesin is expressed in this microorganism. Interestingly, this hypothesis is fully testable and replacing the C-terminal end of P40/P90 by the C-terminal end of P110 should restore the full function of P40/P90 in *Mge*^{Mpn} cells.

Figure CV. 3.1_2. Clustal-O sequence alignments. A) Sequence alignment fragment of the *M. pneumoniae* P1 and *M. genitalium* P140 C-terminal. E1, Engelman motif localized in the transmembrane region. **B)** Sequence alignment fragment of the *M. pneumoniae* P40/P90 and *M. genitalium* P110 C-terminal. E2 and E3, Engelman motifs localized in the transmembrane region.

Integration of previous structural knowledge with the *in vivo* functional data obtained in this work provides important clues for a better understanding of the functioning of Naps in *Mge and Mpn*, although many questions remain open about the adhesion and gliding motility mechanisms. The possibility to express mycoplasma adhesins in a surrogate host opens a new framework allowing structure-function studies otherwise difficult species such as *Mpn*. Studying the adhesion and gliding mechanism of this pathogen in *Mge* could also be helpful to identify mycoplasma factors involved in tissue tropism. These results can help in the development of vaccines and therapeutics for inhibiting the infectivity of this respiratory pathogen.

GENERAL DISCUSSION

GD. 1. General Discussion

GD. 1. General discussion

The Nap complex is a macromolecular structure specialized in cytadherence. It is composed of the P110 and P140 adhesins in *M. genitalium*, and P40/P90 and P1 in *M. pneumoniae*[70,299,353,432] [**Burgos R. *et al*., 2006; Scheffer M. P. *et al*., 2017; Aparicio D. *et al*., 2020; Vizarraga D. *et al.*, 2020**]. In this work we try to expand the mechanistic knowledge of these complexes using different structural and *in vivo* approaches.

The tridimensional structure of the Nap from *M. genitalium*, described in chapter I, indicates a loose interface between P140 and P110 heterodimers in the extracellular region, suggesting that the subunits are held together mainly by interactions in the intracellular and transmembrane regions. This important result is consistent with the recent structural advances of P1 and P40/P90 structures of *M. pneumoniae*[432] [**Vizarraga D. *et al*., 2020**].

Most membrane proteins have transmembrane domains made up of bundles of hydrophobic alpha-helices. The lateral association of transmembrane helices within the lipid bilayer is a key stage in the folding of membrane proteins. It may also play a role in signalling across cell membranes. Based on this observation, in chapter III we have investigated by mutational analysis the possible contributions of the "GXXXG" Engelman motifs, found in the transmembrane region of adhesins, to the organization and functioning of the Nap complex. Mutations in these highly conserved Engelman motifs, has been found to alter adhesion and motility, providing important clues about the possible dimer formation mechanism of these adhesins. This behaviour could be similar to thar observed in some eukaryotic cell adhesion receptors. Integrins are also heterodimeric transmembrane proteins formed by noncovalent association of an α and a β-subunit. Each subunit contains a large extracellular domain, a single transmembrane spanning α-helix and a short cytoplasmic tail[522] [**Carman C. V. and Springer T. A., 2003**]. Different types of α integrins can combine with different β counterparts, forming a variety of heterodimers. The way in which transmembrane integrin homomeric interactions take place is by an interaction that also involves a "GXXXG" Engelman motif[523] [**Arkin I. T. and Brunger A. T., 1998**].

In chapters I and III, we have also found that Naps undergo large structural rearrangements, thereby alternating between "open" and "closed" conformations, which are associated with attachment and release to the cell receptor, respectively. To avoid been trapped in the overall most stable state, the cycling between "open" and "closed" conformations would require a net input of energy at the level of every Nap. The binding site in P110 could be regulated by the interaction with P140 as found in *M. pneumoniae*[353] [**Vizarraga D. *et al*., 2020**]. This may be the reason why P1 of *M. pneumoniae*, was expected to contain the binding site. In the Cryo-EM map

of P1, the weak density of the C-terminal domain indicates flexibility with respect to the N-terminal domain proving that P1 can experience significant conformational changes[353] [**Vizarraga D. *et al*., 2020**]. This is consistent with the structure of the complex of *M. pneumoniae* adhesin P1 and the Fab fragment from the monoclonal antibody P1/MCA4, determined in this work. The P1/MCA4 epitope involves residues of the C-terminal domain of P1 only and is totally inaccessible in the "open" (ready for binding to SOs) conformation of the Nap complex. Therefore, for the P1/MCA4 epitope to be exposed, the adhesion complex has to experience a major rearrangement with respect to the "open" conformation, pivoting around static P40/P90 subunits anchored by interactions of their Engelman motifs. The conformation where P1/MCA4 binds must be unsuitable for attachment to SOs, as binding of antibody P1/MCA4 slows and induces detachment of moving *M. pneumoniae* cells only. Therefore, although P40/P90 and P110 contain the binding site to the sialic acid cell receptors, P1 and P140 have still to be seen as a major player in the Nap functioning during gliding and also in the adhesion to host cells of *M. pneumoniae* and *M. genitalium,* respectively. Moreover, proteins others than the Nap components, including accessory proteins of the terminal organelle, or PrpC/PrkC, are known to be essential for binding and gliding[278,303,305,306,363,418] [**Chang H. Y. *et al*., 2011; Hasselbring B. M. *et al*., 2012; Page C. A. & Krause D. C. 2013; Romero-Arroyo C. E. *et al.* 1999; Burgos R. *et al*., 2007; García-Morales L. *et al*., 2016**]. These proteins might support functioning and conformation of the Naps to play its roles.

The presence of several residues with a potential regulatory role makes the Nap complex an excellent candidate to integrate the signals from different external and internal stimulus and to provide a response by modulating the gliding motility and cytadherence capacity of mycoplasma cells. Unfortunately, how the Nap could internalize and transmit the signals to intracellular effectors is still unknown. However, we have found phosphosites in P110 and P140, and together with the phenotype characterization of these phosphorylated residues mutant strains obtained, could help in understanding the cross-talk communication between extra- and intracellular regions. All these results ttogether reinforce the view that the Nap complex is not a passive element to attach mycoplasmas to the gliding surfaces and reveal that adhesins are able to modulate the mycoplasma movements.

In chapters I, II and III, we have taken advantage of the structural data recently obtained to design and generate different *M. genitalium* strains with mutations in key residues of these proteins. Our results reveal that cythadherence capacity and gliding motility of this bacterium can be modulated by introducing single amino acid substitutions in P110 and P140. Of note, residues located outside of the sialic acid receptor binding site, are also important to sustain adherence and motility.

Gliding of *M. pneumoniae* cells is always in the direction of the attachment organelle, which indicates that the gliding machinery, including the Naps at the cell surface, should provide a well-defined directionality. To achieve a directional gliding, the release of the sialylated receptors is as essential as the binding because mycoplasma cells cannot move forward if they remain anchored to the surface receptors where they have first attached. In the Nap, the conformational changes required by the foot/leg activity during gliding have to be synchronized with the binding/release to the cell receptors, which are thought to be randomly distributed on the host surface. Many mycoplasmas, including *M. genitalium* and *M. pneumoniae*, have curved terminal organelles and draw circular paths when they glide over solid surfaces[265] [**Hatchel J. M. and Balish M. F., 2008**]. Since gliding is essential for infection on mucosal surfaces[310] [**Jordan J. L. *et al*., 2007**] and the curvature of *M. genitalium* terminal organelle correlates well with the diameter of the circular tracks[276] [**Burgos R. *et al*., 2008**], this type of movement could be important for mycoplasma pathogenicity. Interestingly, some mutant strain presented in this work, shows an increased amount of cells describing circular paths, also with a reduced diameter when compared to that exhibited by WT cells. All these results together reinforce the view that the Nap complex is not a passive element to attach mycoplasmas to the gliding surfaces and reveal that adhesins are able to modulate the mycoplasma movements.

The alarming increase of antibiotic resistance makes a search for alternative means of fighting these bacterial infections imperative. Adherence of *M. genitalium* and *M. pneumoniae* to host target epithelial cells is one of the initial stages of the infectious process and as for other bacteria, it represents a key step in pathogenesis. Of note, bacteria adhered to cell surfaces are better able to acquire nutrients, further enhancing their ability to survive and infect the host. Therefore, the use of agents that interfere with the ability of bacteria to adhere to eukaryotic cells represents an attractive approach to combat bacterial infections. Remarkably, because anti-adhesive agents are not bactericidal, the propagation and spread of resistant strains is much less likely to occur than as a result of exposure to antibiotics.

In chapter II of this work, we have reported the atomic-level characterization of the structural features governing the recognition of sialoglycan ligands by the main cytadhesins from *M. pneumoniae* and *M. genitalium*, defining the molecular basis of ligand specificity of these bacterial virulence factors. Although the two cytoadhesins show different binding sites and shapes, P110 and P90/P40 similarly recognize *N*- and *O*-glycans, showing similar epitopes. In all predicted complexes, the sialic acid is the residue that principally contributes to the binding. Thus, these data demonstrate that the mode of action of *Mycoplasma* cytoadhesins is very different from that of bacterial adhesins, such as Siglec-like streptococcal adhesins, despite a remarkable topological similarity with their sugar binding site[438,447] [**Di Carluccio C. *et al*., 2021;**

Di Carluccio C. *et al.*, 2024]. In the light of this finding, we could integrate the structural information obtained unravelling the molecular basis for sialoglycan recognition and ligand specificity. This analysis will enable the design of species-specific anti-adhesive compounds. In this regard, the use of saccharides structurally similar to those of the bacterial receptor ligand for anti-adhesion therapy has been widely documented; these receptor analogues act by competitive binding inhibition. The first study demonstrating the anti-adhesive efficacy of a saccharide-based host receptor analog describes the use of methyl alpha-D-mannopyranoside to prevent colonization of the urinary tract of mice by *Escherichia coli*[524] [Aronson M. *et al.*, 1979]. Likewise, patients with acute otitis externa positive for *Pseudomonas aeruginosa* were treated by local administration of a mixture of galactose, mannose and N-acetylneuraminic acid[525] [Beuth J. *et al.*, 1996]. A few years later, Dubois and colleagues successfully treated rhesus monkeys naturally infected by *Helicobacter pylori* with sialyl-3'-lactose, a specific inhibitor of adhesion of this pathogen to human gastric tissue culture cells[526] [Mysore J. V. *et al.*, 1999]. Overall, these results demonstrate that saccharide receptor analogues offer a safe and effective strategy for treating a variety of bacterial infections. However, despite the many beneficial attributes associated with anti-adhesion therapy, there are downsides to this approach that need to be overcome before anti-adhesion could gain broad validity in the treatment of a wide range of infections. One of the main practical problems in the use of competition-based anti-adhesion inhibitors is to achieve high enough avidity to efficiently compete with bacteria, which often carry hundreds of adhesion molecules on their surface. In keeping with this, the concentration of carbohydrates required for effective inhibition of adhesion *in vitro* are usually high, in the millimolar range. As it has been achieved in this work, getting a better knowledge of the molecular bases of the cytadhesin-ligand recognition will be helpful in future studies to improve the screening for sialoglycan-based analogues. These molecules could present increased specificity and binding affinity for the cytadhesin, allowing the development of more efficient competitive binding inhibitors as anti-adhesion therapy for mycoplasma infections.

In addition to their roles in cytadherence and motility, *M. pneumoniae* and *M. genitalium* adhesins are immunodominant proteins and constitute the main target of host antibodies during infection[223,225,228,527–529] [Ma L. *et al.*, 2015; Wood G. E. *et al.*, 2013; Wood G. E. *et al.*, 2017; Atkinson T. P. *et al.*, 2008; Chourasia B. K. *et al.*, 2014; Jacobs E. *et al.*, 1990]. Comparatively, P1 and P40/P90 from *M. pneumoniae* present many sequence insertions, which amount to more than 200 extra residues in each protein, with respect to their orthologues P140 and P110 in *M. genitalium*. Interestingly, most of the insertions correspond to disordered regions in the structures of the *M. pneumoniae* proteins[353] [Vizarraga D. *et al.*, 2020]. The

comparative study done in this work of P1 and P140 reveals that both adhesins share similar immunogenicity properties, and provides several polypeptide candidates to be used for *M. genitalium* serological diagnostic. Additionally, the sequence identity between P40/P90 and P1 from *M. pneumoniae*, and P110 and P140 from M. *genitalium*, increases from the N-terminal to the C-terminal domain, becoming highest in the transmembrane and cytoplasmic regions (43%). The increased variation of the sequences from the most exposed regions of the Nap, the N-terminal domains, can reflect specific attachment and motility requirements but also a mycoplasma survival strategy related with enhanced antigenic variability. This fact, together with the presence of multiple copies of the adhesin genes in the genomes of several mycoplasmas supports the hypothesis that in each species, the adhesin genes may have evolved to mediate adherence to different hosts and tissues.

Finally, described in chapter V, we have found that the major adhesins from *M. pneumoniae*, P1 and P40/P90, are functional in *M. genitalium*. Thus, demonstrating that *M. genitalium* could be used as a surrogate host to express and characterize *M. pneumoniae* adhesins, opening a new framework for new structure-function studies otherwise difficult in *M. pneumoniae*, and which could be also helpful to identify mycoplasma factors involved in tissue tropism.

M. pneumoniae P116 is also a strongly immunogenic protein[495] [**Drasbek M. *et al*., 2004**], thus also making it a promising target for therapeutics[490] [**Svenstrup H. F. *et al*., 2002**]. In chapter IV of this work, we have reported the structural and functional characterization of P116. This protein was originally reported to contribute to host-cell adhesion and is an essential protein for the viability of *M. pneumoniae* cells[112] [**Lluch-Senar M. *et al*. 2015**].

Unlike the Nap complex, that concentrates at the tip structure of the cells, we observed that P116 are distributed uniformly across the whole surface of the *M. pneumoniae* cells and adhesion and motility were unaffected when adding antibodies against this protein. The P116 structure has a previously uncharacterized fold with a lipid-accessible cavity, in which a diversity of lipids can be bound, confirming the capacity of P116 to extract lipids from serum. Interestingly, despite its broad lipid range, P116 still shows a high specificity, largely enriching certain lipids such us sphingomyelin (SM), phosphatidylcholine (PC) and cholesterol, which are the most abundant membrane lipids in *M. pneumoniae*[485] [**Bittman R., 1993**].

Taken together, the P116 structure and our insights into different P116 conformations and the P116 complex formation with HDL reveal a mechanism by which *Mycoplasma species* extract lipids from the environment and most likely incorporate them into their own membrane. This system appears to be unmatched by any other known prokaryotic or eukaryotic lipid carrier[497,498] [**Zhang L. *et al*., 2012; Zhang M. *et al*., 2018**], and requires further investigation.

Integration of previous structural knowledge, the information obtained from the different structural approaches and with the *in vivo* functional data obtained in this work provides important clues for a better understanding of the functioning of Naps in *M. pneumoniae* and *M. genitalium*. Although many questions remain open about the adhesion and gliding motility mechanisms. Our results about the role of mycoplasma adhesins, indicate critical residues for the Nap functioning. These results, together with previous studies showing the potential of pneumococcal adhesin based vaccines[530] [**Seo J-Y. *et al*., 2002**], pave the way to the development of effective vaccines and alternative strategies of anti-adhesion therapies based on blocking the first stages of the infection by mycoplasmas from the *pneumoniae* cluster. Development of non-antibiotic therapies is essential when an increase number of reports, that manifest the failing of antibiotics in the treatment of infections with these microorganisms, is depicting a severe thread for public health in the next years.

CONCLUSIONS

CHAPTER I: STRUCTURE AND MECHANISM OF THE NAP ADHESION COMPLEX FROM THE HUMAN PATHOGEN *Mycoplasma genitalium*

- The Nap is composed by two P140-P110 heterodimers and undergoes large structural rearrangements, alternating between "open" and "closed" conformations.
- The "open" conformation corresponds to an *in situ* abundant state, ready-to-bind to sialylated cell receptors. The "closed" conformation corresponds to an *in situ* less abundant state, where the tight interaction of the extracellular regions of P140 and P110 occlude the cell receptor binding site.
- Unique or double substitutions in residues within potassium pocket of P110 have an important impact on the cytadherence and motility properties of *M. genitalium*.

In vivo characterization of the P110-W838F mutant reveals an important role for potassium ion in the regulation of P110 activity and gliding motility in *M. genitalium*.

- *In vivo* analyses of the P110-R834G mutant indicate the presence of cells with heterogeneous amounts of adhesins.
- Double substitution H381A-H382A in P140 modifies the cytadherence and motility properties of *M. genitalium*.
- P1 and P140 adhesins share similar immunogenicity properties.
- Epitopes of six P1 mAbs inhibiting adhesion and patient's sera are located mainly in exposed areas of the surface of P1 adhesin.
- P1-like epitopes are located mainly exposed in the surface of P140, suggesting that they are also accessible to the antibodies.
- P140 amino acid sequences homologous to most P1 epitopes could be useful for *M. genitalium* serological diagnostic.

- Five specifics threonine and serine of *M. genitalium* P140 and six specifics threonine and serine of P110 adhesins had been found to be phosphorylated *in vivo*.

- Reversible phosphorylation events play an important role in *M. genitalium* gliding motility.

- G37ΔMG_109 mutant strains present a significant high duplication time compared with the wild-type strain.

- Cells from G37ΔMG_109 mutant strain (*prkC M. genitalium* KO mutant) glided at approximately half the frequency of wild-type cells.

CHAPTER II: MOLECULAR BASIS OF BACTERIAL LECTINS RECOGNITION OF EUKARYOTIC GLYCANS: THE CASE OF *Mycoplasma pneumoniae* AND *Mycoplasma genitalium* CYTOADHESINS

- Adhesins P110 and P40/P90 recognize *N*- and *O*-glycans bearing α-2,3 and α-2,6 sialic acid and the binding epitopes of these ligands has been defined by STD-NMR.

- The binding of P110 and P40/P90 adhesins is based in extensive and predominant interactions with the sialic acid (Neu5Ac-AcHN moiety) and both adhesins share similar ligand-protein interactions characteristics

-The sialic acid anchors the ligand to the binding site of the proteins.

- The majority of the interactions involved mainly the Neu5Ac residue whereas the other sugar units did not significantly contribute to the binding process.

- In the bound state, the glycosidic linkage between sialic acid and galactose of 3'SLn ligand adopts specific conformations according to the values of the Φ dihedral angle around the Neu5Ac-α-(2,3)-Gal linkage, explaining the high binding affinity for this ligand.

- In the bound state the glycosidic linkage between sialic acid and galactose of 6'SLn ligand is in equilibrium between different conformations according to the values of the Φ and ω dihedral angle around the Neu5Ac-α-(2,3)-Gal linkage.

- Molecular dynamics simulations indicate that the P110 adhesin is stabilized in the presence of the potassium (K^+) ion.

CHAPTER III: DYNAMICS OF THE NAP COMPLEX AND ADHESION MECHANISMS OF THE HUMAN PATHOGENS *Mycoplasma pneumoniae* AND *Mycoplasma genitalium*

- Large conformational rearrangements occur in P1 of motile cells. However, only small or no conformational changes seem to occur in P40/P90 during the Nap attachment/detachment cycle associated with the “open /closed” conformations.
- The P1/MCA4-Fab binds to a structural epitope centered around the Thr1426-Asp1438 segment which is fully located in the C-domain of P1.
- The P1/MCA4-Fab structural epitope becomes accessible to antibodies only when the Nap is in the "closed" conformation.
- GxxxG motif present in P140’s transmembrane domain seems to not contribute in the dimerization process of the Nap complex.
- Engelman motifs E2 and E3 from P110 (P40/P90 homologue) are essential for cell adhesion.
-The large rearrangements that take place in the C-domain of P1 during the attachment/detachment cycle of a Nap require also displacements of the transmembrane helix. Such back and forth displacements might allow a cross-talk communication between extra- and intracellular regions.

CHAPTER IV: ESSENTIAL PROTEIN P116 EXTRACTS CHOLESTEROL AND OTHER INDISPENSABLE LIPIDS FOR *Mycoplasmas*

- P116 protein from *Mycoplasma pneumoniae* is not involved in cell adhesion.
- P116 protein structure from *M. pneumoniae* has a novel “five fingers” fold.
- P116 is able to extract lipids from bovine serum and human HDL.
- The N-terminal domain of P116 is near the C terminus, which anchors the protein on the mycoplasma membrane.
- The P116 core is a very flexible domain that enables alternating wringing motion.
- P116 could undergo a rolling movement on the mycoplasma membrane, thus facilitating the transport of cholesterol and other essential lipids from the environment to the cell membrane.
- P116 has affinity for a broad range of lipids, with a preference for sphingomyelin, phosphatidylcholine and cholesterol.

CHAPTER V: HETEROLOGOUS EXPRESSION OF *Mycoplasma pneumoniae* MAJOR ADHESINS IN THE CLOSE RELATED SPECIES *Mycoplasma genitalium*

- The major adhesins from *Mycoplasma pneumoniae* P1 and P40/P90 are functional in *Mycoplasma genitalium,* allowing structure-function studies otherwise difficult in *M. pneumoniae*.
- The adhesion and motile defects observed in *M. genitalium* cells expressing *M. pneumoniae* adhesins, might be explained by the different amino acid sequences in the C-term ends of P1 and P40/P90 adhesins.
- P40/P90 is proteolytically processed in *M. genitalium*, which is consistent with the auto-processing activity described for this adhesin.
- The chimeric *M. genitalium* strain expressing *M. pneumoniae* adhesins represents a suitable model to determine the factors involved in tissue tropism.

MATERIALS AND METHODS

MM. 1. Biologic Material

MM. 2. DNA manipulation

MM. 3. Protein Analysis Methods

MM. 4. Time-lapse microcinematography

MM. 5. Quantification of the hemadsorption of *Mycoplasma* strains

MM. 6. Epifluorescence Microscopy

MM. 7. Electron Microscopy

MM. 8. Crystallography and X-ray structure

MM. 9. Protein-Ligand interaction analyses

MM. 10. Growth Analysis

MM. 1. Biologic Material

MM. 1.1. Bacterial strains

All bacterial strains used in this work are listed below. *E. coli* strains were preserved in LB medium with 15% glycerol (v/v) at -80ºC. *M. genitalium* strains were kept in SP4 medium without adding glycerol at -80ºC, as the high concentration of foetal bovine serum present in the culture medium acts as a cryoprotector.

Table MM. 1.1. *Escherichia coli* strains used in this work.

Escherichia coli	
XL1-Blue	Strain used for cloning purposes. It is deficient in recombination and has a high transformation efficiency. *end*A1 *gyr*A96(nal^R) *thi*1 *rec*A1 *rel*A1 *lac gln*V44 *hsd*R17(r_k^- m_k^+) F' [::Tn10 *pro*AB$^+$ *lac*I^q Δ(*lac*Z). It is resistant to nalidixic acid and tetracycline.
	Strain used for cloning manipulations.
BL21(DE3)	Strain used for recombinant protein expression. It contains the RNA polymerase from phage T7 under the control of the lacUV5 promoter sequence, which is inducible with IPTG. This feature allows high expression levels of genes cloned under the control of the T7 promoter, present for example in pET protein expression plasmids. Complete genotype: F$^-$*ompT gal dcm lon hsdS*$_B$ ($r_B^-m_B^-$) λ (DE3 [*lacI lacUV5-T7 p07 ind1 sam7 nin5*]) [*malB*$^+$]$_{K-12}$ (λ^S).
	Strain used for recombinant protein expression.

MM. 1.1.1. Chapter I strains

Table MM. CI. 1.1.1. *Mycoplasma genitalium* strains used in Chapter I: Structure and mechanism of the nap adhesion complex from the human pathogen *Mycoplasma genitalium.*

***Mycoplasma genitalium* strain**	
G37	WT
	Used as a WT strain in this study. Origin: ATCC 33530
ΔMG_192	G37 ΔMG_192::*tetM*438
	Deletion of the MG_192 gene by allelic exchange. It is resistant to tetracycline. Origin: Burgos R. *et al.,* (2006)
P110-WT	ΔMG_192 *tetM*::MTn*Pac*MG_192
	Re-introduction of a MG_192 wild-type allele in a ΔMG_192 mutant. It is resistant to tetracycline and puromycin. Origin: Aparicio, D. *et al.*, (2018)
P110-R600A	ΔMG_192 MG_018(19720)::MTn*Pac*MG_192-R600A
	Introduction of a MG_192 allele bearing a R600A substitution in a ΔMG_192 mutant. It is resistant to tetracycline and puromycin. Origin: This work
P110-RQD	ΔMG_192 MG_018(22272)::MTn*Pac*MG_192-R600A-Q460A-D461A

	Introduction of a MG_192 allele bearing a R600A, Q460A and D461A substitutions in a ΔMG_192 mutant. It is resistant to tetracycline and puromycin. Origin: This work
P110-Y830A	ΔMG_192 *tetM*(663)::MTn*Pac*MG_192-Y830A
	Introduction of a MG_192 allele bearing a Y830A substitution in a ΔMG_192 mutant. It is resistant to tetracycline and puromycin. Origin: This work
P110-R834G	ΔMG_192 *tetM*(985)::MTn*Pac*MG_192-R834G
	Introduction of a MG_192 allele bearing a R834G substitution in a ΔMG_192 mutant. It is resistant to tetracycline and puromycin. Origin: This work
P110-D836L	ΔMG_192 MG_018(22281)::MTn*Pac*MG_192-D836L
	Introduction of a MG_192 allele bearing a D836L substitution in a ΔMG_192 mutant. It is resistant to tetracycline and puromycin. Origin: This work
P110-W838F	ΔMG_192 MG_140-MG_141(179151)::MTn*Pac*MG_192-W838F
	Introduction of a MG_192 allele bearing a W838F substitution in a ΔMG_192 mutant. It is resistant to tetracycline and puromycin. Origin: This work
P110-G389F	ΔMG_192 MG_355(452667)::MTn*Pac*MG_192-G839F
	Introduction of a MG_192 allele bearing a G839F substitution in a ΔMG_192 mutant. It is resistant to tetracycline and puromycin. Origin: This work
ΔMG_191	G37 ΔMG_191::*tetM*438
	Deletion of the MG_192 gene by allelic exchange. It is resistant to tetracycline. Origin: Burgos R. *et al.,* (2006)
P140-WT	ΔMG_191 MgPar8-BE(349311)::MTn*Pac*MG_191
	Re-introduction of a MG_191 wild-type allele in a ΔMG_191 mutant. It is resistant to tetracycline and puromycin. Origin: This work
P140-HH	ΔMG_191 MG_210-MG_480(250095)::MTn*Pac*MG_191-H831A-H832A
	Introduction of a MG_191 allele bearing a H831A and H832A substitutions in a ΔMG_191 mutant. It is resistant to tetracycline and puromycin. Origin: This work

***Mycoplasma genitalium* strain**	
G37	WT
	Used as a WT strain in this study. Origin: ATCC 33530
ΔMG_108	G37ΔMG_108::Lox72
	Deletion of the MG_108 gene by allelic exchange. It only keeps the Cre-Lox72 scar. Origin: This work
ΔMG_109	G37ΔMG_109:: *pacM*438
	Deletion of the MG_192 gene by allelic exchange. It is resistant to puromycin. Origin: Martínez-Torrò C. 2020 and This work

***Mycoplasma genitalium* strain**	
G37	WT
	Used as a WT strain in this study. Origin: ATCC 33530
P140-S1406A	ΔMG_191 MG_460 (564542)::MTn*Pac*MG_191-S1406A
	Introduction of a MG_191 allele bearing a P140: S1406A substitution in a ΔMG_191 mutant. It is resistant to tetracycline and puromycin. Origin: This work
P140-T1401A	ΔMG_191 MG_328 (412144)::MTn*Pac*MG_191-S1401A
	Introduction of a MG_191 allele bearing a P140: T1401A substitution in a ΔMG_191 mutant. It is resistant to tetracycline and puromycin. Origin: This work
	ΔMG_191 MgPar5-KL (231219)::MTn*Pac*MG_191-S1415A

P140-T1415A	Introduction of a MG_191 allele bearing a P140: T1415A substitution in a ΔMG_191 mutant. It is resistant to tetracycline and puromycin. Origin: This work
P140-S1418A	ΔMG_191 MgPar7-KL (314466)::MTn*Pac*MG_191-S1418A
	Introduction of a MG_191 allele bearing a P140: S1418A substitution in a ΔMG_191 mutant. It is resistant to tetracycline and puromycin. Origin: This work
P140-S1418E	ΔMG_191 MG_411 (513063)::MTn*Pac*MG_191-S1418E
	Introduction of a MG_191 allele bearing a P140: S1418E substitution in a ΔMG_191 mutant. It is resistant to tetracycline and puromycin. Origin: This work
P140-T1428A	ΔMG_191 MG_428 (534002)::MTn*Pac*MG_191-S1428A
	Introduction of a MG_191 allele bearing a P140: T1428A substitution in a ΔMG_191 mutant. It is resistant to tetracycline and puromycin. Origin: This work
P140-S1406A + T1401A	ΔMG_191 MG_343 (439566)::MTn*Pac*MG_191-S1406A-T1401A
	Introduction of a MG_191 allele bearing P140: S1406A and T1401A substitutions in a ΔMG_191 mutant. It is resistant to tetracycline and puromycin. Origin: This work
P140-S1406E + T1401E	ΔMG_191 Intergenic region MG_446-MG_447 (550568)::MTn*Pac*MG_191-S1406E-T1401E
	Introduction of a MG_191 allele bearing P140: S1406E and T1401E substitutions in a ΔMG_191 mutant. It is resistant to tetracycline and puromycin. Origin: This work
P140-S1418A + T1428A	ΔMG_191 Intergenic region MgPar5-LM-MG_194 (231652)::MTn*Pac*MG_191-S1418A-T1428A
	Introduction of a MG_191 allele bearing P140: S1418A and T1428A substitutions in a ΔMG_191 mutant. It is resistant to tetracycline and puromycin. Origin: This work
P140-S1418E + T1428E	ΔMG_191 MG_116 (143191)::MTn*Pac*MG_191-S1418E-T1428E
	Introduction of a MG_191 allele bearing P140: S1418E and T1428E substitutions in a ΔMG_191 mutant. It is resistant to tetracycline and puromycin. Origin: This work
ΔMG_191	G37 ΔMG_191::*tetM*438
	Deletion of the MG_192 gene by allelic exchange. It is resistant to tetracycline. Origin: Burgos R. *et al.,* (2006)
P140-WT	ΔMG_191 MgPar8-BE (349311)::MTn*Pac*MG_191
	Re-introduction of a MG_191 wild-type allele in a ΔMG_191 mutant. It is resistant to tetracycline and puromycin. Origin: This work
P140-HH	ΔMG_191 MG_210-MG_480(250095)::MTn*Pac*MG_191-H831A-H832A
	Introduction of a MG_191 allele bearing P140: H831A and H832A substitutions in a ΔMG_191 mutant. It is resistant to tetracycline and puromycin. Origin: This work

MM. 1.1.2. Chapter II strains

Table MM. CII. 1.1.2. *Mycoplasma genitalium* strains used in Chapter II: Molecular basis of bacterial lectins recognition of eukaryotic glycans: the case of *Mycoplasma pneumoniae* and *Mycoplasma genitalium* cytadhesins.

***Mycoplasma genitalium* strain**	
G37	WT
	Used as a WT strain in this study. Origin: ATCC 33530
ΔMG_192	G37 ΔMG_192::*tetM*438
	Deletion of the MG_192 gene by allelic exchange. It is resistant to tetracycline. Origin: Burgos R. *et al.,* (2006)
P110-WT	ΔMG_192 *tetM*::MTn*Pac*MG_192

	Re-introduction of a MG_192 wild-type allele in a ΔMG_192 mutant. It is resistant to tetracycline and puromycin. Origin: Aparicio, D. *et al.*, (2018)
P110-N182A	ΔMG_192 MG_191 (222461)::MTn*Pac*MG_192-N182A
	Introduction of a MG_192 allele bearing a N182A substitution in a ΔMG_192 mutant. It is resistant to tetracycline and puromycin. Origin: This work

MM. 1.1.3. Chapter III strains

Table MM. CIII. 1.1.3. *Mycoplasma genitalium* strains used in Chapter III: Dynamics of the nap complex and adhesion mechanisms of the human pathogens *Mycoplasma pneumoniae* and *Mycoplasma genitalium.*

***Mycoplasma genitalium* strain**	
G37	WT
	Used as a WT strain in this study. Origin: ATCC 33530
G37ΔAdh	G37ΔMG_191-ΔMG_192::Lox72
	Deletion of the MG_191 and MG_192 genes by allelic exchange. It only keeps the Cre-Lox72 scar. Origin: This work
G37ΔAdh::COM	G37ΔAdh MG_ RS01600 (327226)::MTn*Pac*MG_191/MG_192
	Re-introduction, by transposon insertion, of a MG_191 and MG_192 wild-type alleles in a G37ΔAdh mutant. It is resistant to puromycin. Origin: This work
G37ΔAdh::COM (MutE1)	G37ΔAdh Intergenic region MG_498-MG_263 (320162)::MTn*Pac*MG_191-G1372F-G1376F /MG_192
	Re-introduction of a MG_191 and MG_192 alleles bearing **P140E1: G1372F-G1376F** substitutions, in a G37ΔAdh mutant. It is resistant to puromycin. Origin: This work
G37ΔAdh::COM (MutE2; MutE3)	G37ΔAdh Intergenic region MG_ 192.1-MgPar5 (229341)::MTn*Pac*MG_191/MG_192-G947F-G951F-G960F-G964F
	Re-introduction of a MG_191 and MG_192 alleles bearing **P110E2: G947F-G951F** and **P110E3: G960F-G964F** substitutions, in a G37ΔAdh mutant. It is resistant to puromycin. Origin: This work
G37ΔAdh::COM (MutE1; MutE2; MutE3)	G37ΔAdh Intergenic region MG_ 068-MgPar1 (84579)::MTn*Pac*MG_191- G1372F-G1376F /MG_192-G947F-G951F-G960F-G964F
	Re-introduction of a MG_191 and MG_192 alleles bearing **P140E1: G1372F-G1376F**, **P110E2: G947F-G951F** and **P110E3: G960F-G964F** substitutions, in a G37ΔAdh mutant. It is resistant to puromycin. Origin: This work
G37ΔAdh::COM (MutE2)	G37ΔAdh MG_228-dhfR (275110)::MTn*Pac*MG_191/MG_192-G947F-G951F
	Re-introduction of a MG_191 and MG_192 alleles bearing **P110E2: G947F-G951F** substitutions, in a G37ΔAdh mutant. It is resistant to puromycin. Origin: This work
G37ΔAdh::COM (MutE3)	G37ΔAdh MG_443 (548794)::MTn*Pac*MG_191/MG_192-G960F-G964F
	Re-introduction of a MG_191 and MG_192 alleles bearing **P110E3: G960F-G964F** substitutions, in a G37ΔAdh mutant. It is resistant to puromycin. Origin: This work

G37ΔAdh::COM (MutE1; MutE2)	G37ΔAdh MgPar7-KL (314635)::MTn*Pac*MG_191- G1372F-G1376F /MG_192-G947F-G951F
	Re-introduction of a MG_191 and MG_192 alleles bearing **P140E1: G1372F-G1376F** and **P110E2: G947F-G951F** substitutions, in a G37ΔAdh mutant. It is resistant to puromycin. Origin: This work
G37ΔAdh-COM (MutE1; MutE3)	G37ΔAdh MG_316 (394912)::MTn*Pac*MG_191- G1372F-G1376F /MG_192-G960F-G964F
	Re-introduction of a MG_191 and MG_192 alleles bearing **P140E1: G1372F-G1376F** and **P110E3: G960F-G964F** substitutions, in a G37ΔAdh mutant. It is resistant to puromycin. Origin: This work

MM. 1.1.4. Chapter IV strains

Table MM. CIV. 1.1.4. *Mycoplasma genitalium* strains used in Chapter IV: Essential protein p116 extracts cholesterol and other indispensable lipids for *Mycoplasmas.*

Mycoplasma strain	
MPN129	WT
	Used as a WT strain in this study. Origin: ATCC 29342

MM. 1.1.5. Chapter V strains

Table MM. CV. 1.1.5. *Mycoplasma genitalium* strains used in Chapter V: Heterologous expression of *mycoplasma pneumoniae* major adhesins in the close related species *Mycoplasma genitalium.*

Mycoplasma strain	
G37	WT
	Used as a WT strain in this study. Origin: ATCC 33530/NCTC 10195
MPN129	WT
	Used as a WT strain in this study. Origin: ATCC 29342
ΔMG_191	G37 ΔMG_191::*tetM*438
	Deletion of the MG_192 gene by allelic exchange. It is resistant to tetracycline. Origin: Burgos R. *et al.,* (2006)
ΔMG_192	G37 ΔMG_192::*tetM*438

	Deletion of the MG_192 gene by allelic exchange. It is resistant to tetracycline. Origin: Burgos R. *et al.,* (2006)
G37ΔAdh	G37ΔMG_191-ΔMG_192::Lox72
	Deletion of the MG_191 and MG_192 genes by allelic exchange. It only keeps the Cre-Lox72 scar. Origin: This work
G37ΔAdh::COM	G37ΔAdh MG_ RS01600 (327226)::MTn*Pac*MG_191/MG_192
	Re-introduction, by transposon insertion, of a MG_191 and MG_192 wild-type alleles in a G37ΔAdh mutant. It is resistant to puromycin. Origin: This work
G37ΔAdh::MPN	G37ΔAdh MG_281 (343662)::MTn*Pac*MPN_141/MPN_142
	Re-introduction, by transposon insertion, of a MPN_141 and MG_142 wild-type alleles in a G37ΔAdh mutant. It is resistant to puromycin. Origin: This work
G37ΔAdh::MPN-CS	G37ΔAdh MgPar7 (313199)::MTn*Pac*MPN_141/MPN_142-R445S-A446S-R455S-A456S
	Re-introduction, by transposon insertion, of a MPN_141 and MG_142 alleles bearing P40/P90: R445S-A446S-R455S-A456S substitutions in a G37ΔAdh mutant. It is resistant to puromycin. Origin: This work
G37ΔAdh::MPN ΔSII	G37ΔAdh MG_067 (82408)::MTn*Pac*MPN_141/MPN_142-ΔL395-T414
	Re-introduction, by transposon insertion, of a MPN_141 and MG_142 alleles bearing P40/P90: L395-T414 deletion in a G37ΔAdh mutant. It is resistant to puromycin. Origin: This work
G37ΔMG_317 (ΔHMW3)	G37 MG_317::pMTn*tetM*438
	MG_317 truncated gene by transposon insertion. It is resistant to tetracycline. Origin: Pich O. Q. *et al.,* (2009)

MM. 1.2. Culture mediums and bacterial growth conditions

MM. 1.2.1. Culture of *E. coli* strains

E. coli XL1-Blue strain was used for cloning procedures due to its recombination deficiency and its high transformation efficiency. It is also endonuclease I (*endA*) deficient, thus providing yield of DNA miniprerp. This strain is resistant to tetracycline (coded in the F' episome) and nalidixic acid (because of a mutation in the A subunit of DNA gyrase). Its complete genotype is listed as

follows: *end*A1 *gyr*A96(nal^{R}) *thi*1 *rec*A1 *rel*A1 *lac gln*V44 *hsd*R17(r_k^- m_k^+) F' [::Tn10 *pro*AB$^+$ *lac*I^q Δ(*lac*Z)M15].

E. coli XL1-Blue was grown in Luria-Bertani liquid LB (Lysogeny Broth) medium[531] [**Sambrook J. *et. al*., 1989**]. This is one of the most widely used broths for the growth of bacteria and it is composed of bactotryptone 1%$_{w/v}$ (Sharlau Microbiology, Thermo-Fisher-Scientific), yeast extract 0.5%$_{w/v}$ (Thermo-Fisher-Scientific) and NaCl 1%$_{w/v}$. This media is autoclaved 15 min at 121ºC and stored at RT (liquid) or 4ºC (plates).

Liquid cultures were inoculated in a laminar flow cabinet, in LB medium overnight (O/N) and grown at 37ºC and 250 rpm in an orbital shaking incubator with a maximum 1:5 volume proportion for proper aeration. Cells were recovered by centrifugation. An isolated colony or 10 µL from a working stock were used to inoculate 3 mL of LB or 20 µL from a working stock to inoculate 50-100 mL of LB to obtain greater quantities of plasmid DNA for electroporation purposes. For larger volumes, 1% inoculum from a starter culture grown until OD_{600}≈1 was used. Antibiotic selection was added to the culture in all cases to prevent plasmid loss.

Solid cultures were also inoculated in a laminar flow cabinet to isolate single colonies upon transformation. A Digralsky spreader was used to spread the transformant cells on the plate. Solid LB medium was prepared by adding Bacteriological agar 1.5%$_{w/v}$ (Thermo-Fisher-Scientific) to liquid LB before autoclaving. Before cooling, this mixture was dispensed on 90 mm petri dishes and stored at 4ºC. Colonies of *E. coli* were isolated by seeding on solid LB medium dishes and growing O/N at 37ºC in an incubator. Colonies were picked up with a sterile wood stick or a pipette tip and expanded in 3 mL of LB overnight O/N at 37ºC. Once characterized, *E. coli* strains were preserved in LB supplemented with 15%$_{v/v}$ of sterile glycerol at -80ºC.

The following supplements were used for liquid and solid LB medium:

- Ampicillin (Sigma-Aldrich/Merk): stock solution was prepared at 200 mg/mL in MilliQ H_2O and sterilized filtering through a 0.22 µm filter (Merck-Millipore). The stock was conserved at -20ºC and used at a final concentration of 100 µg/mL (1:2000).

- Tetracycline (Sigma-Aldrich/Merk): stocks were prepared at 5 mg/mL in 70% ethanol and sterilized by filtering the solution through a 0.22 µm filter (Merck-Millipore). The 1 mL aliquots were conserved at -20ºC and covered in aluminium foil to protect the antibiotic from the light, as it is a photosensitive compound. The working concentration for XL1-Blue strains is 10 µg/mL (1:500).

- Isopropyl β-D-1-thiogalactopyranoside (IPTG) (Sigma-Aldrich/Merk): stocks were prepared at 1M in sterile MilliQ H_2O and stored at -20ºC. IPTG is used at a working concentration of 1mM (1:1000) and it induced transcription of genes under the control of the lac operator.

- 5-bromo-4-chloro-3-indolyl-β-D-galactopyranoside (X-Gal) (AMRESCO, VWR-Avantor): stocks were prepared dissolving 40 mg of X-Gal in 1 mL of N,N-dimethylformamide. X-Gal is used in LB plates as it is an analogue of lactose that yields an insoluble blue compound used to distinguish a successful cloning with blue/white screening. It is used at a final concentration of 40 µg/mL (1:1000). These plates need to be stored in the dark covered with aluminium foil as X-Gal is photosensitive.

MM. 1.2.2. Culture of *M. genitalium* strains

M. genitalium was grown in Spiroplasma Medium 4 (SP4). It is a very rich medium recommended for culturing mycoplasmas and spiroplasmas[532] [**Tully J. G. *et al.*, 1979**]. The medium is prepared in two steps: base and supplementation. The base is composed of PPLO Broth 3.5 g/L (Becton Dickinson), Bactotryptone 10 g/L (Becton Dickinson), Bactopeptone 5.3 g/L (Becton Dickinson) and Glucose 5 g/L (Sigma-Aldrich/Merk). The mix is dissolved in MilliQ H_2O and adjusted to pH 7.8 with NaOH 2M. To prepare SP4 agar plates, Bactoagar 0.8%$_{w/v}$ was added before autoclaving at 121ºC for 15 minutes.

After autoclavation and once the SP4 base was cooled down (not under 56ºC I solid SP4 is desired), it was supplemented. For 500 mL SP4 broth preparation 50 mL 2%$_{w7v}$ Yeastolate (Becton Dickinson), 6 mL 0.1%$_{w/v}$ Phenol Red pH 7 (Sigma-Aldrich/Merk), 25 mL 10x CMRL (Life Technologies), 17.5 mL fresh yeast extract, 85 mL Fetal Bovine Serum (Life Technologies), 1.71 mL glutamine 29.2 mg/mL (Sigma-Aldrich/Merk) and 250 µL ampicillin 200 mg/mL (Sigma-Aldrich/Merk) were added to the base. The pH was adjusted again to 7.8 with NaOH 2M and the mixture was filtered through a 0.22 µm Stericup (Merk-Millipore) to ensure the medium was clear of any residual live yeast cell.

The following components were used with SP4 when needed:

- Yeastolate 2%: 8 g Yeastolate (Becton-Dickinson) dissolved in 400 mL MilliQ H_2O and autoclaved at 121ºC for 15 minutes. Stored at 4ºC.
- Yeast extract 25%$_{w/v}$: 250 g of fresh yeast was dissolved in 1L MilliQ H2O and autoclaved at 115ºC for 10 minutes. Then, it was centrifugated at 400xg for 10 minutes to pellet the yeast cells. Supernatants were autoclaved again at 115ºC for 10 minutes and aliquoted in 20 mL. For extra security, the aliquots were centrifugated again at 400xg for 10 minutes before storing them at -20ºC.

- Phenol Red 0.1 pH 7: 0.4 g Phenol Red (Sigma-Aldrich/Merk) dissolved in 400 mL MilliQ H_2O. The pH was adjusted carefully to 7 using NaOH 2M. Stored at 4ºC after autoclaving at 121ºC for 15 minutes.
- Fetal Bovine Serum (FBS) (Life Technologies): it was heated up to 56ºC for 30 minutes in order to inactivate the complement system. Then, it was aliquoted in sterility in a laminar flow cabinet and 43 mL aliquots were stored at -20ºC.
- Ampicillin (Sigma-Aldrich/Merk): stock solution was prepared as described before and used at a final concentration of 100 µg/mL (1:2000) to prevent bacterial contamination.
- Tetracycline (Sigma-Aldrich/Merk): stock solution was prepared as described before. It was used at a working concentration of 2.5 µg/mL (1:2000) to select strains carrying the marker gene TetM438[244] [**Pich O. Q. *et al.*, 2006b**]. It was used avoiding light exposure as it is photosensitive.
- Chloramphenicol (Sigma-Aldrich/Merk): stocks were prepared at 34 mg/mL in 70% ethanol and sterilized by filtering through a 0.22 µm filter (Merk-Millipore). Aliquots of 1 mL were stored at -20ºC. It was used at a working concentration of 17 µg/mL (1:2000) to select strains carrying the marker gene *cat*M438[309] [**Calisto B. M. *et al.*, 2012**] that provides chloramphenicol resistance.
- Puromycin (Life Technologies): the stock solution (10 mg/mL) was stored at -20ºC. It was used at a final concentration of 3.3 µg/mL (1:3000) to select strains carrying the *pac* marker[249] (described in **Algire M. A. *et al.*, 2009**) under the control of the MG_438 promoter[209] [**Torres-Puig S. *et al.*, 2015**], as with tetracycline and chloramphenicol gene markers. Puromycin stock solution was kept in the dark as it is a photosensitive compound.

MM. 1.2.3. Culture of *M. pneumoniae* strain

Similar to what it has been explained above for *M. genitalium*, *M. pneumoniae* M129 strain was grown in cell culture flasks containing SP4 or PPLO media and incubated at 37 ºC with or without 5% CO_2. Surface-attached mycoplasmas were harvested using a cell scraper and resuspended in medium or suitable buffers for experiments.

MM. 1.2.4. Culture of eukaryotic cells

NSI myeloma cells[533] [**Köhler G. and Milstein C., 2005**] were grown in RPMI 1640 medium supplemented with 10% foetal bovine serum (FBS) and 50 µg mL^{-1} gentamicin (complete RPMI). Hybridomas were selected in complete RPMI supplemented with HAT media and BM-Condimed (Sigma-Aldrich/Merk).

MM. 1.3. Bacterial transformation

MM.1.3.1. DNA transformation in *E. coli* XL1-Blue strain

Competence of cells from *E. coli* XL1-Blue strain was achieved using the standard Inoue method described in Sambrook *et al.*, 1989. Aliquots of 900 µL of competent cells were cooled in liquid nitrogen and stored at -80ºC. Plasmids were transformed into XL1-Blue competent cells by using a standard heat shock protocol also described in[531] **Sambrook J. *et al.*, 1989**, where cells were shocked at 42ºC for 90 seconds.

M. genitalium cultures were inoculated in a class 2 laminar flow cabinet and incubated at 37ºC in a 5% CO_2 atmosphere. Liquid cultures were grown in 5, 20 or 35 mL of SP4 in 25, 75 or 175 cm^2 tissue culture flasks (SPL Life Sciences), respectively. The inoculum used varied highly depending on the strain or the experiment, ranging from 15 µL to 200 µL. Cultures were kept at 37ºC until mid-long phase (usually about 3-4 days) and then they were processed. For adherent strains, the medium was aspired and cells were recovered with fresh medium using a cell scrapper (SPL Life Sciences). For non-adherent strains, the cells were centrifuged at 12000 rpm for 15 minutes. Then, the supernatant was discarded and pelleted cells were recovered in the desired medium.

For solid cultures, the plated quantity depended on the experiment that was being performed. For viability assays, the cellular suspensions were serially diluted until 10^{-6} and 10 µL drops of different dilutions were plated. For transposon delivery, 100 µL of a 0, 10^{-1} and 10^{-2} dilutions were plated onto SP4 agar plates. And to achieve homologous recombination with a suicide plasmid, 200 µL of non-diluted cellular suspension were plated. Individual colonies could be observed after 10-14 days using a binocular stereomicroscope. The isolated colonies were selected with a permanent marker using the stereomicroscope and recovered in the laminar flux cabin using sterile cut microtips. These colonies were cultures in 25 cm^2 flasks with 5 mL of SP4 and the proper concentration of the selection marker. Some growth can be observed after 7-10 days depending on the strain and the mutant can be recovered by aspiring the medium and residual agar and scrapping the cells in 500 µL or 1 mL of fresh SP4. Stocks were stored at -80ºC without the addition of glycerol, due to the high concentration of FBS in SP4 medium that permits cryopreservation.

MM. 1.3.2. *M. genitalium* transformation and screening for mutants

M. genitalium was transformed by electroporation as described by[251] **Reddy S. P. *et al.*, 1996**, adapting a protocol used to *M. pneumoniae* transformation by[234] **Hedreyda C. T. *et al.*, 1993**. The protocol used in this laboratory is a slightly modified version detailed as follows:

- Inoculum of a *M. genitalium* strain in a 75 cm^2 flask with 20 mL SP4.

- After 3-4 days at 37ºC and 5% CO_2, the culture usually reached the mid-log phase. Then, 10 mL of SP4 were discarded and cells were scrapped in the remaining volume.
- The scrapped cells in 10 mL SP4 were filtered through a 0.45 filter (Millipore) to disaggregate cell clusters and increase transformation efficiency. Then, 3-5 mL were inoculated in a new 75 cm^2 flask with 15-17 mL of fresh SP4 or 8-10 mL were seeded in a 175 cm^2 flask with 25-27 mL of fresh SP4 if several transformations (more than 4) were desired. The flask was left overnight at the incubator.
- The next day, medium was aspirated and cells were washed three times with Electroporation Buffer (8mM HEPES, 272 mM sucrose, pH 7.2-7.4). Then, cells were scraped in the remaining residual medium, recovered in a microtube and the volume was adjusted depending on the number of transformations to be performed.
- 100 µL of the cellular suspension were mixed with 10 µg (for transposition) or 30 µg (for gene replacement using suicide plasmid and pCre plasmid[261] [**Mariscal A. M. *et al*., 2016**]) of plasmid DNA.
- Immediately after mixing the cells with the plasmid DNA, the mixture was placed into a 0.2mm gapped electroporation cuvette (VWR) and electroporated at 2500 V, 250 Ω and 25 mF with an electroporation system (ECM 620-630 BTX) or Gene Pulser Xcell Microbial System 100/240 V 50/60 Hz electroporator (BioRad). Electroporation timer constants ranged from 4.0 to 6.0 milliseconds. After electroporation, cuvettes were immediately put on ice.
- After 15 minutes on ice, cells were resuspended with 900 µL of fresh SP4 and transferred to a sterile microtube. Tubes were incubated at 37ºC and 5% CO_2 for 3-4 hours in order to allow the expression of the resistance marker.
- Finally, cells were plated on SP4 agar plates with the corresponding antibiotic. As a control, viable cells on SP4 agar plates without antibiotic could also be seeded.

There were two modifications to this protocol if the parental strain was non-adherent:

a) The culture was not filtered through a 0.45 µm filter but forced through a 25G needle syringe 8-10 times. This is because of the natural aggregation of non-adherent cells that would highly decrease the number of cells that passed through the filter.
b) As they do not adhere to the plastic surface, the three washes with electroporation buffer were performed by centrifugating the cells three times at 12000 rpm for 15 minutes at 4ºC, in a 1.5 mL microtube.

Transposon insertion point of the selected clones bearing the different mutations/constructions presented in this work are descripted above in **Table MM. 1.1.1_CI, 1.1.2_CII, 1.1.3_CIII, 1.1.4_CIV and 1.1.5_CV**.

When transforming with the pCre plasmid, after the incubation for the expression of the resistance marker, 0.8-1 mL of the cell suspension were dispensed in a 75 cm^2 flask supplemented with Gentamicin 50mg/mL. After 3 days (72h) of incubation at 37ºC and 5% CO_2, the cells were plated on SP4 agar plates without antibiotic for mutant selection. Usually, cells are scraped-off the flask, resuspended in 1mL of SP4 and 100 µL of a 0 to 10^{-5} dilutions are plated. Colonies should appear in 10-14 days and normally, picked them up of the 10^{-2} or 10^{-3} dilution plate.

MM. 2. DNA manipulation

MM. 2.1. Plasmid DNA extraction

Extraction of plasmid DNA (pDNA) was carried out using a 1.5- 3 mL of an O/N *E. coli* culture and the *GeneJET Plasmid Miniprep Kit* (Thermo-Fisher-Scientific), following manufacturer instructions (the supplied guidelines). The quantity of plasmid DNA obtained depended on the copy number of the plasmid. For high copy number plasmid, up to 10 µg of pDNA were usually obtained. Minipreparations were used for cloning purposes.

If larger amounts of pDNA were needed, a 50- or 100-mL O/N *E. coli* culture was processed using the GenElute HP Midiprep Kit (Sigma-Aldrich/Merk), following manufacturer's instructions. In order to increase the concentration, pDNA was precipitated after elution with 0.7 volumes of isopropanol and 0.1 volumes of 0.3 M ammonium acetate. The mix was centrifugated at 18000xg and 4ºC for 45 minutes. The supernatant was discarded and the pellet was washed once with 70% ethanol. Then, the supernatant was discarded again and the pellet was vacuum dried. The dried pellet was resuspended with 100 µL Electroporation Buffer, as midipreparations were used to transform *M. genitalium*. Suspension was left O/N at 4ºC and stored at -20ªC after quantification. Typically, up to 300 µg of pDNA could be obtained.

MM. 2.2. Genomic DNA extraction of *M. genitalium* strains

This protocol is divided in two working zones.

<u>In Laminar air flow cabinet</u>

- Firs, the medium was removed out of the flask and the cells were washed two times with PBS 1x. If the strains are non-adherent, cells were recovered by centrifugation 20 min at 12000 rpm and transferred to an Eppendorf. Then cells were also washed two times with PBS 1x.
- 500 µl of solution I (0.1M Tris-HCl pH 8; 0,5M NaCl; 10mM EDTA) was added to the flask or the Eppendorf.
- Cells were scraped off and collected in an Eppendorf tube.
- 12.5 µl of SDS 20% was added, mixed gently and let it 5 minutes at RT.

- Finally, 5 µL of proteinase K (100 µg/ml) was added.

Outside Laminar air flow cabinet (open phenol-chloroform in fume hood)

- Cells were incubated 1 hour at 55ºC, shaking it gently every few min.
- The DNA was extracted with 1 vol. of phenol-chloroform without vortexing, and recovered by centrifugation 10 min at 13000 rpm.
- The upper phase was collected in an Eppendorf tube using a cut pipette tip.
- The phenol-chloroform extraction was repeated one more time. This second time collecting the upper phase in a red cap tube.
- The genomic DNA was precipitated, in the same tube, with 2 volumes of absolute ethanol, mixing gently until a cotton appeared.
- The cotton was transferred to an Eppendorf tube and recovered by centrifugation during 5 min at 14000 rpm.
- The pellet was washed with 1 ml of 70% ethanol. Detaching the pellet, a little, and recovered another time by centrifugation 2 min at 14000 rpm.
- Finally, the pellet was dried at vacuum and resuspended in 0.2% TE buffer (Tris-HCl 10mM pH 8, EDTA 1mM), sometimes with 15 µg/mL of RNase A (Life Technologies). Suspension was left O/N at 4ºC, vortexed and stored at -20ºC.

MM. 2.3. Obtention of *M. genitalium* and *M. pneumoniae* lysates

With screening purpose, to isolate genomic DNA (gDNA) from *M. genitalium* in a faster and easy way, the following protocol (adapted for our lab) was followed:

- Inoculum of the desired *M. genitalium* strain to screen in a 25 cm^2 flask with 5 mL of SP4 and supplemented with the required antibiotics. The culture was grown until late exponential phase.
- The medium was aspirated and cells were washed twice in 1 mL PBS 1x (Sigma-Aldrich/Merk). Then, cells were scrapped off in 1 mL PBS 1x, transferred to a microcentrifuge tube and centrifuged at 12000 rpm for 10 min. For non-adherent strains, cells were centrifuged in SP4 and washed twice in PBS 1x.
- PBS was aspirated and the pellet (usually a small one) was lysed using 20-50 µL of lysis buffer (0.1 M Tris-HCl pH 8.5, 0.05% Tween-20, 250 µg/mL proteinase K). An optimal disaggregation of the pellet by pipetting up and down was important to achieve a good lysis. The mix was incubated at 37ºC for 1 hour.
- Then, proteinase K was inactivated at 95ºC for 10 minutes.
- Lysates were stored at -20ºC.

1-2 µL of the lysate were used for PCR screening and 5 µL were usually enough for Sanger sequencing.

MM. 2.4. DNA quantification

DNA quantification was determined using a "NanoDrop" 1000 Spectrophotometer (Thermo-Fisher-Scientific), or Nano-300 Micro Spectrophotometer (Allsheng), following the manufacturer's instructions.

MM. 2.5. DNA amplification

DNA amplification for molecular cloning purposes was carried out with *Phusion High Fidelity DNA polymerase* (Thermo-Fisher-Scientific), following manufacturer's instructions. Taq DNA polymerase (Sigma-Aldrich Merk) was employed in mutant screenings. DNA was amplified by PCR in a MJ Mini Thermal Cycler (Bio-Rad). 10-50 ng of DNA template were usually used, 200 µM of dNTP mix (Sigma-Aldrich/Merk), 0.2 µM of each oligonucleotide, 1x HF Green Buffer (Phusion) or 1x PCR reaction buffer (Taq), and 0.6 U of the Phusion polymerase or 1.25 U of the Taq polymerase.

Usually, PCR fragments were joined by Splicing by Overlap Extension (SOE) PCR. This method is based in the use of oligonucleotides with 5' overhang that is complementary to the 3' end of the fragment to be fused with. Both fragments are amplified separately, purified and they are mixed in the next PCR reaction. In this new reaction, they will be annealed together and using the forward primer of the first fragment and the reverse oligonucleotide of the second fragment they will generate a new product. This technique allows the merge several DNA fragments without the use of restriction enzymes nor ligation reactions.

MM. 2.6. Gel electrophoresis and DNA quantification

Following standard procedures[531] [**Sambrook J. *et al*., 1989**], agarose gels were used to separate DNA fragments and PCR products. Depending on the size of these fragments, the concentration of agarose (SeaKem LE Agarose) ranged from 0.7-2%$_{(w/v)}$ and it was diluted in 1xTAE buffer (40 mM Tris, 20 mM acetic acid and 1 mM EDTA). Usually, DNA samples were already mixed with a commercial loading buffer (*Phusion Green HF buffer* or *FastDigest Green buffer*, both from Thermo-Fisher- Scientific). If not, samples were diluted with loading buffer (40 mM Tris-Acetate pH 8, 1 mM EDTA, Bromophenol Blue 250 µg/mL, xylene cyanol 250 µg/mL and 30% glycerol) before loading them into the agarose gel.

Electrophoresis gels were run at 65-90V for 60-90 minutes in 1x TAE Buffer. Molecular weight was estimated using *GeneRuler^{TM} 1 kb Plus DNA Ladder* (Thermos-Fisher- Scientific). Then, the

agarose gel was stained with *RedSafe™* (iNtRON Biotechnology) or Midori Green Advance (Nippon Genetics). Both DNA staining solutions were used at 0.02%$_{(v/v)}$. The gel was incubated with the staining buffer for 30-40 min in an orbital shaker. Then, it was visualized under UV or black light in a *GelDoc™ XR+ Imaging System* (Bio-Rad) for screening purposes or under a Spectroline TC-365A transilluminator (Spectronics Corporation) to recover DNA bands from the agarose gel. DNA from agarose gels was later extracted using *NucleoSpin Gel and PCR Clean-up* kit (Macherey-Nagel). Following manufacturer's instructions.

MM. 2.7. DNA digestion/restriction

DNA fragments were digested using *FastDigest™* restriction enzymes (Thermo-Fisher-Scientific), following the manufacturer's guidelines. Restriction of DNA was used for plasmid screenings and DNA cloning.

MM. 2.8. Ligation of DNA fragments

DNA fragments were ligated into previously digested plasmids with T4 DNA ligase (Sigma-Aldrich/Merk or Thermo-Fisher-Scientific). Reactions were performed at room temperature for 1-2 hours or O/N at 16ºC, depending on the specifications of the ligase and the DNA end (longer time for blunt ands, shorter for sticky ends).

MM. 2.9. DNA sequencing

Genomic DNA, plasmids and PCR products were Sanger sequenced at Servei de Genòmica I Bioinformàtica (UAB). Reactions were performed with the *BigDye® 3.0 Terminator* kit (Applied Biosystems) and analyzed in an ABI PRISM 3130xl Genetic Analyzer (Applied Biosystems).

MM. 2.10. Plasmid construction for *Mycoplasma* transformation

A total of 38 plasmids were constructed and used in this work, for the obtention of the different *M. genitalium* mutants. The list can be found in the Appendices organized by chapter. Strategies on the construction of the different vectors were similar but it varies depending on the desired approach.

Plasmids to generate knock-out (KO) mutants in *M. genitalium*: KO mutants in *M. genitalium* were generated replacing the gene of interest with an antibiotic resistance marker by a doble crossover event. This gene replacement was achieved via transformation with a suicide plasmid bearing the antibiotic cassette neighbored by 1kb of the upstream and downstream regions of the gene to be replaced. The resistance marker was under the control of a constitutive promoter and flanked with lox61 and lox71 sequences, in order to finally obtain a free of any antibiotic

selectable marker mutant strain by transformation with the pCre[261] [Mariscal A. M., *et al*., 2016] plasmid (Figure MM. 2.10_1).

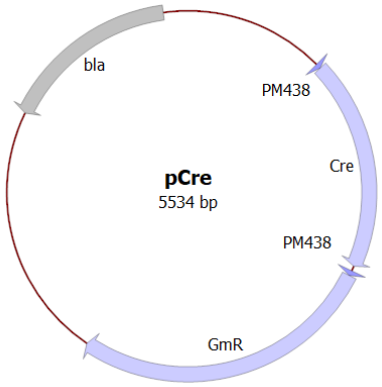

Figure MM. 2.10_1. pCre schematic representation. *bla* indicates the ampicillin resistance gene. Cre indicates the Cre recombinase coding gene under the control of MG_438 promoter and GmRS438 indicates the gentamicin resistance gene (aac(6')-aph(2'') gene) under the MG_438 promoter.

Upstream and downstream regions as well as the antibiotic marker were amplified by PCR. Then, upstream (UR) and downstream (DR) region amplicons were mixed and used as a template to ligate and amplify them by SOE-PCR. Then, this insert was cloned in an *Eco*RV-digested pBE[244] [Pich O. Q. *et al*., 2006b]. Finally, the resulting resistance marker amplicon was digested with specific restriction enzymes and ligated into the similarly digested pBE containing the UR and DR regions obtained before. The suicide plasmids obtained were used to transform *M. genitalium* and contain the designed amplicons of the upstream region, marker and downstream region for each KO generated.

Plasmids bearing minitransposons to re-introduce or overexpress genes in *M. genitalium:* to re-introduce or overexpress genes, a miniTn4001-derived transposon bearing a copy of the gene of interest was employed. The extra copy was amplified from genomic DNA of *M. genitalium* or an intermediate pBE derivative vector[244] [Pich O. Q, *et al*., 2006b], previously obtained for the cloning procedure. Usually, the gene was amplified with its own promoter or, in some cases, adding a 5' tail with the sequence of the MG_191 promoter (the one that drives the transcription of the adhesion operon in *M. genitalium*). It was cloned into the pMTnPac[534] [Torres-Puig S. *et al*., 2018] plasmid (Figure MM. 2.10_2) previously digested with the corresponding restriction enzyme and used to transform *M. genitalium*.

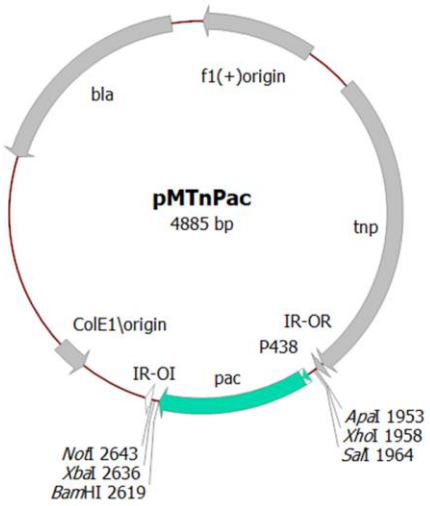

Figure MM. 2.10_2. Schematic representation of pMTnPac plasmid backbone. Restriction sites used for cloning are indicated. Puromycin acetyl transferase (*pac*) gene is depicted as a cyan arrow.

Most of the plasmid inserts were created by DNA fragment joined together by Splicing by Overlap Extension PCR (SOE-PCR). This technique is based in the amplification of a DNA fragment using oligonucleotides with a 5' overhang complementary to the end of the molecule to be fused with. Mixing both DNA fragments in the same PCR reaction, they will be annealed together and extended generating a new product formed by the unification of both fragments. This technique allows the ligation of several DNA pieces without the use of restriction enzymes nor DNA ligases (**Figure MM. 2.10_3**). For base substitutions introduction, site-directed mutagenesis was adapted to this method for creating a specific mutation in a known sequence. Primers containing the base changes of interest as a non-complementary break in the primer sequence were used in the PCR reaction. As the primers are extended, the resulting amplification product includes the non-complementary bases, which replace the original sequence.

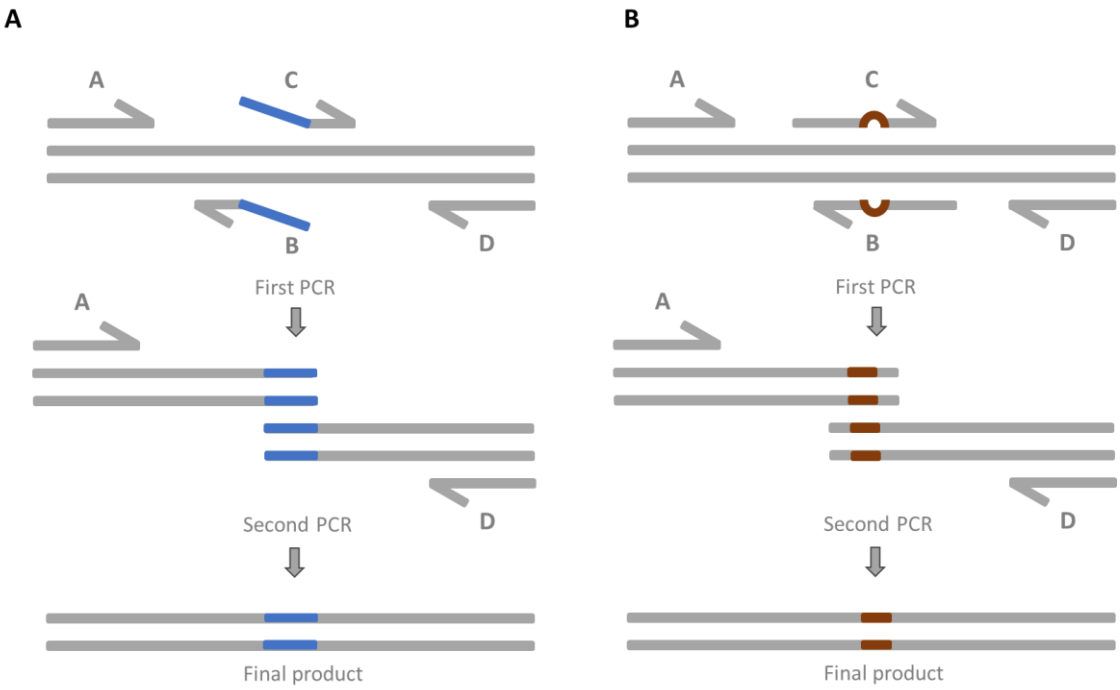

Figure MM. 2.10_3. Schematic representation of Splicing by Overlap Extension PCR (SOE-PCR) method. A) Primer extension for insertion. Primers B and C contain the sequence that will be inserted (indicated by the blue line). The first round of PCR uses two reactions with primer pairs A/B and C/D. The two resulting PCR products are mixed with primer pair A/D for the second round of PCR. The overlapping regions of the two, first-round PCR products allow the strands to hybridize, and the second round of PCR creates the final, full-length product with the desired insertion. **B) PCR for base substitutions.** Primers containing the base changes of interest as a non-complementary break in the primer sequence (indicated by the brown bubble) are used in a PCR reaction. As the primers are extended, the resulting amplification product includes the non-complementary bases, which replace the original sequence.

Other plasmid inserts were created by ExSite PCR. This technique enables the amplification of a region using primers oriented in the reverse direction (**Figure MM. 2.10_4**). In this case, reverse primers were designated to contain a 5' phosphorylated end, allowing the two ends to be ligated together following amplification. An adaptation of this method was used in this work to introduce mutations in previously cloned sequences. When PCR is used for site-directed mutagenesis, the forward primers were designed to include the desired change, which in this study were base substitution and deletion. The mutation is incorporated into the amplicon during the PCR protocol, replacing or deleting the original sequence. Mutations introduced by PCR can only be incorporated into regions of sequence complementary to the primers and not regions between the primers.

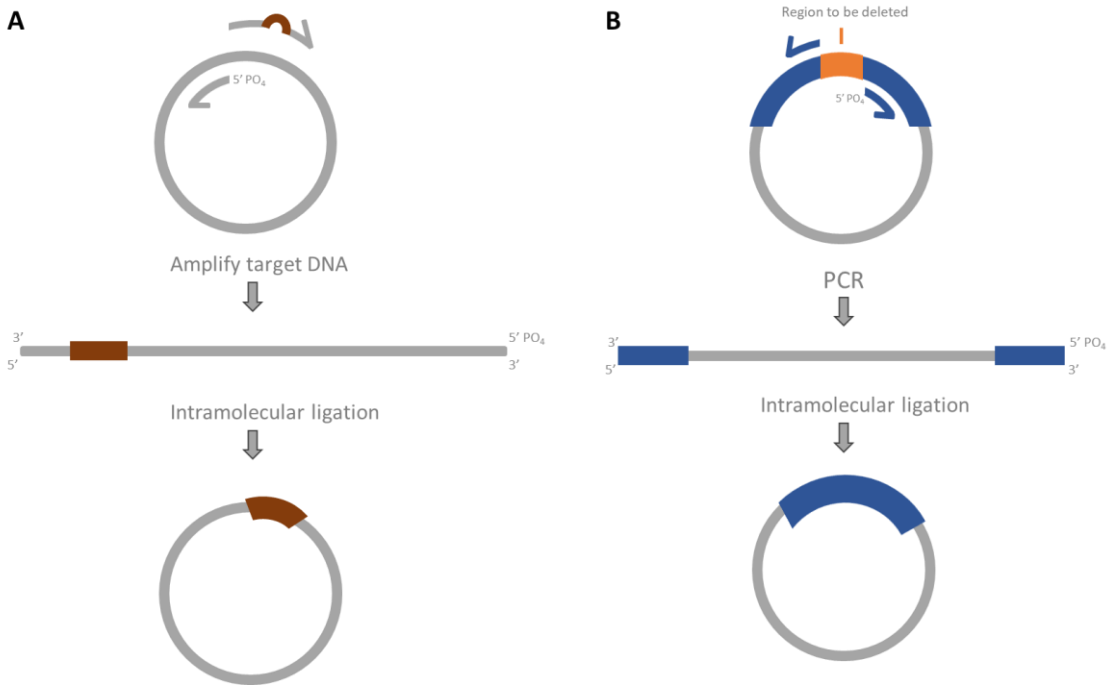

Figure MM. 2.10_4. Schematic representation of ExSite PCR method. A) Inverse PCR for a substitution. One of the two primers contain the mutation of interest (indicated by the brown bubble). In this case, reverse primer contains 5' phosphorylated end to allow the two ends to be ligated together following amplification. PCR is used to amplify the entire circular plasmid to create a linear template that contains the substituted sequence. This fragment is then circularized by intramolecular ligation and the resulting plasmid is transformed into host bacteria for propagation. **B) Inverse PCR for a deletion.** This method uses primers that hybridize to regions on either side of the area to be deleted. In this case, the reverse primer contains 5' phosphorylated end, allowing the two ends to be ligated together following amplification. PCR with a high-fidelity DNA polymerase leaves blunt ends and creates a linearized fragment that is missing the deleted region. This fragment is then circularized by intramolecular ligation and the resulting plasmid is transformed into host bacteria for propagation.

Plasmids used in this work and their construction are explained in greater detail in **Appendices Table A. CI. 1.2, CII. 2.2, CIII. 3.2 and CV. 5.2**. Maps were created with the "Maps" Software (from Molecular Biology Laboratory).

MM. 2.11. Oligonucleotides used in this work

All oligonucleotides used in this work can be found in the Appendices organized by Chapter.

MM. 3. Protein Analysis Methods

MM. 3.1. *Mycoplasma* protein extraction and quantification

To obtain *M. genitalium* or *M. pneumoniae* protein extracts for analysis, mid-long phase cultures grown in 75 cm^2 flasks were washed 4 times with 1x PBS (Sigma-Aldrich/Merk) and scrapped off in 125 µL 1x PBS. Then, cells were lysed with 25 µL 6x Laemmli sample buffer (0.375 M Tris-HCl pH 6.8, 12% SDS, 60% glycerol, 0.6% β-mercaptoethanol and 0.003% bromophenol blue) and

boiled for 10 minutes to fully denature proteins. Protein extractions were cooled down and stored at -20ºC. For non-adherent strains, cells were recovered by centrifugation at 12000 rpm for 15 minutes. Then, the supernatant was discarded and pelleted cells were resuspended in the same volume, 125 µL 1x PBS, and lysed in the same way as it has been mentioned just above.

Protein extracts were quantified using Pierce™ BCA Protein Assay Kit (Thermo-Fisher-Scientific), following manufacturer's instructions, or using "NanoDrop" 1000 Spectrophotometer (Thermo-Fisher-Scientific) or Nano-300 Micro Spectrophotometer (Allsheng), following the manufacturer's instructions.

MM. 3.2. Protein electrophoresis

Proteins were loaded into denaturing polyacrylamide gels to separate them according to their molecular weight. SDS-PAGE gels were prepared according to standard procedures[535] [**Shapiro A. L. *et al.*, 1967**] using 40% acrylamide:bisacrylamide (37:5:1) solution (Bio-Rad or Panreac) and polymerized in the *Mini-PROTEAN® handcast system* (Bio-Rad). The final concentration of acrylamide in the resolving (or running) gel ranged between 10 and 15%, depending on the molecular weight range of the target proteins. Acrylamide concentration on the stacking gel was fixed at 4%. *PageRuler™ Unstained Protein Ladder* (Thermo-Fisher-Scientific) was used as a molecular weight marker. For Western Blotting, *PageRuler™ Prestained Protein Ladder* or *PageRuler™ Plus Prestained Protein Ladder* (Thermo-Fisher-Scientific) was the selected ladder.

Gels were run with amperage fixed at 20-30 mA for 90-120 minutes in 1x Running Buffer (25mM Tris, 192 mM glycine, 0.1% SDS). The endpoint was determined with the bromophenol blue front and depended on the target molecular weight range to be resolved.

MM. 3.3. Staining

Once the electrophoresis was over, gels were washed with distilled water to remove traces of SDS and then stained with Coomassie solution (0.1% Coomassie $R250_{(w/v)}$, 10% acetic acid (v/v), 40% methanol (v/v)) for 30 minutes in agitation, and unstained in 10% acetic acid and sponges were used to accelerate the process; or directly stained with InstantBlue® Coomassie Protein Stain (ISB1L-Abcam).

MM. 3.4. Western blot method

For specific detection of *M. genitalium* or *M. pneumoniae* proteins, SDS-PAGE gels were electro-transferred to PVDF membranes using cold Towbin buffer (25mM Tris, 192mM Glycine, 20% Methanol (v/v)) following the standard protocols described in[536,537] **Towbin H. *et al.*, 1979 and Mahmood T. and Yang P. C., 2012**.

Table MM. 3.4. Antibodies used in this study.

Antibody	Host	Dilution	Conjugated enzyme	Source
Anti-mouse IgG (H+L) Alexa Fluor 555	Goat	1:250		Invitrogen
Polyclonal anti-Mouse IgG (H+L)	Goat	1:3000	HRP	Bio-Rad
Polyclonal anti-MG_191/MG_192 (Nap)	Mouse	1:1000	-	This work
Polyclonal anti-MPN141 (P1)	Mouse	1:10/1:1000/1:2000	-	This work. Sprankel L. *et al.*, 2023
Polyclonal anti-MPN142 (P40P90)	Mouse	1:10/1:1000	-	This work
Polyclonal anti-MPN141 N-domain	Mouse	1:10/1:1000	-	This work.
Monoclonal anti-MPN141 (P1/MCA4)	Mouse	1:100/1:3000	-	Seto S. *et al.* 2005 (unpublished) This work
Polyclonal anti-MPN213 (P116)	Mouse	1:10/1:1000/1:2000	-	This work. Sprankel L. *et al.*, 2023

Membranes were probed with the appropriate primary antibody in blocking solution, which was then detected using a secondary antibody conjugated with horseradish peroxidase (Bio-Rad). Bioluminescence reaction was catalyzed with *Luminata Forte*^{TM} *Western HRP* substrate (Sigma-Aldrich/Merck-Millipore). Visualization and image optimization was performed in a CHEMIDOC MP Imaging System (Bio-Rad) using QuantityOne® software (Bio-Rad) and Odyssey XF LI-COR Imaging System (LI-COR) using LI-COR software.

MM. 3.5. Recombinant proteins expression and purification

MM. 3.5.1. Cloning, expression, and purification of P110N, P140, and P110

The region corresponding to the MG_192 (P110) gene from *M. genitalium* (strain G37, residues 23–827, P110N) was amplified from a synthetic clone (**Appendices Table A. CI. 1.5**) using primers P110N-F and P110N-R as Forward and Reverse, respectively (**Appendices Table A. CI. 1.1**). The PCR fragment was cloned into the expression vector pOPINE[538] [**Berrow N. S., *et al.*, 2007**] (gift from Ray Owens plasmid #26043, Addgene, Watertown, USA) to generate a C-end His_6-tagged protein. The recombinant protein was obtained after expression in B834 (DE3) cells (Merck,

Darmstadt, Germany) at 20 °C O/N upon induction with 1 mM IPTG at an optical density at 600 nm (OD_{600}) of 0.6. Cells were harvested and lysed in 1× phosphate-buffered saline (PBS) buffer by sonication. Subsequently, the cell extract was centrifuged at 25000 ×*g* at 4 °C and the supernatant applied to a 5 ml His-trap column (GE Healthcare, Pittsburgh, USA) equilibrated with 1× PBS as binding buffer and 1× PBS with 500 mM imidazole as elution buffer. Soluble aliquots of His_6-tagged P110N were pooled and loaded onto a HiLoad Superdex 200 16/60 column (GE Healthcare) in buffer consisting of 50 mM Tris pH 7.4 and 150 mM NaCl. The region corresponding to the MG_192 (P110) gene from *M. genitalium* (strain G37, residues 23–938, P110) was amplified from a synthetic clone (**Appendices Table A. CI. 1.5**) using primers P110-F and P110-R as Forward and Reverse, respectively (**Appendices Table A. CI. 1.1**). The region corresponding to the MG_191 (P140) gene from *M. genitalium* (strain G37, residues 23–1351) was amplified from a synthetic clone (**Appendices Table A. CI. 1.5**) using primers P140-F and P140-R as Forward and Reverse, respectively (**Appendices Table A. CI. 1.1**). Protein production and purification for P140 and P110 followed the same protocol as for P110N[75] [**Aparicio D. *et al*., 2018**].

MM. 3.5.2. Cloning, expression and purification of P1 and P1 fragments

The coding sequences for constructs of P1 and the C-terminal domain of P1 were amplified from the synthetic clone of MPN_141 (P1) gene from *M. pneumoniae* (Genscript) (**Appendices Table A. CIII. 3.6**), using primers P1-F and P1-R for P1 (29-1521), P1Ct1400_F and P1R for P1 C-terminal (1400-1521), P1Ct1376_F and P1-R for P1 C-terminal (1376-1521) (**Appendices Table A. CI. 1.1**). The coding sequences for constructs of P40/P90 were amplified from the synthetic clone of MPN_142 (P40/P90) gene from *M. pneumoniae* (Genscript) (**Appendices Table A. CIII. 3.6**), using primers P40P90_F and P40P90_R (23-1114). The PCR fragments were cloned into the expression vector pOPINE[538] (Addgene) [**Berrow N. S., *et al*., 2007**] to add a C-end His_6-tag to the resulting constructs. Recombinant proteins were obtained after expression with B834 (DE3) cells (Merck), with IPTG at 0.8 mM and 22ºC overnight. The cell pellets were lysed in 1xPBS at pH 7.4 and 40mM Imidazole (binding buffer) and centrifuged at 20000 rpm at 4ºC. Supernatant was charged into a His-Trap 5ml column (GE Healthcare) and eluted with a buffer containing 400 mM imidazole. Soluble aliquots were concentrated and loaded in a Superdex 200 GL 10/300 column (GE Healthcare) with a Tris-HCl 20 mM buffer (pH 7.4) and 150 mM NaCl.

MM. 3.5.3. Cloning, expression and purification of P116 constructs

Regions corresponding to the *mpn213* gene from *M. pneumoniae* were amplified from synthetic clones (**Appendices Table A. CIV. 4.2**) using different primers for each construct: P116-F_{30} and P116-R_{957} for P116 (30–957); P116-F_{13} and P116-R_{957} for P116 (13–957); P116-F_{212} and P116-R_{862}

for P116 (212–862); and P116-FW_{681A} and P116-RW_{681A} to generate variant P116 W681A (**Appendices Table CIV. 4.1**). PCR fragments were cloned into the expression vector pOPINE[538] [**Berrow N. S., *et al*., 2007**] (Addgene) to generate constructs, with a C-end His_6-tag. Recombinant proteins were obtained after expression at 22 °C in B834 (DE3) cells (Merck), upon induction with 0.6 mM IPTG at an optical density at 600 nm (OD_{600}) of 0.8. Cells were collected and lysed by French press in binding buffer (20 mM Tris-HCl pH 7.4, 40 mM imidazole and 150 mM NaCl) and centrifuged at 49000 x*g* at 4 °C. Supernatant was loaded onto a His-Trap 5 ml column (GE Healthcare) that was pre-equilibrated in binding buffer and elution buffer (20 mM Tris-HCl pH 7.4, 400 mM imidazole and 150 mM NaCl). Soluble aliquots were pooled and loaded onto a Superdex 200 GL 10/300 column (GE Healthcare) in a protein buffer (20 mM Tris-HCl pH 7.4 and 150 mM NaCl).

To obtain empty P116, 2.6% Triton X-100 was added to the protein sample and incubated for 1.5 hours at room temperature. Subsequent purification followed the same methodology described above, but also included a wash step with the binding buffer plus 1.3% Triton X-100, followed by extensive washing with at least 20 column volumes of wash buffer (20 mM Tris-HCl pH 7.4, 20 mM imidazole) before eluting the samples from the column. P116 was concentrated with Vivaspin 500 centrifugal concentrators (10000 MWCO PES, Sartorius) to a final concentration of > 0.5 mg/mL.

To refill P116 with lipids, the empty protein was incubated with approximately 1 mL FBS per mg P116 for 2 hours at 30 °C while still bound on the column. After extensive washing with at least 40 column volumes of wash buffer, elution and concentration were performed as described above.

MM. 3.6. Purification of Nap complex (P110 and P140) from *M. genitalium* cells

A P110-His strain was generated for purification of the Nap complexes from *M. genitalium* G37 cells (ATCC 33530). Produced by genetic engineering[299] [**Scheffer, M. P. *et al.*, 2017**], the strain carries a 6xHis-tag insertion in the MG_192 (P110) gene. Different numbers of litters (normally, between 1L and 4L) of the P110-His strain grown in SP4 medium in suspension at 37 °C at 100 rpm. was harvested by centrifugation (16000 ×g, 4 °C, 30 minutes). The pellet was washed twice with PBS with calcium and magnesium, followed by cell disruption by sonication in PBS in the presence of 1mM EDTA, 5mM β-mercaptoethanol, 0.1mM PMSF, and EDTA-free cocktail of protease inhibitors (Roche Diagnostics, Mannheim, Germany), following manufacturer instructions. The pellet generated after centrifugation (70000 ×g, 4 °C, 30 minutes) was

resuspended in 75mM Tris pH 7.4, 400mM NaCl, 5% glycerol, and 2% n-octyl-β-D-glucopyranoside detergent (OG) by homogenization in a glass homogenizer. Solubilization of membranes was done overnight at 4 °C in an orbital shaker. Solubilized membranes were centrifuged at 50000 ×g, 30-40 min (4 °C) and the supernatant was purified by Ni^{2+}-affinity chromatography HisTrap™ HP (Cytiva) in 75mM Tris pH 7.4, 400mM NaCl, 5% glycerol, and 0.5% OG detergent. The purified Nap complex was obtained by Superose 6 size-exclusion chromatography Superose® 6 Increase 10/300 GL (Cytiva) equilibrated with the same buffer.

MM. 3.7. Antibodies production, validation and purification

The research complies with all relevant ethical regulations. The experimental procedures to immunize mice and obtain polyclonal and monoclonal antibodies were approved by the Ethics Committee on Animal and Human Experimentation from the "Universitat Autonòma de Barcelona" under the document CEEAH 1002R3R2R.

MM. 3.6.1. Polyclonal antibodies obtention

Polyclonal antibodies obtention for P110, P140 and Nap from *M. genitalium*

Polyclonal antisera anti-P110, anti-P140 and anti-Nap were prepared by immunizing BALB/C mice with the respective recombinant proteins and Nap purification described above. Sera were obtained by cardiac puncture of properly euthanized mice just before splenectomy and tittered using serial dilutions of each antigen. Titers of the different polyclonal sera were determined as the IC_{50} value from four parameter logistic plots and found to be approximately 1/10000.

Polyclonal antibodies obtention for P1 and P40/P90 from *M. pneumoniae*

Polyclonal antisera anti-P1, anti-P1 fragments and anti-P90/P40 were prepared by immunizing BALB/C mice with the respective recombinant proteins and polypeptides described above[353] [**Vizarraga D. *et al*., 2020**]. Sera were obtained by cardiac puncture of properly euthanized mice just before splenectomy and tittered using serial dilutions of each antigen. Titers of the different polyclonal sera were determined as the IC_{50} value from four parameter logistic plots and found to be approximately between 1/2500 and 1/4000.

Polyclonal antibodies obtention for P116 from *M. pneumoniae*

Two BALB/C mice were serially immunized with four intraperitoneal injections, each one containing 150 µg of recombinant P116 ectodomain (residues 30–957) in 200 µL of PBS with no adjuvants. The last injection was delivered four days before splenectomy. Polyclonal sera were obtained by cardiac puncture of properly euthanized mice just before splenectomy and titered using serial dilutions of the antigen. The titer of each polyclonal serum was determined as the

IC_{50} value from four parameter logistic plots and found to be approximately 1/4000 for both sera.

MM. 3.6.1. Monoclonal antibodies obtention, sequencing and mapping

Production and sequencing of the monoclonal antibody P1/MCA4

A *mpn141* (P1) gene fragment was amplified by PCR from genomic DNA of *M. pneumoniae* M129 strain using primers P1F_2 and P1R_2 (**Appendices Table A. CIII. 3.1**). The amplified fragment was inserted into *Nco*I and *Xho*I site of pET-30c (+) expression vector, resulting the pP1-8 plasmid. *E. coli* BL21(DE3) was transformed by the pP1-8 for expression of a recombinant P1 peptide containing Ala1160 to Gln1518 of the P1 of M129 strain. The recombinant P1 was purified by His-tag affinity chromatography and used to immunize mice for production of anti-P1 monoclonal antibody. The monoclonal antibody P1/MCA4 was selected by ELISA screening and showed high specificity to P1 in Western blotting analysis and immunofluorescence microscopy of living *M. pneumoniae* cells. The amino acid sequence of P1/MCA4 was determined at GenScript (Tokyo, Japan) by cloning and sequencing of the cDNAs of antibody mRNA from P1/MCA4 producing hybridoma cell. The obtained sequences for a single H chain and two L chain of the P1/MCA4 (**Appendices Figure A. CIII. 3.5**) were deposited into the DDBJ/ENA/GenBank databases under the accession numbers LC600310, LC600311 and LC600312**.**

For P1-Fab fragment purification, monoclonal antibody P1/MCA4 against P1 was diluted up to 2 mg mL^{-1} in 1xPBS buffered at pH 8.0 and mixed with 0.1mg/ml of Papain (previously activated in 20mM L-cysteine, 20 mM EDTA and 1xPBS pH 7.0) in a relation 1:40 (Protein:Papain) and incubated during 4 hours at 37ºC. To stop digestion, 10% of the final volume of Iodine acetamide was added. The digested solution was loaded onto HiTrap Protein G 5ml with Binding buffer (20 Mm Na_2HPO_4 pH 7.0) and Elution buffer (0.1 M Glycine-HCl pH 2.7). Soluble aliquots were concentrated and loaded in a Superdex 75 GL 10/300 column (GE Healthcare) with a Tris-HCl 20 mM pH 7.4 and 150 mM NaCl buffer. Complexes of P1-mAb and P1-Fab were formed by mixing both proteins in a ratio 2:1 and 1:1, respectively.

For epitope mapping of P1/MCA4, a series of plasmids that express recombinant P1 peptides were constructed (**Appendices Table A. CIII. 3.4**). These plasmids were generated by partial deletion of the pP1-8 plasmid using specific primer sets and PrimeSTAR Mutagenesis Basal kit (Takara Bio, Shiga, Japan). Recombinant P1 peptides were produced in *E. coli* BL21(DE3) harboring the plasmids, separated by 10-20% gradient-gel SDS-PAGE, and transferred to nitrocellulose membranes. Recombinant P1 peptides on membranes were reacted with 0.5

µg/ml P1/MCA4. After wash of the membranes, binding of the P1/MCA4 to P1 peptide was detected by anti-mouse IgG, HRP conjugate secondary antibody (Promega, Madison, WI, USA) and EzWestBlue W substrate (Atto, Tokyo, Japan).

Monoclonal antibodies obtention for P116 from *M. pneumoniae*

Isolated B lymphocytes from the immunized mice were fused to NSI myeloma cells[533] [**Köhler G. and Milstein C., 2005**] to obtain stable hybridoma cell lines producing monoclonal antibodies, as previously described[539] [**Guasch A. *et al.*, 2020**]. Supernatants from hybridoma cell lines derived from single fused cells were first investigated by indirect ELISA screening against the recombinant P116 ectodomain. Positive clones were also tested by Western blot against protein profiles from *M. pneumoniae* cell lysates and by immunofluorescence using whole, non-permeabilized *M. pneumoniae* cells (see below). Only those clones with supernatants revealing a single 116 kDa band in protein profiles and also exhibiting a consistent fluorescent staining of *M. pneumoniae* cells were selected and used in this work.

MM. 3.8. Chromatography-mass spectrometry (LC-MS) analysis

MM.3.8.1. Liquid chromatography-mass spectrometry (LC-MS) analysis

P140 and P110 proteomics analysis (LC–MS/MS)

LC-MS analysis was performed by the Proteomics Laboratory at CSIC/UAB. Following the purification procedure described above, a sample of the Nap (containing P140 and P110 proteins) in PBS 2X and 0.5% n-octyl-β-D-glucopyranoside detergent (OG) (0.5 µg/ µL) were in-liquid digested following LP-CSIC/UAB internal procedure LP/IT/03. An aliquot of 2 µg was taken to be analyzed directly by LC-MS/MS. The remaining sample was evaporated to dryness to follow the phosphorylation enrichment procedure (TiO_2 enrichment).

The MS system used was an LTQ XL Orbitrap-Velos (Thermo-Fisher- Scientific) equipped with a nanoESI ion source. A 20% of the enriched sample (or 2 ug from the total sample) was loaded into the chromatographic system consisting in a C18 preconcentration cartridge (Agilent Technologies) connected to a 15 cm long, 100 µm i.d. C18 column (Nikkyo Technos Co.). The separation was done at 0.4 µL/min in a 60-min acetonitrile gradient from 3 to 35% (solvent A: 0.1% formic acid, solvent B: acetonitrile 0.1% formic acid). The HPLC system was composed of an Agilent 1200 capillary nano pump, a binary pump, a thermostated micro injector and a micro switch valve. The LTQ XL Orbitrap-Velos was operated in the positive ion mode with a spray voltage of 1.7 kV. The spectrometric analysis was performed in a data dependent mode or target mode.

Data dependent mode; acquiring a full scan followed by 10 MS/MS scans of the 10 most intense signals detected in the MS scan from the global list. The full MS (range 400-1600) was acquired in the Orbitrap with a resolution of 60.000. The MS/MS spectra were done in the linear ion-trap. Target mode; acquiring a full scan followed by 5 MS/MS scans of the 5 most intense signals detected in the MS scan from the peptide list added (phosphopeptides detected in data dependent mode), for those MS/MS scans where the loss of the phosphate moiety was detected (24.5, 32.66, 49.0, 98.0 m/z), an MS3 was acquired. The full MS (range 400-1650) was acquired in the Orbitrap with a resolution of 60.000. The MS/MS spectra were done in the linear ion-trap. The database search was performed with Proteome Discoverer v1.4, with the following parameters: peptide mass tolerance 20 ppm, fragment tolerance 0.6 Da, enzyme set as Trypsin and allowance up to 1 missed cleavage, dynamic modification of methionine oxidation (+16 Da), N-terminal acetylation (+42), and S-T-Y phosphorylation (+79.96), fixed modification of cysteine carbamidomethylation (+57 Da). The database used for searching was created by combination of Mycoplasma genitalium database (04_21) and the protein sequences given by the user. Final results were filtered by peptide rank 1, peptide confidence high (1% FDR) and search engine rank 1.

P116 Proteomics analysis (LC–MS/MS)

LC-MS analysis was performed by the Proteomics Laboratory at CSIC/PRBB. Protein samples were reduced with TCEP and cysteines alkylated with IAA (Thermo-Fisher-Scientific). Subsequent proteolytic digests were performed using S-TRAPs (Protifi), according to the manufacturer's instructions. Peptides were further desalted and purified on Isolute C18 SPE cartridges (Biotage, Sweden) and dried in an Eppendorf concentrator (Eppendorf).

After solubilization in 0.1% formic acid (FA) in ACN/water (95/5, vol/vol), samples were subjected to LC–MS/MS analysis on a nanoElute (Bruker) system, equipped with C18 analytical column (15 cm × 75 µm, particle size: 1.9 µm (PepSep)) coupled to a timsTOF Pro 2 mass spectrometer (Bruker).

Samples were loaded directly onto the analytical column with twice the sample pick-up volume with buffer A. Peptides were separated on the analytical column at 60 °C with a flow rate of 500 nL/minute, with the following gradient: 2 to 35% B in 17.8 minutes, 35 to 95% B in 0.5 minutes and constant 90% B for 2.4 minutes with buffer A (0.1% FA in water) and buffer B (0.1% FA in acetonitrile).

Peptides eluting from the column were ionized online using a captive spray ion-source and analyzed in DDA-PASEF mode with a cycle time of 100 ms and 4 PASEF-MS/MS events. Spectra were acquired over the mass range of 100–1,700 *m/z* and a mobility window of 0.85–1.3 Vs/cm^2.

Data analysis was performed in FragPipe 18 using MSFragger 3.5 for database searches[540] [**Kong, A. T. *et al*., 2017**]. Raw files were recalibrated, search parameters automatically optimized and searched against the combined Uniprot reference proteomes for *M. pneumoniae, E. coli* and *Bos taurus* (UP000000808, UP000000625, UP000162055; obtained 2022-06-23).

The database search space was restricted to tryptic peptides with a length of 7–50 amino acids, allowing for up to two missed cleavages and with a minimum of one unique peptide per protein group. Carbamidomethylation of cysteine was set as a fixed modification and oxidation of methionine, as well as N-terminal acetylation, were set as variable modifications. Percolator was used to estimate the number of false positive identifications, and the results were filtered for a strict target false discovery rate (FDR) < 0.01.

P116 Lipidomic analysis (LC–MS/MS)

LC-MS analysis was performed by the Proteomics Laboratory at CSIC/PRBB. Lipid samples, with an equivalent of 10 µg of protein, were extracted using a modified MTBE/Methanol extraction protocol[541] [**Vasilopoulou C. G. *et al*., 2020**] and submitted to LC–MS/MS analysis using a nanoElute (Brukrt) system, equipped with C18 analytical column (15 cm × 75 µm, particle size: 1.9 µm (PepSep)), coupled to a timsTOF Pro 2 mass spectrometer (Bruker).

Samples were loaded directly onto the analytical column with twice the sample pick-up volume with buffer A. Lipids were separated on the analytical column at 60 °C with a flow rate of 400 nL/minute, with the following gradient: 1% B for 1 minute, 1 to 30% B in 2 minute, 30 to 51% B in 4 minutes, 51 to 61% B in 5 minutes, 61 to 70% B in 5 minutes, 70 to 99% B in 5 minutes and constant 99% B for 13 minutes. This was followed by column re-equilibration with buffer A (ACN/water (60/40, vol/vol) with 10 mM ammonium formate and 0.1% FA) and buffer B (2-propanol/ACN (90/10, vol/vol) with 10 mM ammonium formate and 0.1% FA).

Lipids eluting from the column were ionized online using a captive spray ion source and were analyzed in two replicates for positive and negative mode using DDA-PASEF with a ramp time of 100 ms and 3 PASEF-MS/MS events. Spectra were acquired over the mass range from 50–1,550 *m/z* and a mobility window from 0.55–1.95 Vs/cm^2.

Raw data were converted into .ibf files and analyzed using the MS-DIAL lipidomic pipeline (version 4.9[542] [**Tsugawa H. *et al*., 2020**]) with default processing parameters for timsTOF data.

Identified lipids were aligned to a pooled control sample and filtered by blank abundances (sample intensity/blank intensity >5). Intensities were normalized by mTIC, exported and further analyzed in R using the "lipidr" package[543] [**Mohamed A. M. *et al*., 2020**].

MM. 3.8.2. Size Exclusion Chromatography (SEC-MALS)

Preparation of P140–P110 and P140–P110N complexes and SEC-MALS analysis

Central fractions of the Superdex 200 16/60 column (GE Healthcare) from P140 and either P110N or P110 were mixed in a 1:1 ratio to a final concentration of ∼11 mg/ml (measured with an absorption coefficient of 1.32). Each mixture was incubated for 30 min at room temperature to obtain the heterodimeric complex. For protein oligomerization experiments, prior to sample injections, the multi-angle light scattering (MALS, WYATT Technologies & Corporation) detector was normalized with 25 µl of BSA at 5 mg/ml. Then 150 µl of each purified P140, P110, and P140–P110 sample at 0.6, 2, and 0.5 mg/ml, respectively, were injected at 0.5 ml/min using a Superdex 200 increase 10/300 GL column (GE Healthcare) equilibrated with a running buffer consisting of 50 mM Tris pH 7.4 and 150 mM NaCl. All samples were purified by filtering through 0.22 µm filters.

P1-Fab SEC-MALS analysis and Multi angle light scattering

Molecular weights were measured using a Superdex 200 10/300 GL (GE HEalthcare) column in a Prominence liquid chromatography system (Shimadzu) connected to a DAWN HELEOS II multi-angle light scattering (MALS) detector and an Optilab T-REX refractive index (dRI) detector (Wyatt Technology). ASTRA 7 software (Wyatt Technology) was used for data processing and result analysis. A dn/dc value of 0.185 mL g^{-1} (typical of proteins) was assumed for calculations.

P116 SEC-MALS analysis and multi-angle light scattering

Molecular weights were measured from P116 samples using a Superose 6 10/300 GL (GE Healthcare) column in a Prominence liquid chromatography system (Shimadzu) connected to a DAWN HELEOS II multi-angle light scattering (MALS) detector and an Optilab T-REX refractive index (dRI) detector (Wyatt Technology). ASTRA 7 software (Wyatt Technology) was used for data processing and analysis. An increment of the specific refractive index in relation to concentration changes (dn/dc) of 0.185 mL/g (typical of proteins) was assumed for calculations.

MM. 3.8.3. Matrix-assisted laser desorption/ionization-mass spectrometry (MALDI-MS)

P116 samples MALDI-MS analysis

All samples were mixed in a 1:1 ratio with sDHB (Super-DHB, Bruker) matrix solution (50 mg mL in 50% acetonitrile (ACN), 50% water, and 0.1% trifluoroacetic acid). Subsequently, 1 µL aliquots

of the mixture were deposited on a BigAnchor MALDI target (Bruker) and allowed to dry and crystallize at ambient conditions.

MS spectra were acquired on a rapifleX MALDI-TOF/TOF (Bruker, Germany) in the mass range of 20000–120000 *m/z* in linear positive mode for intact protein measurements and in the mass range of 100–1600 *m/z* in reflector positive mode for lipid measurements. The Compass 2.0 (Bruker) software suite was used for spectra acquisition and processing.

MM. 3.9. HDL isolation and determination of cholesterol transfer rate

Human HDL (density 1.063–1.210 g/mL) was isolated from plasma of healthy donors through sequential gradient density ultracentrifugation, using potassium bromide for density adjustment, at 100000 x*g* for 24 hours with an analytical fixed-angle rotor (50.3, Beckman Coulter). The amount of cholesterol and apolipoprotein A1 were determined enzymatically and by an immunoturbidimetric assay, respectively, using commercial kits adapted for a COBAS 6000 autoanalyzer (Roche Diagnostics, Rotkreuz, Switzerland). Radiolabeled HDLs were prepared in the following way: 10 µCi of either [1,2-^{3}H(N)] free cholesterol or [1,2-^{3}H(N)] cholesteryl oleate (Perkin Elmer) were mixed with absolute ethanol, and the solvent was dried under a stream of N_2. HDL (0.5 mL, 2.25 g/L of ApoA1) was added to the tubes containing the radiotracers, as appropriate, and then incubated for 16 hours in a 37ºC bath[544] [**Cedó L. *et al.*, 2020**]. The labelled HDLs (both ^{3}H-cholesterol-containing and ^{3}H-cholesteryl oleate-containing HDLs) were re-isolated by gradient density ultracentrifugation at 1.063–1.210 g/mL and dialyzed against PBS through gel filtration chromatography. Specific activities of ^{3}H-cholesterol-containing and ^{3}H-cholesteryl oleate-containing HDLs were 1221 and 185 counts per minute (cpm)/nmol, respectively. The cholesterol transfer to P116 (1 g/L) was measured after adding either [^{3}H] free cholesterol-containing or [^{3}H] cholesteryl oleate-containing HDL (0.5 g/L of APOA1) and incubation for 2 hours at 37ºC. HDL and P116 were separated by a His-Trap HP affinity and size-exclusion columns (**Figure CIV. 2.9_1**). The radioactivity associated with each P116 and HDL fraction was measured through liquid scintillation counting. The percentage of [^{3}H] cholesterol transferred per mL was determined for each condition. The specific activities for each radiotracer were used to calculate the amount of free cholesterol and cholesteryl ester transferred from HDL to P116. Total cholesterol levels in the HDL fraction were determined enzymatically by using a commercial kit adapted for a COBAS 6000 autoanalyzer (ref 03039773190, Roche Diagnostics). Human APOA1 levels were determined in both the HDL and purified P116 fractions by an assay (ref 3032566122, Roche Diagnostics) that used anti-APOA1 antibodies that react with the antigen in the sample to form antigen–antibody complexes,

which, after agglutination, were measured turbidimetrically in the COBAS 6000 autoanalyzer (**Appendices Table A. CIV. 4.4**).

MM. 4. Time-lapse microcinematography

MM. 4.1. Time-lapse microcinematography

Gliding properties of the *M. genitalium* and *M. pneumoniae* wild type and mutant strains were analyzed by time-lapse microcinematography as previously described[519] [**García-Morales L., *et al*., 2016**], but with some modifications. Samples from mid-log phase cell cultures were grown overnight on eight-well ibiTreat µ-slides (Ibidi, Gräfelfing, Germany) filled with 200 µl of SP4 medium. Prior to the observation, medium was replaced with fresh SP4 prewarmed at 37 °C and cell movement was examined at 37 °C and 5% CO_2 using a Nikon Eclipse TE 2000-E inverted microscope equipped with a CO_2 Microscope Cage Incubation System (Okolab, San Bruno, USA). Images were captured at 2 s intervals for a total of 2 min for all different strains. The frequency of motile cells was determined by examining a minimum of 250 isolated cells of each strain. Given that cells of the P110-W838F mutant were mainly aggregated, only 64 individual cells could be analyzed. Mean velocities were obtained from the analysis of at least 25 motile, isolated cells, by measuring the travelled distance and dividing this value by the time spent in microcinematography. Analysis of the gliding properties was performed using the ImageJ software with the MTrack2, MTrackJ, wrMTrack, and Stack Deflicker plugins (https://imagej.nih.gov/ij/).

Effects of antibody sera on mycoplasma cells were investigated by time lapse cinematography of *M. pneumoniae* cells growing in IBIDI 8-well chamber slides using SP4 medium supplemented with 3% gelatin prewarmed at 37ºC. Each well was seeded with about 10^5 CFUs and incubated for 12-24 h in 200 µL SP4 supplemented with 3% gelatin. Prior to observation, the medium was replaced with fresh SP4 supplemented with 3% gelatin and pre-warmed at 37°C. After incubation for 10 minutes at 37 ºC and 5% CO_2, the slide was placed in a Nikon Eclipse TE 2000-E inverted microscope equipped with a Microscope Cage Incubation System (Okolab) at 37 ºC. Images were captured at 0.5 s intervals for a total observation time of 10 min, and the different antibodies were dispensed directly into the wells after the first 50-60 seconds of observation. Frequencies of motile cells and detached cells before adding the different antibodies were calculated from the images collected between 0 and 50-60 seconds of observation, depending the cinematography. Frequencies of motile cells and detached cells after adding the different antibodies were calculated from the pictures collected in the last minute of observation, between 50-60 seconds and 10 minutes of observation.

Time-lapse microcinematography images were captured with an Orca Fusion camera (Hamamatsu) controlled by NIS-Elements BR software (Nikon).

MM. 5. Quantification of the hemadsorption of *Mycoplasma* strains

Hemadsorption (HA) was quantified using flow cytometry (FC) as previously described[509] [García-Morales L., 2014] with few modifications. Fluorophore SYBR Green I (Life technologies) binds to nucleic acids and is used in this method due to the different content of nucleic acids between mycoplasma cells and hRBCs. After this staining, populations of mycoplasma cells, mycoplasma aggregates, hRBCs and hRBCs with attached mycoplasmas can be separated and measured. 10^9 mycoplasma cells were used during the HA assay. FACS data was acquired using a FACSCalibur (Becton Dickinson) equipped with an air-cooled 488 nm argon laser and a 633 nm red diode laser. FC data were analysed with the CellQuest-Pro software and FACSDiva software (Becton Dickinson). Side-angle-scatter (SSC-H), Forward Scatter-Height (FSC-H), green fluorescence (FL1-H detector, 530/30 filter) and red autofluorescence (FL3-H detector, 670LP filter) were used to quantify the different cell types used.

Binding of mycoplasma cells to hRBCs can be modelled using the equation: $M_f = 1 - \frac{B_{max}[RBC\}}{K_d + [RBC]}$

This equation corresponds to an inverse Langmuir isothermal kinetic function, where M_f is the fraction of free mycoplasma cells, [*RBC*] is the number of FC events in R2 region per µL, B_{max} the maximum fraction of mycoplasmas cells bound to RBCs and K_d is the dissociation constant of the binding reaction[509] [García-Morales L., 2014]. Similar to other kinetic analyses performed on binding reactions involving a ligand and a receptor, the lower K_d and the higher B_{max} are indicative of the stronger HA activity of the tested cells. Plots and data fitting to inverse Langmuir isotherm curves were performed by using the Prism 7 software (GraphPad).

In previous works, our lab demonstrated the suitability of a FACS-based hemadsorption assay to quantify the HA of *M. genitalium* cells[75] [Aparicio D. *et al.*, 2018]. In the current study, we used FACS to assess the cytadherence of a series of adhesin mutants. K_d and B_{max} values for all mutants' strains analyzed are listed per chapter in **Appendices Tables A. CI. 1.3, CII. 2.3, CII. 3.3 and CV. 5.3.**

MM. 6. Epifluorescence Microscopy

MM. 6.1. Immunofluuorescence microscopy

The immunofluorescence staining of mycoplasma cells on chamber slides was similar to previously described[271,510] [Nakane D. *et al.*, 2015; Sprankel L. *et al.*, 2023b], with several modifications. All mycoplasma cells were washed with PBS containing 0.02% Tween 20 (PBS-T)

except cells from *M. genitalium* G37ΔAdh strain and Engelman motif mutant strains, which were washed in PBS containing 136 mM sucrose (PBS-Suc), prewarmed at 37 °C. Then, each well was fixed with 200 µL of 3% paraformaldehyde (w/v) and 0.1% glutaraldehyde. Cells were washed three times with PBS-T (or PBS-Suc), and slides were immediately treated with 3% BSA in PBS-T (blocking solution) for 30 minutes. The blocking solution was removed and each well was incubated for 1 hour with 200 µL of the primary antibodies diluted in blocking solution. We have used a 1/2000 dilution for all polyclonal sera; a 1/10 dilution was used for monoclonal antibodies from hybridoma supernatants. Wells were washed three times with PBS-T or PBS-Suc and incubated for 1 hour with a 1/2000 dilution of a goat anti-mouse Alexa 555 secondary antibody (Invitrogen) in blocking solution. Wells were then washed three times with PBS-T or PBS-Suc and incubated for 20 minutes with 100 µL of a solution of Hoechst 33342 10 µg μL^{-1} in PBS-T or PBS-Suc. Wells were finally washed once with PBS-T and replenished with 200 µL of PBS before microscopic examination. Cells were examined by phase contrast and epifluorescence in an Eclipse TE 2000-E inverted microscope (Nikon). Phase contrast images, 4',6-diamidino-2-phenylindole (DAPI, excitation 387/11 nm, emission 447/60 nm) and Texas Red (excitation 560/20 nm, emission 593/40 nm) epifluorescence images were captured with an Orca Fusion camera (Hamamatsu) controlled by NIS-Elements BR software (Nikon).

MM. 7. Electron Microscopy

MM. 7.1. Negative staining transmission electron microscopy

For the OG solubilized Nap complex, empty Nanodiscs and Nanodiscs filled with Nap molecules grids with continuous carbon films (Electron Microscopy Sciences, Hatfield Pennsylvania, PA, USA) were glow-discharged and the sample (ranging 6-12 µg/mL) was adsorbed to the grid at RT for 40-50 s. After washing two times with Milli-Q water, the grids were stained with 1% (w/v) uranyl acetate for 10-20 s. Images were recorded on a TEM Hitachi H7000 25-125kV (200 KV) transmission electron microscope (Tokyo, Japan) equipped with a CCD GATAN ES500W Erlangshen camera.

MM. 7.2. Scanning Electron Microscopy

Scanning Electron Microscopy (SEM) was performed adapted from what was described previously[277] [**Pich O.Q. *et al*., 2009**]. For the Scanning Electron Microscopy (SEM) analysis, the *M. genitalium* cultures were grown to mid-long phase over glass and round coverslips in a 24-well plate with fresh SP4. For non-adherent mutant strains, the coverslips were treated in advance with 0.2 mg/mL Poly-L-Lysine to allow the cells to stick to the surface of the glass. The inoculum depended on the stock concentration and usually ranged between 5-10 µL of *M.*

genitalium strains. The *Mge*-WT and the mutant strains were grown overnight and washed twice with 1 mL 0.1M PB. Then, the cells were fixed with 2% paraformaldehyde and 2.5% glutaraldehyde (v/v) dissolved in 0.1M PB for two hours in the dark and room temperature. Samples were then washed again with 0.1M PB and dehydrated sequentially with increasing ethanol solutions (25, 50, 75 and 100% ethanol), 10 minutes for each solution. Once in 100% ethanol, samples were sent to Servei de Microscòpia (UAB) and immediately critical-point dried in a *K850 Critical Point Dryer* (Emitech) and then they were sputter coated with gold. Samples were observed using a MERLIN FE-SEM microscope (ZEISS). Images were analyzed with *ImageJ* software (NIH).

MM. 7.3. Cryo-electron tomography (Cryo-ET)

MM. 7.3.1. Cryo-ET and sub-tomogram averaging of *M. genitalium* cells

Ghost cells were prepared in a similar manner as reported previously[299] [**Scheffer M. P. *et al*., 2017**]. Briefly, cells of the adherently growing *M. genitalium* G37 strain (ATCC 33530) were cultivated on 300-mesh lacey carbon EM grid (PLANO GmbH, Wet zlar, No. S166-3) in 3 ml SP4 medium, rinsed for 1 min with PBS before incubation with 20 mM TEA pH 7.5, 0.5 M KCl, and 1% (v/v) Triton X-100 for 1–5 min in the Vitrobot Mark IV (Thermo-Fisher-Scientific, Waltham, USA) humidity chamber at 95% humidity and 15 °C. Before plunge freezing, 5 nm gold fiducial markers (Protein A-conjugated to gold beads, Cell Biology Department, UMC Utrecht) were added. Tilt-series were recorded using SerialEM 3.5.8[545] [**Mastronarde D. N., 2005**] on a 300 kV Titan Krios (Thermo-Fisher-Scientific) in energy-filtered transmission electron microscopy (EFTEM) mode using a GIF Quantum® SE post-column energy filter (Gatan, Inc., California, USA) set to 20 eV slit width. A K2 Summit detector (Gatan Inc.) was operated in counting mode with a dose rate of ~1.0e^-/pixel/s, using a frame rate of 0.25 s and a total dose in the range of 40–50e^-/Å^2. A nominal magnification of ×64000 was used with the K2 in super-resolution mode, resulting in a pixel size of 1.1 Å/pixel. The tilt-series generally covered an angular range from –60° to +60° with an angular increment of 3° and defocus set between –2 and –4 µm using either dose symmetric or bidirectional acquisition. Tomograms were reconstructed by super-sampling SART[546] [**Kunz M. and Frangakis A. S., 2014**] with 3D contrast transfer function (CTF) correction. For volume visualization and isosurface rendering, the EMpackage in Amira was used (Thermo-Fisher-Scientific)[547] [**Zivanov J. *et al*., 2018**]. Sub-tomogram averaging was performed in a similar manner as reported previously[299] [**Scheffer M. P. *et al*., 2017**]. In short, Nap complexes were manually selected and pre-aligned according to their orientation on the membrane, which provided a strong constraint lowering the degrees of freedom for sub-tomogram averaging. This first pre-aligned average was used as the starting reference template for the iterative sub-

tomogram averaging procedure, thus completely avoiding any initial model bias. The "open" structure for the Cryo-ET data is maintained when using the "closed" structure as a starting reference (**Appendices Figure A. CI. 1.4_1**). We then averaged 11000 Nap sub-tomograms. Post-processing involved refinement by projection matching and dose weighting of the wedge components. After classification, 8800 Nap sub-tomograms were included in the final average. All processing was performed using sub-tomograms with a voxel size of 0.44 nm. The 0.5 criterion was used for resolution estimation. For classification of sub-tomograms, the averaged particles were normalized, and single projection slices in *X*, *Y*, and *Z* directions were extracted using custom MATLAB scripts, which are available on GitHub (https://github.com/uermel/Artiatomi). Subsequently, the two-dimensional (2D) projection slices were imported into Relion[547] [**Zivanov J. *et al*., 2018**] and 2D classification without image alignment was performed. Constituent sub-tomograms from the respective 2D classes were summed together to create 3D classes. Molecular graphics rendering and analyses were performed with either UCSF Chimera[408] [**Pettersen E. F. *et al*., 2004**] or UCSF ChimeraX[548] [**Goddard T. D. *et al*., 2018**] (Resource for Biocomputing, Visualization, and Informatics at the University of California, San Francisco, USA). In all cases, rigid-body transformations were used to fit X-ray structures into the Cryo-EM density maps using the fit-in-map function in UCSF Chimera.

MM. 7.3.2. Cryo-ET and sub-tomogram averaging of *M. pneumoniae* cells

M. pneumoniae M129 cells of an adherently growing culture were scraped in a final volume of 1 mL of SP4 medium and washed three times in PBS. This solution was mixed with fiducial markers (Protein A conjugated to 5 nm colloidal gold: Cell biology department, University Medical Centre Utrecht). From this stock, a 3.5-µL drop was applied to a (45 s) glow-discharged R1.2/1.3 C-flat grid (Electron Microscopy Science), and plunge-frozen in liquid ethane (Vitrobot Mark IV, Thermo-Fisher-Scientific) at 100% relative humidity, 4ºC, and a nominal blot force of –1, with a wait and blotting time of 10 seconds.

Tilt-series were recorded using SerialEM v3.8[545] [**Mastronarde D. N., 2005**] at a nominal magnification of ×105000 (1.3 Å per pixel) in nanoprobe EFTEM mode at 300 kV with a Titan Krios (Thermo-Fisher-Scientific) electron microscope equipped with a GIF Quantum S.E. post-column energy filter in zero loss peak mode and a K2 Summit detector (Gatan). The total dose per tomogram was 120 $e^{-}/Å^2$, and the tilt series covered an angular range from −60° to 60° with an angular increment of 3° and a defocus set at −3 µm. Tomograms were reconstructed by super-sampling SART[546] [**Kunz M. and Frangakis A. S., 2014**] with a 3D CTF correction[549] [**Kunz M. and Frangakis A. S., 2014**].

MM. 7.4. Cryo-electron microscopy (Cryo-EM)

MM. 7.4.1. Single-particle Cryo-EM and image processing of the P140-P110 heterodimer and Nap complex

For single-particle Cryo-EM, a 3.5 µl aliquot of 20 µg/ml purified P140–P110 heterodimer, or 25 µg/ml purified Nap complex, was applied to a (30 s) glow-discharged R1.2/1.3 Quantifoil grid (Quantifoil, Großlöbichau, Germany), and plunge-frozen in liquid ethane (Vitrobot Mark IV, Thermo-Fisher-Scientific) at 100% humidity, 4ºC, blot force –3, wait time 60 s, with a blotting time of 15 s for the heterodimer and 20 s for the Nap complex. Dose-fractionated movies were collected at a nominal magnification of ×130000 (1.05 Å per pixel) in nanoprobe EFTEM mode at 300 kV with a Titan Krios (Thermo-Fisher-Scientific) electron microscope using a GIF Quantum S.E. post-column energy filter in zero loss peak mode and a K2 Summit detector (Gatan Inc.). For the heterodimer, 32 frames of 0.2 s each were collected and for the Nap complex 34 frames per micrograph were collected. The camera was operated in dose-fractionation counting mode with a dose rate of ~7.7 electrons per $Å^2$ s^{-1} for the heterodimer and ~7.4 electrons per $Å^2$ s^{-1} for the Nap complex, resulting in both cases in a total dose of ~50 electrons per $Å^2$. Defocus values ranged from –1 to –4 µm with marginal (<0.1 µm) astigmatism.

Relion 3.0 was used for the whole-image processing workflow[547] [**Zivanov J. *et al*., 2018**] unless stated otherwise. Beam-induced motion correction was performed using UCSF MotionCor2[550] [**Zheng S. Q. *et al*., 2017**]. The CTF of each micrograph was estimated using GCTF[551] [**Zhang K., 2016**]. As reference for autopicking the heterodimer, the crystal structure filtered to 20 Å was used. As a reference for the Nap complex, the crystal structure of the dimer was fitted into the Cryo-ET data and subsequently lowpass filtered to 20 Å. Cross-checking experiments with Laplacian-of-Gaussian autopicking were performed for the Nap to verify that the structure was not reference-biased. For the heterodimer, 1024402 particles were extracted from 2751 micrographs, and for the Nap complex, 160203 particles were extracted from 2225 micrographs, using a 270-pixel box in both cases. All images were normalized to make the average intensity of the background equal to zero during pre-processing. False-positive particles were removed manually or by unsupervised 2D classification. The CTF-refinement function from Relion 3.0 was used to perform per-particle defocus estimation using a search range from 300 nm around the estimated values from the whole micrographs. To correct for local motion and for radiation damage, we used the Bayesian polishing function of Relion 3.0, in which the resolution-dependent decay caused by radiation damage is taken into account[552] [**Scheres S. H., 2012**]. The polished particles were subjected to another round of 2D classification to remove remaining junk particles. The remaining 404064 particles for the heterodimer and 28000 particles for the

Nap complex were used for 3D classification using the initially generated density map filtered to 60 Å as reference. For the heterodimer, six classes were generated using 3D classification, of which one class (37009 particles) showed electron density in the stalk region for P110 and was refined using 3D auto-refine. For the Nap complex, six classes were generated using 3D classification, of which two classes (11737 particles) were tetrameric. The one tetrameric class containing 5612 particles was refined using 3D auto-refine. Gold-standard Fourier shell correlations (FSCs) were calculated during the 3D refinement between two independently refined halves of the data. The resulting map was post-processed to exclude solvent regions from the FSC calculation and to perform sharpening with a temperature factor of –78 $Å^2$ for the heterodimer and –218 $Å^2$ for the Nap complex resulting in a global resolution of 4.1 Å for the heterodimer and 9.8 Å for the Nap complex, using the 0.143 criterion. Local resolution was estimated using Relion 3.0, showing high resolution in the core regions of the dimer and low resolution in the surface and stalk regions (**Appendices Figure A. CI. 1.6_1 and CI. 1.6_2**).

MM. 7.4.2. P1-Fab Single-particle Cryo-EM, model building and refinement of the binary complex

To prevent preferred orientations, Octylthioglucoside (OG) was added to solution of purified P1-Fab (P1/MCA4) complex to adjust the final concentration of OG to 0.9% (w/l). 2.6 µL of sample solution was applied to a glow-discharged Au-coated Quantifoil holey carbon grid (R1.2/1.3, Cu, 200 mesh), blotted for 4 sec at 4 °C in 100% humidity and plunged into frozen liquid ethane using a Vitrobot Mark IV (Thermo-Fisher-Scientific). The grid was inserted into a CRYO ARM 300 (JEOL) operating at an acceleration voltage of 300 kV. Cryo-EM images were recorded with a K3 direct electron detector (Gatan) in CDS mode with an energy filter at a slit width of 20 eV. Data were automatically collected using the SerialEM software (https://bio3d.colorado.edu/SerialEM/) at a physical pixel size of 0.49 Å with 50 frames at a dose of 2.0 e^-/ $Å^2$ per frame and an exposure time of 2.86 sec per movie with a defocus ranging from -0.5 to -1.5 µm. A total of 27122 movies were collected for P1-Fab complex.

The movie frames were subjected to beam-induced movement correction using MotionCor2.1[550] [**Zheng S. Q. *et al.*, 2017**] and contrast transfer function (CTF) was evaluated using Gctf[551] [**Zhang K., 2016**]. Approximately 2000 particles were manually selected from 20 micrographs to perform two-dimensional (2D) classification. Using a good 2D class average image, a total of 4312408 particle images were automatically picked and 2D classifications were performed using RELION-3.1[547] [**Zivanov J. *et al.*, 2018**]. A total of 1252491 particles were selected for building the initial model of the P1-Fab complex using CryoSPARC2[553] [**Punjani A. *et al.*, 2017**] and subjected to 3D classification into 8 classes using RELION-3.1. The selected

particles were re-extracted at a pixel size of 0.49 Å and subjected to three 3D refinement, two CTF refinement and Bayesian polishing. After selection of particles using no-alignment 3D classification, a total of 352039 particles were subjected to two 3D refinement and CTF refinement. The final 3D refinement and post-processing yielded maps with global resolutions of 2.39 Å, according to the 0.143 criterion of the Fourier shell correlation (**Appendices Table A. CIII. 3.8**). Local resolution was estimated using RELION-3.1. Processing strategy is described in **Appendices Figure A. CIII. 3.8_1**.

The model of the P1-Fab complex was built based on the Cryo-EM density map. Previous published crystal structure of P1 (PDB ID: 6RC9) was docked into the EM density map using UCSF Chimera[553] [**Punjani A. *et al*., 2017**]. N-domain, C-domain of P1 and Fab were manually repositioned and refined iteratively using COOT[554] [**Emsley P. and Cowtan K., 2004**] and PHENIX real space refinement[555] [**Afonine P. V. *et al*., 2018**]. The statistics of the 3D reconstruction and model refinement are summarized in **Appendices Table A. CIII. 3.8**. The final refined structure has been deposited in the EMDB with code 8ROR.

MM. 7.4.3. P1-Fab Single-particle Cryo-EM of the ternary complex

2.6 µL of sample solution was applied to a glow-discharged Quantifoil holey carbon grid (R1.2/1.3, Cu, 200 mesh), blotted for 4 sec at 4°C in 100% humidity and plunged into frozen liquid ethane using a Vitrobot Mark IV. The grid was inserted into a CRYO ARM 300 operating at an acceleration voltage of 300 kV. Cryo-EM images were recorded with a K3 direct electron detector in CDS mode with an energy filter at a slit width of 20 eV. Data were automatically collected using the SerialEM software (https://bio3d.colorado.edu/SerialEM/) at a physical pixel size of 0.87 Å with 40 frames at a dose of 2.0 e^{-}/ $Å^{2}$ per frame and an exposure time of 3.3 sec per movie with a defocus ranging from -0.8 to -1.8 µm. A total of 7,938 movies were collected for P40/P90-P1-Fab complex.

The movie frames were subjected to beam-induced movement correction using MotionCor2.1[550] [**Zheng S. Q. *et al*., 2017**] and CTF was evaluated using Gctf[551] [**Zhang K., 2016**]. Using blob picker program of CryoSPARC2, a total of 9565198 particle images were automatically picked and 2D classifications were performed using CryoSPARC2[553] [**Punjani A. *et al*., 2017**]. A total of 1070120 particles were selected for building the initial model of the P40/P90-P1-Fab complex using CryoSPARC2. However, due to preferred orientation, an accurate initial structure could not be obtained. Therefore, we did not perform 3D reconstruction for high-resolution structure determination, but performed 3D refinement to confirm how P40/P90 and Fab are bound to P1. The selected particles were re-extracted at a pixel size of 0.87 Å and subjected to

3D refinement. The final 3D refinement and post-processing yielded maps with global resolutions of below 10 Å, according to the 0.143 criterion of the Fourier shell correlation (**Appendices Table A. CIII. 3.8**).

MM. 7.4.4. P116 Single-particle Cryo-EM, model building and refinement

For single-particle Cryo-EM, a 3.5-µL drop of purified P116 (100–400 µg/mL in 20 mM Tris, pH 7.4 buffer or 600 µg/mL in 20 mM Tris, 2 mM CHAPSO, pH 7.4 buffer) or P116 mixed with HDL (250 µg/mL P116 and 1116 µg/mL HDL in 20 mM Tris, pH 7.4 buffer) was applied to a 45 s glow-discharged R1.2/1.3 C-flat grid (Electron Microscopy Science), and plunge-frozen in liquid ethane (Vitrobot Mark IV, Thermo-Fisher-Scientific) at 100% relative humidity, 4 °C, a nominal blot force of –3, and a wait time of 0.5 seconds, with a blotting time of 12 s. Before freezing, Whatman 595 filter papers were incubated for 1 hour in the Vitrobot chamber at 100% relative humidity and 4 °C.

Dose-fractionated movies of P116, P116 refilled and P116 mixed with HDL were collected with SerialEM v3.8[545] [**Mastronarde D. N., 2005**] at a nominal magnification of ×130000 (1.05 Å per pixel) in nanoprobe EFTEM mode at 300 kV with a Titan Krios (Thermo-Fisher-Scientific) electron microscope equipped with a GIF Quantum S.E. post-column energy filter in zero loss peak mode and a K2 Summit detector (Gatan). For P116, P116 refilled and P116 with HDL, a total of 4376, 4019 and 3114 micrographs with 34, 29 and 30 frames per micrograph and a frame time of 0.2 seconds were collected. The camera was operated in dose-fractionation counting mode with a dose rate of ~8 electrons per $Å^2\ s^{-1}$, resulting in a total dose of 50 electrons per $Å^2\ s^{-1}$. Defocus values ranged from –1 to –3.5 µm.

For P116 empty, dose-fractionated movies were collected using EPU 2.12 (Thermo-Fisher-Scientific) at a nominal magnification of ×105000 (0.831 Å per pixel) in nanoprobe EFTEM mode at 300 kV with a Titan Krios G2 electron microscope (Thermo-Fisher-Scientific), equipped with a BioQuantum-K3 imaging filter (Gatan), operated in zero loss peak mode with 20 eV energy slit width. In total, 15299 micrographs with 50 frames per micrograph and frame time of 0.052 seconds were collected. The K3 camera was operated in counting mode with a dose rate of ~16 electrons per $A^2\ s^{-1}$, resulting in a total dose of 50 electrons per $Å^2\ s^{-1}$. Defocus values ranged from −0.8 to −3.5 µm.

CryoSPARC v3.2[553] [**Punjani A. *et al*., 2017**] was used to process the Cryo-EM data, unless stated otherwise. Beam-induced motion correction and CTF estimation were performed using CryoSPARC's own implementation. Particles were initially clicked with the Blob picker using a particle diameter of 200–300 Å. Particles were then subjected to unsupervised 2D classification.

For the final processing, the generated 2D averages were taken as templates for the automated particle picking; for the processing of P116 with HDL, no template picking was performed. In total, 3463490, 4532601 particles, 2930863 particles and 262981 particles were picked and extracted with a binned box size of 256 pixels for P116, P116 empty, P116 refilled and P116 with HDL, respectively. False-positive picks were removed by two rounds of unsupervised two-dimensional classification. The remaining 1324330 particles (P116), 1140275 particles (P116 empty), 1311526 particles (P116 refilled) and 46277 particles (P116 with HDL) were used to generate an ab initio reconstruction with three classes followed by a subsequent heterogeneous refinement with three classes. For the final processing, 1315362 particles (P116), 633332 particles (P116 empty), 1311526 particles (P116 refilled) and 46277 particles (P116 with HDL) were used. For the remaining particles, the beam-induced specimen movement was corrected locally.

The CTF was refined per group on the fly within the non-uniform refinement. The obtained global resolution of the homodimer was 3.3 Å (P116), 4 Å (P116 empty), and 3.5 Å (P116 refilled) (**Figure CIV. 2.4_2, Appendices Figure A. CIV. 4.3_1 and Appendices Table A. CIV. 4.3**). To analyze the sample with regard to its flexibility, the particles were subjected to the 3D variability analysis of CryoSPARC, which was used to display the continuous movements of the protein.

The initial tracing of the core domain was performed manually with Coot[554] [**Emsley P. and Cowtan K., 2004**]. It contained numerous gaps and ambiguities that were slowly polished by alternating cycles of refinement using the 'Real Space' protocol in the program Phenix[556,557] [**Headd J. J. *et al.* 2012; Afonine P. V. *et al*., 2012**] and manual reinterpretation and rebuilding with Coot. The tracing and assignment of specific residues in the N-terminal domain were very difficult owing to the low local resolution of the map for this domain, and only a partial interpretation was achieved. Using Robetta and AlphaFold[471] [**Jumper J. *et al*. 2021**], we obtained different predictions of the N-terminal domain structure using different parts of the sequence. The highest ranked predictions, selected using the partial experimental structure already available, were obtained with AlphaFold for residues 81–245, which allowed us to complete the building of the N-terminal domain according to the Cryo-EM map. The root-mean-square deviation between the AlphaFold prediction and the experimental model was 2.6 Å for 104 (63%) structurally equivalent residues. Some residues at the N end of the N-terminal domain were difficult to identify and were represented as alanines in the final model. The whole P116 model was then refined using Phenix, and the final refined structure was deposited in the EMDB under code EMD-15274 (**Appendices Table A. CIV. 4.3**).

MM. 7.5. Surface Plasmon Resonance

MM. 7.5.1. Surface plasmon resonance of the P140 and P140-P110 complex

For binding assay experiments, a Biacore 3000 biosensor platform (GE Biosystems) equipped with a research-grade streptavidin-coated biosensor chip SA was used. The chip was docked into the instrument and preconditioned with three 1-min injections of 1 M NaCl in 50 mM NaOH. Both 3SL-PAA-biotin and 6SL-PAA-biotin (Carbosynth) oligosaccharides were injected over the second and third flow cell, respectively, at 10 µg/ml diluted in HBS-P (10 mM Hepes, pH 7.4, 0.15 M NaCl, and 0.005% P20). The first cell was left blank to serve as a reference. The running buffer consisted of HBS-P at a flow rate of 30 µl/min and the immobilization levels acquired were ~160 and ~180 response units for 3SL-PAA-biotin and 6SL-PAA-biotin, respectively. A series of diluted purified extracellular P140 and P140–P110 samples in HBS-P (1.25, 2.5, 5, 10, and 20 µM) were injected over the flow cell surface at 30 µl/min. Interaction analysis were performed at 25 °C and the protein was allowed to associate and dissociate for 60 and 90 s, respectively, followed by a 30 s regeneration injection step of 0.05% SDS at 30 µl/min.

MM. 8. Crystallography and X-ray structure

MM. 8.1. Crystallization of P140 alone and the P140–P110N complex

Screening for initial crystallization conditions was performed with 150 nl droplets in 96-well plates on a Cartesian robot (Cartesian (TM) Dispensing Systems) for both P140 alone and the P140–P110N complex. Optimized crystals from P140 were prepared by mixing 1 µl P140 at 6.5 mg/ml and 1 µl reservoir solution containing 20% PEG3350, 0.1 M BisTris Propane pH 7.5, and 0.2 M sodium sulphate hydrate at 20 °C in hanging drop in 24-well plates. Crystals from the P140–P110N complex were prepared by mixing 1 µl of P140–P110N complex at 10.95 mg/ml and 1 µl reservoir solution containing 23% PEG 500MME, 4% PGA, and 0.1 M sodium cacodylate pH 6.5 at 20 °C in hanging drop in 24-well plates. All crystals were flash-cooled in liquid nitrogen with 20% glycerol as a cryoprotectant.

MM. 8.2. X-ray data collection and structure determination

X-ray diffraction experiments were performed at the Xaloc Beamline (ALBA, Spain). Data were processed with Xia2[558] [**Winter G., 2010**] using XDS[559] [**Kabsch W., 2010**], Aimless and Pointless[560] [**Evans P., 2006**] from the CCP4i suite of programs[561] [**CCP4, 1994**]. P140 crystals belong to the space group C2 with six subunits in the asymmetric unit, while P140–P110N crystals belong to the space group $P2_1$ and contain four heterodimers in the crystal asymmetric unit. For the P140–P110N crystals, a partial molecular replacement solution was obtained with Phaser software[562] [**McCoy A. J., 2007**] using the N-terminal domain of the available structures

of P110 (PDB code 6RT3) as a search model. In these P140–P110N crystals, an initial mask was tentatively defined for P140 using the sub-tomogram averaged map of a whole Nap complex obtained from Cryo-ET images of *M. genitalium* ghost cells. Density modification in the crystal of the P140–P110N complex, by iterative non-crystallographic symmetry averaging and solvent flattening followed by phase extension with DM[563] [**Cowtan K. D. and Main P., 1996**], allowed us to obtain a rough density for P140, in which a few secondary structural elements were recognizable. This density was sufficient to provide an initial molecular replacement solution for the P140 crystals (with six subunits in the asymmetric unit) and for crystals of the orthologous protein P1 from *M. pneumoniae* (now deposited in the PDB with code 6RC9). Averaging within and between crystals, while updating and refining the masks, provided electron density maps from which it was possible to progressively build in parallel the structures of P140 and P1. The weak selenium methionine anomalous data, available from both the P140 and the P140–P110N crystals, were used to confirm the sequence assignment to the P140 structure. Final models were traced with Coot[554] [**Emsley P. and Cowtan K., 2004**] and refined with Refmac5[564] [**Murshudov G. N. *et al*., 2011**] (**Appendices Table A. CI. 1.7**).

MM. 9. Protein-Ligand interaction analyses

MM. 9.1. Ligands

The 3'sialylactosamine (3'SLn) and 6'sialylactosamine (6'SLn) were purchased from Tokyo Chemical Industry Co., Ltd. The sialyl-T-antigen linked to the threonine (sTa-Thr) was chemically synthesized as previously reported[565] [**Schwarz J. B. *et al*., 1999**]. The biantennary N-glycans were provided from GlyTech, Inc[566] [**Kajihara Y. *et al*., 2004**].

MM. 9.2. Fluorescence spectroscopy

Steady-state fluorescence experiments were performed on a Fluoromax-4 spectrofluorometer from Horiba Scientific (Edison, USA). All the measurements were acquired at a controlled temperature of 25°C, the excitation wavelength was selected at 280 nm and the emission spectra collected between 290 and 500 nm. The slits were set to 5 nm for both the excitation and emission monochromators. All the spectra were recorded after an equilibration time of 3 minutes in a 1 cm path-length quartz cuvette, under constant stirring.

A fixed concentration of both P110 and P40/P90 proteins (purified as previously described in this section) was selected at 0.07 µM in 1,2 mL PBS buffer (pH 7.4) and titrated by adding small amounts of each ligand 3'SLn, 6'SLn, sTa-Thr in the range from 0 to 6.5µM (1–100 µL of a ligand stock solution of 84µM). In these conditions, it was possible to observe the quenching of protein

fluorescence in presence of the three different ligands; in particular, no ligand emission interference was observed.

Data analysis was performed using the software Origin 1 8.1. Specifically, the binding curves were obtained by plotting F/F_{max} values versus ligand concentrations, where F and F_{max} are fluorescence intensities in presence and in absence of the ligands, respectively. The binding constants (K_b) were determined by non-linear regression with One Site-Specific Binding model, as described in detail in[441,567,568] [**Ribeiro M. M. *et al.*, 2008; Oliva R. *et al.*, 2019; Forgione R. E. *et al.*, 2020**].

MM. 9.3. NMR analysis

The NMR experiments were recorded on a Bruker AVANCE NEO 600 MHz equipped with a cryo probe. Data acquisition and processing were performed with TOPSPIN 4.1.1 software. All NMR samples were prepared in 50mM deuterate phosphate buffer (NaCl 140 mM, Na2HPO4 10 mM, KCl 3 mM, pH 7.4 and the [D4] (trimethylsilyl) propionic acid, sodium salt (TSP, 10µM) was used as internal reference to calibrate all the spectra. The chemical shifts of the glycan ligands were assigned by 1H, COSY, TOCSY, NOESY and HSQC experiments[569] [**Speciale I. *et al.*, 2022**].

Tr-NOESY analysis**:** homonuclear 2D 1H-1H NOESY experiments were carried out by using data sets of 2048x512 points and mixing times of 200 ms. Protein to ligand ratios from 1:20 to 1:50 were used[570] [**Angulo M. J. *et al.*, 2006**].

STD NMR analysis**:** all the NMR spectra were acquired in the same conditions for P110 and P40/P90, using protein concentrations of 20µM and ligand concentrations of 1mM (protein:ligand ratio of 1:50) and temperature of 298K. Control experiments with the ligands and proteins in the absence of the protein and the ligand, respectively, were performed to optimize STD NMR parameters[571] [**Mayer B. *et al.*, 2001**]. STD NMR experiments were acquired with 64K data points and zero-filled prior to processing and a number of scans of 72 and 128. The protein resonances were selectively irradiated using 40 Gauss pulses with a length of 50ms, setting the off-resonance pulse frequency at 40 ppm and the on-resonance pulse at 0 and 7.5 ppm. All STD experiments were performed by using the sequence “stddiffesgp” with an excitation sculpting with gradient pulses (esgp) for the suppression of water signals. A saturation time of 2 s were used for all STD-NMR experiments. By using these conditions, no STD signals were observed in the control STD NMR spectra of the ligands alone.

The epitope mapping of ligands was achieved by the calculation of the ratio $(I_0 - I_{sat})/I0$, where $(I_0 - I_{sat})$ is the intensity of the signal in the STD NMR spectrum and I_0 is the peak intensity referred to the unsaturated reference spectrum (off-resonance). The highest STD signal was set to 100% and all the other STD were normalized to this value.

MM. 9.4. MM and MD simulations

Molecular dynamics calculations of 100 ns on ligands alone and bound to the proteins P110 and P40/P90 were carried out by using the AMBER 18 software package[572] [**Case D. A. *et al.*, 2023**] in explicit water using the following forcefields: Glycam06j-1 for the glycans and FF14SB for the proteins. All the oligosaccharides were built up and minimized by using Maestro package and the carbohydrate builder utility of the glycam website (www.glycam.com), and then the torsional angles were set to the values obtained through the molecular mechanics calculations. First, the ligands were manually docked into the proteins binding pocket according to the published structures (PDB used: 6RUT and 6TLZ for P110 and P40/P90 respectively). Before the MD simulation, the complexes were minimized using Sander tools. The molecules were neutralized by adding Na^+ ions and then hydrated with an octahedral box of TIP3P water of the proper size and the remote interactions were calculated using a cut-off of 10 Å applying *tleap* module of the AMBER package. The MD calculations were performed by using the PMEMD.CUDA implementation within AMBER 18 package. Periodic boundary conditions were applied, as well as the smooth particle mesh Ewald method to represent the electrostatic interactions, with a grid space of 1 Å. A restriction to the protein, which was gradually released, was applied and the system was minimized. Furthermore, the whole system was slowly heated from 0 to 300 K using a weak restrain on the solute and then, the system was equilibrated at 300 K using constant pressure and removing the restrains on the solute. Concerning the complexes of P110 and P40/P90 with sTa-Thr, the value of the peptide dihedral angle (O-CB-CA-N) was restrained approximately at 60 degrees.

Coordinates were obtained to acquire 10000 structures representing the progression of the dynamics. The trajectories were assessed using the *ptraj* module in AMBER 18 and the MD results were visualized using the VMD program[573] [**Humphrey W. *et al.*, 1996**]. A cluster analysis of the MD trajectory was applied based on ligand RMSD, employing the K-means algorithm integrated into the *ptraj* module. The representative structures of the most populated clusters were selected to depict the complexes interactions. Multiple representative poses were chosen for each MD simulation. The identification of hydrogen bonds was computed using the CPPTAJ module within AMBER 18, defining a hydrogen bond as forming between an acceptor heavy atom (A), a donor hydrogen atom (H), and a donor heavy atom (D). The distance cut-off was chosen at 3 Å, and the A-H-D angle cut-off was set to 135°. The frequency of protein-ligand bonds formed during the dynamics was reported with a 5 Å cut-off.

MM. 10. Growth Analysis

To measure the replication rates of several *M. genitalium* and *M. pneumoniae* strains, a mid-long phase culture grown in a 25 cm^2 flask with 5 mL SP4 was used. The medium was aspirated and the cells were resuspended in 3 mL of fresh SP4. Then, 300 µL of the cellular suspension were inoculated in the firs (or seventh) row of a 96-well plate. 100 µL of the first well was inoculated into the next well (second/eighth) row that contained 200 µL of fresh SP4, thus diluting 1/3 the initial concentration (**Figure MM. 10_1**). This process was repeated four more times (until the sixth/twelfth row), therefore achieving a final 1/243 dilution. In the sixth/twelfth well, 100 µL were discarded after mixing by pipetting up and down three times to leave the final volume at 200 µL. The 96-well plated was sealed with transparent tape to diminish condensation and incubated at 37ºC and 5% CO_2 for 7-8 days.

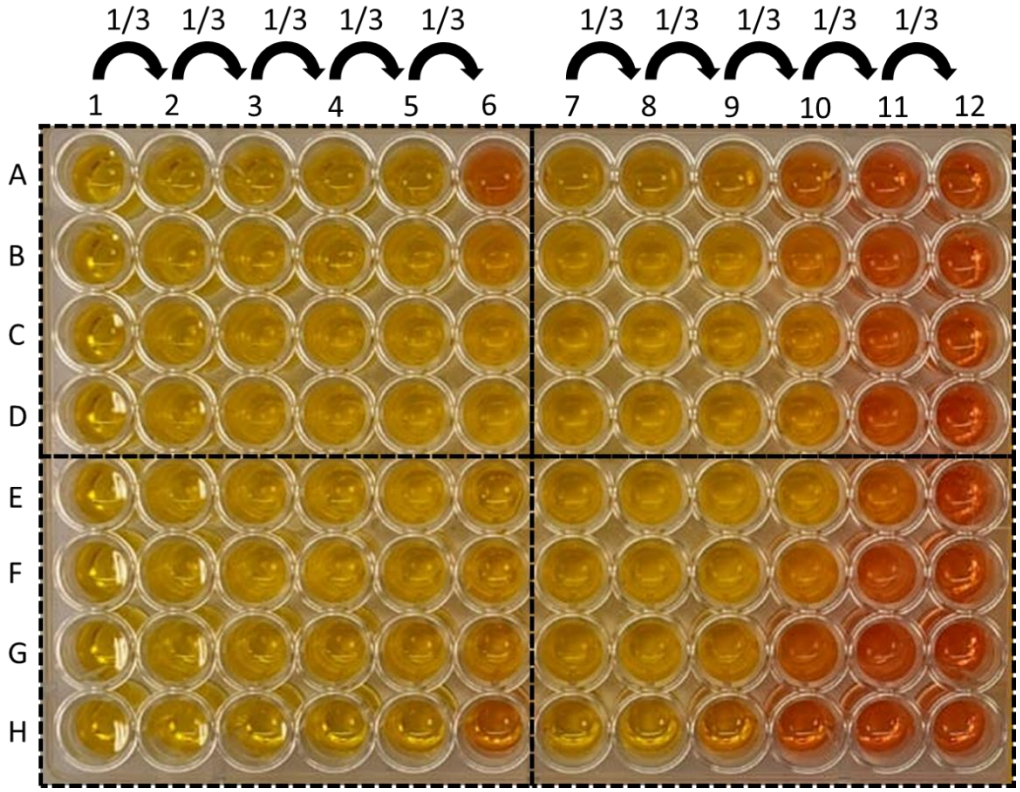

Figure MM. 10_1. Schematic representation/Representative picture of a "real" 96-well plate used for growth kinetics of mycoplasma cells/strains. 300 µL of each strain was inoculated in the first (or seventh) row and it was diluted sequentially with SP4 until the sixth (or twelfth) row. For instance, 300 µL of a G37 strain was seeded at the A1 well; 100 µL of the A1 well was inoculated into the A2 well that contained 200 µL of SP4. Next, 100 µL of the A2 well was seeded into the A3 well, 100 µL of the A3 well was transferred to the A4 well. This process was repeated until the A6 well was reached. Then, after pipetting up and down several times, 100 µL of the A6 well were discarded in order to leave the final volume at 200 µL. Four technical repeats were performed for each strain (A1-A6, B1-B6, C1-C6 and D1-D6, for instance), as it is represented by a dotted line square.

The plate was placed into a Tecan Sunrise Absorbance Microplate Reader (Tecan) adapted with an external chamber designed to maintain the temperature conditions. This microplate reader was used to extrapolate the replication rates by measuring the colorimetric change of the medium at 550 nm. The alteration of the spectrum is related to the microorganism growth, as the metabolism of the bacteria acidifies the initial pH from 7.8 (red) to 6 (yellow). Then a growth curve was generated for each dilution and the inflection point was inferred. Next, the inflection points were plotted in a graphic, using the Napierian logarithm of the dilution as the "x" coordinate for each dilution. Once all the inflection points were plotted and aligned, the equation of the line was obtained and the doubling time (g) was inferred suing the slope (μ, growth rate constant) of the line, as described in the formula for exponential growth of bacteria ($g=\ln 2/(1/\mu)$). This method is an adaptation of the one reported in[158] [**Karr J. R. *et al*., 2012**].

For each analysis, there was a total of 800 lectures, one every 15 min for up to eight days. The readings were stored in an Excel datasheet and analyzed as described after the measurements were over. In order to obtain the readings, a proprietary software of Tecan spectrophotometer (Magellan) was used. A software developed by Jaume Piñol was used to ease the downstream analysis of the data. In addition, a Python script was designed to organize each dataset (the absorbance values of the dilutions of the four technical replicates) in an individual Excel sheet. Then, the same script analyzed the data and provides the curve parameters needed to extrapolate the duplication time. Once all the parameters were calculated, the script was designed to summarize all the growth data in a global Excel sheet, thus providing the average replication time for each strain using the four technical repeats per plate. The Python script can be consulted and downloaded from[420] [**Martinez-Torró C., 2020**].

After running this script, the user must run the Solver complement for each dilution in order to obtain the real adjusted value. Thus, this program reduces the analysis of the reads from several hours to less than five minutes, as it only takes seconds to calculate the adjusted values for each dilution using Solver. The results of each technical repeat are gathered as they are calculated in the Global sheet, as the script has set the necessary formulas to gather the values to calculate the average replication time for each strain.

APPENDICES

A. 1. Appendix of Chapter I

A. 1.1. List of oligonucleotides used in Chapter I

Appendices Table A. CI. 1.1. List of oligonucleotides used in Chapter I: Structure and mechanism of the nap adhesion complex from the human pathogen *Mycoplasma genitalium.*

Primer name	Sequence 5'→ 3'[a]	Use
Construction of mutants of *M. genitalium*		
Complementation of ΔP110 mutant with different P110 variants		
COMmg192-F (*Apa*I)	AGTGGGCCCACTAACAAAAAACAAATTAGTGATGTTGTTA GTGATTGTGTGAAAAAAATTGTTTATAATTAAGTTTGTATG AAAACAATGAGAAAACAG	Cloning: Build pMTnPacP110 with the different P110 substitutions
COMmg192-R (*Xho*I)	AGTCTCGAGCTAACTTTTGGTTTCTTCTG	
R600Amg192-F	CCTGAAAACGCGGGTGCTAGT	
R600Amg192-R	ACTAGCACCCGCGTTTTCAGG	
Q460AD461Amg192-F	AGTTTTTCAATCGCTGCCACCTTCAGCTTTG	
Q460AD461Amg192-R	AAAGCTGAAGGTGGCAGCGATTGAAAAACTCCC	
Y830Amg192-F	GGTTAGCACCTAGTGCCACAGAAAACAGGG	
Y830Amg192-R	CCCTGTTTTCTGTGGCACTAGGTGCTAACC	
R834Gmg192-F	GTTACACAGAAAACGGGGTTGATGCATGGG	
R834Gmg192-R	CCCATGCATCAACCCCGTTTTCTGTGTAAC	
D836Lmg192-F	CAGAAAACAGGGTTTTGGCATGGGGTAAAG	
D836Lmg192-R	CTTTACCCCATGCCAAAACCCTGTTTTCTG	
W838Fmg192-F	GTTGATGCATTTGGTAAAGTTG	
W838Fmg192-R	CAACTTTACCAAATGCATCAAC	
G839Amg192-F	GATGCATGGGCTAAAGTTGAG	
G839Amg192-R	CTCAACTTTAGCCCATGCATC	
Complementation of ΔP140 mutant with different P140 variants		
COMmg191-F (*Apa*I)	AGTGGGCCCACTAACAAAAAACAAATTAGTGATG	Cloning: Build pMTnPacP140 with the different P140 substitutions
COMmg191-R (*Sal*I)	AGTGTCGACTTATTGTTTTACTGGAGGTTT	
H381AH382Amg191-F	CCGAAGTGAAACGCCGCTGGGATCTGGGATTAC	
H381AH382Amg191-R	ATCCCAGATCCCAGCGGCGTTTCACTTCGG	
P140XbaI-F	TCTAGACAGTGATGGTACCC	

P140T1401A-F	GCTAAAGCAGTTGGTAGTGTC	
P140T1401-R (5' Ph)	*CAAGACATCAACCTTTTTGT	
P140S1406A-F	GCTGTCTTTAAAGAGATCATTAAC	
P140S1406-R (5' Ph)	*ACCAACTGCTTTGGTCAAG	
P140T1415A-F	GCTGGGATCTCTAACGCTCC	
P140T1415-R (5' Ph)	*TCTGTTAATGATCTCTTTAAAGAC	
P140S1418A-F	GCTAACGCTCCTAAGAAGTTA	
P140S1418E-F	GAAAACGCTCCTAAGAAGTTA	
P140S1418-R (5' Ph)	*GATCCCTGTTCTGTTAATG	
P140T1428A-F	GCTCCAACCAAACCAACTC	
P140T1428E-F	GAACCAACCAAACCAACTC	
P140T1428-R (5’ Ph)	*AGCTTGTTTTAACTTCTTAGG	
P140T1401A-S1406A-F	GCTAAAGCAGTTGGTGCTGTCTTTAAAGAGATCATTAAC	
P140T1401E-S1406E-F	GAAAAAGCAGTTGGTGAAGTCTTTAAAGAGATCATTAAC	
MG_108 null mutant		
dMG_108-BEFw	TACGAATTACATAACCTTTGTGC	To create an MG_108 defective mutant
dMG_108-BERev	GGATCCATGCACCTCTCGAGATGATCATTAGCAGCTTGCAT	
dMG_108-BDFw	CTCGAGAGGTGCATGGATCCCATTAACAAATACTATTTCCA	
dMG_108-BDRev	ATGGAACTCTACCAACTAACA	
Lox71p438Fwd (*Xho*I)	CTCGAGTACCGTTCGTATAATGTATGCTATACGAAGTTATT AGTATTTAGAATTAATAAAGT	
CatLox66Rev (*Bam*HI)	GGATCCTACCGTTCGTATAGCATACATTATACGAAGTTATT TACGCCCCGCCCTGCCACT	
Oligonucleotides used in sequencing and screening reactions		
Pac-Up	GTAGCTAATCTAACAGTAGG	To sequence DNA inserts cloned in a miniTnPac
Pac-Dw	GTCCTAGAACTTGGTGTATG	To determine miniTnPac Tnp insertion point
RTPCRmg192-F	TCCCCTAATGAATTGCGAAG	To screen for MG_191/MG_192 variants and to
RTPRCmg192-R	CAGGGGCAATTGATTTAAGC	

RTPCRmg191-F	CTGGAGAGAACCCAGGATCA	sequence DNA inserts cloned in a miniTnPac
Tnp3	GATTCATGATTATATCGATCAAC	
SEQmg191a-F	GGTTAGTTTCTATGATGCAC	
SEQmg191b-F	GATACAGCTACTGTACCTAG	
SEQmg191c-F	GTTCTACCTTCGATCAGTTC	
SEQmg191d-F	GCATTACTCCATACCTATGG	
SEQmg191e-F	ATTAACACCATCACCACTAC	
Cat-Up	TTCTTTACGATGCCATTGG	
SCRΔMG_108-F	ATCATAACCTTTAATAGTGATC	To screen for MG_108 null mutant
SCRΔMG_108-R	GCTTGCATTAAAGGTAAGTC	
SCRFloxΔMG_108-F	CAAGCTAAGATAGAGTTTCAAC	
Fup17	GTAAAACGACGGCCAGT	Universal Forward primer
Rup17	GGAAACAGCTATGACCATG	Universal Reverse primer
Cloning of P110 and P140 different constructs for recombinant expression/purification		
P110-R	GTGATGGTGATGTTTAGGCAGTGCTGCAAAC	To amplify P110 construct gene
P110N-F	AGGAGATATACCATGGCACTGGCAAATACCTTTC	To amplify P110N construct gene
P110N-R	GTGATGGTGATGTTTTGCCAGACCACCATTATTGG	
P140-F	AGGAGATATACCATGGGTGTTATTACCGGTGTTG	To amplify P140 construct gene
P140-R	GTGATGGTGATGTTTATCTGCCCACTGATTAAACG	

[a] Restriction sites of the primers are underlined.

A. 1.2. Plasmid construction and generation of mutants in Chapter I

Appendices Table A. CI. 1.2. List of plasmids used to create the strains used in Chapter I: Structure and mechanism of the nap adhesion complex from the human pathogen *Mycoplasma genitalium.*

Plasmid name	Aim	Source
pBE	pBE derivative vector used in the cloning procedures	Pich O. Q. *et al.*, 2006b
pMTnPac	Minitransposon bearing the puromycin resistance gene	Torres-Puig S. *et al.*, 2018

pMTnPac-P110-WT	To complement P110 (MG_192) gene. Also used as a template to obtain P110 gene variants for cloning	This work
pMTnPac-P110-R600A	To complement P110 (MG_192) gene bearing a R600A substitution	This work
pMTnPac-P110-RQD	To complement P110 (MG_192) gene bearing a R600A, Q460A and D461A substitutions	This work
pMTnPac-P110-Y830A	To complement P110 (MG_192) gene bearing a Y830A substitution	This work
pMTnPac-P110-R834G	To complement P110 (MG_192) gene bearing a R834G substitution	This work
pMTnPac-P110-D836L	To complement P110 (MG_192) gene bearing a D836L substitution	This work
pMTnPac-P110-W838F	To complement P110 (MG_192) gene bearing a W838F substitution	This work
pMTnPac-P110-G839F	To complement P110 (MG_192) gene bearing a G839F substitution	This work
pMTnPac-P140-WT	To complement P140 (MG_191) gene	This work
pMTnPac-P140-HH	To complement P140 (MG_191) gene bearing a H831A and H832A substitutions	This work
pBE-P140-C-ter	Intermediate pBE derivative vector used as a template in the cloning process to obtain P140 gene variants for the other clonings	This work
pMTnPac-P140-S1406A	To complement P140 (MG_191) gene bearing a S1406A substitution	This work
pMTnPac-P140-T1401A	To complement P140 (MG_191) gene bearing a T1401A substitution	This work
pMTnPac-P140-T1415A	To complement P140 (MG_191) gene bearing a T1415A substitution	This work
pMTnPac-P140-S1418A	To complement P140 (MG_191) gene bearing a S1418A substitution	This work
pMTnPac-P140-S1418E	To complement P140 (MG_191) gene bearing a S1418E substitution	This work
pMTnPac-P140-T1428A	To complement P140 (MG_191) gene bearing a T1428A substitution	This work

pMTnPac-P140-S1406A+T1401A	To complement P140 (MG_191) gene bearing a S1406A and T1401A substitutions	This work
pMTnPac-P140-S1406E+T1401E	To complement P140 (MG_191) gene bearing a S1406E and T1401E substitutions	This work
pMTnPac-P140-S1418A+T1428A	To complement P140 (MG_191) gene bearing a S1418A and T1428A substitutions	This work
pMTnPac-P140-S1418E+T1428E	To complement P140 (MG_191) gene bearing a S1418E and T1428E substitutions	This work
pΔMG_108	Suicide vector pBE derivative used to create the *Mge* MG_108 defective mutant. Selectable marker: chloramphenicol flanked with *lox* sequences	This work

A. 1.2.1. Construction of pΔMG108 plasmid and generation of ΔMG_108 mutant strain

The suicide plasmid pBEΔMG_108 was designed to generate a G37 *M. genitalium* MG_108 (PrpC) null mutant strain by gene replacement or homologous recombination (HR). First, a 1 kb flanking upstream region (UR) to the MG_108 gene was PCR-amplified using the dMG_108-BEFw and dMG_108-BERev primers. Similarly, a 1 kb flanking downstream region (DR) to the MG_108 gene was PCR-amplified with the dMG_108-BDFw and dMG_108-BDRev primers. *mg107, mg108 and mg109* are overlapping genes and seems to belong to the same transcriptional operon. For this reason, the UR and DR maintain the first and final nucleotides of the *mg108*, respectively (63.4 % of the *mg*108 coding region deleted, bases 22 to 517). In parallel, a "lox" version of the CmM438 selectable marker[534] [**Torres-Puig S. *et al.*, 2018**] was PCR-amplified with the Lox71p438-Fwd (*Xho*I) and CatLox66-Rev (*Bam*HI) primers, obtaining the CmM438 flanked with the lox61 and lox71 sequences. Then, the UR and DR PCR products were joined by PCR with the dMG_108-BEFw and dMG_108-BDRev primers. The resulting PCR product was cloned into an *Eco*RV-digested pBE plasmid[244] [**Pich O. Q. *et al.*, 2006**]. Finally, the resulting CmM438 amplicon was digested with *Xho*I and *Bam*HI restriction enzymes and ligated into the similarly digested pBE containing the UR and DR regions obtained before.

This plasmid was used to obtain the G37ΔMG_108 chloramphenicol resistant mutant strain (**Appendices Figure A. CI. 1.2.1_1**). Electroporation of this mutant with the pCre plasmid[261] [**Mariscal A. M., *et al.*, 2016**] that contains the Cre recombinase allowed us to obtain the G37ΔMG_108 strain, free of any antibiotic selectable marker.

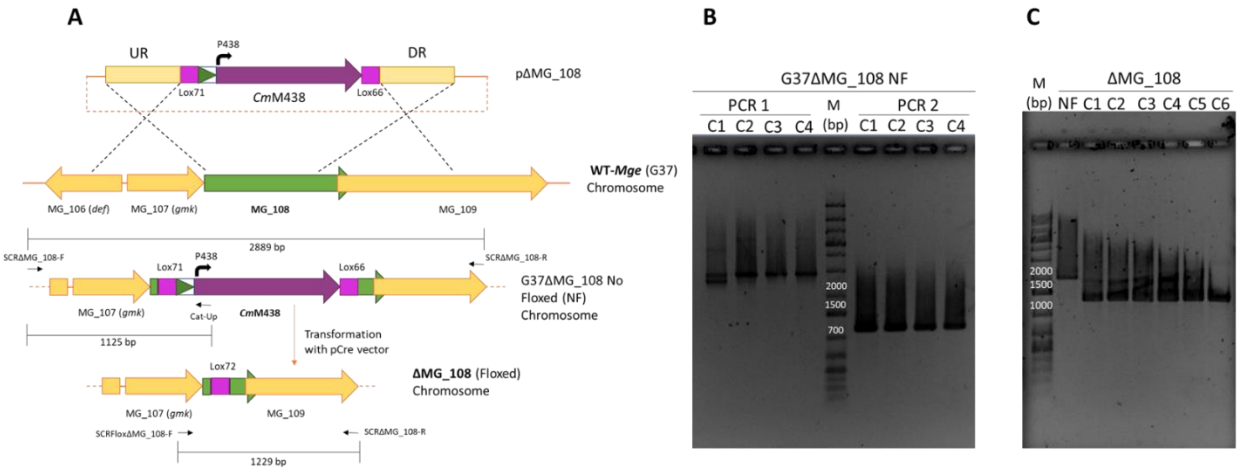

Appendices Figure A. CI. 1.2.1_1. Construction of ΔMG_108 null mutant. A) Schematic representation illustrating the construction of the *M. genitalium* MG_108 null mutant by homologous recombination. Arrows indicate the approximate location of the primers used for screening. **B)** Electrophoresis gel demonstrating the replacement of the MG_108 locus by the *Cm*M438 marker in different ΔMG_108 non floxed (NF) mutant clones. PCR1, reaction using SCRΔMG_108-F and SCRΔMG_108-R primers; PCR2, reaction using SCRΔMG_108-F and Cat-Up primers. **C)** Electrophoresis gel demonstrating the loss of the *Cm*M438 marker by the Cre recombinase in different ΔMG_108 mutant clones. NF, control reaction with the genomic DNA of a ΔMG_108 non floxed mutant clone.

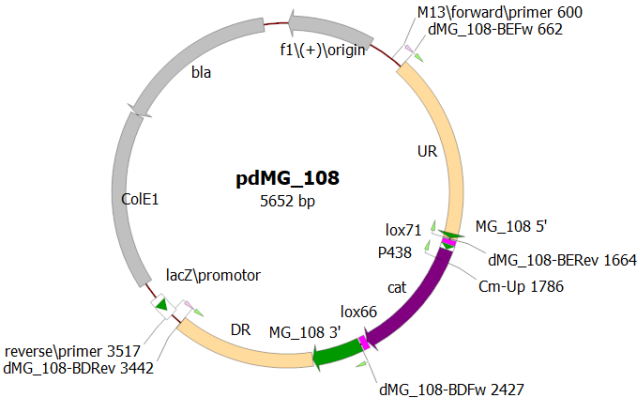

Appendices Figure A. CI. 1.2.1_2. pΔMG_108 plasmid map. Oligonucleotides used for cloning are drawn as little green arrows. UR, homologous upstream region; DR, homologous downstream region; *bla*, β-lactamase; lacZ/promotor, *lacZ* gene promoter; *cat*, *Cm*M438 marker with the MG_438 promoter flanked with lox71 and lox66 sequences.

A. 1.2.2. Construction of pMTnPac-P110-WT, pMTnPacP140-WT, pMTnPacP110-mutant variants and pMTnPacP140-HH

The strategies followed for the construction of the different vectors were similar. Plasmids carrying the miniTn4001-derived transposon were used to re-introduce genes in the *M. genitalium* chromosome. Plasmid pMTnPac[465] [Aparicio D. *et al.*, 2020] (**Figure MM. 2.10_2**) was digested with *ApaI-XhoI* or *ApaI-SalI* and ligated with similarly digested inserts.

The MG_191 gene coding for P140 was amplified using chromosomal DNA from strain G37 with primers COMmg191-F (*Apa*I) and COMmg191-R (*Sal*I) (**Appendices Table A. CI. 1.1**). Primer COMmg191-F (*Apa*I) carries the P140 promoter, which was identified in a previous study[574] [**Musatovova O. *et al*., 2003**]. The resulting amplicon was digested with *Apa*I and *SalI* and ligated to a similarly digested pMTnPac plasmid[534] [**Torres-Puig S. *et al*., 2018**] to create pMTnPacP140-WT. The P140- HH variant was created in a two-step PCR procedure, using DNA from plasmid pMTnPacP140-WT as a template and primers COMmg191-F/ H381AH382Amg191-R and H381AH382Amg191-F/COMmg191-R, respectively. The resulting amplicons of the previous PCR reactions, were used as a template to reconstitute the mutated MG_191 allele by SOE-PCR with primers COMmg191-F and COMmg191-R. The mutated MG_191 allele was also digested with *Apa*I and *Sal*I and ligated to a similarly digested pMTnPac plasmid to create pMTnPacP140-HH. Sequencing analysis of the TnPacP140-WT and TnPacP140-HH minitransposons using primers Tnp3, RTPCRmg191-F, SEQmg191a-F, SEQmg191b-F, SEQmg191c-F, SEQmg191d-F, SEQmg191e-F and Pac-Up, ruled out the presence of additional mutations within the MG_191 sequence. The resulting pMTnPacP140 plasmid (**Appendices Table A. CI. 1.2 and Figure A. CI. 1.2.2_1**) derivatives were transformed to a *M. genitalium* ΔMG_191 null mutant[70] [**Burgos R. *et al.*, 2006**] to create the P140-WT and P140-HH strains. Identification of the minitransposon insertion site in the individual clones was done by sequencing using the Pac-Dw primer and chromosomal DNA as a template.

Similarly, P110 variants were generated in a two-step PCR procedure using DNA from plasmid pMTnPacP110-WT as a template[432] [**Aparicio D. *et al*., 2020**]. For each mutant, the first PCR round was performed using primer COMmg192-F (*Apa*I) and the specific mg192 reverse primer listed in **Appendices Table A. CI. 1.1** or primer COMmg192-R (*Xho*I) and the specific mg192 forward primer. To obtain the different full-length MG_192 alleles, we conducted SOE-PCR using the specific amplicon pair obtained for each mutant as template (R600A, Y830A, R834G, D836L, W838F and G839A) and primers COMmg192-F (*Apa*I) and COMmg192-R (*Xho*I). Then, the mutated P110 alleles were digested with *Apa*I and *Xho*I and ligated to a similarly digested pMTnPac plasmid[534] [**Torres-Puig S. *et al*., 2018**] to generate the corresponding pMTnPacP110 plasmid series (**Appendices Table A. CI. 1.2 and Figure A. CI. 1.2.2_2**). The P110 variant carrying the triple substitution RQD was obtained using primers Q460AD461Amg192-F and -R to introduce the double substitution Q460A and D461A into the pMTnPacP110-R600A plasmid, which was used as DNA template for the PCR reaction. Sequencing analysis of the different pMTnPacP110 minitransposons using primers Tnp3, RTPCR192-F, RTPCR192-R and Pac-Up, ruled out the presence of additional mutations in the MG_192 sequence. These plasmids were

transformed to a *M. genitalium* ΔMG_192 null mutant[70] [Burgos R. *et al.*, 2006] to create the different P110 variant strains. Identification of the minitransposon insertion site in the individual clones was done by sequencing using the Pac-Dw primer and chromosomal DNA as template.

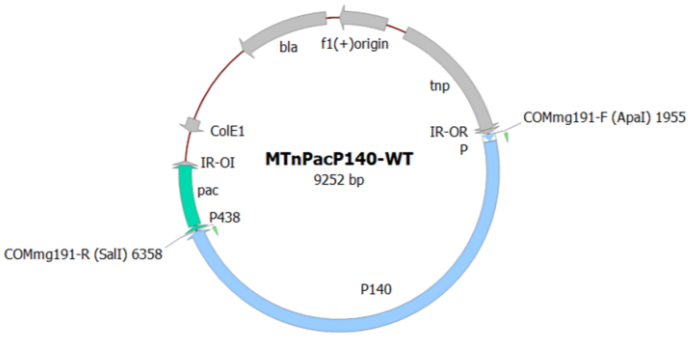

Appendices Figure A. CI. 1.2.2_1. pMTnPacP140-WT plasmid map. Primers used to build this plasmid are highlighted as little green arrows. P140, MG_191 gene sequence; P, MG_191 own promoter; IR, inverted repeat; P438, MG_438 promoter; *pac*, puromycin acetyl transferase marker; tnp, transposase; *bla*, β-lactamase.

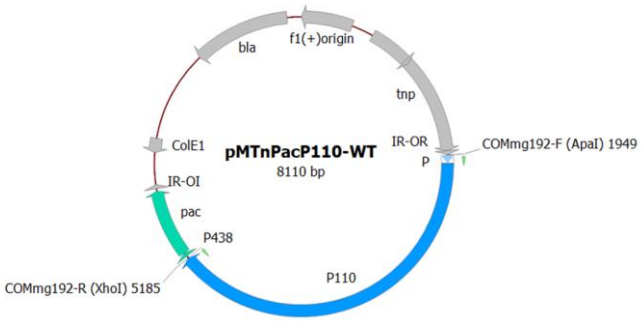

Appendices Figure A. CI. 1.2.2_2. pMTnPacP110-WT plasmid map. Primers used to build this plasmid are highlighted as little green arrows. P110, MG_192 gene sequence; P, MG_191 own promoter; IR, inverted repeat; P438, MG_438 promoter; *pac*, puromycin acetyl transferase marker; tnp, transposase; *bla*, β-lactamase.

A. 1.2.3. Construction of the pBE-P140-C-ter and the other pMTnPacP140 C-terminal mutant variants

To generate P140 (MG_191) variants carrying specific mutations in residues of the C-terminal, first the MG_191 C-terminal region was amplified using primers P140XbaI-F and COMmg191-R (*Sal*I). The resulting PCR product was cloned into an *Eco*RV-digested pBE plasmid[244] [Pich O. Q. *et al.*, 2006b], obtaining the pBE-P140-C-ter. Using the pBE-P140-C-ter as a template and the specific primers for each mutant (**Appendices Table A. CI. 1.1**) the target mutations in the MG_191 C-terminal region were introduced by ExSite-PCR. Then, the pBE derivatives plasmids containing the C-terminal of the P140 allele with the desired mutations were re-ligated and mutant P140 C-terminal region excised by digestion with *Xba*I and *Sal*I restriction enzymes.

Finally, DNA fragments with mutant P140 C-terminal region were ligated into a pMTnPacP140-WT plasmid previously digested with *Xba*I and *Sal*I, to generate the corresponding pMTnPacP140 plasmid series (**Appendices Figure A. CI. 1.2.3**).

Sequencing analysis of the different pMTnPacP140 minitransposons constructs using primer Pac-Up, ruled out the presence of additional mutations in the C-terminal of the MG_191 sequence. These plasmids were transformed into the *M. genitalium* ΔMG_191 null mutant[70] [**Burgos R. *et al.*, 2006**] to create the different P140 variant strains. Identification of the minitransposon insertion site in the individual clones was done by sequencing using the Pac-Dw primer and chromosomal DNA as a template.

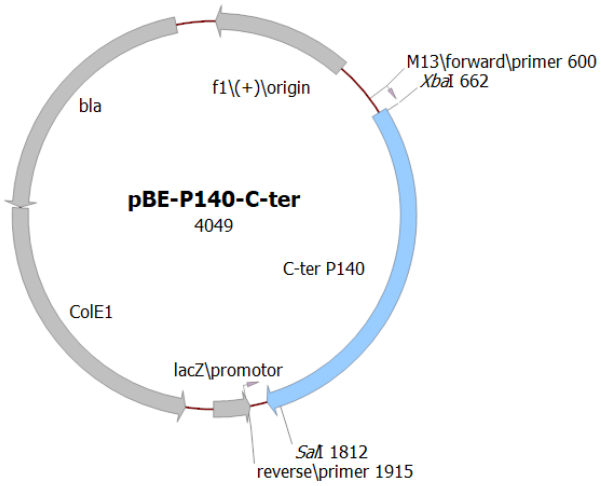

Appendices Figure A. CI. 1.2.3. pBE-P140-C-ter plasmid map. C-ter P140, MG_191 C-terminal region; lacZ/promotor, *lacZ* gene promoter; *bla*, β-lactamase. Enzyme restriction excision sites used in cloning are depicted.

A. 1.3. Results compilation of the cytadherence capacity of *M. genitalium* strains analysed in Chapter I

Appendices Table A. CI. 1.3. Summary table with the K_d, B_{max} values and other characteristics of all mutant strains analysed in Chapter I.

Strain	K_d values ± SE	B_{max} values ± SE	Affected HA parameter	Flask-Adherent	Adhesins expression levels[a]
G37 (WT-*Mge*)	$1.2x10^3 \pm 1.1x10^2$	0.89±0.02	-	Yes	4
P110-WT	$1.6x10^3 \pm 1.6x10^2$	0.89±0.02	-	Yes	4
P110-Y830A	$3x10^4 \pm 1.0x10^4$	1.81±0.40	↑ K_d, ↑ B_{max}	Yes	4

P110-R834G	$1.1x10^3±3.6x10^2$	0.62±0.05	↓ B_{max}	Yes	3
P110-D836L	$1.6x10^3±55$	0.95±0.01	-	Yes	3
P110-W838F	$2x10^4±1.8x10^4$	0.84±0.43	↑ K_d	Yes	2
P110-G839F	NA	NA	NA	No	0
P110-R600A	$2.2x10^4±1.4x10^4$	0.62±0.25	↑ K_d, ↓ B_{max}	No	1
P110-RQD	NA	NA	*NA*	No	0
P140-WT	$1.5x10^3±1.4x10^2$	0.90±0.02	-	Yes	3
P140-HH	$2.9x10^4$	1.79	↑ K_d, ↑ B_{max}	Yes	3
P140-S1406A	$3.0x10^3±6.5x10^2$	0.86±0.06	↑ K_d	Yes	4
P140-T1401A	$6.4x10^3±1.2x10^3$	0.96±0.08	↑ K_d	Yes	4
P140-T1415A	$2.7x10^3±4.4x10^2$	0.89±0.05	↑ K_d	Yes	4
P140-S1418A	$2.1x10^3±3.9x10^2$	0.97±0.05	↑ K_d	Yes	4
P140-S1418E	$2.6x10^3±3.1x10^2$	1.03±0.04	↑ K_d, ↑ B_{max}	Yes	4
P140-T1428A	$3.0x10^3±5.3x10^2$	1.02±0.06	↑ K_d, ↑ B_{max}	Yes	4
P140-S1418A + T1428A	$2.7x10^3±4.0x10^2$	1.06±0.05	↑ K_d, ↑ B_{max}	Yes	4
P140-S1418E + T1428E	$8.0x10^3±1.3x10^3$	1.10±0.08	↑ K_d, ↑ B_{max}	Yes	4
P140-S1406A + T1401A	$1.7x10^3±4.3x10^2$	0.89±0.05	↑ K_d	Yes	4
P140-S1406E + T1401E	$2.3x10^3±2.8x10^2$	0.91±0.03	↑ K_d	Yes	4

[a] Illustrative value scale from 0 (without adhesins) to 4 (WT).

A. 1.4. Cryo-ET and sub-tomogram averaging of *M. genitalium* cells

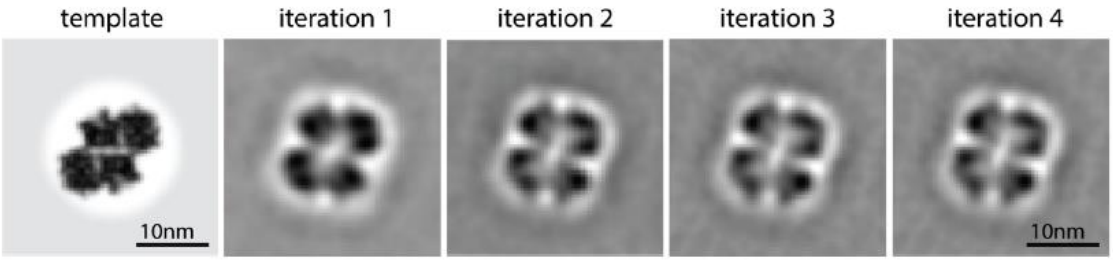

Appendices Figure A. CI. 1.4_1. Sub-tomogram averaging experiment using the crystal structure tetramer as a starting reference. When using the 'closed' tetramer structure (crystal structure packing unit) as a starting reference, the sub-tomogram averaging procedure still converges to the open structure after 5 iterations. Scale bar is 10 nm.

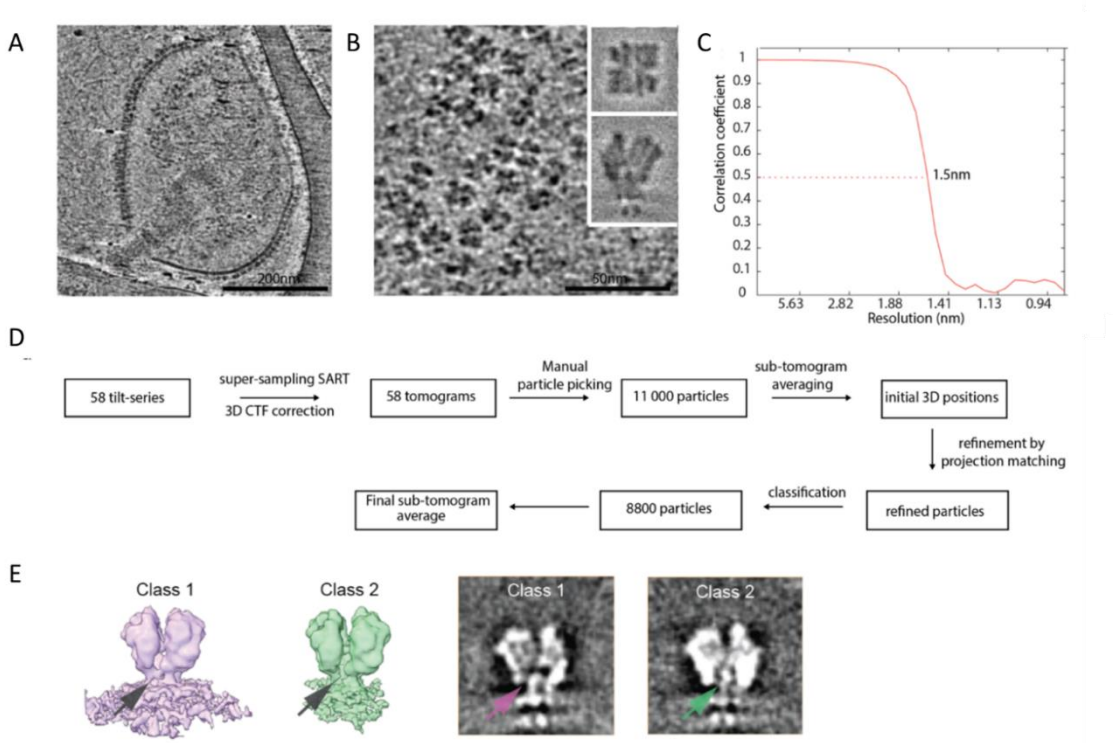

Appendices Figure A. CI. 1.4_2. Cryo-ET of *M. genitalium* cells. A) A 0.88 nm thick slice through a representative tomogram (58 tomograms were used in total) of a detergent-permeabilized *M. genitalium* cell. **B)** A zoomed in top view of the Nap complexes found on the cell in (A). Insets show slices through the top view (upper inset) and side view (lower-inset) of the sub-tomogram average. **C)** Fourier shell correlation of the subtomogram average showing a resolution of 15 Å at the 0.5 criterion. **D)** Flowchart showing the processing pipeline from the raw tilt-series to the final sub-tomogram average. **E)** Different classes observed during subtomogram averaging, class 1 (in purple) shows well resolved stalks (arrows), whereas class 2 (in green) shows less well-resolved stalks. Particles from class 1 were used in the final average. Adapted from **Aparicio D. *et al.*, 2020**.

A. 1.5. Synthetic DNA

Appendices Table A. CI. 1.5. Synthetic clones obtained from Geneart. Start and stop codons of the full-length MG_191 and MG_192 genes are highlighted in green.

Synthetic clone for *M. genitalium* P140
CGAATTGAAGGAAGGCCGTCAAGGCCGCATTTAATTAAACAAGTTTGTACAAAAAAGCAGGCTCTGGAAGTTCTGTTTCAGGGTCCGAGCGGTGCAATGAAAACCATGCGTAAACAAATTTA TAAAAAAGCCTATTGGCTGCTGCTGCCGTTTCTGCCGCTGGCACTGGCAAATACCTTTCTGGTTAAAGAGGATAGCAAAAACGTTACCGCATATACCCCGTTTGCAACCCCGATTACCGATAGC AAAAGCGATCTGGTTAGCCTGGCACAGCTGGATAGCAGCTATCAGATTGCAGATCAGACCATTCATAACACCAACCTGTTTGTGCTGTTCAAAAGCCGTGATGTGAAAGTGAAATATGAAAGC AGCGGCAGCAACAACATTAGCTTTGATAGCACCAGCCAGGGTGAAAAACCGAGCTATGTTGTTGAATTTACCAACAGCACCAATATCGGCATTAAATGGACCATGGTGAAGAAATATCAGCT GGATGTTCCGAATGTGAGCAGCGATATGAATCAGGTTCTGAAAAACCTGATTCTGGAACAGCCGCTGACCAAATATACCCTGAATAGCAGCCTGGCAAAAGAAAAAGGTAAAACCCAGCGTG AAGTTCATCTGGGTAGCGGTCAGGCAAATCAGTGGACCAGCCAGCGTAATCAGCATGATCTGAATAATAATCCGAGCCCGAATGCAAGCACCGGTTTTAAACTGACCACCGGTAATGCATATC GTAAACTGAGCGAAAGCTGGCCGATTTATGAACCGATTGATGGCACCAAACAGGGTAAAGGTAAAGATAGCAGCGGTTGGAGCAGCACCGAAGAAAATGAAGCAAAAAATGATGCACCGA GCGTTAGCGGTGGTGGTAGCAGCAGCGGCACCTTTAATAAATATCTGAATACCAAACAGGCCCTGGAAAGCATTGGTATTCTGTTTGATGATCAGACACCGCGTAATGTTATTACCCAGCTGT ATTATGCAAGCACCAGCAAACTGGCAGTGACCAATAATCATATTGTGGTTATGGGCAATAGCTTTCTGCCGAGCATGTGGTATTGGGTTGTTGAACGTAGCGCACAAGAAAATGCCAGCAATA AACCGACCTGGTTTGCAAATACCAATCTGGATTGGGGTGAGGATAAACAGAAACAGTTGTTGAAAACCAGCTGGGCTATAAAGAAACCACCAGTACCAATAGCCACAACTTTCATAGCAAA AGCTTTACCCAGCCTGCATATCTGATTAGCGGTATTGATAGCGTGAACGATCAGATTATCTTCAGCGGTTTTAAAGCAGGTAGCGTTGGTTATGATAGCAGCAGCAGCAGTAGCAGCTCAAGC AGCAGCTCAACCAAAGATCAGGCACTGGCATGGTCAACCACCACCAGTCTGGATAGCAAAACCGGTTATAAAGATCTGGTGACCAATGATACCGGTCTGAATGGTCCGATTAATGGTAGCTTT AGCATCCAGGATACCTTTAGCTTTGTTGTTCCGTATAGCGGCAATCATACCAATAATGGCACCACCGGTCCGATTAAAACCGCATATCCGGTTAAAAAAGATCAGAAAAGCACCGTGAAAATT AATAGCCTGATTAATGCCACACCGCTGAATAGCTATGGTGATGAAGGTATTGGTGTTTTTGATGCACTGGGCCTGAACTATAACTTCAAAAGCAATCAAGAACGTCTGCCGAGCCGTACCGAT CAGATTTTTGTTTATGGTATTGTGAGCCCGAATGAACTGCGTAGCGCAAAAAGCAGCGCAGATAGCACCGGTAGCGATACCAAAGTTAATTGGAGCAATACCCAGAGCCGTTATCTGCCGGTT CCGTATAATTATAGCGAAGGTATTATTGATGCCGACGGTTTTAAACGTCCGGAAAATCGTGGTGCAAGCGTTACCACCTTTAGCGGTCTGAAAAGCATTGCACCGGATGGTTTTGCAAATAGC ATTGCAAATTTTAGCGTGGGTCTGAAAGCAGGTATTGATCCGAATCCGGTTATGAGCGGTAAAAAAGCAAATTATGGTGCCGTTGTTCTGACCCGTGGTGGTGTTGTTCGTCTGAATTTTAATC CGGGTAATGATAGCCTGCTGAGCACCACCGATAATAATATTGCACCGATCAGCTTTAGCTTTACCCCGTTTACCGCAGCAGAAAGCGCAGTTGATCTGACCACCTTTAAAGAAGTGACCTATAA CCAAGAAAGCGGTCTGTGGTCCTATATTTTTGATAGCAGCCTGAAACCGAGCCATGATGGTAAACAGACACCGGTTACCGACAATATGGGTTTTAGCGTTATTACCGTTAGCCGTACCGGTAT TGAACTGAATCAGGATCAGGCAACCACCACCCTGGATGTTGCACCGAGCGCACTGGCAGTTCAGAGCGGTATTCAGAGCACCACCCAGACCCTGACCGGAGTTCTGCCGCTGAGCGAAGAAT TTAGCGCAGTTATTGCAAAAGATAGCGATCAGAATAAAATCGACATTTACAAAAATAATAATGGCCTGTTTGAAATTGATACCCAGCTGAGCAATAGCGTTGCAACCAATAATGGTGGTCTGG CACCGAGCTATACCGAAAATCGTGTTGATGCATGGGGCAAAGTTGAATTTGCAGATAATTCAGTTCTGCAGGCACGTAATCTGGTTGATAAAACCGTGGATGAGATTATTAACACACCGGAAA TCCTGAACAGCTTTTTTCGTTTTACCCCTGCATTCGAAGATCAGAAAGCAACCCTGGTGGCAACCAAACAGAGCGATACCAGCCTGAGCGTTAGTCCGCGTATTCAGTTCCTGGATGGCAATTT TTATGACCTGAATAGCACCATTGCCGGTGTTCCGCTGAATATTGGTTTTCCGAGCCGTGTTTTTGCAGGTTTTGCAGCACTGCCTGCATGGGTTATTCCGGTTAGCGTTGGTAGCAGCGTTGGC ATTCTGTTTATTCTGCTGGTTCTGGGTCTGGGTATTGGTATTCCGATGTATCGTGTTCGTAAACTGCAGGATGCCAGCTTTGTGAACGTGTTTAAAAAAGTTGATACCCTGACCACCGCAGTTG GTAGCGTTTATAAAAAGATTATCACCCAGACCGGTGTGGTTAAAAAGCACCGAGTGCACTGAAAGCAGCAAATCCGAGCGTTAAAAAACCGGCAGCATTTCTGAAACCGCCTGTTCAGCCTC CGAGCAAACCGGAAGGTGAACAGAAAGCAGTTGAAGTTAAAAGCGAGGAAACCAAAAGCTAAACCCAGCTTTCTTGTACAAAGTGGTGGCGCGCCCTGGGCCTCATGGGCCTTCCTTTCACT GCC
Synthetic clone for *M. genitalium* P110
CGAATTGAAGGAAGGCCGTCAAGGCCGCATTTAATTAAACAAGTTTGTACAAAAAAGCAGGCTCTGGAAGTTCTGTTTCAGGGTCCGAGCGGTGCAATGCATCAGCCGAAAAAACGTCTGGC AAAAAAAAGCTGGGCATTTCTGACCGCAGCACTGACCCTGGGTGTTATTACCGGTGTTGGTGGTTATTTTCTGTTTAACCAGAATAAACAGCGTAGCAGCGTTAGCAATTTTGCATATCAGCCG AAACAGCTGAGCGTTAAACATCAGCAGGCAGTTGATGAAACCCTGACCCCGTGGACCTGGAATAATAATAATTTTTCAAGCCTGAAAATTACCGGTGAAAATCCGGGTAGCTTTGGTCTGGTT CGTAGCCAGAATGATAATCTGAATATTAGCAGCGTGACCAAAAATAGCAGCGACGATAATCTGAAATATCTGAATGCCGTCGAGAAATATCTGGATGGTCAGCAGAATTTTGCCATTCGTCGC TATGATAATAATGGTCGTGCCCTGTATGATATTAACCTGGCAAAAATGGAAAATCCGAGCACCGTTCAGCGTGGTCTGAATGGTGAACCGATTTTTGATCCGTTTAAAGGTTTTGGTCTGACCG GTAATGCACCGACCGATTGGAATGAAATTAAAGGTAAAGTTCCGGTTGAGGTTGTTCAGAGTCCGCATAGCCCGAATCTGTATTTTGTTCTGCTGGTTCCGAAAGTTGCCCTGGAATACCATA ATCTGAACAATCAGGTGGTGAAAGAAAGCCTGGAAGTTAAAGCAACCCAGAGCAGCTTTAATCCGACCAGCGTCTGCAGAAAGATAGTCCGGTTAAAGATAGCAGCAAACAGGGTGAAAA ACTGAGCGAAACCACCGCAAGCAGCATGAGCAGCGGTATGGCAACCAGCACCCGTGCAAAAGCACTGAAAGTTGAAGTTGAACGTGGTAGCCAGAGCGATAGCCTGCTGAAAAATGATTTT GCAAAAAAACCGCTGAAGCATAAAAACAGCAGCGGTGAAGTTAAACTGGAAGCCGAAAAAGAATTTACCGAAGCATGGAAACCGCTGCTGACCACCGATCAGATTGCACGTGAAAAAGGTA TGGGTGCAACCGTTGTTAGCTTTTATGATGCACCGTATAGCGAAAATCATACCGCATTTGGTCTGGTGGATCATATTGATCCGAAAAAAATGGTCGAGAATTATCCGCCTAGCTGGAAAACCCC GAAATGGAATCATCATGGCATCTGGGATTATAATGCACGTAATCTGCTGCTGCAGACCACCGGTTTTTTTAATCCGCGTCGTCATCCGGAATGGTTTGATGAAGGTCAGGCAAAAGCAGATAA TACCAGTCCGGGTTTTAAAGTTGGTGATACCGATCATAAAAAAGATGGCTTTAAAAAAAATAGCTCCAGCCCGATTGCACTGCCGTTTGAAGCATATTTTGCCAATATTGGTAATATGGTGGCC ATTGGTAACAGCGTGTTTATTTTTGGTGGTAATGGTCATGCCACCAAAATGTTTACCACCAATCCGCTGAGCATTGGTGTGTTTCGTATCAAATATACCGATAATTTTAGCAAAAGCAGCGTTAC CGGTTGGCCGTATGCAGTTCTGTTTGGTGGTCTGATTAATCCGCAAACCAATGGTCTGAAAGATCTGCCGCTGGGCACCAATCGTTGGTTTGAATATGTTCCGCGTATGGCAGTTAGCGGTGT TAAATGGGTTGGTAATCAGCTGGTTCTGGCAGGCACCCTGACCATGGGTGATACCGCAACCGTTCCGCGTCTGAAATATGATCAGCTGGAAAAACATCTGAATCTGGTTGCACAGGGTCAGG GTCTGCTGCGTGAAGATCTGCAGATTTTTACCCCGTATGGTTGGGCAAATCGTCCGGATATTCCGGTTGGTGCATGGCTGCAGGATGAAATGGGTAGCAAATTTGGTCCGCACTATTTTCTGA ACAACCCGGATATTCAGGACAATGTGAATAATGATACCGTGGAAGCACTGATCAGCAGCTATAAAAATACCGACAAACTGAAACACGTGTATCCGTATCGTTATAGCGGTCTGTATGCATGGC AGCTGTTTAATTGGAGCAATAAACTGACCAATACACCGCTGAGCGCCAATTTTGTTAACGAAAATAGCTATGCACCGAATAGCCTGTTTGCAGCAATTCTGAATGAAGATCTGCTGACCGGTCT GAGCGATAAAATTTTTTATGGCAAAGAGAACGAATTTGCCGAAAATGAAGCCGATCGTTTTAATCAGCTGCTGAGCCTGAATCCGAATCCGAATACCAATTGGGCACGTTATCTGAATGTTGT TCAGCGTTTTACCACCGGTCCGAATCTGGATAGCAGCACCTTTGATCAGTTTCTGGATTTTCTGCCGTGGATTGGTAATGGTAAACCGTTTAGCAATAGCCCGAGCCCGAGCACCAGCGCCAGC AGTAGTACACCGCTGCCGACCTTAGCAATATTAATGTTGGTGTGAAAAGCATGATCACCCAGCATCTGAATAAAGAAAATACCCGCTGGGTGTTTATCCCGAATTTTAGTCCGGATATTTGGA CCGGTGCAGGTTATCGTGTTCAGAGCGCAAATCAGAAAAATGGTATTCCGTTCGAACAGGTTAAACCGAGCAATAATAGCACCCCGTTTGATCCGAATAGCGACGATAACAAAGTTACCCCGA GCGGTGGTAGCAGCAAACCGACCACCTATCCGGCACTGCCGAATAGCATTAGCCCGACCAGCGATTGGATTAATGCACTGACCTTTACCAACAAAAATAATCCGCAGCGTAACCAACTGCTGC TGCGTAGCCTGCTGGGCACCATTCCGGTTCTGATTAATAAAAGCGGTGATAGCAACGATCAGTTCAACAAAGATAGCGAACAGAAATGGGACAAAACCGAAACCAATGAAGGTAATCTGCCT GGTTTTGGTGAAGTTAATGGTCTGTATAATGCAGCTCTGCTGCACACCTATGGTTTTTTTGGCACCAATACCAATAGCACCGATCCGAAAATTGGCTTTAAAGCAGATAGCAGCAGCTCAAGTA GCAGCACCCTGGTTGGTAGCGGTCTGAATTGGACCAGCCAGGATGTTGGTAATCTGGTTGTTATTAACGATACCAGCTTTGGTTTTCAGCTGGGTGGTTGGTTTATTACCTTTACCGATTTCATT CGTCCGCGTACCGGTTATCTGGGTATTACCCTGAGCAGCCTGCAGGATCAGACCATTATTTGGGCAGATCAGCCGTGGACCAGCTTTAAAGGTAGCTATCTGGATAGTGATGGCACCCCGAAA AGCCTGTGGGATCCGACCGCACTGAAAAGCCTGCCGAATAGTAGCACCACCTATGATACCAATCCGACCCTGAGCCCGAGCTTTCAGCTGTATCAGCCGAATAAAGTTAAAGCATATCAGACC ACCAATACCTATAATAAACTGATTGAACCGGTTGATGCAACCAGCGCAGCAACCAATATGACCAGTCTGCTGAAACTGCTGACCACGAAAAACATTAAAGCCAAACTGGGTAAAGGCACCGCC AGCAGCCAGGGTAATAATAATGGTGGTGGTGTTAGCCAGACCATTAATACCATTACCACCACCGGTAATATTAGCGAAGGTCTGAAAGAAGAAACCAGCATTCAGGCAGAAACCCTGAAAAA ATTCTTCGATAGCAAACAGAATAATAAAAGCGAAATCGGCATTGGCGATAGCACCTTTACCAAAATGGATGGTAAACTGACCGGTGTTGTTAGCACACCGCTGGTTAATCTGATTAATGGTCA GGGTGCAACCAGCGATAGCGATACCGAAAAAATTAGCTTTAAACCGGGTAACCAGATCGACTTTAATCGTCTGTTTACCCTGCCGGTTACCGAACTGTTTGATCCTAATACCATGTTCGTGTAT GATCAGTATGTTCCGCTGCTGGTGAATCTGCCGAGCGGTTTTGATCAGGCAAGCATTCGTCTGAAAGTGATTAGCTATAGCGTGGAAAATCAGACCCTGGGCGTTCGTCTGGAATTTAAAGAT CCGCAGACCCAGCAGTTTATTCCGGTGCTGAATGCAAGCAGCACCGGTCCGCAGACCGTTTTTCAGCCGTTTAATCAGTGGGCAGATTATGTTCTGCCGCTGATTGTTACCGTTCCGATTGTTG TGATTATTCTGAGCGTTACCCTGGGTCTGACCATTGGTATTCCGATGCATCGTAATAAAAAAGCACTGCAGGCAGGTTTTGACCTGAGCAATAAAAAAGTTGACGTTCTGACCAAAGCCGTTG GTAGCGTTTTTAAAGAAATTATTAACCGCACCGGCATTAGCAATGCACCGAAAAAACTGAAACAGGCAACCCCGACCAAACCGACCCCGAAAACCCCTCCGAAACCGCCTGTTAAACATAAGT AAACCCAGCTTTCTTGTACAAAGTGGTGGCGCGCCCTGGGCCTCATGGGCCTTCCTTTCACTGCC

A. 1.6. Single-particle Cryo-EM and image processing of the P140-P110 heterodimer and Nap complex

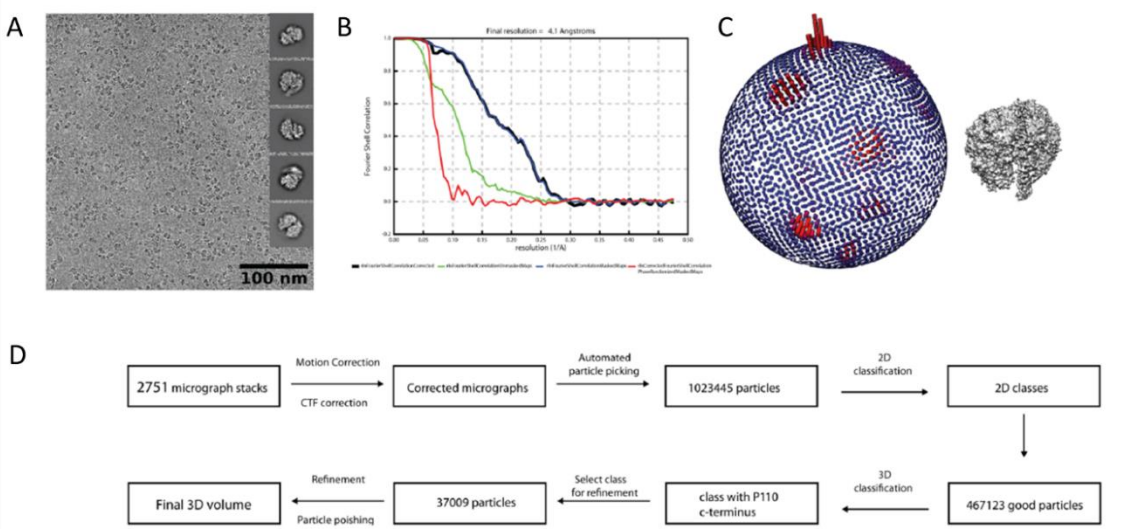

Appendices Figure A. CI. 1.6_1. Processing of Cryo-EM data from the extracellular regions of P140-P110. **A**) Representative Cryo-electron micrograph of P140-P110 heterodimers with a subset of 2D classes as insets (2751 micrographs were recorded in total). **B)** Fourier shell correlation showing a resolution of 4.1 Å using the 0.143 criteria. **C)** Angular distribution plot of images corresponding to the final 3D volume that displays anisotropy. **D)** Flowchart showing the processing pipeline from the micrograph stacks to the final 3D volume. Adapted from **Aparicio D. *et al.*, 2020**.

Appendices Table A. CI. 1.6_1. Single particle analysis data collection. Adapted from **Aparicio D. *et al.*, 2020**.

	P140-P110N	NAP complex
Data collection		
Microscope	FEI Titan Krios	FEI Titan Krios
Detector	Gatan K2 Summit	Gatan K2 Summit
Acquisition software	SerialEM 3.7	SerialEM 3.7
Magnification	130,000x	130,000x
Pixel size (Å)	1,05	1,05
Total electron dose (e- / Å²)	50	50
Dose rate (Å2 / s-1)	7,7	7,4
number of frames	32	34
Defocus range (μm)	-1 to -4	-1 to -4
Micrographs used	2.751	2.225
Processing		
Software	Relion 3.0 beta	Relion 3.0 beta
Motion correction	UCSF MotionCor2	UCSF MotionCor2
CTF estimation	GCTF v 1.06	GCTF v 1.06
Total extracted particles	1.024.402	160.203
After 2D Classification	467.123	28.000
Number of 3D classes	6	6
Number of refined particles	37.009	5.612
Symmetry	/	C2
Map sharpening B factor (Å²)	-78	-218
Resolution FSC 0.143 (Å)	4,1	9,8

Appendices Table A. CI. 1.6_2. Correlation and clash-score values from rigid-body fitted crystal structures. Adapted from Aparicio D. *et al.*, 2020.

	Correlation#/clash-score^		
	Cryo-EM (P140-P110 heterodimer)	Cryo-EM ("Closed" Nap conformation)	Cryo-ET ("Open" Nap conformation)
P140	0.74 / 13.55	-	-
P110	0.73 / 13.55	-	-
P140	-	0.95 / 12.13	0.94 / 10.39
P110	-	0.94 / 12.42	0.94 / 10.39

#Real-space correlation of the fitted models into the corresponding electron density maps. Fitting was based on the local optimization algorithm of Chimera4

^The "clash-score" is defined as the number of serious overlaps (> 0.4 Å) per 1000 atoms (Molprobity[575] [Davis I. W., *et al.*, 2004]).

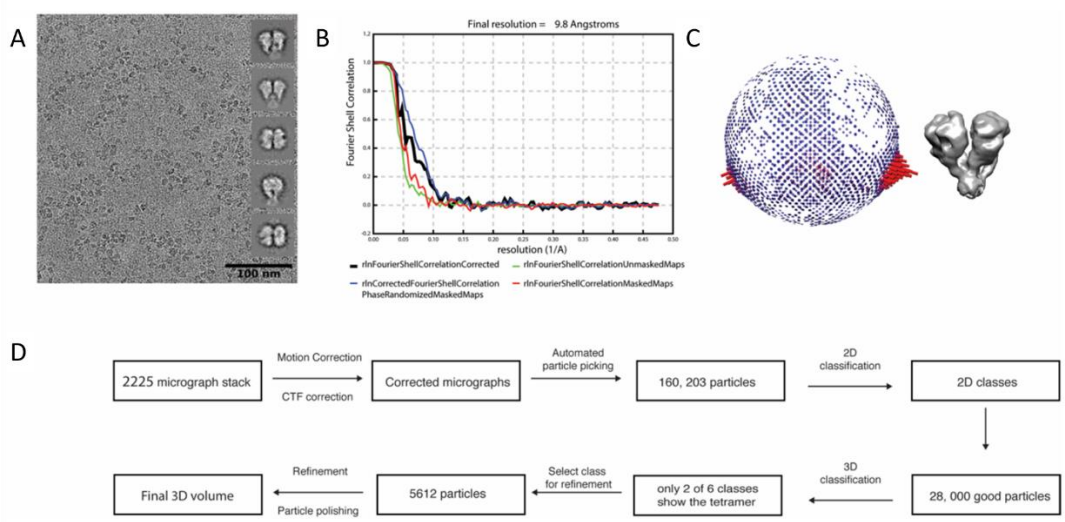

Appendices Figure A. CI. 1.6_2. Image and data Cryo-EM processing of the Nap complex A) Representative Cryo-electron micrograph of Nap complexes with a subset of 2D classes as insets (2225 micrographs were recorded in total). **B)** Fourier shell correlation of the Cryo-EM map showing a resolution of 9.8 Å. **C)** Angular distribution plot of the final 3D volume. **D)** Flowchart showing the processing pipeline from the micrograph stacks to the final 3D volume. Adapted from Aparicio D. *et al.*, 2020.

A. 1.7. Crystallization of P140 alone and the P140–P110N complex

Appendices Table A. CI. 1.7. Data collection and refinement statistics. Adapted from **Aparicio D. *et al.*, 2020**.

Data collection and Refinement Statistics [a]		
	P140	**P140-P110N**
Data collection		
Space group	C2	$P2_1$
Cell dimensions		
a,b,c (Å)	459.19, 116.65, 285.64	150.99, 157.28, 192.36
α,β,γ (°)	90.00, 124.20, 90.00	90.00, 93.81, 90.00
Unique reflections	123183 (6159)	189359 (784)
Resolution (Å)	189.88-3.26 (3.58-3.26)	157.28-2.65 (2.70-2.65)
Wavelength (Å)	0.9791	0.9789
Rmeas (%)[b]	0.15 (0.67)	0.58 (2.11)
I/σI	5.8 (1.6)	6.6 (1.5)
CC(1/2)	0.98 (0.74)	0.87 (0.343)
Completeness (Spherical)	63.5 (13.2)	73.3 (6.1)
Completeness (Ellipsoidal)	86.1 (57.9)	90.8 (44.4)
Redundancy	3.1 (2.6)	6.8 (6.8)
Refinement Statistics		
Resolution	37.36-3.26	121.66-2.65
Num. of reflections	123103	189358
R_{Work} (%)[c]	18.4	18.70
R_{free} (%)[d]	20.5	22.4
No. residues	1292	2134
No. ligands	0	0
Solvent content (%)	67.36	46
Av. B-factor (Å^2)	80.85	40.36
Coor. Error (Å)[e]	0.42	0.36
Rms dev.bonds (Å)	0.01	0.01
Rms dev.angles (°)	1.27	1.25

[a] Values in parentheses correspond to the highest resolution shell.
[b] $R_{sym} = \Sigma_{hkl}\Sigma_i|I_i(hkl) - \langle I(hkl)\rangle| / \Sigma_{hkl}\Sigma_i I_i(hkl)$, where $I_i(hkl)$ is the intensity of an observation and $\langle I(hkl)\rangle$ is the mean value of observations for a unique reflection.
[c] $R_{cryst} = \Sigma_h|Fo(h) - Fc(h)| / \Sigma_h|Fo(h)$, where Fo and Fc are the observed and calculated structure-factor amplitudes, respectively.
[d] R_{free} was calculated with 5% of data, which was excluded from the refinement.
[e] Based on maximum likelihood.

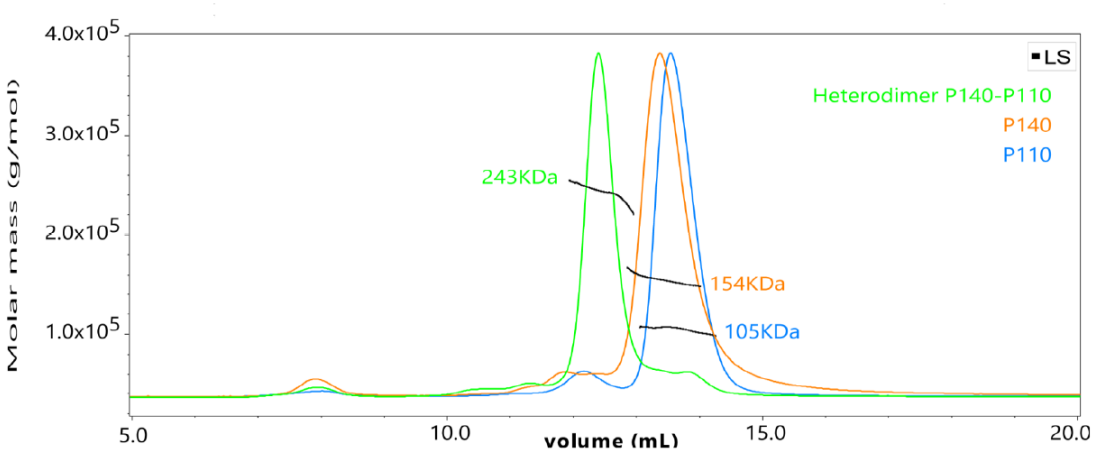

Appendices Figure A. CI. 1.7_1. SEC-MALS measurements. MALS measurements indicate that essentially only heterodimers are detected when mixing equimolecular amounts of P110 and P140. Adapted from **Aparicio D. *et al.*, 2020**.

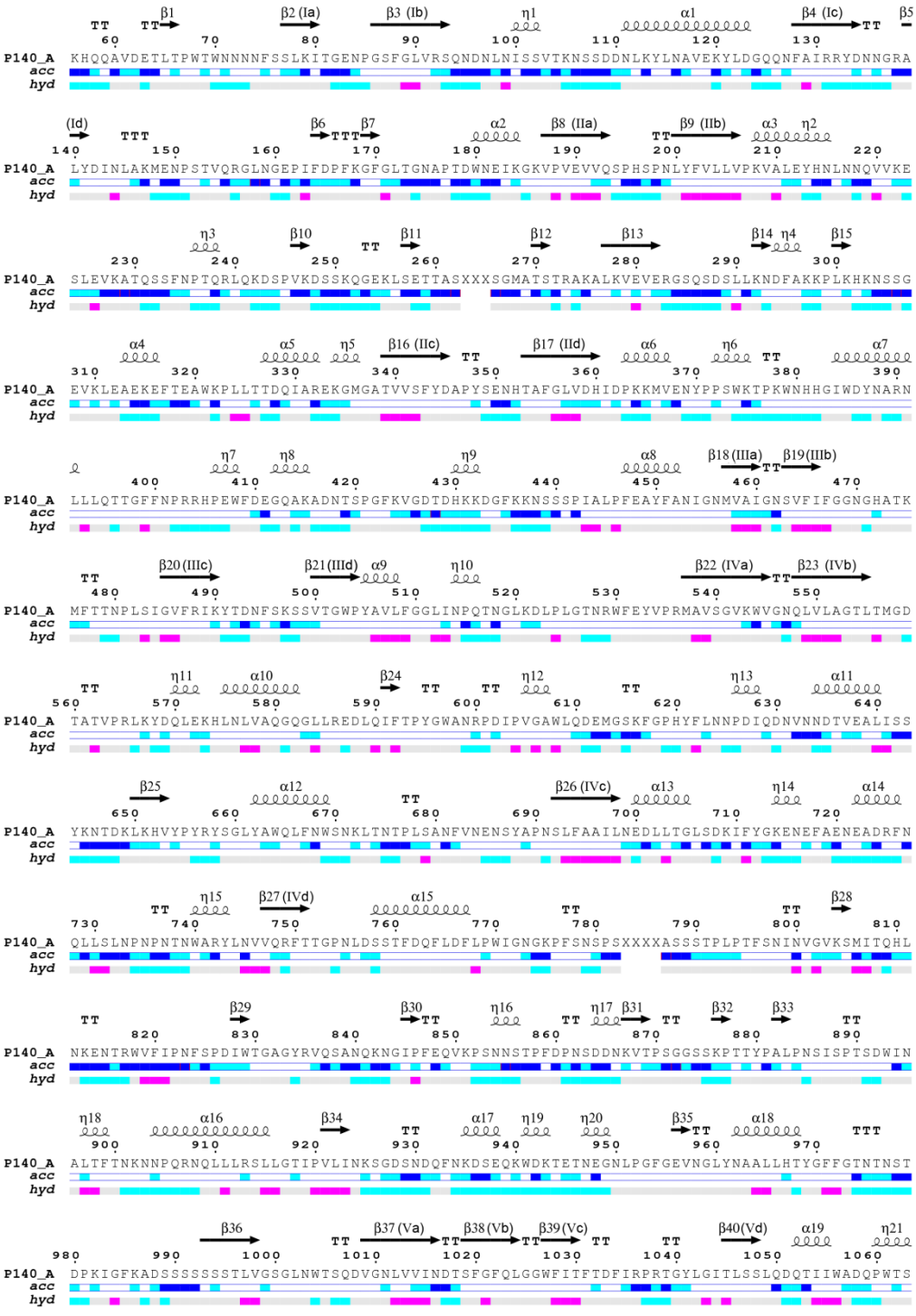
P140_A
acc
hyd

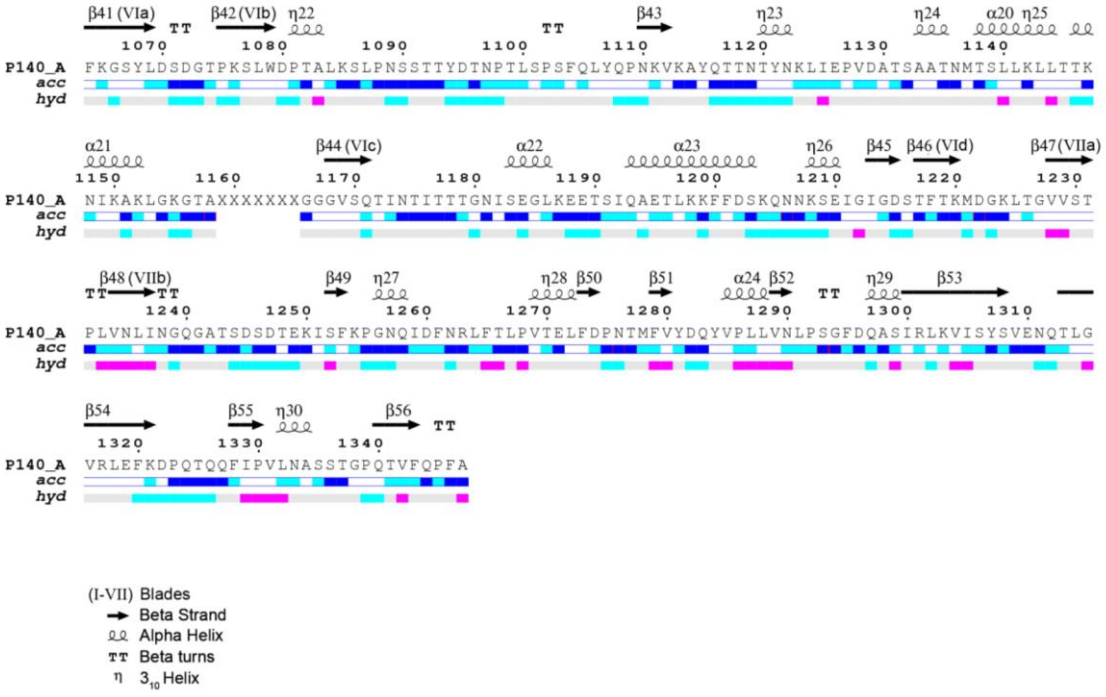

Appendices Figure A. CI. 1.7_2. P140 sequence and secondary structural elements. Amino acid sequence of the extracellular region of P140, with the corresponding secondary structural elements (helices with squiggles, strands with arrows and turns with TT letters) (Endscript2[511] [**Robert X. *et al.*, 2014**]). The seven blades (or β-sheets) in the propeller are represented by roman numerals (I-VII). Bars below the sequence show solvent accessibility (blue is accessible, cyan is intermediate, white is buried) and hydropathy (pink is hydrophobic, cyan is hydrophilic). Adapted from **Aparicio D. *et al.*, 2020**.

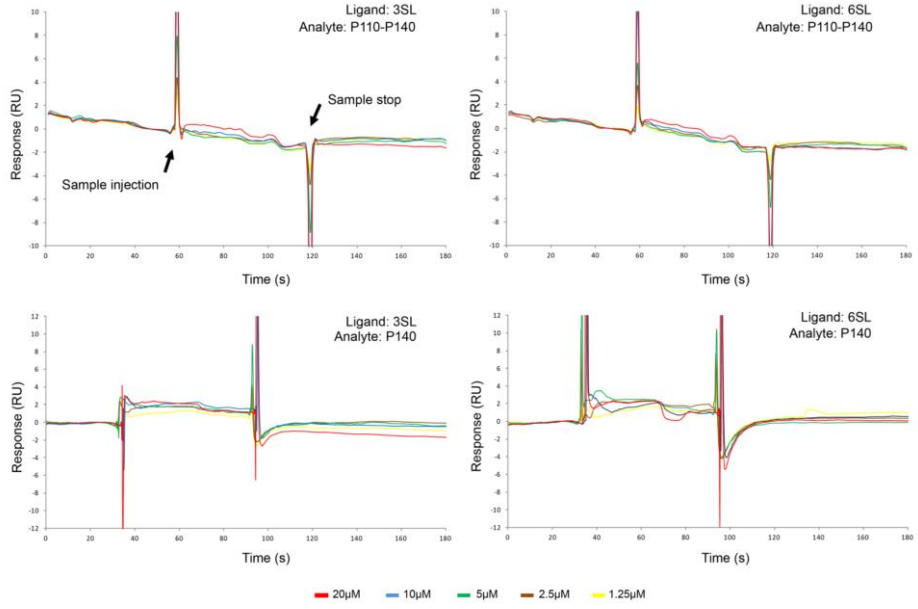

Appendices Figure A. CI. 1.7_3. Surface Plasmon Resonance (SPR). Surface Plasmon Resonance sensorgrams showing no binding for the extracellular P140-P110 heterodimer (top panels) and for P140 (bottom panels) against increasing amounts of 3SL (left panels) and 6SL (right panels). Adapted from **Aparicio D. *et al.*, 2020**.

A. 1.8. P140 and P110 proteomics analysis (LC–MS/MS)

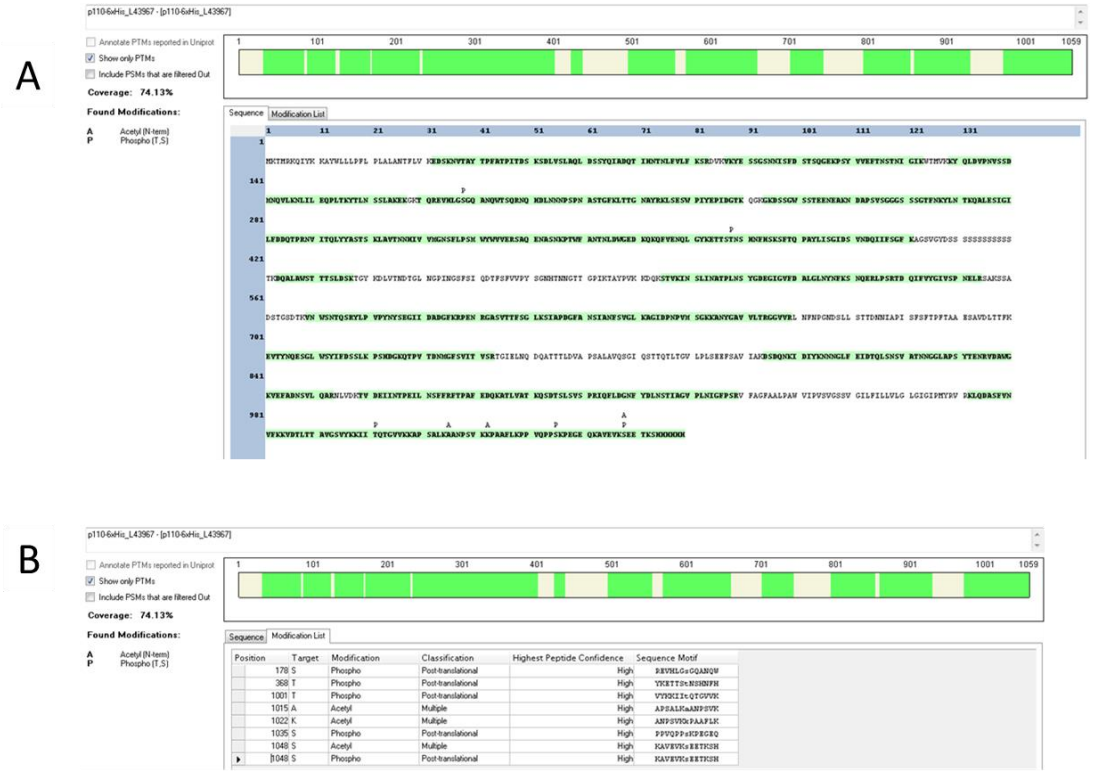

Appendices Figure A. CI. 1.8_1. A) Sequence coverage and phosphorylation sites in *M. genitalium* P110 adhesin. B) Modification list.

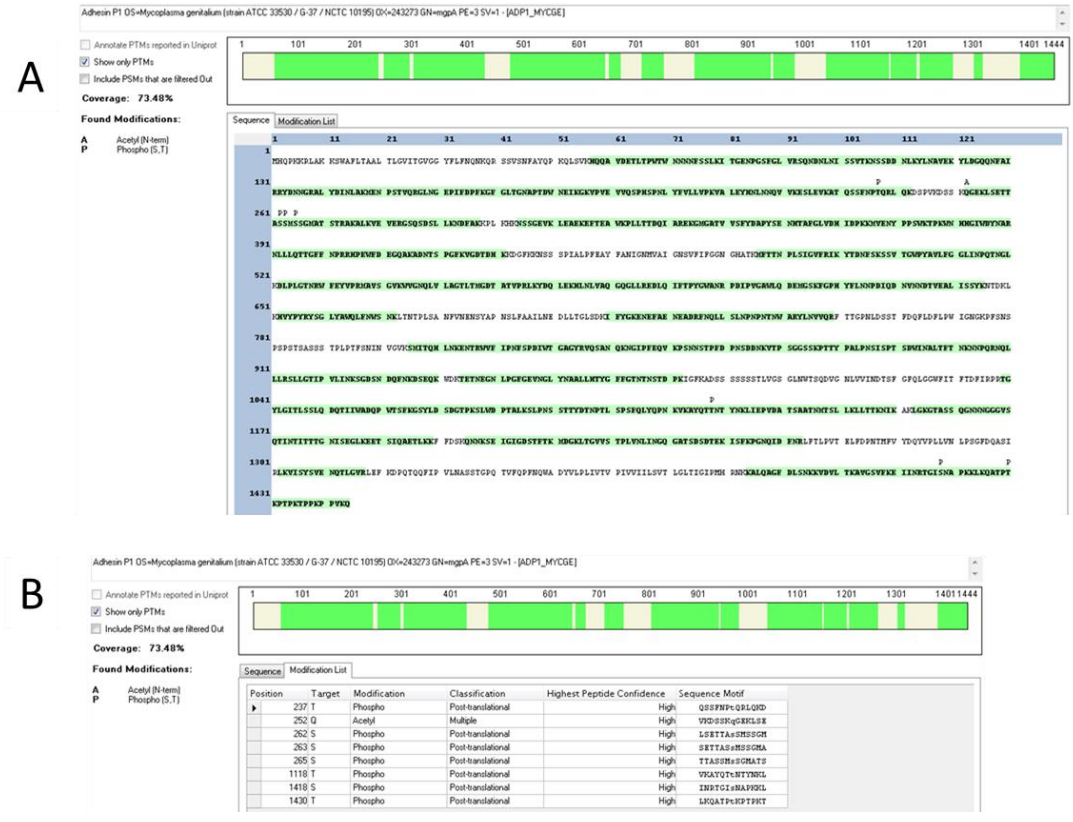

Appendices Figure A. CI. 1.8_2. A) Sequence coverage and phosphorylation sites in *M. genitalium* P140 adhesin. B) Modification list.

Appendices Table A. CI. 1.8_1. Phosphopeptides detected in TiO_2 enriched sample for P140 and P110 proteins of interest in data dependent mode (without peptide list**) and target model (**with peptide list**).**

		Data dependet mode		Target mode	
Sequence	**Protein**	**# PSMs**	**ptmRS Best Site Probabilities**	**# PSMs**	**ptmRS Best Site Probabilities**
LKQATPtKPTPK	p140	3	T7(Phospho): 100	25	T7(Phospho): 98.99
KPAAFLKPPVQPPsKPEGEQK	p110	3	S14(Phospho): 100	19	S14(Phospho): 100
ETTStNSHNFHSK	p110	2	T5(Phospho): 82.22	9	T5(Phospho): 93.9
TGIsNAPK	p140	2	S4(Phospho): 99.91	10	S4(Phospho): 99.82
qGEKLSETTAssMSSGMATSTR	p140	1	S6(Phospho): 20; T8(Phospho): 20; T9(Phospho): 20; S11(Phospho): 20; S12(Phospho): 20; S14(Phospho): 20; S15(Phospho): 20; T19(Phospho): 20; S20(Phospho): 20; T21(Phospho): 20	ND	-
AVEVKsEETK	p110	1	S6(Phospho): 100	17	S6(Phospho): 100
TGIsNAPKK	p140	1	S4(Phospho): 99.85	8	S4(Phospho): 100
EVHLGsGQANQWTSQR	p110	1	S6(Phospho): 100	20	S6(Phospho): 100
AYQTtNTYNK	p140	1	T5(Phospho): 99.62	6	T5(Phospho): 99.5
LSETTASSmsSGmATSTR	p140	1	S8(Phospho): 44.83; M9(Oxidation): 100; S11(Phospho): 44.83; M13(Oxidation): 100	6	M9(Oxidation): 100; S11(Phospho): 99.02; M13(Oxidation): 100
ATQSSFNPtQR	p140	1	T9(Phospho): 100	30	T9(Phospho): 100
KIItQTGVVK	p110	1	T4(Phospho): 99.92	ND	-

A. 2. Appendix of Chapter II

A. 2.1. List of oligonucleotides used in Chapter II

Appendices Table A. CII. 2.1. List of oligonucleotides used in Chapter II: Molecular basis of bacterial lectins recognition of eukaryotic glycans: the case of *Mycoplasma pneumoniae* and *Mycoplasma genitalium* cytadhesins.

Primer name	Sequence 5'→ 3'[a]	Use
Construction of mutants of *M. genitalium*		
N182Amg192-F	GTAGTGGGCAAGCAGCTCAGTGAACCAGTCA	
N182Amg192-R	TGACTGGTTCACTGAGCTGCTTGCCCACTAC	
COMmg192-F (*Apa*I)	AGTGGGCCCACTAACAAAAAACAAATTAGTGATGTT GTTAGTGATTGTGTGAAAAAAATTGTTTATAATTAA GTTTGTATGAAAACAATGAGAAAACAG	Cloning: Build pMTnPacP110-N182A
COMmg192-R (*Xho*I)	AGTCTCGAGCTAACTTTTGGTTTCTTCTG	
Oligonucleotides used in sequencing and screening reactions		
Pac-Up	GTAGCTAATCTAACAGTAGG	To sequence DNA inserts cloned in the miniTnPac
RTPCRmg192-F	TCCCCTAATGAATTGCGAAG	
RTPRCmg192-R	CAGGGGCAATTGATTTAAGC	
Tnp3	GATTCATGATTATATCGATCAAC	
COMmg192-F (*Apa*I)	AGTGGGCCCACTAACAAAAAACAAATTAGTGATGTT GTTAGTGATTGTGTGAAAAAAATTGTTTATAATTAA GTTTGTATGAAAACAATGAGAAAACAG	To screen for MG_192 mutation
Pac-Dw	GTCCTAGAACTTGGTGTATG	To determine miniTnPac Tnp insertion point

[a] Restriction sites of the primers are underlined.

A. 2.2. Plasmid construction and generation of mutants in Chapter II

Appendices Table A. CII. 2.2. List of plasmids used to create the strains used in Chapter II: Molecular basis of bacterial lectins recognition of eukaryotic glycans: the case of *Mycoplasma pneumoniae* and *Mycoplasma genitalium* cytadhesins.

Plasmid name	Aim	Source
pBE	pBE derivative vector used in the cloning procedures	Pich O. Q. *et al*., 2006b
pMTnPac	Minitransposon bearing the puromycin resistance gene	Torres-Puig S. *et al*., 2018
pMTnPac-P110-WT	To complement P110 (MG_192) gene. Also used as a template to obtain P110 gene variant for cloning	This work

pMTnPac-P110-N182A	To complement P110 (MG_192) gene bearing a N182A substitution	This work

A. 2.2.1. Construction of pMTnPacP110-N182A mutant variant

Similarly to what has been previously explained, P110-N182A variant were generated in a two-step PCR procedure using DNA from plasmid pMTnPacP110-WT as a template[465] [**Aparicio D. *et al.*, 2020**]. The first PCR round was performed using primer COMmg192-F (*Apa*I) and the specific N182Amg192-R reverse primer listed in **Appendices Table A. CII. 2.1**, and primer COMmg192-R (*Xho*I) and the specific N182Amg192-F forward primer. To obtain the full-length MG_192 allele, we conducted SOE-PCR using the specific amplicon pair obtained as template and primers COMmg192-F (*Apa*I) and COMmg192-R (*Xho*I). Then, the mutated P110 allele was digested with *Apa*I and *Xho*I and ligated to a similarly digested pMTnPac plasmid[534] [**Torres-Puig S. et al., 2018**] to generate the corresponding pMTnPacP110-N182A plasmid (**Appendices Table A. CII. 2.2 and Figure A. CII. 2.2.1**). Sequencing analysis of the minitransposon using primers Tnp3, RTPCR192-F, RTPCR192-R, COMmg192-F (*Apa*I) and Pac-Up, ruled out the presence of additional mutations in the MG_192 sequence. This plasmid was transformed to a *M. genitalium* ΔMG_192 null mutant[70] [**Burgos R. *et al.*, 2006**] to create the P110-N182A variant strains. Identification of the minitransposon insertion site in the individual clones was done by sequencing using the Pac-Dw primer and chromosomal DNA as template.

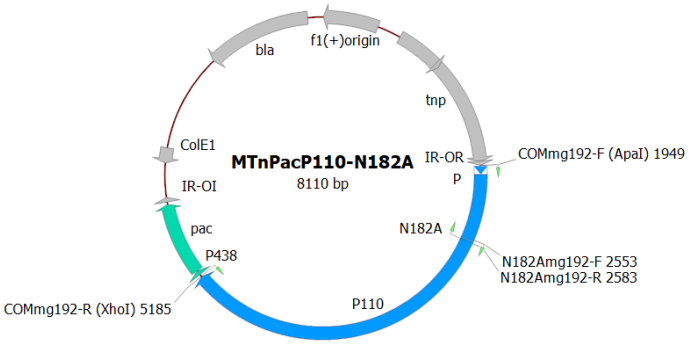

Appendices Figure A. CII. 2.2.1. pMTnPacP110-N182A plasmid map. Primers used to build this plasmid are highlighted as little green arrows. P110, MG_192 gene sequence; P, MG_191 own promoter; N182A, base substitution location of this P110 gene sequence variant; IR, inverted repeat; P438, MG_438 promoter; *pac*, puromycin acetyl transferase marker; tnp, transposase; *bla*, β-lactamase.

A. 3. Appendix of Chapter III

A. 3.1. List of oligonucleotides used in Chapter III

Appendices Table A. CIII. 3.1. List of oligonucleotides used in Chapter III: Dynamics of the nap complex and adhesion mechanisms of the human pathogens *Mycoplasma pneumoniae* and *Mycoplasma genitalium.*

Primer name	Sequence 5' → 3'[a]	Use
Construction of mutants of *M. genitalium*		
Doble adhesins null mutant		
MgParBEFw	ATCATTACCATTATCAATG	Cloning: Build pBEΔAdh
MgParBERev	GGATCCATGCACCTCTCGAGACAAACTTAATTATAAACAAT	
MgParBDFw	CTCGAGAGGTGCATGGATCCTAGTTTTTAACCTTTCAATAAC	
MgParBDRev	CTACTATTGCTAGGTTTCAC	
Lox71p438Fwd (*Xho*I)	CTCGAGTACCGTTCGTATAATGTATGCTATACGAAGTTATTAGTATTTAGAATTAATAAAGT	
CatLox66Rev (*Bam*HI)	GGATCCTACCGTTCGTATAGCATACATTATACGAAGTTATTTACGCCCCGCCCTGCCACT	
Complementation of the null mutant		
COMmg191-F (*Apa*I)	AGTGGGCCCACTAACAAAAAACAAATTAGTGATG	Cloning: Build pMTnPacCOM (MG_191/MG_192)
COMmg191/192-R (*Sal*I)	AGTGTCGACATCCACTCTCTAAATTGCAAGTTTAG	
Engelman Motif mutants		
EngMotifP140-F	TTTTTAACGATTTTTATTCCAATGCACAGAAAC	Cloning: Build pMTnPacCOM:MG_191/MG_192 with the different Engelman Motif substitutions
EngMotifP140-R (5' Ph)	*CAAAGTAACACTAAGGATAATC	
EngMotifP110-F	TTTTCTTCAGTTTTTATCTTGTTTATCTTGTTAGTCTTATTTCTTGGGATTTTTATCCCAATGTACAGGGTAAGA	
EngMotifP110a-F	TTTTCTTCAGTTTTTATCTTGTTTATCTTGTTAGTC	
EngMotifP110-R (5' Ph)	*TACTGATACAGGGATCACCCA	
EngMotifP110b-F	TTTCTTGGGATTTTTATCCCAATGTACAGGGTAAGA	
EngMotifP110b-R (5' Ph)	*TAAGACTAACAAGATAAACAAG	
Oligonucleotides used in sequencing and screening reactions		
Pac-Up	GTAGCTAATCTAACAGTAGG	To sequence DNA inserts cloned in a miniTnPac
Pac-Dw	GTCCTAGAACTTGGTGTATG	To determine miniTnPac Tnp insertion point
COMmg191-R (*Sal*I)	AGTGTCGACTTATTGTTTTACTGGAGGTTT	To sequence DNA inserts cloned in a miniTnPac
Fup17	GTAAAACGACGGCCAGT	Universal Forward primer

Rup17	GGAAACAGCTATGACCATG	Universal Reverse primer
SCRMgPar-F	GTCTGTTTGCCATCTATGACA	To screen for MG_191/MG_192 null mutants
SCRMgPar-R	GAGCCACCTGAAGTGACTT	
SCRCre-F	ACTGCAGATCAATGTGCTAG	
SCRCre-R	CGCTTTTGTTGTTTGAGTC	
Tc-F	GAATTCTAGTATTTAGAATTAATAAAG	
Cm-R	CAGTACTGCGATGAGTGGCA	
Cloning of P1 and P40/P90 different constructs for recombinant expression/purification		
P1F	AGGAGATATACCATGACCGTGGTTGGTCACTTTACC	Cloning for recombinant expression
P1R	GTGATGGTGATGTTTATCCGGCCACTGGTTGAACGG	
P1F_2	AGGCCATGGCGGCCTTTCGTGGCAGTTG	
P1R_2	GTGCTCGAGTCATAAATACTAAGCGGGTT	
P1Ct1400_F	AGGAGATATACCATGGCGGATACCGGTCCGCAG	
P1Ct1376_F	AGGAGATATACCATGAAAATGAACGATGACGTTG	
P40P90_F	AGGAGATATACCATGAGCCTGGCGAACACCTATCTGCTG	
P40P90_R	GTGATGTGTATGTTTGCTCGGCACGCGCCGCAAAACC	

[a] Restriction sites of the primers are underlined.

A. 3.2. Plasmid construction and generation of mutants in Chapter III

Appendices Table A. 3.2. List of plasmids used to create the strains used in Chapter III: Dynamics of the nap complex and adhesion mechanisms of the human pathogens *Mycoplasma pneumoniae* and *Mycoplasma genitalium.*

Plasmid name	Aim	Source
pBE	pBE derivative vector used in the cloning procedures	Pich O. Q, *et al.*, 2006b
pMTnPac	Minitransposon bearing the puromycin resistance gene	Torres-Puig S. *et al.*, 2018
pΔAdh (pΔMG_191/MG_192)	Suicide vector pBE derivative used to create the *Mge* MG_191/MG_192 defective mutant. Selectable marker: chloramphenicol flanked with *lox* sequences	This work
pBE-COMP110P140-WT (pBE-*Mge*Adh)	Intermediate pBE derivative vector used in the cloning process. Also used	This work

	as a template to obtain P110 and P140 gene variants for the other clonings	
pMTnPac-P110P140-WT (pMTnPac*Mge*Adh)	To complement P110 (MG_192) and P140 (MG_191) genes.	This work
pMTnPac-P110P140-E1 (pMTnPac*Mge*AdhE1)	To complement P110 (MG_192) and P140 (MG_191) genes bearing P140 G1372F and G1376F substitutions	This work
pMTnPac-P110P140-E2E3 (pMTnPac*Mge*AdhE2E3)	To complement P110 (MG_192) and P140 (MG_191) genes bearing P110 G947F, G951F, G960F and G964F substitutions	This work
pMTnPac-P110P140-E1E2E3 (pMTnPac*Mge*AdhE1E2E3)	To complement P110 (MG_192) and P140 (MG_191) genes bearing P140 G1372F and G1376F; P110 G947F, G951F, G960F and G964F substitutions	This work
pMTnPac-P110P140-E2 (pMTnPac*Mge*AdhE2)	To complement P110 (MG_192) and P140 (MG_191) genes bearing P110 G947F and G951F substitutions	This work
pMTnPac-P110P140-E3 (pMTnPac*Mge*AdhE3)	To complement P110 (MG_192) and P140 (MG_191) genes bearing P110 G960F and G964F substitutions	This work
pMTnPac-P110P140-E1E2 (pMTnPac*Mge*AdhE1E2)	To complement P110 (MG_192) and P140 (MG_191) genes bearing P140 G1372F and G1376F; P110 G947F and G951F substitutions	This work
pMTnPac-P110P140-E1E3 (pMTnPac*Mge*AdhE1E3)	To complement P110 (MG_192) and P140 (MG_191) genes bearing P140 G1372F and G1376F; P110 G960F and G964F substitutions	This work

A. 3.2.1. Construction of pΔAdh (ΔMG_191/MG_192) plasmid and generation of *Mge*$^{ad-}$ (G37ΔAdh) mutant strain

The suicide plasmid pΔAdh (pBEΔMG_191/MG_192) was designed to generate a G37 *M. genitalium* MG_191 (P140) and MG_192 (P110) null mutant strain by gene replacement or homologous recombination (HR). First, a 1 kb flanking upstream region (UR) to the MG_191 gene was PCR-amplified using the MgParBEFw and MgParBERev primers. Similarly, a 1 kb flanking downstream region (DR) to the MG_192 gene was PCR-amplified with the MgParBDFw and MgParBDRev primers (**Appendices Table A. CIII. 3.1**). In parallel, a "lox" version of the *Cm*M438 selectable marker[534] [**Torres-Puig S. *et al.*, 2018**] was PCR-amplified with the Lox71p438-Fwd (*Xho*I) and CatLox66-Rev (*Bam*HI) primers, obtaining the *Cm*M438 flanked with the lox61 and lox71 sequences. Then, the UR and DR PCR products were joined by PCR with the MgParBEFw and MgParBDRev primers. The resulting PCR product was cloned into an *Eco*RV-digested pBE plasmid[244] [**Pich O. Q. *et al.*, 2006b**]. Finally, the resulting *Cm*M438 amplicon was digested with *Xho*I and *Bam*HI restriction enzymes and ligated into the similarly digested pBE containing the UR and DR regions obtained before.

This plasmid, pΔAdh (**Appendices Table A. 3.2 and Figure A. CIII. 3.2.1_1**), was used to obtain the G37ΔAdh chloramphenicol resistant mutant strain. Electroporation of this mutant with the pCre plasmid[261] [**Mariscal A. M., *et al.*, 2016**] (**Figure MM. 2.10_1**) that contains the Cre recombinase allowed us to obtain the *Mge*$^{ad-}$ (G37ΔAdh) strain, free of any antibiotic selectable marker (**Appendices Figure A. CIII. 3.2.1_2**). This strain was used as the recipient strain to transform all the pMTnPac plasmids generated in Chapter III and V.

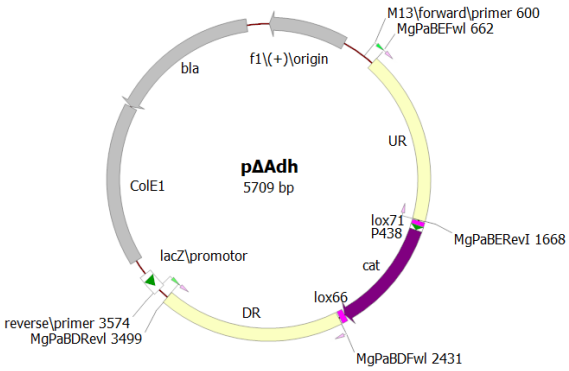

Appendices Figure A. CIII. 3.2.1_1. pΔAdh plasmid map. Oligonucleotides used for cloning are drawn as little pink arrows. UR, homologous upstream region; DR, homologous downstream region; *bla*, β-lactamase; lacZ/promotor, *lacZ* gene promoter; *cat*, *Cm*M438 marker with the MG_438 promoter flanked with lox71 and lox66 sequences.

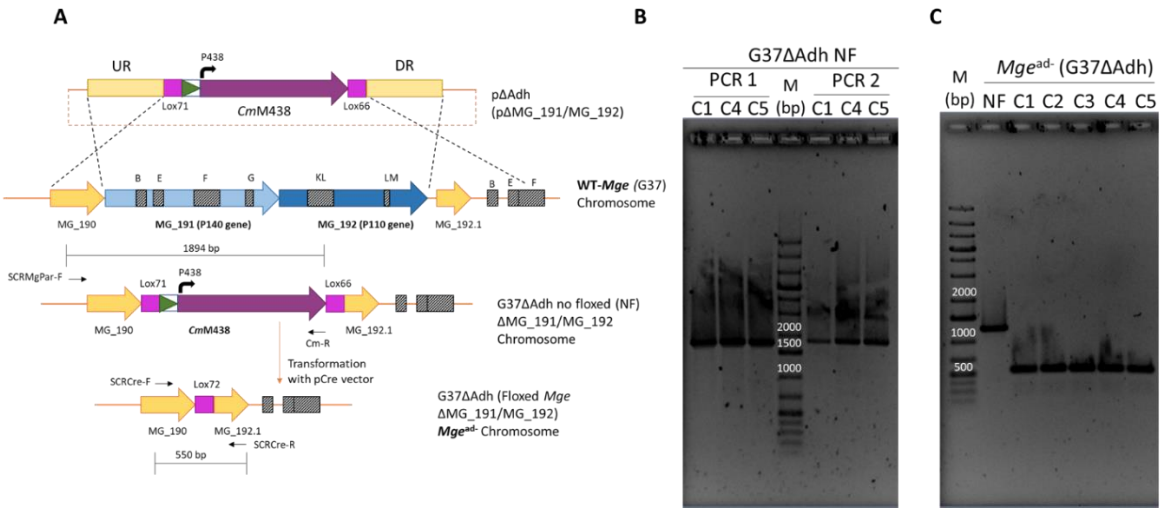

Appendices Figure A. CIII. 3.2.1_2. Construction of ΔMG_108 null mutant. A) Schematic representation illustrating the construction of the *M. genitalium* MG_191 and MG_192 double null mutant by homologous recombination. Arrows indicate the approximate location of the primers used for screening. **B)** Electrophoresis gel demonstrating the replacement of the MG_191 and MG_192 locus by the *Cm*M438 marker in different *Mge*$^{ad-}$ (ΔG37Adh) non floxed (NF) mutant clones. PCR1, reaction using SCRMgPar-F and Cm-R primers; PCR2, reaction using Tc-F and SCRMgPar-R primers (not schematized). **C)** Electrophoresis gel demonstrating the loss of the *Cm*M438 marker by the Cre recombinase in different *Mge*$^{ad-}$ (ΔG37Adh) mutant clones. NF, control reaction with the genomic DNA of a *Mge*$^{ad-}$ (ΔG37Adh) non floxed mutant clone.

A. 3.2.2. Construction of pBE-COMP140P110-WT (pBE-*Mge*Adh), pMTnPac*Mge*Adh and generation of *Mge*^{Mge} mutant strain

MG_191 and MG_192 genes from the chromosome of *M. genitalium* G37 strain were amplified by PCR using COMmg191-F (*Apa*I) and COMmg191/192-R (*Sal*I) primers (**Appendices Table A. CIII. 3.1**). The resulting PCR product was cloned into an *Eco*RV-digested pBE plasmid to create the pBE-COMP140P110-WT (pBE-*Mge*Adh) (**Appendices Table A. 3.2 and Figure A. CIII. 3.2.2_1**). At the same time, the amplicon was digested with the *Apa*I and *Sal*I restriction enzymes and ligated to a similarly digested pMTnPac plasmid[534] [**Torres-Puig S. *et al.*, 2018**] to create the pMTnPac-P140P110-WT (pMTnPac*Mge*Adh) (**Appendices Table A. 3.2 and Figure A. CIII. 3.2.2_2**). This plasmid was used to reintroduce the wild-type alleles of the MG_191 and MG_192 genes to the G37ΔAdh mutant. The COMmg192-F (*Apa*I) primer includes the upstream region (70 nucleotides) of the MG_191 gene, which contains a strong promoter identified in a previous study[574] [**Musatovova O. *et al.*, 2003**]. This promoter was used to drive the transcription of the transposon-encoded copy of the MG_191 and MG_192 genes in all mutants.

Sequencing analysis of the pMTnPac-P140P110-WT construct using primers Tnp3, RTPCR192-F, RTPCR192-R, and Pac-Up, ruled out the presence of additional mutations in the MG_191 and MG_192 sequences. This plasmid was transformed into the *M. genitalium* G37ΔAdh null mutant (this work) to create the *Mge*^{Mge} complemented mutant strain (G37ΔAdh::COM). Identification

of the minitransposon insertion site in the indvidual clones was done by sequencing using the Pac-Dw primer and chromosomal DNA as a template.

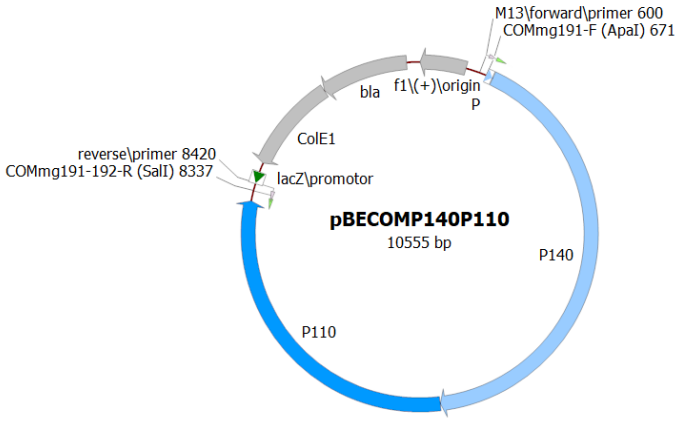

Appendices Figure A. CIII. 3.2.2_1. pBE-COMP140P110-WT (pBE-*Mge*Adh) plasmid map. Oligonucleotides used for cloning are drawn as little green arrows; P110, MG_192 gene sequence; P140, MG_191 gene sequence; P, MG_191 own promoter; *bla*, β-lactamase; lacZ/promotor, *lacZ* gene promoter.

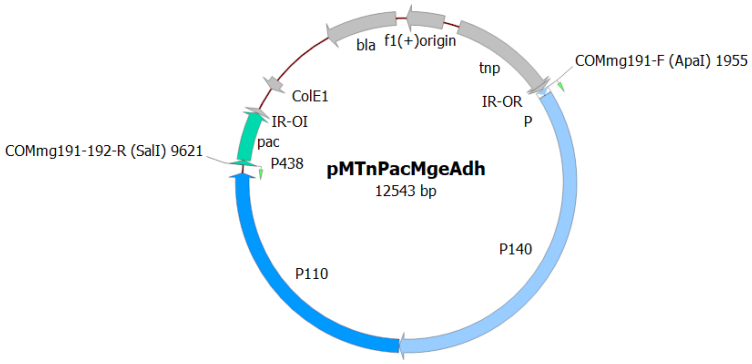

Appendices Figure A. CIII. 3.2.2_2. pMTnPac-P140P110-WT (pMTnPac*Mge*Adh) plasmid map. Oligonucleotides used for cloning are drawn as little green arrows; P110, MG_192 gene sequence; P140, MG_191 gene sequence; P, MG_191 own promoter; *bla*, β-lactamase; IR, inverted repeat; P438, MG_438 promoter; *pac*, puromycin acetyl transferase marker; tnp, transposase.

A. 3.2.3. Construction of pMTnPac*Mge*Adh Engelman motifs mutant variants

As previously described, ExSite PCR method was used to generate P140 (MG_191) and P110 (MG_192) variants carrying specific mutations in residues of the Engelman motifs of these proteins. Using the pBE-COMP140P110-WT (pBE-*Mge*Adh) as a template and the specific primers for each mutant (**Appendices Table A. CIII. 3.1**) the target mutation or combination of mutations in the Engelman motifs of the P140 and P110 adhesins were introduced. Then, the pBE-COMP140P110 (pBE-*Mge*Adh) derivatives plasmids containing the P110 and P140 alleles with the desired mutations were re-ligated and mutant alleles of P140 and P110 were excised

by digestion with *Apa*I and *Sal*I restriction enzymes. Finally, these DNA fragments were ligated into a pMTnPac plasmid[534] [Torres-Puig S. *et al.*, 2018] previously digested with *Apa*I and *Sal*I, to generate the corresponding pMTnPac-P140P110 Engelman motif mutations plasmid series (**Appendices Table A. 3.2 and Figure A. CIII. 3.2.3**).

Sequencing analysis of the different pMTnPac-P140P110 constructs using primers Tnp3, RTPCR192-F, RTPCR192-R, and Pac-Up, ruled out the presence of additional mutations in the MG_191 and MG_192 sequences. These plasmids were transformed into the *M. genitalium* G37ΔAdh null mutant (this work) to create the different P140 and P110 Engelman motif variant strains. Identification of the minitransposon insertion site in the individual clones was done by sequencing using the Pac-Dw primer and chromosomal DNA as a template.

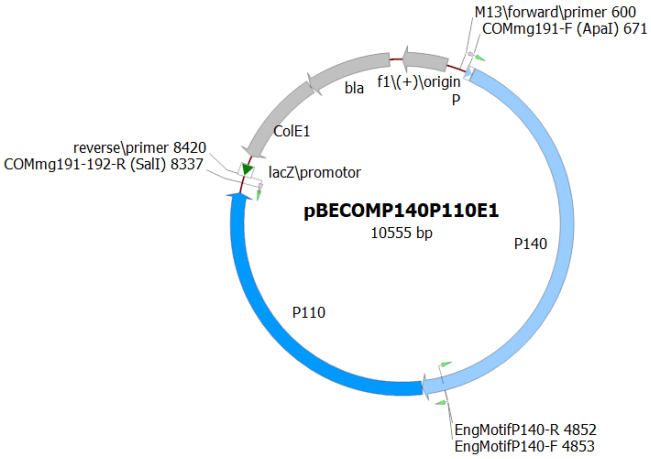

Appendices Figure A. CIII. 3.2.3. pBE-COMP140P110-E1 (pBE-*Mge*AdhE1) plasmid map. Exemplification of one of the pMTnPac-P140P110 Engelman motif mutations plasmid series created. Oligonucleotides used for cloning are drawn as little green arrows; P110, MG_192 gene sequence; P140, MG_191 gene sequence; P, MG_191 own promoter; *bla*, β-lactamase; lacZ/promotor, *lacZ* gene promoter.

A. 3.3. Results compilation of the cytadherence capacity of *M. genitalium* strains analysed in Chapter III

Appendices Table A. CIII. 3.3. Summary table with the K_d, B_{max} values and other characteristics of all mutant strains analysed in Chapter III.

Strain	K_d values ± SE	B_{max} values ± SE	Affected HA parameter	Flask-Adherent	Adhesins expression levels[a]
G37 (WT-*Mge*)	$1.0x10^3 \pm 2.5x10^2$	0.85±0.05	-	Yes	4
G37ΔAdh	NA	NA	NA	No	0
G37ΔAdh::COM	$1.5x10^3 \pm 2.8x10^2$	0.90±0.04	-	Yes	4
G37ΔAdh::COM (E1)	$1.5x10^3 \pm 1.6x10^2$	0.85±0.02	-	Yes	4

G37ΔAdh::COM (E2; E3)	NA	NA	NA	No	4
G37ΔAdh::COM (E1; E2; E3)	$0.5x10^3±8.0x10^2$	0.13±0.04	↓ K_d, ↓ B_{max}	No	4
G37ΔAdh::COM (E2)	$2.5x10^3±1.2x10^3$	0.72±0.10	↑ K_d ↓ B_{max}	Yes	4
G37ΔAdh::COM (E3)	$2.8x10^3±7.2x10^2$	0.57±0.05	↑ K_d, ↓ B_{max}	Yes	4
G37ΔAdh::COM (E1; E2)	$0.6x10^3±2.2x10^2$	0.68±0.05	↓ K_d, ↓ B_{max}	Yes	4
G37ΔAdh-COM (E1; E3)	$1.0x10^3±4x10^2$	0.49±0.05	↓ B_{max}	Yes	4

[a] Illustrative value scale from 0 (without adhesins) to 4 (WT).

A. 3.4. Plasmids used for expression of P1 protein for epitope mapping of P1/MCA4

The corresponding pP1-8 plasmid was constructed by inserting a PCR amplified fragment of P1 gene into the *Nco*I and *Xho*I sites of pET-30c(+) expression vector. The remaining plasmids were constructed by deletion of the pP1-8 using specific primer set and PrimeSTAR Mutagenesis Basal kit (Takara Bio, Shiga, Japan).

Appendices Table A. CIII. 3.4. Plasmids used for expression of P1 protein fragments for epitope mapping of P1/MCA4.

No.	Plasmids	Primers used for plasmid construction*		Plasmid size	Recombinant P1 fragment	M.W. (kDa) **	Bind to P1/MC4***
1	pP1-8	5'-AGGCCATGGCGGCCTTTCGTG GCAGTTG -3'	5'-GTGCTCGAGTCATAAATACTAAGC GGGTT -3'	6789	A1160 - Q1518	43,4	+
2	pP1-8d-N1	5'-TTATTGATTAGTATTTATGACTC GAGCAC -3'	5'-AATACTAATCAATAAACAGCGGTA TGT -3'	6246	A1160 - D1446	35,4	+
3	pP1-8d-N2	5'-CGCTGTTTTAGTATTTATGACTC GAGCAC -3'	5'-AATACTAAAACAGCGGTATGTACT GGT -3'	6240	A1160 - F1444	35,2	+
4	pP1-8d-N3	5'-ACATACCGTAGTATTTATGACTC GAGCAC -3'	5'-AATACTACGGTATGTACTGGTCAT ACA -3'	6234	A1160 - P1442	34,9	+
5	pP1-8d-N4	5'-ACCAGTACTAGTATTTATGACTC GAGCAC -3'	5'-AATACTAGTACTGGTCATACACCA ACA -3'	6228	A1160 - Y1440	34,7	+
6	pP1-8d-N5	5'-TGTATGACTAGTATTTATGACTC GAGCAC -3'	5'-AATACTAGTCATACACCAACATAG TTA -3'	6222	A1160 - D1438	34,4	+
7	pP1-8d-N6	5'-TGGTGTATTAGTATTTATGACTC GAGCAC -3'	5'-AATACTAATACACCAACATAGTTA CCG -3'	6219	A1160 - Y1437	34,3	-
8	pP1-8d-N7	5'-TGTTGGTGTAGTATTTATGACTC GAGCAC -3'	5'-AATACTACACCAACATAGTTACCG GAT -3'	6216	A1160 - V1436	34,1	-
9	pP1-8d-N8	5'-TAACTATGTAGTATTTATGACTC GAGCAC -3'	5'-AATACTACATAGTTACCGGATCAA ACA -3'	6210	A1160 - M1434	33,9	-

No.	Plasmids	Primers used for plasmid construction*		Plasmid size	Recombinant P1 fragment	M.W. (kDa) **	Bind to P1/MC4
10	pP1-8d-N9	5'-ATCCGGTATAGTATTTATGACTCGAGCAC -3'	5'-AATACTATACCGGATCAAACAGATCGG -3'	6204	A1160 – V1432	33,7	-
11	pP1-8d-C1	5'-AGGCCATGACTATGTTGGTGTATGACCA -3'	5'-ACATAGTCATGGCCTTGTCGTCGTC -3'	5970	T1433 - Q1518	14,7	-
12	pP1-8d-C2	5'-AGGCCATGCCGGTAACTATGTTGGTGTA -3'	5'-TTACCGGCATGGCCTTGTCGTCGTC -3'	5976	P1431 - Q1518	14,9	-
13	pP1-8d-C3	5'-AGGCCATGTTTGATCCGGTAACTATGTT -3'	5'-GATCAAACATGGCCTTGTCGTCGTC -3'	5982	F1429 - Q1518	15,2	-
14	pP1-8d-C4	5'-AGGCCATGGATCTGTTTGATCCGGTAAC -3'	5'-ACAGATCCATGGCCTTGTCGTCGTC -3'	5988	D1427 - Q1518	15,4	-
15	pP1-8d-C5	5'-AGGCCATGACCGATCTGTTTGATCCGGT -3'	5'-GATCGGTCATGGCCTTGTCGTCGTC -3'	5991	T1426 - Q1518	15,5	+
16	pP1-8d-C6	5'-AGGCCATGGTCACCGATCTGTTTGATCC -3'	5'-CGGTGACCATGGCCTTGTCGTCGTC -3'	5994	V1425 - Q1518	15,6	+
17	pP1-8d-C7	5'-AGGCCATGGCTGACACTGGTCCACAA -3'	5'-TGTCAGCCATGGCCTTGTCGTCGTC -3'	6069	A1400 – Q1518	18,4	+
18	pP1-8d-C8	5'-AGGCCATGAAGATGAATGACGATGTT -3'	5'-TCATCTTCATGGCCTTGTCGTCGTC -3'	6141	K1376 – Q1518	21	+

* NcoI and XhoI sites of the primers used for pP1-8 plasmid construction are underlined.

** Molecular weight of recombinant P1 fragments including His- and S-tag sequences (45 aa: 5 kDa) from the pET-30c(+) expression vector.

A. 3.5. Production and sequencing of the monoclonal antibody P1/MCA4

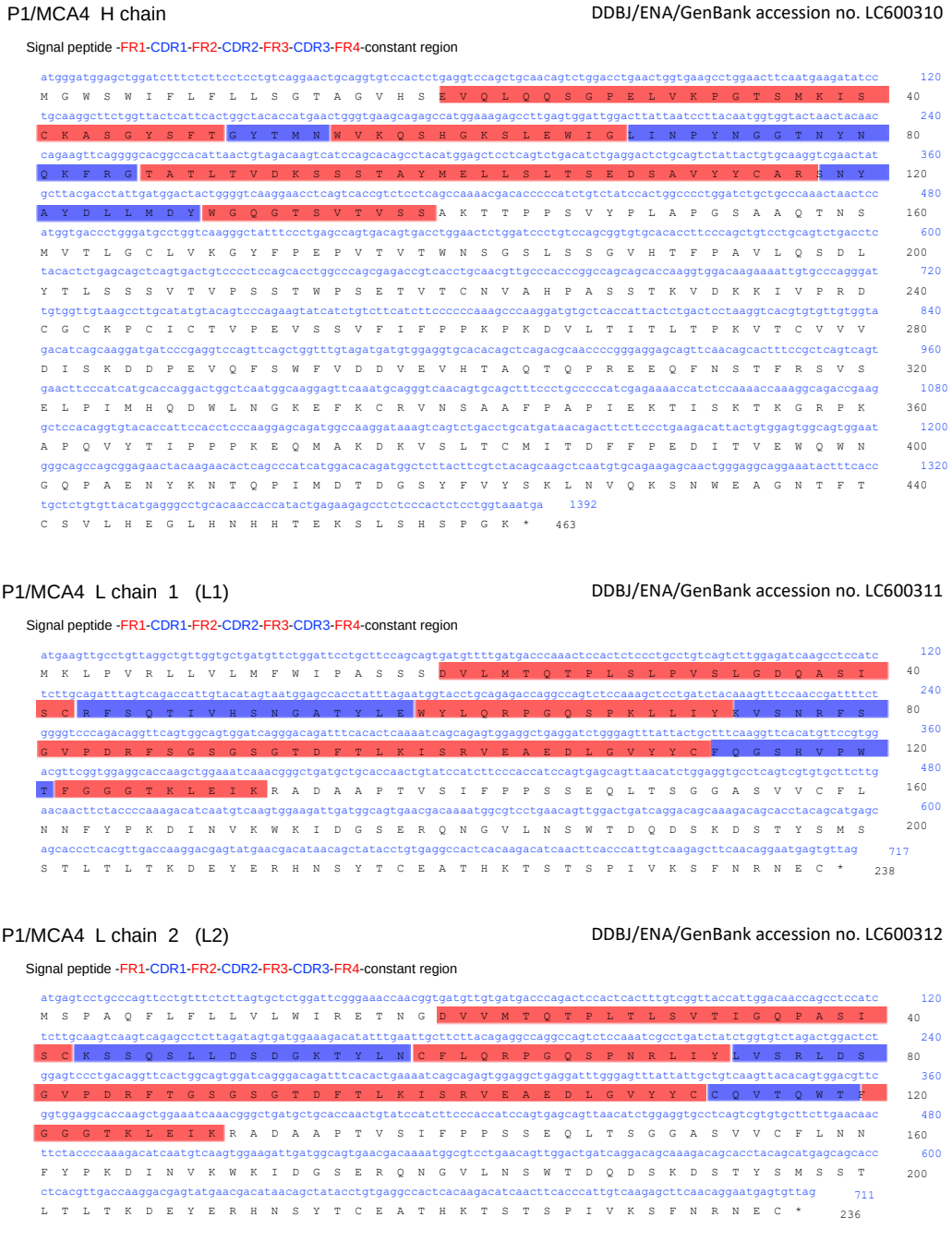

Appendices Figure A. CIII. 3.5. Nucleotides and amino-acids sequences corresponding to the Heavy and the (two) Light chains from Mab P1/MCA4.

A. 3.6. Synthetic DNA

Appendices Table A. CIII. 3.6. Synthetic clones obtained from Genscript. Start and stop codons of the full-length *mpn141* and *mpn142* (P1 and P40/P90 genes) are highlighted in green.

Synthetic clone for *M. pneumoniae* P1
ATGCACCAGACCAAGAAAACCGCGCTGAGCAAGAGCACCTGGATCCTGATTCTGACCGCGACCGCGAGCCTGGCGACCGGTCTGACCGTGGTTGGTCACTTTACCAGCACCACCACCACCCT GAAACGTCAGCAATTCAGCTATACCCGTCCGGACGAAGTTGCGCTGCGTCACACCAACGCGATCAACCCGCGTCTGACCCCGTGGACCTACCGTAACACCAGCTTCAGCAGCCTGCCGCTGAC CGGCGAGAACCCGGGTGCGTGGGCGCTGGTGCGTGACAACAGCGCGAAGGGTATTACCGCGGGTAGCGGCAGCCAGCAAACCACCTATGATCCGACCCGTACCGAAGCGGCGCTGACCGC GAGCACCACCTTTGCGCTGCGTCGTTACGACCTGGCGGGTCGTGCGCTGTATGATCTGGACTTCAGCAAACTGAACCCGCAGACCCCGAACCGTGATCAAACCGGTCAGATCACCTTCAACCC GTTTGGTGGCTTCGGTCTGAGCGGTGCGGCGCCGCAGCAATGGAACGAGGTTAAAAACAAGGTGCCGGTTGAAGTGGCGCAAGACCCGAGCAACCCGTACCGTTTTGCGGTTCTGCTGGTG CCGCGTAGCGTGGTTTACTATGAACAGCTGCAACGTGGTCTGGGCCTGCCGCAGCAACGTACCGAGAGCGGTCAGAACACCAGCACCACCGGTGCGATGTTCGGCCTGAAAGTGAAGAACG CGGAAGCGGATACCGCGAAAAGCAACGAGAAGCTGCAGGGTGCGGAAGCGACCGGTAGCAGCACCACCAGCGGTAGCGGTCAAAGCACCCAGCGTGGTGGCAGCAGCGGTGACACCAAA GTTAAGGCGCTGAAGATCGAGGTGAAGAAAAAGAGCGATAGCGAAGACAACGGCCAGCTGCAACTGGAGAAAAACGATCTGGCGAACGCGCCGATTAAGCGTAGCGAGGAAAGCGGTCA AAGCGTTCAGCTGAAAGCGGACGATTTTGGTACCGCGCTGAGCAGCAGCGGTAGCGGTGGCAACAGCAACCCGGGTAGCCCGACCCCGTGGCGTCCGTGGCTGGCGACCGAGCAGATCCAC AAAGACCTGCCGAAGTGGAGCGCGAGCATCCTGATTCTGTACGATGCGCCGTATGCGCGTAACCGTACCGCGATTGATCGTGTTGACCACCTGGATCCGAAGGCGATGACCGCGAACTACCC GCCGAGCTGGCGTACCCCGAAATGGAACCACCACGGTCTGTGGGACTGGAAGGCGCGTGATGTGCTGCTGCAGACCACCGGCTTCTTTAACCCGCGTCGTCACCCGGAATGGTTTGACGGTG GCCAAACCGTTGCGGATAACGAGAAGACCGGTTTTGATGTGGACAACAGCGAAAACACCAAACAAGGCTTCCAGAAAGAGGCGGATAGCGACAAAAGCGCGCCGATTGCGCTGCCGTTTGA GGCGTATTTCGCGAACATTGGTAACCTGACCTGGTTTGGCCAGGCGCTGCTGGTTTTCGGTGGCAACGGTCATGTTACCAAGAGCGCGCACACCGCGCCGCTGAGCATTGGTGTTTTTCGTGT GCGTTACAACGCGACCGGTACCAGCGCGACCGTTACCGGCTGGCCGTATGCGCTGCTGTTCAGCGGTATGGTGAACAAACAGACCGACGGCCTGAAGGATCTGCCGTTTAACAACAACCGTT GGTTCGAATACGTTCCGCGTATGGCGGTGGCGGGTGCGAAATTTGTTGGCCGTGAGCTGGTGCTGGCGGGTACCATTACCATGGGTGACACCGCGACCGTTCCGCGTCTGCTGTATGATGAG CTGGAAAGCAACCTGAACCTGGTGGCGCAGGGTCAAGGCCTGCTGCGTGAAGACCTGCAGCTGTTCACCCCGTACGGTTGGGCGAACCGTCCGGATCTGCCGATTGGCGCGTGGAGCTCTTC TAGCAGCAGCAGCCACAACGCGCCGTACTATTTTCACAACAACCCGGACTGGCAAGATCGTCCGATCCAGAACGTGGTTGACGCGTTCATTAAACCGTGGGAGGATAAAAACGGCAAGGACG ATGCGAAGTACATCTATCCGTACCGTTATAGCGGCATGTGGGCGTGGCAAGTTTATAACTGGAGCAACAAGCTGACCGACCAGCCGCTGAGCGCGGATTTTGTGAACGAAAACGCGTACCAG CCGAACAGCCTGTTCGCGGCGATTCTGAACCCGGAGCTGCTGGCGGCGCTGCCGGACAAGGTTAAGTACGGCAAAGAGAACGAATTTGCGGCGAACGAGTATGAACGTTTCAACCAAAAG C TGACCGTGGCGCCGACCCAGGGTACCAACTGGAGCCACTTCAGCCCGACCCTGAGCCGTTTTAGCACCGGTTTCAACCTGGTTGGCAGCGTGCTGGACCAGGTTCTGGATTATGTGCCGTGG ATCGGTAACGGCTACCGTTATGGTAACAACCACCGTGGCGTGGACGATATTACCGCGCCGCAAACCAGCGCGGGTAGCAGCAGCGGCATTAGCACCAACACCAGCGGTAGCCGTAGCTTTCT GCCGACCTTCAGCAACATCGGTGTTGGCCTGAAAGCGAACGTGCAAGCGACCCTGGGTGGCAGCCAGACCATGATTACCGGTGGCAGCCCGCGTCGTACCCTGGACCAAGCGAACCTGCAG CTGTGGACCGGTGCGGGCTGGCGTAACGACAAAGCGAGCAGCGGTCAGAGCGATGAAAACCACACCAAGTTTACCAGCGCGACCGGTATGGACCAGCAGGGTCAGAGCGGTACCAGCGCG GGTAACCCGGACAGCCTGAAACAGGATAACATCAGCAAGAGCGGTGATAGCCTGACCACCCAAGACGGCAACGCGATTGATCAGCAAGAGGCGACCAACTACACCAACCTGCCGCCGAACC TGACCCCGACCGCGGACTGGCCGAACGCGCTGAGCTTTACCAACAAGAACAACGCGCAACGTGCGCAGCTGTTCCTGCGTGGTCTGCTGGGCAGCATCCCGGTTCTGGTGAACCGTAGCGGT AGCGACAGCAACAAATTCCAAGCGACCGATCAAAAGTGGAGCTACACCGACCTGCACAGCGATCAGACCAAACTGAACCTGCCGGCGTATGGTGAAGTTAACGGCCTGCTGAACCCGGCGCT GGTTGAAACCTACTTTGGTAACACCCGTGCGGGTGGCAGCGGTAGCAACACCACCAGCAGCCCGGGTATCGGCTTCAAAATTCCGGAACAGAATAACGACAGCAAAGCGACCCTGATTACCC CGGGCCTGGCGTGGACCCCGCAGGATGTTGGTAACCTGGTGGTTAGCGGCACCACCGTGAGCTTTCAACTGGGTGGCTGGCTGGTTACCTTTACCGACTTCGTGAAGCCGCGTGCGGGTTAC CTGGGCCTGCAACTGACCGGTCTGGATGCGAGCGATGCGACCCAACGTGCGCTGATTTGGGCGCCGCGTCCGTGGGCGGCGTTCCGTGGTAGCTGGGTTAACCGTCTGGGCCGTGTTGAGA GCGTGTGGGATCTGAAAGGTGTGTGGGCGGACCAGGCGCAAAGCGATAGCCAAGGTAGCACCACCACCGCGACCCGTAACGCGCTGCCGGAACACCCGAACGCGCTGGCGTTCCAAGTTA GCGTGGTTGAGGCGAGCGCGTATAAACCGAACACCAGCAGCGGTCAGACCCAAAGCACCAACAGCAGCCCGTACCTGCACCTGGTTAAGCCGAAAAAGGTGACCCAGAGCGACAAACTGGA CGATGACCTGAAGAACCTGCTGGATCCGAACCAAGTGCGTACCAAACTGCGTCAGAGCTTTGGTACCGACCACAGCACCCAGCCGCAACCGCAGAGCCTGAAGACCACCACCCCGGTTTTCG GTACCAGCAGCGGCAACCTGAGCAGCGTGCTGAGCGGTGGCGGTGCGGGCGGTGGCAGCAGCGGTAGCGGCCAGAGCGGTGTTGATCTGAGCCCGGTTGAAAAGGTGAGCGGTTGGCTG GTTGGTCAACTGCCGAGCACCAGCGACGGTAACACCAGCAGCACCAACAACCTGGCGCCGAACACCAACACCGGCGAACAACAACGTTGGTTGGTGTTGCCGTCTGAGCGAGAGCAACGCGGCGA AAATGAACGATGACGTTGACGGTATCGTTCGTACCCCGCTGGCGGAGCTGCTGGATGGTGAGGGTCAGACCGCGGATACCGGTCCGCAGAGCGTTAAATTCAAGAGCCCGGACCAGATCGA TTTTAACCGTCTGTTCACCCACCCGGTGACCGACCTGTTTGATCCGGTTACCATGCTGGTGTACGACCAATATATTCCGCTGTTCATCGATATTCCGGCGAGCGTGAACCCGAAAATGGTTCGTC TGAAGGTGCTGAGCTTTGACACCAACGAACAGAGCCTGGGTCTGCGTCTGGAGTTCTTTAAACCGGATCAAGACACCCAGCCGAACAACAACGTTCAAGTGAACCCGAACAACGGTGACTTC CTGCCGCTGCTGACCGCGAGCAGCCAAGGTCCGCAGACCCTGTTTAGCCCGTTCAACCAGTGGCCGGATTACGTTCTGCCGCTGGCGATCACCGTGCCGATCGTGGTTATTGTTCTGAGCGTG ACCCTGGGTCTGGCGATCGGCATTCCGATGCACAAAAACAAGCAAGCGCTGAAAGCGGGTTTTGCGCTGAGCAACCAGAAAGTTGACGTGCTGACCAAGGCGGTTGGTAGCGTGTTCAAGG AGATCATTAACCGTACCGGCATTAGCCAAGCGCCGAAACGTCTGAAGCAGACCAGCGCGGCGAAACCGGGTGCGCCGCGTCCGCCGGTTCCGCCGAAACCGGGCGCGCCGAAGCCGCCGGT GCAGCCGCCGAAAAAGCCGGCGTAA
Synthetic clone for *M. pneumoniae* P40/P90
ATGAAGAGCAAACTGAAGCTGAAACGTTATCTGCTGTTCCTGCCGCTGCTGCCGCTGGGTACCCTGAGCCTGGCGAACACCTATCTGCTGCAAGATCACAACACCCTGACCCCGTACACCCCG TTTACCACCCCGCTGAACGGTGGCCTGGATGTGGTTCGTGCGGCGCACCTGCACCCGAGCTATGAGCTGGTTGACTGGAAACGTGTTGGTGATACCAAACTGGTGGCGCTGGTTCGTAGCGC GCTGGTGCGTGTTAAGTTCCAGGACACCACCAGCAGCGATCAAAGCAACACCAACCAGAACGCGCTGAGCTTTGACACCCAAGAAAGCCAGAAAGCGCTGAACGGTAGCCAAAGCGGCAGC AGCGACACCAGCGGTAGCAACAGCCAGGATTTCGCGAGCTATGTGCTGATTTTTAAAGCGGCGCCGCGTGCGACCTGGGTTTTCGAGCGTAAGATCAAACTGGCGCTGCCGTACGTGAAACA AGAAAGCCAGGGTAGCGGCGATCAGGGCAGCAACGGTAAAGGCAGCCTGTATAAGACCCTGCAAGACCTGCTGGTTGAGCAACCGGTTACCCCGTACACCCCGAACGCGGGTCTGGCGCGT GTGAACGGTGTTGCGCAAGATACCGTTCACTTCGGTAGCGGCCAGGAAAGCAGCTGGAACAGCCAACGTAGCCAGAAGGGTCTGAAAAACAACCCGGGCCCGAAAGCGGTTACCGGTTTTA AGCTGGACAAAGGCCGTGCGTATCGTAAGCTGAACGAGAGCTGGCCGGTGTACGAACCGCTGGACAGCACCAAAGAGGGTAAAGGCAAAGATGAAAGCAGCTGGAAGAACAGCGAGAAA ACCACCGCGGAAAACGACGCGCCGCTGGTTGGTATGGTTGGTAGCGGTGCGGCGGGTAGCGCGAGCAGCCTGCAGGGTAACGGCAGCAACAGCAGCGGTCTGAAAAGCCTGCTGCGTAGC GCGCCGGTGAGCGTTCCGCCGAGCAGCACCAGCAACCAGACCCTGAGCCTGAGCAACCCGGCGCCGGTGGGCCCGCAAGCGGTGGTTAGCCAACCGGCGGGTGGCGCGACCGCGGCGGTG AGCGTTAACCGTACCGCGAGCGATACCGCGACCTTCAGCAAGTACCTGAACACCGCGCAAGCGCTGCACCAGATGGGTGTGATCGTTCCGGGCCTGGAGAAATGGGGTGGCAACAACGGTA CCGGCGTGGTTGCGAGCCGTCAAGACGCGACCAGCACCAACCTGCCGCATGCGGCGGGTGCGAGCCAGACCGGTCTGGGTACCGGTAGCCCGCGTGAGCCGGCGCTGACCGCGACCAGCC AACGTGCGGTTACCGTTGTTGCGGGTCCGCTGCGTGCGGGTAACAGCAGCGAAACCGACGCGCTGCCGAACGTGATTACCCAGCTGTATCACACCAGCACCGCGCAACTGGCGTACCTGAAC GGTCAGATCGTGGTTATGGGCAGCGACCGTGTTCCGAGCCTGTGGTACTGGGTGGTTGGCGAGGATCAAGAAAGCGGCAAAGCGACCTGGTGGGCGAAGACCGAGCTGAACTGGGGTACC GATAAGCAAAAACAGTTCGTGGAAAACCAGCTGGGCTTTAAGGACGATAGCAACGGCGACAGCAAAAACAGCAACCTGAAGGCGCAAGGTCTGACCCAGCCGGCGTATCTGATTGCGGGCC TGGACGTGGTTGCGGATCACCTGGTGTTCGCGGCGTTTAAAGCGGGTGCGGTTGGCTATGACATGACCACCGATAGCAGCGCGAGCACCTACAACCAAGCGCTGGCGTGGAGCACCACCGC GGGTCTGGACAGCGATGGTGGCTACAAGGCGCTGGTTGAAAACACCGCGGGTCTGAACGGCCCGATCAACGGTCTGTTCACCCTGCTGGATACCTTTGCGTATGTGACCCCGGTTAGCGGCA TGAAAGGTGGCAGCCAAAACAACGAGGAAGTGCAGACCACCTACCCGGTTAAGAGCGACCAGAAAGCGACCGCGAAGATTGCGAGCCTGATCAACGCGAGCCCGCTGAACAGCTATGGTG ACGATGGCGTGACCGTTTTCGATGCGCTGGGTCTGAACTTCAACTTTAAGCTGAACGAGGAACGTCTGCCGAGCCGTACCGACCAACTGCTGGTGTACGGCATTGTTAACGAGAGCGAACTG AAAAGCGCGCGTGAGAACGCGCAGAGCACCAGCGACGATAACAGCAACACCAAGGTTAAATGGACCAACACCGCGAGCCACTACCTGCCGGTGCCGTACTATTACAGCGCGAACTTTCCGG AGGCGGGTAACCGTCGTCGTGCGGAACAACGTAACGGCGTGAAGATCAGCACCCTGGAAAGCCAGGCGACCGATGGTTTCGCGAACAGCCTGCTGAACTTTGGCACCGGTCTGAAGGCGG GTGTGGACCCGGCGCCGGTTGCGCGTGGCCACAAGCCGAACTATAGCGCGGTGCTGCTGGTTCGTGGTGGCGTGGTTCGTCTGAACTTTAACCCGGACACCGATAAACTGCTGGACAGCACC GATAAGAACAGCGAGCCGATTAGCTTCAGCTACACCCCGTTTGGTAGCGCGGAAAGCGCGGTGGACCTGACCACCCTGAAAGATGTTACCTATATCGCGGAGAGCGGCCTGTGGTTCTACAC CTTTGACAACGGTGAAAAACCGACCTATGATGGCAAGCAGCAACAGGTTAAGAACCGTAAAGGTTACGCGGTGATTACCGTTAGCCGTACCGGCATCGAGTTCAACGAAGATGCGAACACCA CCACCCTGAGCCAGGCGCCGGCGGCGCTGGCGGTCAAAACGGTATTGCGAGCAGCCAGGACGATCTGACCGGCATCCTGCCGCTGAGCGACGAGTTCAGCGCGGTGATTACCAAGGACCA AACCTGGACCGGTAAAGTTGATATCTATAAGAACACCAACGGCCTGTTTGAGAAAGACGATCAGCTGAGCGAAAACGTGAAGCGTCGTGACAACGGTCTGGTTCCGATCTACAACGAAGGTA TCGTGGACATTTGGGGCCGTGTTGATTTTGCGGCGAACAGCGTTCTGCAGGCGCGTAACCTGACCGACAAGACCGTGGATGAGGTTATTAACAACCCGGACATCCTGCAAAGCTTCTTTAAGT TCACCCCGGCGTTTGATAACCAGCGTGCGATGCTGGTTGGTGAAAAACCAGCGACACCACCCTGACCGTTAAGCCGAAAATTGAGTATCTGGACGGTAACTTCTACGGCGAAGATAGCAAA ATCGCGGGTATTCCGCTGAACATTGATTTTCCGAGCCGTATCTTTGCGGGTTTTGCGGCGCTGCCGAGCTGGGTGATCCCGGTGAGCGTTGGTAGCAGCGTTGGCATCCTGCTGATTCTGCTG ATCCTGGGCCTGGGTATCGGCATTCCGATGTATAAGGTTCGTAAACTGCAAGACAGCAGCTTCGTGGATGTTTTTAAGAAAGTGGACACCCTGACCACCGCGGTGGGTAGCGTTTACAAGAA AATCATTACCCAGACCAGCGTGATCAAGAAAGCGCCGAGCGCGCTGAAAGCGGCGAACAACGCGGCGCCGAAAGCGCCGGTTAAACCGGCGGCGCCGACCGCGCCGCGTCCGCCGGTGCA GCCGCCGAAGAAAGCGTAA

A. 3.7. SEC-MALS analysis and Multi angle light scattering

A

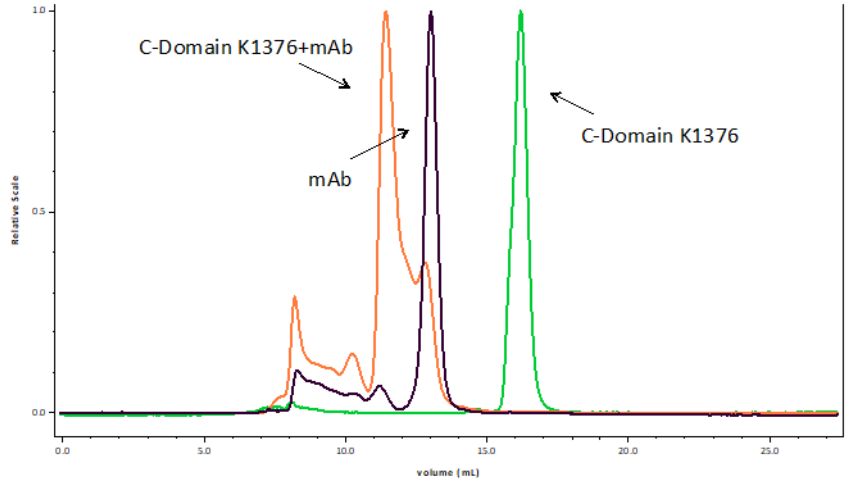

Peak	Mw (KDa)	Mass Fraction (%)
C-Domain K1376	18.92 ± 0.07	100.00
mAb	148.44 ± 0.20	100.00
C-Domain K1376+mAb	189.53 ± 0.21	67.10

B

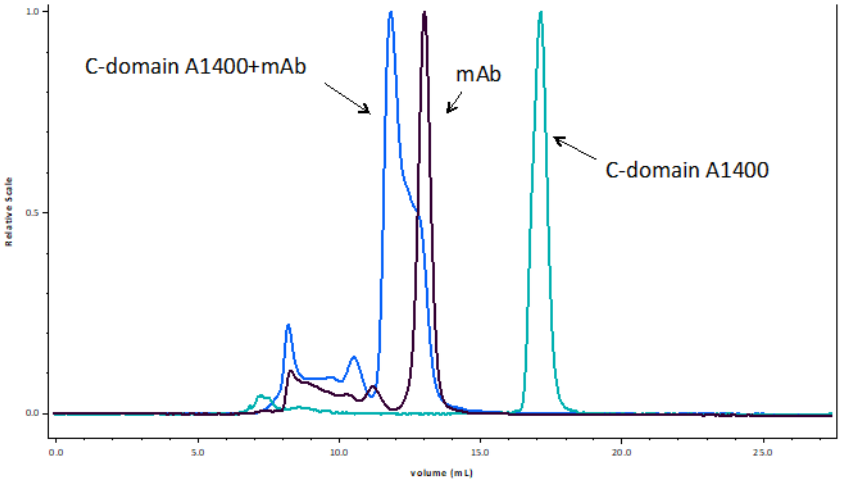

Peak	Mw (KDa)	Mass Fraction (%)
C-Domain A1376	15.79 ± 0.09	100.00
mAb	148.44 ± 0.20	100.00
C-Domain A1376+ mAb	179.44 ± 0.21	57.07

Appendices Figure A. CIII. 3.7_1. Analysis by MALS of samples containing Mab P1/MCA4 and the C-terminal domain constructs from P1. In each of the two samples containing the Mab P1/MCA4 and a construct of the C-terminal domain from P1 is clear the presence of a complex with molecular weight of ~179.4 and 189.5 kDa, for constructs A1400 (A) and K1376 (B), respectively.

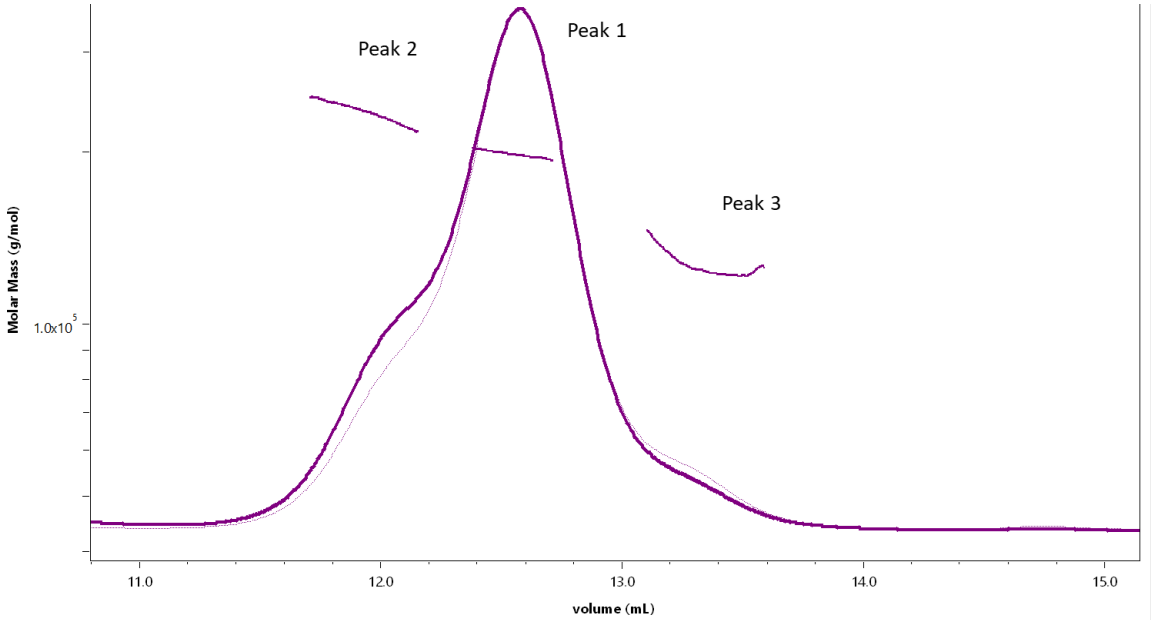

Peak	Mw (KDa)	Mass Fraction (%)
Peak 1	198.48±0.12	62.60
Peak 2	231.69±0.29	23.55
Peak 3	129.04±0.65	13.84

Appendices Figure A. CIII. 3.7_2. MALS analysis of a sample containing P1, P40/P90 and Fab(P1/MCA4). Analysis by MALS of a purified sample containing equimolecular amounts of P1, P40/P90 and the Fab(P1/MCA4), indicated the presence of a mixture of species, although none corresponding clearly to the ternary complex.

A. 3.8. Cryo-electron microscopy (Cryo-EM)

Appendices Table A. CIII. 3.8. Cryo-EM data collection of the P1-Fab and of the P1-P40/P90-(Fab) complexes and model refinement of the P1-Fab complex.

	P1-Fab	P40/P90-P1
PDB ID	8ROR	-
Data collection		
Microscope	CRYO ARM 300 (JEOL)	CRYO ARM 300 (JEOL)
Voltage (kV)	300	300
Detector	K3 direct (Gatan)	K3 direct (Gatan)
Data collection software	SerialEM	SerialEM
Energy Filter	Slit width of 20 eV	Slit width of 20 eV
Electron dose (e^-/ Å^2)/Frame	2.0	2.0
Pixel size (Å)	0.49	0.87
Defocus range (μm)	-0.5 to -1.5	-0.8 to -1.8
Frames	50	40
Movie number	27122	7983
Data processing		
Processing software	RELION-3.1	cryoSPARC2
Number of extracted particles	4312408	9565198
EMDB code	EMD-19402	EMD-19403
Map resolution (Å) at: FSC=0.143 (unmasked/masked)	2.39	<10
Refinement		
Software	PHENIX	
Models used (PDB code)	6RC9	
Atoms (Non-H)	14210	
Protein residues	1789	
Ligands	-	
Waters	269	
Bonds (r.m.s.d)		
Length (Å)	0.004	
Angles (o)	0.659	
B-factor (Å^2)	83.53	
MolProbity score	2.72	
Clashcore	27.36	
Rotamer outliers (%)	3.79	
Ramachandran plot		
Favored (%)	94.82	
Allowed (%)	5.07	
Disallowed (%)	0.11	
CC (volume)	0.83	
CC (mask)	0.83	

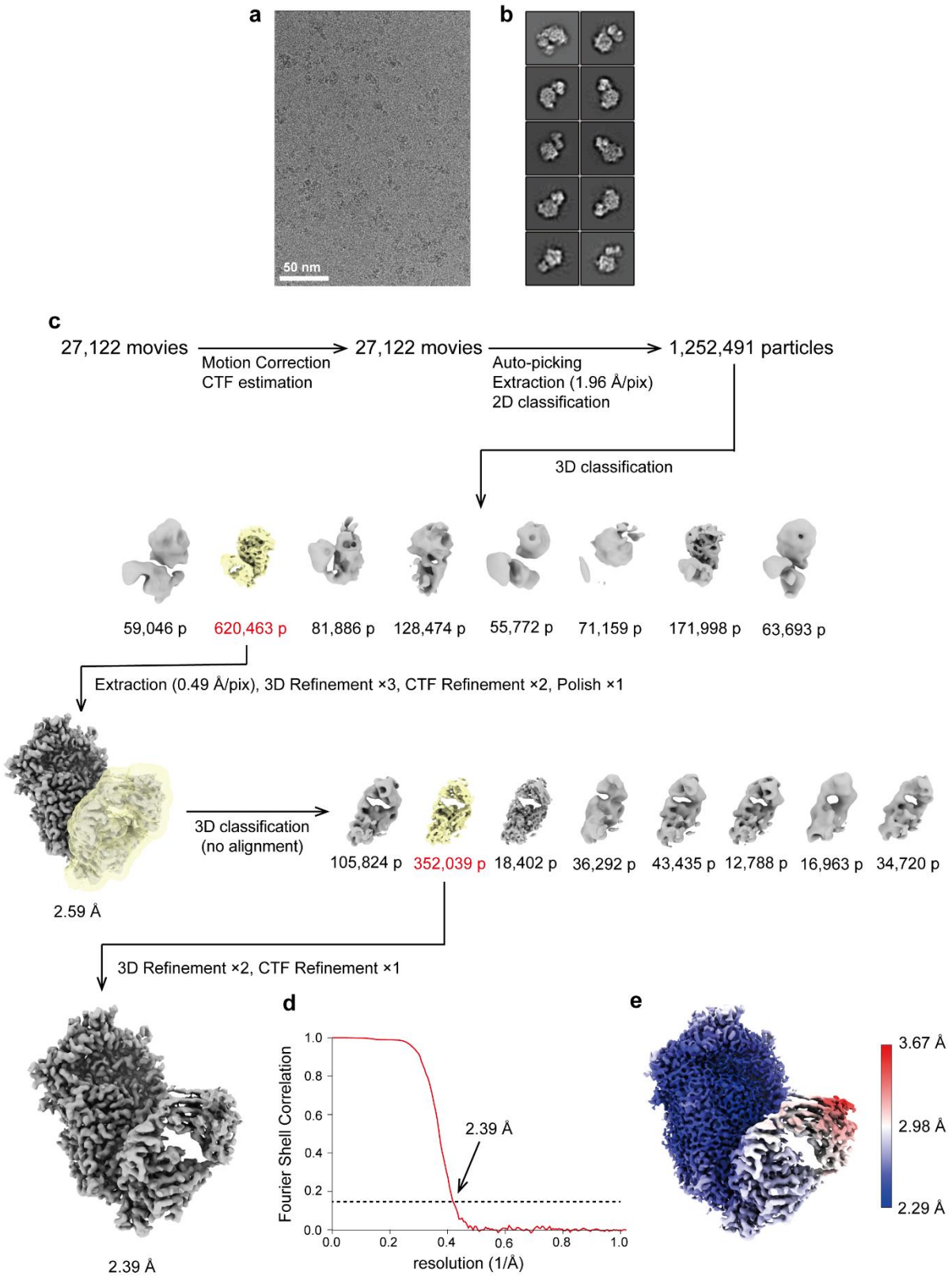

Appendices Figure A. CIII. 3.8_1. Cryo-EM structure determination of the P1-Fab(P1/MCA4) complex.

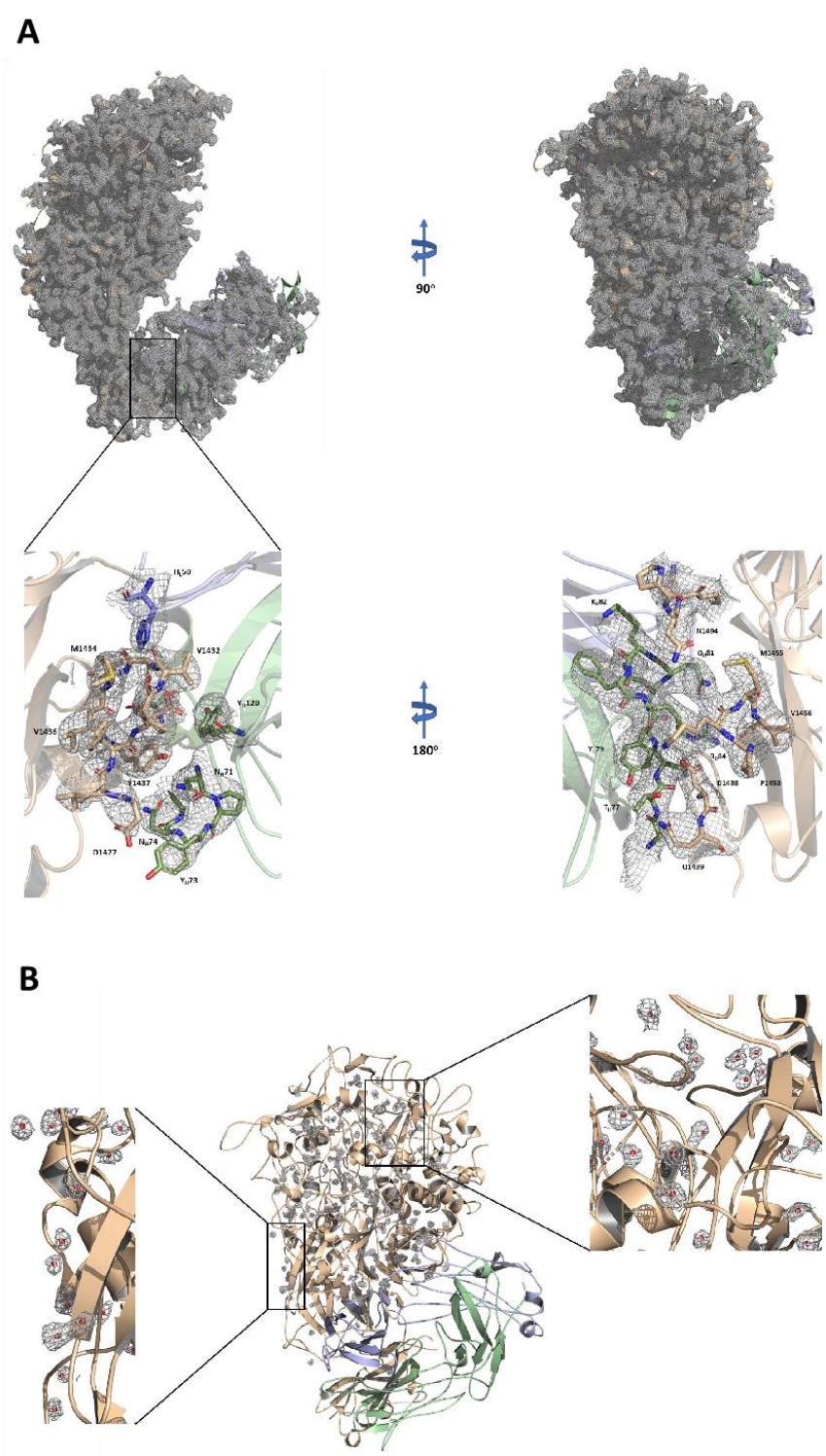

Appendices Figure A. CIII. 3.8_2. Map quality of the P1-Fab(P1/MCA4) complex: Identification of solvent molecules. A) Two 90° apart views of the whole Cryo-EM map of the P1-Fab(P1/MCA4) complex. The map is crispy, with well-defined side chains, for most of P1 and also for the Fab variable module (V_L-V_H). Inset shows the map at the epitope-paratope interface (same color code as in chapter IV). **B)** The quality of the map allowed the identification of a large number of solvent molecules in the N-terminal domain of P1.

A. 3.9. Monoclonal/polyclonal antibodies inhibition assays

Appendices Table A. CIII. 3.9. Monoclonal/polyclonal antibodies inhibition assays.

		Before AS				After AS						
PCA	**MCN replicate**	**Total**	**Non-Motile**	**Motile**	**%Motile Cells**	**Total**	**Non-Motile**	**Motile**	**%Motile Cells**	**RT_{50} (min)**	**Detached cells**	**% Detached cells**
P1	**1**	436	44	392	89,9	111	105	6	5,4	6,95	325	74,5
	2	225	22	203	90,2	73	73	0	0,0	3,99	152	67,6
	3	135	16	119	88,1	34	34	0	0,0	3,00	101	74,8
				Mean	**89,4**			**Mean**	**1,8**	**4,65**		**72,3**
				SE	**0,6**			**SE**	**1,8**	**1,19**		**2,4**
P40/P90	**1**	464	40	424	91,4	133	40	93	69,9	NA	331	71,3
	2	110	18	92	83,6	89	19	70	78,7	NA	21	19,1
				Mean	**87,5**			**Mean**	**74,3**			**45,2**
				SE	**3,9**			**SE**	**4,4**			**26,1**
P1N-ter	1	575	25	550	95,7	231	30	201	87,0	NA	344	59,8
	2	581	26	555	95,5	234	38	196	83,8	NA	347	59,7
				Mean	**95,6**			**Mean**	**85,4**			**59,8**
				SE	**0,1**			**SE**	**1,6**			**0,1**
Negative Control	**1**	242	21	221	91,3	123	21	102	82,9	NA	119	49,2
	2	110	10	100	90,9	60	13	47	78,3	NA	50	45,5
	3	302	38	264	87,4	121	40	81	66,9	NA	181	59,9
				Mean	**89,9**			**Mean**	**76,1**			**51,5**
				SE	**1,2**			**SE**	**4,8**			**4,3**

		Before AS				After AS				
PCA	**MCN replicate**	**Total**	**Non-Motile**	**Motile**	**%Motility**	**Total**	**Non-Motile**	**Motile**	**%Motility**	**RT_{50} (min)**
P1	**1**	175	5	170	97,1	172	172	0	0	3,40
	2	162	6	156	96,3	168	168	0	0	3,04
	3	415	11	404	97,3	408	338	70	17,2	5,38
	4	360	8	352	97,8	372	361	11	3,0	4,61
	5	527	20	507	96,2	424	424	0	0	4,08
	6	692	40	652	94,2	692	692	0	0	3,79
				Mean	**96,5**			**Mean**	**3,4**	**4,05**
				SE	**0,5**			**SE**	**2,8**	**0,35**
P40/P90	**1**	181	7	174	96,1	149	7	142	95,3	NA
	2	313	9	304	97,1	340	13	327	96,2	NA
	3	216	9	207	95,8	183	8	175	95,6	NA
				Mean	**96,4**			**Mean**	**95,7**	
				SE	**0,4**			**SE**	**0,3**	
P1N-ter	**1**	524	52	472	90,1	441	55	386	87,5	NA
	2	424	87	337	79,5	453	87	366	80,8	NA
	3	747	49	698	93,4	747	54	693	92,8	NA
	4	588	43	545	92,7	588	49	539	91,7	NA
				Mean	**88,9**			**Mean**	**88,2**	
				SE	**3,2**			**SE**	**2,7**	
Negative Control	**1**	117	6	111	94,9	114	6	108	94,7	NA
	2	230	8	222	96,5	257	12	245	95,3	NA
	3	176	6	170	96,6	177	6	171	96,6	NA
	4	124	4	120	96,8	125	4	121	96,8	NA
	5	417	18	399	95,7	418	16	402	96,2	NA
				Mean	**96,3**			**Mean**	**96,5**	
				SE	**0,3**			**SE**	**0,1**	

		Before AS				After AS				
MCA	**MCN replicate**	**Total**	**Non-Motile**	**Motile**	**%Motility**	**Total**	**Non-Motile**	**Motile**	**%Motility**	**RT_{50} (min)**
P1-MCA4	**1**	349	5	344	98,6	349	349	0	0	2,63
	2	184	6	178	96,7	168	168	0	0	2,18
	3	142	5	137	96,5	142	142	0	0	3,09
				Mean	**97,3**			**Mean**	**0**	**2,6**
				SE	**0,7**			**SE**	**0**	**0,26**

A. 4. Appendix of Chapter IV

A. 4.1. List of oligonucleotides used in Chapter IV

Appendices Table CIV. 4.1. List of oligonucleotides used in Chapter IV: Essential protein p116 extracts cholesterol and other indispensable lipids for *Mycoplasmas.*

Primer name	Sequence 5' → 3'	Use
Cloning of P116 different constructs for recombinant expression/purification		
P116-F30	AGGAGATATACCATGAACAAGACCCACCAGGTTGAG	To amplify P116 (30–957) construct gene
P116-F13	AGGAGATATACCATGGGCACCGTTGGCACCACCGCG	To amplify P116 (13-957) construct gene
P116-R957	GTGATGGTGATGTTTACCCAGACGGTCAACGGTGATTTG	To amplify P116 (30–957 and 13-957) constructs gene
P116-F212	AGGAGATATACCATGGGTGTTGATGTGTTCGAG	To amplify P116 (212–845) construct gene
P116-R845	GTGATGGTGATGTTTGCTGATGTCCAGCTCCAG	To amplify P116 (212–845) construct gene
P116-FW681A	TTCCCGGGTTATGGTGCGGCGAAGGGTGTTGTG	To generate P116 W681A variant
P116-RW681A	CACAACACCCTTCGCCGCACCATAACCCGGGAA	To generate P116 W681A variant

A. 4.2. Synthetic DNA

Appendices Table A. CIV. 4.2. Synthetic DNA for P116. Start and stop codons of the full-length *mpn213* (P116 gene) are highlighted in green.

Synthetic clone for *M. pneumoniae* P116
ATGAAACTGAGCGCGATTATTAGCCTGAGCGTTGCGGGCACCGTTGGCACCACCGCGGTTGTTGTTCCGACCACCATTACCCTGGTTAACAAGACCCACCAGGTTGAGCACGAAAGCGAGCA GAGCGACTTTCAAGATATTCGTTTCGGTCTGAACAGCGTGAAGCTGCCGAAAGCGCAGCCGGCTGCGGCGACCCGTATCACCGTTGAGAACGGCACCGATAAGCTGGTGAACTACAAAAGCA GCCCGCAGCAACTGTTCCTGGCGAAAAACGCGCTGAAGGACAAACTGCAGGGCGAGTTTGACAAGTTCCTGAGCGATGCGAAAGCGTTTCCGGCGCTGACCGCGGACCTGCAGGAATGGGT TGATCAGCAACTGTTCAACCCGAACCAGAGCTTCTTCGACCTGAGCGCGCCGCGTAGCAACTTTACCCTGAGCAGCGACAAGAAAGCGAGCCTGGATTTCATTTTTCGTTTCACCAACTTCACC GAGAGCGTTCAACTGCTGAAGCTGCCGGAAGGCGTGAGCGTGGTTGTGGACAGCAAACAGAGCTTTGATTACTATGTTAACGCGAGCGCGCAAAAGCTGCTGGTGCTGCCGCTGAGCCTGC CGGACTACACCCTGGGTCTGAACTATATGTTCGATCACATCACCCTGAACGGCAAGGTTGTGAACAAATTTAGCTTCAACCCGTTTAAAACCAACCTGAACCTGGCGTTCAGCAACGTTTATAA CGGTGTTGATGTGTTCGAGGCGCAGAAGAACCTGGTTGGCAAGGGCAAATACCTGAACACCCACGTGAAAGCGGAAGACGTTAAGAAAGATGTGAACGCGAACATCAAGAACCAGTTTGAC ATTGCGAAAATCATTGCGGAGCTGATGGGCAAGGCGCTGAAAGAATTTGGTAACCAGCAAGAGGGCCAACCGCTGAGCTTCCTGAAGGTTATGGACAAGGTGAAAGAAGATTTTGAGAAAC TGTTCAACCTGGTTCGTCCGGGTCTGGGCAAGTTCGTGAAGGACCTGATCCAGAGCAGCAGCCAAGCGGAAAACAAGATCACCGTGTACAAACTGATCTTCGACAACAAGAAAACCATCCTG AACCTGCTGAAGGAACTGAGCATTCCGGAGCTGAACAGCAGCCTGGGTCTGGTTGACGTGCTGTTCGATGGTATCACCGACAGCGATGGCCTGTATGAGCGTCTGCAGAGCTTTAAGGACCT GATTGTTCCGGCGGTGAAGACCAACGAAAAAACCGCGGCGCTGAGCCCGCTGATTGAGGAACTGCTGACCCAGAAAGACACCTACGTTTTCGATCTGATCCAAAAGCACAAAGGTATTCTGA CCAACCTGCTGAAGAACTTTCTGGCGGACTTCCAGAAAAGCACCCCGTTTATGGCGGATCAAGTGGCGATCTTTACCGAACTGTTCGACAACGAGGGTGCGTTTGACCTGTTCGGCGAGGCG GACTTTGTTGATAAAATCGCGGAACTGTTCCTGACCAAGCGTACCGTGAAAAACGGCGAAAAGATTGAAACCAAAGACAGCCTGCTGGTTACCAGCCTGAAGAGCCTGCTGGGCGAGAAAG TTGCGGCGCTGGGCGACCTGCTGGATAGCTATATCTTCAAGAACGAACTGCTGAACCGTAGCGTTGAAGTGGCGAAAGCGGAGGCGAAGGACACCAAAGGTGCGACCGATTACAAGAAAG AGCAGGCGAAGGCGCTGAAGAAACTGTTCAAACACATCGGCGAAAACACCCTGAGCAAGACCAACCTGGATAAAATTACCCTGAAAGAGGTGAAAAACACCGAAAACGTGGAGCTGGAGG AAACCGAAACCACCCTGAAGGTGAAGAAACTGGACGTTGAATATAAAGTGGAGCTGGGTAACTTTGAGATCAAGAACGGCCTGATTAAAGCGATGCTGGAGTTCCTGCCGGACACCAAGGA TCTGGAAACCACCCTGGATAAGCTGCTGTTCAAAGGCGAGAGCTACAAGGCGATGAAGGACAAGTACATCAAAGAAGGCTTCCCGGGTTATGGTTGGGCGAAGGGTGTTGTGCCGGGTGCG TTTGAAAGCATCGAGAACACCTTCAAAAGCGCGATCGATAAGACCAAAAGCATTCGTGACCTGTTTGGTGATATGCTGTTCGGCAACGACCTGAGCAGCGTTAAGGAAACCGATAGCTTTATC ACCCTGGGTGGCAGCTTCGACATTAAATATGGTGGCGAGAACCTGAACGTTCTGCCGGCGTACTATAGCCTGATCAACAGCGAAATTGGTTACCAGATCATTGGCGTGGACACCACCATTGAT GCGACCAAGGTTAAAGTGGAACTGAAGAACAAAGAGTATAAGGGTAAAAGCCCGGCGATCAACGGCCAGGTTAAACTGAGCCAGAGCTTCTTCAACGTGTGGACCAACATGTTCGACAGCA TCACCAAGCAGATTTTTCAAAAGAAATACGAGTTCAAGGACAACATTCAAGTGTTTGCGCGTAACGAAGATAACACCAGCCGTCTGGAGCTGGACATCAGCGATCCGGAACAGCGTGTTATTC CGTTTGCGTTCGTGGACGGTTTCGGCATCCAACTGAAGGCGGTTGATAAAAACATTACCAAGGAAGCGGGTAACACCGAGCCGAAGAGCCCGGTGATCCAGCTGTATGAAGCGCTGAACAA GGAGAAAGACCAAAAACAGCAAAGCAAGCAGAGCCCGAAACAACTGGATACCAAGACCCAGCTGGGTTACCTGCTGAAACTGGGCGACAACTGGAGCAAGGACGATTATAAAAGCCTGAT TGACGATACCATCATTAACAACAACTACCTGGAGGCGAGCTTCAACAGCAAAATCACCGTTGACCGTCTGGGTATCCCGATTGATCTGTGGCTGTTTAAAATCTGGCCGAAATTCAACCTGGAA ATTCCGATGCAGGGTAGCCTGCAACTGTACAGCAGCAGCGTGATCTTCCCGTACGGCATTTATGACACCAGCGTTCAGGATGCGGCGAAGATCGTGAAACGTCTGAACTTTACCGACATGGGT TTTAAGCTGAACGATCCGAAGCCGAACTTTTGGTTTGTTGGTTTCTAA

A. 4.3. P116 Single-particle Cryo-EM, model building and refinement

Appendices Table A. CIV. 4.3. Cryo-EM data collection, refinement and validation statistics. Adapted from **Sprankel L. *et al.*, 2023**.

	P116 (EMD-15274)	P116 empty (EMD-15275)	P116 refilled (EMD-15276)	P116+HDL (EMD-15277)
Data collection and processing				
Microscope	FEI Titan Krios	FEI Titan Krios	FEI Titan Krios	FEI Titan Krios
Detector	Gatan K2 Summit	Gatan K3 Summit	Gatan K2 Summit	Gatan K2 Summit
Acquisition Software	SerialEM 3.8	EPU 2.12	SerialEM 3.8	SerialEM 3.8
Magnification	×130,000	×105,000	×130,000	×130,000
Voltage (kV)	300	300	300	300
Electron exposure ($e^-/Å^2$)	50	50	50	50
Defocus range (μm)	−1 to −3.5	−1 to −3.5	−1 to −3.5	−1 to −3.5
Pixel size (Å)	1.05	0.831	1.05	1.05
Symmetry imposed	C_1	C_1	C_1	C_1
Initial particle images	3,463,490	4,532,601	2,930,863	262,981
Final particle images	1,315,362	633,322	1,311,526	46,277
Map Resolution (Å)	3.3	4	3.5	8.6
FSC threshold	0.143	0.143	0.143	0.143
Map resolution range (Å)	2.5–5	3.5–6	3–7	7–12
Number of frames	34	50	29	30
Micrographs used	4,367	15,299	4,019	3,114
Processing software	cryoSPARC v3.3.2	cryoSPARC v3.3.2	cryoSPARC v3.3.2	cryoSPARC v3.3.2
Motion correction	cryoSPARC v3.3.2	cryoSPARC v3.3.2	cryoSPARC v3.3.2	cryoSPARC v3.3.2
CTF estimation	cryoSPARC v3.3.2	cryoSPARC v3.3.2	cryoSPARC v3.3.2	cryoSPARC v3.3.2
Particle images after 2D classification	1,324,330	1,140,275	1,311,526	46,277
Map sharpening B factor	−117	−105	−131	−490

Refinement	P116 (PDB 8A9A)	P116 empty (PDB 8A9B)
Initial model used (PDB code)	/	8A9A
Model resolution (Å)	3.3	4
FSC threshold	0.143	0.143
Model resolution range (Å)	2.5–5.0	3.5–6.0
Map sharpening *B* factor ($Å^2$)	−94	−105
Model composition		
Non-hydrogen atoms	12,772	6,386
Protein residues	1,618	809
Ligands	0	0
B factors ($Å^2$)		
Protein	51.22	35.30
Ligand	0	
R.m.s. deviations		
Bond lengths (Å)	0.003	0.027
Bond angles (°)	0.651	1.197
Validation		
MolProbity score	2.18	2.52
Clashscore	12	20
Poor rotamers (%)	0.14	0.71
Ramachandran plot		
Favored (%)	89.34	84
Allowed (%)	10.53	15
Disallowed (%)	0.13	1

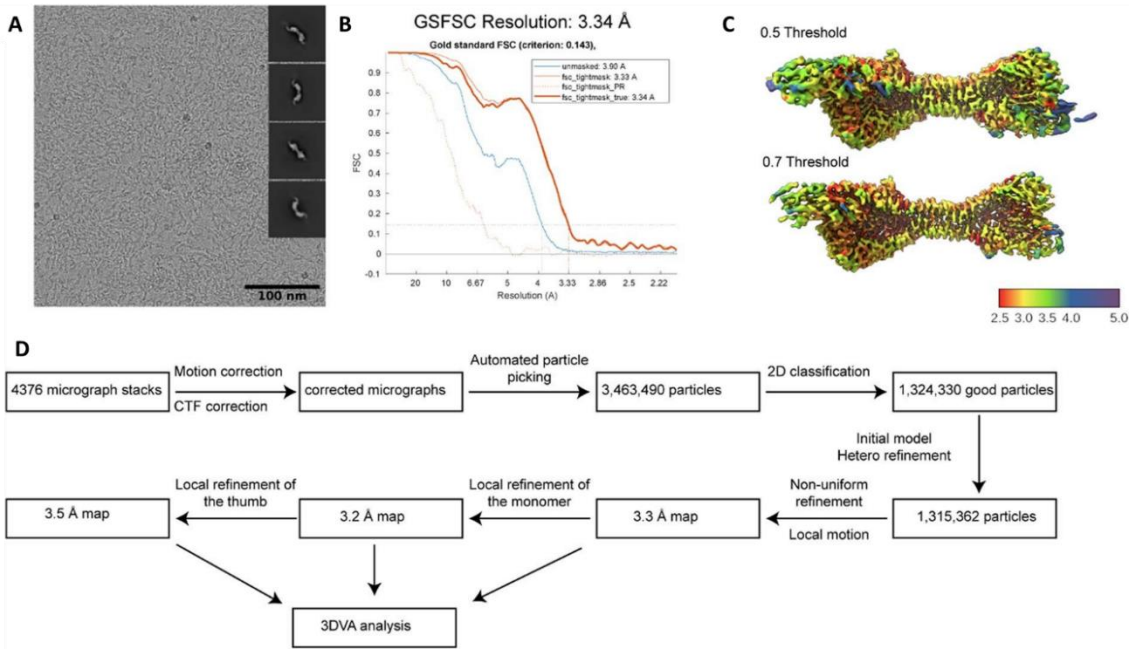

Appendices Figure A. CIV. 4.3_1. Overview of Cryo-EM processing of P116. A) Representative Micrograph and obtained 2D classes used for template picking. **B)** Fourier shell correlation of P116 reports a final resolution of 3.3 Å according to the 0.143 cut-off criteria. **C)** Local resolution map at different thresholds of the Cryo-EM density map (C1 symmetry) of P116 ranging from 2.5 to 5 Å. (**d**) Schematic processing overview for the P116 construct. The processing for P116 empty, P116 refilled and P116 + HDL was carried out in a similar manner. Adapted from **Sprankel L. *et al.*, 2023**.

A. 4.4. HDL isolation and determination of cholesterol transfer rate

Appendices Table A. CIV. 4.4. Relative level of ApoAI in both HDL in the radioactive assay and P116 after incubating with HDL. Adapted from **Sprankel L. *et al.*, 2023**.

	ApoAI (mg/mL)
HDL	
Free cholesterol-radiolabeled form	0.2272
Esterified cholesterol-radiolabeled form	0.2272
P116 after incubating with HDL	
Empty	0.00
Refilled	0.00

A. 4.5. Adhesion and motility inhibition assay

Appendices Table A. CIV. 4.5. Adhesion and motility inhibition assay. Number of cell detachments and motility status in microcinematography (MCN) replicates of *M. pneumoniae* cells before and after adding polyclonal antibodies (PCA) vs P1 and P116. A negative control was performed by incubating cells in the same medium (PBS - 10% FBS) but no antibodies were added. Mean, standard deviation (SD) and standard error (SE) were computed from the frequencies of detached cells in each replicate. Adapted from **Sprankel L. *et al.*, 2023**.

		Before AS (nº Cells)				After AS (nº Cells)					
PCA	MCN replicate	Total	Non-Motile	Motile	% Motility	Total	Non-Motile	Motile	% Motility	Detached Cells	% Detached Cells
P1	**1**	46	5	41	89,1	15	11	4	26,7	37	90,2
	2	20	1	19	95,0	4	4	0	0,0	19	100,0
	3	131	3	128	97,7	31	24	7	22,6	121	94,5
	4	15	0	15	100,0	9	9	0	0,0	15	100,0
	5	397	9	388	97,7	122	89	33	27,0	355	91,5
				Mean	**95,9**			**Mean**	**15,3**	**Mean**	**95,1**
				SD	**4,2**			**SD**	**14,0**	**SD**	**4,6**
				SE	**1,9**			**SE**	**6,3**	**SE**	**2,1**
P116	**1**	170	5	165	97,1	112	7	105	93,8	60	36,4
	2	79	7	72	91,1	45	8	37	82,2	35	48,6
	3	51	5	46	90,2	35	5	30	85,7	16	34,8
	4	42	5	37	88,1	30	6	24	80,0	13	35,1
	6	61	4	57	93,4	31	4	27	87,1	30	52,6
				Mean	**91,9**			**Mean**	**85,8**		
				SD	**3,4**			**SD**	**5,3**	**Mean**	**40,2**
				SE	**1,5**			**SE**	**2,4**	**SD**	**8,5**
										SE	**3,8**
Negative Control	**1**	29	4	25	86,2	12	4	8	66,7	17	68,0
	2	49	2	47	95,9	31	5	26	83,9	21	44,7
	3	32	4	28	87,5	17	4	13	76,5	15	53,6
				Mean	**89,9**			**Mean**	**75,7**	**Mean**	**53,8**
				SD	**5,3**			**SD**	**8,6**	**SD**	**11,8**
				SE	**3,0**			**SE**	**5,0**	**SE**	**6,8**

A. 5. Appendix of Chapter V

A. 5.1. List of oligonucleotides used in Chapter V

Appendices Table A. CV. 5.1. List of oligonucleotides used in Chapter V: Heterologous expression of *mycoplasma pneumoniae* major adhesins in the close related species *Mycoplasma genitalium.*

Primer name	Sequence 5' → 3'[a]	Use
Construction of mutants of *M. genitalium*		
Doble adhesins null mutant		
MgPaBEFwl	ATCATTACCATTATCAATG	Cloning: Build pBEΔAdh
MgPaBERevl	GGATCCATGCACCTCTCGAGACAAACTTAATTATAAACAAT	
MgPaBDFwl	CTCGAGAGGTGCATGGATCCTAGTTTTTAACCTTTCAATAAC	
MgPaBDRevl	CTACTATTGCTAGGTTTCAC	
Lox71p438Fwd (*Xho*I)	CTCGAGTACCGTTCGTATAATGTATGCTATACGAAGTTATTAGTATTTAGAATTAATAAAGT	
CatLox66Rev (*Bam*HI)	GGATCCTACCGTTCGTATAGCATACATTATACGAAGTTATTTACGCCCCGCCCTGCCACT	
Complementation of the null mutant with *Mge* adhesins		
COMmg191-F (*Apa*I)	AGTGGGCCCACTAACAAAAAACAAATTAGTGATG	Cloning: Build pMTnPacCOM (MG_191/MG_192)
COMmg191/192-R (*Sal*I)	AGTGTCGACATCCACTCTCTAAATTGCAAGTTTAG	
Complementation of the null mutant with *Mpn* adhesins		
COMmpn141-F (*Not*I)	AGTGCGGCCGCACTAACAAAAAACAAATTAGTGATGTTGTTAGTGATTGTGTGAAAAAAATTGTTTATAATTAAGTTTGTATGCACCAAACCAAAAAAACTGCCTTG	Cloning: Build pMTnPacCOM (MPN_141/MPN_142)
COMmpn142-R (*Xba*I)	AGTTCTAGATTAAGCCTTTTTAGGTGGTTGG	
Complementation of the null mutant with *Mpn* adhesins with P40/P90 double cleavage site substitution		
MPN142MutDobleP.Tall-R	TTCACTGCTATTGCCGGAGGAAAGGGGGCCAGCAACCAC CGTGACGGAGGACTGTGACGTTGCGGT	Cloning: Build pMTnPacCOM (MPN_141/MPN_142 CS Mutation)
MPN142MutDobleP.Tall-F	ACCGCAACGTCACAGTCCTCCGTCACGGTGGTTGCTGGCC CCCTTTCCTCCGGCAATAGCAGTGAA	
Complementation of the null mutant with *Mpn* adhesins with complete P40/P90 SII deletion		
Del.SII_P40/P90-R	CCCCGGAACAATCACCCCCATCT	Cloning: Build pMTnPacCOM (MPN_141/MPN_142 SII Deletion)
Del.SII_P40/P90-F (5' Phos)	*GATGCCCTACCGAATGTCATCAC	
Oligonucleotides used in sequencing and screening reactions		
SCRMgPaFw	GTCTGTTTGCCATCTATGACA	To screen for MG_191/MG_192 null mutants
SCRMgPaRev	GAGCCACCTGAAGTGACTT	
SCRCre-F	ACTGCAGATCAATGTGCTAG	
SCRCre-R	CGCTTTTGTTGTTTGAGTC	
Cm-Up	CAACGGTGGTATATCCAG	
Cm-Dw	CAGTACTGCGATGAGTGGCA	
SCRMutP.TallMPN142-R	GAGCTCGGTTTTCGCTCATC	To screen for mutations in MPN_141/MPN_142

Mpn142-F	ATGAAATCGAAGCTAAAGTTAAAAC	To screen for MPN_141/MPN_142 SII Deletion
Pac-Up	GTAGCTAATCTAACAGTAGG	To sequence DNA inserts cloned in a miniTnPac
Pac-Dw	GTCCTAGAACTTGGTGTATG	To determine miniTnPac Tnp insertion point
COMmg191-R (*Sal*I)	AGTGTCGACTTATTGTTTTACTGGAGGTTT	To sequence DNA inserts cloned in a miniTnPac
Fup17	GTAAAACGACGGCCAGT	Universal Forward primer
Rup17	GGAAACAGCTATGACCATG	Universal Reverse primer

[a] Restriction sites of the primers are underlined.

A. 5.2. Plasmid construction and generation of mutants

Appendices Table A. CV. 5.2_1. List of plasmids used to create the strains used in Chapter V: Heterologous expression of *mycoplasma pneumoniae* major adhesins in the close related species *Mycoplasma genitalium.*

Plasmid name	Aim	Source
pBE	pBE derivative vector used in the cloning procedures	Pich O. Q. *et al.*, 2006b
pMTnPac	Minitransposon bearing the puromycin resistance gene	Torres-Puig S. *et al.*, 2018
pΔAdh (pΔMG_191/MG_192)	Suicide vector pBE derivative used to create the *Mge* MG_191/MG_192 defective mutant. Selectable marker: chloramphenicol flanked with *lox* sequences	This work
pBE-COMP110P140-WT (pBE-*Mge*Adh)	Intermediate pBE derivative vector used in the cloning process. Also used as a template to obtain	This work

	P110 and P140 gene variants for the other clonings	
pBE-COMP1P40/P90-WT (pBE-*Mpn*Adh)	Intermediate pBE derivative vector used in the cloning process. Also used as a template to obtain P1 (MPN141) and P40/P90 (MPN142) gene variants for the other clonings	This work
pMTnPac*Mge*Adh (pMTnPac-P110P140-WT)	To complement P110 (MG_192) and P140 (MG_191) genes. Also used as a template to obtain P110 and P140 gene variants for other clonings	This work
pMTnPac*Mpn*Adh (pMTnPac-P1P40/P90-WT)	To complement P40/P90 (MPN142) and P1 (MPN141) genes. Also used as a template to obtain P40/P90 and P1 gene variants for other clonings	This work
pMTnPac*Mpn*Adh-CS	To complement P40/P90 (MPN142) and P1 (MPN141) genes bearing P40/P90: R445S-A446S-R455S-A456S substitutions	This work
pMTnPac*Mpn*Adh-ΔSII	To complement P40/P90 (MPN142) and P1 (MPN141) genes bearing a P40/P90 L395-T414 (SII) deletion	This work

Appendices Table A. CV. 5.2_2. Insertion points of the pMTnPac*Mge*Adh and pMTnPac*Mpn*Adh variants in the chromosome of G37ΔAdh derivatives.

Strain	Disrupted gene or genome region	Insertion point*	Orientation#
G37ΔAdh::COM (*Mge*^{Mge})-C1	Middle MG_RS01600	327226	se
G37ΔAdh::COM (*Mge*^{Mge})-C2	MG_497-MG_261 (Intergenic region)	315411	se
G37ΔAdh::COM (*Mge*^{Mge})-C3	MG_310	386708	as

G37ΔAdh::MPN (*Mge*^{Mpn})-C1	MG_281	343662	se
G37ΔAdh::MPN (*Mge*^{Mpn})-C2	MG_032	37490	as
G37ΔAdh::MPN (*Mge*^{Mpn})-C3	MG_213	253947	as
G37ΔAdh::MPN-CS (*Mge*$^{Mpn-CS}$)-C1	MG_210-MG_480 (Intergenic region)	249996	as
G37ΔAdh::MPN-CS (*Mge*$^{Mpn-CS}$)-C2	MG_192.1	229190	se
G37ΔAdh::MPN-CS (*Mge*$^{Mpn-CS}$)-C3	MgPar7	252667	as
G37ΔAdh::MPN ΔSII (*Mge*^{MpnΔSII})-C1	MG_32-MG_033 (Intergenic region)	39033	as
G37ΔAdh::MPN ΔSII (*Mge*^{MpnΔSII})-C2	MG_067	82408	as
G37ΔAdh::MPN ΔSII (*Mge*^{MpnΔSII})-C3	MG_110	137821	as

*Coordinates of the G37 genome corresponding to the transposon insertion point determined by sequencing with the Pac-Up and Pac-Dw primers.

[#]as, transposon insertion in antisense orientation with respect to the disrupted gene; se, transposon insertion in sense orientation with respect to the disrupted gene.

Mutants highlighted in bold were taken as reference in the Wester blot analysis.

A. 5.2.1. Construction of pBE-COMP1P40/P90-WT (pBE-*Mpn*Adh), pMTnPac*Mpn*Adh and generation of *Mge*^{Mpn} mutant strain

MPN141 and MPN142 genes from the chromosome of *M. pneumoniae* 129 strain were amplified by PCR using COMmpn141-F (*Not*I) and COMmpn142-R (*Xba*I) primers (**Appendices Table A. CV. 5.1**). The resulting PCR product was cloned into an *Eco*RV-digested pBE plasmid to create the pBE-COMP1P40/P90-WT (pBE-*Mpn*Adh) (**Appendices Table A. CV. 5.2 and Figure A. CV. 5.2.1_1**). At the same time, the amplicon was digested with the *Not*I and *Xba*I restriction enzymes and ligated to a similarly digested pMTnPac plasmid[534] [**Torres-Puig S. *et al.*, 2018**] to create the pMTnPac-P1P40/P90-WT (pMTnPac*Mpn*Adh) (**Appendices Table A. CV. 5.2 and Figure A. CV. 5.2.1_2**). This plasmid was used to reintroduce the wild-type alleles of the MPN141 and MPN142 genes to the G37ΔAdh mutant. The COMmpn141-F (*Not*I) primer also includes the upstream region (70 nucleotides) of the endogenous MG_191 gene, which contains a strong promoter identified in a previous study[574] [**Musatovova O. *et al.*, 2003**]. This promoter was used to drive the transcription of the transposon-encoded copy of the MPN141 and MPN142 genes in all mutants.

Sequencing analysis of the pMTnPac-P1P40/P90-WT construct using primers Tnp3, Mpn142-F, COMmpn141-F (*Not*I), and Pac-Dw, ruled out the presence of additional mutations in the MPN141 and MPN142 sequences. This plasmid was transformed into the *M. genitalium*

G37ΔAdh null mutant (this work) to create the the *Mge*^{Mpn} complemented mutant strain (G37ΔAdh::MPN).. Identification of the minitransposon insertion site in the individual clones was done by sequencing using the Pac-Up primer and chromosomal DNA as a template.

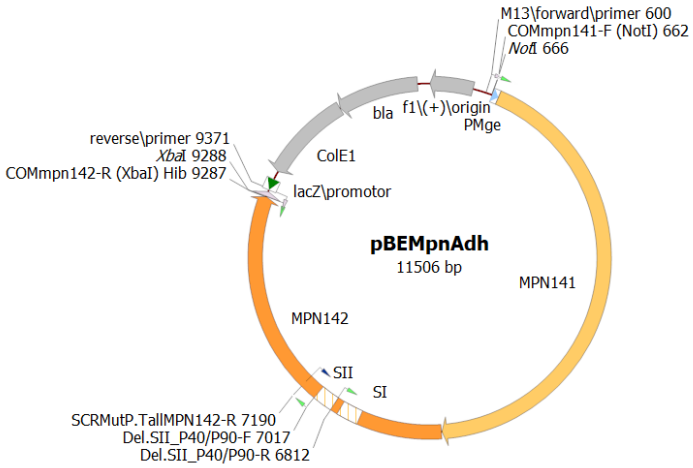

Appendices Figure A. CV. 5.2.1_1. pBE-COMP1P40/P90-WT (pBE-*Mpn*Adh) plasmid map. Oligonucleotides used for cloning are drawn as little green arrows; MPN141, P1 gene sequence; MPN142, P40/P90 gene sequence; P*Mge*, *M. genitalium* MG_191 own promoter; *bla*, β-lactamase; lacZ/promotor, *lacZ* gene promoter; SI, insertion I; SII, insertion II.

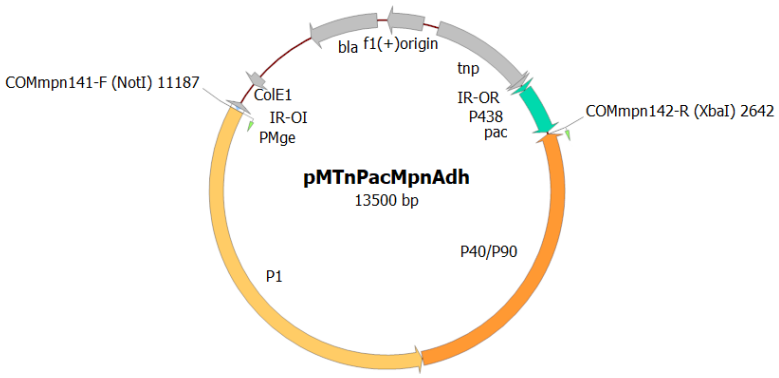

Appendices Figure A. CV. 5.2.1_2. pMTnPac-P1P40/P90-WT (pMTnPac*Mpn*Adh) plasmid map. Oligonucleotides used for cloning are drawn as little green arrows; P1, MPN141 gene sequence; P40/P90, MPN142 gene sequence; P*Mge*, *M. genitalium* MG_191 own promoter; *bla*, β-lactamase; IR, inverted repeat; P438, MG_438 promoter; *pac*, puromycin acetyl transferase marker; tnp, transposase.

A. 5.2.2. Construction of pMTnPac-*Mpn*Adh mutant variants and generation of *Mge*$^{Mpn\text{-}CS}$ and *Mge*$^{Mpn\text{-}\Delta SII}$ mutant strains

To generate P40/P90 variants carrying specific mutations in the cleavage site (CS) and insertion II (SII) region, the target mutations in the MPN142 gene were introduced also by ExSite-PCR using the pBE-COMP1P40/P90-WT as a template and the specific primers for each mutant (**Appendices Table A. CV. 5.1**). Then, plasmids containing the P1 and P40/P90 alleles with the desired mutations were re-ligated and mutant P1 and P40/P90 alleles excised by digestion with *Not*I and *Xba*I restriction enzymes. Finally, DNA fragments with mutant alleles were ligated into a pMTnPac plasmid previously digested with *Not*I and *Xba*I, to generate the corresponding pMTnPac-P1P40/P90 (pTnPac*Mpn*Adh) plasmid series (**Appendices Figure A. CV. 5.2.2**).

Sequencing analysis of the different pMTnPacCOMP140P110 constructs using primers Tnp3, Mpn142-F, SCRMutP.TallMPN142-R, COMmpn141-F (*Not*I), and Pac-Dw, ruled out the presence of additional mutations in the MPN141 and MPN142 sequences. These plasmids were transformed into the *M. genitalium* G37ΔAdh null mutant (this work) to create the two P40/P90 strains *Mge*$^{Mpn\text{-}CS}$ (**Appendices Figure A. CV. 5.2.2**) and *Mge*$^{Mpn\text{-}\Delta SII}$ (insertions regions exemplified in **Appendices Figure A. CV. 5.2.1_1**). Identification of the minitransposon insertion site in the individual clones was done by sequencing using the Pac-Up primer and chromosomal DNA as a template.

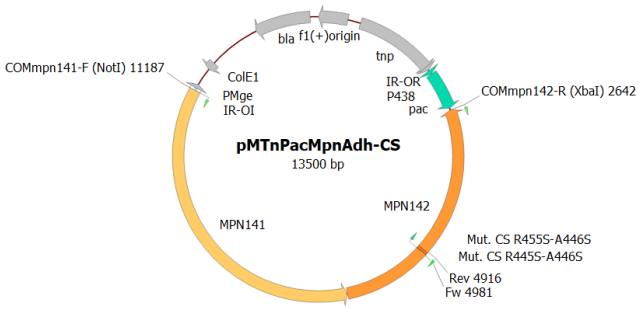

Appendices Figure A. CV. 5.2.2. pMTnPac-P1P40/P90-CS (pMTnPac*Mpn*Adh-CS) plasmid map. Exemplification of one of the two **pMTnPac-P1P40/P90** mutations plasmid created. Oligonucleotides used for cloning are drawn as little green arrows; MPN141, P1 gene sequence; MPN142, P40/P90 gene sequence; P*Mge*, *M. genitalium* MG_191 own promoter; *bla*, β-lactamase; IR, inverted repeat; P438, MG_438 promoter; *pac*, puromycin acetyl transferase marker; tnp, transposase.

A. 5.3. Results compilation of the cytadherence capacity of *M. genitalium* strains analysed in Chapter V

Appendices Table A. CV. 5.3. Summary table with the K_d, B_{max} values and other characteristics of all mutant strains analysed in Chapter V.

Strain	K_d values ± SE	B_{max} values ± SE	Affected HA parameter (vs WT-*Mge*)	Affected HA parameter (vs WT-*Mpn*)	Flask-Adherent	Adhesins expression levels[a]
G37 (WT-*Mge*)	$1.2x10^3 \pm 2.6\ x10^2$	0.86±0.05	-	↑ B_{max}	Yes	4
MPN129 (WT-*Mpn*)	$1.0x10^3 \pm 1\ x10^3$	0.24±0.06	↓ B_{max}	-	Yes	4
G37ΔAdh::COM	$1.5x10^3 \pm 2.8\ x10^2$	0.90±0.04	-	↑ B_{max}	Yes	4
G37ΔAdh::MPN	$1.6x104 \pm 3.2\ x10^3$	0.95±0.10	↑ K_d, ↑ B_{max}	↑ K_d, ↑ B_{max}	Yes	4

[a] Illustrative value scale from 0 (without adhesins) to 4 (WT).

A. 5.4. Clustal-O multiple sequence alignments

```
P40/P90 (MPN142)    ---MKSKLKLKRYLLFLPLLPLGTLSLANTYLLQ-DHNTLTPYTPFTTPLNGG-LDVVRA    55
   P110 (MG192)     MKTMRKQIYKKAYWLLLPFLPL---ALANTFLVKEDSKNVTAYTPFATPITDSKSDLVSL    57
                       *:.::  * * *:**:***   :****:*:: * :.:* ****:**:...  *:*

P40/P90 (MPN142)    AHLHPSYELVDWKRVGDTKLVALVRSALVRVKFQDTTSSDQSNTNQNALSFDTQESQKAL    115
   P110 (MG192)     AQLDSSYQIADQT-IHNTNLFVLFKSRDVKVKYESSGS--------NNISFDST------    102
                    *:*. **::.* . : :*:*..*.:*  *:**::.: *        * :***:

P40/P90 (MPN142)    NGSQSGSSDTSGSNSQDFASYVLIFKAA--PRATWVFERKIKLALPYVKQESQGSGDQGS    173
   P110 (MG192)     ------------SQGEKPSYVVEFTNSTNIGIKWTMVKKYQLDVPNVS-----------    138
                             .. :  ***: *. :     .*.: :* :* :* *.

P40/P90 (MPN142)    NGKGSLYKTLQDLLVEQPVTPYTPNAGLARVNGVAQDTVHFGSGQESSWNSQRSQKGLKN    233
   P110 (MG192)     ---SDMNQVLKNLILEQPLTKYTLNSSLAKEKGKTQREVHLGSGQANQWTSQRNQHDLNN    195
                       ..: :.*::*::***:* ** *:.**: :* :*  **:**** ..*.***.*:.*:*

P40/P90 (MPN142)    NPGPKAVTGFKLDKGRAYRKLNESWPVYEPLDSTKEGKGKDESSWKNSEKTTAENDAPLV    293
   P110 (MG192)     NPSPNASTGFKLTTGNAYRKLSESWPIYEPIDGTKQGKGKDSSGWSSTEENEAKNDAPSV    255
                    **.*:* ***** .*.*****.****:***:*.**:*****.*.*..:*:. *:**** *

P40/P90 (MPN142)    GMVGSGAAGSASSLQGNGSNSSGLKSLLRSAPVSVPPSSTSNQTLSLSNPAPVGPQAVVS    353
   P110 (MG192)     SGG-------------------------------------------------------    258
                    .

P40/P90 (MPN142)    QPAGGATAAVSVNRTASDTATFSKYLNTAQALHQMGVIVPGLEKWGGNNGTGVVASRQDA    413
   P110 (MG192)     ---------------GSSSGTFNKYLNTKQALESIGILFDD-------------------    284
                               .*.:.**.***** ***..:*::. .

P40/P90 (MPN142)    TSTNLPHAAGASQTGLGTGSPREPALTATSQRAVTVVAGPLRAGNSSETDALPNVITQLY    473
   P110 (MG192)     ------------------------------------------------QTPRNVITQLY    295
                                                                    ::  *******

P40/P90 (MPN142)    HTSTAQLAYLNGQIVVMGSDRVPSLWYWVVGED---QESGKATWWAKTELNWGTDKQKQF    530
   P110 (MG192)     YASTSKLAVTNNHIVVMGNSFLPSMWYWVVERSAQENASNKPTWFANTNLDWGEDKQKQF    355
                    ::**::**  *.:*****.. :**:***** ..   : *.* **:*:*:*:** ******

P40/P90 (MPN142)    VENQLGFKDDSNSDSKNSNLKAQGLTQPAYLIAGLDVVADHLVFAAFKAGAVGYDMTTDS    590
   P110 (MG192)     VENQLGYKETTSTNS--HNFHSKSFTQPAYLISGIDSVNDQIIFSGFKAGSVGYDSSSSS    413
                    ******:*: :.::*   *:::::.:*******:*:* * *:::*:.****:**** ::.*

P40/P90 (MPN142)    ----SASTYNQALAWSTTAGLDSDGGYKALVENTAGLNGPINGLFTLLDTFAYVTPVSGM    646
   P110 (MG192)     SSSSSSSTKDQALAWSTTTSLDSKTGYKDLVTNDTGLNGPINGSFSIQDTFSFVVPYSGN    473
                        *:** :********:.***. *** ** * :******** *:: ***::*.* **

P40/P90 (MPN142)    KGGSQNNEEVQTTYPVKSDQKATAKIASLINASPLNSYGDDGVTVFDALGLNFNFKLNEE    706
   P110 (MG192)     HTNNGTTGPIKTAYPVKKDQKSTVKINSLINATPLNSYGDEGIGVFDALGLNYNFKSNQE    533
                    : .. ..  ::*:****.***:*.** *****:*******:*: ********:*** *:*

P40/P90 (MPN142)    RLPSRTDQLLVYGIVNESELKSARENAQSTSDDNSNTKVKWTNTASHYLPVPYYYSANFP    766
   P110 (MG192)     RLPSRTDQIFVYGIVSPNELRSAKSSADST---GSDTKVNWSNTQSRYLPVPYNYSEGII    590
                    ********::*****. .**:**:..*:**   .*:***:*:** *:****** ** .:

P40/P90 (MPN142)    EAGNRRRAEQRNG--VKISTLESQATDGFANSLLNFGTGLKAGVDPAPVARGHKPNYSAV    824
   P110 (MG192)     DADGFKRPENRGASVTTFSGLKSIAPDGFANSIANFSVGLKAGIDPNPVMSGKKANYGAV    650
                    :*.. :* *:*..  ..:* *:* * ******: **..*****:** **  *:* **.**

P40/P90 (MPN142)    LLVRGGVVRLNFNPDTDKLLDSTDKNSEPISFSYTPFGSAESAVDLTTLKDVTYIAESGL    884
   P110 (MG192)     VLTRGGVVRLNFNPGNDSLLSTTDNNIAPISFSFTPFTAAESAVDLTTFKEVTYNQESGL    710
                    :*.***********..*.**.:**:*  *****:*** :**********:*:***  ****

P40/P90 (MPN142)    WFYTFDNGEKPTYDGKQQQVKNRKGYAVITVSRTGIEFNEDANTTTLSQAPAALAVQNGI    944
   P110 (MG192)     WSYIFDSSLKPSHDGKQTPVTDNMGFSVITVSRTGIELNQDQATTTLDVAPSALAVQSGI    770
                    * * **.. **::****  *.:. *::***********:*:*  ****. **:*****.**
```

```
P40/P90 (MPN142)    ASSQDDLTGILPLSDEFSAVITKDQTWTGKVDIYKNTNGLFEKDDQLSENVKRRDNGLVP    1004
   P110 (MG192)     QSTTQTLTGVLPLSEEFSAVIAKDSD-QNKIDIYKNNNGLFEIDTQLSNSVATNNGGLAP    829
                     *: : ***:****:******:**.   .*:*****.***** * ***:.*  .:.**.*

P40/P90 (MPN142)    IYNEGIVDIWGRVDFAANSVLQARNLIDKTVDEVINNPDILQSFFKFTPAFDNQRAMLVG    1064
   P110 (MG192)     SYTENRVDAWGKVEFADNSVLQARNLVDKTVDEIINTPEILNSFFRFTPAFEDQKATLVA    889
                     *.*. ** **:*:** *********.******:**.*:**:***:*****::*:* **.

P40/P90 (MPN142)    EKTSDTTLTVKPKIEYLDGNFYGEDSKIAGIPLNIDFPSRIFAGFAALPSWVIPVSVGSS    1124
   P110 (MG192)     TKQSDTSLSVSPRIQFLDGNFYDLNSTIAGVPLNIGFPSRVFAGFAALPAWVIPVSVGSS    949
                     * ***:*:*.*:*::******. :*.***:****.****:********:**********

P40/P90 (MPN142)    VGILLILLILGLGIGIPMYKVRKLQDSSFVDVFKKVDTLTTAVGSVYKKIITQTSVIKKA    1184
   P110 (MG192)     VGILFILLVLGLGIGIPMYRVRKLQDASFVNVFKKVDTLTTAVGSVYKKIITQTGVVKKA    1009
                    ****:***:**********:******:***:**********************.*:***

P40/P90 (MPN142)    PSALKAANNAAPKAPVKPAAPTAPRPPVQPPKKA*----------------     1218
   P110 (MG192)     PSALKAANPSVKKPA------AFLKPPVQPPSKPEGEQKAVEVKSEETKS*     1053
                    ******** :. *        :  :******.*
```

Appendices Figure A. CV. 5.4_1. Clustal-O alignment of *M. pneumoniae* P40/P90 and M. *genitalium* P110.

```
  P1 (MPN141)       MHQTKKTALSKSTWILILTAT-ASLATGLTVVGHFTSTTTTLKRQQFSYTRPDEVALRHT    59
P140 (MG191)        MHQPKK-RLAKKSWAFLTAALTLGVITGVGGYFLFNQNKQRSSVSNFAY-QPKQLSVKHQ    58
                    *** **  *:*.:* :: :*   .: **:     *....   . .:*:* :*.::::::*

  P1 (MPN141)       NAINPRLTPWTYRNTSFSSLPLTGENPGAWALVRDNSAKGIT----AGSGSQQTTYDPTR    115
P140 (MG191)        QAVDETLTPWTWNNNNFSSLKITGENPGSFGLVRSQNDNLNISSVTKNSSDDNLKY-LNA    117
                    :*::  *****:.*..**** :******::.***.:. :        .*..:: .*  .

  P1 (MPN141)       TEAALTASTTFALRRYDLAGRALYDLDFSKLN-PQTPTRDQTGQITFNPFGGFGLSGAAP    174
P140 (MG191)        VEKYLDGQQNFAIRRYDNNGRALYDINLAKMENPSTVQRGLNGEPIFDPFKGFGLTGNAP    177
                    .*  * .. .**:****  ******::::*:: *.*  *. .*:  *:** ****:* **

  P1 (MPN141)       QQWNEVKNKVPVEVAQDPSNPYRFAVLLVPRSVVYYEQLQRGLGLPQQRTESGQNTSTTG    234
P140 (MG191)        TDWNEIKGKVPVEVVQSPHSPNLYFVLLVPKVALEYHNLNNQVVKESLEVKATQSS--FN    235
                     :***:*.******.*.* .*  : *****: .: *.:*:. :   . ..:: *.:   .

  P1 (MPN141)       AMFGLKVKNAEADTAKSNEKLQGAEATGSSTTSGSGQSTQRGGSSGDTKVKALKIEVKKK    294
P140 (MG191)        PTQRLQKDSPVKDSSKQGEKLSET--T---------ASSMSSGMATSTRAKALKVEVERG    284
                        *: ..   *::*..***. :  *           *:  .* : .*:.****:**::

  P1 (MPN141)       SDSEDNGQLQLEKNDLANAPIKRSEESGQSVQLKADDFGTALSSSGSGGNSNPGSPTPWR    354
P140 (MG191)        SQSD-----SLLKNDFAKKPLKHKNSSGEVKLE----------------AEKEFTEAWK    322
                    *:*:     .* ***:*: *:*:.:.**:                     ::      *:

  P1 (MPN141)       PWLATEQIHKDLPKWSASILILYDAPYARNRTAIDRVDHLDPKAMTANYPPSWRTPKWNH    414
P140 (MG191)        PLLTTDQIAREK-GMGATVVSFYDAPYSENHTAFGLVDHIDPKKMVENYPPSWKTPKWNH    381
                    * *:*:** ::    .*::: :*****:.*:**:. ***:*** *. ******:******

  P1 (MPN141)       HGLWDWKARDVLLQTTGFFNPRRHPEWFDGGQTVADNEKTGFDVDNSENTKQGFQKEADS    474
P140 (MG191)        HGIWDYNARNLLLQTTGFFNPRRHPEWFDEGQAKADNTSPGFKVGDTDHKKDGFKKN---    438
                    **:**::**::******************** **: *** . **.*.::::.*:**:*:

  P1 (MPN141)       DKSAPIALPFEAYFANIGNLTWFGQALLVFGGNGHVTKSAHTAPLSIGVFRVRYNATGTS    534
P140 (MG191)        -SSSPIALPFEAYFANIGNMVAIGNSVFIFGGNGHATKMFTTNPLSIGVFRIKYTDNFSK    497
                     .*:****************:. :*:::::******.**   * ********::*. . :.

  P1 (MPN141)       ATVTGWPYALLFSGMVNKQTDGLKDLPFNNNRWFEYVPRMAVAGAKFVGRELVLAGTITM    594
P140 (MG191)        SSVTGWPYAVLFGGLINPQTNGLKDLPLGTNRWFEYVPRMAVSGVKWVGNQLVLAGTLTM    557
                    ::*******:**.*::* **:******:..************:*.*:**.:******:**

  P1 (MPN141)       GDTATVPRLLYDELESNLNLVAQGQGLLREDLQLFTPYGWANRPDLPIGAWSSSSSSSHN    654
P140 (MG191)        GDTATVPRLKYDQLEKHLNLVAQGQGLLREDLQIFTPYGWANRPDIPVGAWLQDEMGSKF    617
                    ********* **:**.:*****************:***********:*:*** ... .*:

  P1 (MPN141)       APYYFHNNPDWQDRPIQNVVDAFIKPWEDKNGKDDAKYIYPYRYSGMWAWQVYNWSNKLT    714
P140 (MG191)        GPHYFLNNPDIQDNVNNDTVEALISSYKN---TDKLKHVYPYRYSGLYAWQLFNWSNKLT    674
                    .*:** **** **.  ::.*:*:*. :::   .*. *::********::***::*******

  P1 (MPN141)       DQPLSADFVNENAYQPNSLFAAILNPELLAALPDKVKYGKENEFAANEYERFNQKLTVAP    774
P140 (MG191)        NTPLSANFVNENSYAPNSLFAAILNEDLLTGLSDKIFYGKENEFAENEADRFNQLLSLNP    734
                    : ****:*****:* ********** :**:.* **: ******** ** :**** *:: *

  P1 (MPN141)       TQGTNWSHFSPTLSRFSTGFNLVGSVLDQVLDYVPWIGNGYRYGNNHRGVDDITAPQTSA    834
P140 (MG191)        NPNTNWARYLNVVQRFTTGPNLDSSTFDQFLDFLPWIGNGKPFSNSPSP-------ST--    785
                    . .***:::  .:.**:** ** .*.:**.**::******  :.*.          .*

  P1 (MPN141)       GSSSGISTNTSGSRSFLPTFSNIGVGLKANVQATLGGSQTMITGGSPRRTLDQANLQLWT    894
P140 (MG191)        ---------SASSSTPLPTFSNINVGVKSMITQHLNKENT------RWVFIPNFSPDIWT    830
                             ::.* : *******.**:*: :   *. .:*          : : . ::**

  P1 (MPN141)       GAGWRNDKASSGQSDENHTKFTSATGMDQQGQSGTS-AGNPDSLKQDNISKSGDSLTTQD    953
P140 (MG191)        GAGYRVQSANQKNG----IPFEQV------KPSNNSTPFDPN---------SDDNKVTP-    870
                    ***:* :.*.. :.      * ..        *..*   :*:         *.*. .*
```

```
  P1 (MPN141)       GNAIDQQEATNYTNLPPNLTPTADWPNALSFTNKNNAQRAQLFLRGLLGSIPVLVNRSGS    1013
P140 (MG191)        --SGGSSKPTTYPALPNSISPTSDWINALTFTNKNNPQRNQLLLRSLLGTIPVLINKSGD    928
                      : ...: *.*  ** .::**:** ***:****** ** **:**.***:****:*:**.

  P1 (MPN141)       DSNKFQA-TDQKWSYTDLHSDQTKLNLPAYGEVNGLLNPALVETYFGNTRAGGSGSNTTS    1072
P140 (MG191)        SNDQFNKDSEQKWDKTE----TNEGNLPGFGEVNGLYNAALLHTYGFFGT-----NTNST    979
                    ..::*:  ::***. *:     .: ***.:****** * **:.**          ....:

  P1 (MPN141)       SPGIGFKIPEQNNDSKATLITPGLAWTPQDVGNLVVS-GTTVSFQLGGWLVTFTDFVKPR    1131
P140 (MG191)        DPKIGFKADSS-SSSSSTLVGSGLNWTSQDVGNLVVINDTSFGFQLGGWFITFTDFIRPR    1038
                    .* ****  .. ..*.:**:  ** ** ********  .*:..******::*****::**

  P1 (MPN141)       AGYLGLQLTGLDASDATQRALIWAPRPWAAFRGSWVNRLGRVESVWDLKGVWADQAQSDS    1191
P140 (MG191)        TGYLGITLSSLQ-----DQTIIWADQPWTSFKGSYLDSDGTPKSLWDPTALKSLPNSSTT    1093
                    :****: *:.*:     :::*** :**::*:**:::  *  :*:** ..: :   .* :

  P1 (MPN141)       QGSTTTATRNALPEHPNALAFQVSVVEASAYKPNTSSGQTQSTNSSPYLHLVKPKKVTQS    1251
P140 (MG191)        YD-----TNPTL--SPS---F-------QLYQPNKVKAY---QTTNTYNKLIEPVDATSA    1133
                     .     *. :*   *.   *       . *:**. ..     .:. * :*::* ..*.:

  P1 (MPN141)       DKLDDDLKNLLDPNQVRTKLRQSFGTDHSTQPQPQSLKTTTPVFGTSSGNLSSVLSGGGA    1311
P140 (MG191)        ATNMTSLLKLLTTKNIKAKLGKG----------------------------TASSQGNNN    1165
                     .   .* :**  :::::** :.                             ::  .*..

  P1 (MPN141)       GGGSSGSGQSGVDLSPVEKVSGWLVGQLPSTSDGNTSSTNNLAPNTNTGNDVVGVGRLSE    1371
P140 (MG191)        GGGVSQT------INTITT-TGNISEGLKEETSIQAETLKKFFDSKQNNKSEIG---IGD    1215
                    *** * :      :. : . :* :   * . :. ::.: :::  ..:..:. :*   :.:

  P1 (MPN141)       SNAAKMNDDVDGIVRTPLAELLDGEGQTADTGPQSVKFKSPDQIDFNRLFTHPVTDLFDP    1431
P140 (MG191)        STFTKMDGKLTGVVSTPLVNLINGQGATSDSDTEKISFKPGNQIDFNRLFTLPVTELFDP    1275
                    *. :**:..: *:* ***.:*::*:* *:*:. :.:.**  :********* ***:****

  P1 (MPN141)       VTMLVYDQYIPLFIDIPASVNPKMVRLKVLSFDTNEQSLGLRLEFFKPDQDTQPNNNVQV    1491
P140 (MG191)        NTMFVYDQYVPLLVNLPSGFDQASIRLKVISYSVENQTLGVRLEFKDPQ-----------    1324
                     **:*****:**::::*:..:   :****:*:..::*:**:**** .*:

  P1 (MPN141)       NPNNGDFLPLLTASSQGPQTLFSPFNQWPDYVLPLAITVPIVVIVLSVTLGLAIGIPMHK    1551
P140 (MG191)        ---TQQFIPVLNASSTGPQTVFQPFNQWADYVLPLIVTVPIVVIILSVTLGLTIGIPMHR    1381
                       . :*:*:*.*** **** :*.***** ****** :******* ******* ******:

  P1 (MPN141)       NKQALKAGFALSNQKVDVLTKAVGSVFKEIINRTGISQAPKRLKQTSAAKPGAPRPPVPP    1611
P140 (MG191)        NKKALQAGFDLSNKKVDVLTKAVGSVFKEIINRTGISNAPKKLKQATPTKPTPKTPPKPP    1441
                    **:**:*** ***:************************:***:***:: :**    ** **

  P1 (MPN141)       KPGAPKPPVQPPKKPA* 1627
P140 (MG191)        VKQ*------------- 1444
```

Appendices Figure A. CV. 5.4_2. Clustal-O alignment of *M. pneumoniae* P1 and M. *genitalium* P140.

BIBLIOGRAPHY

1. Woese, C. R., Maniloff, J. & Zablen, L. B. Phylogenetic analysis of the mycoplasmas. *Proc. Natl. Acad. Sci. U. S. A.* **77**, 494–498 (1980).
2. Fraser, C. M. *et al.* The minimal gene complement of Mycoplasma genitalium. *Science* **270**, 397–403 (1995).
3. Tully, J. G. *Molecular and Diagnostic Procedures in Mycoplasmology*. (1995).
4. do Nascimento, N. C. *et al.* Genome Sequence of Mycoplasma parvum (Formerly Eperythrozoon parvum), a Diminutive Hemoplasma of the Pig. *Genome Announc.* **1**, e00986-13 (2013).
5. Razin, S. Molecular biology and genetics of mycoplasmas (Mollicutes). *Microbiol. Rev.* **49**, 419–455 (1985).
6. Barré, A., de Daruvar, A. & Blanchard, A. MolliGen, a database dedicated to the comparative genomics of Mollicutes. *Nucleic Acids Res.* **32**, D307-310 (2004).
7. *Bergey's Manual® of Systematic Bacteriology: Volume Four The Bacteroidetes, Spirochaetes, Tenericutes (Mollicutes), Acidobacteria, Fibrobacteres, Fusobacteria, Dictyoglomi, Gemmatimonadetes, Lentisphaerae, Verrucomicrobia, Chlamydiae, and Planctomycetes*. (Springer New York, New York, NY, 2010). doi:10.1007/978-0-387-68572-4.
8. Taylor-Robinson, D. & Bébéar, C. Antibiotic susceptibilities of mycoplasmas and treatment of mycoplasmal infections. *J. Antimicrob. Chemother.* **40**, 622–630 (1997).
9. Gaurivaud, P., Laigret, F. & Bove, J. M. Insusceptibility of members of the class Mollicutes to rifampin: studies of the Spiroplasma citri RNA polymerase beta-subunit gene. *Antimicrob. Agents Chemother.* **40**, 858–862 (1996).
10. Inamine, J. M., Ho, K. C., Loechel, S. & Hu, P. C. Evidence that UGA is read as a tryptophan codon rather than as a stop codon by Mycoplasma pneumoniae, Mycoplasma genitalium, and Mycoplasma gallisepticum. *J. Bacteriol.* **172**, 504–506 (1990).
11. Navas-Castillo, J., Laigret, F., Tully, J. G. & Bové, J. M. [Mollicute Acholeplasma florum possesses a gene of phosphoenolpyruvate sugar phosphotransferase system and it uses UGA as tryptophan codon]. *C. R. Acad. Sci. III* **315**, 43–48 (1992).
12. Citti, C., Maréchal-Drouard, L., Saillard, C., Weil, J. H. & Bové, J. M. Spiroplasma citri UGG and UGA tryptophan codons: sequence of the two tryptophanyl-tRNAs and organization of the corresponding genes. *J. Bacteriol.* **174**, 6471–6478 (1992).
13. Harwick, H. J., Kalmanson, G. M. & Guze, L. B. Human Diseases Associated with Mycoplasmas—With an Appendix on Simple Culture Techniques. *Calif. Med.* **116**, 1–7 (1972).
14. Klieneberger, E. The natural occurrence of pleuropneumonia-like organism in apparent symbiosis with Strrptobacillus moniliformis and other bacteria. *J. Pathol. Bacteriol.* **40**, 93–105 (1935).
15. EDWARD, D. G. FF. & FREUNDT, E. A. Proposal for Mollicutes as name of the class established for the order Mycoplasmatales. *Int. J. Syst. Evol. Microbiol.* **17**, 267–268 (1967).
16. Razin, S. The Genus Mycoplasma and Related Genera (Class Mollicutes). in *The Prokaryotes* (eds. Dworkin, M., Falkow, S., Rosenberg, E., Schleifer, K.-H. & Stackebrandt, E.) 836–904 (Springer US, New York, NY, 2006). doi:10.1007/0-387-30744-3_29.
17. Baseman, J. B. & Tully, J. G. Mycoplasmas: sophisticated, reemerging, and burdened by their notoriety. *Emerg. Infect. Dis.* **3**, 21–32 (1997).
18. Combaz-Söhnchen, N. & Kuhn, A. A Systematic Review of Mycoplasma and Ureaplasma in Urogynaecology. *Geburtshilfe Frauenheilkd.* **77**, 1299–1303 (2017).
19. Razin, S., Yogev, D. & Naot, Y. Molecular Biology and Pathogenicity of Mycoplasmas. *Microbiol. Mol. Biol. Rev.* **62**, 1094–1156 (1998).
20. Nikfarjam, L. & Farzaneh, P. Prevention and detection of Mycoplasma contamination in cell culture. *Cell J.* **13**, 203–212 (2012).
21. Rottem, S. & Barile, M. F. Beware of mycoplasmas. *Trends Biotechnol.* **11**, 143–151 (1993).
22. Taylor-Robinson, D. & Jensen, J. S. Mycoplasma genitalium: from Chrysalis to multicolored butterfly. *Clin. Microbiol. Rev.* **24**, 498–514 (2011).

23. Kumar, A., Rahal, A., Chakraborty, S., Verma, A. K. & Dhama, K. Mycoplasma agalactiae, an Etiological Agent of Contagious Agalactia in Small Ruminants: A Review. *Vet. Med. Int.* **2014**, 286752 (2014).
24. Nicholas, R. a. J. & Ayling, R. D. Mycoplasma bovis: disease, diagnosis, and control. *Res. Vet. Sci.* **74**, 105–112 (2003).
25. Provost, A. *et al.* Contagious bovine pluropneumonia. *Rev. Sci. Tech. Int. Off. Epizoot.* **6**, 565–679 (1987).
26. Barden, J. A. & Decker, J. L. Mycoplasma Hyorhinis Swine Arthritis. I. Clinical and Microbiologic Features. *Arthritis Rheum.* **14**, 193–201 (1971).
27. Maes, D. *et al.* Update on Mycoplasma hyopneumoniae infections in pigs: Knowledge gaps for improved disease control. *Transbound. Emerg. Dis.* **65 Suppl 1**, 110–124 (2018).
28. Stipkovits, L. & Kempf, I. Mycoplasmoses in poultry. *Rev. Sci. Tech. Int. Off. Epizoot.* **15**, 1495–1525 (1996).
29. Minion, F. C. Molecular pathogenesis of mycoplasma animal respiratory pathogens. *Front. Biosci. J. Virtual Libr.* **7**, d1410-1422 (2002).
30. Woese, C. R. Bacterial evolution. *Microbiol. Rev.* **51**, 221–271 (1987).
31. Inagaki, Y., Bessho, Y. & Osawa, S. Lack of peptide-release activity responding to codon UGA in Mycoplasma capricolum. *Nucleic Acids Res.* **21**, 1335–1338 (1993).
32. Inagaki, Y., Bessho, Y., Hori, H. & Osawa, S. Cloning of the Mycoplasma capricolum gene encoding peptide-chain release factor. *Gene* **169**, 101–103 (1996).
33. Kenri, T. *et al.* Identification of a new variable sequence in the P1 cytadhesin gene of Mycoplasma pneumoniae: evidence for the generation of antigenic variation by DNA recombination between repetitive sequences. *Infect. Immun.* **67**, 4557–4562 (1999).
34. Rocha, E. P. C. & Blanchard, A. Genomic repeats, genome plasticity and the dynamics of Mycoplasma evolution. *Nucleic Acids Res.* **30**, 2031–2042 (2002).
35. Bhugra, B. & Dybvig, K. Identification and characterization of IS1138, a transposable element from Mycoplasma pulmonis that belongs to the IS3 family. *Mol. Microbiol.* **7**, 577–584 (1993).
36. Dybvig, K. & Maniloff, J. Integration and lysogeny by an enveloped mycoplasma virus. *J. Gen. Virol.* **64 (Pt 8)**, 1781–1785 (1983).
37. King, K. W. & Dybvig, K. Nucleotide sequence of Mycoplasma mycoides subspecies Mycoides plasmid pKMK1. *Plasmid* **28**, 86–91 (1992).
38. Tu, A. H., Voelker, L. L., Shen, X. & Dybvig, K. Complete nucleotide sequence of the mycoplasma virus P1 genome. *Plasmid* **45**, 122–126 (2001).
39. Voelker, L. L. & Dybvig, K. Sequence analysis of the Mycoplasma arthritidis bacteriophage MAV1 genome identifies the putative virulence factor. *Gene* **233**, 101–107 (1999).
40. Maniloff, J. Evolution of wall-less prokaryotes. *Annu. Rev. Microbiol.* **37**, 477–499 (1983).
41. Rogers, M. J. *et al.* Construction of the mycoplasma evolutionary tree from 5S rRNA sequence data. *Proc. Natl. Acad. Sci. U. S. A.* **82**, 1160–1164 (1985).
42. Weisburg, W. G. *et al.* A phylogenetic analysis of the mycoplasmas: basis for their classification. *J. Bacteriol.* **171**, 6455–6467 (1989).
43. Tully, J. G., Bové, J. M., Laigret, F. & Whitcomb, R. F. Revised Taxonomy of the Class Mollicutes: Proposed Elevation of a Monophyletic Cluster of Arthropod-Associated Mollicutes to Ordinal Rank (Entomoplasmatales ord. nov.), with Provision for Familial Rank To Separate Species with Nonhelical Morphology (Entomoplasmataceae fam. nov.) from Helical Species (Spiroplasmataceae), and Emended Descriptions of the Order Mycoplasmatales, Family Mycoplasmataceae. *Int. J. Syst. Evol. Microbiol.* **43**, 378–385 (1993).
44. Gupta, R. S. & Oren, A. Necessity and rationale for the proposed name changes in the classification of Mollicutes species. Reply to: 'Recommended rejection of the names Malacoplasma gen. nov., Mesomycoplasma gen. nov., Metamycoplasma gen. nov., Metamycoplasmataceae fam. nov., Mycoplasmoidaceae fam. nov., Mycoplasmoidales ord. nov., Mycoplasmoides gen. nov., Mycoplasmopsis gen. nov. [Gupta, Sawnani, Adeolu, Alnajar and Oren 2018] and all proposed species comb. nov. placed therein', by M. Balish et al. (Int J Syst Evol Microbiol, 2019;69:3650–3653). *Int. J. Syst. Evol. Microbiol.* **70**, 1431–1438 (2020).
45. Gupta, R. S., Sawnani, S., Adeolu, M., Alnajar, S. & Oren, A. Phylogenetic framework for the phylum Tenericutes based on genome sequence data: proposal for the creation of a new order Mycoplasmoidales ord. nov., containing two new families Mycoplasmoidaceae fam. nov. and

Metamycoplasmataceae fam. nov. harbouring Eperythrozoon, Ureaplasma and five novel genera. *Antonie Van Leeuwenhoek* **111**, 1583–1630 (2018).
46. Gupta, R. S., Son, J. & Oren, A. A phylogenomic and molecular markers based taxonomic framework for members of the order Entomoplasmatales: proposal for an emended order Mycoplasmatales containing the family Spiroplasmataceae and emended family Mycoplasmataceae comprised of six genera. *Antonie Van Leeuwenhoek* **112**, 561–588 (2019).
47. Hamasuna, R., Osada, Y. & Jensen, J. S. Isolation of Mycoplasma genitalium from first-void urine specimens by coculture with Vero cells. *J. Clin. Microbiol.* **45**, 847–850 (2007).
48. Himmelreich, R. *et al.* Complete sequence analysis of the genome of the bacterium Mycoplasma pneumoniae. *Nucleic Acids Res.* **24**, 4420–4449 (1996).
49. Yus, E. *et al.* Impact of genome reduction on bacterial metabolism and its regulation. *Science* **326**, 1263–1268 (2009).
50. Meloni, G. A., Bertoloni, G., Busolo, F. & Conventi, L. Colony morphology, ultrastructure and morphogenesis in Mycoplasma hominis, Acholeplasma laidlawii and Ureaplasma urealyticum. *J. Gen. Microbiol.* **116**, 435–443 (1980).
51. Miles, R. J. Catabolism in mollicutes. *J. Gen. Microbiol.* **138**, 1773–1783 (1992).
52. Taylor, R. R., Varsani, H. & Miles, R. J. Alternatives to arginine as energy sources for the non-fermentative Mycoplasma gallinarum. *FEMS Microbiol. Lett.* **115**, 163–167 (1994).
53. Keçeli, S. A. & Miles, R. J. Differential inhibition of mollicute growth: an approach to development of selective media for specific mollicutes. *Appl. Environ. Microbiol.* **68**, 5012–5016 (2002).
54. Pollack, J. D. Mycoplasma genes: a case for reflective annotation. *Trends Microbiol.* **5**, 413–419 (1997).
55. Dahl, J. The role of cholesterol in mycoplasma membranes. *Subcell. Biochem.* **20**, 167–188 (1993).
56. Maier, T. *et al.* Large-scale metabolome analysis and quantitative integration with genomics and proteomics data in Mycoplasma pneumoniae. *Mol. Biosyst.* **9**, 1743–1755 (2013).
57. Carvalho, F. M. *et al.* DNA repair in reduced genome: The Mycoplasma model. *Gene* **360**, 111–119 (2005).
58. Dillingham, M. S., Soultanas, P., Wiley, P., Webb, M. R. & Wigley, D. B. Defining the roles of individual residues in the single-stranded DNA binding site of PcrA helicase. *Proc. Natl. Acad. Sci. U. S. A.* **98**, 8381–8387 (2001).
59. Estevão, S., van der Spek, P. E., van Rossum, A. M. C. & Vink, C. Uncoupling of the apyrimidinic/apurinic endonucleolytic and 3'→5' exonucleolytic activities of the Nfo protein of Mycoplasma pneumoniae through mutation of specific amino acid residues. *Microbiology* **160**, 1087–1100 (2014).
60. Witte, G., Hartung, S., Büttner, K. & Hopfner, K.-P. Structural biochemistry of a bacterial checkpoint protein reveals diadenylate cyclase activity regulated by DNA recombination intermediates. *Mol. Cell* **30**, 167–178 (2008).
61. Bork, P. *et al.* Exploring the Mycoplasma capricolum genome: a minimal cell reveals its physiology. *Mol. Microbiol.* **16**, 955–967 (1995).
62. Burgos, R., Wood, G. E., Young, L., Glass, J. I. & Totten, P. A. RecA mediates MgpB and MgpC phase and antigenic variation in Mycoplasma genitalium, but plays a minor role in DNA repair. *Mol. Microbiol.* **85**, 669–683 (2012).
63. Brocchi, M., Vasconcelos, A. T. R. D. & Zaha, A. Restriction-modification systems in Mycoplasma spp. *Genet. Mol. Biol.* **30**, 236–244 (2007).
64. Calisto, B. M. *et al.* Crystal structure of a putative type I restriction-modification S subunit from Mycoplasma genitalium. *J. Mol. Biol.* **351**, 749–762 (2005).
65. Dybvig, K., Cao, Z., French, C. T. & Yu, H. Evidence for type III restriction and modification systems in Mycoplasma pulmonis. *J. Bacteriol.* **189**, 2197–2202 (2007).
66. Bergemann, A. D., Whitley, J. C. & Finch, L. R. Taxonomic significance of differences in DNA methylation within the 'Mycoplasma mycoides cluster' detected with restriction endonucleases MboI and DpnI. *Lett. Appl. Microbiol.* **11**, 48–51 (1990).
67. Halden, N. F., Wolf, J. B. & Leonard, W. J. Identification of a novel site-specific endonuclease produced by Mycoplasma fermentans: discovery while characterizing DNA binding proteins in T lymphocyte cell lines. *Nucleic Acids Res.* **17**, 3491–3499 (1989).
68. Krause, D. C. & Baseman, J. B. Mycoplasma pneumoniae proteins that selectively bind to host cells. *Infect. Immun.* **37**, 382–386 (1982).

69. Fisseha, M., Göhlmann, H. W., Herrmann, R. & Krause, D. C. Identification and complementation of frameshift mutations associated with loss of cytadherence in Mycoplasma pneumoniae. *J. Bacteriol.* **181**, 4404–4410 (1999).
70. Burgos, R. *et al.* Mycoplasma genitalium P140 and P110 Cytadhesins Are Reciprocally Stabilized and Required for Cell Adhesion and Terminal-Organelle Development. *J. Bacteriol.* **188**, 8627–8637 (2006).
71. Pich, O. Q., Burgos, R., Ferrer-Navarro, M., Querol, E. & Piñol, J. Role of Mycoplasma genitalium MG218 and MG317 cytoskeletal proteins in terminal organelle organization, gliding motility and cytadherence. *Microbiology* **154**, 3188–3198 (2008).
72. Indiková, I. *et al.* Role of the GapA and CrmA cytadhesins of Mycoplasma gallisepticum in promoting virulence and host colonization. *Infect. Immun.* **81**, 1618–1624 (2013).
73. Razin, S., Kahane, I., Banai, M. & Bredt, W. Adhesion of mycoplasmas to eukaryotic cells. *Ciba Found. Symp.* **80**, 98–118 (1981).
74. Baseman, J. B., Banai, M. & Kahane, I. Sialic acid residues mediate Mycoplasma pneumoniae attachment to human and sheep erythrocytes. *Infect. Immun.* **38**, 389–391 (1982).
75. Aparicio, D. *et al.* Mycoplasma genitalium adhesin P110 binds sialic-acid human receptors. *Nat. Commun.* **9**, 4471 (2018).
76. Taylor-Robinson, D., Davies, H. A., Sarathchandra, P. & Furr, P. M. Intracellular location of mycoplasmas in cultured cells demonstrated by immunocytochemistry and electron microscopy. *Int. J. Exp. Pathol.* **72**, 705–714 (1991).
77. Lo, S. C. *et al.* Adhesion onto and invasion into mammalian cells by mycoplasma penetrans: a newly isolated mycoplasma from patients with AIDS. *Mod. Pathol. Off. J. U. S. Can. Acad. Pathol. Inc* **6**, 276–280 (1993).
78. Jensen, J. S., Blom, J. & Lind, K. Intracellular location of Mycoplasma genitalium in cultured Vero cells as demonstrated by electron microscopy. *Int. J. Exp. Pathol.* **75**, 91–98 (1994).
79. Winner, F., Rosengarten, R. & Citti, C. In vitro cell invasion of Mycoplasma gallisepticum. *Infect. Immun.* **68**, 4238–4244 (2000).
80. Blaylock, M. W., Musatovova, O., Baseman, J. G. & Baseman, J. B. Determination of infectious load of Mycoplasma genitalium in clinical samples of human vaginal cells. *J. Clin. Microbiol.* **42**, 746–752 (2004).
81. Ueno, P. M. *et al.* Interaction of Mycoplasma genitalium with host cells: evidence for nuclear localization. *Microbiol. Read. Engl.* **154**, 3033–3041 (2008).
82. Andreev, J., Borovsky, Z., Rosenshine, I. & Rottem, S. Invasion of HeLa cells by Mycoplasma penetrans and the induction of tyrosine phosphorylation of a 145-kDa host cell protein. *FEMS Microbiol. Lett.* **132**, 189–194 (1995).
83. McGowin, C. L., Popov, V. L. & Pyles, R. B. Intracellular Mycoplasma genitalium infection of human vaginal and cervical epithelial cells elicits distinct patterns of inflammatory cytokine secretion and provides a possible survival niche against macrophage-mediated killing. *BMC Microbiol.* **9**, 139 (2009).
84. Shepard, M. C. *et al.* Ureaplasma urealyticum gen. nov., sp. nov.: Proposed Nomenclature for the Human T (T-Strain) Mycoplasmas. *Int. J. Syst. Evol. Microbiol.* **24**, 160–171 (1974).
85. Dienes, L. & Edsall, G. Observations on the L-Organism of Klieneberger. *Proc. Soc. Exp. Biol. Med.* **36**, 740–744 (1937).
86. Taylor-Robinson, D. & Furr, P. M. Update on sexually transmitted mycoplasmas. *Lancet Lond. Engl.* **351 Suppl 3**, 12–15 (1998).
87. Waites, K. B. & Talkington, D. F. Mycoplasma pneumoniae and Its Role as a Human Pathogen. *Clin. Microbiol. Rev.* **17**, 697–728 (2004).
88. Clarivet, B. *et al.* Prevalence of Chlamydia trachomatis, Neisseria gonorrhoeae and Mycoplasma genitalium in asymptomatic patients under 30 years of age screened in a French sexually transmitted infections clinic. *Eur. J. Dermatol. EJD* **24**, 611–616 (2014).
89. Philibert, P. *et al.* High Prevalence of Asymptomatic Sexually Transmitted Infections among Men Who Have Sex with Men. *J. Clin. Med.* **3**, 1386–1391 (2014).
90. Henning, D. *et al.* Asymptomatic Mycoplasma genitalium infection amongst marginalised young people accessing a youth health service in Melbourne. *Int. J. STD AIDS* **25**, 299–302 (2014).
91. Manhart, L. E. Mycoplasma genitalium: An Emergent Sexually Transmitted Disease? *Infect. Dis. Clin. North Am.* **27**, 779–792 (2013).

92. Mårdh, P. A. Mycoplasma hominis - a neglected human pathogen. *Eur. J. Clin. Microbiol.* **2**, 303–308 (1983).
93. Ireland, D. J. & Keelan, J. A. The Maternal Serological Response to Intrauterine Ureaplasma sp. Infection and Prediction of Risk of Pre-Term Birth. *Front. Immunol.* **5**, 624 (2014).
94. Zhang, N. *et al.* Are Ureaplasma spp. a Cause of Nongonococcal Urethritis? A Systematic Review and Meta-Analysis. *PLoS ONE* **9**, e113771 (2014).
95. Sweeney, E. L., Dando, S. J., Kallapur, S. G. & Knox, C. L. The Human Ureaplasma Species as Causative Agents of Chorioamnionitis. *Clin. Microbiol. Rev.* **30**, 349–379 (2017).
96. Blanchard, A. & Montagnier, L. AIDS-associated mycoplasmas. *Annu. Rev. Microbiol.* **48**, 687–712 (1994).
97. Grau, O. *et al.* Association of Mycoplasma penetrans with human immunodeficiency virus infection. *J. Infect. Dis.* **172**, 672–681 (1995).
98. Jiang, X., Lv, Y.-Q., Zhang, J.-N., Shi, Y.-L. & Xu, F.-F. Mycoplasma penetrans infection is a potential cause of immunoglobulin A nephropathy: a new animal model. *J. Nephrol.* **26**, 470–475 (2013).
99. Tsai, S., Wear, D. J., Shih, J. W. & Lo, S. C. Mycoplasmas and oncogenesis: persistent infection and multistage malignant transformation. *Proc. Natl. Acad. Sci. U. S. A.* **92**, 10197–10201 (1995).
100. Tully, J., Cole, R., Taylor-Robinson, D. & Rose, D. A NEWLY DISCOVERED MYCOPLASMA IN THE HUMAN UROGENITAL TRACT. *The Lancet* **317**, 1288–1291 (1981).
101. Taylor-Robinson, D., Gilroy, C. B., Horowitz, S. & Horowitz, J. Mycoplasma genitalium in the joints of two patients with arthritis. *Eur. J. Clin. Microbiol. Infect. Dis. Off. Publ. Eur. Soc. Clin. Microbiol.* **13**, 1066–1069 (1994).
102. TULLY*, J. G., TAYLOR-ROBINSON, D., ROSE, D. L., COLE, R. M. & BOVE, J. M. Mycoplasma genitalium, a New Species from the Human Urogenital Tract. *Int. J. Syst. Evol. Microbiol.* **33**, 387–396 (1983).
103. McGowin, C. L. & Anderson-Smits, C. Mycoplasma genitalium: An Emerging Cause of Sexually Transmitted Disease in Women. *PLoS Pathog.* **7**, (2011).
104. Harish, S. Sexually transmitted infection by Mycoplasma genitalium: A short review. *J. Skin Sex. Transm. Dis.* **3**, 46–50 (2021).
105. Torrone, E. A. *et al.* Prevalence of Urogenital Mycoplasma genitalium Infection, United States, 2017 to 2018. *Sex. Transm. Dis.* **48**, e160 (2021).
106. Gnanadurai, R. & Fifer, H. Mycoplasma genitalium: A Review. *Microbiol. Read. Engl.* **166**, 21–29 (2020).
107. Fernández-Huerta, M. *et al.* Single-Locus-Sequence-Based Typing of the mgpB Gene Reveals Transmission Dynamics in Mycoplasma genitalium. *J. Clin. Microbiol.* **58**, e01886-19 (2020).
108. Jensen, J. S., Cusini, M., Gomberg, M. & Moi, H. 2016 European guideline on Mycoplasma genitalium infections. *J. Eur. Acad. Dermatol. Venereol. JEADV* **30**, 1650–1656 (2016).
109. van der Schalk, T. E., Braam, J. F. & Kusters, J. G. Molecular basis of antimicrobial resistance in Mycoplasma genitalium. *Int. J. Antimicrob. Agents* **55**, 105911 (2020).
110. Machalek, D. A. *et al.* Prevalence of mutations associated with resistance to macrolides and fluoroquinolones in Mycoplasma genitalium: a systematic review and meta-analysis. *Lancet Infect. Dis.* **20**, 1302–1314 (2020).
111. Manhart, L. E., Broad, J. M. & Golden, M. R. Mycoplasma genitalium: should we treat and how? *Clin. Infect. Dis. Off. Publ. Infect. Dis. Soc. Am.* **53 Suppl 3**, S129-142 (2011).
112. Lluch-Senar, M. *et al.* Defining a minimal cell: essentiality of small ORFs and ncRNAs in a genome-reduced bacterium. *Mol. Syst. Biol.* **11**, 780 (2015).
113. Eaton, M. D., Meiklejohn, G. & van Herick, W. STUDIES ON THE ETIOLOGY OF PRIMARY ATYPICAL PNEUMONIA : A FILTERABLE AGENT TRANSMISSIBLE TO COTTON RATS, HAMSTERS, AND CHICK EMBRYOS. *J. Exp. Med.* **79**, 649–668 (1944).
114. Somerson, N. L., Taylor-Robinson, D. & Chanock, R. M. Hemolyin production as an aid in the identification and quantitation of Eaton agent (Mycoplasma pneumoniae). *Am. J. Hyg.* **77**, 122–128 (1963).
115. Waites, K. B., Xiao, L., Liu, Y., Balish, M. F. & Atkinson, T. P. Mycoplasma pneumoniae from the Respiratory Tract and Beyond. *Clin. Microbiol. Rev.* **30**, 747 (2017).
116. Søndergaard, M. J., Friis, M. B., Hansen, D. S. & Jørgensen, I. M. Clinical manifestations in infants and children with Mycoplasma pneumoniae infection. *PLOS ONE* **13**, e0195288 (2018).
117. Gao, L.-W. *et al.* The epidemiology of paediatric Mycoplasma pneumoniae pneumonia in North China: 2006 to 2016. *Epidemiol. Infect.* **147**, e192 (2019).

118. Zhu, Y., Tang, X., Lu, Y., Zhang, J. & Qu, J. Contemporary situation of community-acquired pneumonia in China: A systematic review. *J. Transl. Intern. Med.* **6**, 26–31 (2018).
119. Xu, W. *et al.* Detection of Viruses and Mycoplasma pneumoniae in Hospitalized Patients with Severe Acute Respiratory Infection in Northern China, 2015–2016. *Jpn. J. Infect. Dis.* **71**, 134–139 (2018).
120. Kutty, P. K. *et al.* Mycoplasma pneumoniae Among Children Hospitalized With Community-acquired Pneumonia. *Clin. Infect. Dis.* **68**, 5–12 (2019).
121. Kumar, S., Roy, R. D., Sethi, G. & Saigal, S. R. Mycoplasma pneumoniae infection and asthma in children. *Trop. Doct.* **49**, 117–119 (2019).
122. Kassisse, E., García, H., Prada, L., Salazar, I. & Kassisse, J. Prevalence of Mycoplasma pneumoniae infection in pediatric patients with acute asthma exacerbation. *Arch. Argent. Pediatr.* **116**, 179–185 (2018).
123. Esposito, S. *et al.* Cytokine secretion in children with acute Mycoplasma pneumoniae infection and wheeze. *Pediatr. Pulmonol.* **34**, 122–127 (2002).
124. Narita, M. Pathogenesis of extrapulmonary manifestations of Mycoplasma pneumoniae infection with special reference to pneumonia. *J. Infect. Chemother.* **16**, 162–169 (2010).
125. Narita, M. Classification of Extrapulmonary Manifestations Due to Mycoplasma pneumoniae Infection on the Basis of Possible Pathogenesis. *Front. Microbiol.* **7**, (2016).
126. Giavina-Bianchi, P. & Kalil, J. Mycoplasma pneumoniae infection induces asthma onset. *J. Allergy Clin. Immunol.* **137**, 1024–1025 (2016).
127. Wang, K. *et al.* Mycoplasma pneumoniae and Respiratory Virus Infections in Children With Persistent Cough in England: A Retrospective Analysis. *Pediatr. Infect. Dis. J.* **30**, 1047 (2011).
128. Takahashi, N. *et al.* Acute respiratory distress syndrome caused by Mycoplasma pneumonia without elevated pulmonary vascular permeability: a case report. *J. Thorac. Dis.* **8**, (2016).
129. Meyer Sauteur, P. M. *et al.* Frequency and Clinical Presentation of Mucocutaneous Disease Due to Mycoplasma pneumoniae Infection in Children With Community-Acquired Pneumonia. *JAMA Dermatol.* **156**, 144–150 (2020).
130. Meyer Sauteur, P. M., Goetschel, P. & Lautenschlager, S. Mycoplasma pneumoniae and mucositis – part of the Stevens-Johnson syndrome spectrum. *JDDG J. Dtsch. Dermatol. Ges.* **10**, 740–745 (2012).
131. Harr, T. & French, L. E. Toxic epidermal necrolysis and Stevens-Johnson syndrome. *Orphanet J. Rare Dis.* **5**, 39 (2010).
132. Prindaville, B., Newell, B. D., Nopper, A. J. & Horii, K. A. Mycoplasma pneumoniae–Associated Mucocutaneous Disease in Children: Dilemmas in Classification. *Pediatr. Dermatol.* **31**, 670–675 (2014).
133. Meyer Sauteur, P. M. *et al.* Infection with and Carriage of Mycoplasma pneumoniae in Children. *Front. Microbiol.* **7**, (2016).
134. Groot, R. C. A. de, Sauteur, P. M. M., Unger, W. W. J. & Rossum, A. M. C. van. Things that could be Mycoplasma pneumoniae. *J. Infect.* **74**, S95–S100 (2017).
135. Spuesens, E. B. M., Sauteur, P. M. M., Vink, C. & Rossum, A. M. C. van. Mycoplasma pneumoniae infections – Does treatment help? *J. Infect.* **69**, S42–S46 (2014).
136. Cao, B., Qu, J.-X., Yin, Y.-D. & Eldere, J. V. Overview of antimicrobial options for ycoplasma pneumoniae pneumonia: focus on macrolide resistance. *Clin. Respir. J.* **11**, 419–429 (2017).
137. Khoury, T. *et al.* Increased rates of intensive care unit admission in patients with Mycoplasma pneumoniae: a retrospective study. *Clin. Microbiol. Infect.* **22**, 711–714 (2016).
138. Chen, Y.-C., Hsu, W.-Y. & Chang, T.-H. Macrolide-Resistant Mycoplasma pneumoniae Infections in Pediatric Community-Acquired Pneumonia. *Emerg. Infect. Dis.* **26**, 1382–1391 (2020).
139. Zhou, Y. *et al.* More Complications Occur in Macrolide-Resistant than in Macrolide-Sensitive Mycoplasma pneumoniae Pneumonia. *Antimicrob. Agents Chemother.* **58**, 1034–1038 (2014).
140. Hutchison, C. A. *et al.* Global transposon mutagenesis and a minimal Mycoplasma genome. *Science* **286**, 2165–2169 (1999).
141. Glass, J. I. *et al.* Essential genes of a minimal bacterium. *Proc. Natl. Acad. Sci. U. S. A.* **103**, 425–430 (2006).
142. Christen, B. *et al.* The essential genome of a bacterium. *Mol. Syst. Biol.* **7**, 528 (2011).
143. Gibson, D. G. *et al.* Complete chemical synthesis, assembly, and cloning of a Mycoplasma genitalium genome. *Science* **319**, 1215–1220 (2008).
144. Gibson, D. G. *et al.* Creation of a bacterial cell controlled by a chemically synthesized genome. *Science* **329**, 52–56 (2010).

145. Hutchison, C. A. *et al.* Design and synthesis of a minimal bacterial genome. *Science* **351**, aad6253 (2016).
146. Vickers, C. E. The minimal genome comes of age. *Nat. Biotechnol.* **34**, 623–624 (2016).
147. Balish, M. F. Mycoplasma pneumoniae, an underutilized model for bacterial cell biology. *J. Bacteriol.* **196**, 3675–3682 (2014).
148. Weiner, J., Herrmann, R. & Browning, G. F. Transcription in Mycoplasma pneumoniae. *Nucleic Acids Res.* **28**, 4488–4496 (2000).
149. Güell, M. *et al.* Transcriptome complexity in a genome-reduced bacterium. *Science* **326**, 1268–1271 (2009).
150. Maier, T. *et al.* Quantification of mRNA and protein and integration with protein turnover in a bacterium. *Mol. Syst. Biol.* **7**, 511 (2011).
151. Yus, E. *et al.* Transcription start site associated RNAs in bacteria. *Mol. Syst. Biol.* **8**, 585 (2012).
152. Kühner, S. *et al.* Proteome organization in a genome-reduced bacterium. *Science* **326**, 1235–1240 (2009).
153. Schmidl, S. R. *et al.* The stability of cytadherence proteins in Mycoplasma pneumoniae requires activity of the protein kinase PrkC. *Infect. Immun.* **78**, 184–192 (2010).
154. Párraga-Niño, N., Colomé-Calls, N., Canals, F., Querol, E. & Ferrer-Navarro, M. A comprehensive proteome of Mycoplasma genitalium. *J. Proteome Res.* **11**, 3305–3316 (2012).
155. van Noort, V. *et al.* Cross-talk between phosphorylation and lysine acetylation in a genome-reduced bacterium. *Mol. Syst. Biol.* **8**, 571 (2012).
156. Wodke, J. A. H. *et al.* Dissecting the energy metabolism in Mycoplasma pneumoniae through genome-scale metabolic modeling. *Mol. Syst. Biol.* **9**, 653 (2013).
157. Lluch-Senar, M. *et al.* Comprehensive Methylome Characterization of Mycoplasma genitalium and Mycoplasma pneumoniae at Single-Base Resolution. *PLOS Genet.* **9**, e1003191 (2013).
158. Karr, J. R. *et al.* A whole-cell computational model predicts phenotype from genotype. *Cell* **150**, 389–401 (2012).
159. McGowin, C. L. & Totten, P. A. The Unique Microbiology and Molecular Pathogenesis of Mycoplasma genitalium. *J. Infect. Dis.* **216**, S382–S388 (2017).
160. Ito, S. *et al.* Fulminant Mycoplasma pneumoniae pneumonia with marked elevation of serum soluble interleukin-2 receptor. *Intern. Med. Tokyo Jpn.* **34**, 430–435 (1995).
161. Radisic, M., Torn, A., Gutierrez, P., Defranchi, H. A. & Pardo, P. Severe acute lung injury caused by Mycoplasma pneumoniae: potential role for steroid pulses in treatment. *Clin. Infect. Dis. Off. Publ. Infect. Dis. Soc. Am.* **31**, 1507–1511 (2000).
162. Rawadi, G. & Roman-Roman, S. Mycoplasma membrane lipoproteins induced proinflammatory cytokines by a mechanism distinct from that of lipopolysaccharide. *Infect. Immun.* **64**, 637–643 (1996).
163. McGowin, C. L., Ma, L., Martin, D. H. & Pyles, R. B. Mycoplasma genitalium-encoded MG309 activates NF-kappaB via Toll-like receptors 2 and 6 to elicit proinflammatory cytokine secretion from human genital epithelial cells. *Infect. Immun.* **77**, 1175–1181 (2009).
164. Wu, Y. *et al.* Mycoplasma genitalium lipoproteins induce human monocytic cell expression of proinflammatory cytokines and apoptosis by activating nuclear factor kappaB. *Mediators Inflamm.* **2008**, 195427 (2008).
165. Hallamaa, K. M., Tang, S.-L., Ficorilli, N. & Browning, G. F. Differential expression of lipoprotein genes in Mycoplasma pneumoniae after contact with human lung epithelial cells, and under oxidative and acidic stress. *BMC Microbiol.* **8**, 124 (2008).
166. Goret, J. *et al.* Surface lipoproteome of Mycoplasma hominis PG21 and differential expression after contact with human dendritic cells. *Future Microbiol.* **11**, 179–194 (2016).
167. Shimizu, T. Inflammation-inducing Factors of Mycoplasma pneumoniae. *Front. Microbiol.* **7**, 414 (2016).
168. Halbedel, S., Hames, C. & Stülke, J. Regulation of carbon metabolism in the mollicutes and its relation to virulence. *J. Mol. Microbiol. Biotechnol.* **12**, 147–154 (2007).
169. Blötz, C. & Stülke, J. Glycerol metabolism and its implication in virulence in Mycoplasma. *FEMS Microbiol. Rev.* **41**, 640–652 (2017).
170. Stroud, R. M. *et al.* Glycerol facilitator GlpF and the associated aquaporin family of channels. *Curr. Opin. Struct. Biol.* **13**, 424–431 (2003).

171. Vilei, E. M. & Frey, J. Genetic and biochemical characterization of glycerol uptake in mycoplasma mycoides subsp. mycoides SC: its impact on H(2)O(2) production and virulence. *Clin. Diagn. Lab. Immunol.* **8**, 85–92 (2001).
172. Schmidl, S. R. *et al.* A trigger enzyme in Mycoplasma pneumoniae: impact of the glycerophosphodiesterase GlpQ on virulence and gene expression. *PLoS Pathog.* **7**, e1002263 (2011).
173. Hames, C., Halbedel, S., Hoppert, M., Frey, J. & Stülke, J. Glycerol metabolism is important for cytotoxicity of Mycoplasma pneumoniae. *J. Bacteriol.* **191**, 747–753 (2009).
174. Szczepanek, S. M., Boccaccio, M., Pflaum, K., Liao, X. & Geary, S. J. Hydrogen peroxide production from glycerol metabolism is dispensable for virulence of Mycoplasma gallisepticum in the tracheas of chickens. *Infect. Immun.* **82**, 4915–4920 (2014).
175. Cross, C. E. *et al.* Oxygen radicals and human disease. *Ann. Intern. Med.* **107**, 526–545 (1987).
176. Thomas, D. C. The phagocyte respiratory burst: Historical perspectives and recent advances. *Immunol. Lett.* **192**, 88–96 (2017).
177. Kannan, T. R. & Baseman, J. B. ADP-ribosylating and vacuolating cytotoxin of Mycoplasma pneumoniae represents unique virulence determinant among bacterial pathogens. *Proc. Natl. Acad. Sci. U. S. A.* **103**, 6724–6729 (2006).
178. Hardy, R. D. *et al.* Analysis of pulmonary inflammation and function in the mouse and baboon after exposure to Mycoplasma pneumoniae CARDS toxin. *PloS One* **4**, e7562 (2009).
179. Li, G. *et al.* High co-expression of TNF-α and CARDS toxin is a good predictor for refractory Mycoplasma pneumoniae pneumonia. *Mol. Med. Camb. Mass* **25**, 38 (2019).
180. Daubenspeck, J. M. *et al.* Mycoplasma genitalium Biofilms Contain Poly-GlcNAc and Contribute to Antibiotic Resistance. *Front. Microbiol.* **11**, 585524 (2020).
181. Renaudin, H., Tully, J. G. & Bebear, C. In vitro susceptibilities of Mycoplasma genitalium to antibiotics. *Antimicrob. Agents Chemother.* **36**, 870–872 (1992).
182. Haggerty, C. L. *et al.* Failure of cefoxitin and doxycycline to eradicate endometrial Mycoplasma genitalium and the consequence for clinical cure of pelvic inflammatory disease. *Sex. Transm. Infect.* **84**, 338–342 (2008).
183. Björnelius, E. *et al.* Antibiotic treatment of symptomatic Mycoplasma genitalium infection in Scandinavia: a controlled clinical trial. *Sex. Transm. Infect.* **84**, 72–76 (2008).
184. Falk, L., Fredlund, H. & Jensen, J. S. Tetracycline treatment does not eradicate Mycoplasma genitalium. *Sex. Transm. Infect.* **79**, 318–319 (2003).
185. Falk, L., Fredlund, H. & Jensen, J. S. Symptomatic urethritis is more prevalent in men infected with Mycoplasma genitalium than with Chlamydia trachomatis. *Sex. Transm. Infect.* **80**, 289–293 (2004).
186. Wikström, A. & Jensen, J. S. Mycoplasma genitalium: a common cause of persistent urethritis among men treated with doxycycline. *Sex. Transm. Infect.* **82**, 276–279 (2006).
187. Jensen, J. S. Mycoplasma genitalium infections. Diagnosis, clinical aspects, and pathogenesis. *Dan. Med. Bull.* **53**, 1–27 (2006).
188. Ferwerda, A., Moll, H. A. & de Groot, R. Respiratory tract infections by Mycoplasma pneumoniae in children: a review of diagnostic and therapeutic measures. *Eur. J. Pediatr.* **160**, 483–491 (2001).
189. Guo, D.-X. *et al.* Epidemiology and mechanism of drug resistance of Mycoplasma pneumoniae in Beijing, China: A multicenter study. *Bosn. J. Basic Med. Sci.* **19**, 288–296 (2019).
190. Wang, Y. *et al.* Increased Macrolide Resistance Rate of M3562 Mycoplasma pneumoniae Correlated With Macrolide Usage and Genotype Shifting. *Front. Cell. Infect. Microbiol.* **11**, 675466 (2021).
191. Braam, J. F., van Dommelen, L., Henquet, C. J. M., van de Bovenkamp, J. H. B. & Kusters, J. G. Multidrug-resistant Mycoplasma genitalium infections in Europe. *Eur. J. Clin. Microbiol. Infect. Dis. Off. Publ. Eur. Soc. Clin. Microbiol.* **36**, 1565–1567 (2017).
192. Couldwell, D. L. & Lewis, D. A. Mycoplasma genitalium infection: current treatment options, therapeutic failure, and resistance-associated mutations. *Infect. Drug Resist.* **8**, 147–161 (2015).
193. Zhang, Q., Guo, Z. & MacDonald, N. E. Vaccine Preventable Community-acquired Pneumonia in Hospitalized Children in Northwest China. *Pediatr. Infect. Dis. J.* **30**, 7 (2011).
194. Lahiry, A., Fan, Y., Stimple, S. D., Raith, M. & Wood, D. W. Inteins as tools for tagless and traceless protein purification. *J. Chem. Technol. Biotechnol.* **93**, 1827–1835 (2018).
195. Yu, H., Karunakaran, K. P., Jiang, X. & Brunham, R. C. Subunit vaccines for the prevention of mucosal infection with Chlamydia trachomatis. *Expert Rev. Vaccines* **15**, 977–988 (2016).

196. Fitch, W. M., Peterson, E. M. & de la Maza, L. M. Phylogenetic analysis of the outer-membrane-protein genes of Chlamydiae, and its implication for vaccine development. *Mol. Biol. Evol.* **10**, 892–913 (1993).
197. Pal, S., Theodor, I., Peterson, E. M. & de la Maza, L. M. Immunization with the Chlamydia trachomatis Mouse Pneumonitis Major Outer Membrane Protein Can Elicit a Protective Immune Response against a Genital Challenge. *Infect. Immun.* **69**, 6240–6247 (2001).
198. Dumke, R. & Jacobs, E. Antibody Response to Mycoplasma pneumoniae: Protection of Host and Influence on Outbreaks? *Front. Microbiol.* **7**, (2016).
199. Nogueira, W. G. *et al.* Computational identification of putative common genomic drug and vaccine targets in Mycoplasma genitalium. *Genomics* **113**, 2730–2743 (2021).
200. Moxon, R., Reche, P. A. & Rappuoli, R. Editorial: Reverse Vaccinology. *Front. Immunol.* **10**, 2776 (2019).
201. Khan, S. *et al.* Proteome-wide mapping and reverse vaccinology-based B and T cell multi-epitope subunit vaccine designing for immune response reinforcement against Porphyromonas gingivalis. *J. Biomol. Struct. Dyn.* **40**, 833–847 (2022).
202. Akter, A. *et al.* Computational approach for identifying immunogenic epitopes and optimizing peptide vaccine through in-silico cloning against Mycoplasma genitalium. *Heliyon* **10**, (2024).
203. Vink, C., Rudenko, G. & Seifert, H. S. Microbial antigenic variation mediated by homologous DNA recombination. *FEMS Microbiol. Rev.* **36**, 917–948 (2012).
204. Shao, W., Li, X., Goraya, M. U., Wang, S. & Chen, J.-L. Evolution of Influenza A Virus by Mutation and Re-Assortment. *Int. J. Mol. Sci.* **18**, 1650 (2017).
205. Dehon, P. M. & McGowin, C. L. The Immunopathogenesis of Mycoplasma genitalium Infections in Women: A Narrative Review. *Sex. Transm. Dis.* **44**, 428–432 (2017).
206. Qin, L., Chen, Y. & You, X. Subversion of the Immune Response by Human Pathogenic Mycoplasmas. *Front. Microbiol.* **10**, 1934 (2019).
207. Citti, C., Nouvel, L.-X. & Baranowski, E. Phase and Antigenic Variation In Mycoplasmas. *Future Microbiol.* **5**, 1073–1085 (2010).
208. Dumke, R., Schurwanz, N. & Jacobs, E. Characterisation of subtype- and variant-specific antigen regions of the P1 adhesin of Mycoplasma pneumoniae. *Int. J. Med. Microbiol. IJMM* **298**, 483–491 (2008).
209. Torres-Puig, S., Broto, A., Querol, E., Piñol, J. & Pich, O. Q. A novel sigma factor reveals a unique regulon controlling cell-specific recombination in Mycoplasma genitalium. *Nucleic Acids Res.* **43**, 4923–4936 (2015).
210. Torres Puig, S. Study of a master regulator of recombination in Mycoplasma genitalium. (2017).
211. Burgos, R. & Totten, P. A. MG428 is a novel positive regulator of recombination that triggers mgpB and mgpC gene variation in Mycoplasma genitalium. *Mol. Microbiol.* **94**, 290–306 (2014).
212. Peterson, S. N., Hu, P. C., Bott, K. F. & Hutchison, C. A. A survey of the Mycoplasma genitalium genome by using random sequencing. *J. Bacteriol.* **175**, 7918–7930 (1993).
213. Peterson, S. N. *et al.* Characterization of repetitive DNA in the Mycoplasma genitalium genome: possible role in the generation of antigenic variation. *Proc. Natl. Acad. Sci. U. S. A.* **92**, 11829–11833 (1995).
214. Ruland, K., Wenzel, R. & Herrmann, R. Analysis of three different repeated DNA elements present in the P1 operon of Mycoplasma pneumoniae: size, number and distribution on the genome. *Nucleic Acids Res.* **18**, 6311–6317 (1990).
215. Su, C. J., Chavoya, A. & Baseman, J. B. Regions of Mycoplasma pneumoniae cytadhesin P1 structural gene exist as multiple copies. *Infect. Immun.* **56**, 3157–3161 (1988).
216. Ma, L. *et al.* Mycoplasma genitalium: an efficient strategy to generate genetic variation from a minimal genome. *Mol. Microbiol.* **66**, 220–236 (2007).
217. Spuesens, E. B. M. *et al.* Sequence variations in RepMP2/3 and RepMP4 elements reveal intragenomic homologous DNA recombination events in Mycoplasma pneumoniae. *Microbiol. Read. Engl.* **155**, 2182–2196 (2009).
218. Spuesens, E. B. M. *et al.* Variation in a surface-exposed region of the Mycoplasma pneumoniae P40 protein as a consequence of homologous DNA recombination between RepMP5 elements. *Microbiol. Read. Engl.* **157**, 473–483 (2011).
219. Fookes, M. C. *et al.* Mycoplasma genitalium: whole genome sequence analysis, recombination and population structure. *BMC Genomics* **18**, 993 (2017).

220. Iverson-Cabral, S. L., Astete, S. G., Cohen, C. R., Rocha, E. P. C. & Totten, P. A. Intrastrain heterogeneity of the mgpB gene in Mycoplasma genitalium is extensive in vitro and in vivo and suggests that variation is generated via recombination with repetitive chromosomal sequences. *Infect. Immun.* **74**, 3715–3726 (2006).
221. Iverson-Cabral, S. L., Astete, S. G., Cohen, C. R. & Totten, P. A. mgpB and mgpC sequence diversity in Mycoplasma genitalium is generated by segmental reciprocal recombination with repetitive chromosomal sequences. *Mol. Microbiol.* **66**, 55–73 (2007).
222. Ma, L. *et al.* Extensive variation and rapid shift of the MG192 sequence in Mycoplasma genitalium strains from patients with chronic infection. *Infect. Immun.* **82**, 1326–1334 (2014).
223. Ma, L., Jensen, J. S., Mancuso, M., Myers, L. & Martin, D. H. Kinetics of Genetic Variation of the Mycoplasma genitalium MG192 Gene in Experimentally Infected Chimpanzees. *Infect. Immun.* **84**, 747–753 (2015).
224. Razin, S. & Jacobs, E. Mycoplasma adhesion. *J. Gen. Microbiol.* **138**, 407–422 (1992).
225. Atkinson, T. P., Balish, M. F. & Waites, K. B. Epidemiology, clinical manifestations, pathogenesis and laboratory detection of Mycoplasma pneumoniae infections. *FEMS Microbiol. Rev.* **32**, 956–973 (2008).
226. Hardy, R. D. *et al.* Mycoplasma pneumoniae induces chronic respiratory infection, airway hyperreactivity, and pulmonary inflammation: a murine model of infection-associated chronic reactive airway disease. *Infect. Immun.* **70**, 649–654 (2002).
227. McGowin, C. L., Spagnuolo, R. A. & Pyles, R. B. Mycoplasma genitalium rapidly disseminates to the upper reproductive tracts and knees of female mice following vaginal inoculation. *Infect. Immun.* **78**, 726–736 (2010).
228. Wood, G. E., Patton, D. L., Cummings, P. K., Iverson-Cabral, S. L. & Totten, P. A. Experimental Infection of Pig-Tailed Macaques (Macaca nemestrina) with Mycoplasma genitalium. *Infect. Immun.* **85**, e00738-16 (2017).
229. Minion, F. C., Jarvill-Taylor, K. J., Billings, D. E. & Tigges, E. Membrane-associated nuclease activities in mycoplasmas. *J. Bacteriol.* **175**, 7842–7847 (1993).
230. Dybvig, K., Sitaraman, R. & French, C. T. A family of phase-variable restriction enzymes with differing specificities generated by high-frequency gene rearrangements. *Proc. Natl. Acad. Sci. U. S. A.* **95**, 13923–13928 (1998).
231. Dybvig, K. & Cassell, G. H. Transposition of gram-positive transposon Tn916 in Acholeplasma laidlawii and Mycoplasma pulmonis. *Science* **235**, 1392–1394 (1987).
232. King, K. W. & Dybvig, K. Plasmid transformation of Mycoplasma mycoides subspecies mycoides is promoted by high concentrations of polyethylene glycol. *Plasmid* **26**, 108–115 (1991).
233. Minion, F. C. & Kapke, P. A. Transformation of mycoplasmas. *Methods Mol. Biol. Clifton NJ* **104**, 227–234 (1998).
234. Hedreyda, C. T., Lee, K. K. & Krause, D. C. Transformation of Mycoplasma pneumoniae with Tn4001 by electroporation. *Plasmid* **30**, 170–175 (1993).
235. Xavier, J. C., Patil, K. R. & Rocha, I. Systems biology perspectives on minimal and simpler cells. *Microbiol. Mol. Biol. Rev. MMBR* **78**, 487–509 (2014).
236. Maglennon, G. A. *et al.* Development of a self-replicating plasmid system for Mycoplasma hyopneumoniae. *Vet. Res.* **44**, 63 (2013).
237. Cordova, C. M. M. *et al.* Identification of the Origin of Replication of the Mycoplasma pulmonis Chromosome and Its Use in oriC Replicative Plasmids. *J. Bacteriol.* **184**, 5426–5435 (2002).
238. Lee, S.-W., Browning, G. F. & Markham, P. F. Development of a replicable oriC plasmid for Mycoplasma gallisepticum and Mycoplasma imitans, and gene disruption through homologous recombination in M. gallisepticum. *Microbiology* **154**, 2571–2580 (2008).
239. Lee, S.-W., Browning, G. F. & Markham, P. F. Development of a replicable oriC plasmid for Mycoplasma gallisepticum and Mycoplasma imitans, and gene disruption through homologous recombination in M. gallisepticum. *Microbiol. Read. Engl.* **154**, 2571–2580 (2008).
240. Sharma, S. *et al.* Development and Host Compatibility of Plasmids for Two Important Ruminant Pathogens, Mycoplasma bovis and Mycoplasma agalactiae. *PLoS ONE* **10**, e0119000 (2015).
241. Dhandayuthapani, S., Rasmussen, W. G. & Baseman, J. B. Disruption of gene mg218 of Mycoplasma genitalium through homologous recombination leads to an adherence-deficient phenotype. *Proc. Natl. Acad. Sci.* **96**, 5227–5232 (1999).

242. Mahairas, G. G. & Minion, F. C. Transformation of Mycoplasma pulmonis: demonstration of homologous recombination, introduction of cloned genes, and preliminary description of an integrating shuttle system. *J. Bacteriol.* **171**, 1775–1780 (1989).
243. Krishnakumar, R. *et al.* Targeted chromosomal knockouts in Mycoplasma pneumoniae. *Appl. Environ. Microbiol.* **76**, 5297–5299 (2010).
244. Pich, O. Q., Burgos, R., Planell, R., Querol, E. & Piñol, J. Comparative analysis of antibiotic resistance gene markers in Mycoplasma genitalium: application to studies of the minimal gene complement. *Microbiol. Read. Engl.* **152**, 519–527 (2006).
245. Hasselbring, B. M., Page, C. A., Sheppard, E. S. & Krause, D. C. Transposon mutagenesis identifies genes associated with Mycoplasma pneumoniae gliding motility. *J. Bacteriol.* **188**, 6335–6345 (2006).
246. Pich, O. Q., Burgos, R., Ferrer-Navarro, M., Querol, E. & Piñol, J. Mycoplasma genitalium mg200 and mg386 genes are involved in gliding motility but not in cytadherence. *Mol. Microbiol.* **60**, 1509–1519 (2006).
247. Mahairas, G. G. & Minion, F. C. Random insertion of the gentamicin resistance transposon Tn4001 in Mycoplasma pulmonis. *Plasmid* **21**, 43–47 (1989).
248. Hahn, T. W., Mothershed, E. A., Waldo, R. H. & Krause, D. C. Construction and analysis of a modified Tn4001 conferring chloramphenicol resistance in Mycoplasma pneumoniae. *Plasmid* **41**, 120–124 (1999).
249. Algire, M. A. *et al.* New selectable marker for manipulating the simple genomes of Mycoplasma species. *Antimicrob. Agents Chemother.* **53**, 4429–4432 (2009).
250. Lyon, B. R., May, J. W. & Skurray, R. A. Tn4001: a gentamicin and kanamycin resistance transposon in Staphylococcus aureus. *Mol. Gen. Genet. MGG* **193**, 554–556 (1984).
251. Reddy, S. P., Rasmussen, W. G. & Baseman, J. B. Isolation and characterization of transposon Tn4001-generated, cytadherence-deficient transformants of Mycoplasma pneumoniae and Mycoplasma genitalium. *FEMS Immunol. Med. Microbiol.* **15**, 199–211 (1996).
252. Pour-El, I., Adams, C. & Minion, F. C. Construction of mini-Tn4001tet and its use in Mycoplasma gallisepticum. *Plasmid* **47**, 129–137 (2002).
253. Montero-Blay, A., Miravet-Verde, S., Lluch-Senar, M., Piñero-Lambea, C. & Serrano, L. SynMyco transposon: engineering transposon vectors for efficient transformation of minimal genomes. *DNA Res. Int. J. Rapid Publ. Rep. Genes Genomes* **26**, 327–339 (2019).
254. Bergemann, A. D., Whitley, J. C. & Finch, L. R. Homology of mycoplasma plasmid pADB201 and staphylococcal plasmid pE194. *J. Bacteriol.* **171**, 593–595 (1989).
255. Lartigue, C., Blanchard, A., Renaudin, J., Thiaucourt, F. & Sirand-Pugnet, P. Host specificity of mollicutes oriC plasmids: functional analysis of replication origin. *Nucleic Acids Res.* **31**, 6610–6618 (2003).
256. Shahid, M. A., Marenda, M. S., Markham, P. F. & Noormohammadi, A. H. Development of an oriC vector for use in Mycoplasma synoviae. *J. Microbiol. Methods* **103**, 70–76 (2014).
257. Li, J. *et al.* Development of a replicative plasmid for gene expression in Mycoplasma bovis. *J. Microbiol. Methods* **108**, 12–18 (2015).
258. Ishag, H. Z. A. *et al.* A replicating plasmid-based vector for GFP expression in Mycoplasma hyopneumoniae. *Genet. Mol. Res. GMR* **15**, (2016).
259. Ishag, H. Z. A., Xiong, Q., Liu, M., Feng, Z. & Shao, G. Development of oriC-plasmids for use in Mycoplasma hyorhinis. *Sci. Rep.* **7**, 10596 (2017).
260. Blötz, C. *et al.* Development of a replicating plasmid based on the native oriC in Mycoplasma pneumoniae. *Microbiol. Read. Engl.* **164**, 1372–1382 (2018).
261. Mariscal, A. M., González-González, L., Querol, E. & Piñol, J. All-in-one construct for genome engineering using Cre-lox technology. *DNA Res. Int. J. Rapid Publ. Rep. Genes Genomes* **23**, 263–270 (2016).
262. Breton, M. *et al.* First report of a tetracycline-inducible gene expression system for mollicutes. *Microbiol. Read. Engl.* **156**, 198–205 (2010).
263. Qi, L. S. *et al.* Repurposing CRISPR as an RNA-guided platform for sequence-specific control of gene expression. *Cell* **152**, 1173–1183 (2013).
264. Mariscal, A. M. *et al.* Tuning Gene Activity by Inducible and Targeted Regulation of Gene Expression in Minimal Bacterial Cells. *ACS Synth. Biol.* **7**, 1538–1552 (2018).

265. Hatchel, J. M. & Balish, M. F. Attachment organelle ultrastructure correlates with phylogeny, not gliding motility properties, in Mycoplasma pneumoniae relatives. *Microbiology* **154**, 286–295 (2008).
266. Meng, K. E. & Pfister, R. M. Intracellular structures of Mycoplasma pneumoniae revealed after membrane removal. *J. Bacteriol.* **144**, 390–399 (1980).
267. Seybert, A., Herrmann, R. & Frangakis, A. S. Structural analysis of Mycoplasma pneumoniae by cryo-electron tomography. *J. Struct. Biol.* **156**, 342–354 (2006).
268. Henderson, G. P. & Jensen, G. J. Three-dimensional structure of Mycoplasma pneumoniae's attachment organelle and a model for its role in gliding motility. *Mol. Microbiol.* **60**, 376–385 (2006).
269. Kawamoto, A. *et al.* Periodicity in Attachment Organelle Revealed by Electron Cryotomography Suggests Conformational Changes in Gliding Mechanism of Mycoplasma pneumoniae. *mBio* **7**, e00243-16 (2016).
270. Gonzalez-Gonzalez, L. Functional and structural analyses of the terminal organelle of Mycoplasma genitalium. (Universitat Autònoma de Barcelona, 2015).
271. Nakane, D., Kenri, T., Matsuo, L. & Miyata, M. Systematic Structural Analyses of Attachment Organelle in Mycoplasma pneumoniae. *PLoS Pathog.* **11**, e1005299 (2015).
272. Krause, D. C. & Balish, M. F. Cellular engineering in a minimal microbe: structure and assembly of the terminal organelle of Mycoplasma pneumoniae. *Mol. Microbiol.* **51**, 917–924 (2004).
273. Nakane, D. & Miyata, M. *Gliding Mechanism of the Mycoplasma Pneumoniae Subgroup: Implications from Studies on Mycoplasma Mobile*. (2013).
274. Dyson, H. J. & Wright, P. E. Intrinsically unstructured proteins and their functions. *Nat. Rev. Mol. Cell Biol.* **6**, 197–208 (2005).
275. Burgos, R., Pich, O. Q., Querol, E. & Piñol, J. Functional analysis of the Mycoplasma genitalium MG312 protein reveals a specific requirement of the MG312 N-terminal domain for gliding motility. *J. Bacteriol.* **189**, 7014–7023 (2007).
276. Burgos, R., Pich, O. Q., Querol, E. & Piñol, J. Deletion of the Mycoplasma genitalium MG_217 gene modifies cell gliding behaviour by altering terminal organelle curvature. *Mol. Microbiol.* **69**, 1029–1040 (2008).
277. Pich, O. Q., Burgos, R., Querol, E. & Piñol, J. P110 and P140 Cytadherence-Related Proteins Are Negative Effectors of Terminal Organelle Duplication in Mycoplasma genitalium. *PLoS ONE* **4**, e7452 (2009).
278. García-Morales, L., González-González, L., Querol, E. & Piñol, J. A minimized motile machinery for Mycoplasma genitalium. *Mol. Microbiol.* **100**, 125–138 (2016).
279. Stevens, M. K. & Krause, D. C. Mycoplasma pneumoniae cytadherence phase-variable protein HMW3 is a component of the attachment organelle. *J. Bacteriol.* **174**, 4265–4274 (1992).
280. Hahn, T. W., Willby, M. J. & Krause, D. C. HMW1 is required for cytadhesin P1 trafficking to the attachment organelle in Mycoplasma pneumoniae. *J. Bacteriol.* **180**, 1270–1276 (1998).
281. Krause, D. C. & Balish, M. F. Structure, function, and assembly of the terminal organelle of Mycoplasma pneumoniae. *FEMS Microbiol. Lett.* **198**, 1–7 (2001).
282. Balish, M. F., Hahn, T. W., Popham, P. L. & Krause, D. C. Stability of Mycoplasma pneumoniae cytadherence-accessory protein HMW1 correlates with its association with the triton shell. *J. Bacteriol.* **183**, 3680–3688 (2001).
283. Willby, M. J. & Krause, D. C. Characterization of a Mycoplasma pneumoniae hmw3 mutant: implications for attachment organelle assembly. *J. Bacteriol.* **184**, 3061–3068 (2002).
284. Willby, M. J. *et al.* HMW1 is required for stability and localization of HMW2 to the attachment organelle of Mycoplasma pneumoniae. *J. Bacteriol.* **186**, 8221–8228 (2004).
285. Chaudhry, R., Varshney, A. K. & Malhotra, P. Adhesion proteins of Mycoplasma pneumoniae. *Front. Biosci. J. Virtual Libr.* **12**, 690–699 (2007).
286. Relich, R. F. & Balish, M. F. Insights into the function of Mycoplasma pneumoniae protein P30 from orthologous gene replacement. *Microbiology* **157**, 2862–2870 (2011).
287. Cloward, J. M. & Krause, D. C. Loss of co-chaperone TopJ impacts adhesin P1 presentation and terminal organelle maturation in Mycoplasma pneumoniae. *Mol. Microbiol.* **81**, 528–539 (2011).
288. Seto, S. & Miyata, M. Attachment Organelle Formation Represented by Localization of Cytadherence Proteins and Formation of the Electron-Dense Core in Wild-Type and Mutant Strains of Mycoplasma pneumoniae. *J. Bacteriol.* **185**, 1082–1091 (2003).

289. Balish, M. F., Santurri, R. T., Ricci, A. M., Lee, K. K. & Krause, D. C. Localization of Mycoplasma pneumoniae cytadherence-associated protein HMW2 by fusion with green fluorescent protein: implications for attachment organelle structure. *Mol. Microbiol.* **47**, 49–60 (2003).
290. Seto, S., Layh-Schmitt, G., Kenri, T. & Miyata, M. Visualization of the Attachment Organelle and Cytadherence Proteins of Mycoplasma pneumoniae by Immunofluorescence Microscopy. *J. Bacteriol.* **183**, 1621–1630 (2001).
291. Hasselbring, B. M., Jordan, J. L., Krause, R. W. & Krause, D. C. Terminal organelle development in the cell wall-less bacterium Mycoplasma pneumoniae. *Proc. Natl. Acad. Sci. U. S. A.* **103**, 16478–16483 (2006).
292. Kenri, T. *et al.* Use of fluorescent-protein tagging to determine the subcellular localization of mycoplasma pneumoniae proteins encoded by the cytadherence regulatory locus. *J. Bacteriol.* **186**, 6944–6955 (2004).
293. Hasselbring, B. M. & Krause, D. C. Proteins P24 and P41 function in the regulation of terminal-organelle development and gliding motility in Mycoplasma pneumoniae. *J. Bacteriol.* **189**, 7442–7449 (2007).
294. Cloward, J. M. & Krause, D. C. Mycoplasma pneumoniae J-domain protein required for terminal organelle function. *Mol. Microbiol.* **71**, 1296–1307 (2009).
295. Miyata, M. & Hamaguchi, T. Integrated Information and Prospects for Gliding Mechanism of the Pathogenic Bacterium Mycoplasma pneumoniae. *Front. Microbiol.* **7**, 960 (2016).
296. Kelley, L. A. & Sternberg, M. J. E. Protein structure prediction on the Web: a case study using the Phyre server. *Nat. Protoc.* **4**, 363–371 (2009).
297. Layh-Schmitt, G., Podtelejnikov, A. & Mann, M. Proteins complexed to the P1 adhesin of Mycoplasma pneumoniae. *Microbiol. Read. Engl.* **146 (Pt 3)**, 741–747 (2000).
298. Nakane, D., Adan-Kubo, J., Kenri, T. & Miyata, M. Isolation and Characterization of P1 Adhesin, a Leg Protein of the Gliding Bacterium Mycoplasma pneumoniae. *J. Bacteriol.* **193**, 715–722 (2011).
299. Scheffer, M. P. *et al.* Structural characterization of the NAP; the major adhesion complex of the human pathogen Mycoplasma genitalium. *Mol. Microbiol.* **105**, 869–879 (2017).
300. Seto, S., Kenri, T., Tomiyama, T. & Miyata, M. Involvement of P1 Adhesin in Gliding Motility of Mycoplasma pneumoniae as Revealed by the Inhibitory Effects of Antibody under Optimized Gliding Conditions. *J. Bacteriol.* **187**, 1875–1877 (2005).
301. Iverson-Cabral, S. L., Wood, G. E. & Totten, P. A. Analysis of the Mycoplasma genitalium MgpB Adhesin to Predict Membrane Topology, Investigate Antibody Accessibility, Characterize Amino Acid Diversity, and Identify Functional and Immunogenic Epitopes. *PloS One* **10**, e0138244 (2015).
302. Jordan, J. L., Berry, K. M., Balish, M. F. & Krause, D. C. Stability and subcellular localization of cytadherence-associated protein P65 in Mycoplasma pneumoniae. *J. Bacteriol.* **183**, 7387–7391 (2001).
303. Chang, H.-Y., Jordan, J. L. & Krause, D. C. Domain analysis of protein P30 in Mycoplasma pneumoniae cytadherence and gliding motility. *J. Bacteriol.* **193**, 1726–1733 (2011).
304. Hasselbring, B. M., Jordan, J. L. & Krause, D. C. Mutant analysis reveals a specific requirement for protein P30 in Mycoplasma pneumoniae gliding motility. *J. Bacteriol.* **187**, 6281–6289 (2005).
305. Romero-Arroyo, C. E. *et al.* Mycoplasma pneumoniae protein P30 is required for cytadherence and associated with proper cell development. *J. Bacteriol.* **181**, 1079–1087 (1999).
306. Hasselbring, B. M., Sheppard, E. S. & Krause, D. C. P65 truncation impacts P30 dynamics during Mycoplasma pneumoniae gliding. *J. Bacteriol.* **194**, 3000–3007 (2012).
307. Krause, D. C. *et al.* Transposon mutagenesis reinforces the correlation between Mycoplasma pneumoniae cytoskeletal protein HMW2 and cytadherence. *J. Bacteriol.* **179**, 2668–2677 (1997).
308. Popham, P. L., Hahn, T.-W., Krebes, K. A. & Krause, D. C. Loss of HMW1 and HMW3 in noncytadhering mutants of Mycoplasma pneumoniae occurs post-translationally. *Proc. Natl. Acad. Sci. U. S. A.* **94**, 13979–13984 (1997).
309. Calisto, B. M. *et al.* The EAGR box structure: a motif involved in mycoplasma motility. *Mol. Microbiol.* **86**, 382–393 (2012).
310. Jordan, J. L. *et al.* Protein P200 Is Dispensable for Mycoplasma pneumoniae Hemadsorption but Not Gliding Motility or Colonization of Differentiated Bronchial Epithelium. *Infect. Immun.* **75**, 518–522 (2007).
311. Kawakita, Y. *et al.* Structural Study of MPN387, an Essential Protein for Gliding Motility of a Human-Pathogenic Bacterium, Mycoplasma pneumoniae. *J. Bacteriol.* **198**, 2352–2359 (2016).

312. Cloward, J. M. & Krause, D. C. Functional domain analysis of the Mycoplasma pneumoniae co-chaperone TopJ. *Mol. Microbiol.* **77**, 158–169 (2010).
313. Broto, A., Piñol Ribas, J. & Querol Murillo, E. Anàlisi funcional de dominis de proteïnes implicades en la motilitat de Mycoplasma genitalium. (Universitat Autònoma de Barcelona, Barcelona, 2015).
314. Hasselbring, B. M. & Krause, D. C. Cytoskeletal protein P41 is required to anchor the terminal organelle of the wall-less prokaryote Mycoplasma pneumoniae. *Mol. Microbiol.* **63**, 44–53 (2007).
315. Martinelli, L. *et al.* Structure-Guided Mutations in the Terminal Organelle Protein MG491 Cause Major Motility and Morphologic Alterations on Mycoplasma genitalium. *PLoS Pathog.* **12**, e1005533 (2016).
316. Wilson, M. H. & Collier, A. M. Ultrastructural study of Mycoplasma pneumoniae in organ culture. *J. Bacteriol.* **125**, 332–339 (1976).
317. Shimizu, T. & Miyata, M. Electron microscopic studies of three gliding Mycoplasmas, Mycoplasma mobile, M. pneumoniae, and M. gallisepticum, by using the freeze-substitution technique. *Curr. Microbiol.* **44**, 431–434 (2002).
318. Hegermann, J., Herrmann, R. & Mayer, F. Cytoskeletal elements in the bacterium Mycoplasma pneumoniae. *Naturwissenschaften* **89**, 453–458 (2002).
319. McBride, M. J. Bacterial gliding motility: multiple mechanisms for cell movement over surfaces. *Annu. Rev. Microbiol.* **55**, 49–75 (2001).
320. Jarrell, K. F. & McBride, M. J. The surprisingly diverse ways that prokaryotes move. *Nat. Rev. Microbiol.* **6**, 466–476 (2008).
321. Miyata, M. *et al.* Tree of motility – A proposed history of motility systems in the tree of life. *Genes Cells* **25**, 6–21 (2020).
322. Hug, L. A. *et al.* A new view of the tree of life. *Nat. Microbiol.* **1**, 16048 (2016).
323. Castelle, C. J. & Banfield, J. F. Major New Microbial Groups Expand Diversity and Alter our Understanding of the Tree of Life. *Cell* **172**, 1181–1197 (2018).
324. Miyata, M. Centipede and inchworm models to explain Mycoplasma gliding. *Trends Microbiol.* **16**, 6–12 (2008).
325. Mizutani, M., Tulum, I., Kinosita, Y., Nishizaka, T. & Miyata, M. Detailed Analyses of Stall Force Generation in Mycoplasma mobile Gliding. *Biophys. J.* **114**, 1411–1419 (2018).
326. Nishikawa, M. S. *et al.* Refined Mechanism of Mycoplasma mobile Gliding Based on Structure, ATPase Activity, and Sialic Acid Binding of Machinery. *mBio* **10**, e02846-19 (2019).
327. Matsuike, D. *et al.* Structure and Function of Gli123 Involved in Mycoplasma mobile Gliding. *J. Bacteriol.* **205**, e00340-22 (2023).
328. Miyata, M. Unique centipede mechanism of Mycoplasma gliding. *Annu. Rev. Microbiol.* **64**, 519–537 (2010).
329. Wolgemuth, C. W., Igoshin, O. & Oster, G. The motility of mollicutes. *Biophys. J.* **85**, 828–842 (2003).
330. Jurkovic, D. A., Hughes, M. R. & Balish, M. F. Analysis of energy sources for Mycoplasma penetrans gliding motility. *FEMS Microbiol. Lett.* **338**, 39–45 (2013).
331. Mizutani, M. & Miyata, M. Behaviors and Energy Source of Mycoplasma gallisepticum Gliding. *J. Bacteriol.* **201**, e00397-19 (2019).
332. Vicente, M., Gomez, M. J. & Ayala, J. A. Regulation of transcription of cell division genes in the Escherichia coli dcw cluster. *Cell. Mol. Life Sci. CMLS* **54**, 317–324 (1998).
333. Ayala, J. A., Garrido, T., De Pedro, M. A. & Vicente, M. Chapter 5 Molecular biology of bacterial septation. in *New Comprehensive Biochemistry* (eds. Ghuysen, J.-M. & Hakenbeck, R.) vol. 27 73–101 (Elsevier, 1994).
334. Zhao, Y. *et al.* Cell division gene cluster in Spiroplasma kunkelii: functional characterization of ftsZ and the first report of ftsA in mollicutes. *DNA Cell Biol.* **23**, 127–134 (2004).
335. Bredt, W. Motility and multiplication of Mycoplasma pneumoniae. A phase contrast study. *Pathol. Microbiol. (Basel)* **32**, 321–326 (1968).
336. Martínez-Torró, C. *et al.* Functional Characterization of the Cell Division Gene Cluster of the Wall-less Bacterium Mycoplasma genitalium. *Front. Microbiol.* **12**, 695572 (2021).
337. Lluch-Senar, M., Querol, E. & Piñol, J. Cell division in a minimal bacterium in the absence of ftsZ. *Mol. Microbiol.* **78**, 278–289 (2010).
338. Eraso, J. M. *et al.* The highly conserved MraZ protein is a transcriptional regulator in Escherichia coli. *J. Bacteriol.* **196**, 2053–2066 (2014).

339. Maeda, T., Tanaka, Y., Takemoto, N., Hamamoto, N. & Inui, M. RNase III mediated cleavage of the coding region of mraZ mRNA is required for efficient cell division in Corynebacterium glutamicum. *Mol. Microbiol.* **99**, 1149–1166 (2016).
340. Fisunov, G. Y. *et al.* Binding site of MraZ transcription factor in Mollicutes. *Biochimie* **125**, 59–65 (2016).
341. Kimura, S. & Suzuki, T. Fine-tuning of the ribosomal decoding center by conserved methyl-modifications in the Escherichia coli 16S rRNA. *Nucleic Acids Res.* **38**, 1341–1352 (2010).
342. Kyuma, T. *et al.* Ribosomal RNA methyltransferases contribute to Staphylococcus aureus virulence. *FEBS J.* **282**, 2570–2584 (2015).
343. Zou, J. *et al.* Studies on Aminoglycoside Susceptibility Identify a Novel Function of KsgA To Secure Translational Fidelity during Antibiotic Stress. *Antimicrob. Agents Chemother.* **62**, e00853-18 (2018).
344. Xu, X. *et al.* Beyond a Ribosomal RNA Methyltransferase, the Wider Role of MraW in DNA Methylation, Motility and Colonization in Escherichia coli O157:H7. *Front. Microbiol.* **10**, 2520 (2019).
345. Margolin, W. Themes and variations in prokaryotic cell division. *FEMS Microbiol. Rev.* **24**, 531–548 (2000).
346. Dai, K. & Lutkenhaus, J. ftsZ is an essential cell division gene in Escherichia coli. *J. Bacteriol.* **173**, 3500–3506 (1991).
347. Beall, B. & Lutkenhaus, J. FtsZ in Bacillus subtilis is required for vegetative septation and for asymmetric septation during sporulation. *Genes Dev.* **5**, 447–455 (1991).
348. Margolin, W., Wang, R. & Kumar, M. Isolation of an ftsZ homolog from the archaebacterium Halobacterium salinarium: implications for the evolution of FtsZ and tubulin. *J. Bacteriol.* **178**, 1320–1327 (1996).
349. Sun, Q. & Margolin, W. FtsZ dynamics during the division cycle of live Escherichia coli cells. *J. Bacteriol.* **180**, 2050–2056 (1998).
350. Errington, J., Daniel, R. A. & Scheffers, D.-J. Cytokinesis in bacteria. *Microbiol. Mol. Biol. Rev. MMBR* **67**, 52–65, table of contents (2003).
351. Kasai, T. *et al.* Role of Binding in Mycoplasma mobile and Mycoplasma pneumoniae Gliding Analyzed through Inhibition by Synthesized Sialylated Compounds. *J. Bacteriol.* **195**, 429–435 (2013).
352. Loomes, L. M. *et al.* Erythrocyte receptors for Mycoplasma pneumoniae are sialylated oligosaccharides of Ii antigen type. *Nature* **307**, 560–563 (1984).
353. Vizarraga, D. *et al.* Immunodominant proteins P1 and P40/P90 from human pathogen Mycoplasma pneumoniae. *Nat. Commun.* **11**, 5188 (2020).
354. Nagai, R. & Miyata, M. Gliding motility of Mycoplasma mobile can occur by repeated binding to N-acetylneuraminyllactose (sialyllactose) fixed on solid surfaces. *J. Bacteriol.* **188**, 6469–6475 (2006).
355. Rottem, S. Interaction of mycoplasmas with host cells. *Physiol. Rev.* **83**, 417–432 (2003).
356. Mernaugh, G. R., Dallo, S. F., Holt, S. C. & Baseman, J. B. Properties of Adhering and Nonadhering Populations of Mycoplasma genitalium. *Clin. Infect. Dis.* **17**, S69–S78 (1993).
357. Baseman, J. B., Lange, M., Criscimagna, N. L., Giron, J. A. & Thomas, C. A. Interplay between mycoplasmas and host target cells. *Microb. Pathog.* **19**, 105–116 (1995).
358. Dallo, S. F. & Baseman, J. B. Intracellular DNA replication and long-term survival of pathogenic mycoplasmas. *Microb. Pathog.* **29**, 301–309 (2000).
359. Cohen, C. R. *et al.* Mycoplasma genitalium infection and persistence in a cohort of female sex workers in Nairobi, Kenya. *Sex. Transm. Dis.* **34**, 274–279 (2007).
360. Citti, C. & Blanchard, A. Mycoplasmas and their host: emerging and re-emerging minimal pathogens. *Trends Microbiol.* **21**, 196–203 (2013).
361. Svenstrup, H. F., Fedder, J., Abraham-Peskir, J., Birkelund, S. & Christiansen, G. Mycoplasma genitalium attaches to human spermatozoa. *Hum. Reprod. Oxf. Engl.* **18**, 2103–2109 (2003).
362. Collier, A. M. Attachment of Mycoplasma genitalium to the ciliated epithelium of human fallopian tubes. in *Recent advances in mycoplasmology.* 730–732 (1990).
363. Burgos, R., Pich, O. Q., Querol, E. & Piñol, J. Functional Analysis of the Mycoplasma genitalium MG312 Protein Reveals a Specific Requirement of the MG312 N-Terminal Domain for Gliding Motility. *J. Bacteriol.* **189**, 7014–7023 (2007).
364. Reddy, S. P., Rasmussen, W. G. & Baseman, J. B. Molecular cloning and characterization of an adherence-related operon of Mycoplasma genitalium. *J. Bacteriol.* **177**, 5943–5951 (1995).

365. Dallo, S. F., Kannan, T. R., Blaylock, M. W. & Baseman, J. B. Elongation factor Tu and E1 beta subunit of pyruvate dehydrogenase complex act as fibronectin binding proteins in Mycoplasma pneumoniae. *Mol. Microbiol.* **46**, 1041–1051 (2002).
366. Balasubramanian, S., Kannan, T. R. & Baseman, J. B. The surface-exposed carboxyl region of Mycoplasma pneumoniae elongation factor Tu interacts with fibronectin. *Infect. Immun.* **76**, 3116–3123 (2008).
367. Yueyue, W. *et al.* Pathogenicity and virulence of Mycoplasma genitalium: Unraveling Ariadne's Thread. *Virulence* **13**, 1161–1183 (2022).
368. Gründel, A., Friedrich, K., Pfeiffer, M., Jacobs, E. & Dumke, R. Subunits of the Pyruvate Dehydrogenase Cluster of Mycoplasma pneumoniae Are Surface-Displayed Proteins that Bind and Activate Human Plasminogen. *PloS One* **10**, e0126600 (2015).
369. Gründel, A., Pfeiffer, M., Jacobs, E. & Dumke, R. Network of Surface-Displayed Glycolytic Enzymes in Mycoplasma pneumoniae and Their Interactions with Human Plasminogen. *Infect. Immun.* **84**, 666–676 (2015).
370. Thomas, C., Jacobs, E. & Dumke, R. Characterization of pyruvate dehydrogenase subunit B and enolase as plasminogen-binding proteins in Mycoplasma pneumoniae. *Microbiol. Read. Engl.* **159**, 352–365 (2013).
371. Dumke, R., Hausner, M. & Jacobs, E. Role of Mycoplasma pneumoniae glyceraldehyde-3-phosphate dehydrogenase (GAPDH) in mediating interactions with the human extracellular matrix. *Microbiol. Read. Engl.* **157**, 2328–2338 (2011).
372. Alvarez, R. A., Blaylock, M. W. & Baseman, J. B. Surface localized glyceraldehyde-3-phosphate dehydrogenase of Mycoplasma genitalium binds mucin. *Mol. Microbiol.* **48**, 1417–1425 (2003).
373. Szczepanek, S. M. *et al.* Vaccination of BALB/c Mice with an Avirulent Mycoplasma pneumoniae P30 Mutant Results in Disease Exacerbation upon Challenge with a Virulent Strain. *Infect. Immun.* **80**, 1007–1014 (2012).
374. Techasaensiri, C. *et al.* Variation in colonization, ADP-ribosylating and vacuolating cytotoxin, and pulmonary disease severity among mycoplasma pneumoniae strains. *Am. J. Respir. Crit. Care Med.* **182**, 797–804 (2010).
375. Ofek, I., Hasty, D. L. & Sharon, N. Anti-adhesion therapy of bacterial diseases: prospects and problems. *FEMS Immunol. Med. Microbiol.* **38**, 181–191 (2003).
376. Sharon, N. Carbohydrates as future anti-adhesion drugs for infectious diseases. *Biochim. Biophys. Acta BBA - Gen. Subj.* **1760**, 527–537 (2006).
377. Moonens, K. & Remaut, H. Evolution and structural dynamics of bacterial glycan binding adhesins. *Curr. Opin. Struct. Biol.* **44**, 48–58 (2017).
378. Mernaugh, G. R., Dallo, S. F., Holt, S. C. & Baseman, J. B. Properties of Adhering and Nonadhering Populations of Mycoplasma genitalium. *Clin. Infect. Dis.* **17**, S69–S78 (1993).
379. Burgos, R. *et al.* Mycoplasma genitalium P140 and P110 cytadhesins are reciprocally stabilized and required for cell adhesion and terminal-organelle development. *J. Bacteriol.* **188**, 8627–37 (2006).
380. Scheffer, M. P. *et al.* Structural characterization of the NAP; the major adhesion complex of the human pathogen *Mycoplasma genitalium*. *Mol. Microbiol.* **105**, 869–879 (2017).
381. García-Morales, L., González-González, L., Querol, E. & Piñol, J. A minimized motile machinery for Mycoplasma genitalium. *Mol. Microbiol.* **100**, 125–138 (2016).
382. Nakane, D., Adan-Kubo, J., Kenri, T. & Miyata, M. Isolation and characterization of P1 adhesin, a leg protein of the gliding bacterium Mycoplasma pneumoniae. *J. Bacteriol.* **193**, 715–22 (2011).
383. Aparicio, D. *et al.* Mycoplasma genitalium adhesin P110 binds sialic-acid human receptors. *Nat. Commun.* **9**, 4471 (2018).
384. Otto, M. Physical stress and bacterial colonization. *FEMS Microbiol. Rev.* **38**, 1250–1270 (2014).
385. Herman-Bausier, P. *et al.* Staphylococcus aureus clumping factor A is a force-sensitive molecular switch that activates bacterial adhesion. *Proc. Natl. Acad. Sci. U. S. A.* **115**, 5564–5569 (2018).
386. Connell, I. *et al.* Type 1 fimbrial expression enhances Escherichia coli virulence for the urinary tract. *Proc. Natl. Acad. Sci.* **93**, 9827–9832 (1996).
387. Sauer, M. M. *et al.* Catch-bond mechanism of the bacterial adhesin FimH. *Nat. Commun.* **7**, 10738 (2016).
388. Choudhury, D. *et al.* X-ray Structure of the FimC-FimH Chaperone-Adhesin Complex from Uropathogenic Escherichia coli. *Science* **285**, 1061–1066 (1999).
389. Greenwood, J. A. & Murphy-Ullrich, J. E. Signaling of de-adhesion in cellular regulation and motility. *Microsc. Res. Tech.* **43**, 420–432 (1998).

390. Laverty, D. *et al.* Cryo-EM structure of the human α1β3γ2 GABAA receptor in a lipid bilayer. *Nature* 10.1038/s41586-018-0833–4 (2019) doi:10.1038/s41586-018-0833-4.
391. Sartori-Rupp, A. *et al.* Correlative cryo-electron microscopy reveals the structure of TNTs in neuronal cells. *Nat. Commun.* **10**, 342 (2019).
392. Hospenthal, M. K. *et al.* The Cryoelectron Microscopy Structure of the Type 1 Chaperone-Usher Pilus Rod. *Struct. England1993* **25**, 1829-1838.e4 (2017).
393. Li, H. & Thanassi, D. G. Use of a combined cryo-EM and X-ray crystallography approach to reveal molecular details of bacterial pilus assembly by the chaperone/usher pathway. *Curr. Opin. Microbiol.* **12**, 326–332 (2009).
394. Peng, G. *et al.* Crystal Structure of Bovine Coronavirus Spike Protein Lectin Domain. *J. Biol. Chem.* **287**, 41931–41938 (2012).
395. Shang, J. *et al.* Cryo-EM structure of infectious bronchitis coronavirus spike protein reveals structural and functional evolution of coronavirus spike proteins. *PLoS Pathog.* **14**, e1007009 (2018).
396. Walls, A. C. *et al.* Glycan shield and epitope masking of a coronavirus spike protein observed by cryo-electron microscopy. *Nat. Struct. Mol. Biol.* **23**, 899–905 (2016).
397. Turk, M. & Baumeister, W. The promise and the challenges of cryo-electron tomography. *FEBS Lett.* **594**, 3243–3261 (2020).
398. Lučić, V., Rigort, A. & Baumeister, W. Cryo-electron tomography: The challenge of doing structural biology in situ. *J. Cell Biol.* **202**, 407–419 (2013).
399. Sprankel, L., Scheffer, M. P., Manger, S., Ermel, U. H. & Frangakis, A. S. Cryo-electron tomography reveals the binding and release states of the major adhesion complex from Mycoplasma genitalium. *PLOS Pathog.* **19**, e1011761 (2023).
400. Cao, B. *et al.* High Prevalence of Macrolide Resistance in Mycoplasma pneumoniae Isolates from Adult and Adolescent Patients with Respiratory Tract Infection in China. *Clin. Infect. Dis.* **51**, 189–194 (2010).
401. Parrott, G. L., Kinjo, T. & Fujita, J. A Compendium for Mycoplasma pneumoniae. *Front. Microbiol.* **7**, 513 (2016).
402. Bradshaw, C. S. *et al.* Azithromycin failure in Mycoplasma genitalium urethritis. *Emerg. Infect. Dis.* **12**, 1149–1152 (2006).
403. Sharon, N. Carbohydrates as future anti-adhesion drugs for infectious diseases. *Biochim. Biophys. Acta BBA - Gen. Subj.* **1760**, 527–537 (2006).
404. Jones, D. T. Protein secondary structure prediction based on position-specific scoring matrices. *J. Mol. Biol.* **292**, 195–202 (1999).
405. Loukachevitch, L. V. *et al.* Structures of the Streptococcus sanguinis SrpA Binding Region with Human Sialoglycans Suggest Features of the Physiological Ligand. *Biochemistry* **55**, 5927–5937 (2016).
406. Pyburn, T. M. *et al.* A structural model for binding of the serine-rich repeat adhesin GspB to host carbohydrate receptors. *PLoS Pathog.* **7**, e1002112 (2011).
407. Krissinel, E. & Henrick, K. Inference of Macromolecular Assemblies from Crystalline State. *J. Mol. Biol.* **372**, 774–797 (2007).
408. Pettersen, E. F. *et al.* UCSF Chimera—A visualization system for exploratory research and analysis. *J. Comput. Chem.* **25**, 1605–1612 (2004).
409. García-Morales, L., González-González, L., Costa, M., Querol, E. & Piñol, J. Quantitative assessment of Mycoplasma hemadsorption activity by flow cytometry. *PloS One* **9**, e87500 (2014).
410. Burgos, R. *et al.* Mycoplasma genitalium P140 and P110 Cytadhesins Are Reciprocally Stabilized and Required for Cell Adhesion and Terminal-Organelle Development. *J. Bacteriol.* **188**, 8627–8637 (2006).
411. Russ, W. P. & Engelman, D. M. The GxxxG motif: A framework for transmembrane helix-helix association11Edited by G. von Heijne. *J. Mol. Biol.* **296**, 911–919 (2000).
412. Seto, S., Kenri, T., Tomiyama, T. & Miyata, M. Involvement of P1 Adhesin in Gliding Motility of Mycoplasma pneumoniae as Revealed by the Inhibitory Effects of Antibody under Optimized Gliding Conditions. *J. Bacteriol.* **187**, 1875–1877 (2005).
413. Vizarraga, D. *et al.* Immunodominant proteins P1 and P40/P90 from human pathogen Mycoplasma pneumoniae. *Nat. Commun.* **11**, 1–3 (2020).

414. Himmelreich, R., Plagens, H., Hilbert, H., Reiner, B. & Herrmann, R. Comparative analysis of the genomes of the bacteria Mycoplasma pneumoniae and Mycoplasma genitalium. *Nucleic Acids Res.* **25**, 701–712 (1997).
415. Absalon, C. *et al.* CpgA, EF-Tu and the stressosome protein YezB are substrates of the Ser/Thr kinase/phosphatase couple, PrkC/PrpC, in Bacillus subtilis. *Microbiology* **155**, 932–943 (2009).
416. Pereira, S. F. F., Goss, L. & Dworkin, J. Eukaryote-Like Serine/Threonine Kinases and Phosphatases in Bacteria. *Microbiol. Mol. Biol. Rev. MMBR* **75**, 192–212 (2011).
417. Shah, I. M., Laaberki, M.-H., Popham, D. L. & Dworkin, J. A Eukaryotic-like Ser/Thr Kinase Signals Bacteria to Exit Dormancy in Response to Peptidoglycan Fragments. *Cell* **135**, 486–496 (2008).
418. Page, C. A. & Krause, D. C. Protein kinase/phosphatase function correlates with gliding motility in Mycoplasma pneumoniae. *J. Bacteriol.* **195**, 1750–1757 (2013).
419. Karr, J. R. *et al.* A whole-cell computational model predicts phenotype from genotype. *Cell* **150**, 389–401 (2012).
420. Martínez-Torró, C. Transcriptional Regulation of Cell Division and Metal Uptake in Mycoplasma genitalium. (Universitat Autònoma de Barcelona, Cerdanyola del Vallès, 2020).
421. Hatchel, J. M. & Balish, M. F. Attachment organelle ultrastructure correlates with phylogeny, not gliding motility properties, in Mycoplasma pneumoniae relatives. *Microbiol. Read. Engl.* **154**, 286–95 (2008).
422. Jordan, J. L. *et al.* Protein P200 Is Dispensable for Mycoplasma pneumoniae Hemadsorption but Not Gliding Motility or Colonization of Differentiated Bronchial Epithelium . **75**, 518–522 (2007).
423. Seo, J.-Y. Cross-Protective Immunity of Mice Induced by Oral Immunization with Pneumococcal Surface Adhesin A Encapsulated in Microspheres. *Infect. Immun.* **70**, 1143–1149 (2002).
424. Pizarro-Cerdá, J. & Cossart, P. Bacterial adhesion and entry into host cells. *Cell* **124**, 715–727 (2006).
425. Loveless, R. W. & Feizi, T. Sialo-oligosaccharide receptors for Mycoplasma pneumoniae and related oligosaccharides of poly-N-acetyllactosamine series are polarized at the cilia and apical-microvillar domains of the ciliated cells in human bronchial epithelium. *Infect. Immun.* **57**, 1285–1289 (1989).
426. Williams, C. R. *et al.* Distinct Mycoplasma pneumoniae Interactions with Sulfated and Sialylated Receptors. *Infect. Immun.* **88**, e00392-20 (2020).
427. Talkington, D. F., Waites, K. B., Schwartz, S. B. & Besser, R. E. Emerging from Obscurity: Understanding Pulmonary and Extrapulmonary Syndromes, Pathogenesis, and Epidemiology of Human Mycoplasma pneumoniae Infections. in *Emerging Infections 5* 57–84 (John Wiley & Sons, Ltd, 2001). doi:10.1128/9781555816988.ch4.
428. Kashyap, S. & Sarkar, M. Mycoplasma pneumonia: Clinical features and management. *Lung India Off. Organ Indian Chest Soc.* **27**, 75–85 (2010).
429. Ona, S., Molina, R. L. & Diouf, K. Mycoplasma genitalium: An Overlooked Sexually Transmitted Pathogen in Women? *Infect. Dis. Obstet. Gynecol.* **2016**, (2016).
430. Smullin, C. P. *et al.* Prevalence and incidence of Mycoplasma genitalium in a cohort of HIV-infected and HIV-uninfected pregnant women in Cape Town, South Africa. *Sex. Transm. Infect.* **96**, 501–508 (2020).
431. Hu, P. C. *et al.* Mycoplasma pneumoniae Infection: Role of a Surface Protein in the Attachment Organelle. *Science* **216**, 313–315 (1982).
432. Aparicio, D. *et al.* Structure and mechanism of the Nap adhesion complex from the human pathogen Mycoplasma genitalium. *Nat. Commun.* **11**, 2877 (2020).
433. Vizarraga, D., Torres-Puig, S., Aparicio, D. & Pich, O. Q. The Sialoglycan Binding Adhesins of Mycoplasma genitalium and Mycoplasma pneumoniae. *Trends Microbiol.* **29**, 477–481 (2021).
434. Taylor, G. Sialidases: structures, biological significance and therapeutic potential. *Curr. Opin. Struct. Biol.* **6**, 830–837 (1996).
435. Gaskell, A., Crennell, S. & Taylor, G. The three domains of a bacterial sialidase: a β-propeller, an immunoglobulin module and a galactose-binding jelly-roll. *Structure* **3**, 1197–1205 (1995).
436. Varki, N. M. & Varki, A. Diversity in cell surface sialic acid presentations: implications for biology and disease. *Lab. Investig. J. Tech. Methods Pathol.* **87**, 851–857 (2007).
437. Roberts, D. D., Olson, L. D., Barile, M. F., Ginsburg, V. & Krivan, H. C. Sialic Acid-Dependent Adhesion of Mycoplasma pneumoniae to Purified Glycoproteins. *J. Biol. Chem.* **264**, 9289–9293 (1989).
438. Carluccio, C. D. *et al.* Molecular recognition of sialoglycans by streptococcal Siglec-like adhesins: toward the shape of specific inhibitors. *RSC Chem. Biol.* **2**, 1618–1630 (2021).

439. Chernova, O. A., Medvedeva, E. S., Mouzykantov, A. A., Baranova, N. B. & Chernov, V. M. Mycoplasmas and Their Antibiotic Resistance: The Problems and Prospects in Controlling Infections. *Acta Naturae* **8**, 24–34 (2016).
440. Di Carluccio, C. *et al.* Investigation of protein-ligand complexes by ligand-based NMR methods. *Carbohydr. Res.* **503**, 108313 (2021).
441. Forgione, R. E. *et al.* Unveiling Molecular Recognition of Sialoglycans by Human Siglec-10. *iScience* **23**, 101231 (2020).
442. Poppe, L., Stuike-Prill, R., Meyer, B. & van Halbeek, H. The solution conformation of sialyl-alpha (2---6)-lactose studied by modern NMR techniques and Monte Carlo simulations. *J. Biomol. NMR* **2**, 109–136 (1992).
443. Page, M. J. & Di Cera, E. Role of Na+ and K+ in Enzyme Function. *Physiol. Rev.* **86**, 1049–1092 (2006).
444. Black, C. B., Huang, H.-W. & Cowan, J. A. Biological coordination chemistry of magnesium, sodium, and potassium ions. Protein and nucleotide binding sites. *Coord. Chem. Rev.* **135–136**, 165–202 (1994).
445. Manchee, R. J. & Taylor-Robinson, D. Utilization of Neuraminic Acid Receptors by Mycoplasmas. *J. Bacteriol.* **98**, 914–919 (1969).
446. Sobeslavsky, O., Prescott, B. & Chanock, R. M. Adsorption of Mycoplasma pneumoniae to Neuraminic Acid Receptors of Various Cells and Possible Role in Virulence. *J. Bacteriol.* **96**, 695–705 (1968).
447. Di Carluccio, C. *et al.* Molecular Insights into O-Linked Sialoglycans Recognition by the Siglec-Like SLBR-N (SLBRUB10712) of Streptococcus gordonii. *ACS Cent. Sci.* **10**, 447–459 (2024).
448. Bensing, B. A. *et al.* Origins of glycan selectivity in streptococcal Siglec-like adhesins suggest mechanisms of receptor adaptation. *Nat. Commun.* **13**, 2753 (2022).
449. Waites, K. B., Xiao, L., Liu, Y., Balish, M. F. & Atkinson, T. P. Mycoplasma pneumoniae from the Respiratory Tract and Beyond. *Clin. Microbiol. Rev.* **30**, 747 (2017).
450. Parrott, G. L., Kinjo, T. & Fujita, J. A Compendium for Mycoplasma pneumoniae. *Front. Microbiol.* **7**, (2016).
451. Rangroo, R. *et al.* The Severity of the Co-infection of Mycoplasma pneumoniae in COVID-19 Patients. *Cureus* **14**, (2022).
452. Sauteur, P. M. M. *et al.* Pneumonia outbreaks due to re-emergence of Mycoplasma pneumoniae. *Lancet Microbe* **0**, (2024).
453. Mazzolini, R. *et al.* Engineered live bacteria suppress Pseudomonas aeruginosa infection in mouse lung and dissolve endotracheal-tube biofilms. *Nat. Biotechnol.* (2023) doi:10.1038/S41587-022-01584-9.
454. Henderson, G. P. & Jensen, G. J. Three-dimensional structure of Mycoplasma pneumoniae's attachment organelle and a model for its role in gliding motility. *Mol. Microbiol.* **60**, (2006).
455. Miyata, M. & Hamaguchi, T. Integrated Information and Prospects for Gliding Mechanism of the Pathogenic Bacterium Mycoplasma pneumoniae. *Front. Microbiol.* **7**, (2016).
456. Seybert, A., Herrmann, R. & Frangakis, A. S. Structural analysis of Mycoplasma pneumoniae by cryo-electron tomography. *J. Struct. Biol.* **156**, (2006).
457. Nakane, D., Kenri, T., Matsuo, L. & Miyata, M. Systematic Structural Analyses of Attachment Organelle in Mycoplasma pneumoniae. *PLoS Pathog.* **11**, (2015).
458. Kawamoto, A. *et al.* Periodicity in Attachment Organelle Revealed by Electron Cryotomography Suggests Conformational Changes in Gliding Mechanism of Mycoplasma pneumoniae. *mBio* **7**, (2016).
459. Mizutani, M., Sasajima, Y. & Miyata, M. Force and Stepwise Movements of Gliding Motility in Human Pathogenic Bacterium Mycoplasma pneumoniae. *Front. Microbiol.* **12**, (2021).
460. Krause, D. C., Leith, D. K., Wilson, R. M. & Baseman, J. B. Identification of Mycoplasma pneumoniae proteins associated with hemadsorption and virulence. *Infect. Immun.* **35**, (1982).
461. Scheffer, M. P. *et al.* Structural characterization of the NAP; the major adhesion complex of the human pathogen Mycoplasma genitalium. *Mol. Microbiol.* **105**, (2017).
462. Vizarraga, D. *et al.* Immunodominant proteins P1 and P40/P90 from human pathogen Mycoplasma pneumoniae. *Nat. Commun.* **11**, (2020).
463. Vizarraga, D., Torres-Puig, S., Aparicio, D. & Pich, O. Q. The Sialoglycan Binding Adhesins of Mycoplasma genitalium and Mycoplasma pneumoniae. *Trends Microbiol.* **29**, 477–481 (2021).
464. Williams, C. R. *et al.* Distinct mycoplasma pneumoniae interactions with sulfated and sialylated receptors. *Infect. Immun.* **88**, (2020).

465. Aparicio, D. *et al.* Structure and mechanism of the Nap adhesion complex from the human pathogen Mycoplasma genitalium. *Nat. Commun.* **11**, (2020).
466. Aparicio, D. *et al.* Mycoplasma genitalium adhesin P110 binds sialic-acid human receptors. *Nat. Commun.* **9**, (2018).
467. Sprankel, L., Scheffer, M. P., Manger, S., Ermel, U. H. & Frangakis, A. S. Cryo-electron tomography reveals the binding and release states of the major adhesion complex from Mycoplasma genitalium. *PLoS Pathog.* **19**, e1011761 (2023).
468. Sprankel, L. *et al.* Essential protein P116 extracts cholesterol and other indispensable lipids for Mycoplasmas. *Nat. Struct. Mol. Biol.* **30**, (2023).
469. Seto, S., Kenri, T., Tomiyama, T. & Miyata, M. Involvement of P1 adhesin in gliding motility of Mycoplasma pneumoniae as revealed by the inhibitory effects of antibody under optimized gliding conditions. *J. Bacteriol.* **187**, (2005).
470. van Zundert, G. C. P. *et al.* The HADDOCK2.2 Web Server: User-Friendly Integrative Modeling of Biomolecular Complexes. *J. Mol. Biol.* **428**, 720–725 (2016).
471. Jumper, J. *et al.* Highly accurate protein structure prediction with AlphaFold. *Nature* **596**, 583–589 (2021).
472. Evans, R. *et al.* Protein complex prediction with AlphaFold-Multimer. 2021.10.04.463034 Preprint at https://doi.org/10.1101/2021.10.04.463034 (2022).
473. Pich, O. Q., Burgos, R., Querol, E. & Piñol, J. P110 and P140 cytadherence-related proteins are negative effectors of terminal organelle duplication in Mycoplasma genitalium. *PloS One* **4**, e7452 (2009).
474. Burgos, R. *et al.* Mycoplasma genitalium P140 and P110 cytadhesins are reciprocally stabilized and required for cell adhesion and terminal-organelle development. *J. Bacteriol.* **188**, 8627–8637 (2006).
475. Miyata, M. Centipede and inchworm models to explain Mycoplasma gliding. *Trends Microbiol.* **16**, 6–12 (2008).
476. Seybert, A. *et al.* Cryo-electron tomography analyses of terminal organelle mutants suggest the motility mechanism of Mycoplasma genitalium. *Mol. Microbiol.* **108**, 319–329 (2018).
477. Kasai, T. *et al.* Role of binding in Mycoplasma mobile and Mycoplasma pneumoniae gliding analyzed through inhibition by synthesized sialylated compounds. *J. Bacteriol.* **195**, 429–435 (2013).
478. Mizutani, M. & Miyata, M. Behaviors and Energy Source of Mycoplasma gallisepticum Gliding. *J. Bacteriol.* **201**, (2019).
479. Tsiodras, S., Kelesidis, I., Kelesidis, T., Stamboulis, E. & Giamarellou, H. Central nervous system manifestations of Mycoplasma pneumoniae infections. *J. Infect.* **51**, 343–354 (2005).
480. Jiang, Z., Li, S., Zhu, C., Zhou, R. & Leung, P. H. M. Mycoplasma pneumoniae Infections: Pathogenesis and Vaccine Development. *Pathogens* **10**, 119 (2021).
481. Razin, S., Yogev, D. & Naot, Y. Molecular Biology and Pathogenicity of Mycoplasmas. *Microbiol. Mol. Biol. Rev.* **62**, 1094–1156 (1998).
482. Gaspari, E. *et al.* Model-driven design allows growth of Mycoplasma pneumoniae on serum-free media. *NPJ Syst. Biol. Appl.* **6**, 33 (2020).
483. Razin, S., Argaman, M. & Avigan, J. CHEMICAL COMPOSITION OF MYCOPLASMA CELLS AND MEMBRANES. *J. Gen. Microbiol.* **33**, 477–487 (1963).
484. Leon, O. & Panos, C. Long-chain fatty acid perturbations in Mycoplasma pneumoniae. *J. Bacteriol.* **146**, 1124–1134 (1981).
485. Bittman, R. Mycoplasma membrane lipids. Chemical composition and transbilayer distribution. *Subcell. Biochem.* **20**, 29–52 (1993).
486. Mohn, W. W. *et al.* The Actinobacterial mce4 Locus Encodes a Steroid Transporter,. *J. Biol. Chem.* **283**, 35368–35374 (2008).
487. Pandey, A. K. & Sassetti, C. M. Mycobacterial persistence requires the utilization of host cholesterol. *Proc. Natl. Acad. Sci. U. S. A.* **105**, 4376–4380 (2008).
488. Damy, S. B. *et al.* Mycoplasma pneumoniae and/or Chlamydophila pneumoniae inoculation causing different aggravations in cholesterol-induced atherosclerosis in apoE KO male mice. *BMC Microbiol.* **9**, 194 (2009).
489. Huang, Z. & London, E. Cholesterol lipids and cholesterol-containing lipid rafts in bacteria. *Chem. Phys. Lipids* **199**, 11–16 (2016).

490. Svenstrup, H. F., Nielsen, P. K., Drasbek, M., Birkelund, S. & Christiansen, G. Adhesion and inhibition assay of Mycoplasma genitalium and M. pneumoniae by immunofluorescence microscopy. *J. Med. Microbiol.* **51**, 361–373 (2002).
491. Krause, D. C., Leith, D. K., Wilson, R. M. & Baseman, J. B. Identification of Mycoplasma pneumoniae proteins associated with hemadsorption and virulence. *Infect. Immun.* **35**, 809–817 (1982).
492. Baseman, J. B., Cole, R. M., Krause, D. C. & Leith, D. K. Molecular basis for cytadsorption of Mycoplasma pneumoniae. *J. Bacteriol.* **151**, 1514–1522 (1982).
493. Washburn, L. R. & Somerson, N. L. Lipoproteins as substitutes for serum in Mycoplasma culture medium. *J. Clin. Microbiol.* **10**, 586–589 (1979).
494. Phillips, M. C. Molecular Mechanisms of Cellular Cholesterol Efflux. *J. Biol. Chem.* **289**, 24020–24029 (2014).
495. Drasbek, M., Nielsen, P. K., Persson, K., Birkelund, S. & Christiansen, G. Immune response to Mycoplasma pneumoniae P1 and P116 in patients with atypical pneumonia analyzed by ELISA. *BMC Microbiol.* **4**, 7 (2004).
496. O'Reilly, F. J. *et al.* In-cell architecture of an actively transcribing-translating expressome. *Science* **369**, 554–557 (2020).
497. Zhang, L. *et al.* Structural basis of transfer between lipoproteins by cholesteryl ester transfer protein. *Nat. Chem. Biol.* **8**, 342–349 (2012).
498. Zhang, M. *et al.* Structural basis of the lipid transfer mechanism of phospholipid transfer protein (PLTP). *Biochim. Biophys. Acta BBA - Mol. Cell Biol. Lipids* **1863**, 1082–1094 (2018).
499. Aparicio, D. *et al.* Mycoplasma genitalium adhesin P110 binds sialic-acid human receptors. *Nat. Commun.* **9**, 4471 (2018).
500. Vizarraga, D., Torres-Puig, S., Aparicio, D. & Pich, O. Q. The Sialoglycan Binding Adhesins of Mycoplasma genitalium and Mycoplasma pneumoniae. *Trends Microbiol.* **29**, 477–481 (2021).
501. Inanime, J. M., Loechel, S. & Ping-chuan, H. Analysis of the nucleotide sequence of the *P1* operon of *Mycoplasma pneumoniae*. *Gene* **73**, 175–183 (1988).
502. Waldo, R. H. & Krause, D. C. Synthesis, Stability, and Function of Cytadhesin P1 and Accessory Protein B/C Complex of Mycoplasma pneumoniae. *J. Bacteriol.* **188**, 569–575 (2006).
503. Inamine, J. M. *et al.* Nucleotide sequence of the P1 attachment-protein gene of *Mycoplasma pneumoniae*. *Gene* **64**, 217–229 (1988).
504. Sperker, B., Hu, P. -c. & Herrmann, R. Identification of gene products of the P1 operon of Mycoplasma pneumoniae. *Mol. Microbiol.* **5**, 299–306 (1991).
505. Layh-Schmitt, G. & Herrmann, R. Localization and biochemical characterization of the ORF6 gene product of the Mycoplasma pneumoniae P1 operon. *Infect. Immun.* **60**, 2906–2913 (1992).
506. Widjaja, M., Berry, I. J., Pont, E. J., Padula, M. P. & Djordjevic, S. P. P40 and P90 from Mpn142 are Targets of Multiple Processing Events on the Surface of Mycoplasma pneumoniae. *Proteomes* **3**, 512–537 (2015).
507. Torres-Puig, S., Broto, A., Querol, E., Piñol, J. & Pich, O. Q. A novel sigma factor reveals a unique regulon controlling cell-specific recombination in Mycoplasma genitalium. *Nucleic Acids Res.* **43**, 4923–4936 (2015).
508. Pich, O. Q., Burgos, R., Ferrer-Navarro, M., Querol, E. & Piñol, J. Role of Mycoplasma genitalium MG218 and MG317 cytoskeletal proteins in terminal organelle organization, gliding motility and cytadherence. *Microbiology* **154**, 3188–3198 (2008).
509. García-Morales, L., González-González, L., Costa, M., Querol, E. & Piñol, J. Quantitative Assessment of Mycoplasma Hemadsorption Activity by Flow Cytometry. *PLoS ONE* **9**, e87500 (2014).
510. Sprankel, L. *et al.* Essential protein P116 extracts cholesterol and other indispensable lipids for Mycoplasmas. *Nat. Struct. Mol. Biol.* **30**, 321–329 (2023).
511. Robert, X. & Gouet, P. Deciphering key features in protein structures with the new ENDscript server. *Nucleic Acids Res.* **42**, W320–W324 (2014).
512. Russell, C. J., Hu, M. & Okda, F. A. Influenza hemagglutinin protein stability, activation, and pandemic risk. *Trends Microbiol.* **26**, 841–853 (2018).
513. Tang, J. *et al.* Dynamic and Geometric Analyses of Nudaurelia capensis ωVirus Maturation Reveal the Energy Landscape of Particle Transitions. *J. Mol. Recognit. JMR* **27**, 230–237 (2014).
514. Johnson, J. E., Domitrovic, T., Matsui, T., Castells-Graells, R. & Lomonossoff, G. Dynamics and stability in the maturation of a eukaryotic virus: a paradigm for chemically programmed large-scale macromolecular reorganization. *Arch. Virol.* **166**, 1547–1563 (2021).

515. Minamino, T. & Macnab, R. M. Domain Structure of Salmonella FlhB, a Flagellar Export Component Responsible for Substrate Specificity Switching. *J. Bacteriol.* **182**, 4906–4914 (2000).
516. Sadilkova, L. *et al.* Single-step affinity purification of recombinant proteins using a self-excising module from Neisseria meningitidis FrpC. *Protein Sci. Publ. Protein Soc.* **17**, 1834–1843 (2008).
517. Björnfot, A.-C., Lavander, M., Forsberg, Å. & Wolf-Watz, H. Autoproteolysis of YscU of Yersinia pseudotuberculosis Is Important for Regulation of Expression and Secretion of Yop Proteins. *J. Bacteriol.* **191**, 4259–4267 (2009).
518. Miyata, M. & Hamaguchi, T. Integrated information and prospects for gliding mechanism of the pathogenic bacterium Mycoplasma pneumoniae. *Front. Microbiol.* **7**, (2016).
519. García-Morales, L., González-González, L., Querol, E. & Piñol, J. A minimized motile machinery for Mycoplasma genitalium. *Mol. Microbiol.* **100**, 125–38 (2016).
520. Seybert, A. *et al.* Cryo-electron tomography analyses of terminal organelle mutants suggest the motility mechanism of Mycoplasma genitalium. *Mol. Microbiol.* **108**, 319–329 (2018).
521. Pich, O. Q., Burgos, R., Ferrer-Navarro, M., Querol, E. & Pinol, J. Mycoplasma genitalium mg200 and mg386 genes are involved in gliding motility but not in cytadherence. *Mol. Microbiol.* **60**, 1509–1519 (2006).
522. Carman, C. V. & Springer, T. A. Integrin avidity regulation: are changes in affinity and conformation underemphasized? *Curr. Opin. Cell Biol.* **15**, 547–556 (2003).
523. Arkin, I. T. & Brunger, A. T. Statistical analysis of predicted transmembrane alpha-helices. *Biochim. Biophys. Acta* **1429**, 113–128 (1998).
524. Aronson, M. *et al.* Prevention of colonization of the urinary tract of mice with Escherichia coli by blocking of bacterial adherence with methyl alpha-D-mannopyranoside. *J. Infect. Dis.* **139**, 329–332 (1979).
525. Beuth, J., Stoffel, B. & Pulverer, G. Inhibition of bacterial adhesion and infections by lectin blocking. *Adv. Exp. Med. Biol.* **408**, 51–56 (1996).
526. Mysore, J. V. *et al.* Treatment of Helicobacter pylori infection in rhesus monkeys using a novel antiadhesion compound. *Gastroenterology* **117**, 1316–1325 (1999).
527. Wood, G. E. *et al.* Persistence, Immune Response, and Antigenic Variation of Mycoplasma genitalium in an Experimentally Infected Pig-Tailed Macaque (Macaca nemestrina). *Infect. Immun.* **81**, 2938 (2013).
528. Chourasia, B. K., Chaudhry, R. & Malhotra, P. Delineation of immunodominant and cytadherence segment(s) of Mycoplasma pneumoniae P1 gene. *BMC Microbiol.* **14**, 108 (2014).
529. Jacobs, E., Pilatschek, A., Gerstenecker, B., Oberle, K. & Bredt, W. Immunodominant epitopes of the adhesin of Mycoplasma pneumoniae. *J. Clin. Microbiol.* **28**, 1194–1197 (1990).
530. Seo, J.-Y. *et al.* Cross-Protective Immunity of Mice Induced by Oral Immunization with Pneumococcal Surface Adhesin A Encapsulated in Microspheres. *Infect. Immun.* **70**, 1143 (2002).
531. Sambrook, J., Fritsch, E. F. & Maniatis, T. *Molecular Cloning: A Laboratory Manual*. (Cold Spring Harbor Laboratory, 1989).
532. Tully, J. G., Rose, D. L., Whitcomb, R. F. & Wenzel, R. P. Enhanced isolation of Mycoplasma pneumoniae from throat washings with a newly-modified culture medium. *J. Infect. Dis.* **139**, 478–482 (1979).
533. Köhler, G. & Milstein, C. Continuous cultures of fused cells secreting antibody of predefined specificity. 1975. *J. Immunol. Baltim. Md 1950* **174**, 2453–2455 (2005).
534. Torres-Puig, S. *et al.* Activation of σ20-dependent recombination and horizontal gene transfer in Mycoplasma genitalium. *DNA Res. Int. J. Rapid Publ. Rep. Genes Genomes* **25**, 383–393 (2018).
535. Shapiro, A. L., Viñuela, E. & Maizel, J. V. Molecular weight estimation of polypeptide chains by electrophoresis in SDS-polyacrylamide gels. *Biochem. Biophys. Res. Commun.* **28**, 815–820 (1967).
536. Towbin, H., Staehelin, T. & Gordon, J. Electrophoretic transfer of proteins from polyacrylamide gels to nitrocellulose sheets: procedure and some applications. *Proc. Natl. Acad. Sci. U. S. A.* **76**, 4350–4354 (1979).
537. Mahmood, T. & Yang, P.-C. Western blot: technique, theory, and trouble shooting. *North Am. J. Med. Sci.* **4**, 429–434 (2012).
538. Berrow, N. S. *et al.* A versatile ligation-independent cloning method suitable for high-throughput expression screening applications. *Nucleic Acids Res.* **35**, e45 (2007).
539. Guasch, A. *et al.* Structure of P46, an immunodominant surface protein from Mycoplasma hyopneumoniae: interaction with a monoclonal antibody. *Acta Crystallogr. Sect. Struct. Biol.* **76**, 418–427 (2020).

540. Kong, A. T., Leprevost, F. V., Avtonomov, D. M., Mellacheruvu, D. & Nesvizhskii, A. I. MSFragger: ultrafast and comprehensive peptide identification in mass spectrometry-based proteomics. *Nat. Methods* **14**, 513–520 (2017).
541. Vasilopoulou, C. G. *et al.* Trapped ion mobility spectrometry and PASEF enable in-depth lipidomics from minimal sample amounts. *Nat. Commun.* **11**, 331 (2020).
542. Tsugawa, H. *et al.* A lipidome atlas in MS-DIAL 4. *Nat. Biotechnol.* **38**, 1159–1163 (2020).
543. Mohamed, A., Molendijk, J. & Hill, M. M. lipidr: A Software Tool for Data Mining and Analysis of Lipidomics Datasets. *J. Proteome Res.* **19**, 2890–2897 (2020).
544. Cedó, L. *et al.* LDL Receptor Regulates the Reverse Transport of Macrophage-Derived Unesterified Cholesterol via Concerted Action of the HDL-LDL Axis. *Circ. Res.* **127**, 778–792 (2020).
545. Mastronarde, D. N. Automated electron microscope tomography using robust prediction of specimen movements. *J. Struct. Biol.* **152**, 36–51 (2005).
546. Kunz, M. & Frangakis, A. S. Super-sampling SART with ordered subsets. *J. Struct. Biol.* **188**, 107–115 (2014).
547. Zivanov, J. *et al.* New tools for automated high-resolution cryo-EM structure determination in RELION-3. *eLife* https://elifesciences.org/articles/42166 (2018) doi:10.7554/eLife.42166.
548. Goddard, T. D. *et al.* UCSF ChimeraX: Meeting modern challenges in visualization and analysis. *Protein Sci.* **27**, 14–25 (2018).
549. Kunz, M. & Frangakis, A. S. Three-dimensional CTF correction improves the resolution of electron tomograms. *J. Struct. Biol.* **197**, 114–122 (2017).
550. Zheng, S. Q. *et al.* MotionCor2: anisotropic correction of beam-induced motion for improved cryo-electron microscopy. *Nat. Methods* **14**, 331–332 (2017).
551. Zhang, K. Gctf: Real-time CTF determination and correction. *J. Struct. Biol.* **193**, 1–12 (2016).
552. Scheres, S. H. W. A Bayesian View on Cryo-EM Structure Determination. *J. Mol. Biol.* **415**, 406–418 (2012).
553. Punjani, A., Rubinstein, J. L., Fleet, D. J. & Brubaker, M. A. cryoSPARC: algorithms for rapid unsupervised cryo-EM structure determination. *Nat. Methods* **14**, 290–296 (2017).
554. Emsley, P. & Cowtan, K. Coot: model-building tools for molecular graphics. *Acta Crystallogr. D Biol. Crystallogr.* **60**, 2126–2132 (2004).
555. Afonine, P. V. *et al.* Real-space refinement in PHENIX for cryo-EM and crystallography. *Acta Crystallogr. Sect. Struct. Biol.* **74**, 531–544 (2018).
556. Headd, J. J. *et al.* Use of knowledge-based restraints in phenix.refine to improve macromolecular refinement at low resolution. *Acta Crystallogr. D Biol. Crystallogr.* **68**, 381–390 (2012).
557. Afonine, P. V. *et al.* Towards automated crystallographic structure refinement with phenix.refine. *Acta Crystallogr. D Biol. Crystallogr.* **68**, 352–367 (2012).
558. Winter, G. xia2: an expert system for macromolecular crystallography data reduction. *J. Appl. Crystallogr.* **43**, 186–190 (2010).
559. Kabsch, W. XDS. *Acta Crystallogr. D Biol. Crystallogr.* **66**, 125–132 (2010).
560. Evans, P. Scaling and assessment of data quality. *Acta Crystallogr. D Biol. Crystallogr.* **62**, 72–82 (2006).
561. Project, C. C. & Number 4. The CCP4 suite: programs for protein crystallography. *Acta Crystallogr. D Biol. Crystallogr.* **50**, 760–763 (1994).
562. McCoy, A. J. Solving structures of protein complexes by molecular replacement with Phaser. *Acta Crystallogr. D Biol. Crystallogr.* **63**, 32–41 (2007).
563. Cowtan, K. D. & Main, P. Phase combination and cross validation in iterated density-modification calculations. *Acta Crystallogr. D Biol. Crystallogr.* **52**, 43–48 (1996).
564. Murshudov, G. N. *et al.* REFMAC5 for the refinement of macromolecular crystal structures. *Acta Crystallogr. D Biol. Crystallogr.* **67**, 355–367 (2011).
565. Schwarz, J. B. *et al.* A Broadly Applicable Method for the Efficient Synthesis of α-O-Linked Glycopeptides and Clustered Sialic Acid Residues. *J. Am. Chem. Soc.* **121**, 2662–2673 (1999).
566. Kajihara, Y. *et al.* Prompt Chemoenzymatic Synthesis of Diverse Complex-Type Oligosaccharides and Its Application to the Solid-Phase Synthesis of a Glycopeptide with Asn-Linked Sialyl-undeca- and Asialo-nonasaccharides. *Chem. – Eur. J.* **10**, 971–985 (2004).
567. Ribeiro, M. M. B., Franquelim, H. G., Castanho, M. A. R. B. & Veiga, A. S. Molecular interaction studies of peptides using steady-state fluorescence intensity. Static (de)quenching revisited. *J. Pept. Sci. Off. Publ. Eur. Pept. Soc.* **14**, 401–406 (2008).

568. Oliva, R. *et al.* Encapsulating properties of sulfobutylether-β-cyclodextrin toward a thrombin-derived antimicrobial peptide. *J. Therm. Anal. Calorim.* **138**, 3249–3256 (2019).
569. Speciale, I. *et al.* Liquid-state NMR spectroscopy for complex carbohydrate structural analysis: A hitchhiker's guide. *Carbohydr. Polym.* **277**, 118885 (2022).
570. Angulo, J. *et al.* Blood Group B Galactosyltransferase: Insights into Substrate Binding from NMR Experiments. *J. Am. Chem. Soc.* **128**, 13529–13538 (2006).
571. Mayer, M. & Meyer, B. Group Epitope Mapping by Saturation Transfer Difference NMR To Identify Segments of a Ligand in Direct Contact with a Protein Receptor. *J. Am. Chem. Soc.* **123**, 6108–6117 (2001).
572. Case, D. A. *et al.* AmberTools. *J. Chem. Inf. Model.* **63**, 6183–6191 (2023).
573. Humphrey, W., Dalke, A. & Schulten, K. VMD: Visual molecular dynamics. *J. Mol. Graph.* **14**, 33–38 (1996).
574. Musatovova, O., Dhandayuthapani, S. & Baseman, J. B. Transcriptional starts for cytadherence-related operons of Mycoplasma genitalium. *FEMS Microbiol. Lett.* **229**, 73–81 (2003).
575. Davis, I. W., Murray, L. W., Richardson, J. S. & Richardson, D. C. MolProbity: structure validation and all-atom contact analysis for nucleic acids and their complexes. *Nucleic Acids Res.* **32**, W615–W619 (2004).